Multimodal and Advanced Interferometric Second Harmonic Generation Microscopy for an Improved Characterization of Biopolymers in Cells and Tissues

Maxime Pinsard

Université du Québec
Institut National de la Recherche Scientifique (INRS)
Centre Energie Matériaux Télécommunications (EMT)

Doctoral Thesis

Multimodal and Advanced Interferometric Second Harmonic Generation Microscopy for an Improved Characterization of Biopolymers in Cells and Tissues

By

Maxime Pinsard

A thesis submitted for the achievement of the degree of
Philosophiae Doctor (PhD)
in Energy and Materials Sciences

March 19th 2020

Jury Members

President of the jury and Internal Examiner	José Azaña INRS-EMT
External Examiner	Feruz Ganikhanov University of Rhode Island
External Examiner	Virginijus Barzda University of Toronto
Director of Research	François Légaré INRS-EMT

Abstract

Multiphoton microscopy is a paramount paradigm for tissue imaging and characterization in biology, and more generally in material sciences. Within it, second harmonic generation (SHG) has become the gold standard for *in-situ* 3D visualization of tissues containing a widespread biopolymer: fibrillar collagen. SHG's intrinsic properties, being the result of a highly coherent exciting wave being inelastically scattered, allows these types of materials to be specifically revealed, among which are also myosin in muscles, and various nonlinear crystals.

However, the optical coherence of SHG also means that the images contain the result of complex interferences, and not the actual structure of the material. Partly because of this problem, many techniques have been proposed to enhance SHG, and to fully benefit of its numerous properties: the direction of generation can be probed, its sensitivity to polarization, or its relative phase.

Interferometric Second-Harmonic Generation microscopy (I-SHG), and its application to biological tissues, have allowed for the relative phase to be measured. This technique has been increasingly better controlled, but lacked a real incorporation with other multiphoton techniques. It was also quite long and complicated to use, and measured only the phase, without taking advantage of other parameters.

This dissertation first portrays the general context around SHG, before detailing the process itself. Directional and polarization-resolved SHG are then presented and applied to the analysis of a complex collagen-rich tissue: the equine meniscus in a joint. A property of Gaussian beams being focused, the Gouy phase-shift, which explains some SHG imaging artifacts in stacked structures, is then reported to be measurable with I-SHG's phase retrieval. Afterwards, I-SHG was used to decouple these artefactual interferences from the real structure of samples containing alternating polarities, while also enhancing the structure's visibility.

I-SHG was subsequently made compatible with laser-scanning schemes, which greatly enhanced its speed. This was applied to *in-situ* imaging of the microtubules' polarity during an embryo mitosis. Because this "fast I-SHG" still presented some experimental latencies, a single-scan paradigm (1S-ISHG) was implemented, using an electro-optic modulator that changes the relative phase of the interferograms within the conventional pixels of the image. The complete optical, hardware and software controls required for these improvements are detailed as well.

This one order of magnitude speed enhancement remains to be utilized to characterize dynamic processes requiring an imaging speed below the Hz scale, or for large-scale studies. Menisci could also be further investigated in multimodal microscopy coupled to I-SHG.

Keywords: scanning microscopy; second harmonic (SHG); interferometry; multiphoton microscopy; biological tissues; collagen; phase contrast; polarity; muscle; meniscus

Résumé

Microscopie de Génération de Seconde Harmonique Multimodale et Interférométrique pour une Caractérisation Améliorée des Biopolymères dans les Cellules et Tissus

La microscopie multiphoton est primordiale pour l'imagerie des tissus biologiques et de certains matériaux. La Génération de Seconde Harmonique (SHG) est en particulier une référence pour l'imagerie 3D des tissus contenant un biopolymère très répandu: le collagène. Les propriétés intrinsèques de la SHG, qui résulte de la diffusion inélastique d'une onde excitatrice très cohérente, permettent de révéler spécifiquement ce type de structures, parmi lesquelles figurent aussi la myosine des muscles, ou certains cristaux non-linéaires.

Cependant, la cohérence optique de la SHG signifie également que les images contiennent la résultante d'interférences complexes, et non la structure réelle du matériau. Pour cela, de nombreuses techniques ont été proposées pour améliorer la SHG, et tirer pleinement parti de ses nombreuses propriétés: la direction de la génération, sa sensibilité à la polarisation ou sa phase relative peuvent être sondées. La microscopie de Génération de Seconde Harmonique Interférométrique (I-SHG), et son application aux tissus biologiques, a permis de mesurer la phase. Cette technique a été de mieux en mieux maîtrisée, mais sans être réellement intégrée à d'autres techniques multiphoton. Elle était aussi assez longue et compliquée à utiliser, et ne mesurait que la phase, sans tirer parti d'autres paramètres.

Cette thèse présente d'abord le contexte général autour de la SHG, avant de détailler cette dernière. La SHG directionnelle et résolus en polarisation sont ensuite utilisées pour l'analyse du collagène d'un tissu complexe: le ménisque des articulations équines. Une propriété des faisceaux Gaussiens subissant une focalisation, le déphasage de Gouy, est ensuite démontrée mesurable par I-SHG. Cette dernière explique notamment certains artefacts d'imagerie par SHG dans des structures en empilement. Ensuite, ces interférences artéfactuelles sont découplées par I-SHG de la structure réelle dans des échantillons contenant des alternances de polarité, ce qui produit aussi une meilleure visibilité de la structure.

La I-SHG est ensuite rendue compatible avec un balayage laser, ce qui améliore considérablement sa vitesse. Ceci est appliqué à l'imagerie *in situ* de la polarité des microtubules au cours d'une mitose embryonnaire. Puisque cette "I-SHG rapide" présentait encore quelques latences expérimentales, elle a été ensuite réduite à un seul balayage de l'échantillon (1S-ISHG), via un modulateur électro-optique qui déphase les interférogrammes au sein même des pixels de l'image. Le contrôle optique, matériel et logiciel nécessaire à ces améliorations sont également détaillés.

Cette amélioration de la vitesse (un ordre de grandeur) pourra servir à caractériser des processus dynamiques, ou pour des études à grande échelle. Le ménisque pourra également bénéficier d'un couplage microscopie multimodale - ISHG.

Mots-clés: microscopie à balayage ; seconde harmonique (SHG) ; interférométrie ; microscopie multiphoton ; tissus biologiques ; collagène ; contraste de phase ; polarité ; muscle ; ménisque

Gratitude

Pour commencer, je suis reconnaissant envers François Légaré de m'avoir pris en thèse de microscopie non-linéaire, et à Stéphane Bancelin qui m'a bien formé au labo et aux rouages de l'INRS, et m'a surtout guidé dans mes premiers projets et fait participer aux siens. I'd like to acknowledge Prof Ganikhanov, Azaña and Barzda for accepting to be in my thesis jury. Je souhaite aussi remercier chaleureusement Marie-Claire Schanne-Klein qui m'a accueuilli plusieurs mois au L.O.B à Polytechnique Paris et m'a aidé à mettre en forme plusieurs articles: sans toi, Marie-Claire, cette thèse n'aurait probablement pas vu le jour !

There are many people that helped during this PhD, the following are just few of them: Carol from the INRS workshop, and Philippe from ALLS for their technical help. Special kudos have to be delivered to Antoine L., who helped me a lot with my issues in the lab: sorry for having bothered you that much, I had a lot of questions and demands ! Likewise, I'm also grateful to the tech support of the numerous optics and electronics companies I have contacted, and to the Stackoverflow, GitHub and NIforum communities who provided an incredible amount of direct and indirect information helpful in this PhD. I must also cite Charles-André C., Mathieu L. and Maxime R. who successfully transferred to me the knowledge of microscopy and I-SHG, and CY Coté's Axis Photonique for their collaboration on the phase-scanner. Je souhaite tout particulièrement remercier Elissa, qui a accepté de reprendre le flambeau de la présidence du CEISME, et Nazar, Vincent, Nico S. qui m'ont expliqué son fonctionnement. I'll also keep a good memory of the executive bureau: Lei for being such a great treasurer, the help of Zineb, Zouina, but also the new generation with Nico M., Joey and Elissa, and H. Sabourin for our participation at the Professor assembly.

I'd like to thank Heide for the organization of the group, and her very helpful inputs in the text of my manuscripts (thanks also Michael Greschner for that!). This thesis is also the result of a vast collaboration between several labs, which I'd like to acknowledge: the veterinary school in St-Hyacinthe (Sheila Laverty, Hélène and Julia), Prof. Patten at INRS-IAF, Magali Millecamps from McGill, Boris and Sébastien from the LMN, Lucas and Thameur from A. Pignolet's team, Esen from M-A Gauthier's lab, and the last but certainly not the least: Jarno van der Kolk from L. Rammuno's team in UOttawa whose help was decisive in our publications.

Gratitude to the Razarri's team (Andrea, Younggyun, Lucas, Xin Jin...), notably for our great time spent in conferences ;), and also to the GRK program especially Franz Loechner and Anna Spaethe, as well as all people in Jena that welcomed me in the program and during my stay in 2019. Je remercie tous les membres du L.O.B. à Polytechnique Paris, notamment Margaux, Yoann, Joséphine, grâce à qui j'ai pu m'intégrer et passer 3 mois vraiment très fun à Palaiseau ! Merci également à tous ceux avec qui j'ai pu travailler dans le labo à Varennes: Margaux, Jérémy, je crois qu'on s'est bien amusé malgré les aléas du microscope ! Merci à Nedgine et à Adrien de m'avoir supporté dans le bureau ;)

Je tiens enfin à souligner les bons moments passés aux activités sportives de l'INRS: le soccer (Vincent W., Nico S., Vincent G., Guilmot ...), le squash (Simon V., Pilar, Patrick, Alonso, JF, Stass, Romain, Marc-André) mais surtout le hockey - extérieur et intérieur! - (Jérémie, Loik, Nico S., Romain, Joel, Antoine L., Philippe, Cuauhtémoc, Blaise...) ! Un clin d'oeil particulier à l'équipe d'électro-chimie de l'INRS (Mohamed, Victor, Etienne, Gaetan...), notamment pour nos belles séances au blocshop ! Merci au bus de l'INRS qui m'a permis de découvrir des livres incroyables. Je remercie bien évidemment tous mes proches, amis et famille de France et d'ici, pour leur soutient indispensable, même s'ils oublient un peu vite qu'une thèse ici, c'est pas 3 ans !!

A tous ceux que j'ai oublié, vous êtes les meilleurs.

Merci à tous !

Author's presentation

Maxime Pinsard has performed an engineer formation at ESPCI Paris in France, in physics, chemistry and biology. He specialized for the last year at Institut d'Optique Graduate School (IOGS), in the master Laser, Optics, Matter. During these years, he had the opportunity to do internships in the biophotonics domain: 6 months in an industry of fiber laser, Amplitude System near Bordeaux, and several research fellowships in labs: Institut Langevin in OCT imaging, and Institut Curie in optical particle tracking for super-resolution imaging.
He was then hired in the multiphoton microscopy lab at INRS, from where the following work was done.

Figure 1: In the multiphoton microscopy lab at INRS-EMT, Varennes, 2018.

Synopsis - Sommaire récapitulatif (fr)

-1.1 Introduction

La microscopie multiphoton (MPM) a été, au cours des 30 dernières années, de plus en plus considérée comme un paradigme majeur pour l'imagerie des tissus biologiques, et de certains matériaux [180, 28, 256, 53]. La MPM une technique de microscopie optique limitée par la diffraction, sa résolution axiale est donc régit par la longueur d'onde de la source excitatrice utilisée. Comme la "fenêtre biologique" des tissus biologiques (où la diffusion et l'absorption restent limitées) est dans le proche infrarouge (NIR, 700-1300nm), la résolution en MPM reste sub-micrométrique [35, 97]. Le contraste d'imagerie est obtenu par génération d'effets non-linéaires in-situ, ce qui présente de nombreux avantages : la possibilité de n'imager qu'un seul type de structure à la fois (renforçant ainsi le contraste), une bonne pénétration (jusqu'à 500 μm [255]) et une sélectivité en profondeur (quelques μm), une faible invasivité (rendant possible des images in vivo), une résolution 3D sub-micrométrique et le fait que la quantité de signal généré ne soit pas limitée dans le temps [255].

La MPM est aussi multimodale puisqu'elle permet la combinaison de plusieurs effets non-linéaires, chacun capturé par une voie de détection séparée : la fluorescence excitée à deux photons (2PEF), la génération de seconde (SHG) ou de troisième (THG) harmonique, et la diffusion Raman cohérente anti-Stokes (CARS) ou Stokes (SRS) [255]. La Génération de Seconde Harmonique (SHG) est en particulier devenue la référence pour l'imagerie 3D la moins invasive possible de tissus contenant un biopolymère constituant jusqu'à 30% de la masse totale des protéines chez un mammifère: le collagène [35]. Chacune des techniques est spécifique : par exemple, la diffusion Raman sonde la nature chimique alors que la génération d'harmoniques est plutôt sensible à la structure 3D (voir Fig. 2). Leur combinaison va donc fournir une description assez exhaustive de la zone imagée : on comprend aisément le développement rapide et soutenu de la MPM dans de nombreux domaines allant de l'oncologie jusqu'à l'embryologie ou aux neurosciences [255].

La génération de seconde harmonique (SHG), en particulier, image uniquement les milieux denses ne possédant pas de centre de symétrie : ceci la rend spécifique à certains types de structures inorganiques (e.g. les cristaux biréfringents, certaines couches épitaxiées) [12] ou organiques (e. g. la cellulose [117, 80], le collagène [76, 35, 150], la tubuline [146, 9, 231] ou encore la myosine [223, 69, 169]). Étant un processus paramétrique, elle ne fait pas intervenir de transfert électronique ce qui rend la relaxation de l'interaction quasi-instantanée, contrairement à la fluorescence excitée à deux photons qui prend plusieurs ns [33]. Elle évite aussi le photo-blanchiment et limite grandement la phototoxicité : rien n'empêche a priori de réaliser des images en continu de l'échantillon sans le dégrader [255]. Enfin, l'intensité SHG a une dépendance quadratique (jusqu'à la limite du volume focal) avec le nombre d'harmonophores (des milieux permettant la SHG) [27] ce qui conduit à un contraste élevé. Elle a aussi l'avantage, par rapport à la fluorescence à deux photons, d'être un processus cohérent : il y a donc une relation de phase définie

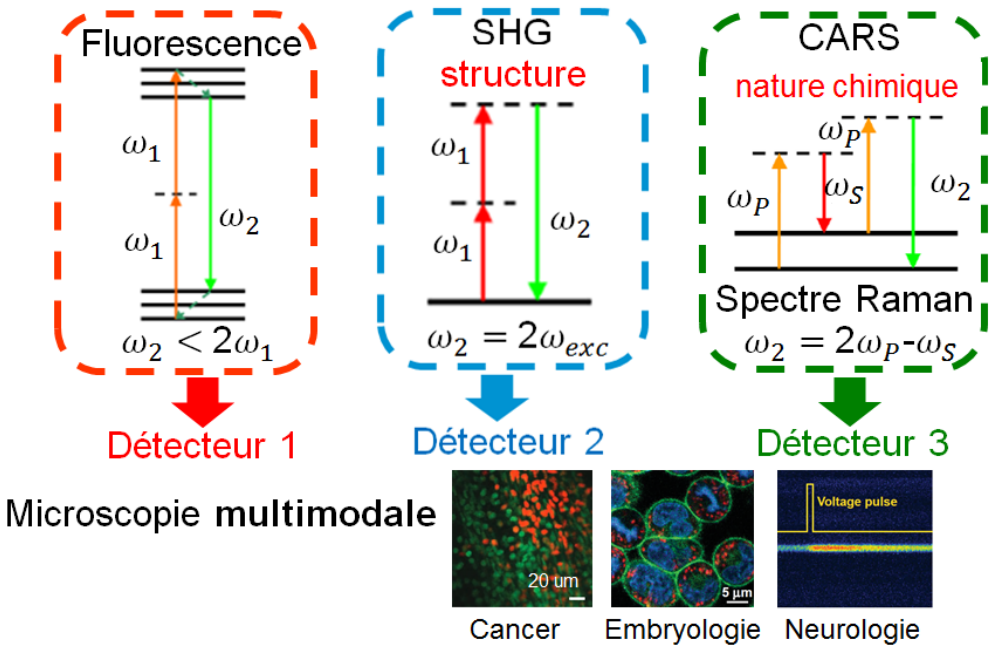

Figure 2: Description des différents processus multiphotons, et applications. Images tirées de [255].

entre la SHG créée et l'onde excitatrice, et cette propriété peut être mesurée en plus de l'amplitude seule [174, 175].

-1.2 Problématique / présentation du sujet de recherche

La compréhension des mécanismes de création de la SHG comme son amplification par interférences constructives à l'intérieur de milieux complexes (les structures biologiques par exemple) mérite encore d'être affinée, et nécessite parfois des études au cas-par-cas étant donné la grande variété des structures possibles. De plus, la cohérence optique de la SHG signifie également que les images contiennent la résultante d'interférences complexes, et non la structure réelle du matériau. Pour cela, de nombreuses techniques ont été proposées, également pour améliorer la SHG et tirer pleinement parti de ses nombreuses propriétés. La SHG directionnelle ou "forward and backward" (F/B SHG) utilise ainsi la direction de la génération, qui est uniquement vers l'avant (*forward*) et vers l'arrière (*backward*), la proportion relative des deux dépendants de l'agencement 3D du matériau imagé ([174], fig. 7.29). La sensibilité à la polarisation peut être sondée par p-SHG ("*polarization-resolved* SHG"), grâce au couplage avec la polarimétrie ce qui permet de mesurer l'alignement des dipoles au sein d'une image, et de déduire des paramètres structurels [83, 85, 99, 58, 76]. Enfin, la microscopie SHG peut être couplée à l'interférométrie (I-SHG) afin de mesurer la phase relative du signal SHG, ce qui permet de remonter à la polarité relative des structures [174, 175]. Il consiste en un interféromètre à un bras où une SHG dite "de référence" est générée colinéairement au faisceau d'excitation (dans un cristal non-linéaire, BBO par exemple), puis ceux-ci sont injectés dans le microscope de façon classique. Un déphaseur (ici une plaque de verre rotative) permet d'agir sur les deux faisceaux de fréquence respectivement ω et 2ω pour changer leur différence de phase, et ainsi acquérir des interférogrammes (voir Fig. 3).

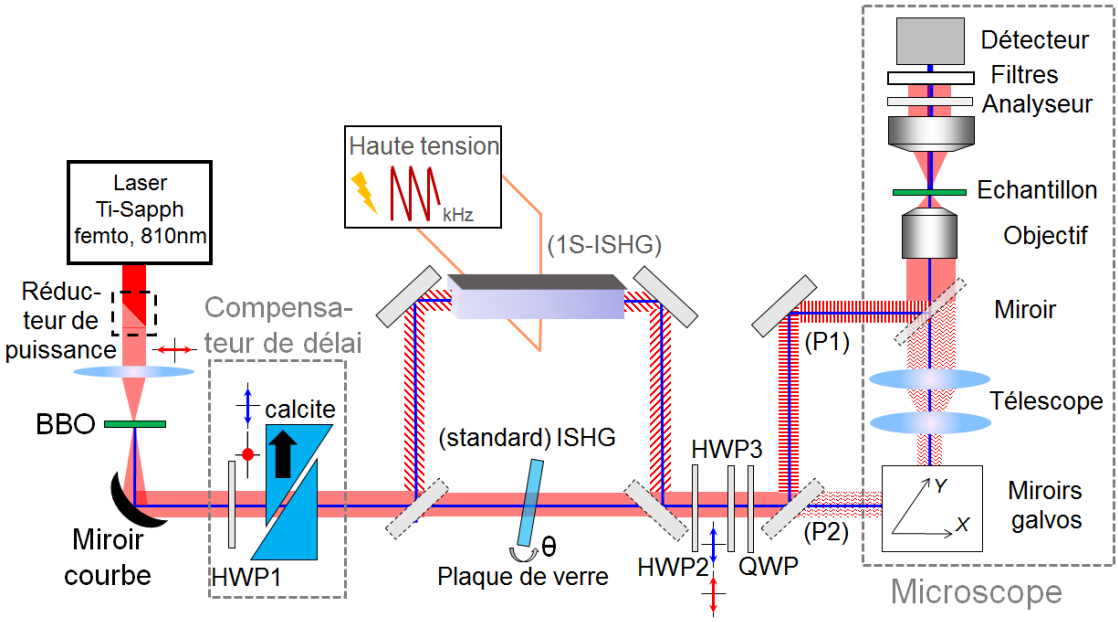

Figure 3: Montage pour la microscopie de génération de seconde harmonique interférométrique. Toutes les possibilités et chemin optiques sont représentées: la I-SHG standard, et la I-SHG mono-scan (1S-ISHG, présentée après). De plus, les différentes possibilités de balayage sont représentées : balayage par échantillon (P1), et balayage par laser (P2). HWP: lame demi-onde (1 et 2: à 810nm seulement, 3: à 810 et 405nm). QWP: lame quart d'onde.

Ce travail a été réalisé par mon prédécesseur Maxime Rivard avec des impulsions picosecondes pour s'affranchir des problèmes de décalage temporel, et en utilisant un laser de direction statique pour s'affranchir des problèmes d'aberrations induites par le balayage laser (l'échantillon est alors balayé par translation) [174, 175, 177]. Il a été ensuite progressivement amélioré par mes collègues Charles-André Couture et Stéphane Bancelin en rendant possible l'utilisation d'impulsions femtosecondes [46, 45], ce qui rapproche a priori le montage de celui d'un microscope de SHG classique (e.g. tel que dans [27, 35]). Le but est en effet d'inclure dans un montage de microscopie SHG standard un simple module « add-on » qui permette de réaliser la microscopie I-SHG : celui-ci sera alors plus à même d'être utilisé directement par tout laboratoire soucieux d'ajouter, à moindre coût, un nouveau mode de contraste à leur appareil.

Cependant ces améliorations viennent avec des compromis sur la qualité des interférences produites (donc de la précision de la phase mesurée) et la robustesse de l'alignement, autrement dit la facilité d'utilisation de ce mode de contraste et sa stabilité au fil des acquisitions. Il est donc apparu nécessaire de retrouver la qualité de l'interférométrie de la méthode initiale tout en gardant les avantages acquis lors des transformations du montage : l'augmentation drastique du signal généré grâce aux impulsions femtosecondes d'une part, et la rapidité d'acquisition des images grâce à un balayage laser de l'échantillon d'autre part. Ceci est d'autant plus vrai que les futures études s'orientent vers l'analyse de structures dynamiques tel que l'imagerie de la mitose [9], dont la forme et/ou la position évoluent rapidement dans le temps ($<$ 10 s voire moins), étant donné que la I-SHG sur structure statique a déjà été un succès. De plus, même pour les structures statiques, une augmentation de la précision de mesure de phase est la bienvenue afin de sonder des structures plus complexes ou des propriétés plus précises.

En outre, la I-SHG pourrait également être utilisée de façon multimodale, en la couplant à d'autres extensions de la SHG ou à des moyens d'imagerie complémentaires. En considérant que la SHG sert en général à imager des structures à symétrie cylindrique qui sont souvent polaires, chirales et optiquement

actives (collagène, myosine, tubuline, cf Fig. 2.1), la CD-SHG (SHG par dichroïsme circulaire) peut permettre de mesurer la polarité des fibrilles de collagène hors-plan par exemple (Fig. 4 c)). Leur alignement dans le plan focal est mesurable par SHG résolue en polarisation (Fig. 4 b)), et la I-SHG vient compléter en donnant le sens du dipôle via sa polarité (Fig. 4 a)). Toutes ces améliorations de

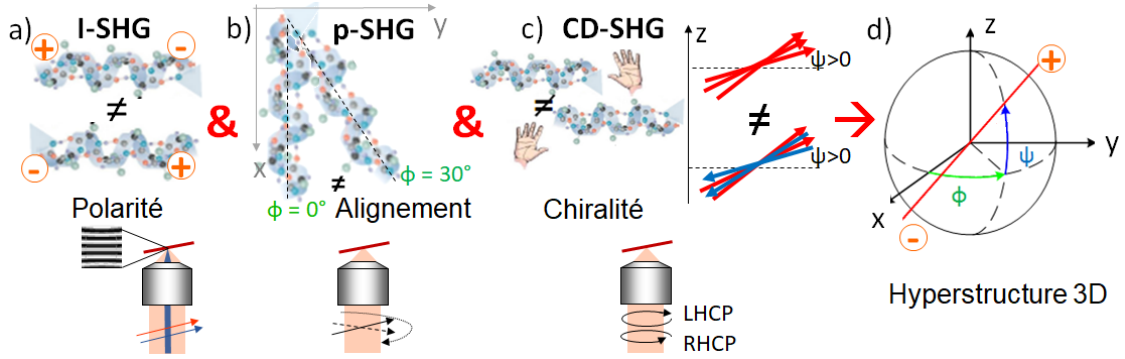

Figure 4: Description complète de la polarité des fibrilles de collagène par couplage multimodal de la I-SHG avec la CD-SHG et la p-SHG. (a) I-SHG mesurant la polarité des fibrilles (b) p-SHG donnant l'azimut de la direction de la fibrille dans le plan de l'image (alignement). (c) CD-SHG donnant la polarité des fibrilles hors plan, sensible à leur chiralité. LHCP (resp. RHCP) = polarisation circulaire gauche (resp. droite). (d) L'alignement 3D et la polarité complète des fibrilles peut alors être reconstruit (hyperstructure).

la SHG doivent cependant être acquises de façon *successive* car l'onde excitatrice doit être modifiée, contrairement aux techniques multimodales utilisant des longueurs d'ondes différentes (fluorescence, CARS) qui ont l'avantage de pouvoir être mise en place *simultanément* avec des détecteurs différents (voir Fig. 2).

Enfin, la I-SHG ne mesurait jusqu'alors que la phase du signal SHG, alors que l'équation d'interférence (2.23) permet a priori de calculer d'autres grandeurs intéressantes concernant la structure du matériau. On peut aussi ajouter que des études à large échelle, souvent utiles en biologie, pourrait être menées si la I-SHG devenait une technique aussi routinière que la SHG standard. Pour cela, il faudrait grandement améliorer la facilité d'alignement, d'acquisition et de traitement des données, mais aussi la vitesse d'acquisition en elle-même pour permettre l'imagerie d'un grand nombre de zones en une seule journée (souvent limitante, car l'alignement du faisceau risque de changer les jours suivants). Cela permettrait en plus d'imager des structures qui bougent au fil du temps sans problème d'artefacts dus aux mouvements. Cette thèse se propose donc d'aborder ces différents aspects et de tenter de les résoudre au maximum.

-1.3 Microscopie multimodale appliquée au ménisque articulaire

Un 1er enjeu est de rajouter des modes de contraste à la SHG et à l'I-SHG afin de caractériser plus en détail les échantillons imagés. En plus de la polarité dans le plan de l'image, l'orientation dans le plan (par p-SHG, décrit dans l'article de 4 et dans l'annexe C), ainsi que la polarité hors-plan (par CD-SHG, cf annexe C.4). La détermination de la nature chimique des molécules par CARS viendrait enfin compléter l'analyse et permettraient l'étude de cas biologiques complexes. Le ménisque articulaire en fait partie : c'est un fibrocartilage composé majoritairement de fibrilles de collagène de type I et II agencées en une structure tridimensionnelle non triviale [151, 129, 4]. Il y a 2 ménisques par genoux (médial, latéral), ceux-ci ont la forme d'un "C" (vu du dessus) dont l'épaisseur décroît du bord vers le centre, si bien qu'une section coronaire a une forme triangulaire: voir Fig. 5 E.

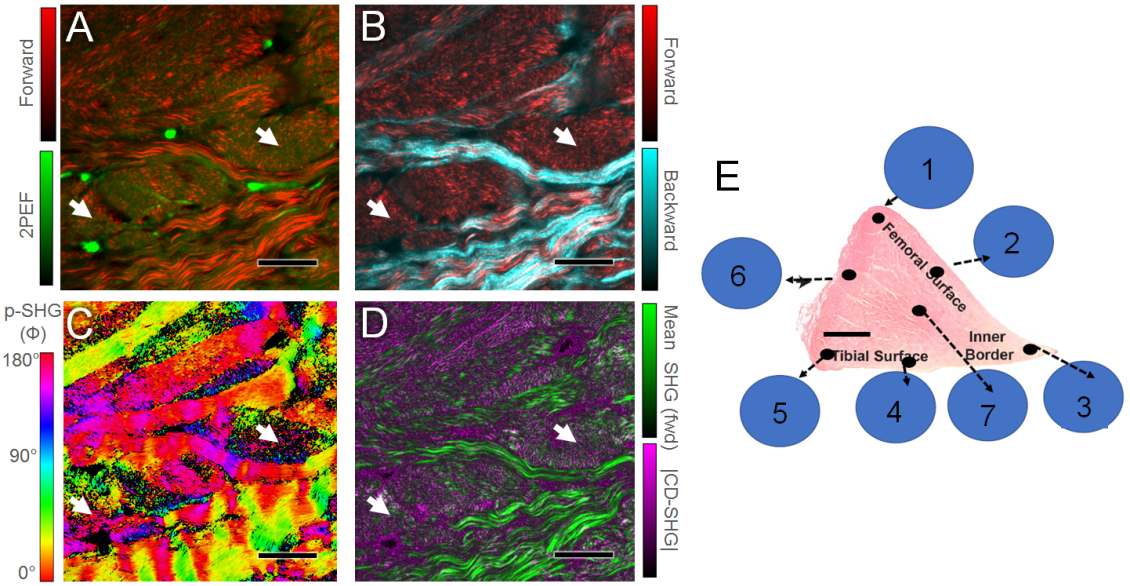

Figure 5: Images de la surface tibiale d'un ménisque de l'articulation du genou d'un cheval adulte sain (médial, gauche, postérieur). (A) Composite de la SHG *forward* (rouge) et de la fluorescence à 2 photons (2PEF, vert). (B) Composite de la SHG *forward* (vers l'avant, rouge) et *backward* (vers l'arrière, cyan). Le signal SHG *backward* est multiplié par un facteur $\times$23 pour être affiché et comparé au *forward*. (C) Alignement dans le plan des fibrilles de collagène par p-SHG, chaque angle correspondant à une couleur donnée indiquée sur l'échelle à gauche. (D) Composite de la SHG *forward* (vert) et de la CD-SHG en valeur absolue (magenta). Barre d'échelle : 50μm. Ces images ont été prises avec le microscope de Marie-Claire Schanne-Klein au L.O.B. (Palaiseau, France). (E) Ménisque complet où les différentes zones utilisées pour cartographier l'échantillon sont représentées (barre d'échelle 0.8cm): Fémoral externe (1), surface fémorale (2), pointe (3), surface tibiale (4), tibial externe (5), externe (6) et centre ou intrasubstance (7).

Comme le ménisque mesure plusieurs cm de large (voir Fig. 5 E), il faut choisir une région d'intérêt pour l'imager en microscopie, même si un balayage par platine motorisée peut produire des images de plusieurs mm en une seule fois (cf 4). Le "triangle" est donc habituellement décomposée en 5 à 7 zones (ou plus) représentées sur la Fig. 5 E: l'article présenté en 4 se restreint par exemple à la partie centrale (7). Nous avons choisis ici de montrer une autre zone, extraite de la surface tibiale (4) et montrant les divers modes de contraste de la microscopie multimodale. La fluorescence à 2 photons (2PEF, vert sur la Fig. 5 A) fait principalement ressortir les chondrocytes, l'autofluorescence du collagène étant assez faible. En revanche, les fibrilles de collagène (type I et II mélangés) sont visibles par SHG (rouge). Un autre composite (Fig. 5 B) compare la SHG émise vers l'avant (*forward*, rouge) et celle émise vers l'arrière (*backward*, cyan): les fibrilles formant les "faisceaux" (*fascicles* en anglais) orthogonaux au plan de l'image, selon le modèle proposé par Andrews *et al.* [4], sont surtout visible en *forward*. Ceci est conforme à la théorie de la dépendance du patron de radiation avec l'angle de la structure 2D, généralement admise et présentée dans [254] (voir aussi Fig. 2.8). Sur cette image la SHG *backward* est multipliée par un facteur $\times$23 pour comparaison, et fait surtout ressortir des assemblages épais de fibrilles que l'on peut identifier comme des sections de feuillet de fibre d'attache, aussi présentées dans le modèle d'Andrews *et al.* [4], ainsi que Fig. 4.1 (g). L'alignement des fibrilles de collagène est confirmé par le tracé de leur orientation locale dans le plan (angle ϕ) obtenu par p-SHG (Fig. 2.8 C), car des directions bien déterminées sont visibles pour les fibres d'attache alors que celle des faisceaux orthogonaux est mal définie (ϕ aléatoire, semblable à un *speckle*). Enfin, la Figure 2.8 D) s'inspire de [189] et vérifie que les portions de l'image ayant un signal de CD-SHG important (en magenta, valeur absolue traduisant un

angle plutôt hors-plan) correspondent à celles ayant un signal d'intensité SHG *forward* petit (en vert), et inversement. On distingue encore ici les fibres d'attache majoritairement dans le plan (avec un signal SHG *forward* fort) et les faisceaux de fibrilles plutôt hors-plan (donc un signal $|\,\mathrm{CD}\,|$ fort).

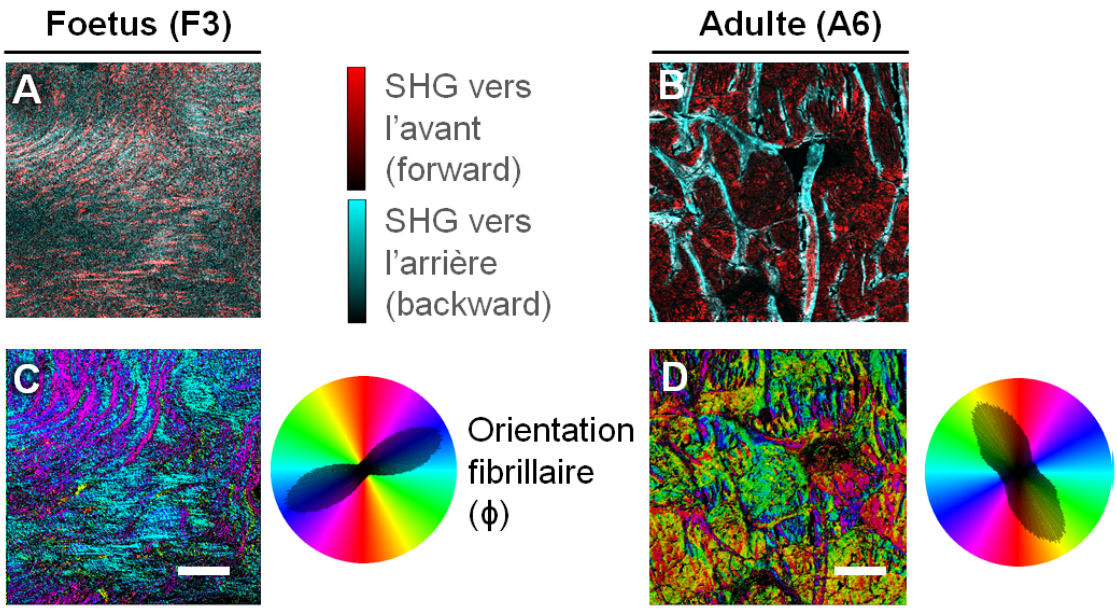

Figure 6: Comparaison F/B SHG (haut, A et B) et P-SHG (bas, C et D) de ménisques de foetus et adultes (zone centrale, extrait du genou de chevaux). Les ménisques immatures (gauche, A et C) présentent un alignement du collagène beaucoup plus homogène que les ménisques adultes (droite, B et D), où des groupements de fibrilles de différentes orientations sont visibles. Barre d'échelle : 200μm.

A l'inverse, le ménisque immature (par exemple celui d'un foetus) ne présente pas cette distinction: très peu de régularité et de structures y sont visibles, et l'organisation du collagène semble soit complètement uniforme, soit aléatoire (voir Fig. 1 et S2, S3 de l'article 4.4), comme le montre l'image de l'alignement des fibrilles par P-SHG de la Fig. 6C, à comparer à la Fig. 6D chez l'adulte. Ainsi, son rapport *forward* sur *backward* est beaucoup plus petit que pour un ménisque adulte : les signaux SHG vers chacune des deux directions sont similaires en intensités (Fig. 6A), alors que des portions très différentes apparaissent en *forward* (rouge) sur *backward* (cyan) pour le ménisque adulte (Fig. 6B).

-1.4 Aspects avancés en microscopie SHG: mesure du déphasage de Gouy et artefacts d'imagerie

Le déphasage de Gouy est expliqué de nombreuses manières dans la littérature [149], et les moyens de la caractériser efficacement sont peu nombreux. Celui-ci implique que la phase d'un faisceau subit un déphasage supplémentaire de π au travers de son focus (la profondeur z variant dans la longueur de Rayleigh et au-delà) [37]:

$$\begin{aligned} &\varphi_{Gouy} = \mathrm{Arctan}\,\frac{z}{z_R} \\ &\Rightarrow \varphi_{Gouy}(z \gg z_R) - \varphi_{Gouy}(z \ll -z_R) = \frac{\pi}{2} - \left(-\frac{\pi}{2}\right) = \pi \end{aligned} \tag{1}$$

Les variations de la phase de Gouy au focus du faisceau d'excitation pourraient par ailleurs venir perturber l'image de phase finale de l'échantillon si celui-ci n'est pas parfaitement plan. Ceci expliquerait un des facteurs qui conduit à la dispersion des mesures de phase relative autour de leur valeur principale, comme on a pu l'observer sur des images de I-SHG d'échantillons biologiques, ou même de cristaux [174, 177].

La I-SHG peut permettre de remonter à cette variation de phase en mesurant la variation axiale de phase relative au voisinage du point focal (Fig. 7 a)): pour ceci, il est nécessaire d'avoir un échantillon qui soit beaucoup moins épais que le volume focal ($\sim 1\mu m$), afin qu'il agisse comme un point source sondant ce volume. Une fibrille de collagène est donc une bonne candidate car son diamètre est en-dessous de 0.5μm, souvent même en-dessous de 0.1μm [107].

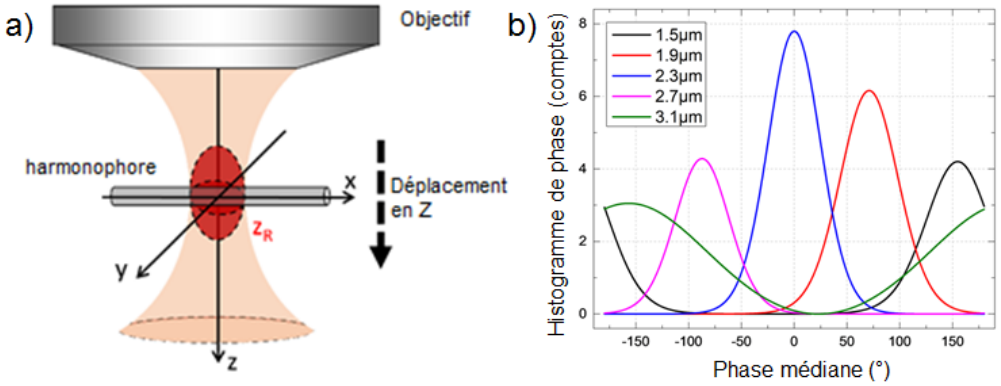

Figure 7: Mesure du déphasage de Gouy par I-SHG. Schéma de la mesure sur un échantillon cylindrique sub-micrométrique en épaisseur (a). Histogrammes de phase associés à différentes positions axiales (Z, seul le contour est représenté). Adapté de l'article 5.

Les interférences ayant lieu au niveau du détecteur, la phase mesurée de la SHG de référence en fonction de la position de l'échantillon ne dépend que de la différence de propagation. Comme la SHG de l'échantillon possède ce même terme de propagation, ils se compensent dans la variation de la phase totale mesurée. En revanche, la SHG de l'échantillon est générée par un très grand nombre de sources secondaires, qui sont déphasés différemment à chaque positions par la phase de Gouy du faisceau Gaussien d'excitation. Ces sources secondaires ne sont pas des faisceaux Gaussiens divergents, ils ne subiront donc pas de déphasage de Gouy supplémentaire. Par contre, la conversion fondamental vers SHG double le déphasage de Gouy (eq. 2):

$$E_{fund} = E_0 e^{i\omega t} e^{i\varphi_{Gouy}} \Rightarrow E_{SHG} \propto (E_{fund})^2 = E_0^2 e^{i2\omega t} e^{i2\varphi_{Gouy}} \quad (2)$$

En mesurant la phase en I-SHG en fonction de la profondeur de focus à travers l'échantillon mince, on obtient donc 2 fois le déphasage de Gouy. Ceci est visible sur la Fig. 7 b) où les positions centrale des histogrammes de Z=1.5μm (black) et Z=3.1μm (green) sont espacées de 360°=2π. On remarque aussi que la largeur des histogrammes est proche de 180° car l'échantillon est en-dehors du volume focal: le signal SHG est alors assez faible, et la précision sur la mesure de phase aussi. Les mesures réalisées au milieu du volume focal sont plus précises car plus de SHG est générée, les histogrammes ont alors une largeur de ~90°. Cette variation de 2π est aussi corroborée par une simulation numérique utilisant la fonction de Green vectorielle et un tenseur de susceptibilité non-linéaire $\chi^{(2)}$ à 2 coefficients, cf Fig. 5.1. Il s'agit d'un modèle plus proche de la réalité que le modèle scalaire de l'équation 1.

Le patron de radiation de la SHG et sa recombinaison sur le détecteur ont également une importance capitale pour la mesure de phase en I-SHG, ainsi que pour l'interprétation des images d'intensité SHG.

Peu d'études prennent en compte l'effet de la forme de ce diagramme d'émission sur l'intensité finale mesurée, qui peut en théorie prendre la forme d'un anneau lorsque le point focal est légèrement en profondeur dans le milieu (une Gausienne 2D s'il est en surface), ou la forme de deux lobes de phases séparées de π[37] (amplitude opposées) si l'on déplace ce point focal à l'interface entre deux milieux de polarités opposées [181] (voir Fig.2 de l'article 6, Fig. 6.2 et Fig. 8).

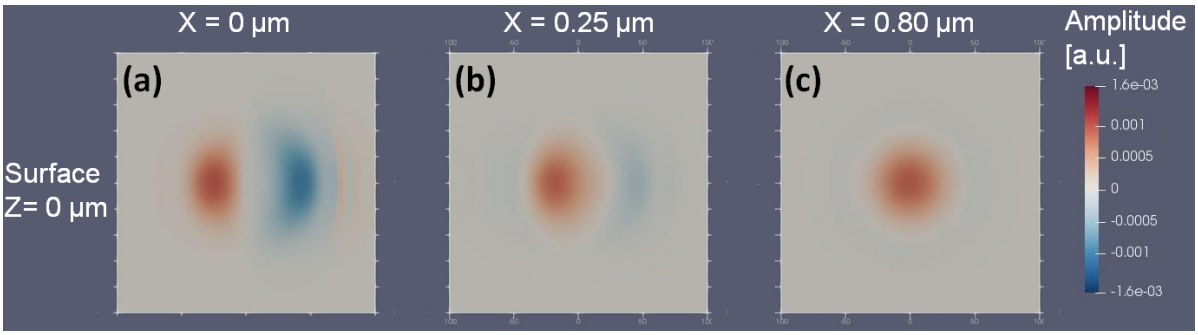

Figure 8: Simulations numériques du patron de radiation de la SHG (en utilisant la formulation de Green), le centre de l'excitation passant d'une interface +/- à une zone homogène (a - c). Le foyer est à la surface du matériau (moitié à la surface et moitié en profondeur).

Ce type de milieu se retrouve par exemple dans le cristal de niobate de lithium périodiquement orienté (PPLN), qui possède des domaines de polarités opposées. On en retrouve aussi dans les muscles: les sarcomères de myosine contiennent le même type d'interfaces (cf fig.1 de l'article 6). Dans le PPLN, les domaines de polarités opposés ne sont pas discernables par SHG, car ils produisent a priori le même signal SHG, en revanche il y a interférence destructive des lobes à l'interface, donc une ligne sombre (voir par exemple [111]). Pourtant, certaines images de PPLN font apparaître au contraire une ligne brillante, comme sur la Fig.9 (haut, gauche). On peut montrer qu'il s'agit en fait de diffusion incohérente, due aux défauts présents à ce type d'interface 6 qui créent alors, via un effet de champ local, un signal de seconde harmonique (SH) très important grâce au nombreuses brisures de symétrie. Ce signal SH n'a pas de direction bien définie contrairement à la SHG normale: il s'ajoute donc au signal total comme une contribution de diffusion, de plus incohérente car ne possédant pas de relation de phase bien définie. En effet, il n'y a pas de franges d'interférence sur cette contribution (voir Fig.6.4), et le signal détecté à cette interface est bien trop élevé (2 fois plus grand que dans les zones homogènes "*bulk*") pour n'être que de la SHG: des simulations numériques (similaires à celles utilisées pour l'étude du déphasage de Gouy) montrent en effet qu'aux interfaces, le signal devrait être nul ou au plus 70% du signal *bulk* si les lobes ne se recouvraient pas, en cas de mauvais alignement (voir Fig.5 de l'article 6).

Ceci n'existe pas dans la myosine, mais il y a quand-même des artefacts, cohérents cette fois, décrits de nombreuses fois dans la littérature [181, 52]: le déphasage de Gouy peut créer des artefacts d'imagerie sur des structures avec des interfaces empilées selon l'axe de la profondeur. Couplé à la possibilité d'interférences plus ou moins marquées entre des interfaces adjacentes dans le plan de l'image, l'imagerie de la myosine peut révéler en fonction de la profondeur des structures "double-bande" où chaque interface est visible (cas "normal"), ou bien des structures "simple-bande" artefactuelles où les changements de polarité ne sont plus visibles (voir Fig. 9, bas). Ceci est expliqué en considérant deux séquences de sarcomères empilées comme sur la Fig. 10, haut: des extrémités de myosine de même signe devrait interférer constructivement et ainsi lier les 2 étages sur l'image SHG (A' bas), mais le déphasage de Gouy de $\pm\pi/4$ aux extrémités du volume focal produit un déphasage de $\pi/2 - (-\pi/2) = \pi$ sur leur SHG: des extrémités de même polarité présenteront donc un mimimum du signal SHG si elles sont espacées de sorte à être contenues aux extrémités du volume focal (A, bas). Un décalage Δ égal à la moitié de la longueur L des sarcomères donnera des jonctions en SHG entre les sarcomères empilés (Fig.

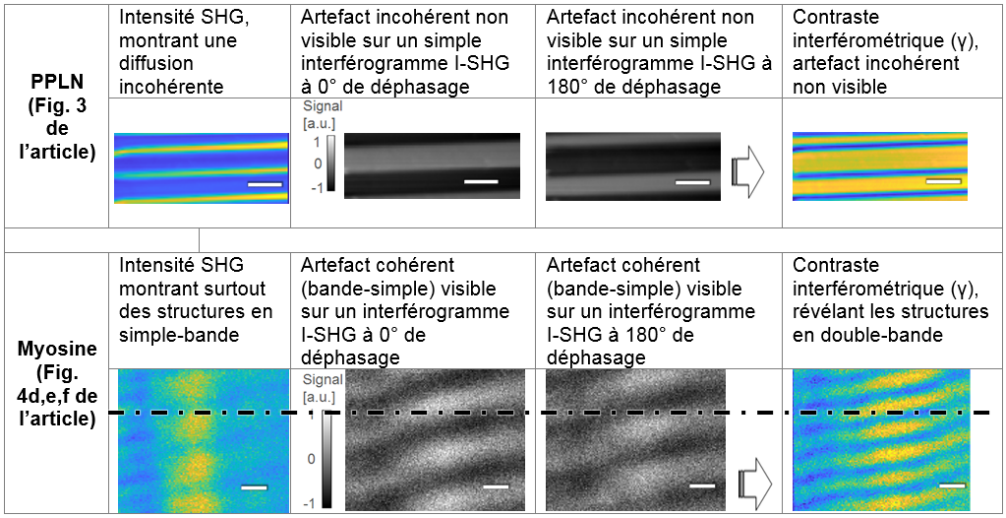

Figure 9: Comparaison de l'élimination des artefacts incohérents et cohérents par I-SHG. (Haut) Images de PPLN de la fig.3 de l'article 6, montrant le contraste γ en I-SHG (droite) et deux interférogrammes à 0° (milieu gauche) et 180° (milieu droit) utilisés pour reconstruire l'image I-SHG. Les artefacts incohérents (bandes brillantes) présents sur l'image d'intensité SHG (gauche) sont directement supprimés sur les interférogrammes. Barre d'échelle: 5μm. (Bas) Même chose, avec la myosine de la fig.4(e) de l'article 6. Les artefacts cohérents (simple-bande) sont aussi visibles sur l'intensité SHG (gauche) mais également sur les interférogrammes (milieu gauche et droite), ceux-ci sont en revanche bien déphasés de π. Les motifs double-bande n'apparaissent que dans le contraste I-SHG γ (droite). Une ligne noire en pointillés guide l'oeil pour comparer les images. Barre d'échelle: 1μm. Adapté de la fig.6 de l'article 6.

10 C), alors que le signe opposé des extrémités de myosine aurait conduit - sans déphasage de Gouy - à un espacement visible des deux séquences (C'). Les structures "simple-bande" en SHG peuvent être expliquées par le cas intermédiaire Δ=L/4: le volume focal capture la jonction oblique des 2 étages, ce qui ajoute du signal entre les creux dus aux interférences destructives entre des polarités opposées.

En rajoutant la SHG de référence (configuration I-SHG), on obtient des interférogrammes qui font encore apparaître l'artefact simple-bande (Fig. 9 milieu bas), car celui-ci est cohérent: ce n'est seulement qu'en reconstruisant l'image de I-SHG (ici le contraste γ) que les double-bandes sont révélées (droite). Par contre, pour le PPLN, l'artefact incohérent n'interfère pas et est donc supprimé directement sur les interférogrammes (Fig. 9 haut, milieu), et donc également sur le contraste γ (droite).

De plus, les images montrent aussi qu'en I-SHG les interfaces ont une visibilité accrue par rapport au reste du matériau, comparé à l'intensité SHG standard: un facteur $\times$5 pour le PPLN et $\times$3 pour la myosine sont reportés (6).

-1.5 Améliorations de l'I-SHG

-1.5.1 Aspects généraux

Comme évoqué précédemment, la I-SHG nécessitait d'être améliorée afin d'être utilisée de façon routinière et à grande échelle. En plus de mesurer l'amplitude du signal SHG (via le contraste interférométrique) en parallèle de la phase, cette technique nécessitait surtout d'être rendue plus rapide et précise. D'autre part, le contraste interférométrique doit être amélioré pour retrouver une valeur proche de l'unité, afin

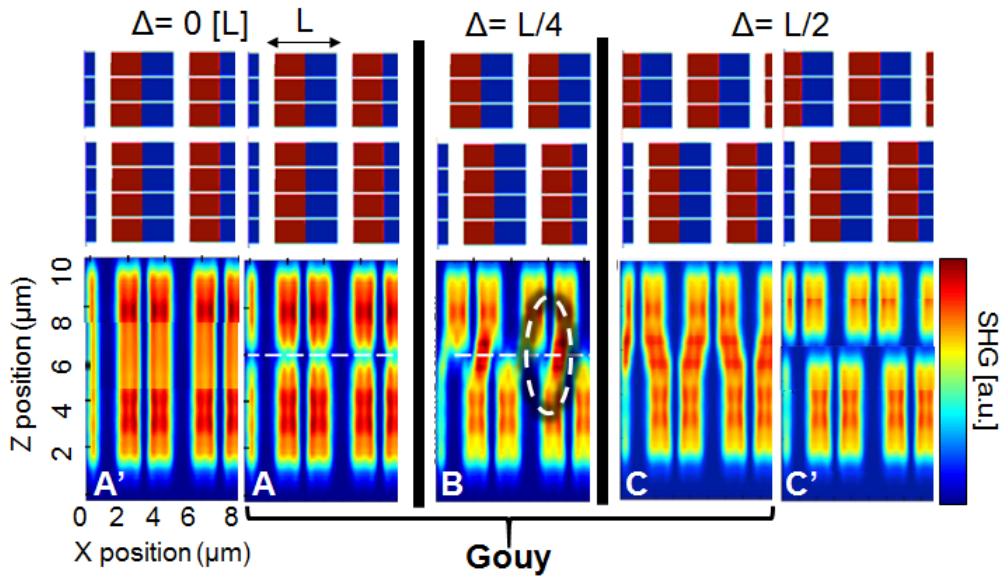

Figure 10: Empilement de deux séquences de sarcomères de myosine dans les muscles présentant des décalages différents, et la conséquence sur leur imagerie par SHG. (Haut) Schéma des positions, avec les extrémités positives en rouge et les extrémités négatives en bleu. (Bas) SHG simulée à partir des arrangements de myosine du dessus. (A)&(A') : avec un offset Δ égal à un nombre entier de fois L (ou 0), (C)&(C') : à la moitié de la longueur L des sarcomères, et (B) : Δ=L/4. Le déphasage de Gouy est considéré dans les case (A), (B), (C), mais pas (A') et (C'). Un exemple de volume focal est indiqué sur (B), bas (oval pointillé blanc). Adapté de [52].

d'assurer la précision des mesures réalisées avec cette technique. Cela implique :
- un meilleur recouvrement spatial des faisceaux qui interfèrent, notamment axial
- une polarisation des deux faisceaux bien rectilignes et parallèles entre elles
- des durées d'impulsions "échantillon" et "référence" égales, avec un *chirp* (dispersion temporelle du 2e ordre) limité

Pour le dernier point, on peut néanmoins montrer que le paramètre important est uniquement la différence de *chirp* entre les deux impulsions qui interfèrent (voir eq. 2.36): l'équation générale pour la I-SHG, prenant en compte les polarisations des 2 faisceaux (référence R et échantillon S, formant respectivement un angle α_1 et α_2 avec l'axe optimal d'excitation de l'échantillon), et les dispersions temporelles du 1er et 2e ordre s'écrit:

$$\boxed{I_{ISHG}(2\omega_0) = I_{SHG,R}(2\omega_0)\cos^2\alpha_1 + I_{SHG,S}(2\omega_0)\cos^2\alpha_2 + \gamma_{\omega_0}\cos\left[\Delta\varphi + \text{effetsChirp}\right]} \tag{3}$$

($\Delta\varphi$ est la différence de phase entre R et S, ω_0 la pulsation optique). Les effets du *chirp* et le contraste γ s'écrivent:

$$\begin{aligned}
&\boxed{\text{effetsChirp} = \frac{0.5}{1+(\sigma_\tau/\tau_d)^4}\left(\frac{\text{délaiGroupe}}{\tau_d}\right)^2 - \frac{1}{2}\,\text{Arctan}\,\frac{\tau_d^2}{\sigma_\tau^2}} \\
&\boxed{\gamma_{\omega_0,2^{nd}} = 2\gamma_0\sqrt{\cos\alpha_1\cos\alpha_2}\,\frac{2}{(1+(\tau_d/\sigma_\tau)^4)^{1/4}}\exp\left[-\frac{0.5}{1+(\tau_d/\sigma_\tau)^4}\left(\frac{\text{délaiGroupe}}{\sigma_\tau}\right)^2\right]}
\end{aligned} \tag{4}$$

avec délaiGroupe $= \sum_j \Delta l_j \Delta k_j'\Big|_{\omega_0}$, $\tau_d^2 = 2\sum_j \Delta GDD_j$ et σ_τ la largeur temporelle de l'impulsion. Le délai de groupe est l'effet de la dispersion temporelle de l'indice optique au 1er ordre, et la "GDD"

celui du 2nd ordre (*chirp*). Ces effets de dispersion temporelle diminuent donc le contraste total des interférences: autant il est aisé de superposer les deux impulsions temporellement en les décalant dans le temps si nécessaire, autant agir sur leur *chirp* pour le rendre nul est très difficile dans un montage où les deux impulsions R et S (à des longueurs d'onde différentes) sont superposées.

Pré-compenser le *chirp* - par exemple avec des miroirs à *chirp* négatif - aura donc comme seul effet d'améliorer le signal de SHG produit dans l'échantillon, car celui-ci a une dépendance linéaire avec la durée de l'impulsion. Ceci peut néanmoins être utile dans des milieux biologiques qui donnent un faible rapport signal-sur-bruit (SNR) en SHG. Pour améliorer le contraste interférométrique, il faudrait pouvoir compenser le *chirp* des deux impulsions séparément, avec des compresseurs fonctionnant chacun à la longueur d'onde de l'impulsion en question.

D'autres facteurs pourraient être responsables de cette dispersion comme la précision de mesure de la phase ou les fluctuations de l'interféromètre, c'est pourquoi il a aussi été nécessaire de s'attaquer à une analyse computationnelle avancée de l'extraction de la phase relative à partir des interférogrammes. Cela consiste en un algorithme à trois étapes, qui converge vers une valeur finale de phase et de déphasage, et dont le nombre d'itérations dépend du rapport signal-sur-bruit de l'échantillon [238, 124]. Un code de dépliage 2D de la phase par proches voisins guidé par qualité a aussi été adapté, ainsi que des procédures pour corriger des aberrations spatiales de forme parabolique ou plane, des déformations périodiques de la phase ou pour lui appliquer une courbe de tendance 2D. Tout le traitement d'images de I-SHG a été condensé dans une interface graphique sous Matlab (GUI) qui permet de changer efficacement les paramètres, de traiter exhaustivement les images et de réaliser des analyses en série (*batch-processing*) et automatisées d'un grand nombre d'acquisitions. Ceci contribue grandement à la réduction du temps nécessaire à réaliser une expérience de I-SHG, car le traitement d'images est souvent négligé dans ce calcul bien qu'il puisse devenir un frein assez important s'il est trop chronophage.

Ces aspects computationnels s'intègrent de façon logique dans le projet de thèse (cf Fig. 11), car ils sont nécessaires à la réalisation de certains points (flèches épaisses), ou permettent une amélioration d'autres aspects (flèches fines). Ainsi le traitement d'image avancé via le GUI et d'autres scripts MatLab sont nécessaires pour l'étude expérimentale des aspects avancée en I-SHG, ainsi que pour la I-SHG mono-scan. Mais ils permettent également d'étudier en profondeur les tissus biologiques tels que la myosine du muscle, et font indirectement parti de la procédure de microscopie multimodale.

De même, la microscopie multimodale et la I-SHG mono-scan nécessitent un contrôle accru du programme d'acquisition, mais vont aussi permettre son expansion en soulevant de nouvelles problématiques à résoudre. Un nouveau programme de contrôle du microscope multiphoton a donc été codé en langage Python, pour pouvoir être le plus compréhensible et adaptable possible, et parce que les projets sus-mentionnés nécessitent une compréhension très poussée des procédés participant au contrôle du microscope et à l'acquisition des images. Cela a permis de synchroniser efficacement le modulateur de phase avec l'acquisition des images, via une interface claire et maîtrisée: voir Fig. 12.

En outre, le système de déclenchement (*trigger*) du moteur de balayage de l'échantillon a également été repensé afin d'améliorer la synchronisation balayage/acquisition des images, ce qui diminue le temps d'acquisition, permet de maîtriser certains paramètres comme la vitesse de scan et évite certains artefacts dus à la translation du moteur.

De plus, il a été nécessaire d'implémenter des nouveaux miroirs galvanométriques car ceux du microscope étaient plus adaptés à une excitation NIR pour produire de la fluorescence qu'à la I-SHG: leur transmission dans le visible autour de 400nm étaient de seulement 1% (>80% dans le NIR), et ils déformaient énormément la polarisation d'excitation, principalement. Ce fut une opportunité de comprendre

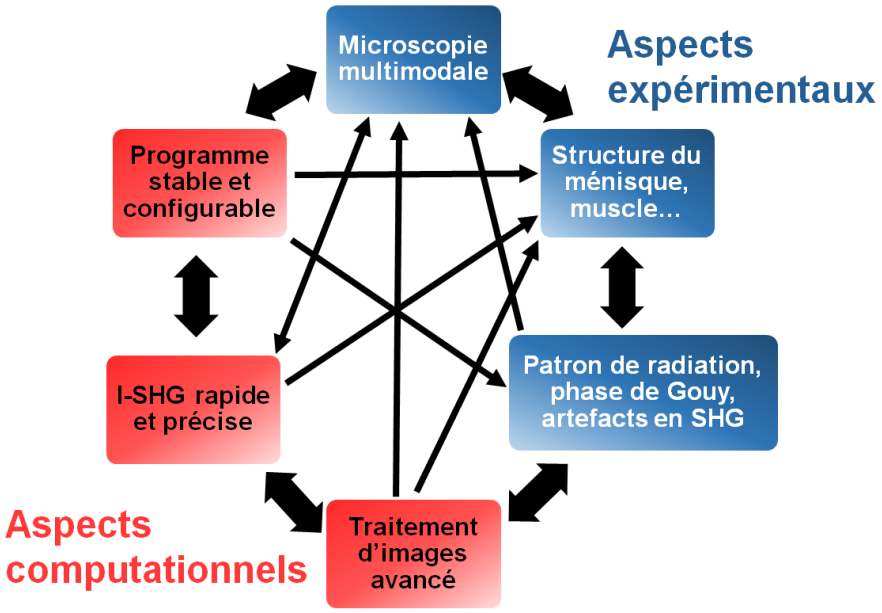

Figure 11: Différentes améliorations et points travaillés de la thèse, avec leurs liens. Les flèches épaisses représentent les liens principaux, et les flèches fines les liens secondaires. Les aspects expérimentaux sont indiqués en bleu, les aspects computationnels en rouge.

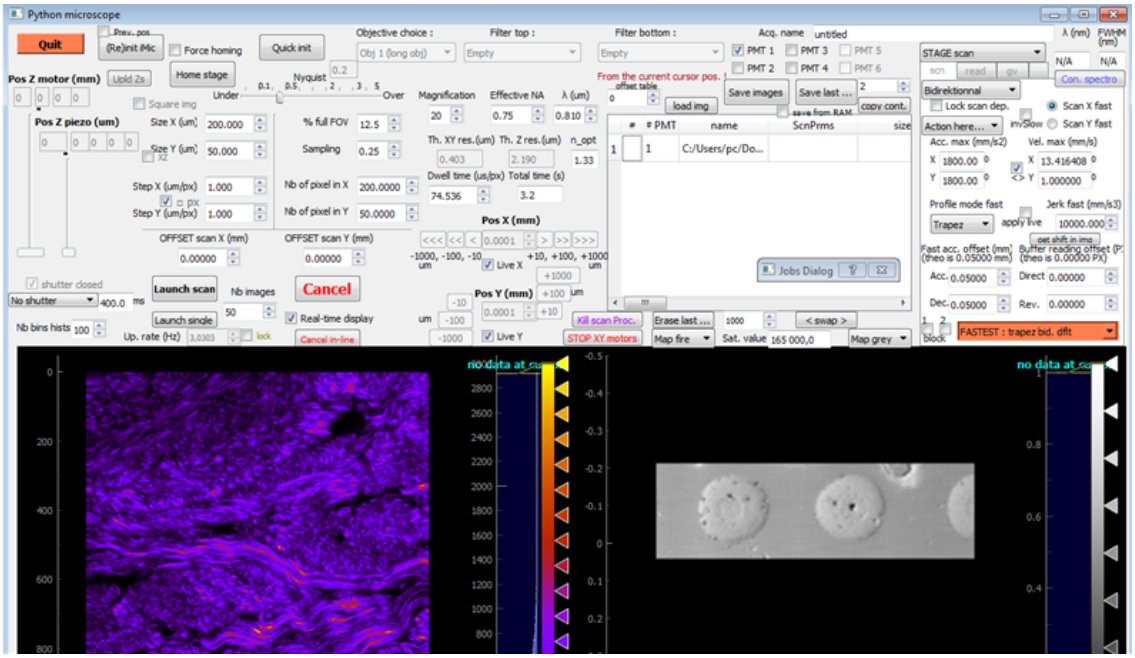

Figure 12: Vue du programme Python pour le contrôle du microscope, intégralement développé durant cette thèse. L'interface graphique permet de contrôler la position en 3D de l'échantillon (gauche), de changer les paramètres de l'acquisition et de sauver les images incluant ces paramètres (milieu), et de régler les variables utilisées par les différents instruments (droite). Une seconde fenêtre permet également de gérer les tâches répétitives.

le fonctionnement de tels miroirs à balayage, pour pouvoir ensuite les contrôler facilement et les adapter à une application avancée: la I-SHG mono-scan (présentée ci-après).

-1.5.2 Vitesse et précision d'acquisition en I-SHG

I-SHG à balayage laser

Comme déjà mentionné, un retour au balayage laser inhérent à tous les microscopes multiphoton est souhaitable afin de rendre la I-SHG compatible et facilement insérable dans un quelconque système existant, mais aussi pour raccourcir le temps d'acquisition de la I-SHG. Une image par balayage non-optimisé de l'échantillon prend ainsi 1.5h (pour 250μm^2 et 0.5μm/pixel, temps différent pour d'autres tailles), mais peut être divisé par plusieurs dizaines en balayage laser. Cette amélioration a été menée par mon collègue Stéphane Bancelin, et est reportée sur l'article 7. Il y a eu 2 limitations à surmonter: d'une part, le télescope des miroirs de balayage (galvos) rajoutait beaucoup de GVM entre les trains d'impulsions "référence" (R) et "échantillon" (S), il fallait donc la pré-compenser tout en gardant des diamètres de faisceaux R et S similaires et une différence de *chirp* raisonnable, pour maintenir un bon contraste interférométrique. D'autre part, les aberrations dues au balayage laser dans l'objectif devaient être corrigées: puisque les faisceaux traversent plus ou moins de verre lors du balayage, il y a un déphasage du centre de l'image vers les bords que l'on voit bien sur la Fig. 13B qui montre la phase mesurée dans une plaque de quartz homogène.

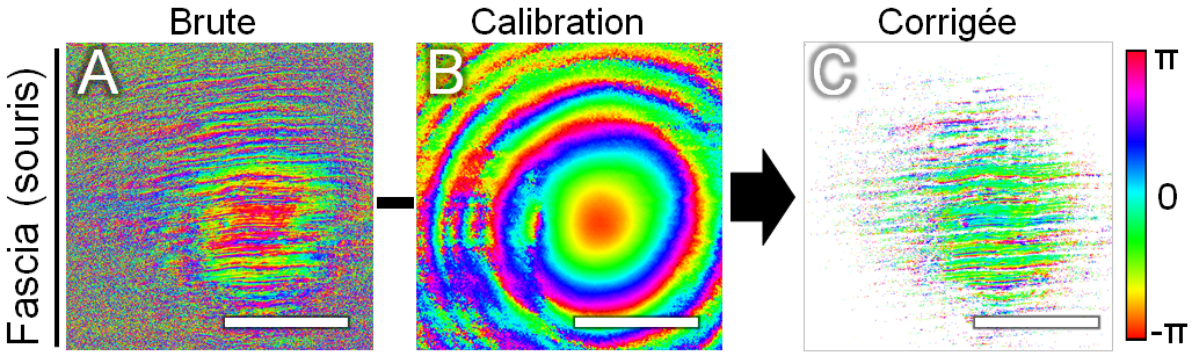

Figure 13: Image de phase d'un fascia du muscle du tibia antérieur de souris, par I-SHG avec balayage laser. (A) Image de phase brute du fascia. (B) Image de phase avec les mêmes paramètres, dans une plaque de quartz homogène. (C) Image de phase du fascia corrigée. Barre d'échelle : 100μm.

L'article associé (7) montre un exemple de I-SHG par balayage laser dans le PPLN (fig.4), utilisé comme échantillon de référence, puis dans un tissu biologique où le SNR est moins bon: le tendon de queue de souris (fig.5). Nous reprenons ici des images prises exactement dans les mêmes conditions (le champ-de-vue complet de 250μm^2 est montré), mais dans un tissu légèrement différent: le fascia du muscle tibial de souris. L'image I-SHG de la phase relative brute (Fig. 13A) montre les aberrations de l'objectif, heureusement elles ne dépendent que de l'alignement et sont les mêmes si on remplace le fascia par du quartz homogène (Fig. 13B). En soustrayant les deux images (la phase est l'argument de $e^{i\varphi}$, donc une division par une référence donne une soustraction des phases) on obtient la phase corrigée (Fig. 13C) qui ne montre ici qu'une seule polarité. Les zones avec trop peu de contraste interférométrique (vues comme du bruit sur l'image brute Fig. 13A) sont filtrées et indiquées en blanc. On voit que la I-SHG exploitable est limitée à une aire de 100μm^2 dû aux aberrations dans l'objectif de microscope (et le télescope des miroirs de balayage). Il est à noter que ce champ de vue peut être amélioré en adaptant mieux le télescope associé aux miroirs de balayage, ce qui a été fait lors de leur renouvellement comme sus-mentionné. De plus, cette publication a aussi traité du nombre optimal de déphasages à utiliser pour retrouver la phase avec une bonne précision. Une étude plus poussée a été menée dans cette thèse et a montré que 2 méthodes différentes d'extraction de la phase à partir des interférogrammes

étaient équivalentes, pourvu qu'elles aient le même nombre de déphasage N_{ps}, la précision sur la phase φ mesurée étant en fait:

$$\delta\varphi \sim \frac{\delta I}{M I_0}\sqrt{\frac{2}{\mathbf{N_{avg}N_{ps}}}} \Leftrightarrow \boxed{\delta\varphi = \frac{1}{M \times \mathsf{SNR}}\sqrt{\frac{2}{\mathbf{N_{avg}N_{ps}}}}} \tag{5}$$

où SNR est le rapport signal-sur-bruit, δI (resp. I_0) les fluctuations d'intensité (resp. l'intensité moyenne) SHG, M le contraste d'interférence et N_{avg} le nombre d'images moyennées (optionnel). L'article montre ainsi qu'il y a peu de différences sur la précision de la mesure de phase si N_{ps} passe de 36 (le pas de phase est alors de 15°) à 9 (le pas de phase est alors de 45°), en tout cas dans un échantillon de tendon où le SNR est plutôt élevé. 9 déphasages sont justement utilisés dans l'étude d'un processus plus rapide, qui nécessite donc une plus grande rapidité d'acquisition: la mitose cellulaire.

Étude d'un échantillon vivant et en mouvement

L'amélioration de la vitesse d'acquisition a donc permis d'envisager l'étude d'échantillons *in vivo*, qui sont souvent problématiques en microscopie dû à leur mouvement 3D ou leur(s) déformation(s). Par exemple, les faisceaux mitotiques s'alignent lors de la métaphase et l'anaphase de la mitose d'une cellule, ce qui permet l'imagerie SHG des microtubules qu'ils contiennent tant que cette orientation perdure (les microtubules non-orientées rendent de milieu plus centro-symmétrique et la SHG s'annule). Un des défis dans l'étude de ce processus est de mesurer la polarité des microtubules lors des différentes phases de la mitose: c'est ce que se propose de faire l'article 8 principalement mené par mon collègue Stéphane Bancelin, sur des embryons de poisson-zèbre. Les microtubules changent d'état en moins d'une minute, heureusement la I-SHG rapide avec balayage laser permet d'acquérir des images de phase avec une résolution temporelle de 45sec. Ceci comprend notamment le temps de ré-ajustement de la position axiale du focus, et de la polarisation, qui doivent suivre les transformations de l'échantillon au cours du temps.

La Figure 14 montre l'évolution des microtubules vue par I-SHG dans cet échantillon, de la métaphase (t0) en passant par l'anaphase (t0+1min), jusqu'à la télophase (t0+3min). Deux interférogrammes en opposition de phase (à 0° (a) et 180° (b)) montrent que les microtubules interfèrent effectivement: le signal passe d'un maximum (a) à un minimum (b) sur le pôle du haut (carré rouge), et inversement pour le pôle du bas. Avec une superposition des deux images codées en rouge et vert, on voit d'autant mieux cette opposition de phase entre les deux pôles, qui ont donc une polarité différente (l'image complète de phase étant montrée sur la fig.3 de l'article).

Comme pour l'étude du déphasage de Gouy, les acquisitions problématiques sont celles du début et de la fin du processus, où le signal SHG est faible et la mesure de phase y est alors assez imprécise. Heureusement, la valeur absolue de la phase est peu importante contrairement à la mesure du déphasage de Gouy, et le niveau de la SHG de référence peut être adapté au faible signal, ce qui améliore la précision de la mesure (contraste optimal). Toutefois, un meilleur rapport signal-sur-bruit bénéficierait grandement à cette étude, tout comme une vitesse d'acquisition plus rapide, qui empêcherait des artefacts dus au mouvement des microtubules pendant l'acquisition.

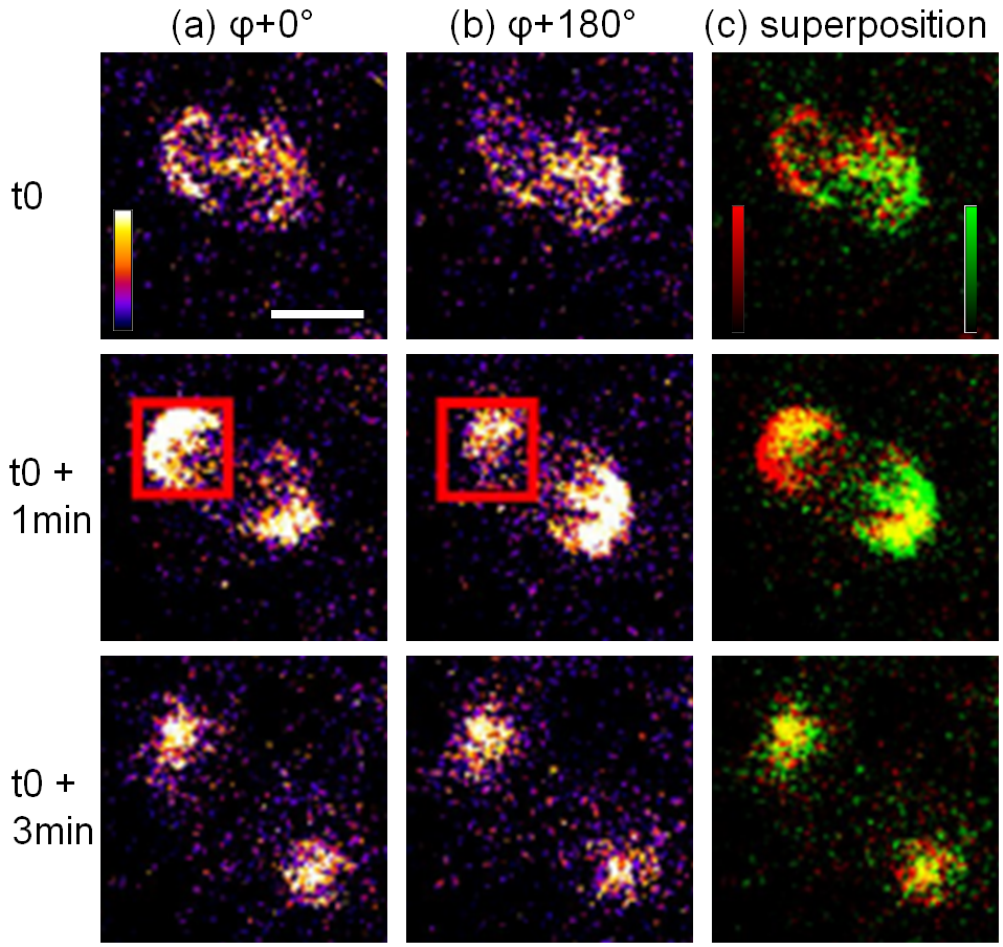

Figure 14: Microtubules d'un embryon de poisson-zèbre vue par I-SHG. Interférogrammes à des déphasages de 0° (a) et 180° (b). Des interférences constructives et destructives se produisent dans les 2 pôles de microtubules, visibles par une inversion de signal entre (a) et (b) à t0+1min (carré rouge). (c) Fusion en 2 couleurs des images acquises de (a) (en rouge) et (b) (en vert). Puissance focale moyenne: 100 mW, tube photomultiplicateur réglé à 1050 V. Barre d'échelle 10μm. Adapté de l'article 8.

I-SHG mono-scan

Le but est de réaliser plusieurs déphasages sub-microseconde lors de l'acquisition de chaque pixel de l'image, afin que toute l'information nécessaire pour retrouver la phase relative de ce pixel soit acquise de façon quasi-simultanée, en tout cas le plus rapproché dans le temps possible (Fig. 15 b). Ceci diffère de la I-SHG "standard" où chaque pixel de phase est reconstruit à partir de ceux des différents interférogrammes, qui sont alors espacés dans le temps d'une durée allant jusqu'au temps d'acquisition d'images entières, c'est-à-dire 45sec ou plus (dépendant de la taille de l'image et du nombre d'interférogrammes). En effet, le déphasage est changé à chaque interférogramme (ou image) et non à chaque pixel (Fig. 15 a).

Seul un module électro-optique (EOM) permet d'atteindre une vitesse suffisante pour déphaser intra-pixels, sans avoir besoin de ralentir d'un facteur trop important la vitesse de balayage (cadences de 50 à 500 kHz). Cela nécessite une synchronisation parfaite avec le système d'acquisition des images, et un modulateur permettant d'agir à la fois sur le faisceau d'excitation et sur la SHG de référence (pour garder un interféromètre à un seul bras, voir Fig. 3). Il est donc nécessaire de recourir à un système

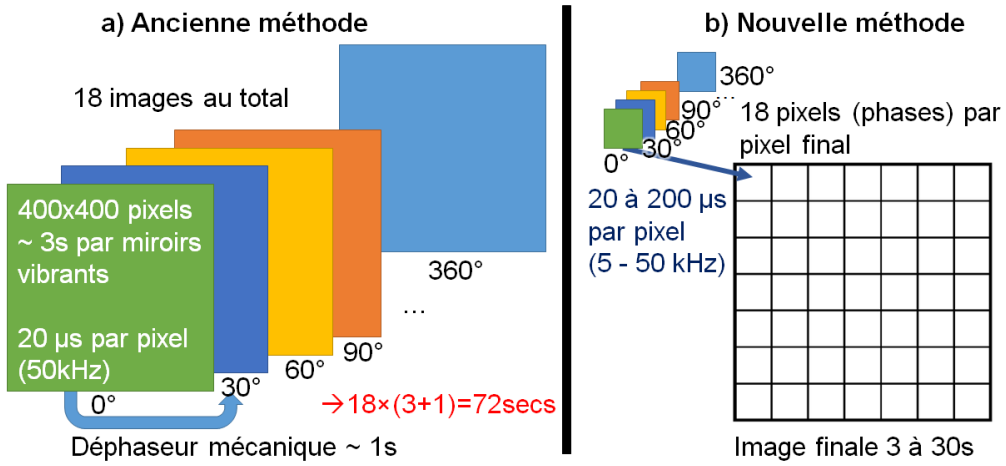

Figure 15: Méthodes standard (a) et rapide (b) pour le déphasage en I-SHG.

personnalisé (ces modulateurs sont généralement conçus pour travailler à une seule longueur d'onde), rendu possible par une collaboration avec la compagnie locale Axis Photonique. Le cristal nécessitant d'avoir, par définition, un indice optique qui varie de façon importante lorsqu'on lui applique un champ électrique (ici une haute tension), il aura aussi dans la plupart des cas une grande variation chromatique. On aura donc des effets de dispersion temporelle du 1er et 2e ordre dus au cristal: ceux du 1er ordre impliquent une GVM, qui peut être compensée en augmentant la quantité de calcite traversée (voir avant). Ceux du 2e ordre (aussi accentués par une épaisseur de calcite supplémentaire) impliquent un *chirp* plus important, et doivent donc être limités pour maintenir un niveau de contraste suffisant à la I-SHG.

Le principe de l'EOM est d'appliquer un déphasage complet à chaque pixel de l'image, pour ensuite diviser ces pixels en sous-pixels qui formeront les N interférogrammes servant à reconstruire l'image finale de I-SHG. Le temps par pixel, qui correspond donc à la durée des rampes de tension, peut être fixé à 20, 200 ou 2000μs. Dans l'article 9, est faite la démonstration de la I-SHG mono-scan (1S-ISHG, voir Fig. 3) sur un échantillon modèle de PPLN, puis est appliqué à deux tissus biologiques: le tendon de queue de souris, ainsi que le ménisque de l'articulation du genou de cheval, imagé par balayage de l'échantillon car le champ de vue doit être suffisamment grand (voir discussion précédente -1.3). Est reporté ici (Fig. 16) un dé-zoom (100μm^2) de la fig.3 de l'article, montrant la phase relative dans un tendon de queue de souris par 1S-ISHG (A et B), et sa comparaison avec la méthode standard (C). Les histogrammes de phase et la carte de couleur correspondante sont indiqués en-dessous des images. On voit que le mode le plus rapide (20μs, A) donne une image de phase moins bien définie et plus bruitée que la I-SHG standard: les distributions des domaines de phase à -$\pi/2$ et $\pi/2$ sont larges de $\sim 0.45\pi$ contre $\sim 0.35\pi$ pour la I-SHG standard (C).

Néanmoins, la discrimination des polarités opposées (phases espacées de π) est quand-même possible, et les images de phase des différents modes seraient les mêmes si cette distinction était uniquement représentée à l'aide d'une carte de couleurs rouge/vert (au lieu "d'arc-en-ciel"), comme utilisée dans les précédentes publications [9, 177, 175]. En augmentant le temps d'exposition (200μs, B), les distributions de phase se resserrent et la précision de la mesure est en effet améliorée: ceci correspond en effet à diminuer les fluctuations d'intensité δI dans l'équation 5), puisque, entre autres, le bruit de grenaille diminue avec $\sqrt{N_{ph}}$ où N_{ph} est le nombre de photons collectés (qui augmente avec le temps d'exposition). Le bruit accru sur la mesure de phase du mode 20μs (A) est d'ailleurs en grande partie dû aux fluctuations

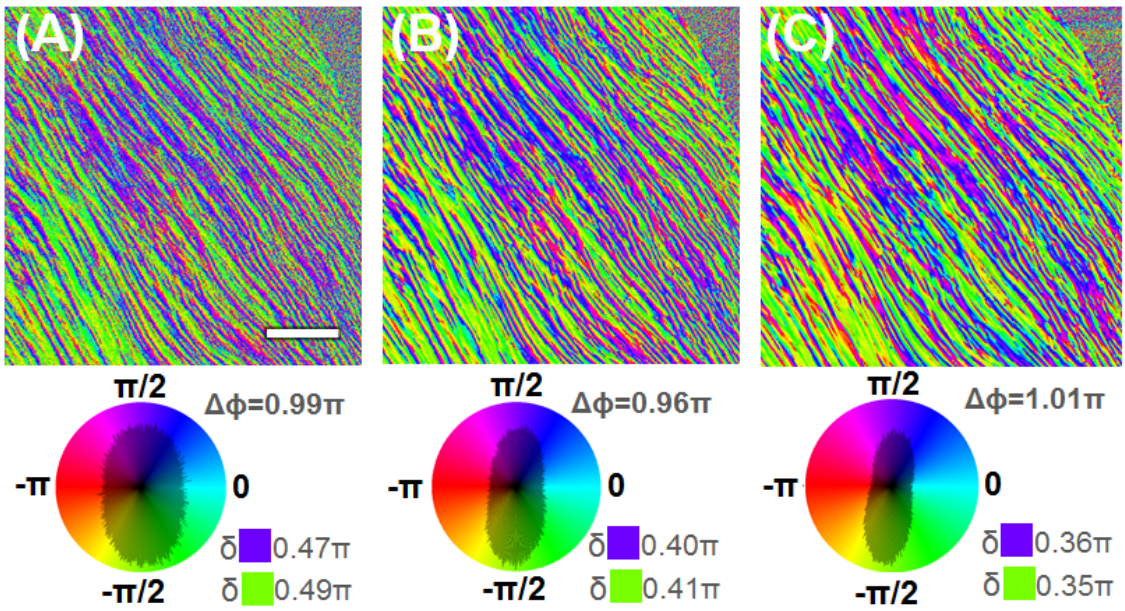

Figure 16: Démonstration de la I-SHG mono-scan dans du tendon de queue de souris (phase relative φ). (A) mode 20μs, (B) mode 200μs et (C) I-SHG standard avec 18 déphasages. Temps d'acquisition: 7sec (A), 53sec (B) et 150sec (D). Précision sur la distance entre les pics $\Delta\varphi$: 0.01π et 0.006π pour (C). Précision sur leur largeur $\delta\varphi$: $\sim$0.01π. Les distributions de phase sont représentées sur un histogramme polaire, où chaque valeur de phase correspond à une couleur. Barre d'échelle: 20μm.

temporelles du laser (autour de 500kHz), qui ne sont plus moyennées avec un temps d'exposition par sous-pixel de $\sim$20/20=1μs. On peut aussi le voir sur la Fig. 17 (ordonnées): la précision sur la mesure de phase varie peu avec les modes 200μs et plus lents (y compris la I-SHG statique standard), mais elle est divisée d'un facteur 2 avec le mode 20μs, et ce avec le PPLN ou le tendon. L'abscisse du graphe (échelle log) montre également que le passage du balayage de l'échantillon (marqueurs carrés bleus) au balayage laser (marqueurs triangles bleus) a permis de diminuer le temps d'acquisition de plus d'un ordre de grandeur, et que le mode 20μs de la 1S-ISHG permet de le diminuer d'un ordre de grandeur supplémentaire. On voit aussi qu'à précision égale, le mode 200μs reste 2 fois plus rapide que la I-SHG standard (triangles oranges versus bleus), et que les modes 2000μs peuvent être exécutés en un temps assez raisonnable ($\sim$10min) si le SNR de l'échantillon requiert un temps d'exposition élevé, ce qui permet une mesure de phase précise.

-1.6 Conclusion et perspectives

-1.6.1 Conclusion générale

Cette thèse a principalement porté sur le couplage de la microscopie de Génération de Seconde Harmonique Interférométrique (I-SHG) à un paradigme global d'imagerie multiphoton, impliquant d'autres techniques de microscopie et une compatibilité améliorée de la I-SHG avec celles-ci. Nous avons commencé par montrer les différents mécanismes influant sur la génération de seconde harmonique, afin d'être en mesure de correctement interpréter les images acquises avec cette technique. De plus, la I-SHG a été présentée en détail, avec ses limitations: entre autres, le fait que le signal mesuré soit le

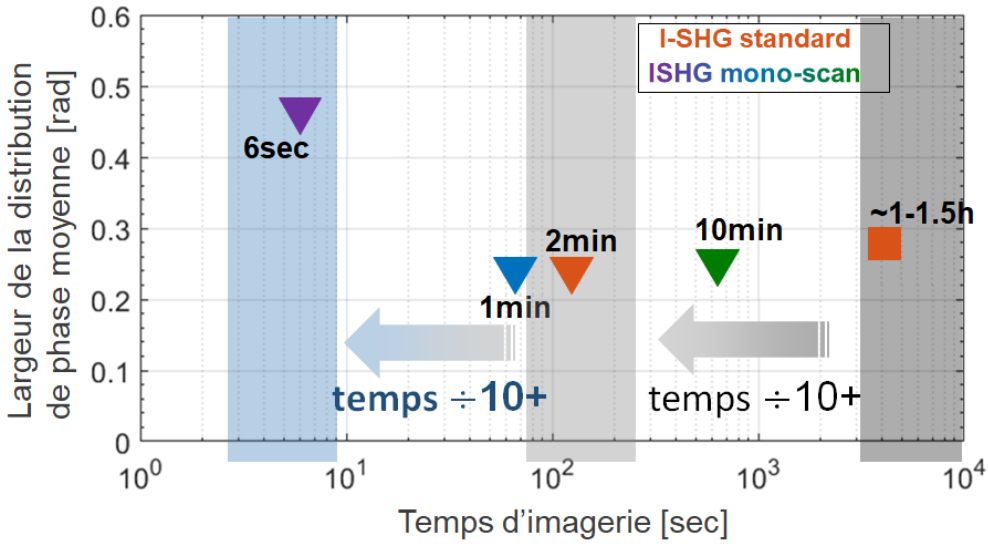

Figure 17: Comparaison du temps d'imagerie en I-SHG pour un balayage de $250\times250\mu m^2$, $0.5\mu m$/px (abscisse, en échelle logarithmique), par rapport à la largeur de distribution de phase (ordonnées), moyennée sur les deux pics de phase de l'échantillon modèle PPLN. Orange = déphaseur statique (I-SHG standard), vert = mode 2000μs, bleu = 200μs, violet = 20μs de la I-SHG mono-scan (1S-ISHG). Les durées correspondant aux acquisitions par balayage de l'échantillon (respectivement au balayage par laser) sont indiquées par des carrés (respectivement des triangles). La durée de la I-SHG standard par balayage de l'échantillon utilisé dans [10] est également indiquée (1.5h).

résultat d'interférences complexes. Pour surmonter ces limitations, il a été nécessaire de s'intéresser aux détails du montage de microscopie, de la production du signal laser jusqu'à l'acquisition des images, en passant par le contrôle électronique et logiciel des différents instruments. En particulier, la géométrie du montage optique et ses composantes ont été repensées pour pouvoir rendre la I-SHG plus versatile (notamment son utilisation avec un balayage laser ou un modulateur électro-optique, EOM), et intégrer d'autres modes de contraste comme le CARS (et sa variante modulée en fréquence, FM-CARS), la fluorescence à 2 photons (2PEF), la SHG résolue en polarisation (p-SHG) ou la SHG par dichroïsme circulaire (CD-SHG). De plus, un nouveau système de balayage laser par miroirs galvanométriques a été implémenté au niveau matériel et logiciel afin d'être plus compatible avec la I-SHG, et la microscopie SHG en général. Enfin, la platine de translation servant au balayage de l'échantillon a été totalement reprogrammée pour pouvoir changer les paramètres d'acquisition, éviter certaines déformations et diminuer le temps d'imagerie. Cette modalité est en effet toujours utile pour visualiser des structures nécessitant un grand champ de vue.

Le second objectif était d'appliquer cette implémentation de plusieurs modalités d'imagerie et grand champ de vue à l'étude du ménisque de l'articulation du genou, qui présente un agencement du collagène beaucoup plus complexe que la plupart des tissus contenant ce biopolymère. En particulier, la microscopie SHG "directionnelle" (*forward* et *backward*) a permis de différencier plusieurs agencements des fibrilles de collagène dans ce tissu: des fibrilles regroupées en fibres épaisses appelées "fibres d'attache", et d'autres formant des paquets dans la direction perpendiculaire appelés "faisceaux". En outre, la maturation de ce tissu a aussi été étudiée via l'alignement des fibrilles de collagène dans le plan d'imagerie par microscopie SHG résolue en polarisation. Cette modalité a montré de surcroit que les ménisques immatures présentent un alignement assez aléatoire du collagène, avec pour certains échantillons un arrangement au contraire très uniforme. Ce n'est qu'avec un tissu plus mature (adulte) que l'on retrouve des paquets assez

homogènes en alignement (faisceaux orthogonaux), délimités par des fibres épaisses (sections de "feuillet d'attache"), conformément au modèle proposé dans une autre étude sur des échantillons bovins [4].

De plus, il a été question d'étudier des aspects avancés de la microscopie SHG, qui pourrait en partie expliquer la complexité de la formation des images. L'un d'eux est le déphasage de Gouy que subit un faisceau en traversant son focus, et qui implique donc une variation de la phase au voisinage du volume focal: c'est donc un aspect très important pour la I-SHG, mais aussi en SHG standard. On a montré que ce déphasage pouvait être directement caractérisé par I-SHG par des mesures sur un échantillon très petit devant la taille du volume focal. Ceci implique aussi que cet effet agit sur toute image de phase de I-SHG, où des structures de même polarité mais légèrement décalées en profondeur présenteront des phases différentes.

Cet effet constitue un artefact aussi en microscopie SHG standard, dans certains agencements à même de lui donner un impact important. Par exemple, on a vu que dans les sarcomères du muscle, les alternances de filaments de myosine pouvaient être agencées en 3D de sorte à produire des artefacts cohérents (simple-bande), en partie dus au déphasage de Gouy. Voulant étudier un échantillon modèle présentant de manière similaire des séries d'interfaces entre deux polarités opposées (le PPLN), nous avons montré qu'il ne possédait pas d'artefacts cohérents, mais que des défauts à l'échelle nanométrique créaient une contribution de diffusion importante. Cela a été l'occasion d'étudier le patron de radiation à ces interfaces par simulations numériques, et ainsi éclaircir ce point peu discuté dans la littérature: la SHG générée à une interface de polarités opposées prend toujours la forme de deux lobes délimités par l'interface, d'amplitude opposée (i.e. déphasés de π). Ces lobes sont donc supposés interférer destructivement une fois recombinés sur le détecteur. Nous avons ainsi montré que la I-SHG permettait de retrouver l'effet de ces interférences destructives (i.e. zéro signal) aux interfaces présentant ces artefacts, et d'augmenter la visibilité de celles ne présentant pas d'artefacts d'un facteur 3 à 5.

Enfin, le dernier objectif a été de bénéficier des améliorations sus-mentionnées pour rendre la I-SHG plus versatile et rapide. Le contrôle des méthodes de balayage a été décisif, mais aussi le développement complet d'une interface logicielle pour le fonctionnement du microscope, la prise d'image, le traitement des données et leur mise en forme. L'imagerie d'un processus dynamique (la mitose cellulaire) nous a permis de constater que la I-SHG femtoseconde par balayage laser pouvait être utilisée, mais a aussi montré les limites expérimentales de ce mode d'acquisition. On a ensuite vu la possibilité d'utiliser l'effet électro-optique pour appliquer le déphasage nécessaire à la I-SHG à une cadence allant jusqu'à celle utilisée pour former les images ($\sim$50kHz), et ce même avec un interféromètre à bras unique agissant sur deux longueurs d'onde différentes. Il a fallu toutefois étudier en détail les mécanismes qui gouvernent le contraste interférométrique: ceux-ci font un peu intervenir le recouvrement spatial des faisceaux, mais surtout leur recouvrement temporel, qu'il faut donc optimiser et corrigeant les dispersions du 1er et 2e ordre impactant les impulsions femtosecondes. Cette avancée a ainsi permis d'appliquer les déphasages pendant l'acquisition des pixels, plutôt qu'entre chaque interférogrammes, ce qui a convertit la I-SHG en une acquisition mono-scan (1S-ISHG). Avec l'échantillon modèle de PPLN et des échantillons de tendon de queue de souris et de ménisque équin, on a montré que ce mode d'acquisition donnait effectivement des résultats similaires à la méthode normale, pourvu que le nombre de photons collectés soit équivalent. La 1S-ISHG permet également d'obtenir des images de I-SHG (phase et amplitude) en un temps égal à celui d'une image de SHG standard si le mode rapide est utilisé. Puisque moins de photons sont collectés, la précision sur la phase est moins bonne mais on peut quand-même retrouver la bonne polarité à chaque pixel (car cela revient juste à discriminer si la phase se situe plutôt autour de $\pi/2$ ou de $-\pi/2$).

Toutes ces améliorations permettent ainsi de développer moins d'efforts expérimentaux et informatiques pour réaliser des images de I-SHG. De plus, nous avons aussi réussi à intégrer la I-SHG dans un

paradigme plus général, qui englobe d'autres variantes de la SHG et de la microscopie multiphoton dans son ensemble. Il reste néanmoins du potentiel pour pousser cette intégration encore plus loin.

-1.6.2 Perspectives

Cette amélioration de la vitesse par plus d'un ordre de grandeur pourra servir à caractériser des processus dynamiques: en particulier, l'imagerie des microtubules pourra grandement en bénéficier, et servir à élucider le débat - en cours dans la littérature - sur la polarité locale et globale de ces protéines dans les dentrites des neurones, ou les fibroblastes. Cela pourra également être appliqué à des études systématiques à grande échelle (grand nombre d'échantillon). Le nouveau programme du microscope, et le couplage multimodal de celui-ci seront d'une grande utilité pour l'étude de futurs échantillons biologiques ou de matériaux optiquement nonlinéaires. Enfin, la structure du ménisque présente encore des parts d'ombre, et pourra également tirer de nombreux bénéfices d'une imagerie par microscopie multimodale alliée à l'I-SHG.

Contents

List of Figures

List of Tables

List of abbreviations

$\chi^{(n)}$	nth-order non-linear susceptibility (n=2,3)
λ	Wavelength of light
μm	micrometer [10^{-6}m]
(P)BS	(Polarization) Beam-Splitter
2D	Two dimensions
3D	Three dimensions
wrt	with respect to
AOI	Angle Of Incidence
BBO	Beta-Barium Borate, a nonlinear crystal.
BW	BandWidth
CARS	Coherent Anti-Stokes Raman Scattering, a coherent parametric four-waves mixing
CCD	Charged-Coupled Device, a video-camera.
CD-SHG	Circular-dichroism SHG
CH, CH2	Chemical bonds carbon-hydrogen
DIC	Differential Interference Contrast
DSP	Digital signal processing
EOM	Electro-Optic Modulator
F/B	Forward over Backward ratio of SHG.
FOV	Field-Of-View, the area imaged by the imaging technique
FROG	Frequency Resolved Optical Gating, an optical characterization technique of ultrashort pulses
fs	femtosecond [10^{-15}s]
FT	Fourier Transform
FWHM	Full-Width at Half-Maximum, width of a distribution/a pulse

FWM	Four-waves mixing, a nonlinear optical process
GDD	Group Delay Dispersion, a 2nd-order dispersion effect (chirp) related to the optical index
GUI	Graphical User Interface
GVM	Group Velocity Mismatch, a dispersion effect related to the optical index
HWP	Half-Wave Plate, an optics applying a π retardation along a given axis
I-SHG, ISHG	Interferometric SHG
IR	Infrared (light)
KD*P	Potassium Dideuterium Phosphate, a nonlinear crystal.
LiNbO3	Lithium Niobate, a nonlinear crystal.
log	Napierian logarithm
MPM	MultiPhoton Microscopy
N.A.(NA)	Numerical aperture of the collecting/focusing optics
nm	nanometer [10^{-9}m]
OCT	Optical Coherence Tomography, a medical imaging technique using light
OPT	Optical Projection Tomography, a medical imaging technique using light
p-SHG	Polarization-resolved SHG
pm	picometer [10^{-12}m]
PMT	Photo-Multiplier Tube, a light detector.
PPLN	Periodically-Poled Lithium Niobate, a nonlinear crystal used for quasi phase-matching.
ps	picosecond [10^{-12}s]
QWP	Quarter-Wave Plate, an optics applying a $\pi/2$ retardation along a given axis
ROI	Region-Of-Interest, a selected fraction of the image
RTP	Rubidium Titanyl Phosphate, a nonlinear crystal.
SHG	Second-Harmonic Generation
SNR	Signal-to-Noise Ratio
SPM	Self-Phase Modulation, a four-wave mixing process
SRS	Stimulated Raman Scattering, a coherent parametric four-waves mixing
THG	Third-Harmonic Generation
TPEF,2PEF	Two-Photon Excited Fluorescence
W.D.	Working Distance of an objective lens

Introduction

This PhD was conducted at INRS-EMT (Varennes, QC, Canada) under the supervision of François Légaré, in the multiphoton microscopy laboratory. This laboratory aims to develop nonlinear optics applied to microscopy in biological samples, as well as inorganic samples ranging from structured materials to thin films. To that end, cooperative work is possible with other labs present at EMT (biochemistry, micro and nano-fabrication, etc.) and other INRS institutions located near Montréal. In 2013, this laboratory reported the implementation of Interferometric-SHG (I-SHG) as a probe of the relative polarity of some proteins arranged in biopolymers. Second-harmonic generation (SHG) microscopy is a nonlinear technique that uses the SHG process inside samples lacking an inversion center, i.e. the conversion of two incident photons into one having twice the optical frequency of the incident light. This technique has become the gold standard for minimally-invasive *in-situ* 3D imaging of some structural proteins like collagen [189], due to its high specificity for these proteins, and its relatively low invasiveness. This tends to replace ([34], Preface) the old gold-standard for this type of imaging, histology ; a technique that cut thin slices of bio-samples to be placed in-vitro for observation, coupled with different staining to enhance the otherwise poor contrast.

However, if coherence can be a true asset of SHG imaging, it is also its main drawback. There can be interferences between all SHG converters, such that an SHG image is the result of these complex interferences, and not a direct image of the structure, as with fluorescence. It is often stated that constructive interferences explain the construction of a strong forward SHG signal, because the coherence length in forward SHG is larger than the focal volume [154]. Yet, structures of opposite polarity can still destructively interfere, and lead to zones with low signal in the image [176]. This implicitly suggests that there are less SHG converters in these areas. This effect can be considered as an imaging artifact: for instance, sarcomeres in muscle present a dip of signal at the overlap of the myosin ends, although this dip is not visible if the scattered light is incoherent as for fluorescence. Furthermore, knowing the

polarity of microtubules could be a milestone for the understanding of various pathologies: cancer on the one hand, as microtubules guide chromosomes during cell mitosis, and Alzheimer disease on the other hand, as they regulate transport in neurons and seemed to show uniform or non-uniform polarity at various scales [7]. In tissues also, the polarity information is crucial for the transparency of cornea, and for mechanical and electrical properties of other collagen-rich ones such as skin, tendon, etc. Measuring the relative polarity locally inside such samples is therefore judicious, and can be done by I-SHG using interferometry to measure the phase of the SHG light, which acquire a supplementary factor of π if the polarity is inverted. This has allowed the microscopy lab to further explain the structure of various tissues (fascia, muscle, tendon, cartilage, etc.) through the work of the previous PhD student M. Rivard and MSc student C.A. Couture [176, 175, 177, 46]. Other microscopy paradigms have also been developed in the lab, such as nonlinear Raman and multiphoton fluorescence.

The goal of this PhD thesis was to further develop and apply these aspects to various biological and non-biological problems, using the different collaborators of Prof. Légaré. Above all, an important part of this project was to enhance the I-SHG technique, which suffered, for instance, from a low acquisition speed. This required a complete re-think of the organization of the microscopy set-up, which was working at its limit in terms of stability and performances. Lastly, it was also planned to continue the collaboration between the LOB in France, initiated by Claire Teulon (former PhD student) and her supervisor Marie-Claire Schanne-Klein (LOB), and my colleague S. Bancelin at INRS. This collaboration aimed at coupling a set of images of the same sample, a part of this set acquired by polarization-resolved SHG (p-SHG) at the LOB, and the other part by I-SHG at INRS. The ultimate goal was to implement these techniques in both laboratories to avoid the inconvenience of dealing with two different set-ups, moreover separated by a long distance. These two techniques are to some extent complementary and, when coupled, allow for the mapping of the 3D orientation of the biopolymers across the sample. Three months of this PhD therefore took place in the LOB in France, where I learnt p-SHG imaging. I then decided to improve its implementation at INRS: some p-SHG measurements had already been performed by M.A. Houle during her Master's, but did not meet the sufficient precision and the advanced analysis required for the new samples we wanted to study. This is the purpose of chapter 4, which shows an application to a complex tissue: the meniscus inside knee-joints. The furthering of I-SHG has been progressive: it was shown that an optical effect called the Gouy phase-shift could be measured (chapter 7), and that this technique allows for the removal of some imaging artifacts in the SHG images (chapter 6). The speed improvement was first performed by adapting I-SHG to laser-scanning set-ups (chapter 7

), which was applied to the study of a dynamic process: the measurement of the polarity of microtubules inside a cell during mitosis (chapter 8). Secondly, to circumvent some limitations encountered in this study, a method that reduces the imaging time by another order of magnitude was implemented: single-scan I-SHG (1S-ISHG), which is the subject of the last chapter (chapter 9) and represents the largest contribution of the project.

Outline

This thesis is presented in the format of a thesis by articles.

Chapter 1 offers a literature review, coupled with important theoretical aspects used throughout the manuscript.

Chapter 2 focuses on SHG microscopy.

Chapter 3 aims to describe the numerous technical aspects treated during the project.

Chapter 4 presents an example of multimodal microscopy applied to a complex tissue, the meniscus.

Chapter 5 shows that coupling SHG microscopy with interferometry allows for the characterization of the Gouy phase-shift through a focal point.

Chapter 6 exposes the elimination of some imaging artifact in SHG microscopy using its enhanced version, interferometric SHG (I-SHG).

Chapter 7 relates the implementation of fast I-SHG using laser-scanning and femtosecond pulses.

Chapter 8 is an application of the article of chapter 7, that benefits from the speed improvement to image the polarity of microtubules in mitotic spindles.

Chapter 9 describes the final goal of the project: the implementation of single-frame I-SHG acquisition using electro-optics.

Part I

Background

Chapter 1

Scanning Microscopy and Nonlinear Optics

The wager of modern Physics is to explain the real by the impossible Alexandre Koyré

This chapter deals with generalities about microscopy, nonlinear optics and the coupling of both. After comparing different medical imaging paradigms, scanning microscopy is described and nonlinear processes are detailed. Finally, multiphoton microscopies are developed and their possible combination is presented.

1.1 Different types of biological imaging and how they compare

Medical imaging is a part of the more general term "biological imaging", and is supposed to be restricted to imaging of parts of the human body. Therefore, its different techniques are supposed to be aimed towards a clinical environment. However, the categorization of the techniques is not that definitive, because all of them are also used in scientific research for technical improvements, and more specifically in biology for characterization of structures or processes that are too small to be detectable with the

human eye. Also, some techniques are not yet in hospitals for reasons other than performances, because it takes efforts and money to generalize a laboratory apparatus to a non-specialist environment. A new technique must indeed prove to have a relative ease-of-use and enhanced performance - compared to the gold standard - in order to be implemented, for both pecuniary reasons and because it is a long process to train new practitioners to use it. That is why some techniques, currently restricted to the specialist literature, may extend their labelling in the future from "biological imaging" to "medical imaging". We present thereafter different biological imaging techniques that are related - or have comparison points - with the project of the thesis.

1.1.1 Introduction to optical microscopies, and nonlinear optics

The first optical microscope was commercialized in 1846 by Carl Zeiss in Jena, Germany ([34], Series Preface). Kholer invented the dark-field microscope in 1903. In 1935, Zernike developed the phase-contrast microscope [252], and Nomarski the differential interference contrast (DIC) microscope in 1952. All these techniques were meant to improve the contrast and resolution of the classical bright-field microscope. However, these techniques need a bright light to work, a well-controlled set-up with no dirt and perfect optics (including the slides), and more problematically a thin sample that does not scatter light too much. The challenge was later to adapt microscopy to overpass the need for controlled *in-vitro* samples, by increasing the light penetration without degradation. In 1969, Davidovits & Egger developed the first laser-scanning microscope [49] using an objective-scanning instead of the sample-scanning previously reported, with a He-Ne laser, and inspired by a patent from Minsky. Now the illumination is point-by-point, to be able to effectively filter the light. Sheppard & Choudhury published in 1977 the first paper mentioning a "confocal microscope", and Brakenhoff described in 1979 an ambitious set-up using sample-scanning. All these advances used the light from the source to image a structure, without conversion: a paradigm change was later made when the detected light was produced by the sample. This means a different color from the excitation one, i.e. a good contrast (and in some cases a non-linearity).

Nonlinear optics had been theoretically predicted back in 1931 by Maria Goeppert-Mayer in her PhD thesis [74], where she described the two-photon absorption process. Indeed, since the electronic levels are quantified, it should be possible to excite electrons to an upper level by using the energy of not only one but several photons, in an additive way. It was applied only 30 years later, shortly after the

invention of the laser in 1961, because a sufficient number of photons must interact in the same spatio-temporal interval for this non-linearity to happen. During this year, Kaiser and Garrett reported the two-photons fluorescence process [108], and Franken *et al.* reported the Second-Harmonic Generation (SHG) in quartz [67]. Even though both are two-photons processes, they are different by their nature: fluorescence is the result of the de-excitation of electrons in a radiative way (the emitted frequency is thus always smaller than the excitation one), while harmonic generation is a resonant process where dipoles inside a given structure will vibrate inelastically if a sufficient photon energy is provided, such that a part of the scattered field will have a frequency that is a multiple of the original frequency (=2 for SHG). Mahan explained two-photons spectroscopy in 1968, Fine & Hansen reported SHG from biological tissue samples in 1971 and later Roth & Freund described SHG from collagen in 1979 [180], but the first image of rat-tail tendon by SHG microscopy was only acquired in 1985 by Freund & Deutsch [68]. Notably, Coherent-Anti-Stokes Raman Scattering (CARS) microscopy was described even before SHG microscopy, in 1982 by Duncan *et al.* [59]. This is a four-wave mixing process, involving a pump laser beam at frequency ω_p and a Stokes laser beam at ω_s. The resonant oscillators can be coherently driven if one of their Raman molecular vibrations is at the beat frequency $\omega_{vib} = \omega_p - \omega_s$, which generates a strong anti-Stokes signal at $\omega_{as} = 2\omega_p - \omega_s$. Since it is a coherent generation, it is several orders of magnitude more intense than the usual spontaneous Raman effect [65].

Later, the publications of Denk *et al.* [53] lead to the rise of multiphoton microscopy, particularly of multiphoton fluorescence. In parallel, Huang *et al.* developed, in 1991, Optical Coherence Tomography (OCT), a technique that exploits interferometry to selectively image the non-scattered photons reflected by a tissue. The resolution is lower than microscopy, but its high penetration depth (several cm) led to this technique being rapidly adopted, as it is in-between microscopy and ultrasound imaging. Probably because of the need for even more photon confinement at focus, Third-Harmonic Generation (THG) microscopy was reported only 10 years after SHG, in 1997 by Barad *et al.* The Abbe/Rayleigh theoretical limit of resolution is essentially half the wavelength, which means 200nm at best for visible light. In 1994, Hell *et al.* described a solution to enhance this resolution by one order of magnitude with a technique called STED (Stimulated-Emission-Depletion fluorescence microscopy). Another 10 years were needed to see the real inception of nanoscopy, also called super-resolution fluorescence microscopy, by improvements to STED and by the publication of a different technique called PALM by Betzig *et al.* in 2006 [184]. These techniques have been also used with multiphoton excitation. Since then,

many improvements in resolution, contrast, imaging depth, acquisition speed, cost and others have been extensively reported in literature[97].

1.1.2 Optical microscopies

Optical microscopies use electromagnetic waves, traditionally with wavelengths that can go from the UV (100-400nm) to the THz ranges (0.1 to 1mm), but most often in or close to the visible range (400-800nm). In 1873, the German E. Abbe studied gratings and showed that the resolving power of the microscope for lines imaging is the famous formula:

$$D = \lambda/(2N.A.) \tag{1.1}$$

Years later, Lord Rayleigh investigated spots (not lines), and showed that their images are Airy disks, which means the theoretical resolution is Abbe's criterion with a 1.22 factor for round points [8], thus generalizing the formula. This is where the term "microscopy" comes from: the resolution is limited by the wavelength, thus in the order of magnitude of the micron. However, this is only true in far-field detection: the propagation actually acts as a low-pass filter, that imposes an exponential decay on the high spatial frequencies (a consequence of diffraction). Thus, in the near-field, it is possible to have a much higher resolution, only limited by the instrument detection and not the wavelength. However, the near-field is by definition at distance much smaller than the wavelength, i.e. below 100nm: the instrument thus must have a probe less than 100nm from the sample. This is the domain of "local probe" imaging, the optical technique for which is called SNOM (Scanning Near-Field Optical Microscopy). This information was obtained in the book "Principles of nano-optics" [144], which we refer to for further knowledge on these techniques. As mentioned earlier, nanoscopy is also completed by the "super-resolution" imaging methods (STED and PALM/STORM). However, these are only applicable to biological samples, as they require staining, dyes or fluorescent proteins in a controlled concentration to reconstruct a sub-diffraction image. The images are still acquired with a diffraction-limited optical microscope, but a non-linearity (for STED), or an image reconstruction (for PALM/STORM) allows us to go beyond this limit. These techniques have opened new possibilities to optical microscopy, such as imaging of the nucleus inside cells: cells can be of various sizes, usually between 1 and 100μm, while their nucleus is much smaller, 10μm in each dimension for human cells. Probing the inside of this structure must therefore be done with the resolution of the super-resolution microscopes: 20nm is the size of assembling of proteins

involved in DNA organization, for instance. Different examples of structures of interest in biology are

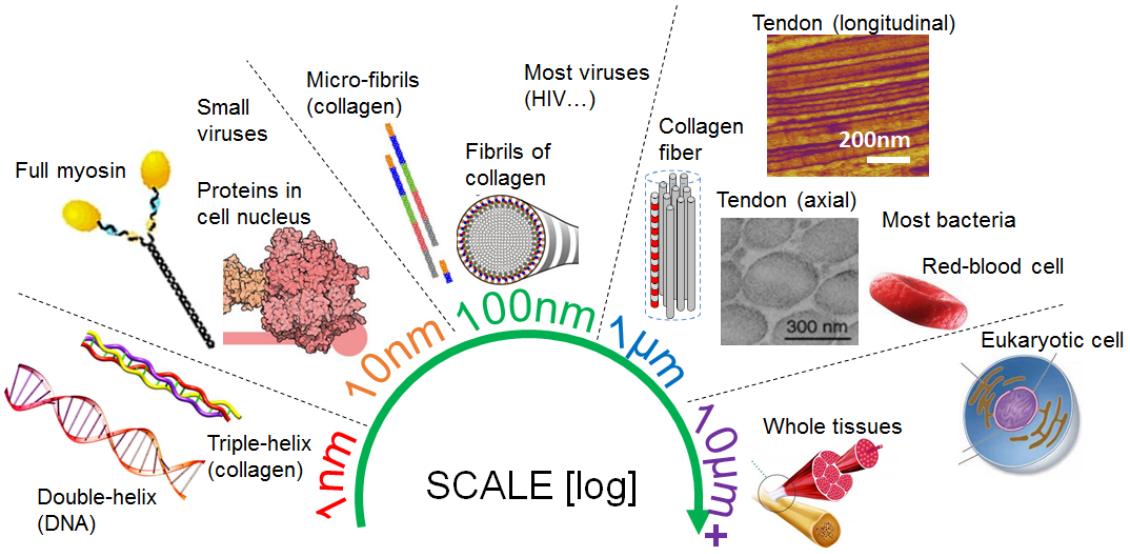

Figure 1.1: Different scaling in biology, from the molecular (nm) to the tissue level (μm). Inspired from [216], fig.1.1.

presented in Fig. 1.1. Optical microscopy is limited to the μm scale, and can thus access collagen fibers, but cannot resolve multiple fibrils which are only a few 10 to 100nm large in diameter. However, its field-of-view usually allows the imaging of full eukaryotic cells, and even large parts of tissues which are from $\sim$100μm to several mm large. Most proteins are below 100nm (in diameter), as well as, for instance, some biopolymers as myosin. The triple-helix of collagen is closer to the nm scale, and so is the double-helix of DNA. The nm resolved images of tendon' fibrils (below 1μm) of Fig. 1.1 were performed with a technique that uses another type of wave for imaging: electronic microscopy.

1.1.3 Electronic microscopies

Electronic microscopies can be divided into two main categories: those which work by reflection (SEM for Scanning Electron Microscopy), and those which work by transmission (TEM for Transmission Electron Microscopy). These microscopies are also limited by diffraction. However, they use a particle that has a mass (electrons), so their associated wavelength is described by the De Broglie equation: $\lambda = h/\sqrt{(2mE)(1+E/2mc^2)}$, where h is the Planck constant, m the mass of the electron, E its energy and c the speed of light in vacuum. For energies of 1-10keV (SEM) to more than 100keV (TEM), the wavelength is then of the order of 10pm to a few pm. The resolution can thus be less than an ängstrom, which is difficult to obtain with electromagnetic waves. The main drawback of electronic microscopies

is the preparation of the samples, which often involves embedding in resin to cut slices thinner than 100nm, the use of electronic markers and a drying and cleaning step, since the sample is inserted in a vacuum chamber.

1.1.4 Optical projection tomography (OPT)

Optical Projection Tomography (OPT) is a type of computed tomography (CT): the same tomographical reconstruction is employed i.e. solving an inverse problem to reconstruct the image [197]. However, it uses visible light (or near-UV, near-IR) and not X-rays. The resolution of OPT is not as good as confocal or multiphoton microscopy (above 1 μm[145]), but OPT can image on much larger 3D sizes (up to 10mm) [197]. Its penetration depth is also comparable to OCT, at a few mm: this technique can easily go deeper, but at a high cost in signal-to-noise ratio [145]. Colored stains can also be imaged in 3D with OPT, whereas microscopy operates with fluorescent dyes instead [197].

1.1.5 Optical coherence tomography (OCT)

Optical Coherence Tomography (OCT) is closer to ultrasound imaging than tomography: it uses a selection of the reflected photons on a structure based on their time-of-flight to select a precise slice (orthogonal to the light propagation) of the sample being imaged. For this, a Michelson interferometer is combined with a low coherence light source [197].

It has similarities with microscopy, for instance in the full-field version, that also uses a microscope objective to have a lateral resolution at the diffraction limit. Its performances (penetration depth, signal-to-noise ratio (SNR)) are mostly limited by the number of photons that are reflected by the Z-plane being imaged.

1.1.6 Comparison of the different techniques

Figure 1.2 shows the techniques used in medical imaging, splitting the ones having a sufficient penetration depth (few cm) to be applied in hospitals from the ones usable only on *ex-vivo* samples and thus are more suitable for biological research or to detect pathologies. OCT is at a position where it is operated both in hospitals and imaging research. Note that the *in-vivo* limit tends to be pushed further as the

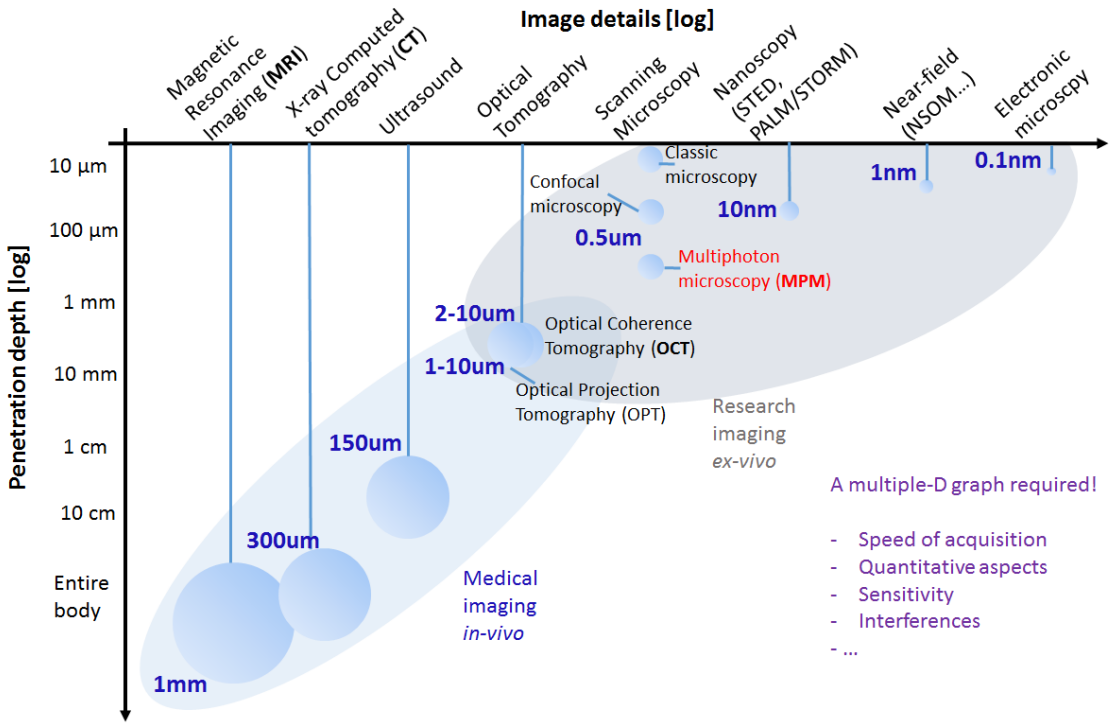

Figure 1.2: Comparison of the different techniques of medical imaging, for the resolution and the depth penetration.

different techniques improve, and optical microscopy could in the future be implemented in hospitals if the penetration depth is sufficient, through the development of endoscopy, for instance.

Of course, this graph is an approximation, because the values of resolution and penetration can vary a lot within a technique if its complexity is increased. Also, as indicated on Fig. 1.2, when determining the suitable imaging technique for a specific purpose, other significant parameters have to be considered: acquisition speed, possibility of quantitative measurements, sensitivity to certain part of the sample, possible interferences or artifacts, etc. The presence of interferences can reduce the reliability, and sensitivity to special types of molecules can be a real asset. Also, the ability to measure quantitative parameters (e.g. like in MRI) can be paramount, and the speed of acquisition can greatly limit the applicability of the technique to some applications that probe dynamic process or moving samples, for instance.

1.2 Nonlinear processes

We will detail nonlinear processes more specifically. Nonlinearities necessitate several photons, but the physical processes can be very different.

1.2.1 Parametric processes

Description

An electron being excited (e.g. by an incoming photon) will travel in its potential: it can travel through a small portion of it - if the excitation is low - which can be approximated as a parabola, which makes the process linear, and is also called elastic by analogy with mechanics. But a larger part of this potential is travelled if the exciting field is strong enough, and the electron or the electron assembly will experience a nonlinear (inelastic) oscillation.

Figure 1.3 a) shows the example of second-harmonic generation (SHG) , which is one of the terms of the Fourier decomposition of the anharmonic response of the electron being excited by a strong electromagnetic field. In other words, this inelastic oscillation of the electrons will be (partially) "transmitted"

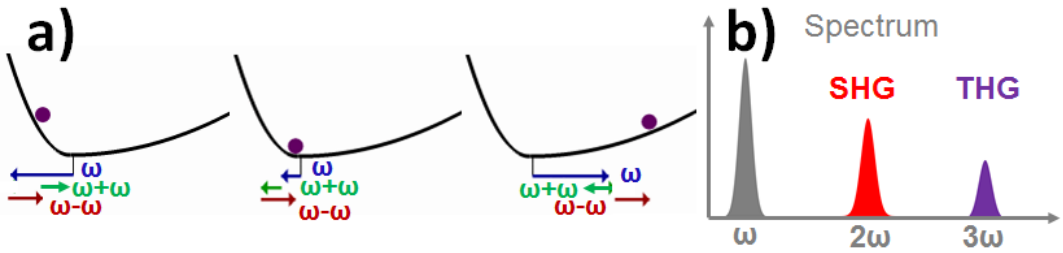

Figure 1.3: a) An electron (purple) is being pushed side-to-side by a sinusoidally-oscillating force induced by the excitating electric field, but because the electron is in an anharmonic potential energy environment (black curve), the electron motion is not sinusoidal. The three arrows show the Fourier decomposition of the motion: the blue arrow corresponds to the ordinary (linear) susceptibility (leading to the same frequency as excitation), the green arrow corresponds to second-harmonic generation (leading to twice the frequency of excitation), and the red arrow corresponds to optical rectification (leading to a difference of frequency equal to 0). Extracted from [187]. b) Corresponding spectra of the parametric processes, showing similar shape and width for excitation and two particular cases: SHG and THG.

to the exciting field, therefore changing its (fundamental) frequency for one of its harmonics. This conversion is thus possible if the medium allows vibrations at these frequencies. Due to the symmetry, it can be shown that any medium having a center of symmetry will anihilate all the Nth harmonics, N being even [20].

All parametric processes have some interesting properties in common, that are not shared by electron-transfer processes:

- the electrons will not be excited to a defined (real) energy level [28]

- the process is instantaneous [28]

- the temporal and spatial coherence of the fundamental photons are preserved [35]: in other words, they conserve phase and directionality information. In particular, the spectrum of the nth harmonic will be similar in width and shape to the fundamental excitation (fig. 1.3 b)).

Multiple harmonic generation

Multiple harmonic generation are multiphoton parametric processes as described before, but which involve a single excitation wavelength. Figure 1.4 shows that a nth harmonic generation *always* happens if a medium has a non-zero, non-linear susceptibility of the nth order, and that the different harmonics are all generated *at the same time*. However, the higher the harmonic is, the higher the number of photons needed to be combined to generate it, so the probability that it happens will be lower. Some media with sufficiently high non-linear properties can generate up to the fourth harmonic (FHG) in quite a large quantity [173]. Within a standard medium and with an average detector, only SHG and THG are

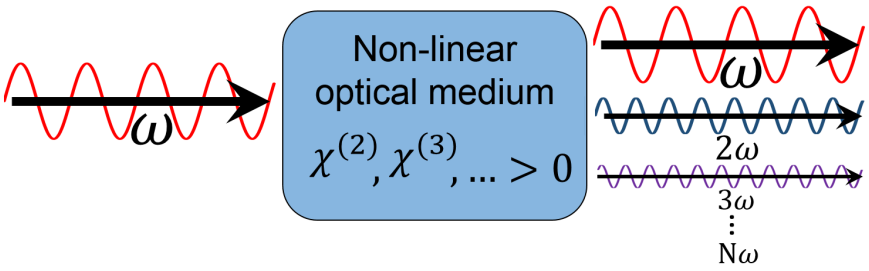

Figure 1.4: Schematic diagram of the multiple harmonic generation, illustrated by the most probable ones: SHG and THG.

usually detected, though. Also, some conditions in the structure and/or orientation of the sample can tune the generation of one process more than others. For instance, SHG can be preferably converted under certain conditions, and in practice the other processes like THG will then remain relatively low. Actually, many conditions affect the conversion to SHG or THG - as will be described later - and the possibilities to convert a large amount of one type of harmonic greatly depends on the structure being excited (homogeneity, symmetries, etc.).

Note that the self-phase modulation and self-focusing are also parametric third-order non-linear processes (see [211] "Nonlinear Index of Refraction", p.369), that involve only one wavelength. For self-phase modulation (SPM), the Kerr effect will modify the optical index, which will produce a non-linear phase relationship [20]. Self-focusing is the exact same effect, but in space instead of time: the wave equation being rigorously similar in space and time, the description is similar to SPM. In practice, the beam will tend to focus itself if the laser intensity is over a threshold, which goes against the normal behavior of a pulse to diverge with propagation because of diffraction.

Sum and difference frequency generation

If two fields of frequency ω_1 and ω_2 are sent on a medium with a non-zero $\chi^{(2)}$, many processes can happen as described by [18]:

$$\begin{aligned}
&P(\omega_1+\omega_1) \propto \chi^{(2)} {E_1}^2 && \text{(SHG 1)}\\
&P(\omega_2+\omega_2) \propto \chi^{(2)} {E_2}^2 && \text{(SHG 2)}\\
&P(\omega_1+\omega_2) \propto 2\chi^{(2)} E_1 E_2 && \text{(SFG)}\\
&P(\omega_1-\omega_2) \propto 2\chi^{(2)} E_1 {E_2}^* \quad \text{or} \quad P(\omega_2-\omega_1) \propto 2\chi^{(2)} E_2 {E_1}^* && \text{(DFG)}\\
&P(\omega_1-\omega_1=0 \;\;\&\;\; \omega_2-\omega_2=0) \propto 2\chi^{(2)}(E_1{E_1}^* + E_2{E_2}^*) && \text{(OR)}
\end{aligned} \tag{1.2}$$

$\chi^{(2)}$ is the nonlinear susceptibility tensor: we will introduce it in detail in the next chapter. For now, we can just consider it as a proportionality factor between the product of electric fields E and the induced polarization $P(\omega)$.

Sum Frequency Generation (SFG) is similar to SHG, as SHG can be considered as a particular case of SFG. Two fields at two different frequencies combine to produce a field whose frequency is the sum of exciting frequencies ($\omega_1 + \omega_2$ here). If one of the exciting frequencies is at the resonance of a chemical bond of the medium, the SFG is enhanced [92]: this effect can be exploited to do, for example, spectroscopy, or to have a better contrast than SHG imaging [90].

The Difference Frequency Generation is the basic principle of an Optical Parametric Oscillator (OPO). Like SFG, two fields at different frequencies combine, but produce a frequency that is the difference of exciting frequencies (ω_1 - ω_2 or ω_2 - ω_1 here). Usually one of the fields is only used to seed the process, and its intensity is much lower [18].

The Optical Rectification (OR) is a special case of DFG where the two frequencies are the same, leading

to a static polarization. It is sometimes referred to when two frequencies of the same pulse are subtracted to give an OR of $\sim$ 10THz for TeraHertz radiation generation [15], but is closer to a DFG process.

Raman processes: CARS and SRS

Coherent Anti-Stokes Raman Scattering (CARS) and Stimulated Raman Scattering (SRS) are third-order processes that consist of an enhancement of the Raman scattering: the medium scatters an excitation photon, but at a lower energy (at a frequency called the Stokes frequency) since another part of the energy is lost to a vibration of a chemical bond. This is the inelastic scattering described by Raman, but selectively enhanced: by sending a second photon at the Stokes frequency (the one of the spontaneous emission), stimulated emission is seeded. SRS uses this emission, but CARS is a bit more complicated, as there is another excitation after the first one (see Fig. 1.5), and the generated frequency is at twice the excitation one, minus the Stokes one (thus called anti-Stokes, because the frequency is higher than the excitation one) [65].

This frequency mixing can lead to a resonance partly linked to a chemical bond, or a parametric process not linked to a chemical bond (non-resonant). The four waves mixing (FWM) process is also an unwanted background process of CARS [138] (see Fig. 1.5). SRS is a process a bit different from the others, as the useful signal is mixed with the excitation one because they have the same wavelength.

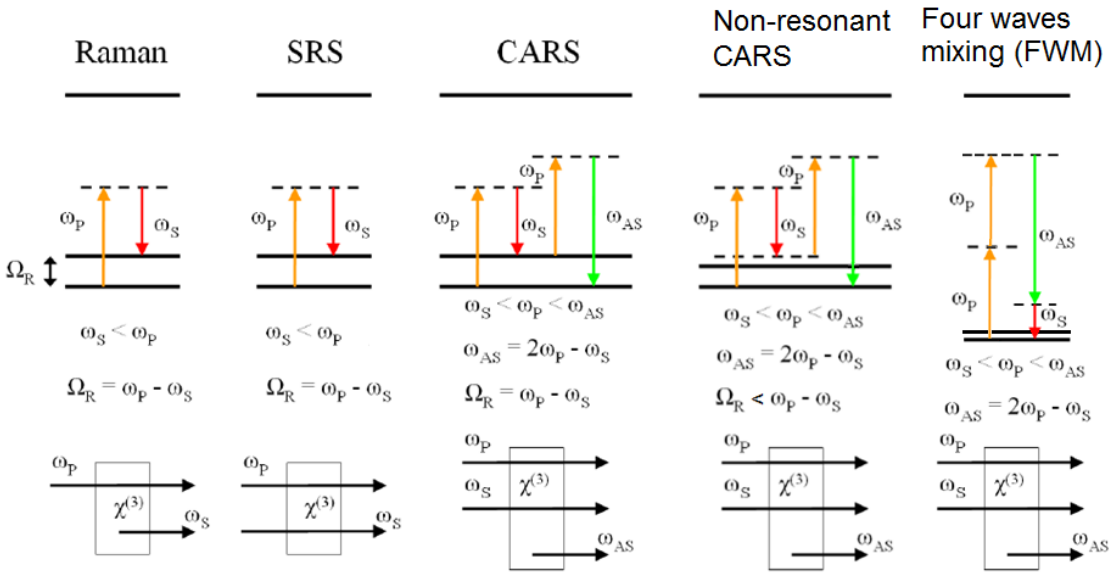

Figure 1.5: Raman parametric processes. Adapted from [174], fig.2.4

1.2.2 Electron-transfer processes

We present here a *substantially different* family of nonlinear processes: nonlinear fluorescence. Here, an electron transfer between two physical levels occurs as described by Fig. 1.6. This excitation can be

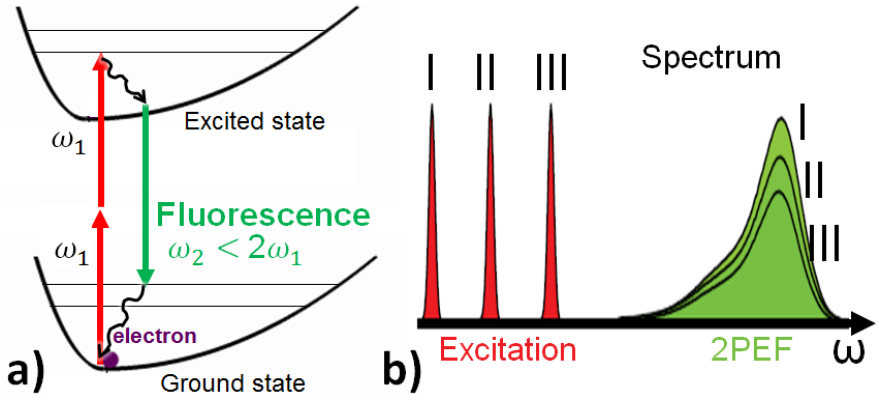

Figure 1.6: a) Two-photons excited fluorescence energy levels. There is a real electron transfer between physical energy levels that has a limited dynamic time (of a few ns). b) Corresponding spectra, showing in red different possible spectra for excitation. In green are the resulting fluorescence spectra, which are broadband and do not change in frequency if the excitation frequency changes, but rather change in intensity. Adapted from [255].

performed with one photon of sufficiently high energy (this is usual fluorescence, used in fluorescence microscopy, for instance), or by the combination of multiple photons if their energy is lower (this is nonlinear fluorescence). Thus two or three photons can combine to excite the electron, which, after, will have some non-radiative de-excitation (phonon-transfer, vibrations modes, etc.), and emit a single photon to return to the ground state (and can have other non-radiative de-excitations). This photon has an energy smaller than the sum of the energy of the photons used for excitation.

(1) Because some non-radiative de-excitation only have a certain probability to occur at the different moments of the process, the energy (and thus the spectrum) of the fluorescence photons is dispersed. Moreover, the fluorescence is emitted by independent emitters that have no relationship and are not synchronized: it is thus logical that the emission is isotropic (no spatial coherence), and with a sample-dependent spectrum (no temporal coherence) [255]. This is shown in Fig. 1.6 b): if the excitation spectrum is shifted in frequency, the multiphoton fluorescence keeps a broadband asymmetrical spectrum whose width and shape are sample-dependent. Only the intensity changes, because the excitation moves around the resonance. The differences between this figure and Fig. 1.3 highlight the different nature of both processes.

(2) The emission is not instantaneous, and the multiphoton fluorescence emission lasts at least a few ns. Thus, the emitted signal cannot be increased by putting the repetition rate of the excitation laser

over $\sim$100MHz ($<$10ns between pulses), as there is a saturation [53].
(3) The electron excitation inside the molecule can also result in instabilities in it that will eventually lead to a structure modification and thus a degradation. After that point, the fluorophore stops its emission, and is "photobleached" [53].
This is the main disadvantage of these processes: even if the photodamages are reduced by the selectivity in depth of multiphoton processes, the electron transfer still induces phototoxicity, and the fluorophores have a limited lifetime due to the unavoidable photobleaching.

1.3 Multiphoton microscopies

Multiphoton microscopies use one or several of the aforementioned processes to enhance the performances of the classical optical microscope. This section reviews the main aspects.

1.3.1 Two main types of microscopy

Most of the multiphoton microscopes, as well as the confocal ones, differ from the classic "wide-field" microscopy configuration. Figure 1.7 shows the differences: a camera is used in wide-field to acquire images at close to video-rate, and the laser illuminates the whole field-of-view without moving. For laser-scanning, the objective is employed for excitation to produce the smallest focal volume possible (possible when a high N.A. objective is used with an overfilling entrance beam), and the laser is scanned over the sample by the scanning mirrors. At every pixel, the signal intensity is recorded by a detector (a photon-counter of an analog photon multiplier). The scan of the sample is more complicated and more time consuming than with wide-field illumination, because the beam must be scanned at a finite speed. Yet it makes sense for nonlinear processes as each part of the sample must be illuminated with a sufficient irradiance. However - as we will see later - new laser technology can allow for the use of wide-field illumination in multiphoton microscopies (MPM). In general, wide-field is used for standard, DIC, phase-contrast, PALM/STORM and conventional fluorescence microscopies. Scanning is reserved for confocal microscopy, MPM and STED.

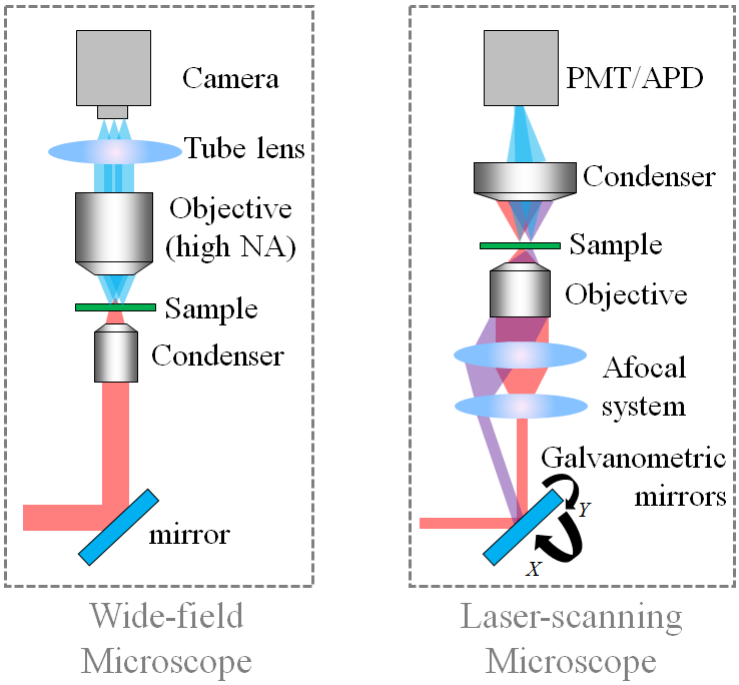

Figure 1.7: Schematics of two configurations in microscopy: a typical wide-field configuration (in transmission, left) versus a laser-scanning one (right). The second path of the excitation when the mirror is tilted is represented in violet for clarity.

1.3.2 Multiphoton fluorescence microscopy

Two-photon excited fluorescence (TPEF or 2PEF) is the most widely used technique in nonlinear microscopy, as it provides good penetration in tissues (thanks to near-IR (NIR) light) while reducing photon damages and photobleaching because of the limited excitation volume [251]. NIR light is preferred because it fits in the "biological window" ([150], p.169), where scattering and absorption from the main components of tissues is limited. Three-photon excited fluorescence (3PEF) can also be utilized to image molecules that absorb at a different frequency than 2PEF [241], but as a 3 photon process it generates less signal than 2PEF. Both use the nonlinear fluorescence process described earlier (1.2.2).

1.3.3 Harmonic microscopies: probing the physical structure

Second-Harmonic (SHG) and Third-Harmonic (THG) generation microscopies use respectively SHG and THG processes, which are some of the parametric processes described earlier. These processes are sensitive to the structure of the material by nature. The SHG is converted only into non-centrosymmetrical structures and is thus very selective: for biological tissues, it concerns collagen, myosin and tubulin

[27], or needs a clear symmetry breaking, as with a membrane surface [33]. The THG does not have this selectivity, but still needs a macroscopic break of symmetry, like an interface, and is therefore very practical for measuring the different interfaces in a medium [33] or enhancing structures smaller than the focal volume [51].

1.3.4 CARS and SRS microscopy: revealing the chemical nature

Raman processes can be enhanced by tuning the excitation laser to reveal certain chemical bonds (CH, CH2, etc.) because the process probes a certain vibrational frequency. Coherent Anti-Stokes Raman Scattering (CARS) microscopy uses two different lasers, a pump beam at a certain frequency and a Stokes beam at a lower frequency. A classic method is to get the pump from an oscillator, and to pump an OPO (Optical Parametric Oscillator) that will produce the Stokes beam [257].
The name "SRS" is actually a bit vague, because it is actually a Stimulated Raman Gain (SRG) (resp. Stimulated Raman Loss (SRL)) that implies a measurable decrease (resp. increase) of the Stokes beam intensity [251]. In SRS, a small signal must be extracted from a large background, which is why a lock-in amplifier is required [34]. This has the advantage to be fully background-free (unlike CARS) if an amplitude modulation is used (FM-SRS) [162].

1.3.5 A multimodal approach

Because these processes all use near-IR excitation light and are produced at the same time, they can be combined inside a single microscope. Filters can be employed to select the different generated wavelengths, and simultaneous acquisition is then performed using many detectors in parallel. The characterization of a given sample is therefore more complete than with only one technique, because CARS provides imaging with a chemical contrast, and SHG/THG with a structural contrast, for instance. This aspect is further developed in chapter 4.

The place of interferometric-SHG

Interferometric-SHG (I-SHG) completes the multimodal approach by revealing the polarity of the different structures in a sample. However, it cannot be acquired simultaneously with standard SHG because it uses the same detected wavelength, and so must be acquired after.

1.4 A more comprehensive comparison of biomedical imaging techniques

To better render all the aspects cited in section 1.1.6, another type of graph is here proposed in Fig. 1.8 taking into account the mentioned details about each techniques: it displays the comparison of a few techniques on the same spider-plot (SHG, 2PEF and CARS microscopies on the left, OPT and OCT on the right), that takes into account different performances. We can see that SHG microscopy's upside is its selectivity, but it can lead to artifacts (which is the subject of chapter 6). 2PEF does not have this problem (but can still made selective) and has the possibility to image a wider range of structures. This is also the case for CARS, however it suffers from a lower contrast due to a nonresonant electronic background. However, 2PEF is more invasive (when markers are used) and is limited in time (photobleaching) compared to the SHG and CARS. We could also compare SHG and histology, as they are often used together (as shown in chapter 4): histology could introduce artifacts as it implies some staining and is more invasive, yet it has shown similar performances as SHG in some cases. This interesting comparison was performed for pancreatic tissue pathology quantification [57]: overall, each application should not rely on a global "gold standard", but rather identify the more suitable imaging paradigm.

On Fig. 1.8 (right) we see that OPT and OCT are quite comparable. They provide a higher penetration depth than multiphoton microscopies, but have a poorer resolution and contrast: the application is not exactly the same.

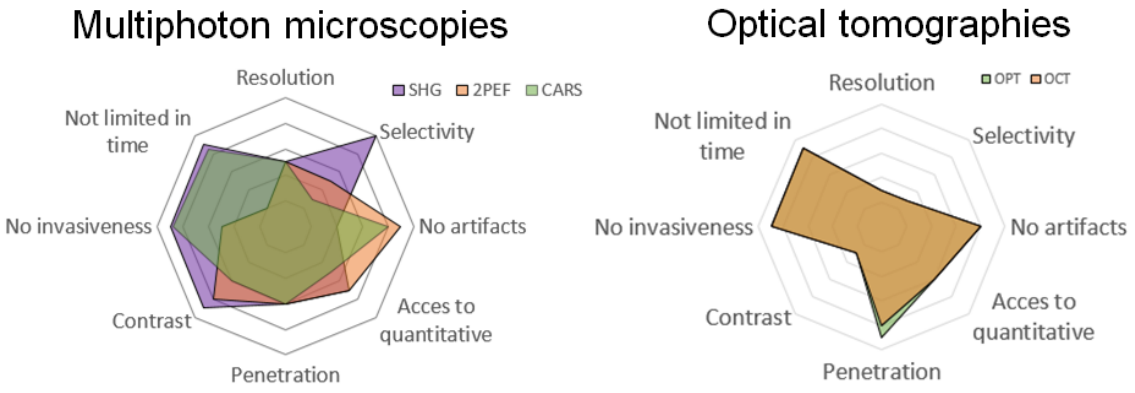

Figure 1.8: Spider plot of performances of the multiphoton microscopies (left) and optical tomographies (right).

Chapter 2

SHG microscopy

This chapter details theoretical aspects related to SHG microscopy. The SHG process is fully explained, some aspects of SHG microscopy are discussed, and some current improvements and possible future routes are described. Finally, interferometric SHG is presented and its main features are detailed.

2.1 Base

2.1.1 SHG building in materials

Birefringence and non-centrosymmetry

The piezoelectricity property is not invariant by a central symmetry, by definition: the Neumann's principle then states that piezoelectric crystals are also not invariant by a central symmetry, i.e. are non-centrosymmetric. The inverse is usually true, the only exception being the 432 class which is cubic and non-centrosymmetric, but not piezoelectric [225] (see fig. 2.1), because piezoelectric charges developed along the 111 polar axes cancel each other out [93]. The two last indices of the $\chi^{(2)}$ tensor are equivalent, such that the class 432 will not exhibit SHG (it should exhibit SFG, though, because for this process the noncentrosymmetry is sufficient as the two last terms are not equivalent). So noncentrosymmetry is not rigorously sufficient for having SHG, it also needs piezoelectricity [87]. In the usual crystals for SHG, we find in pyroelectrics (polar) the mm2 class (KTP, RTP, etc.) and the 3m class (BBO, LiNbO3, LTA, etc.). Others are not pyroelectric (not polar) but have an optical activity such as the 42m class

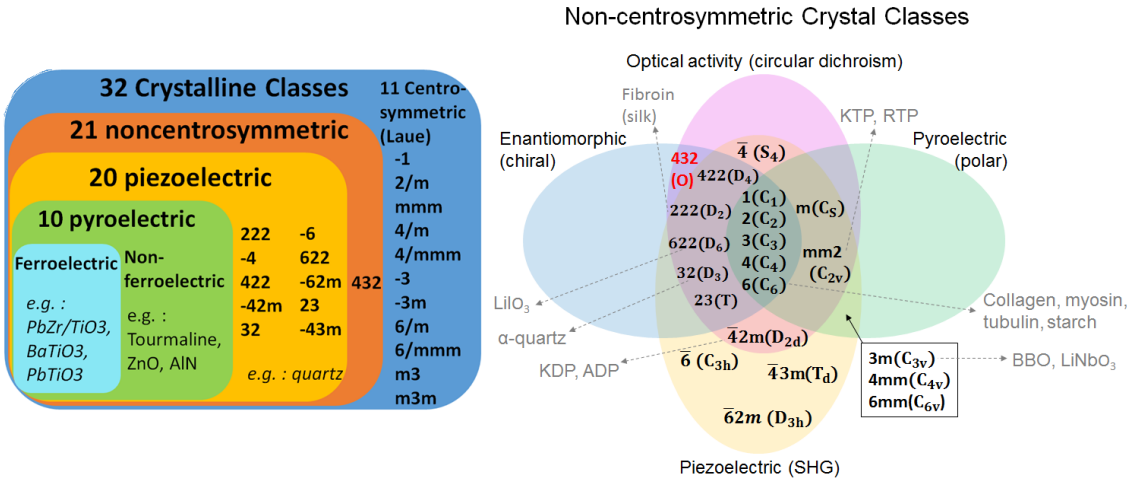

Figure 2.1: (Left) Diagram of the different classes in crystallography, and their correspondence with physical processes. (Right) More detailed description of the non-centrosymmetric classes, involved in SHG (adapted from [87]).

(KDP, ADP, etc.), or can additionally be chiral (e.g. quartz, 32 class for α-quartz and 622 for β-quartz). SHG has also been extensively studied in a sub-part of the pyroelectrics, namely the ferroelectric crystals such as Tetragonal-Tungsten Bronzes (TTB) and others (Calcium Barium Niobate $Ca_xBa_{1-x}Nb_2O_6$, CBN) of the crystalline class "4" (C_4). Ferroelectricity, i.e. polar materials whose spontaneous electric polarization can be reversed by the application of an external electric field, is nevertheless not a property related to any symmetry classes, and is thus verified case-by-case (as shown on Fig. 2.1, left).

Birefringent crystals are optically anisotropic, but that does not mean they are non-centrosymmetric. Actually, these two properties are decorrelated, yet often true at the same time in a given crystal: 18 of the 21 non-centrosymmetric classes are anisotropic, and 9 of the 11 centrosymmetric ones (see [139], Table 3.2). It is impossible to do critical phase-matching in the 3 isotropic non-centrosymmetric classes. We also notice from Fig. 2.1 that all pyroelectric (which are also polar) crystals are piezoelectric (though the inverse is not true), and that all the classes with optical activity are piezoelectric (except the 432 one). In addition, all the chiral classes have an optical activity - and are therefore good candidates for circular dichroism SHG (CD-SHG, as we will see later in C.4) - but the inverse is not true for 4 classes, including 2 polar ones (m and mm2). Lastly, there are some classes that have all the properties: they are piezoelectric, polar and chiral. These classes contain the usual structural proteins imaged by SHG having a cylindrical symmetry (C_6), such as collagen, myosin and tubulin, for instance.

Non-linear susceptibility tensor

For any electromagnetic wave propagating in a medium, the effects of the free charges and of polarization can be grouped in a complex number called the dielectric constant ε (in its general expression) (see [210] "Elements of the Theory of Nonlinear Optics", p.9):

$$\varepsilon(\omega) = \varepsilon_0[n(\omega) + i\alpha(\omega)/4\pi]^2 \tag{2.1}$$

where ε_0 is the dielectric constant in vacuum, $\alpha(\omega)$ and $n(\omega)$ the classic optical index. We define the linear susceptibility as $\chi^{(1)}(\omega) = \varepsilon(\omega) - 1$, which is also a complex number $\chi^{(1)}(\omega) = \chi_R^{(1)}(\omega) + i\chi_I^{(1)}(\omega)$. Thus, one has $n(\omega) = \sqrt{\varepsilon_R(\omega)} = \sqrt{1 + \chi_R^{(1)}(\omega)}$ [210]. For a magnetic material, the relative magnetic permeability μ_R is different from the one in vacuum, and $n(\omega) = \sqrt{\epsilon_R \mu_R}$. Magnetic materials are overall limited to some specific metals called ferromagnetics, which are Fe, Ni and Co mostly, such that the magnetic terms can usually be neglected.

When an excitation field applied to the material is sufficiently intense, the dipoles inside the medium begin to enter into nonlinear oscillations as seen in section 1.2.1, such that the produced polarization can be written as [19]:

$$\overrightarrow{P}(\omega) = \varepsilon_0 \left[\underline{\underline{\chi^{(1)}}} \overrightarrow{E}(\omega) + \underline{\underline{\underline{\chi^{(2)}}}} \overrightarrow{E}(\omega)\overrightarrow{E}(\omega) + \underline{\underline{\underline{\underline{\chi^{(3)}}}}} \overrightarrow{E}(\omega)\overrightarrow{E}(\omega)\overrightarrow{E}(\omega) + ... \right] \tag{2.2}$$

the number n of underlines shows the dimension of the matrix of $\chi^{(n)}$, and arrow-heads denote 1D vectors. If the medium is centro-symmetrical, it is equivalent to write the potential energy function of the force acting on the electrons over +x or -x, such that it is an even function (see [20] 1.4.1). Its decomposition will have only even order terms, meaning its derivative (the electric field) will have only odd order terms. In particular, $\chi^{(2)} = 0$ in such medium. Figure 2.2 shows that a random or an equally-ordered organization of the dipoles lead to a zero $\chi^{(2)}$, the non-zero being obtained only when there is a lack of symmetry center. Because of Kleinman symmetry, and from certain symmetries of the material (e.g. C_∞ for a collagen fibril), the non-linear susceptibility tensor usually reduces to only 2 or 3 components (which are noted d in contracted notations [20]). For instance, d33, d15 = d34 = d31 = d32 in collagen [63], but it is highly dependent on the structure of the medium itself. Other models use 3 different tensor elements which are d33, d31 and d15 ([223], [99]), and find the ratio up to 25 between components [56]. It can also be interesting to write the $\chi^{(n)}$ as a complex number, with a real part that

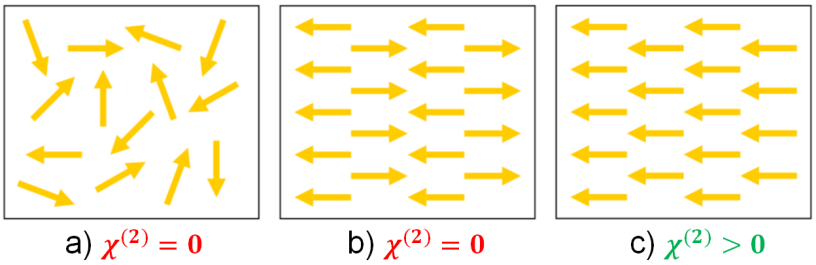

Figure 2.2: Symmetries which have a zero or non-zero nonlinear susceptibility. a) and b) are both centro-symmetrical (a is random and b is equally distributed), whereas c) has dipoles oriented in the same direction. Extracted from [174], fig3.2.

is the standard $\chi^{(n)}$ far from any resonances, and an imaginary part if the electric-dipoles are enhanced near resonance and/or if there are magnetic-dipole and electric-quadrupole effects implying retardation in the nonlinear responses [75].

The nHG process and the $\chi^{(n)}$ can be more extensively explained by the perturbation theory of a harmonic oscillator: for a complete description, reference [19] is suggested.

Different phase-matching

The phase-matching processes are generally true for highly organized materials like crystals: type I or II depending on the polarization of the excitation and converted fields, and a type 0 if the polarization is the same. Their definition can be extended to conversion in inhomogeneous media [85], which is elegant since it sorts processes by the involved polarizations (see Fig. 2.3). For critical phase-matching, if the

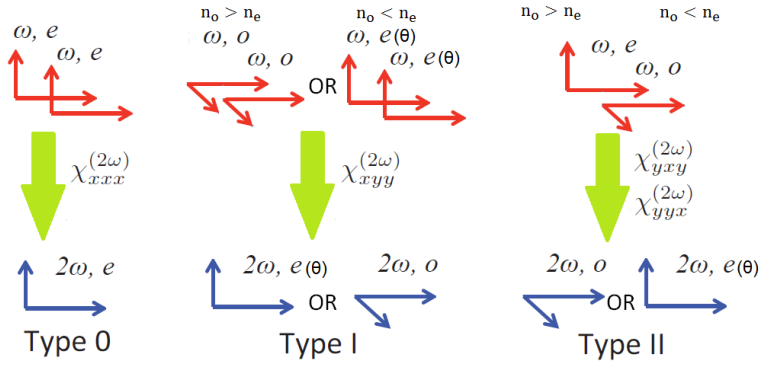

Figure 2.3: Extended definition of phase-matching types in SHG (adapted from [85]).

crystal is uniaxial, it has 2 axes: one axis ordinary "o" and one axis extraordinary "e" (the optical axis). The crystal often has to be tilted by an angle θ so that $n_o(\omega) = n_{e,\theta}(2\omega)$ or $n_{e,\theta}(\omega) = n_o(2\omega)$ at the wanted wavelength. Then the index "seen" by the wave propagating along the tilted extraordinary axis is

sub-scripted e, θ. The SHG wavelength (2ω) will always be on the smallest index (e for negative crystals where $n_o > n_e$ and o for positive ones where $n_o < n_e$), because the optical index increases with the wave frequency.

2.1.2 Hyper-Rayleigh Scattering (HRS) vs SHG

Hyper-Rayleigh Scattering (HRS) is incoherent second-harmonic light, that is usually obtained from solutions where the distribution of the scatterers is more randomized [104]. In such a medium, the produced harmonic field is a random variable [83]. Therefore even if its SHG intensity is proportional to the mean of the orientation of the different scatterers, its HRS is proportional to their variance [104, 83], which leads to a non-zero signal in HRS, but indeed zero in SHG since the mean of such a random variable is 0. HRS is thus a spatially incoherent generation, thought it remains temporally coherent. However, the signal obtained in HRS is usually much smaller than in SHG, because while SHG scales quadratically with the number of scatterers, HRS only has a linear dependency [83], as shown below:

I_{SHG}	I_{HRS}
$\propto \left(\sum E^2\right)^2 \propto N^2E^4$	$\propto NE^4/7$

It is thus logical that HRS is usually not detectable with standard SHG microscope configurations, because the number of scatterers excited in the focal volume is so large that SHG is widely favored [83]. For a more detailed comparison of HRS and SHG, we refer to reference [83] (section 2.2.1.2 "The role of coherence in SHG" in chapter 2.7).

2.1.3 Strong focusing of Gaussian beam

Green's function calculation of the excitation

The focusing of a Gaussian beam does not follow the laws of geometrical optics: the initial waist of the laser and the distance from it must be considered (see [192]). Such a beam is assumed for the following development, and index mismatch as well as polarization distortion at the focus are assumed negligible in the 1st approximation[37]. The incident electric field of excitation can then be written as [37] :

$$E_{inc}(\alpha) = E_0 \exp(-f^2 \sin^2(\alpha)/w^2) \tag{2.3}$$

where α is in the range [0, α_{max}]. α_{max} is the cone angle that is related to the numerical aperture NA $= n \sin \alpha$ (see Fig. 2.4).

We note $\vec{r}_1$ as the vector of the position in the sample. In tight focusing conditions, the vectorial

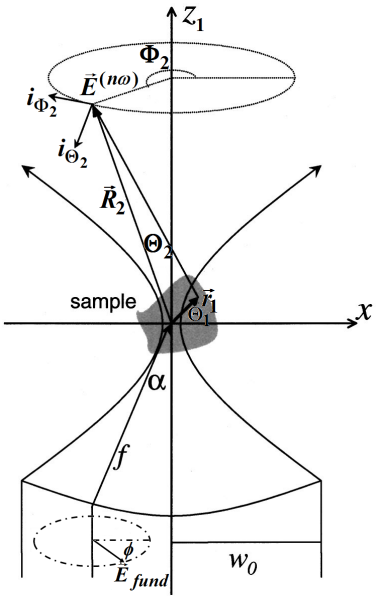

Figure 2.4: Illustration of nHG by a focused laser beam, with definitions of the parameters of the excitation, and the nHG field (adapted from [37]).

Debye theory is used (with no paraxial conditions), such that the fundamental field can be expressed as [81],[171] :

$$\vec{E}_{fund}(r, \Theta_1, \Phi_1) = \frac{ik_1 f}{2} \exp(-ik_1 f) \begin{bmatrix} A_0 + A_2 \cos(2\Phi_1) \\ A_2 \sin(2\Phi_1) \\ 2iA_1 \cos(\Phi_1) \end{bmatrix} \tag{2.4}$$

where the spherical coordinates $\vec{r}_1 = (r_{sph1}, \Theta_1, \Phi_1)$ are used ($\vec{r}_1 = (r_1, \Theta_1, z_1)$ in cylindrical ones), and :

$$\begin{aligned} A_0(\vec{r}_1) &= \int_0^{\alpha_{\max}} \sqrt{\cos\alpha} \sin\alpha \,(1 + \cos\alpha)\, J_0\,(kr_1 \sin\alpha) \exp(ikz_1 \cos\alpha) d\alpha \\ A_1(\vec{r}_1) &= \int_0^{\alpha_{\max}} \sqrt{\cos\alpha} \sin\alpha J_1\,(kr_1 \sin\alpha) \exp(ikz_1 \cos\alpha) d\alpha \\ A_2(\vec{r}_1) &= \int_0^{\alpha_{\max}} \sqrt{\cos\alpha} \sin\alpha \,(1 - \cos\alpha)\, J_2\,(kr_1 \sin\alpha) \exp(ikz_1 \cos\alpha) d\alpha \end{aligned} \tag{2.5}$$

For 2.5 the cylindrical coordinates are employed, such that $z_1 = r_{sph1} \cos\Theta_1$ and $r_1 = r_{sph1} \sin\Theta_1$. The polarization is then distorted by the strong focusing, compared to [37], for instance: this condition

may or may not be important, depending on the situation. Notably, we use the sine condition for the apodization function $P_f = \sqrt{\cos\alpha}$, but others can work depending on the lens (see [82]).

Note that this is supposed to be valid in a homogeneous medium (one n). In a dielectric interfaces, the various reflection components have to be taken into account [82]:

$$\begin{aligned} A_0(\vec{r}_1) &= \int_0^{\alpha_{\max}} f(\alpha_1, z_1, \alpha_n) \left((T_s)^{n-1} + (T_p)^{n-1} \cos\alpha_n \right) \exp(-ik_0 F_n(\alpha_1)) J_0\left(kr_1 \sin\alpha_1\right) d\alpha_1 \\ A_1(\vec{r}_1) &= \int_0^{\alpha_{\max}} f(\alpha_1, z_1, \alpha_n) \left((T_p)^{n-1} \sin\alpha_n \right) \exp(-ik_0 F_n(\alpha_1)) J_1\left(kr_1 \sin\alpha_1\right) d\alpha_1 \\ A_2(\vec{r}_1) &= \int_0^{\alpha_{\max}} f(\alpha_1, z_1, \alpha_n) \left((T_s)^{n-1} - (T_p)^{n-1} \cos\alpha_n \right) \exp(-ik_0 F_n(\alpha_1)) J_2\left(kr_1 \sin\alpha_1\right) d\alpha \end{aligned} \tag{2.6}$$

where $F_n(\alpha_1)$ is the aberration function due to the multiple dielectrics layers:

$$F_n(\alpha_1) = -h_1 n_1 \cos\alpha_1 + h_{n-1} n_{n-1} \cos\alpha_1 + \sum_{j=2}^{N-1} (h_{j-1} - h_j) n_j \cos\alpha_j \tag{2.7}$$

and $f(\alpha_1, z_1, \alpha_n) = \sqrt{\cos\alpha_1} \sin\alpha_1 \exp(ik_n z_1 \cos\alpha_n)$. In the important case of a single dielectric interface, n=2 and $F_2(\alpha_1) = -h(n_1 \cos\alpha_1 - n_2 \cos\alpha_2)$.
The angles α_i are calculated with the laws of refraction, for example : $\cos\alpha_2 = \sqrt{1 - (n_0/n_1 \cos\alpha_1)^2}$.
The Ts and Tp coefficients stands for the Fresnel transmission coefficients for polarizations s and p:

$$t_s(\alpha) = 2n_0 \sqrt{1 - (n_1/n_0 \sin\alpha)^2} / \left(n_0 \sqrt{1 - (n_1/n_0 \sin\alpha)^2} + n_1 \cos\alpha \right) \tag{2.8}$$

and $t_p(\alpha) = 2n_0 \sqrt{1 - (n_1/n_0 \sin\alpha)^2} / \left(n_1 \sqrt{1 - (n_1/n_0 \sin\alpha)^2} + n_0 \cos\alpha \right)$.
This implies that, in tight focusing, some polarization terms appear in directions orthogonal to the polarization of the excitation! This aspect is detailed in section 2.1.3.

Expression of the nonlinear converted field

In a homogeneous system, and under the slowly varying amplitude approximation, with the depletion of the fundamental being neglected, the wave equation for the nth harmonic field is [81]:

$$\nabla\nabla \overrightarrow{E}^{(n\omega)}(\overrightarrow{r}) - k_n^2 \overrightarrow{E}^{(n\omega)}(\overrightarrow{r}) = \frac{4\pi\omega_n^2}{c^2} \overrightarrow{P}^{(n\omega)}(\overrightarrow{r}) \tag{2.9}$$

$\overrightarrow{P}^{(n\omega)}$ is the induced nonlinear polarization at the n-th harmonic frequency.

$$\vec{P}^{(n\omega)}(\vec{r}) = \underbrace{\underline{\chi^{(n)}}}_{\vdots \times n}\vec{E}_{fund}(\vec{r}) \times \overset{n}{\ldots} \times \vec{E}_{fund}(\vec{r}) \tag{2.10}$$

Decomposing the nonlinear tensor of the specific case of SHG (n=2), the reduced notation yields [20]:

$$\begin{bmatrix} P_z^{2\omega} \\ P_y^{2\omega} \\ P_x^{2\omega} \end{bmatrix} = \begin{bmatrix} d_{11} & d_{12} & d_{13} & d_{14} & d_{15} & d_{16} \\ d_{21} & d_{22} & d_{23} & d_{24} & d_{25} & d_{26} \\ d_{31} & d_{32} & d_{33} & d_{34} & d_{35} & d_{36} \end{bmatrix} \begin{bmatrix} E_z^2 \\ E_y^2 \\ E_x^2 \\ 2E_xE_y \\ 2E_xE_z \\ 2E_yE_z \end{bmatrix} \tag{2.11}$$

where the non-zero components for most commonly used media (d_{31}, d_{33} d_{15} in collagen, myosin, d_{22} in $LiNbO_3$) are indicated in color, with the other ones being null. The same color indicates that the elements are equal (in the case of the mentioned media): $\chi^{(2)}_{YYZ} = d_{24} = d_{15} = \chi^{(2)}_{XXZ}$ and $\chi^{(2)}_{ZYY} = d_{32} = d_{31} = \chi^{(2)}_{ZXX}$ because of the C_6 symmetry [247] (d33=$\chi^{(2)}_{XXX}$). The harmonic signal field detected at $\overrightarrow{R}_2(R_2, \Theta_2, \Phi_2)$ is (the volume being integrated in the sample, i.e. $dV = dr_1 \sin(\Theta_1) d\Theta_1 d\Phi_1$):

$$\overrightarrow{E}^{n\omega}\left(\overrightarrow{R}_2\right) = \frac{\omega_n^2}{c^2}\frac{\exp\left(ik_n\left|\overrightarrow{R}_2\right|\right)}{\left|\overrightarrow{R}_2\right|}\iiint_V \exp\left(\frac{-ik_n\overrightarrow{R}_2.\overrightarrow{r}_1}{\left|\overrightarrow{R}_2\right|}\right) \times M(\Theta_2, \Phi_2) \times \begin{bmatrix} P_x^{n\omega}(\overrightarrow{r}_1) \\ P_y^{n\omega}(\overrightarrow{r}_1) \\ P_z^{n\omega}(\overrightarrow{r}_1) \end{bmatrix} \begin{matrix} \overrightarrow{i}_{R_2} \\ \overrightarrow{i}_{\Theta_2} dV \\ \overrightarrow{i}_{\Phi_2} \end{matrix} \tag{2.12}$$

where $M(\Theta_2, \Phi_2) = \begin{bmatrix} 0 & 0 & 0 \\ \cos(\Theta_2)\cos(\Phi_2) & \cos(\Theta_2)\sin(\Phi_2) & -\sin(\Theta_2) \\ -\sin(\Theta_2) & \cos(\Theta_2) & 0 \end{bmatrix}$. Lastly, the SHG integrated power can be written in the general case as:

$$\mathcal{P}^{n\omega} = \frac{1}{2^n\pi} n_{n\omega} c\varepsilon_0 \int {R_2}^2 \left[\vec{E}^{n\omega}\left(\vec{R}_2\right)\right]^2 d\vec{R}_2 \tag{2.13}$$

These expressions are difficult to calculate in the general case, so here we provide the example of reference [31]: collagen, where Kleinman's condition, a cylindrical symmetry and a Gaussian field are assumed, such that there are only two non-zero independent components in the tensor (XXX and XYY). We

define $F_{33,31} = \left(\chi^{(2)}_{XXX}\cos^2\phi + \chi^{(2)}_{XYY}\sin^2\phi\right)$ and $U_1 = \cos\Theta_2\cos\Phi_2 F_{33,31} + \chi^{(2)}_{XYY}\cos\Theta_2\sin\Phi_2\sin 2\phi$, $U_2 = -\sin\Phi_2 F_{33,31} + \chi^{(2)}_{XYY}\cos\Phi_2\sin 2\phi$.

ϕ here is the angle of the polarization (assumed to be linear) of the excitation with respect to the X axis of the laboratory frame. Then, the SHG powers on horizontal and vertical polarizations can be written as:

$$\begin{aligned}\mathcal{P}^{(2\omega)}_{//}(\Theta_2,\Phi_2) &= \frac{n_{2\omega}}{8}\eta^2 c\varepsilon_0 N^2 G(\vec{r}_2)^2 E^4_{fund}\{\cos(\Phi_2-\phi)U_1 - \sin(\Phi_2-\phi)U_2\}^2 \\ \mathcal{P}^{(2\omega)}_{\perp}(\Theta_2,\Phi_2) &= \frac{n_{2\omega}}{8}\eta^2 c\varepsilon_0 N^2 G(\vec{r}_2)^2 E^4_{fund}\{\sin(\Phi_2-\phi)U_1 + \cos(\Phi_2-\phi)U_2\}^2\end{aligned} \tag{2.14}$$

where N and $G(\vec{r}_2)$ are quantities related to the Gaussian parameters: $N = N_V V$ with $V = \sqrt[3]{\pi/2}w_{xy}w_z$ and $G(\vec{r}_2) = \exp\left[\frac{-k^2_{2\omega}}{8}\left(w^2_{xy}\sin^2\Theta_2 + w^2_z[\cos\Theta_2 - \xi]^2\right)\right]$. N_V is the density of harmonophores, and w_{xy} and w_z are the dimensions of the Gaussian focal volume [255]. ξ is the wave-vector reduction factor due to focusing, which accounts for a reduction in axial momentum by its conversion to lateral momentum components within the focus (significant if a high N.A. is used for excitation)[31]. These expressions are useful to calculate the power distribution in 3D, however when dealing with the average SHG power as in P-SHG they are simplified because the radiation pattern is focused on a detector. Therefore, an average on $\vec{r}_2$ is equivalent to considering $\Theta_2 = 0, \Phi_2 = 0$. Also, we will see later (Methods section of article in 4.4) a simpler expression when the frame is rotated to match the collagen fibril.

Is tight-focusing a problem in SHG ?

Here, we will further develop equation 2.6. References [247, 248] investigated the effect of polarization distortion due to tight focusing on SHG, and the possibility to excite axial components of the nonlinear susceptibility tensor. There are two types of excitation components:

- the "paraxial" components, i.e. the usual ones in the XY plane, that excite tensor elements in this plane ($\chi^{(2)}_{XXX}$ and $\chi^{(2)}_{XYY}$ for cylindrical proteins).
- the polarization-distorted components that transfer a portion of the excitation to the propagation axis Z, leading to SHG conversion using "unusual" tensor elements ($\chi^{(2)}_{ZZX}$ and $\chi^{(2)}_{XZZ}$ for cylindrical proteins, which are usually considered equal to $\chi^{(2)}_{XYY}$ [84]).

[247] also provides the relative strength of the polarization distortion: for an excitation originally on the X axis, the ratios of excitation of X:Y:Z at focus is 1:0.1:0.3 with a focusing N.A. of 1.4. Reference

[112] shows that this ratio becomes 1:0.03:0.1 with a N.A. of 0.1 for linearly polarized beams. In standard microscopy, the paraxial approximation is found to be consistent for NA < 0.7 [82], such that the PSF are globally similar for the paraxial and the vectorial models [237]. This does not stand for non-linear processes (e.g. SHG), because of the phase-matching mechanism. Reference [237] states that the vectorial model should be used when NA > 0.3. We can keep in mind that strong N.A., despite generating more SHG intensity, can lead to an uncontrolled excitation of some $\chi^{(2)}$ elements and undesired polarization components in the output field. The relative strengths of these components is of course sample-dependent, because determined by the magnitudes of the $\chi^{(2)}$ elements. For instance, reference [35] states that N.A. below 0.8 can be safely used with neglecting the polarization distortion. In addition, it is shown in [85] that, in collagen, even with a NA close to 1.0, the axial components have a small effect on the non-linear susceptibility tensor measurement, while birefringence and optical dispersion are more critical.

Access to axial elements of the $\chi^{(2)}$

Reference [248] also shows that effective excitation of the axial elements of the $\chi^{(2)}$ can be achieved using a special type of polarization, namely a radial one. Figure 2.5 (a) shows that, in that case, the electric field orientation is always orthogonal to the surface of the beam. By contrast, when it is linearly or circularly polarized, the electric field has a constant orientation over the beam cross-section. For elliptical polarizations (circular being one limit case), this orientation rotates during propagation (Fig. 2.5 (a, middle)). Radially polarized beams are shown to have a doughnut shape [112], and can be generated using a spatial light-modulator (SLM) [248] or a vortex plate [14], for instance. Other special types of polarization may be achieved such as azimuthal, vortex or hybrid ones [226]. Upon focusing, the radial polarization creates an axially polarized field along Z (Fig. 2.5 (c)). This was later confirmed through a recording of field components in a photoresist [93]. By comparison, linear or circular polarization can produce only transverse polarizations at focus (in the XY plane, Fig. 2.5 (b)). Additionally, radial polarizations can be used to generate SHG in collagen whose intensity is constant for every analyzer orientation in the detection path [248]. Thus, radial polarization leads to an axial polarization P_Z (linear) at focus, and the latter leads to a radial polarization in the far-field. A fine tuning of the focusing N.A. can theoretically lead to a polarization at focus that has a ratio of its components Z:XY of 1:1, and even to 5:1 (in intensity) [112].

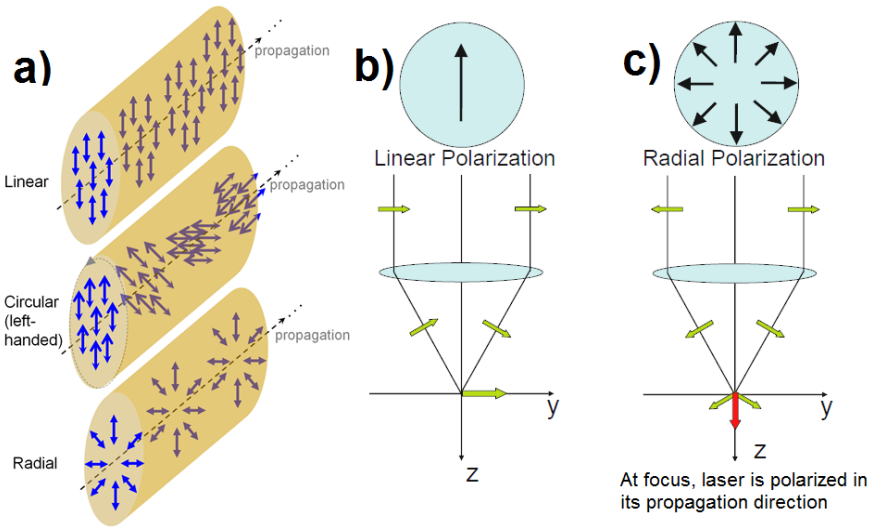

Figure 2.5: Excitation beam with linear, circular, or radial polarization, and its effect at the beam focus. (a) Gaussian beam having linear (top), circular (middle) or radial (bottom) polarization. The linear and circular polarization is the same over the whole cross-section of the beam, while the polarization direction is always orthogonal to the beam surface for the radial one. (b) Effect of the focusing of a linear polarization: the resultant is a standard excitation orthogonal to propagation. (c) The same, but with a radial polarization: the resultant is a polarization parallel to the propagation (red). (b) and (c) have been adapted from [226].

Different complexities for describing a nonlinear generation like SHG

Different methods can be used to describe the harmonic generation processes in media (see 2.1): the simplest give exact, analytical, and simple solutions, but are usually not able to fully describe the process. The plane wave expression is indeed quite misleading because it states that some signal could exist in bulk media, and could even increase with the thickness of the sample, as long as the phase-matching condition is fulfilled. However, if the focal volume is completely in the bulk, the SHG signal vanishes [133, 37]. This phenomenon is well-described by considering a classic Gaussian beam for solving the wave equation (instead of a plane wave). Figure 2.6 also describes - in a diagram - which elements of complexity can be chosen for the calculation of the SHG, and their relative imbrication. The main choices are related to the fundamental field expression, but the complexity of the $\chi^{(2)}$ (with chiral components or not) and the magnetic terms can also increase the complexity of the calculation. The red area indicates the most complex calculation. However, the position in this diagram for a specific application does not usually require a too high level of complexity, as some terms can be neglected (simpler $\chi^{(2)}$ if the material is achiral, for instance).

Type	Phase-match	Paraxial	One polarization	Homogeneo medium	Math model	Form
Plane wave	Yes	Yes	Yes	Yes	Analytical	sinc
Gaussian beam	Yes	Yes	Yes	Yes	Analytical	see table 2.2
Gaussian beam phase mismatch	No	Yes	Yes	Yes	Analytical	Eq. 2.18
Tight focusing	No	No	Yes	Yes	numerical integration	Green's function (see 2.11)
Tight focusing with polarization distortion	No	No	No	Yes	numerical integration	Green's function (see 2.11)
Tight focusing with polarization distortion and dielectric interfaces	No	No	No	No	numerical integration	Green's function (see 2.11)
Maxwell's equations solving	No	No	No	No	numerical integration	FDTD

Table 2.1: Different degrees of complexity to calculate the nonlinear field.

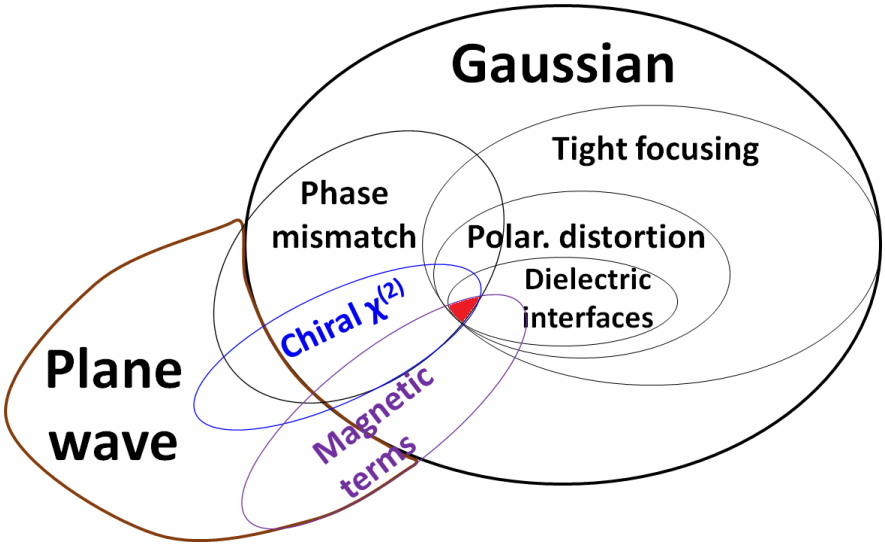

Figure 2.6: Diagram of the complexity of the equations to obtain the nonlinear E-field, with no fundamental depletion. The red area is the most complex calculation.

SHG at interfaces whose plane is orthogonal to the propagation

The nonlinear wave equation with a Gaussian beam can be considered in another expression. Let's consider the fundamental amplitude of the form:

$$A_1 = A_0\sqrt{\frac{2}{\pi}}\frac{z_R}{iq(z)}\exp\left(ik_1\frac{x^2+y^2}{2q(z)}\right) = A_0\sqrt{\frac{2}{\pi}}SphericalGaussian[x,y,z;k_1] \tag{2.15}$$

with $q(z) = z - iz_R$ and $SphericalGaussian$ the function describing a Gaussian envelope with a spherical wave. The wave equation is verified:

$$\left[\partial_x^2 + \partial_y^2 + 2ik_1\partial_z\right] A(x,y,z;k_n) = \frac{\omega_n^2}{c^2}\chi^{(n)} A(x,y,z;k_n) e^{i\Delta kz} \tag{2.16}$$

For the fundamental, the equation has no source term (on the right). For the n-th harmonic, the $\chi^{(n)}$ of the medium must be considered.

The following function is a solution of equation 2.16 (as the spherical envelopes are conserved): $A_n = f(z)SphericalGaussian[x,y,z;k_n]$, with a function f(z) which is thus a solution of the differential equation:

$$f'(z) = -iK\frac{\chi^{(n)}(z)}{q(z)^2} \Rightarrow f(z) = -iK\int_{-\infty}^{z} \frac{\chi^{(n)}(u)}{q(u)^2} du \tag{2.17}$$

with $K = \frac{\omega_n}{2n_n c}\left(A_0\sqrt{\frac{2}{\pi}}\right)^n z_R^2$.

As the total power of a Gaussian beam is $\frac{\pi}{2} I_0 w_0^2$, with I_0 the intensity at the origin (x, y, z = 0), the power scales with the square modulus of f(z). Table 2.2 shows the dependence of the total power with respect to the Z position, if we state that $\chi^{(n)}(z)$ is constant with $z \in [-L/2,\ L/2]$, and 0 otherwise. This implies a difference of behavior for the SHG compared to other processes: there is no selectivity

Condition	SHG	THG
z <= -L/2	0	0
-L/2 < z <= L/2	$\chi^{(2)} \log \frac{iz_R - z}{iz_R + L/2}$	$i\chi^{(3)}(\frac{1}{z - iz_R} - \frac{1}{-L/2 - iz_R})$
z > L/2	$\chi^{(2)} \log \frac{2iz_R - L}{2iz_R + L}$	$i\chi^{(3)} \frac{L}{(L/2)^2 + {z_R}^2}$

Table 2.2: Expressions of f(z)/K for the multi-harmonic generation.

in Z, because the function is not a Lorentzian (or super-Lorentzian), but a log of a ratio. By contrast, the maximum power is obtained when $L = 2z_R$ for THG: the heterogeneities with a dimension close to this value will thus exhibit a high THG signal compared to other structures (see [150] Chap.4). THG microscopy provides here an interesting feature: size selectivity.

No phase-matching

Here, the case where the phase-matching condition is not fulfilled is considered, but the paraxial approximation still holds. This is closer to what happens in real experiments in crystals, and always the case in inhomogeneous media like biological ones. Under these assumptions, the condition $k_n = nk_1$ is still valid, except that $\chi^{(n)}(z)$ becomes $\chi^{(n)}(z)e^{i\Delta kz}$.

For the SHG, in a medium of length L and focus at z_0 [63, 208]:

$$I_{2\omega} = \frac{2\omega^2}{\pi c^2 \epsilon_0 w_0^2 n_{2\omega} n_\omega^2} I_\omega^2 (\chi^{(2)})^2 \left(\int_{z_0}^{z_0+L} \frac{e^{i\Delta kz}}{1+iz/z_R} \right)^2 dz \tag{2.18}$$

For the THG, we can consider the function f integrated over the whole real axis, and use the residue theorem: $f(+\infty) = -iK \int_{-\infty}^{+\infty} \frac{\chi^{(3)} e^{i\Delta ku}}{q(u)^2} du = 2i\pi K \chi^{(3)} \Delta k e^{-\Delta k z_R}$. Then the intensity can be recast as [21]:

$$I_{3\omega} = \left(\frac{3}{2}\right)^4 \frac{\omega^2}{c^4 \epsilon_0^2 n_{3\omega} n_\omega^3} I_\omega^2 (\chi^{(3)})^2 w_0^2 \Delta k^2 z_R^2 e^{-2\Delta k z_R} \tag{2.19}$$

This expression is valid only for the total converted power in a homogeneous medium. The maximum of this function is located at $\Delta k = 1/z_R$ (see Fig. 2.7) ; the perfect phase-matching $\Delta k = 0$ is therefore not the optimal condition to maximize power! This relation shows that the phase-mismatch instead compensates the effect of the Gouy phase-shift in THG. In Fig. 2.7 a), is compared the signal at an

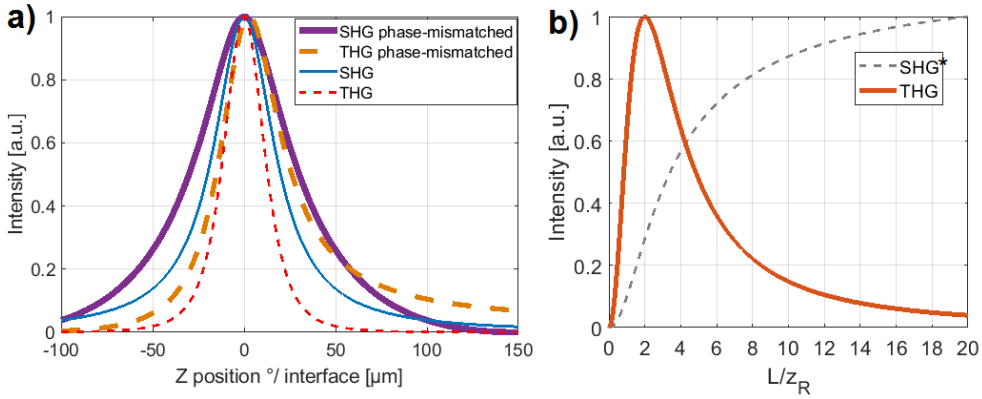

Figure 2.7: Comparison between SHG and THG signal at an interface orthogonal to propagation. (a) SHG and THG signals as a function of Z position relative to the interface boundary. Dashed lines show the non-phase-matched condition (equation 2.19 for THG), and continuous lines show the phase-matched case. (b) SHG and THG signals integrated over the whole sample of thickness L, a function of the ratio of L over the Rayleigh range z_R, for the phase-matched case. The calculation for SHG does not render the experimental behavior. All cases consider Gaussian beams, and numerical calculations are performed.

interface whose plane is orthogonal to propagation, in the different cases presented: SHG and THG, with and without phase-matching. The THG is always narrower than SHG, and can determine the interface precisely. This property for THG actually also holds with interfaces whose plane is collinear to propagation (i.e. interfaces that we see in the 2D microscopy images), because THG probes the volume around the interface, where there is a change of susceptibility or refractive index [150], chap.4. SHG is more restricted: it can image membranes where dipoles are aligned parallel to each other [133], but it has a poor resolution if the interfaces contain no such anti-symmetry. The difference between SHG and THG is well illustrated in reference [146] where SHG and THG images are merged, showing that THG reveals the cell interfaces and SHG only the microtubules inside. Figure 2.7 b) also shows the dependency with the thickness of the interface, but the plot for SHG uses a too simplistic model and is actually not verified experimentally. The signal quickly vanishes when the focus goes in depth, due to a property of focalization: the Gouy phase-shift.

2.1.4 Effect of the Gouy phase-shift

The Gouy phase-shift is responsible for the annihilation of the harmonic signal in bulk materials. The harmonic signal is still created in the bulk, but the phase-mismatch is governed by the Gouy phase-shift that the excitation field accumulates through the focus, which leads to a much smaller effective coherence length [36]: destructive interferences are then stronger than the signal generation. In practice, using the paraxial approximation, we can show that the Gouy phase-shift of the fundamental beam is +-$\pi/4$ at the extremities of the focal volume (Rayleigh range):

$$\phi_G = \mathrm{Arctan}\,(z/z_R\,) \Rightarrow \phi_G(z = \pm z_R) = \pm\pi/4 \tag{2.20}$$

For the n-th harmonic generation, the fundamental at relative phase $\pm\pi$/N is converted to a phase $(\pm\pi/N)^n$. Then, this n-th harmonic's phase experiences a Gouy phase-shift of $\pi/2 \mp \pi/N$. The detected relative phase-shift is then $(\pm\pi/N)^n + \pi/2 \mp \pi/N$. Table 2.3 represents this quantity for THG and SHG. The destructive interferences occur between the signals that are π phase-shifted, i.e. for

	at $\pm\pi$/N	$\Delta(\pm\pi/N)$	Phases of fundamental leading to π phase-shifted harmonics
THG	$\frac{\pi}{N}(N/2 \pm 2)$	4π/N	$\pm\pi/4$ $(z = z_R)$
SHG	$\frac{\pi}{N}(\frac{N}{2} \pm 1)$	2π/N	$\pm\pi/2$ $(z \gg z_R)$

Table 2.3: Gouy phase-shift of the generated harmonic, as a function of the Gouy phase-shift of the fundamental.

$z = z_R$ for THG. Again, THG is shown to have a selectivity in size. Note that the Gouy phase-shift of the THG at $z \gg z_R$ (fundamental at $\pm\pi/2$) is $-\pi/2$, which compensates for the signal generated at z=0. For SHG, the signal at $z \gg z_R$ cancel each other, so the selectivity is not limited to the Rayleigh range, but is much higher (and not well-defined). The phase-matching coherence length condition that is usually used for plane waves [20] must therefore be corrected by an additional term for Gaussian beams:

$$\begin{aligned} |k_2 - 2k_p - 2k_{p,G}|\, l &< \pi \\ |k_3 - 3k_p - 3k_{p,G}|\, l &< \pi \\ |k_{as} - 2k_p + k_s - 2k_{p,G} + k_{s,G}|\, l &< \pi \end{aligned} \tag{2.21}$$

Equation 2.21 shows that for SHG and THG, the coherence length is smaller due to the Gouy phase-shift term (annihilation of signal in the bulk). By contrast, in CARS, the Stokes field is conjugated (emission), but the pump field is not (excitation), which partially cancels their associated Gouy phase-shift terms [36]. We will remember that in CARS (which is also a four-waves mixing phenomena, that involves $\chi^{(3)}$ like THG), the signal increases with the quantity of non-linear medium ([36]), unlike for harmonic processes. Thus, the plot for SHG in Fig. 2.7 b) is actually verified for CARS [36].

2.1.5 Radiation pattern

Forward vs backward ratio

As seen before, SHG and THG are coherent processes and therefore do not emit their signal isotropically: some signal is scattered in the same direction as the fundamental propagation (called forward), and some is scattered in the inverse direction (called backward, or "epi"). Backward generation is a true asset, because some materials that are too thick or opaque do not allow any forward signal collection: the SHG or THG can instead be collected with a microscope in a reflection configuration, in epi detection. The backward implies fundamental wavevectors (k_1) and nHG with an opposite direction: $-k_N$. The coherence length is $L_{coh} = 2/k$, and $k = 2n\pi/\lambda$, thus:

$$L_{coh} \propto 1/(N.n_1 - n_N) \quad \text{whereas} \quad L_{coh,epi} \propto 1/(N.n_1 + n_N) \Rightarrow L_{coh} >> L_{coh,epi} \tag{2.22}$$

The coherence length of epi $L_{coh,epi}$ is much smaller than L_{coh} in forward: the backward nHG signal will always be smaller than the forward.

Effect of scatterer arrangement

In the case of small scatterers extent (e.g. one collagen fibril), Zipfel *et al.* showed that the SHG radiation pattern depends on the scatterer orientation [254] (see Fig. 2.8 (a)): if the longitudinal rod being imaged is orthogonal to propagation, the radiation pattern is like a dipole (red), with the same amount of signal scattered forward and backward. For the case where the rod is turned 90° (parallel to propagation, violet), a symmetry breaking must remain to have SHG: it is assumed that there is an anti-symmetry of dipoles in the focal volume. In that case, the radiation pattern takes the form of two lobes, and the signal is almost exclusively forward oriented (see Fig. 2.8 (a)). This is well illustrated

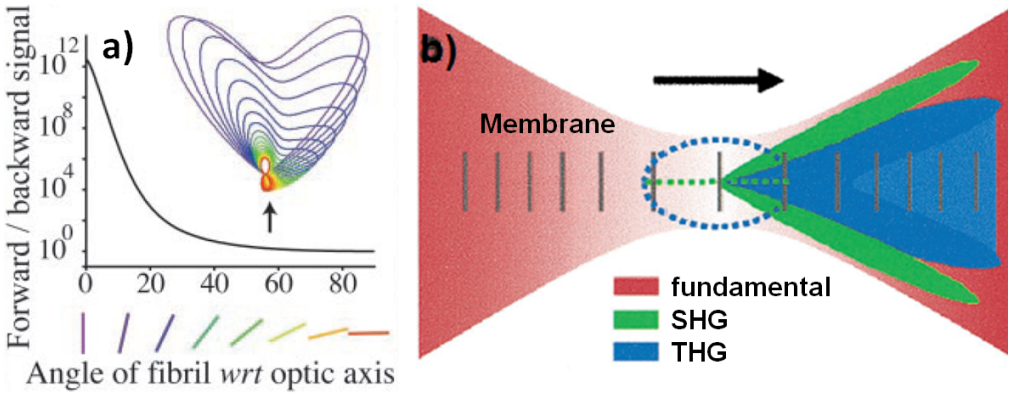

Figure 2.8: SHG radiation pattern as a function of the angle of incidence on a 1D linear medium, and comparison with THG. a) There is a higher F/B ratio if the longitudinal rod being imaged is parallel to propagation rather than orthogonal (extracted from [254]). b), extracted from [133], showing the SHG and THG signals from a rod alignment imaged at grazing incidence, as in membranes (the backward generation is not shown for clarity).

in fig. 2.8 (b) from [133]: the SHG of scatterers aligned along propagation (here at a surface of a membrane) is spread over two side-lobes, while the THG is a more volumetric process (that does not require symmetry breaking) and the emission is then a ring [133]. The two-side lobed pattern thus seems to be reserved for surface generation (the lobes are from either side of the surface, imagine generation in the surface plane is obviously limited), while the ring-like pattern is for volumetric generation: this is also shown in [37], fig.5.

But the SHG is also widely used in volumetric media, where the symmetry breakings - which are often numerous - are ensured by the non-centrosymmetry of the scatterers (due to crystal structure, molecule properties and arrangement). The radiation pattern then depends largely on how deep the

focal volume is positioned in the sample: at surface, the pattern is a 3D Gaussian (like THG) and turns into a ring-like pattern (doughnut) when in depth: see for instance [176] fig.4. We will see in 6 that double-lobes also appear for SHG at interfaces between opposite polarities. Here, we will remember that the forward over backward ratio (F/B) increases with the thickness of the SHG converters along the direction of propagation, or if the longitudinal scatterers tend to be out-of-plane. The simulations in figure 7.29 of the thesis [174] also shows this result, and additionally proves that the SHG signal will be more forward-oriented (F/B higher) if the SHG converters have the same polarity. Moreover, the backward (epi)-generated signal seems to also depend a lot on the wavelength of excitation [78].

A MatLab code was implemented to calculate the radiation pattern power from the Green's function formulation of the previous paragraph. The execution is unfortunately quite long and limits its use in practice. We have teamed up with the laboratory of Lora Ramunno in the Physics Department of UOttawa to obtain the Green's function simulation of these effects, and other configurations. Therefore, for a further characterization of SHG radiation pattern at various interfaces, the reader is referred to the article in chapter 6, especially its fig. 3, its supplementary material and the complementary Fig. 6.2.

2.1.6 Filtering or discriminating the SHG

The SHG has a well-defined spectrum, related to the spectrum of excitation, while the fluorescence one is much broader and only depends on the chemical bonds and electronic structure of the material (see Fig. 1.3 and 1.6). The two-photon excitation (2PEF) fluorescence is therefore decoupled from the SHG, as some non-radiating de-excitations occur and the emitted wavelength will be higher (the energy lower) than the SHG one. For instance, in the case of collagen, the maximum of emitted fluorescence is at 560nm [254]. However, some fluorescence signal could be detected in the SHG window (405+-5nm) when pumped at 810nm, because the 3PEF spectrum is by definition at higher wavelengths than 290nm and could partly lie in this window as well. In particular, if an excitation close to 1000nm is used, then the 3PEF can become quite intense in collagen (and elastin), as the maximum absorption is around 325nm, which is in the UV, and the emission maximum at 400nm [172]! Thus, while it is usually easy to discriminate harmonic processes from multiphoton fluorescence by their central wavelength (using a narrow-band filter for instance), it can be misleading due to spectrum overlap in some cases. To circumvent this problem, the signal versus excitation power law can be verified (e.g. power of 2 for SHG, and 3 for 3PEF). Also, the full spectrum can be acquired with a spectrometer, to control if it

is broadband (fluorescence) or similar to excitation (harmonic process) ; it is also possible to compare the relative strengths of the direct and epi signals, and to use any differences already listed before to differentiate the two processes.

2.1.7 SHG in collagen

Collagen

Collagen represents 25% of the total protein mass in the human body [2]. Collagen's structure is the reason why the corneas is transparent, and why tendons are mechanically resistant. Indeed, the collagen inside cornea is almost crystalline which ensures a good light transmission, while in tendons it is formed of bundles of longitudinal chains at several scales, which provides an extended response to mechanical stretching [86]. Figure 2.9 shows the arrangement of collagen from the nano to the micro-scale: different pitch angles define the helix (a), triple-helix (b) or supercoiling (c) of this biopolymer. The periodicity is of the order of $\sim$1 nm for the helix, and 10 times larger for the triple helix, but it increases dramatically for the supercoiled fibril with a factor $\times$100 (1μm). Similarly, the diameter of the fibril increases to 100nm, while the helices' width is below 1nm. Three main different possibilities then describe the microscopic

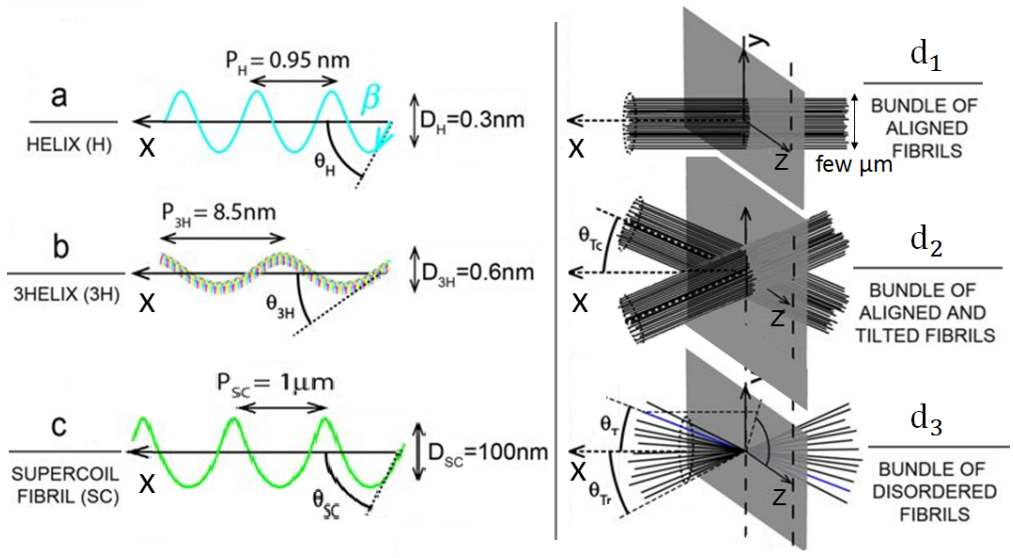

Figure 2.9: Description of the collagen orientation, supercoiling and arrangement at different scales. The triple helices (b) form a supercoiling (c) that is a fibril, and can give three different configurations: bundles of aligned fibrils (d1, e.g. tendon), bundles of aligned but tilted fibrils (d2, e.g. in cornea) or bundles of disordered fibrils (d3, e.g. in immature tissues, bone, fibrocartilage or liver vessels). Adapted from [182].

arrangement of the collagen fibrils: they can be gathered in bundles of aligned fibrils like in tendon or

fascia (fig. 2.9 d1)), or they can form many bundles of aligned fibrils, but tilted with respect to each other (fig. 2.9 d2)): these tilts can be confined in one specific plane, or be out-of-plane. This is the case for tissues having a well-defined order microscopically, but a disorder at the macroscopic level: collagen in skin, aortic artery [182], and some parts of the meniscus [151] (see chapter 4). Lastly, they might not be aligned, but assembled in bundles of disordered fibrils that point in many direction within a limited solid angle (d3 in Fig. 2.9): this can be found in injured or immature tissue, or directly in liver vessels, bone or cartilage (see chapter 4) [182].

SHG building in collagen

The SHG response of collagen seems to originate from the peptide bond itself, which is non-centrosymmetric with opposite charges at its ends [150]. Constructive interferences occur between the bonds that are parallel, and the signal is amplified along the triple helices, up to a length close to the wavelength. For distances longer than that, the phase-shift leads to destructive interferences. Reference [91] lists the molecular groups responsible for the SHG signal in collagen: the methylene group is also paramount.

Thus, only aligned fibrillar collagen (such as type I) can lead to SHG signal. Moreover, because fibrils are packed in fibers, they must be oriented in the same direction so as not to cancel each other. This limits the global SHG signal from fibers.

In conclusion, SHG mapping unfortunately does not provide a map of the fibers (or fibrils) themselves, but must be considered as a complex interference pattern [188, 174]. Other references such as [244] suggest that the SHG in tendon is capable of measuring the fibrils' diameter, with a comparison to measurements from AFM.

SHG in agrochemicals

SHG can arise from cellulose, a polysaccharide biopolymer present in cotton and wood. The signal from bulk cellulose is weak, however, with the most significant one coming from crystalline or nanocrystalline cellulose [117]. Also, it has been shown that crystalline structures are present in epicuticular wax, a layer on plant surface: SHG can be a diagnosis tool for it as well [80]. Lastly, SHG can be generated from starch, another polysaccharide, in higher proportions than in cellulose [164].

SHG building in other structural proteins?

The SHG building inside other proteins having a cylindrical symmetry, like myosin in muscle or tubulin in microtubules, follows roughly the same process as in collagen, partly because they also have a cylindrical symmetry. However, a comprehensive description of the building process must take into account the macroscopic structure of these biomaterials: it therefore has to be done case-by-case. The specific case of myosin is further developed in chapter 6.3. Lastly, we can add that natural silk has been shown to convert SHG [115], as it contains two piezoelectric structural proteins (fibroin and sericin).

2.1.8 Importance of polarization

The exciting beam probes the $\chi^{(2)}$ elements that are in its polarization axis: if the polarization is linear, it concerns only one axis, which can be tilted in the sample frame in certain cases. For instance, a linear polarization can excite d33=$\chi^{(2)}_{XXX}$ if its axis is X, or d34=$\chi^{(2)}_{XXY}$ if its axis is at 45° from X and Y. In that case, d33 will be also excited, as well as d34. However, if the sample frame is unknown, a circular polarization must be used in order to equally excite all the tensor elements. The polarization of the converted SHG (output) is also important to take into consideration, as some tensor elements may generate a SH polarized in the same direction as excitation (at 0°, e.g. $\chi^{(2)}_{XXX}$, $\chi^{(2)}_{YYY}$), but others generate a SH polarized at 45° (with e.g. d26=$\chi^{(2)}_{XXY}$) or 90° (with e.g. d23=$\chi^{(}2)_{YXX}$) from excitation. This output polarization can thus be analyzed with a polarizer to measure some properties of the sample (see p-SHG part). Yet, it has been shown that this polarization can be significantly affected by going through heterogeneous media such as biological tissues [70, 85]. Recent studies show that possible artifacts can be avoided by a careful data processing [84], and that by wavefront shaping it is possible to recover the correct output polarization even through highly scattering media [50].

2.1.9 Photodamages, rate of the laser source

SHG is free from photobleaching, but phototoxicity remains a problem when the fluence is too high, although it is already highly reduced by the confinement of the excitation to the focal volume. In point-scanning microscopy, the fluence is much higher than in whole-field for the same laser source, because the excitation volume is approximately 5e5× smaller, as seen before: this can lead to photodamages. Photodamages in SHG microscopy can of course be thermally damaging, due to a too high average

power, but it seems that photo-induced damages (due to a too high pulse energy or peak power) is a much more important factor in limiting the SHG that can be generated [234]. In transparent media, femtosecond pulses can produce a breakdown, with a formation of little bubbles, above a pulse energy threshold quite similar to the one observed for photo-induced damages (and as low as few nJ/pulses in NIR, 100fs) [234]. Therefore, even if high fluence can lead to these photodamages, it can be interesting to use it for some specific cases.

First, in non-biological - and therefore less photo-sensitive - materials: reducing the pulse rate implies a linear reduction of signal, but maintaining the same average power also allows the energy of the excitation pulse to be linearly increased. Indeed, while the SHG pulse energy scales quadratically with the excitation pulse energy, the detected signal scales only linearly with the inverse of the repetition rate (at constant average power). This is because the sample is excited N times less often if the repetition rate is divided by N, thus the signal is increased by $N^2/\mathrm{N} = \mathrm{N}$. Decreasing the repetition rate of a laser oscillator can thus be a strategy to increase the SHG signal in non-photosensitive media.

Secondly, in biological tissues: unlike whole-field illumination that is confined to the surface ($<250\mu$m), point-scanning can theoretically image up to a few mm [97]. This is achieved by collecting more ballistic photons, i.e. the small amount of the total number of photons that do not lose the information of their original point of emission. A simple strategy is thus to increase the pulse energy, to have a sufficient number of photons at an excitation point far in the depth of the material, and to retrieve a sufficiently high number of SHG photon at the detection point. The problem in the case of fluorescence, related in [97], is the out-of-focus fluorescence that blurs the final image.

Within biological samples, the inverse strategy, however, might be used to keep the energy per pulses at a safe level by increasing the repetition rate, which increases the average power. Indeed, the SHG signal scales linearly with it, as the medium is excited more frequently. A 2 GHz repetition rate allows, for instance, a 15frame/s SHG imaging with a scanning acquisition, where the dwell-time can be reduced thanks to the increased SHG signal (while remaining at an energy per pulses level safe for biological samples) [38]. For multiphoton fluorescence, the ideal delay between two excitation pulses is calculated by considering the relaxation time, and is found to be between 1 and 10 MHz [32]. Care must be taken not to go over the relaxation time of the medium, even more so for multiphoton fluorescences that have a latency time. In SHG, rates at several GHz have been demonstrated safe [193].

2.2 Recent improvements and possible future(s) in SHG

Many improvements in laser-scanning SHG have been made over the 30 years of existence of this technique. We highlight here the most relevant ones that may have implications with the projects of this thesis.

2.2.1 Wide-field SHG

Wide-field (or whole-field) imaging in SHG employs higher energy pulses to perform frame-by-frame capture (e.g. 200x200μm^2) instead of point-by-point, allowing for video-rate imaging (30frame/s or more). We refer to the previous section 1.3.1 for the difference between these two acquisition modes. However, wide-field imaging comes with the drawback of limiting the penetration depth to $\sim$10μm under the surface [97]. Indeed, because all the excitation photons are confined in the focal volume when using a laser-scanning configuration, the local intensity reaches a higher level than in the whole-field configuration: with a NA of 1.1, the focal volume is $0.4 \times 0.4 \times 1 \sim 0.15\mu m^3$, and the excitation volume in whole-field is $140 \times 140 \times 1 \sim 20000\mu m^3$. So, the excitation area is divided by 5e5, and the SHG is reduced by 2.5e11. To retrieve sufficient signal, the pulse rate can be reduced from $\sim$100MHz (as in standard oscillators) to $\sim$10kHz, improving the pulse energy by 1e4 at constant average power. Furthermore, the pulse duration can be reduced by a factor of 10 and still retrieve the same level of SHG signal, as with laser-scanning, going from $\sim$300fs to $\sim$30fs. All of these modifications imply that, most of the time, the use of a new laser source is required. Lasers with a repetition rate of a few kHz are thus employed for this application [152]], enabling the recording of areas which are up to 1000$\times$1000μm^2 [127]]. Note that the team of C. Depeursinge [196] and the team of V. Barzda [253] still showed the possibility of using wide-field SHG using with a 80MHz oscillator, but with a relatively high average power on the sample ($>$3W, whereas there is usually $<$0.1W in MPM). They have also confirmed that a lower repetition rate could allow this technique to reach a sensitivity comparable to scanning SHG microscopy (which they operate in a more recent study [194]), and highlight that the development of more sensitive CCD cameras could also significantly enhance the performances of wide-field SHG.

Temporal focusing is sometimes exploited to reduce the out-of-plane illumination inherent to the wide-field technique, and to improve the axial resolution to a comparable value with point-scanning two-photon microscopy [147]. The set-up uses a "temporal lens", where the frequencies of the pulse are

scattered at the back-focal plane of the microscope objective: each frequency will therefore travel at a different angle to recombine in the end at the focal point. Before the focal point, the spatial chirp makes the effective pulse duration larger than the Fourier limited one, reducing the peak power when the pulse is not in the focal plane [147]. It should be noted that this technique was also employed in scanning multiphoton imaging, enabling a video-rate acquisition thanks to the increase of signal, despite the use of a point scanning scheme [96].

2.2.2 Improved resolution

Some attempts have been made to improve the resolution, using techniques usually applied to other fields of microscopy: structured illumination [246, 230] which provides a $\sim$1.5-fold increase in resolution, and even a 4-fold increase is demonstrated as theoretically achievable in [126]. Another approach is to use a subtracting method as in [224] which is the principle of the SLAM (Switching LAser Mode [72]) applied to SHG, which achieves a $\sim$1.3 times improvement in resolution. Finally, the PSF in SHG is claimed to be not well-defined due to its coherent nature, and some advanced deconvolution algorithms used with an old technique that previously served to improve the SNR, [16] in order to address this issue: a 3.5$\times$ higher SNR can thus be obtained for SHG images [200].

2.2.3 Wavelength-dependent SHG

In multiphoton microscopy, a 900nm excitation wavelength is preferred, because it penetrates more in tissues (due to less scattering) [254] and leads to lower group-velocity dispersion in optical elements [35]. However, the excitation wavelength must remain close to the maximum conversion efficiency of the tissue: for collagen's SHG, this range is between 700 and 800nm [254]. The optimal wavelength for SHG is thus a compromise between conversion efficiency and penetration depth. More recently, some studies used the wavelength dependency of SHG to differentiate between myosin and collagen by changing the wavelength of excitation [78], [25].

2.2.4 Other improvements

Here are listed promising techniques to enhance SHG, however they are only at inception for now:

Hyper-spectral SFG: Sum-Frequency Generation (SFG) microscopy is, like CARS, sensitive to the chemical nature of the medium as it is a process sensitive to molecular vibrations. But like SHG, it also only reveals the non-centrosymmetric structures, and shows a resolution and acquisition speed similar to other multiphoton techniques [92]. Spectrally resolved SFG coupled to a polarization study allows for a characterization of the nonlinear susceptibility tensor of the imaged structure, and to reach higher contrast than non-resonant SHG [90].

Non-conventional SHG in bulk: SHG is not generated in a homogeneous bulk, because a centrosymmetry exists, whereas at the interfaces this symmetry is broken. But under a high concentration of photons in space and time, magnetic-electric and quadrupole-electric interactions can happen, and such a generation is then possible [236].

Unpolarized excitation light: SHG from unpolarized excitation light has been experimentally shown to be independent of the birefringence of the sample and of the polarization distortion that can occur in it (especially in biological ones, see section 2.1.8) [55]. This aspect is further developed in [76].

Stimulated SHG: In its standard use, the SHG only comes from the spontaneously converted signal (with no seed), and the conversion is constrained to a low-level. The authors of [77, 71] used a reference SHG light (similar to I-SHG, see next section) to stimulate the conversion of the SHG inside the sample: both signals are made temporally coincident, with twice as much power for excitation as for the reference beam. With exciting fluence of only a few nJ/μm^2, a factor of amplification of 4 is reported. However, a lock-in detection was used, which requires a modulation (chopper) at a few kHz, and the thickness of the sample has a maximum of two collagen fibrils in order to avoid the phase-mismatch between the fundamental and reference SHG that would happen otherwise [77].

2.3 Interferometric SHG to enhance standard SHG

Interferometric SHG (I-SHG) is the main subject of the thesis [174] chap.5-7, which provides a comprehensive description of this technique using sample-scanning acquisition to avoid the objective phase aberrations, and an excitation with ps pulses such that the temporal dispersion of the beams has a negligible effect. This description is completed in the master memoir [45], that deals with fs pulses and thus has a temporal dispersion compensation. In this thesis we will not repeat every element of the technique for the sake of brevity, but rather emphasize the main points - and especially the new insights

- that were encountered during the continuation of the I-SHG project. Here, we will examine the purely theoretical considerations: the more applied and technical aspects about the experimental configuration are developed in 3.2.

2.3.1 Existing methods to extract the SHG phase

Historical review

The history of the phase measurement of SHG is well-described in [174](chap. 5, p.125), showing that is has been done since 1986 on molecules, and then on ferroelectric crystals in 1992, but the first microscopy image of domain inversions was published only in 1995 [229]. We can cite that [30] measured the phase of the nonlinear susceptibility for the first time in 1965, using a pressurized vacuum box. With the rise of OCT techniques, in 2003 Jiang *et al.* incorporated SHG into an OCT set-up [103] that employed interferometry. Jeon *et al.* [101] anticipated in 2004 that interferences in SHG will be utilized to determine the polarity of ferroelectrics and biological tissues. Very soon after "Interferometric second harmonic generation microscopy" [245] was published, but it wasn't until 2011 that this technique was applied to biological tissues [249]. However, probably shortly before, holographic SHG microscopy was used to image the relative phase in collagen dermis [195]. Notably, heterodyne interferometric CARS was published shortly after the primary I-SHG inception, first proposed by Marks & Boppart in 2004 and applied by Potma *et al.* in 2005 [163] to enhance the CARS contrast and remove its background by separating the real and imaginary parts of the $\chi^{(3)}$. We can also cite that in 1998, heterodyne SHG was already exploited for surface SHG phase measurement [232], and in 1998 and 2003 Wilson *et al.* [242, 243] employed interferometric SHG in spectroscopy (but not microscopy) with 15fs pulses, which also pioneered its later use. The same was done in 1999 [121], with a Babinet-Soleil compensator to perform the phase-shift. Note that [101] also operated with a rotating plate for phase-shifting, just like [41] that also performed in-situ interferences. Finally, the team of V. Barzda developed Interferometric Third Harmonic Generation (I-THG) using the backward-collected signal in 2014 [186].

Holographic SHG imaging

SHG imaging by holography is a wide-field technique (see section 2.2.1) that consists of recording both the amplitude and phase of SHG produced by the sample at video-rate. Interferograms are used to

measure the phase that is reconstructed numerically in post-treatment, thus the name "digital". They are acquired by superimposing, at the detection plane, a SHG signal from the sample (object wave) and the SHG produced by a non-centrosymmetric crystal (reference wave) [193]. Coherence may limit the interference zone in the hologram, but some methods described in [132] and [5] allow one to overcome this problem. The interferograms are recorded either by phase-shifting (the method used for I-SHG), or by off-axis interferometry [193]. The off-axis method simply consists of spatially isolating the good term in the results of the multiplication of the complex amplitudes of object and reference wave.

Numerical focusing

Holography can be exploited to record a whole-field interferogram, which makes use of a Fresnel propagation function to determine the optical field not only in the measured plane, but also in other planes near focus. It is commonly employed to correct the focusing errors [212, 48].

Aberrations correction

The aberrations introduced by the optical elements, especially the microscope objective, must be corrected. For this, a numerical function can be applied to the image since these aberrations are supposed to be predictable, because they are decomposable into Zernike's polynomials [42]. This implies there must first be a classic 2D phase unwrapping to remove phase discontinuity. The correction can also be applied by recording a reference image (without sample), and afterwards dividing the sample amplitude by the reference or subtracting the two phase maps (because the phase is the argument of the exponential, a division of the complex term results in a subtraction of phases) [43]. With classic holography, this is done by simply recording without any sample, whereas in SHG a flat non-centrosymmetric sample (e.g. a crystal) must be used to effectively produce the signal. The problem is this crystal might introduce other aberrations itself [193]. The subtraction technique is similar to what we use for I-SHG galvos scan correction, as we will see later in section 7.

Holographic SHG thus presents many similarities with I-SHG, especially if the phase-shifting technique is used. The main differences remain in the wide-field configuration, and the Mach-Zehnder type of interferometer (splitting and recombination of the arms). Yet it was only applied to crystals or nanocrystals that have a strong $\chi^{(2)}$ like BaTiO_3 [193], probably due to the fact that a too low signal was obtained from samples with weak $\chi^{(2)}$. This is where I-SHG can have a real upside: it can be applied precisely for such samples, like biological tissues.

2.3.2 Basics of I-SHG

I-SHG is, like holography, an interferometry technique. In any interferometer involving two fields, the coherent superposition implies that the amplitudes of both arms are summed at the detector, which creates a cross-term containing the arguments of the complex exponentials. The simplified I-SHG intensity can then be written as (with subscript R being for the reference arm, and S for the sample arm, γ the interference contrast and φ the (full) optical phase):

$$I_{ISHG} = I_R + I_S + \gamma \cos\left[\varphi_R - \varphi_S\right] \tag{2.23}$$

Measuring the relative phase φ_S thus requires extracting the argument of the cosine. Fig. 2.10 explains

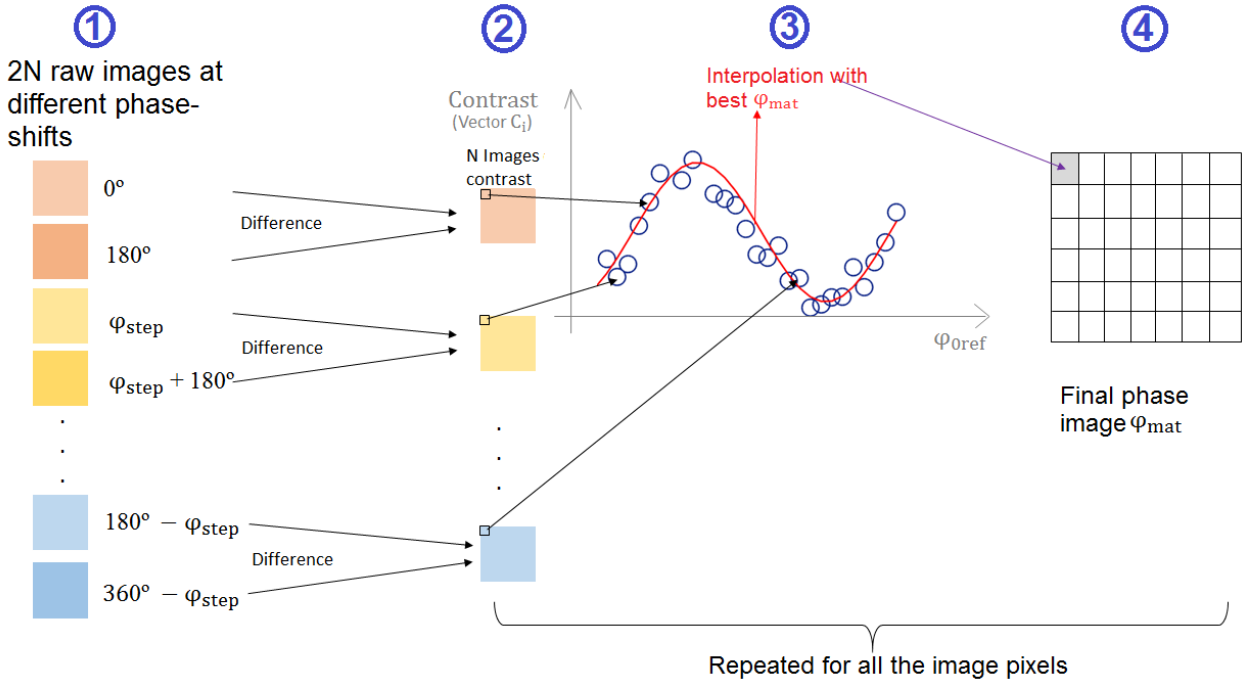

Figure 2.10: Diagram of the algorithm for calculating the phase. The 2N raw images are subtracted 2 by 2 to give N contrast images. Every given pixel at a certain position follows a cosine law with respect to the phase-shift of the interferogram, which can be interpolated to find the optical phase.

that varying the phase-shift (1) between both arms (which basically means varying the optical path of one wave *w.r.t.* the other) makes the cosine argument vary, usually from 0 to 2π (3). Two π phase-shifted interferograms are also usually subtracted (2) to remove the term $I_R + I_S$ in eq. 2.23 (see the thesis [174] eq.3 or section B.3.1). Once the experimental cosine is obtained (blue circles in (3)), a fit can be applied to find its components: amplitude (that is the interference contrast γ), and argument (relative phase φ). The operation is repeated for each pixel of the image (4). This method of fitting

the cosine from several points is called Phase-Shifting Interferometry (PSI): the mathematical details for the phase extraction can be found in Appendix B.3.

2.3.3 Interferometer configurations for I-SHG

Many different options have been listed in the thesis [174] part 5.3) for varying the phase-shift between both arms: a pressure-adjustable gas enclosure, a delay line to produce the reference SHG at a different distance from the sample, a translatable prism pair of calcite, or a rotatable glass plate. Other possibilities are listed here, which for most cases involve a generation of the SHG of the reference arm using a nonlinear crystal (quartz, BBO).

(*) First, some interferometers are completely adapted for microscopy: this is the case of Nomarski's or Mirau's interferometers. In Nomarski's configuration (used in DIC, see Introduction), a Wollaston prism is employed for separating an input wave into two orthogonally-polarized components that will be recombined by another twin prism after having been phase-shifted differently by the sample and sent to the detector where they can interfere (Fig. 2.11, (a)). There is thus no reference wave generated, as the two waves both come from the sample. However, such a set-up would include all the limitations of DIC microscopy, like the problem of thick samples. Mirau's set-up uses a beam splitter to separate the two arms, but placed between the microscope objective and the sample (see Fig. 2.11, (b)): the nonlinear crystal used for reference SHG can be put close to the reference mirror for efficient generation. However, it would require a long working distance objective (which is usually not the best for multiphoton microscopy), and works only in reflection: only the backward or the forward retro-reflected SHG could be exploited.

(*) Second, a delay-line acting on both beams: it takes the same principle as the pressurized gas enclosure, but simply uses the refractive index dispersion of air. It leads to a 1.18rad/cm phase-shift between a fundamental at 800nm and its SHG. This few mm translation per phase-shift is easily achievable by an inexpensive translation motor and presents a linear relationship. It is however rarely used in practice as the delay-line needs to be aligned very accurately to ensure that its translation implies no dis-alignment of the beams, and both beams needs to be perfectly collimated so as to not change the focus position in the end.

(*) Another possibility would be to translate only either the excitation or the reference SHG, after having separated them. Figure 2.12 shows two configurations, a Michelson (a) and a Mach-Zehnder (b): both use the combination of a QWP (quarter-wave plate) and a polarization beam-splitter (PBS) to achieve a

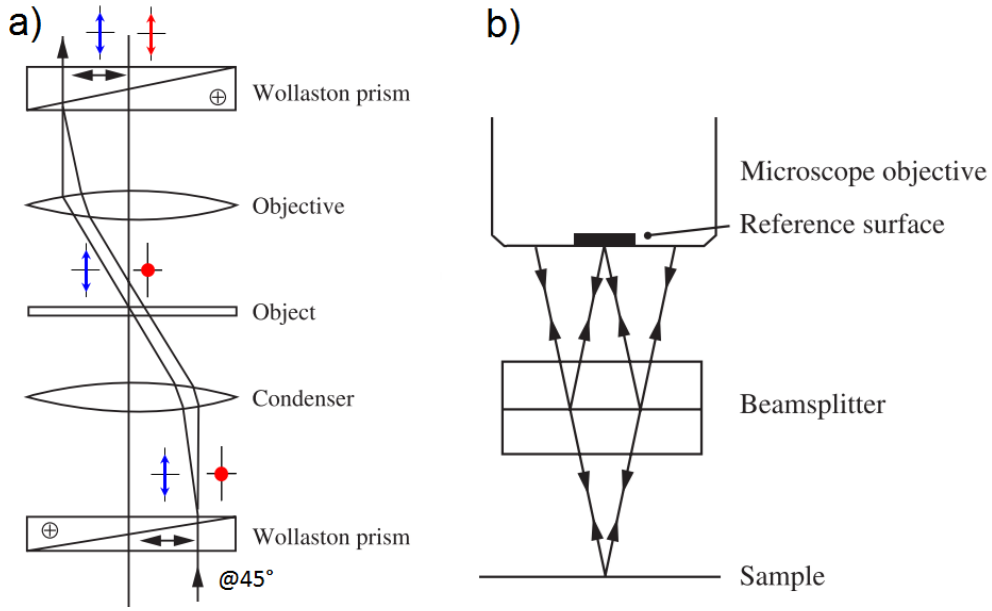

Figure 2.11: (a) A Nomarski interferometer with two Wollaston prisms. (b) A Mirau interferometer close to the focus of a microscope objective. Extracted from [94].

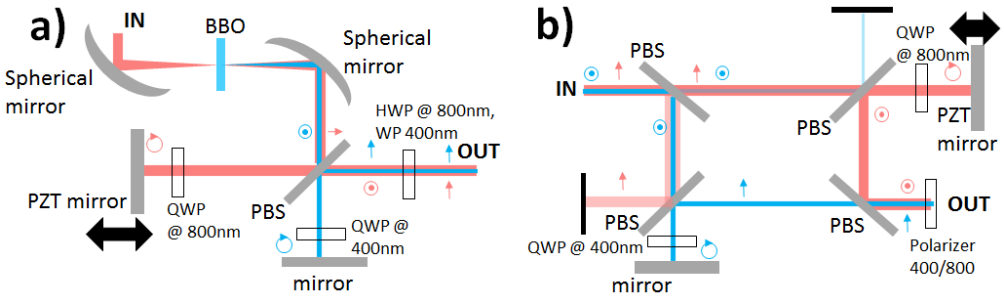

Figure 2.12: (a) A Michelson configuration for interferometric SHG. (b) A Mach-Zehnder configuration. Both set-ups work at the two wavelengths of interest. PBS: polarization beam-splitter, PZT: piezoelectric transducer, QWP: quarter-wave plate, HWP: half-wave plate, BBO: beta-barium borate crystal.

lossless self-reflection of the beam. Two of the PBS can be replaced by dichroic mirrors (which generate more polarization distortion), and the PBS in the bottom path serves to rotate the polarization, to balance the arm lengths and to filter the remaining fundamental. The distance to translate would then be a fraction of the wavelength (plus any multiple of it), reducing the precision of the translating motor to under $\sim$ 100nm. Only a piezo actuator can achieve these steps, with a precision as low as a few nm. (*) Some phase-shifters utilize a diffraction grating with a spatial frequency f, moved by a distance Δ that produces a wavelength-independent phase-shift (at e.g. the 1st order of diffraction) of $2\pi f\Delta$ [47]. Similarly, an acousto-optic cell can be used to produce a temporary grating, or a Zeeman laser can naturally produce a phase-shift [47]. However, they have the disadvantage of selecting only one of the orders of diffraction, implying that the power loss can be quite high [47].

(*) Another smart set-up is to exploit waveplates: as shown on Fig. 2.13, the combination of a QWP and a rotating HWP can be used to apply a $+2\theta$ phase-shift on the fundamental, and a -2θ (total phase-shift of 4θ) to the reference SHG if the fast axis of the HWP is at θ from the horizontal. Since a HWP is invariant by 90° rotations, the maximum phase-shift is then $4\times90=360°$ (2π). After, either a QWP (lossless) or a linear polarizer (2/3 losses) can convert the polarizations back to a linear state [217].

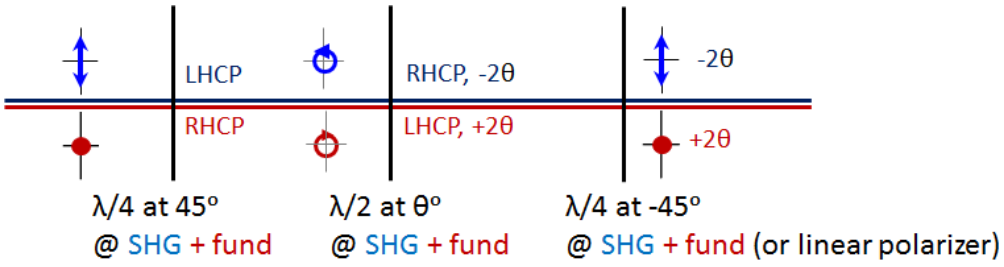

Figure 2.13: Schematic of a phase-shifter composed of waveplates: the quarter-wave plate (QWP) will create a RHCP (resp. LHCP) wave for the fundamental (resp. the reference SHG) wavelength, and the rotation of a half-wave plate (HWP) by an angle θ with respect to the horizontal will phase-shift the waves by $+2\theta$ (resp. -2θ). After, a QWP will convert the polarizations back to a linear state (a linear polarizer can also be used).

Simultaneous interferograms

A possibility to reduce the number of phase shiftings and even get rid of any phase-shifters would be to use a dielectric beam-splitter before the PMTs: two options are given on Fig. 2.14. The first one (a) requires that the reference arm comes independently from the sample arm (thus, does not go through the microscope path). It still necessitates a phase-shifter because, theoretically, a minimum of three interferograms [238] are required to reconstruct the relative phase. The only advantage is thus to divide the acquisition time by 2. The second configuration b) can collect all the interferograms in one shot, if four phase-shifts are assumed to be sufficient to reconstruct the phase. Otherwise, it reduces the acquisition time by a factor of 4 and many phase-shifts are recorded. Its main drawback is that the reference and sample waves must be perfectly linearly polarized, and at 90° from each other, even after crossing the sample thickness. Also, if the polarization of the SHG converted by the sample is along a different direction, the quarter-wave plate and the PBS must be turned accordingly to keep the same polarization transformations.

Both configurations complicate the general set-up, but their main limitation is the decrease of the number of photons collected for one interferogram since they are divided on multiple detectors

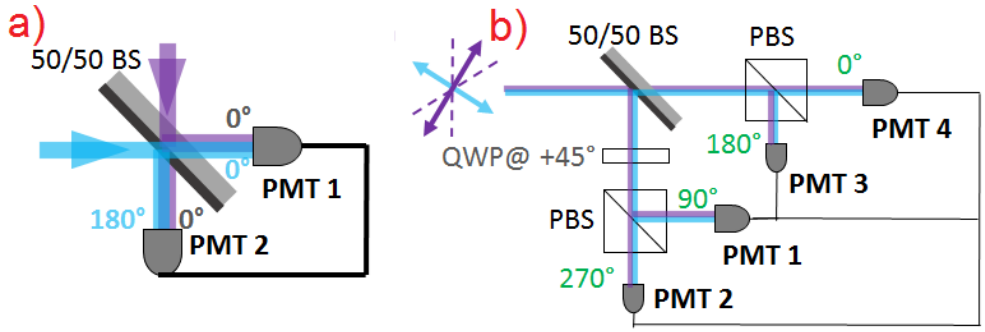

Figure 2.14: Two possible configurations for simultaneous measurement of phase-shifted interferograms. (a) Use of a 50/50 dielectric beam-splitter (BS) that induces a pi phase-shift on the reflected component from low to high optical index (one side of the BS) while the one reflected from high to low optical index is left unchanged (as well as the transmitted ones). The reference (purple) and sample (blue) signals are thus either 0° phase-shifted on one PMT, or 180° phase-shifted on the other one. (b) (inspired from [114]) The reference and sample beam are here orthogonally polarized, respectively at 45° and -45° from the horizontal. Again, the 50/50 beamsplitter (BS) put a 180° phase-shift between reflected and transmitted waves. The quarter-wave plate (QWP) on one arm has its slow axis parallel to the polarization of the reference beam, and will produce an additional +90° phase-shift on it and -90° on the sample beam, without changing the polarizations. The role of the two polarization beam-splitters (PBS) is to equally divide the reference and the sample beam on the two pairs of PMTs, while introducing a 180° phase-shift between them. The final polarizations on each arm will be parallel, and interferences will occur. In the end, there are four arms where the relative phase-shift between both beams is 0 and 180° for the first pair, 180+180+90≡ 90° and 180+180-90≡ 270° for the second pair.

(not to mention the optical losses on each BS, PBS or QWP). Having only one fourth or half of the signal that is "normally" collected can be quite problematic especially in biological samples where the detection sensitivity is often close to maximum, and where the exciting optical power is limited to avoid photodamages.

Lastly, a technique like [58] could be used to extract the phase directly from a (single-shot) spectrogram at each pixel, recorded at the standard pixel rate (∼100kHz), to therefore provide high-speed I-SHG. The limitation determined by the author is the need for quite a large exposure time (up to 1ms) to get a spectrum with sufficient SNR.

2.3.4 Interference fringes on the radiation pattern

The radiation pattern of the collected I-SHG signals can be observed with a CCD camera. By translating the path difference, the fringes or rings appear, depending on the orientation of the reference and the excitation beams, as shown in Fig.2.15. Figure 2.16 shows some examples of such CCD camera images. The first (2.16 a)) shows parallel fringes oriented in a particular direction, meaning that the reference and excitation beam are not exactly collinear when they travel through the microscope. When the alignment is improved, the fringes tend to become a hyperbola (2.16 b)), and turn to rings when the overlap is

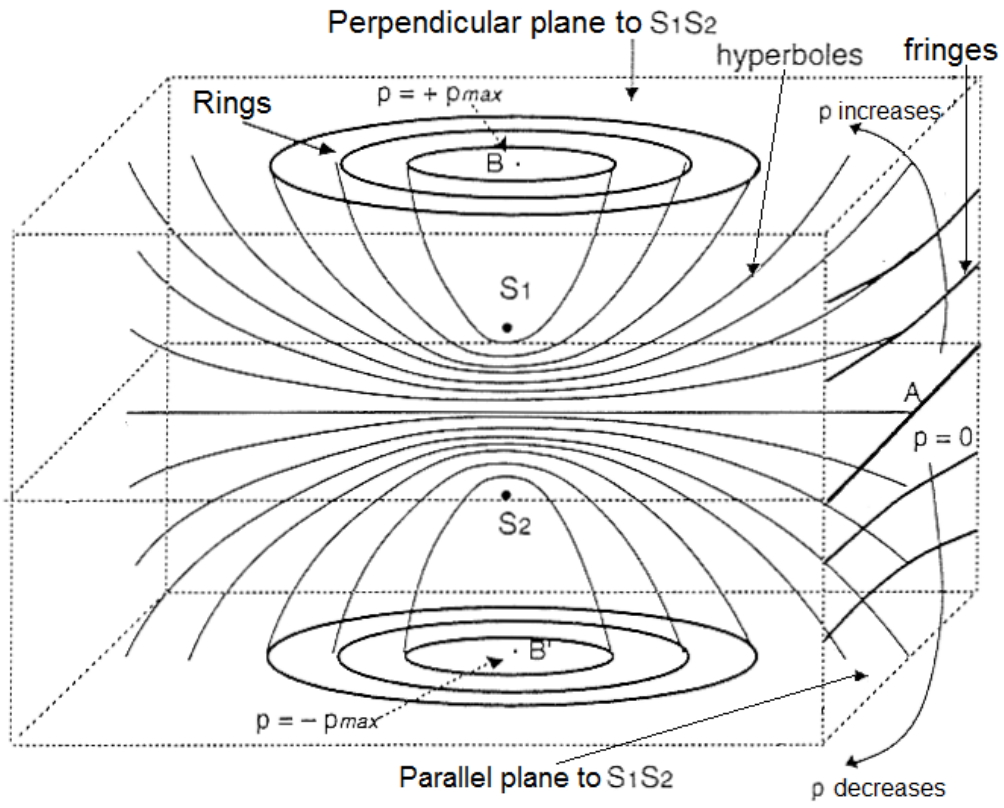

Figure 2.15: Revolution hyperboloid due to two-wave interferences. Figure extracted from [44].

perfect (2.16 c1)). However, if the beam underfills the back focal plane of the microscope objective, the rings are thinner and the contrast change (maximum = constructive, minimum = destructive) does not happen in the full field-of-view (Fig. 2.16 c1 and c2)).

When the two interfering beams are collinear, the pattern of interference is some concentric rings such that the path difference δ depends only on the angle i_n between the center of the pattern and the n-th ring: $\delta = 2e\cos(i_n)$. The variable e here is the optical path difference between the two beams at the center of the pattern. The first ring is bright (constructive interference), thus: $2e\cos(i_1) = k\lambda$ with k being an (unknown) integer. The more the two interfering pulses are shifted in time, the higher k is. The n-th ring radius of the interference pattern (taken from the center) is: $R_n = f'\sqrt{2-(k-n+1)\lambda/e}$, where f' is the equivalent focal length used to image the interference pattern. In a standard Michelson, i > 0 means that the entrance beam is tilted with respect to the arms of the interferometer. On the whole, rings are thus obtained when using a diverging source. In our I-SHG microscopy case, the interferometer is not a Michelson's, but the point is the same: the rings seen on the CCD camera are the consequence of the divergence of both reference and excitation beams. They lead to a decrease of contrast, because it means that rather than having a complete and homogeneous interference over the whole field-of-view,

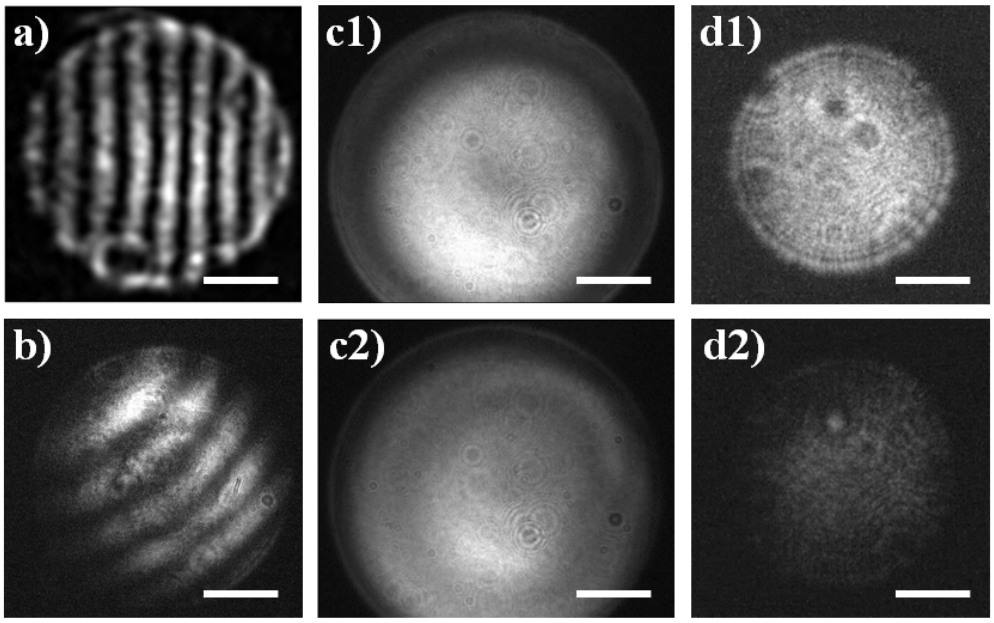

Figure 2.16: Interference pattern on a CCD camera, for different alignment conditions. (a) Vertical fringes, obtained when the reference wave is tilted with respect to the sample wave. (b) Portion of hyperbola, the case in-between fringes and rings. (c1) and (c2) Interference rings, when the two interfering arms are parallel but with a divergence. (d1) and (d2) Flat profile, meaning the two interfering beams are perfectly collinear with no divergence.

different parts of it will interfere differently. Also, these kinds of rings have been shown experimentally to be more sensitive to misalignment. Figure 2.16 (right) shows a constructive (d1) and destructive (d2) pattern when the alignment is perfect: the I-SHG alignment should thus try to reach this flat pattern to ensure the highest contrast.

2.3.5 I-SHG equation with ultrashort pulses

The previous calculations assumed a paraxial plane wave, yet we have seen (section 2.1.3) that in tight-focusing microscopy, at least the Gaussian description of the beam must be considered: in the frequency domain, a Gaussian pulse has a spectral power density as [235]:

$$S(\omega) = |E(\omega)|^2 = \frac{\exp\left(-(\omega-\omega_0)^2/2\sigma_\omega^2\right)}{\sqrt{2\pi}\sigma_\omega} \tag{2.24}$$

The I-SHG total intensity (measured at the detector) is the coherent sum of the electric fields of the reference (R) and sample (S) SHG beams, because the generated SHG are collinear until reaching the

detector [235]:

$$\begin{aligned} &I_{I-SHG}(2\omega) = |E_R(2\omega) + E_S(2\omega)|^2 = |E_R(2\omega)|^2 + |E_S(2\omega)|^2 + 2\,\mathrm{Re}\left[E_R(2\omega)E_S^*(2\omega)\right] \\ &\Leftrightarrow I_{I-SHG}(2\omega) = I_{SHG,R}(2\omega) + I_{SHG,S}(2\omega) + I_{R+S}^{AC}(2\omega) \end{aligned} \tag{2.25}$$

The cross-term $I_{R+S}^{AC}(2\omega)$ is the interference term, which varies in space or time ("AC"). We write the electric field (in the general case) as a product of a term that varies quickly in space and time, and an envelope $A(\omega)$: $E_R(\omega) = A_R(\omega)\exp\left(i(k_R(\omega)l_R - \omega t)\right)$, with $k_{R,0} = 2\pi/\lambda$ the wave vector, and l_R the optical path of the reference beam. The same expression can be written for E_S, and it should be noted that the temporal term in $e^{-i\omega t}$ is canceled out in I_{R+S}^{AC}, I_R and I_S. Also, $\Delta l = l_R - l_S$ depends on the position vector $\vec{r}$. Because the used laser is absolutely not monochromatic, but rather has a spectral width of 10nm (for 100fs at 810nm), $I_{R+S}^{AC}(2\omega)$ is then the superimposition of all the frequencies (ω is the central frequency of the fundamental) [235, 45]:

$$\begin{aligned} &I_{R+S}^{AC}(2\omega) = 2\,\mathrm{Re}\left[\int_{-\infty}^{+\infty} A_R(2\omega)A_S^*(2\omega)\exp\left(-i\Delta\phi(2\omega)\right)d\omega\right] \\ &\text{where}\ \ \Delta\phi(2\omega) = 2k_S(2\omega)l_S - 2k_R(2\omega)l_R \end{aligned} \tag{2.26}$$

Assuming the two interfering pulses have similar envelopes, we can write $S(2\omega) = A_R(2\omega)A_S^*(2\omega)$. The wave vector can be expanded in a Taylor series: $k(\omega) = k(\omega_0) + (\omega - \omega_0)\sum_j \frac{dk}{d\omega}\Big|_{j,\omega_0}$... We limit it here at the 1st order, i.e. we consider only the group velocity mismatch (GVM) for now. The index j is used to sum all the different media where the GVM between the two pulses is significant (glass, calcite ...), and Δl_j is their thickness. We also make the assumption that the envelope of the pulses is symmetrical with respect to the center frequency. Then, the argument of the integral in the equation 2.26 can be split into one term independent of ω, and another one with ω [235]:

$$\begin{aligned} &I_{R+S}^{AC}(\omega) \propto \cos(2k(\omega_0)\Delta l)\int_{-\infty}^{+\infty} S(\omega)\exp\left(-2i\left[\omega-\omega_0\right]\sum_j \Delta l_j\,\Delta k_j'\Big|_{\omega_0}\right)d\omega \\ &\Leftrightarrow I_{R+S}^{AC}(2\omega_0) \propto \cos(2k_0(2\omega_0)\Delta l) \times FourierTransform\left[S(2\omega)\right](2\omega_0) \end{aligned} \tag{2.27}$$

where Δl is the optical path difference between the two pulses. Here we note: $\Delta k_j'\Big|_{\omega_0} = \frac{dk}{d\omega}\Big|_{j,\omega_0}^{R} - \frac{dk}{d\omega}\Big|_{j,\omega_0}^{B}$ the difference of k' between the two pulses (i.e. the GVM) for medium i. We see that the envelope is the Fourier transform (FT) of the spectral power density, which is exactly what the Wiener–Khinchin's theorem states. The standard deviation of the Gaussian $S(2\omega)$ can be expressed as: $\sigma_\omega = 1/\sigma_\tau =$

$2\sqrt{2\log 2}/\sigma_{\tau,FWHM}$. The FT of a Gaussian being also a Gaussian, it yields [235, 45]:

$$I_{R+S}^{AC}(2\omega_0) = 2\gamma_0 \exp\left[-16\log(2)\left(\frac{\sum_j \Delta l_j \, \Delta k_j^{'}\Big|_{\omega_0}}{\sigma_{\tau,FWHM}}\right)^2\right]\cos(2k_0(2\omega_0)\Delta l) \tag{2.28}$$

where γ_0 is a proportionality constant. The interference pattern is thus modulated by a Gaussian envelope that varies with the path difference of the interferometer. Its FWHM is exactly the FWHM of the fundamental! Here the 2nd order dependence of the wave vector $k(\omega)$ with ω is neglected, such that the (temporal) chirp of both pulses is ignored. It can nevertheless become significant for fs pulses, if the GDD (group delay dispersion, related to chirp and this 2nd order effect, see 3.2.2) is over $\sim$5000fs^2 (at 810nm). Furthermore, the considered fields are scalar, because the detection is made along the transmitting axis of a linear polarizer (the analyzer). However, the reference or sample beams may have an angle α with the excited axis of the local $\chi^{(2)}$ of the sample: the considered fields are then $E_R\cos\alpha_1$ and $E_s\cos\alpha_2$.

If the chirp of the pulses is considered, the wave vector must have an additional term in its Taylor series expansion: 2nd order development must be considered : $\frac{1}{2}(\omega-\omega_0)^2\sum_j \frac{d^2k}{d\omega^2}\Big|_{j,\omega_0}$. The difference of phase is then:

$$\Delta\phi(\omega) = k_0(\omega_0)\Delta l + \sum_j \mathrm{dispersion}_{\omega,\omega_0,j} \tag{2.29}$$

where $\mathrm{dispersion}_{\omega,\omega_0,j} = \left(\Delta l_j(\omega-\omega_0)\Delta k_j^{'}\Big|_{\omega_0} + \frac{1}{2}\, l_{d,j}(\omega-\omega_0)^2\Delta k_j^{''}\Big|_{\omega_0}\right)$, $l_{d,j}$ is the thickness of materials (glass, calcite) where the GVD of both pulses is different (i.e. every medium except air, a priori). It is not equal to Δl_j, because the latter is nothing but the optical path difference of both beams in medium j. Similarly to before, $\Delta k_i^{''}\Big|_{\omega_0} = \frac{d^2k}{d\omega^2}\Big|_{i,\omega_0}^{R} - \frac{d^2k}{d\omega^2}\Big|_{i,\omega_0}^{B}$. Substituting this into equation 2.26 leads to:

$$I_{R+S}^{AC}(2\omega_0) = 2\,\mathrm{Re}\left[\exp\left(-ik_0\Delta l\right)\int_{-\infty}^{+\infty} S(\omega)\exp\left(-i\left[\sum_j \mathrm{dispersion}_{\omega,\,\omega_0,j}\right]\right)d\omega\right] \tag{2.30}$$

A calculation similar to equation 2.27 and 2.28 yields ([235] p.208):

$$I_{R+S}^{AC}(2\omega_0) = 2\exp\left(-ik_0\Delta l\right)\mathrm{Re}\left[\frac{\sigma_\tau}{\sqrt{\sigma_\tau^2+i\tau_d^2}}\exp\left(-\frac{1}{2}\frac{\left(\sum_j \Delta l_j \Delta k'_{j,\omega_0}\right)^2}{\sigma_\tau^2 - i\tau_d^2}\right)\right] \tag{2.31}$$

with :

$$\tau_d^2 = 2\sum_j l_{d,j}\Delta k''_{j,\omega_0} \text{ and } \frac{1}{\sigma_\tau^2+i\tau_d^2} = \frac{\sigma_\tau^2}{\sigma_\tau^4+\tau_d^4} - i\frac{\tau_d^2}{\sigma_\tau^4+\tau_d^4} = A + i\,B = r_1\,e^{i\theta_1} \tag{2.32}$$

The real part (A) of this term implies a temporal broadening of I_{R+S}^{AC}, and its imaginary part (B) implies a temporal chirp [235]. One can push the calculation further:

$$\begin{aligned}&\frac{1}{\sqrt{\sigma_\tau^2+i\tau_d^2}} = \sqrt{A+i\,B} = r\,e^{i\theta} \quad \text{with} \quad r = \sqrt{r_1} = \frac{1}{(\sigma_\tau^4+\tau_d^4)^{1/4}} \\ &\text{and } \theta = \frac{1}{2}\theta_1 = \frac{1}{2}\,\mathrm{Arctan}\,\frac{B}{A} = -\frac{1}{2}\,\mathrm{Arctan}\,\frac{\tau_d^2}{\sigma_\tau^2}\end{aligned} \tag{2.33}$$

Thus, placing this into eq. 2.31 (it becomes the real part):

$$\begin{aligned}I_{R+S}^{AC}(2\omega_0) = &\frac{2\sigma_\tau}{(\sigma_\tau^4+\tau_d^4)^{1/4}}\exp\left(-\frac{\sigma_\tau^2}{2(\sigma_\tau^4+\tau_d^4)}(\sum_j \Delta l_j \Delta k'_{j,\omega_0})^2\right) \\ &\times\cos\left(2k(\omega_0)\Delta l + \frac{\tau_d^2}{2(\sigma_\tau^4+\tau_d^4)}(\sum_j \Delta l_j \Delta k'_{j,\omega_0})^2 - \frac{1}{2}\,\mathrm{Arctan}\,\frac{\tau_d^2}{\sigma_\tau^2}\right)\end{aligned} \tag{2.34}$$

There is thus an additional multiplicative term, that will decrease the amplitude of I_{R+S}^{AC} if the difference of chirp $\tau_d^2 \propto \sum_j \Delta GDD_j$ increases (however, it decreases the argument in the exponential and thus the autocorrelation function will be broader, see 3.2.2). In general, we will remember that the chirp will limit the interferometric contrast, and that a smaller pulse bandwidth σ_τ tends to increase it.

The final and global equation for I-SHG - in the general case, considering polarizations - is:

$$\boxed{I_{ISHG}(2\omega_0) = I_{SHG,R}(2\omega_0)\cos^2\alpha_1 + I_{SHG,S}(2\omega_0)\cos^2\alpha_2 + \gamma_{\omega_0}\cos\left[2k_0(\omega_0)\Delta l + \text{chirp\_effect}\right]} \tag{2.35}$$

with $\gamma_{2\omega_0}(\Delta l;\sigma_\tau;\alpha)$ the generalized interferometric contrast, and $I^{AC}_{R+S}(2\omega_0) = \gamma_{\omega_0}\cos\left[2k_0(\omega_0)\Delta l + \text{chirp\_effect}\right]$. If the pulse is Gaussian, and *only the 1st order* of temporal dispersion is considered, chirp_effect $= 0$ and:

$$\boxed{\gamma_{\omega_0,1^{st}}(\Delta l,\sigma_\tau,\alpha_1,\alpha_2) = 2\gamma_0\sqrt{\cos\alpha_1\cos\alpha_2}\exp\left[-16\log(2)\left(\frac{\text{group\_delay}}{\sigma_{\tau,FWHM}}\right)^2\right]} \tag{2.36}$$

For taking into account the 2nd order temporal dispersion, equation 2.34 must be considered:

$$\begin{boxed}{\text{chirp\_effect} = \frac{0.5}{1+(\sigma_\tau/\tau_d)^4}\left(\frac{\text{group\_delay}}{\tau_d}\right)^2 - \frac{1}{2}\operatorname{Arctan}\frac{\tau_d^2}{\sigma_\tau^2}}\\ \boxed{\gamma_{\omega_0,2^{nd}} = 2\gamma_0\sqrt{\cos\alpha_1\cos\alpha_2}\frac{2}{(1+(\tau_d/\sigma_\tau)^4)^{1/4}}\exp\left[-\frac{0.5}{1+(\tau_d/\sigma_\tau)^4}\left(\frac{\text{group\_delay}}{\sigma_\tau}\right)^2\right]}\end{boxed} \tag{2.37}$$

with group_delay $= \sum_j \Delta l_j \Delta k_j'\Big|_{\omega_0}$, $\tau_d^2 = 2\sum_j \Delta GDD_j$ and σ_τ the temporal width of the pulse (see before, or 3.2.2 for an extended definition of group delay and GDD). The dependence on position vector $\vec{r}$ is omitted in intensities, Δl and group_delay for clarity.

Equation 2.35 is the standard expression for two-waves interferences. In experiments, it is easy to have group_delay=0, and the contrast is not too low. As it is more convenient to take $\gamma_{\omega_0}(\Delta l,\sigma_{\tau,FWHM},\alpha_1,\alpha_2) = \gamma$ (independent of the parameters), and $\alpha_1 = \alpha_2 = 0$, these simplifications will be made throughout the thesis, especially in the phase retrieval calculations of Appendix B.3.

Chapter 3

Technical

Last night, I saw a car with the license plate
ARW-357. Can you imagine? Of all the millions
of license plates in the state, what was the chance
that I would see that particular one tonight?
Amazing! Richard Feynman

This chapter aims at describing some technical aspects related to the different projects of the thesis, as well as the changes of the multiphoton microscope and its controlling software, which all make up one significant part of this thesis. Important aspects for building a nonlinear optical microscope are discussed, and I-SHG details and improvements are presented. Finally, notable points about the phase-scanner used for I-SHG are detailed.

3.1 Building and improving a MPM apparatus

3.1.1 Optical arrangement inside microscope for laser-scanning

Usual MPMs employ a laser-scanning system, as already mentioned. Different technologies, such as resonant mirrors, polygonal mirrors, and acousto-optic deflectors can be used instead of the standard galvanometric (galvo) mirrors, especially for speed improvement. But since the pixel rate of MPM is

usually limited to 250kHz [35], non-resonant galvo-mirrors are usually sufficient, especially since they can work over a large range of scan speeds and wavelengths while limiting polarization distortions.

Theory

The galvo mirrors used in laser scanning microscopy are coupled to a microscope objective. This implies various considerations:

- the deflected beam at the back focal plane of the objective must be optically corrected to avoid geometrical aberrations at the focus of the objective

- the back focal plane of the objective must be overfilled to ensure maximum resolution (beam diameter $\sim$ 16mm) on the one hand, but on the other hand the galvo mirrors must be typically under 10mm large to maximize their speed and repeatability. Thus, the beam must be small at the galvos and then magnified before arriving at the objective.

- The mechanical scan angle of the galvo must correspond to the smallest optical scan angle at the focus, such that relatively small optical steps can be performed without entering into the limited mechanical resolution of the galvos: a de-magnification of the scan [40] is needed, which means - again - a magnification of the beam between galvos and objective.

For all these reasons, a telecentric relay is usually implemented. A schematic view of such a set-up is shown in Fig. 3.1A. It consists of the combination of a scan lens and a tube lens, arranged in a double

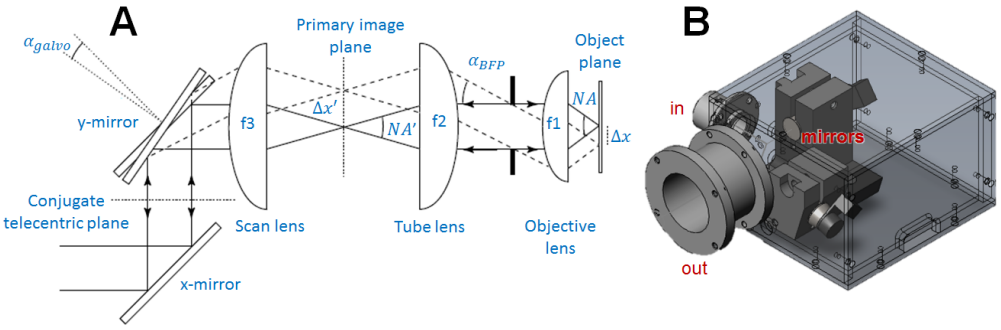

Figure 3.1: Telecentric set-up for galvos scanning. Adapted from [205]

telecentric 4f set-up to obtain best optimal performances [39]. The entrance and exit pupil are then located at infinity.

In Fig. 3.1A, we see that the field-of-view in the focal plane of the objective can be expressed as:

$$FOV = \Delta x = 2 f_{obj} \tan(\alpha_{BFP}) \tag{3.1}$$

where $f_{obj} = f_1$ is the focal length of the objective and α_{BFP} the angle of the deflected beam at the back-focal plane. By definition $f_{obj} = f_{TL}/M_{specs}$, with f_{TL} the tube length and M_{specs} the magnification of the objective ensured by the manufacturer. It is also easy to show that between the scan lens (SL) and the tube lens (TL), one has $\tan(\alpha_{BFP}) = \tan(\alpha_{inc}) f_{SL}/f_{TL}$ [40]. α_{inc} is the angle of the incident beam on the scan lens: by the law of reflection, this angle is twice the mechanical angle $\alpha_{galvo,mech}$ of the galvo mirror with respect to the shaft. Finally, the relationship between an optical scan distance d_x and the mechanical scan angle to impose to the galvo is:

$$d_x = 2\frac{f_{SL}}{M_{specs}} \tan(2\alpha_{galvo,mech}) \Leftrightarrow \alpha_{galvos,mech} = \frac{1}{2} \operatorname{Arctan}\left(\frac{M_{specs} d_x}{2 f_{SL}}\right) \tag{3.2}$$

The tube lens is not present in the final equation, only the scan lens matters here. However, the tube lens does have an effect on the effective magnification: $M_{eff} = \frac{f_{TL}}{f_{TL,specs}} M_{specs}$. $f_{TL,specs}$ is the design tube lens of an infinity-corrected objective which varies depending on the manufacturers, but is usually 200mm (180mm for Olympus). In the real set-up, the magnification will be multiplied by 1.1 because a 200mm tube lens is used with an Olympus objective. Noteworthily, this lens affects the optical aberrations. Indeed, reference [250] shows that the tube lens must have a focal length small enough to ensure approximated paraxial conditions, even at large angles:

$$f_{TL} \leq \frac{f_{TL,specs}}{M_{specs}^2 FOV} \left(D_{TL} M_{specs} - 2NA f_{TL,specs}\right) \tag{3.3}$$

where the subscript "specs" stands for the theoretical value in specifications, and D_{TL} is the tube lens diameter. With classical values of NA=0.8 and a diameter of 30mm, FOV size of 0.6mm and magnification of x20, this value is usually close to 200mm. Provided this condition is respected, it is usually not sufficient to ensure low optical aberrations: custom scan and tube lenses have to be implemented, or expensive multi-purpose ones (containing many lenses) have to be purchased [137, 179, 220]. Even if inexpensive alternatives are possible [170], practical limitations are expected for any given apparatus.

3.1.2 Reasons for replacing the (old) digital galvanometric mirrors

The iMic microscope in our lab comes with galvos mirrors controlled by a Digital Signal Processor (DSP), which is why their control is "digital". However, these galvos present some drawbacks:
(1) they have been in use for a long time, and at some point began to show unexpected errors, noise

and reduced performances. Also, their command unit tended to overheat quickly.
(2) their size was small ($5\times5mm^2$), which limits the usable beam size.
(3) they come with a custom scan lens and tube lens, and as well with a conjugation system in the middle of the mirror pair. However, these optics were likely optimized for near-IR fluorescence excitation. Indeed, they had:
(3a) very poor transmission around 405nm (around 1%), which can force the use of thick nonlinear crystals in I-SHG to have the same level of signal in the reference and sample arms (see section 3.2.1).
(3b) a high polarization distortion, both in ellipticity and direction. This is not suitable for a coherent process like SHG (but can be partially corrected).
(3c) a limited field-of-view (with a "vignetting" effect, see section 3.1.3) due to the imperfect coupling of the scan lens and tube lens (telecentric optics), and to limited performances.
(3d) a difference of focus position in the depth between 810 and 405nm (for I-SHG), because the telecentric optics are achromatic in a limited range: they are not meant to work at the edges of the visible range (like at 405nm).
(3e) a large GVM (for I-SHG) between 405 and 810nm (see section 3.2.1), and a large chirp difference between those wavelengths (estimated $>$ 6000fs^2). This is due to the amount of glass of the (transmission) optics used by the galvos (conjugation ones and telecentric optics). The chirp at 810nm is estimated at 2000fs^2, which also broadens the pulse in standard SHG.
(4) the scan parameters were difficult to control, as the DSP unit only takes full scans in input, formatted in a language specific to the DSP.

Point (1) was later corrected by implementing a large heatsink to reduce overheating, and mainly with a better control of the command and errors by passing from LabView to a new Python program (see section 3.1.5). Point (2) is less significant than expected, because the beam needs to be small: its diameter is increased anyway by the telecentric optics by a factor of 3 to 5 to obtain a slight overfill of the 15-25mm back pupil of the objective. Still, for all the other numerous reasons - and especially to better suit the I-SHG technique (see section 3.2) - new galvos mirrors were implemented, the housing for which can be seen in Fig.3.1B. Their size was chosen at 12.5x12.5mm to avoid any beam clipping. They also incorporate some achromatic doublets working in the visible and NIR, thus correcting points (3a), (3b), (3d), and improving points (3c) and (3e). Lastly, since they have an analog control, point (4) is not a problem anymore.

Maximum FOV without clipping

The old galvos mirrors were already on the microscope, but the optical set-up and path could not be used for the new galvos for various reasons:
- the beam is convergent between the two galvos mirrors (a special configuration, see [205]), and divergent at the exit such that it is corrected by the scan lens after. That is not the case for the new galvos.
- the system (either the scan lens or the tube lens or both) would deform the polarization a lot, because the microscope was conceived for fluorescence imaging that has little concern with this property.
- these lenses are mostly responsible for the poor transmittance of the reference SHG at 400nm (1%)

Thus, a new line was implemented on the microscope using the second floor of the microscope. The new scan lens and tube lens also have to be chosen considering many different criteria:
- the tube lens must not be larger than 200mm to be in the paraxial regime (see eq. 3.3) and in general the closest it can be to 180mm to ensure the effective magnification is the one indicated on the Olympus objective.
- the input beam must have a diameter around 3mm to stay collimated, but not higher than 5mm to not clip on the galvo mirrors and in other parts of the telescope where it will be expanded $\times 4$.
- the path through the armature of the microscope is also limiting: any lens or mirror put inside it must have a maximum diameter of 30mm (which means the beam cannot be tilted at a too large angle).
- any optical element must be positioned at a minimal distance of 150mm from the objective (beyond, there is the injection mirror and the path becomes vertical, so it is inaccessible).

Table 3.1 summarizes the main features and limitations for different set of lenses. Choosing a focal

Focal of scan lens (mm)	Focal of tube lens (mm)	Overfill of tube lens (mm, on one side)	Beam diameter at BFP of objective (mm)	FOV (mm)	Min. pixel step *
40	200	3.1	20	0.5	0.56
50	200	1.3	16	0.6	0.7
50	180	0	14	0.7	0.7

Table 3.1: Summary of the important lengths for the telescope in galvo scanning, for different sets of lenses. Assuming an input beam diameter of 4mm, a maximum deflection angle of $\pm 4°$ (mechanical) as in [205], diameters of respectively 25mm and 30mm for the scan lens and tube lens, a back focal plane diameter of 16mm, and a Gaussian beam. * Considering a 4mV noise on the galvo position.

for the scan lens that is too small (1st line of table) leads to an important clipping on the tube lens (at maximum deflection angle), and to a beam diameter that is slightly too large before the objective. However, the beam is more de-magnified, and a higher resolution can be reached by the galvos, at the price of a smaller effective field-of-view (FOV). If the tube lens focal length is too small (last line of table), the beam is not magnified enough. A compromise has been made by choosing a 50mm scan lens (the achromatic doublet ref. 49-356-INK from Edmund Optics) and a 200m tube lens (the achromatic doublet ref. 49-377-INK from Edmund Optics).

As shown in Fig. 3.2, the tube lens is placed 50mm closer to the objective than it should be (150mm instead of 200mm). This implies that the scan plane - i.e. the virtual plane where the beam is tilted - must be $50 \times \left(\frac{f1}{f2}\right)^2 = 3.3$mm farther from the scan lens to compensate [220].

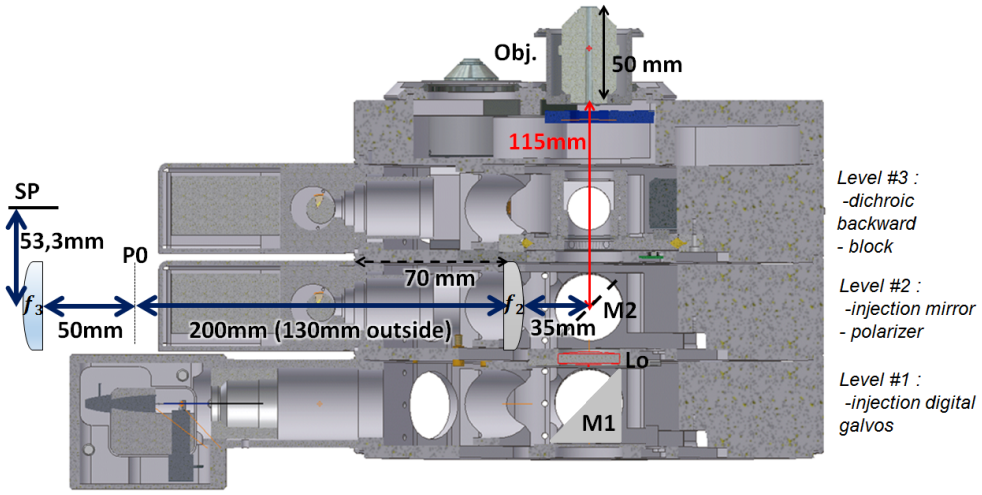

Figure 3.2: Schematic of the iMic microscope used, with the different stages and the telecentric system. SP : scanning plane, P0 : intermediary image plane, f3 : scan lens, f2: tube lens, M2 : relay mirror, Obj. : microscope objective. For the digital galvo path: Lo : tube lens , M1 : relay mirror.

3.1.3 Laser-scanning: FOV considerations

Real FOV in laser-scanning

The theoretical field-of-view (FOV) for an objective (attained in wide-field, for instance) is [202]: $FOV = F.N./\text{Magn.}$ where Magn. is the magnification of the objective, and F.N. the field-number that is usually fixed by the manufacturer. For Olympus, F.N. $= 22mm^2$ so that FOV $= 22/40 = 550\mu m^2$ for a 40 X and 1.1mm for a 20X. Some papers, like [228], for specific applications, tend to exploit the

full FOV by using custom lenses in the scan set-up. In many microscopes however, the focalization by a lens becomes rapidly non-paraxial when used off-axis, and the FOV are then limited to $1/3$ [137] of the values cited above.

Vignetting: this also implies a non-uniform illumination of the sample: the edges have lower intensities (vignetting effect) - noticeable in images of $200\times200\mu m^2$ and a real limitation for $400\times400\mu m^2$ ones - which leads to artifacts, especially when mosaics of images are created to image a large area. [188] suggests dividing the images by a reference, for example an image of a fluorescent plate where a parabolic 2D fitting has been applied to retrieve the shape of the illumination. We put a code for mosaic reconstruction using this correction in appendix C.5.

Laser divergence: the laser has a natural divergence of 1mrad (depending on the beam diameter): a priori, a 1-2m focal lens (converging) can be used to allow the beam to be collimated at the focus of the objective [35], in order to maximize the resolution and the FOV.

Nyquist criterion

The Nyquist criterion [35] states that the sampling frequency must be higher than twice the maximum frequency of the signal, i.e. the step size must be smaller than half of the transverse resolution. For 810nm, with a NA of 0.8, the theoretical resolution is $\sim$0.4μm (see [255] for calculation). So, the step size should theoretically be under 0.2μm.

If this criterion is not satisfied, the highest frequencies in the sample are not resolved, and the microscope is not used at its full capacity. If the step size is much smaller than half the transverse resolution, the image is just over-sampled (redundant information). An oversampling of $1/2.5$ to $1/3$ the transverse resolution is usually advised, because it can help to improve the accuracy of a digital detector (as described in [203]). Also, this allows for compensation of the low-pass filtration that is required for perfect image reconstruction in real optical systems [203].

3.1.4 Microscope configurations, type of objectives and coverslip choice

Up-right microscopes are more suitable for observations of microscopy slides, because the sample is then under a thin coverslip and the immersion medium can be easily applied between it and the objective. Also, an up-right microscope allows for a better detection of forward signals [35].

Inverted configurations are made to observe under a petri dish. Generally, a long working distance objective illuminates the sample, which has the possibility to be in a water bath (for biological media). A water bath (or column) can also be used to avoid retroreflection of the forward signal onto the backward detection (in SHG applications) [119], but would be more difficult to implement on an up-right configuration. For low W.D. objectives, the microscopy slides can be turned upside-down, which enables their imaging with an inverted configuration. The only disadvantage can be gravity acting on the sample, but in most cases the sample is thin and well-maintained.

In an up-right configuration, especially for short W.D. objective, the danger is crashing it into the coverslip while trying to find/optimize the focal plane, which would damage the sample and, more rarely, the objective. This is not really a problem in inverted microscopes, because the illumination objective approaches the sample *from below*: a small lift of the slide (visible with the eye) - even more if the slide is loosely fixed - is a witness of a contact between it and the objective. However, an up-right configuration is mandatory if the sample is imaged in a water bath, with no glass interface (using a water dipping objective, see after).

Configuration	Normal use	Focus finding	Thick water immersion	Retroreflection compensation	Forward detection	Dipping illumination	Dipping collection
Up-right	Micr. slides + coverslip	Hard if low W.D.	Difficult	Difficult	Better	Yes	No
Inverted	Petri dish, coverslip	Easy	Yes	Yes	Good	No	Yes

(*) Objective types

Many types of objectives are available depending on the targeted application, at different price ranges.

Oil immersion objectives are mainly used to achieve high N.A. illumination (because the index of the immersion fluid can be over 1.5), but that is not their only use. A true advantage of these objectives are without doubt their index matching: the refractive index of the immersion fluid can be relatively close to the coverslip's one (glass), resulting in higher Fresnel transmission and lower aberrations. Thus, we conclude that these objectives are very efficient at imaging *through glass*, though at small W.D.

Water-immersion objectives: because the water is more convenient to use and clean, manufacturers invented objectives that replace oil immersion by water (but achieve lower N.A. of course), and thus are useful for samples having a glass coverslip on top.

Water dipping objectives are made to excite or collect light without a glass interface: they are useful

for samples in a water bath (mainly used for *in-vivo* biological samples) - because they can work without aberrations - but a long W.D. is required which can dramatically increase the cost of the lens.

Air objectives are used when the required N.A. is under 0.8. They are relatively convenient as they do not need any fluid (less chances of damaging the objective by the cleaning process). Some of these objectives are *corrected for coverslips* (to avoid aberrations while focusing): their optimal use is for excitation or collection with a sample covered by a coverslip of the correct thickness (see later). We can call them "air immersion" by analogy with the water immersion.

Others are *not corrected for coverslips*, so they should only be used to excite a sample without a coverslip (a microscopy slide turned upside-down with the sample well-stuck on it for an inverted microscope), or collect light directly in contact of the sample. We can call them "air dipping", by analogy with the water dipping.

The two objectives used for this thesis are a 20X air immersion and a 40X water immersion, both from Olympus and with working distance below 0.5mm. The immersion objectives are utilized to image or collect through a coverslip, and usually have a correction ring to adapt to different coverslip thicknesses. But this assumes that the user actually knows the coverslip thickness! Indeed, coverslips labelled "# 1.5H" are the more reliable ones, because their thickness is $170 \pm 5 \mu m$ so that the thickness mismatch is at maximum 5 μm. But in the case of cheaper "#1.5" or "#1" ones, the uncertainty on thickness is up to 30 μm! This becomes a problem when using such objectives with high N.A., as Fig. 3.3 shows: for a N.A. of 0.8 or higher, the illumination/collection efficiency can decrease by more than 60% if the thickness is 30 μm away from the manufacturer's value. The user must therefore take care of controlling the thickness of the coverslips while using such objectives. It is worth noting that some

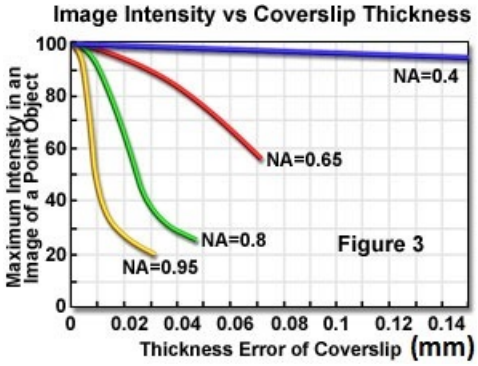

Figure 3.3: Measured average intensity vs the mismatch of coverslip thickness for water-immersion objectives of different N.A. (Reference: Olympus)

companies now offer objectives that support different immersion media (water, silicone oil, glycerine,

oil), like the Zeiss's model LD LCI Plan-Apochromat 25x/0.8 Imm Corr DIC M27. Water objectives also have the disadvantage of the evaporation of the immersion fluid over time (several hours) - especially if the samples is heated, for example at 37° C - which can result in axial drift at first, or complete loss of focus at some point. The loss of water can also occur if the sample is moving. Some companies offer a water dispenser driven by software that helps to solve this issue [120]. In the case where the problem is only the evaporation, smart immersion fluids can be used to replace water: these are oils having the refractive index of water (n=1.33, at 25° C). Every main objective manufacturer has its own (adapted to its objective), but a generic example can be obtained at Cargille's (ref AAA-1.33) [29].

Table 3.2 summarizes the different properties. Generally, the combination of a high N.A. and a long

Immersion Type	Air "Dipping"	Air Immersion	Water Dipping	Water Immersion	Oil
N.A.	<0.8	<0.8	<1.0	<1.2	<1.45
W.D.	long	fair, long	fair, long ($+)	short, fair	short
Use	Focal plane at long distance/trough plastic	Glass coverslip (controlled thickness)	Water bath, water layer, Petri dish	glass coverslip (controlled thickness)	Glass interface
Cleaning	No	No	Evaporation, simple tissue	Evaporation, simple tissue	Alcohol needed

Table 3.2: Comparison of different objectives. Short W.D. are < 0.2mm, fair are in [0.3-0.99] mm, long are > 1 mm, very long are > 3mm

working distance will increase the objective's price a lot. The correction of aberrations over a large wavelength range is also expensive.

(*) NA of collection:

A collector with a NA slightly higher than the excitation one (e.g. 0.9 for 0.8 excitation NA) is required to be sure the whole radiation pattern is collected, especially in SHG ([35]). However, such condensers (which can be microscope objectives) are often placed at a distance less than 1mm from the sample to achieve these NA: they can be inconvenient for thick samples, or prevent the use of water columns to avoid retro-reflection, for instance [119].

3.1.5 A new software code in Python for MPM

A new program coded in Python was implemented throughout this PhD, in order to replace the deficient LabView code used until then. It opened the possibility to do some improvements, enabling smoother

use during experiments. Since the details of this program are useful only for someone wishing to modify it, and for the sake of brevity, the details are included in the appendix (section A.2).

This software allows for (non-exhaustive list), see Fig. 3.4:

- smooth control of all instruments independently: stage for XY scanning, control of objectives and microscope's path, piezo for Z stepping, rotatable glass plate, HWP, QWP, spectrometer, beam shutter, phase-scanner (1).

- full acquisition of the images and transfer to tiff files in the disk: mode galvos (digital or analog), stage-scanning, or static acquisition (3).

- complete control of any scan parameter, with automatic calculation of their inter-dependence (2).

- definition of ROIs on the image, and interactive actions of the user on the scan (4).

- possibility to put "jobs" (5), in queue or not, i.e. automatic procedures to do several scans with a change of some parameters between images.

- an automatic treat of the I-SHG in live, via a call of the MatLab GUI.

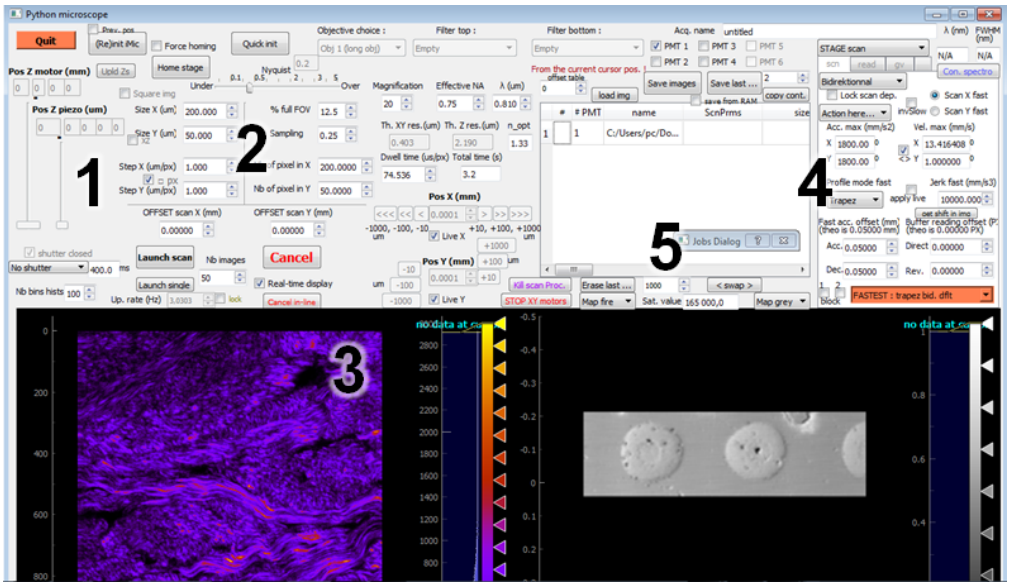

Figure 3.4: Python program for microscope (GUI), integrally developed during this PhD.

3.1.6 Fast and controlled stage-scanning

Sample-scanning has the main advantage of avoiding the inhomogeneities of excitation in the image plane. Also, in the case of precise devices like piezo steppers, the resolution and the minimal move step can be improved as well. Last but not least, a large field-of-view (FOV) can be achieved without mosaic

reconstruction, while limiting the aberration in the objective. This subject is addressed in chapter 4. Table 3.3 summarizes the different advantages and limitations of the different scan methods. We clearly

Type	img time (s)	Optimized exposure time (μs)	Max FOV (mm)	resolution (nm)	Intensity profile
Motorized stage	71[b,d]	58	75[d]	250[d]	flat
Piezo stage	80.2[c]	500	0.2[c]	0.5[c]	flat
Laser scanning device (e.g. galvos)	0.8[a,*]	5	0.4[**]	< 100[***]	2D parabola [188].

Table 3.3: Comparison of scan time for different modes. [a] With a classic image of 400$\times$400μm^2, 1μm/pixel, 20μs exposure time.
[b] Same parameters but exposure time optimized (58μs/px) to have the lowest image time. [c] Based on the 2kHz max frequency of PI's piezo XYZ motors. [d] Considering the Thorlabs MLS203 stage controlled by BBD102 limitations. [**] Limited by the objective FOV capability (dictated by its magnification): here, 20X considered. [***] Value empirically noticed. *With the same exposure time as the one optimized for a motorized stage, this value goes to 9.3sec. When compared to the piezo stage one, this value goes to 80sec.

see the main limitation of doing sample-scanning over a laser-scanning: the imaging time is multiplied by up to 100 (it is worth noting that the exposure time by pixel is usually higher, though). There is, however, no FOV correction needed (see 3.1.6). A motorized stage was chosen in our lab to perform sample scanning: they are usually cheaper than the piezo ones, and can achieve scans over a FOV as large as a few tens of mm in a reasonable time. The scan time can be greatly reduced - and the scanning itself much more controlled - if all the parameters of the scan dynamics are well controlled. This aspect is developed in detail in section A.3, in the appendix so as not to overload the core of the text. We have reported in Fig. 3.5 the comparison of imaging time between a naive implementation of the stage-scanning (far left), and the optimized ones for different modes, for two different scan sizes (two colors). This figure acts as a summary of what is developed in the appendix: the meaning of each scan mode can thus be found there. From this figure we will just keep in mind that this type of scan - if optimized - can be performed 2 to 10 times faster than the standard implementation, which we reported in [10] for instance. The absence of aberrations in the objective in stage-scanning has been a real asset for the implementation of I-SHG (see [174], chap.5), as we will see now.

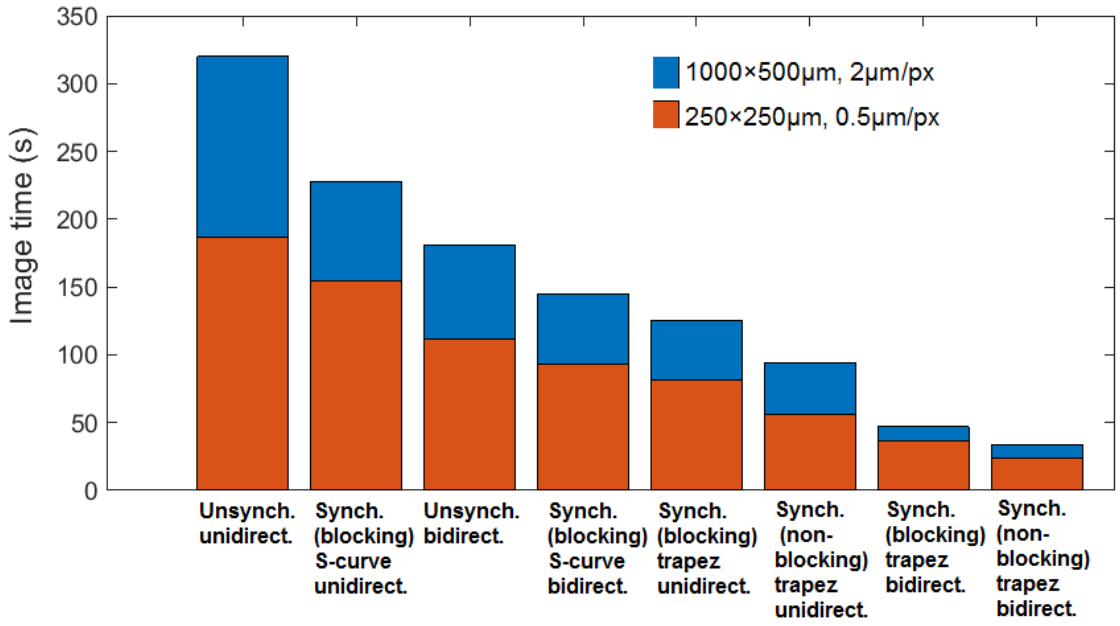

Figure 3.5: Comparison of the imaging time difference between different scanning techniques. The reference scan (blue) is 100x500 pixels, 2μm/pixel, 1800mm/s2 of maximum acceleration. The one in red is 250x250 pixels, 0.5μm/pixel

3.2 Interferometric SHG: practical considerations

3.2.1 Contrast improvement

The full set-up for I-SHG acquisition can be found in Fig.1 of the article of Chapter 9. We will describe here a few methods to enhance the interferometric contrast.

Choosing the correct polarization in I-SHG (and other SHG derivatives)

In many applications (including I-SHG), people have to choose the best linear polarization to excite their sample to have a maximum signal, and to be sure that the polarization is parallel to the collagen fibrils. This choice is often made by optimizing the signal in a reference sample. Also, some people use p-SHG to select only one frame corresponding to the best image: reference [204] gives a review of assessment models and useful parameters for comparison of entropy, pixel contrast and variance.

For having the best contrast, the polarizations of the reference SHG and the sample SHG should be as parallel as possible (see equation 2.35). Figure 3.6 is complementary to part 2.4) of the article. It

shows the optimization of the waveplates used before entering the microscope (half-wave plate, HWP and quarter-wave plate, QWP). For (a) and (b), the QWP angles are put in abscissa, and the HWP angles in ordinates: the polarization direction measured at each set of the two waveplates is color-coded according to the color-wheel on the right (cyan = vertical, red = horizontal). We see that, despite the clear differences between a) and b), it is still possible to find a couple of (angle$_{HWP}$;angle$_{QWP}$) that ensures the same direction of polarization for the 405 (reference) and 810nm (sample) beams. The corresponding angles are indicated by black and white crosses. These angles are also plotted in c), to appreciate the difference in orientation between the 405nm and the 810nm for the chosen waveplates pairs. Except for some angles like the interval [160, 180]° , there are small differences between polarization direction at both wavelengths (a few tens of ° or less).

However, the ellipticity is also important, and must be as small as possible (0 = polarization perfectly linear): in Fig. 3.6d), the measured ellipticity varies from 0.2 to 0.6 or more. Overall, the set of waveplate angles must be chosen carefully, and are different for every case. A finer step for the waveplates angles could also allow us to improve the measured performances for a given polarization direction, by finding the optimal couple (angle$_{HWP}$;angle$_{QWP}$). Note that the use of only a HWP alone (no QWP) is also a possibility that actually works quite well, if there are not too many deforming optics on the path to the microscope. This is the case for the stage-scanning set-up, and to a lesser extent for the new analog galvos configuration. For the digital galvos (the case of Fig. 3.6), the associated scan lens and tube lens (see section 3.1.2 in the Appendix) prevent the use of such a simple arrangement, as can be seen in Fig. 3.6e): some angles (40, 45°) work for both wavelengths, but the majority show high discrepancy in polarization direction and ellipticity between those two wavelengths. Some HWP angles even lead to inverted polarization directions (e.g. HWP=20°). To conclude, this confirms the possibility to use both wavelengths, 405 and 810nm, on the same optical path for I-SHG, and still have good performances in terms of polarization matching, even if some optics distort it a lot like in the digital galvos case. The input polarizations need, however, to be well-controlled using calibrated HWP and QWP.

These calibrations are nevertheless limited to corrections down to $\lambda/4$. Dichroics or special coatings may in rare cases need finer corrections, by smaller sub-multiples of λ: a Babinet-Soleil or Berek compensator can then be used to properly correct the polarizations. However, even if they can be broadband, these compensators correct only one specific wavelength, and have a completely different effect at the SHG one, for instance. It is unclear if some retardance settings can correctly compensate the different retardances that both wavelengths experience in the microscope.

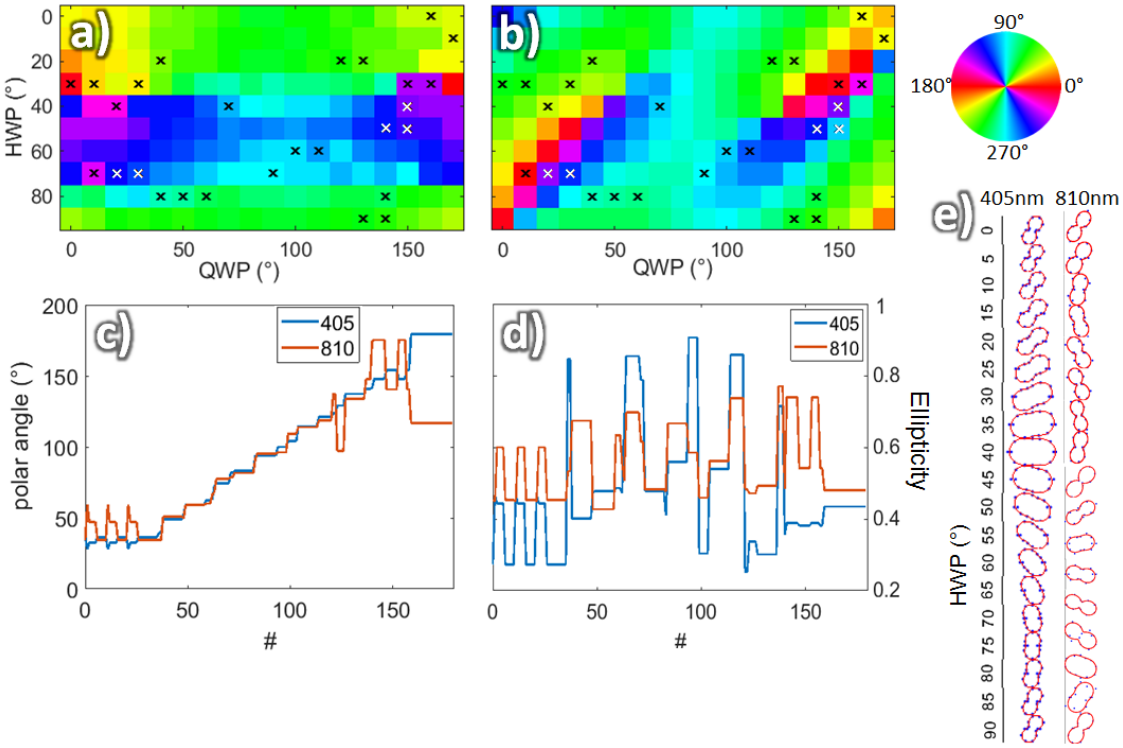

Figure 3.6: Map of the measured polarization at focus, of the fundamental (810nm) and SHG of reference (405nm), using the digital galvos mirrors and the I-SHG set-up with the phase-scanner. The waveplate angles are varied by steps of 10°. (Top) Polarization direction angle measured at 405nm (a) and 810nm (b), as a function of the HWP angle and the QWP angle. The direction is color-coded according to the colorwheel on the right. The directions of polarization that matches for both wavelengths - and that is thus selected for the final polarization control - are indicated by (black and white) crosses. (Bottom) Plot of the different chosen angles: polarization direction (c) and associated ellipticity (d) for both wavelengths, 405nm and 810nm. (e) Full polarization description at 405 and 810nm if only the HWP is used from 0 to 90°. Experimental points are blue markers, fitted by a red curve.

Reference SHG generation

To generate the reference SHG for I-SHG microscopy, a non-linear crystal that works with type I or type II critical phase-matching such as BBO is used. If the thickness of the crystal is too important, the phase-matching conditions are not fulfilled for all the spectral components of the fundamental pump, and the generated SHG may have a shorter spectral width implying a larger temporal width. This is called the phase-matching bandwidth. It is calculated considering the width of the sinc^2 function (with a plane wave approximation 2.1): this function decreases by a factor of 2 at 1.39, and is expressed using the derivative with respect to the wavelength of the phase-matching condition (at 1st order) [213]:

$$\delta\lambda_{FWHM} = \frac{0.44\lambda_0/L}{\left|\frac{dn}{d\lambda}(\omega) - 0.5\frac{dn}{d\lambda}(2\omega)\right|} \tag{3.4}$$

We generally use a type I BBO (28.7° for 800nm, o+o=e), with thickness of 200 or 30μm. Considering that the SHG field experiences n_Θ (and not n_e), $\delta\lambda_{FWHM}(20\mu\text{m}) = 26\text{nm}$ and $\delta\lambda_{FWHM}(30\mu\text{m}) =$

18nm: this is sufficient as the spectral width is 10nm only, but care should be taken when working with BBO thicker than 50μm, because the $\delta\lambda_{FWHM}$ goes under 10nm (for 100fs pulses, 300fs pulses would be fine as they have 3nm bandwidth at 810nm).

Delay/GVM correction

We have seen in 2.3.5 the existence of a Group Velocity Mismatch (GVM)[64], also called temporal walk-off, simply because different wavelengths travel at different speed in all materials.

The GVM leads to a significant variation of the group velocity v_g with λ, which results in a group delay between the two pulses R (reference) and S (sample):

$$\Delta t_g\left(\lambda_1,\lambda_2\right) = L\left[\frac{1}{v_g(\lambda_1)} - \frac{1}{v_g(\lambda_2)}\right] \text{ with } v_g(\lambda_0) = c\left[n(\lambda_0) - \lambda_0 \left.\frac{dn}{d\lambda}\right|_{\lambda_0}\right]^{-1} \tag{3.5}$$

In particular, this implies a delay between a fundamental pulse and its SHG. We see in Fig. 3.7 its dependency on the excitation wavelength. The optical element that provides the higher group delay

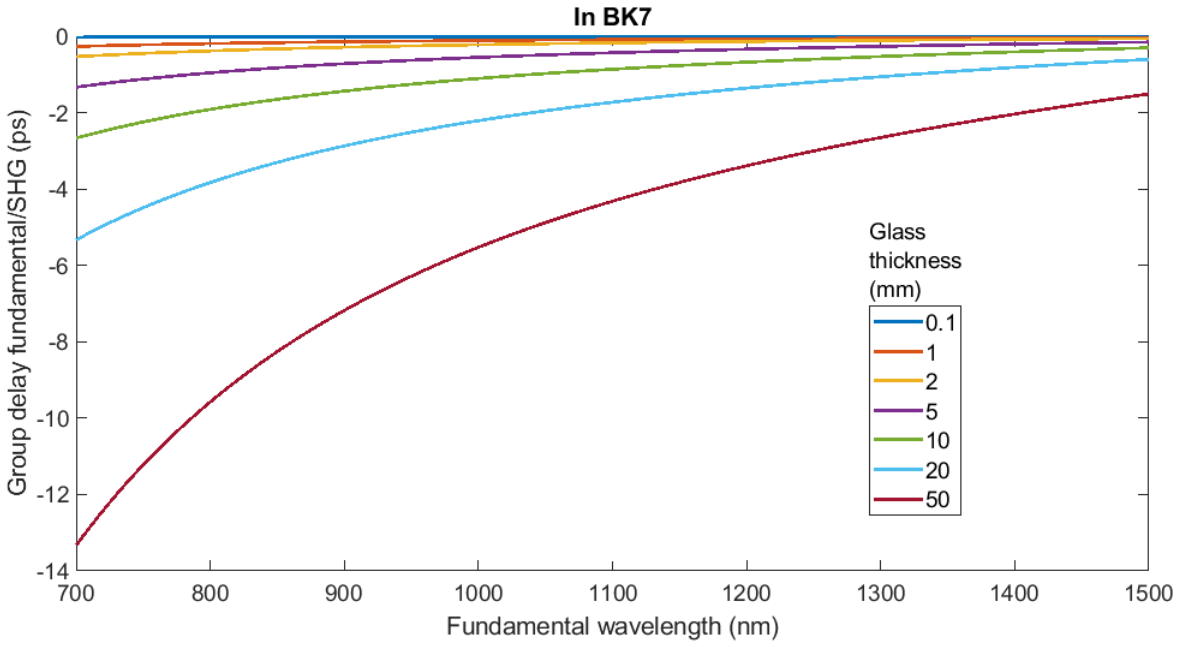

Figure 3.7: Group delay accumulated by SHG pulse with respect to its fundamental, function of the fundamental wavelength in BK7 glass, for different thicknesses travelled. The higher the excitation wavelength, the more negligible the group delay is.

(and that cannot be removed) is the microscope objective. The UPLSAPO 20X (Olympus) represents

around 45mm of (equivalent) BK7 glass, and the UAPO-340 40X around 36 mm (these values have been measured by compensating the delay between pulses, i.e. with an interferometer [45]).

The reasonable condition $\Delta t_g(\lambda_1, \lambda_2) \leq \sigma_\tau$ (where σ_τ is the temporal width of the pulse) can be defined as the threshold over which the group delay temporally separates the two pulses. If the Vanguard laser (12ps, 1064nm) is considered, the delay varies between 3.7 (40X) and 4.6 ps (20X): this effect can be considered as negligible in the first approximation (this condition has indeed been assumed for the first I-SHG experiments [174]).
The Tsunami laser (100fs, 810nm) is at a slightly lower wavelength slightly lower, which increases the group delay: 6.7 (40X) and 8.3ps (20X). Here the delay is around 60 times (6000%) larger than the temporal width of the pulse: there is no overlap between the pulses, and this delay must be corrected. Moreover, applying the mentioned condition, we found that any BK7 optical element whose thickness is higher than 0.65mm must be compensated for (the threshold is at 117mm for the Vanguard at 12ps, see table 3.4). To circumvent this effect, the pulses could be separated, time-delayed by propagation,

-	20X	40X
L verre BK7 (mm)	45	36
Delay 1064/532 nm (ps)	4.6	3.7
Delay 810/405 nm (ps)	8.3	6.7
% of pulse temporal FWHM Vanguard (12ps, 1064nm)	38%	31%
% of pulse temporal FWHM Tsunami (100fs, 810nm)	7000%	5500%
L BK7 max for delay negligible Vanguard (mm)	117	
L BK7 max for delay negligible Tsunami (mm)	0.65	

Table 3.4: Delay of the different microscope objectives

and recombined. If the common path configuration is being kept (for stability), the properties of calcite could be exploited: this is one of the only materials where an NIR fundamental light can travel slower than its SH. For this, the polarizations of the two waves are placed respectively orthogonal and parallel to the optical axis to exploit the high negative birefringence of calcite. The set-up used, similar to a Babinet-Soleil compensator, is described in Fig. 3.8. Two calcite prisms can be translated parallel to their prism angle (18°) so that the total thickness of the pair varies from 10 to 22mm. Because a high GVM has to be compensated for, a configuration where the beams pass four times through the prisms can be made (quadruple pass). For this, two roof mirrors are used to offset the beam vertically and horizontally, respectively (the minimum equivalent thickness is then 40mm). If less calcite has to be used, the vertical roof mirror can be turned to offset the beam horizontally, so that it does get reflected by the 2nd roof mirror, and goes to an output at the same position. Passing an even number of times

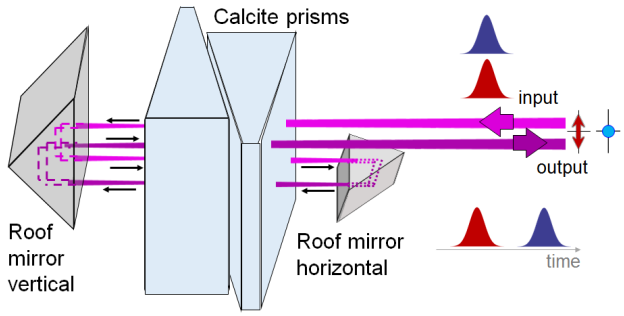

Figure 3.8: Set-up for the GVM correction: two calcite prisms (a-cut, having an 18° face angle) can be translated horizontally such that the total thickness of calcite experienced by the pulses is changed. Their optical axis is horizontal, orthogonal to the right-angled surface, so that the reference SHG having a horizontal polarization will travel faster than the fundamental that is vertically polarized. Two roof mirrors are used to perform a quadruple path in the prisms. The vertical one can be converted to horizontal to perform a double pass, while keeping the same position in input and output (thus by-passing the second one).

in the pair has the advantage to make the travel path of the beam symmetrical, which can compensate for some misalignments.

Other materials for GVM compensation

Materials where $v_g^o(\omega) < v_g^e(\omega)$ (or $v_g^e(\omega) < v_g^o(\omega)$) are not so common. Calcite has a GVM of 0.45 ps/mm and MgF2 (e/o) is 0.11 ps/mm, for the couple of 810/405 nm. BBO has 0.19 ps/mm at $\theta = 39°$ (unusual angle), with no spatial walk-off for this orientation of BBO, providing the crystal is cut at the right angle.

Spatial walk-off of phase-matching

The spatial walk-off (see [210], "Frequency doubling and mixing" p.98) is the fact that the birefringence of the medium will laterally shift the generated nH wave compared to its fundamental, since both experience different optical indices (as they have different polarization). The corresponding angle is:

$$\tan\rho = \frac{n_e(\theta)^2}{2}\frac{dn_e(\theta)}{d\theta} \Leftrightarrow \rho = \mathrm{Arctan}\left[\frac{n_e(\theta)^2}{2}\left(\frac{1}{{n_e}^2} - \frac{1}{{n_o}^2}\right)\sin(2\theta)\right] \tag{3.6}$$

For SHG in type I BBO at 810nm, we found a value of only 3.8° , and even for thicknesses L of several hundreds of μm, the lateral walk-off will only be a few tens of μm (shift=$L\tan\rho$). It can nevertheless be compensated for by using two crystals of thickness L/2, whose optical axes are inverted with respect to the incidence plane. If the 2nd crystal also generates SHG, the walk-off will only be divided by 2

because this crystal is not compensated for. One possibility is then to use a passive (non-generating) crystal of thickness L, coupled to the generating crystal of the same thickness [64].

3.2.2 Chirp compensation

The group delay dispersion (GDD) is the same effect as the GVM ("the red is faster than blue"), but within the pulse itself, thus involving the second derivative of the optical index with respect to the wavelength:

$$GDD(\lambda_0) = L_{material}\frac{{\lambda_0}^3}{2\pi c^2}\frac{d^2n}{d\lambda^2}\bigg|_{\lambda_0} \Rightarrow \sigma_{\tau,out} = \sigma_\tau\sqrt{1+16\,(\log 2)^2\,\frac{GDD^2}{\sigma_\tau^4}} \tag{3.7}$$

For the BBO crystal, at 810nm (initial width 100fs), the broadening is 0.001fs @ 810nm (resp. 0.01fs @ 405nm) for a thickness of 30μm, 0.3fs @ 810nm (resp. 2.1fs @ 405nm) for 5mm. This parameter must then be considered for short pulses $<$ 100fs in BBO, but not here. Many optical elements can lead to positive dispersion, or positive chirp: see table 3.5. For I-SHG, we have seen in eq. 2.34 that for the two pulses (whose wavelengths are different), their difference in chirp only matters for the interferometric contrast: a pre-compensation of the fundamental's chirp will not improve I-SHG. However, the generated SH at a given time t has a quadratic dependence with the peak power of excitation, and the total measured SHG also increases if the pulse duration is higher (longer interaction): overall, the measured SHG is inversely proportional to the pulse's duration. Pre-compensating the chirp can thus be necessary to ensure a sufficient SNR in SHG measurements in some samples without risking damages that come with an increase of excitation power. Overall, one efficient way to maintain a good interferometric contrast is to increase the pulse's duration σ_τ by decreasing its spectral bandwidth, such that the temporal chirp τ_d^2 will have a smaller effect (eq. 2.34): in our set-up, we can extract a 3nm bandwidth from the pulse's spectrum using a transmission filter (Semrock), such that the final duration is 320fs instead of 100fs.

Prism compressor

Prisms disperse light in transmission and can thus be employed as a pulse compressor. Typically, four prisms are needed to perform a compression. Such a system is usually tricky to align because each prism must be at its minimum angle of deviation, and because a 2nd order effect (the dependence of

GDD (in fs^2)	810nm	405nm
Filter Semrock 3nm BW	4000	
Faraday isolator[a]	5400	
BBO 0.2mm thick	15	40
waveplates	180	300
lenses (plano)	150	400
lenses (achromatic doublets)	500	2000
Calcites pair	2000	2600
Objective 20X	2000	5400
EOM[b] 70mm KD*P	3000	7000
EOM 35mm RTP	10000	23000

Table 3.5: Group delay dispersion (GDD) produced by the different optical elements. [a] Old model from Newport. [b] Electro-optic modulator, see later (3.3).

the deviation angle with the prism angle) is used to align a 1st order effect (the dependence of the angular dispersion with the prism angle) [227]. That is why the double-pass prism compressor has been invented : the beam passes through each prism twice, so only two prisms are needed. More recently, R. Trebino's team proposed going even further by passing four-times through a single prism, and using retro-reflecting optics to ensure a good alignment [1], see Fig. 3.9,A). The prism needs to be dispersive

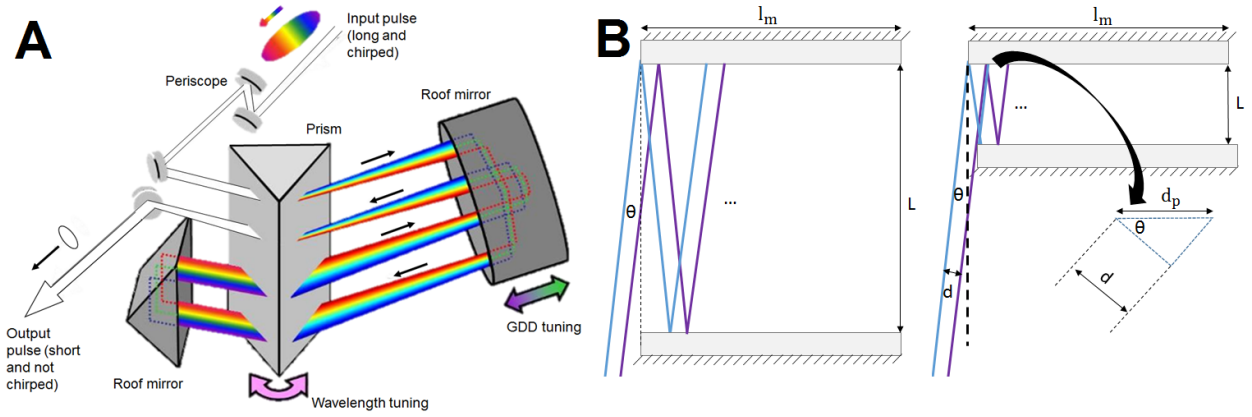

Figure 3.9: Schematic of two chirp compensators: the BOA pulse compressor (A, adapted from Swamp Optics' website), and a chirped mirror pair (B). (B, middle) Random configuration where the space between the chirp mirrors is sufficient but not optimal. (Right) Optimal configuration where L cannot be smaller otherwise the beam would clip on the edge of the mirror. The laser beam is represented by two lines of different colors, for clarity.

enough (lowest Abbe's number possible) to ensure that a sufficiently high GDD can be attained. The GDD is then [140]:

$$GDD_{PRISM} = \frac{\lambda^3}{2\pi c^2}\left[4L_{sep}\left\{\left(\frac{d^2n}{d\lambda^2} + (2n - \frac{1}{n^3})(\frac{dn}{d\lambda})^2\right)\sin\beta - 2(\frac{dn}{d\lambda})^2\cos\beta\right\} + 4\frac{d^2n}{d\lambda^2}(2D_{1/e^2})\right] \tag{3.8}$$

where L_{sep} is the length that separates the apex of prism #1 from the one of prism #2 (in the 4 passes configuration, the distance between the prism apex and the big first retroreflector), n the refractive index (at the designed central wavelength), and β stands for the angle of the dispersed beam after the first prism. This expression assumes that all beams pass through the prism(s) as close as possible to the apex of the prism. When β is small (generally true for ∼100fs pulses and classic prisms), this expression reduces to:

$$GDD_{PRISM} = \frac{\lambda^3}{2\pi c^2}\left[-8L_{sep}(\frac{dn}{d\lambda})^2 + 4\frac{d^2n}{d\lambda^2}(2D_{1/e^2})\right] = \frac{\lambda^3}{2\pi c^2}\left[-4L_{sep}(\frac{dn}{d\lambda})^2 + L_{prism}\frac{d^2n}{d\lambda^2}\right] \quad (3.9)$$

The first term is always negative and states that a higher GDD can be reached if the distance between the first prim and second prism is increased. The second term is always positive: the more prism material the beam encounters, the higher the GDD will be (in positive values). Thus, to reach high negative GDD, this quantity must be as small as possible - and can be used to tune the GDD - meaning that the beam needs to pass through the lower width of the prism (close to the apex) [227].

Grating compressor - 4f

The prism compressor has the disadvantage of being in transmission, which might induce some power loss or other effects on the beam. It is generally safer to work in reflection as much as possible, allowed by gratings (that exist in transmission and reflection). A grating compressor has the advantage of enabling higher GDD than a prism compressor, and it can also compensate nicely for the third order dispersion [227] (in case of pulses under ∼80fs). The total GDD of a grating compressor is [113]:

$$GDD_{GRATINGS} = \frac{m^2\lambda^3 L_g}{2\pi c^2\Lambda^2}\left[1-\left(m\frac{\lambda}{\Lambda}-\sin\theta_i\right)^2\right]^{-3/2} \quad (3.10)$$

What is interesting with a grating compressor is the possibility to use orders of diffraction higher than 1 (m>1), which leads to higher GDD compensation and allows for simultaneous compression of the chirps of pulses at different central wavelengths. In the case of one fundamental beam collinear with its SHG, the calculations show that the ratio of the GDD compensated for the SHG compared to the fundamental scales with $m_{SHG}^2/8$. Therefore, the GDD compensation for the SHG needs to be higher than for the fundamental: $m_{SHG}^2/8 > 1 \Rightarrow m_{SHG} \geq 3$, ideally 4 (to have a ratio 2:1). Moreover, a 4f system can be utilized to filter the bandwidth of the fundamental in the Fourier plane.

Chirped mirrors

Chirped mirrors can be used to introduce negative chirp on pulses. They employ Bragg reflectors to generally achieve -50 to -500 fs^2 at various wavelengths. They can be utilized in pairs, such that around 8 reflections are performed. For instance, Thorlabs offers 1" mirrors with -54fs^2, or a rectangular one 2" large with -175fs^2 per reflection (as of mid-2018). GDD higher than 4000fs^2 are hard to compensate for with such a system. The company UltraFastInnovations can provide routine mirrors with -550fs^2 per reflection.

On Fig. 3.9,B) it is clear that the projected diameter of the beam on the mirror is $d/\cos\theta$ Also, $L = (d/2/\cos\theta)/\tan\theta = d/(2\sin\theta)$ for any θ: taking a certain θ fixes the value of the distance between the chirp mirrors L. Of course θ must not be too small to allow the chirp mirrors to be separated by a distance realistic in the lab. Taking a beam diameter d of 5mm and an AOI angle of 5°, L = 28.7mm, which is very feasible. On the contrary, θ must not be too large to allow a high number of reflections on the chirp mirrors (which will be $N = \text{floor}(l_m/d_p)$). With $\theta = 5°$, d_p is higher than d by only 2μm, which ensures the wanted number of bounces on the mirrors will be achieved. Taking a θ that is too large can also force the chirp mirrors to be too close to each other (in the optimal configuration), which implies an alignment problem.

Summary

Table 3.6 shows that, even if the chirped mirrors are easy to use (easy alignment) and easy to insert into an optical set-up, they come with a trade-off on GDD tunability (dictated by the GDD induced by one reflection) and wavelength tunability (they are designed to work around one central wavelength only). To attain GDD comparable to prism of grating compressors, expensive coatings must be used along with a high number of reflections, very long mirrors or a large number of small ones.

Control of pulses: pulse measurement

The pulse duration of our laser is below 1ps, and thus requires an ultrashort pulse measurement system to deliver the best performances. The so-called SHG-FROG (Frequency Resolved Optical Gating)[206] can be used to retrieve the optical phase and therefore has information about possible spatial and temporal

Type	Wavelength tunability*	GDD tunability	GDD max (fs^2)	Alignment	Limitation
Chirped mirror pair (1")	50nm	Multiple of reflection GDD	-8000	Quite easy	More GDD means less tunability, or more losses
Prism compressor	2000nm	Coarse or fine	-20000	Difficult	Losses, the beam gets large
Grating compressor	2000nm	Coarse or fine	-50000	Difficult	Losses

Table 3.6: Comparison of the different techniques for chirp compensation. Losses are in optical power. * Typical.

chirp. However, this is a bit high-profile for pulses around 100fs, since the third-order dispersion is not significant, and only the duration is aimed to be measured.

Interferometric (or fringes-resolved) autocorrelation (FRAC) is a rather easy way to have this measure, since it only requires a Michelson's interferometer and a SHG crystal. We have recovered an old version of the Femtometer from Femtolasers which allows us - using a piezo driver - to acquire a full autocorrelation trace at a 1Hz rate (see Fig. 3.10). In comparison, an interferometric FROG would be longer (a few minutes) [206], because it uses a motorized translation step-by-step that needs to resolve all the fringes, and the integration time of our spectrometer is constrained to ms, whereas PMTs easily work under μs. However, a non-collinear geometry could be used for FROG, or for autocorrelation (called Intensity Autocorrelation) that can take larger steps, as it does not need to resolve any fringes (just the pulse shape): the acquisition time is greatly reduced, but the alignment is more demanding.
The trace (Fig. 3.10) shows 560 fringes. The fringes are spaced by 1.3fs each at 810nm, and the deconvolution for a Gaussian is 1.7 (for FRAC) [66], leading to a 560*1.3/1.7 = 173fs pulse after passing the Faraday isolator. This is in good agreement with the 178fs found with a (true) FROG.

Since the chirp of the pulses is a sensitive parameter for the contrast, it must be routinely controlled and adjusted. For this, the I-SHG set-up can be exploited. SHG autocorrelation or FROG indeed both rely on the generation of SHG with two delayed pulses. Here, we can delay the SHG of one arm with respect to the fundamental, the latter being converted to SHG so that both waves interfere in the end. Let's assume a highly chirped pulse at FWHM = 500fs, so the delay needs to be scanned over at least 500*1.7*1.7 $\sim$ 1500fs to resolve the full width of the autocorrelation function. Since the phase-shift is $\Delta\varphi = 2\pi c\Delta t/\lambda$, it represents a 7000°phase-shift: impossible to reach with a standard phase-shifter limited to several π, this range can be scanned with the calcite prisms (see Fig. 3.8). This was done

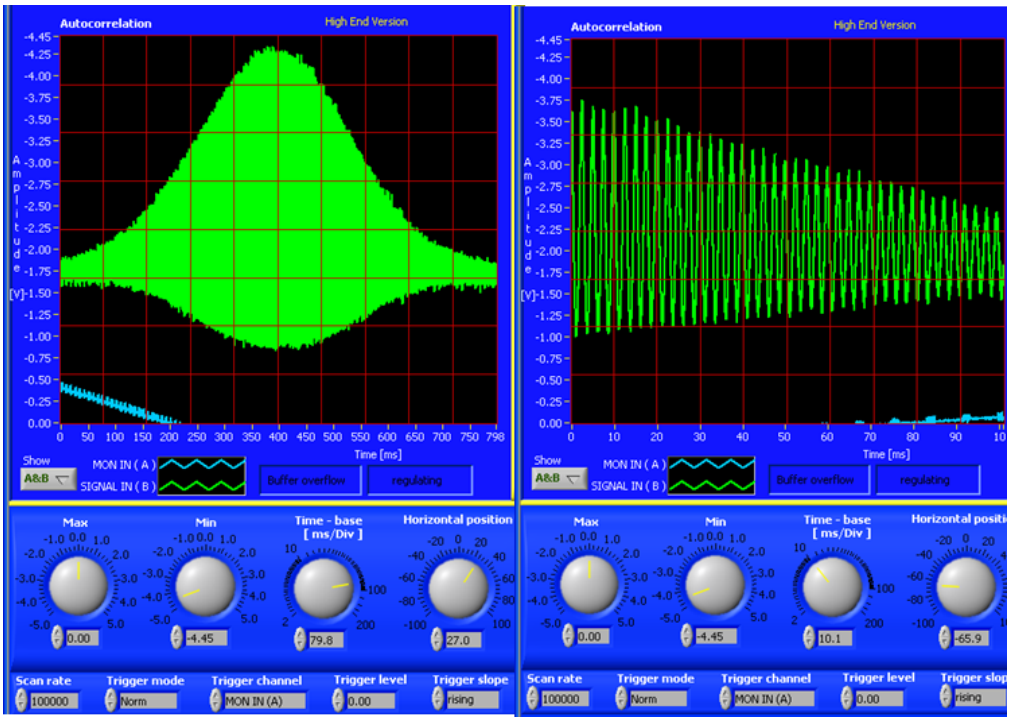

Figure 3.10: Interferometric autocorrelation (FRAC) trace of the pulse passed only in the Faraday isolator, recovered by the Femtometer model 2007 and its software FemtoAcq. The pulse duration is given by the 560 fringes of the FWHM of the trace, leading to a 560x1.3/1.7 = 173fs pulse (at 810nm, the fringes are spaced by 1.3fs each, and the deconvolution factor for a Gaussian is 1.7).

by simply by adding a motorized translation on one calcite prism, and the signal is recorded by the standard PMT for the autocorrelation, or by a spectrometer *in-lieu* of the PMT for the FROG. Since an interferometric (collinear) measure is performed, the scan must resolve the fringes that are spaced by λ/c [66], i.e. 1.35fs for 405nm. This is not a problem for the autocorrelation since the exposure time can be set to few μs, but it represents 7000/1.35*2*5e-3 = 51sec minimum for the FROG, as the exposure time of the spectrometer must be over 5msec. The two SHG fields are summed when interfering, such that the resulting intensity is:

$$
\begin{aligned}
&I_{autoco}(\tau) = \int_{-\infty}^{+\infty} \left| E^2(t) + E^2(t-t_0) \right|^2 dt \\
&= \int_{-\infty}^{+\infty} \Big(E^2(t) + E^2(t-t_0) \Big) \Big(E^2(t) + E^2(t-t_0) \Big)^* dt \\
&= \int_{-\infty}^{+\infty} \Big(E^2(t) E^{*2}(t) \Big)^2 + \Big(E^2(t-t_0) E^{*2}(t-t_0) \Big)^2 dt + \int_{-\infty}^{+\infty} \Big(E^2(t) E^{*2}(t-t_0) \Big) + \Big(E^{*2}(t) E^2(t-t_0) \Big) dt \\
&= \int_{-\infty}^{+\infty} I_{SHG}(t)^2 + I_{SHG}(t-t_0)^2 dt + 2 \int_{-\infty}^{+\infty} \mathrm{Re}\{ E^2(t)\, E^2(t-t_0)^* \} dt \\
&= \text{constants} + SHG\,\text{interferogram}
\end{aligned}
\tag{3.11}
$$

This scan thus leads to a *field* autocorrelation of the SHG pulses, not a standard interferometric autocorrelation. The trace is vertically symmetrical, and its width is smaller if the pulse duration is smaller (more spectral bandwidth), but larger if its chirp is higher (eq. 2.37). The full expression of the autocorrelation is pulse-dependent, and is often complicated to represent as an analytical expression, as it involves functions (like the Gaussian) that do not have primitives. Here we consider the simple case of a Gaussian pulse chirped linearly: $E(t) = E_0 \exp\left[-\frac{1}{2}\frac{t}{\sigma_\tau}(1+i\beta)\right] e^{i\omega t}$ The interferometric autocorrelation is then [54]:

$$I_{FRAC}(t_0) \propto 1+\left\{2+e^{\frac{-\beta^2}{2}\left(\frac{t_0}{\sigma_\tau}\right)^2}\cos 2\omega t_0\right\} e^{\frac{-1}{2}\left(\frac{t_0}{\sigma_\tau}\right)^2} + 4e^{-\frac{3+\beta^2}{8}\left(\frac{t_0}{\sigma_\tau}\right)^2}\cos\left(\frac{\beta}{4}\left(\frac{t_0}{\sigma_\tau}\right)^2\right)\cos\omega t_0 \quad (3.12)$$

Similarly, the SHG field autocorrelation can be calculated as (from equation 3.11):

$$I_{SHG,FA}(t_0) \propto 1+\left\{2+e^{\frac{-\beta^2}{2}\left(\frac{t_0}{\sigma_\tau}\right)^2}\cos 2\omega t_0\right\} e^{\frac{-1}{2}\left(\frac{t_0}{\sigma_\tau}\right)^2} \quad (3.13)$$

There is a constant background, a Gaussian envelope and an oscillating term at 2ω. The unchirped case is when the chirp parameter $\beta = 0$. Figure 3.17 provides some examples of field autocorrelations using calcite, for I-SHG using the phase-scanner or not (see section 3.3.11). This technique has the advantage of measuring the chirp of the pulses in-situ, at the focus of the microscope and not outside of it like standard devices.

However, in the microscopy case, the important information is only to know whether the pulse is FT-limited (minimum temporal width) when being focused in the sample: this can be controlled by, for instance, maximizing the nonlinear signal generated in a crystal. The advantage is that it can be done at the precise location where the pulse should be compressed (here, at the focus of the microscope). However, it is quite challenging as the signal could also vary due to a change of polarization (ellipticity + direction), intensity (losses on the path), alignment, etc. Therefore, it is crucial to also measure the level of the fundamental, and to calculate the ratio I_{SHG}/I_{fund}^2. This ratio should be linear with the pulse duration (see 2.1.2). Figure 3.11 shows the measured ratio of signal at the focus of the microscope (sample = quartz), as a function of the expected GDD. The GDD is calculated from the number of bounces on the chirped mirrors. The theoretical curve (considering the linear dependence of the signal with the pulse duration) is also plotted in red. Each time, the fundamental signal was measured just after the SHG, with the same gain on the detector, but with different optical filters. All the parameters are the same for each configuration, (a) and (b). We see that there is indeed a maximum of the ratio with a

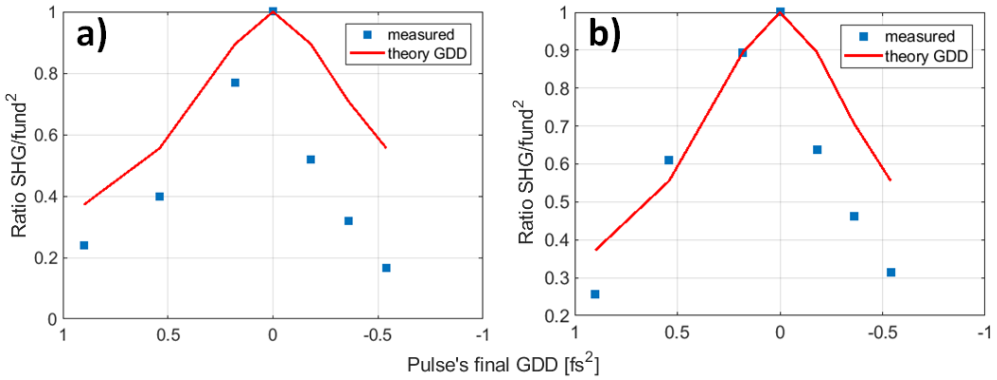

Figure 3.11: Measured signal in microscope as a function of pulse duration. (a) For the stage path, with the phase EOM and the iSHG optics. (b) Same, but with the analog galvos optics in addition.

certain number of bounces (which corresponds to 0 GDD), which is different for the two configurations: the chirped mirrors should be set to this value to have a fundamental pulse approximately FT-limited at the focus of the microscope. Also, the fit does not completely follow the experimental points, likely because of the imprecision of the alignment that changes every time the number of bounces on the chirped mirrors is changed.

Remaining difference in temporal width

Table 3.7 summarizes the remaining chirps on the reference SHG pulse, and the final difference in temporal width compared to the sample's SHG. We see that the galvos lead to a final pulse duration

mode	scan	Number of required bounces (-500fs^2 per bounce)	GDD difference fund/SHG (fs^2)	Temporal width difference (fs)
Motorized optics	stage	21	5000	130 (3)
	galvos	29	8700	240 (9)
EOM	stage	53	21000	500 (48)
	galvos	58	23000	540 (56)

Table 3.7: Summary of the remaining chirps depending on the used configuration for I-SHG. The values or temporal width correspond to an initial width of 100fs (320fs).

twice as high as the stage-scanning configuration (with 100fs pulses), but that the crystal of the EOM is responsible for the higher chirp.

3.2.3 Spatial effect: size of both beams

Previously, we saw that the contrast essentially depends on temporal effects, but spatial ones must also be controlled to be sure the I-SHG occurs in the best conditions. The different configurations are reported in Fig. 3.12 are reported, whether 2 (a) or 3 (b) lenses are used to focalize inside the calcites (see Fig.3.8): the output beam at 810nm (red) has a diameter much more similar to the beam at 405nm (blue) in case b) than in case a). Also, their respective foci inside the calcites are much closer axially in case b) (2 lenses). The calculations of the beam focus and diameters are detailed in Appendix B.1, for

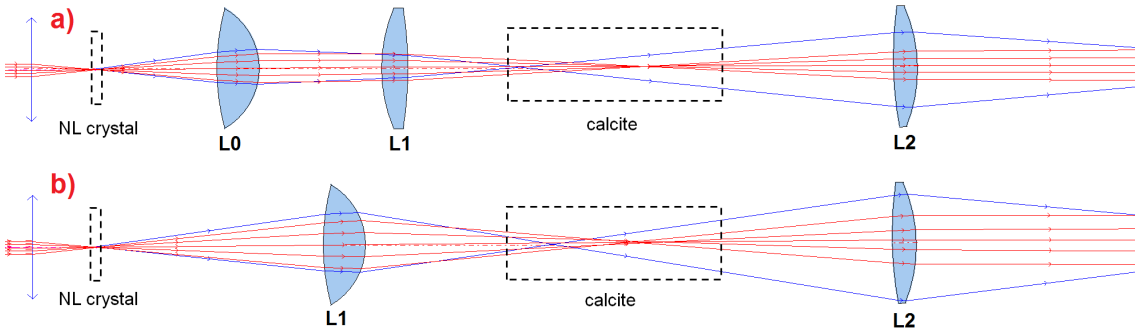

Figure 3.12: (a) The classic 3 lenses configuration. (b) The modified one, with only 2 lenses. The calcite width is large because the beam goes multiple times in the same prisms (see Fig. 3.8).

plane wave and Gaussian beams.

Overall, the 2 lens configuration gives higher performances in terms of diameter difference between the beams (see table B.1), especially when an imperfect lens is used to do the final re-collimation. Since less lenses also means less GVM and less chirp for both of the beams, it is clearly advantageous to use the two lens configuration to ensure the highest interferometric contrast possible. It should also be noted that the focalization of the beam in calcite was found to be necessary experimentally, to be able to pass the beam many times in it and to ensure a good interferometric contrast too.

(*) Effect of the calcite on the beam size

The two beams cross the calcites, and experience a different optical index inside it which could impact the beam focusing. To test this effect, we consider that a perfect lens is used to focalize the beams and find:

$$D_R - D_B = 2\Delta l = 2(L\tan\theta_R - L\tan\theta_B) = 2L\left(\frac{\sin\theta_R}{\sqrt{n_R^2 - n_R\sin\theta_R}} - \frac{\sin\theta_B}{\sqrt{n_B^2 - n_B\sin\theta_B}}\right) \quad (3.14)$$

with $\sin\theta_i = \frac{d/2}{\sqrt{(d/2)^2+{f_i}^2}}$ Considering a total calcite thickness of 60mm, a 4mm diameter beam focalized by a 700mm lens and optical indexes of (1.65 for 810nm (o) and 1.50 for 405 nm (e)), the beam diameter difference between fundamental and SHG is only 30μm larger after the calcites. Even with different lens configuration this should be negligible.

3.2.4 Quantitative study of the number of phase-shifts required and the precision

We calculate here the theoretical number of phase-shifts (i.e. interferograms) required to recover the I-SHG information (phase, amplitude), as a complementary of what is developed in the end of our article [10] (7).

Algorithm to improve the phase extraction

A robust algorithm requiring only 3 phase-shifts (which can be random) to converge, i.e. the minimum number, has been developed by [238]. This consists of three steps:
- first, it is assumed that the background intensity and the modulation amplitude do not change when the phase-shift is applied, but only changes pixel to pixel. This allows us to calculate a 1st value of the optical phase. This is the calculation performed with the standard I-SHG retrieval presented in appendix B.3.
- then, we assume the opposite: there is a change in background intensity and modulation amplitude when applying the phase-shifts, but not between each pixel. The effective phase-shifts between each image are then retrieved.
- these effective phase-shifts are compared with the ones calculated at the previous iteration (iteration 0 corresponding to the imposed ones): if the values are not stabilized (with a given tolerance of few % or below [238]), the algorithm iterates one more time.

This type of algorithm can prove to be very effective, but it must not be forgotten that the precision on the phase can be limited upstream by the SNR or other physical parameters. This algorithm was later improved in 2013 to take into account the effect of spatial tilt on the interferograms, and in 2015 for the effect of external vibrations on it: this is summarized in [123]. Although implemented for measurements with a CCD camera, this algorithm was implemented in the I-SHG code with its 3 versions. However, a converging algorithm could rarely be obtained if only 3 phase-shifts are given at input, and it was unclear

if the many iterations provide a real improvement on the phase for low SNR samples: for standard data treatment, we thus stick to the 1st step, described in appendix B.3

A priori effect of contrast

A test of the interferences is to look at the contrast obtained when looking at the pattern shown in Fig. 2.15, i.e. what is the ratio of the maximum to the minimum signal. The limitations are described in the contrast formula (2.36):
- the time delay between the two pulses (especially if they are below the picosecond time width)
- the spatial shift in the interference plane (walk-off effect of optics, imperfect objective, etc.), leading to a spatial overlap of the two beams
- the spatial shift of the focal points (the two waves diverge differently before the objective, and the latter is not achromatic at 100%, etc.)
- the fact that the two waves are not perfectly polarized linearly, and in the same direction

An interesting result is to plot the cosine-like (eq. 2.35) curve (by taking the 2D median or mean of the frames), see Fig. 3.13. By subtracting two 180°-shifted frames (leading to 'contrast' frames), the contrast is doubled (see eq. (a1) in the article of chap.9, or [174], 5.4, p.137 eq. 5.3). This operation of subtraction can be repeated many times, such that the following vector is obtained:

$$\begin{matrix}[E(0)\\ ...\\ E(N-1)]\end{matrix} \quad with\ E(k) = \sum_{i=0}^{\log_2 M} \binom{\log_2 M}{i} (-1)^i I\left(k \times \mathrm{stp} + i \times 180\right) \tag{3.15}$$

where N is the number of phase-shifts, s the step between phase-shifts, M the number of times the contrast is multiplied and I(k) the interferogram of the k-th phase-shift. For instance, the simple contrast calculation has M = 2, and two interferograms to subtract, and M=8 is sometimes used involving 3 subtractions (eq. (a3) of the article of chap.9). The final number of phase-shifts is $N = 2\phi_{max}/(\log_2 M + 2)/\mathrm{stp}$, where ϕ_{max} is the maximum phase-shift. To properly discretize the cosine curve, the phase-shift range needs to cover 2π. That means $N = 360/s$, thus ϕ_{max} must be chosen according to the step between phase-shifts and the multiplication of the contrast. If stp is fixed (N is constant and equal to 360/stp), multiplying the contrast by a factor M requires us to multiply ϕ_{max} by $\pi(\log_2 M + 2)$: ϕ_{max} needs to be increased by 180° at each doubling of M, for the final cosine curve

to cover the whole range $[0, 2\pi]$ (Fig.3.13). In particular, 3π was used by Rivard *et al.* [174] to have a factor of 2, and 5π allows us to multiply by M=8.

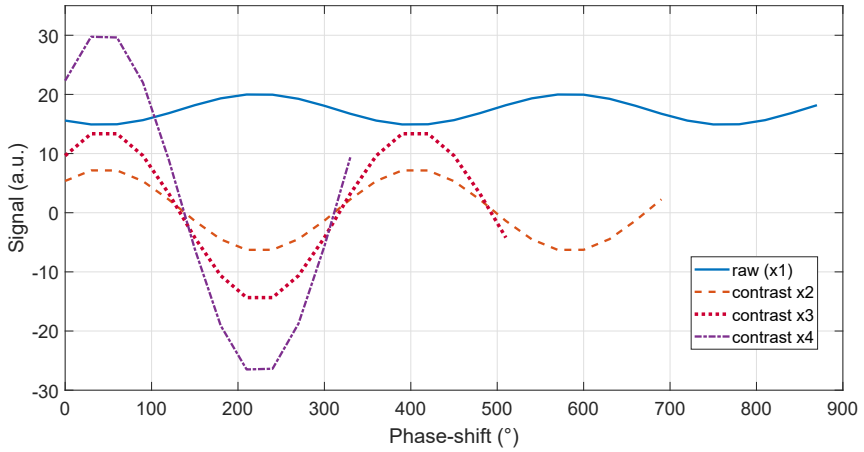

Figure 3.13: Multiplying the contrast by subtraction of interferogram frames. Blue: original cosine term whose phase-shift ranges from 0 to 5π (M=1), Orange dashed: subtraction of frames (M=2) leading to a final range of 4π, Red dotted: 2nd subtraction, final range of 3π (M=4), Violet dotted: 3rd subtraction, final range of 2π (M=8). The step of phase-shift is stp=30°.

More quantitative study - precision

The error in phase calculation has been investigated by Hibino [95] (and more precisely by Brophy [23]), which gives this expression for the standard deviation of the phase $\delta\phi$ under the assumption of an uncorrelated intensity noise with equal variance from frame-to-frame:

$$\delta\varphi \sim \frac{\delta I}{\Gamma M I_0}\sqrt{\frac{1}{2}\sum_{n=1}^{\mathbf{N_{ps}}}(A_n^2 + B_n^2)} \tag{3.16}$$

We will detail the different terms: here, δI is the signal noise, M is the contrast of the fringes, and $\Gamma = \sum_{n=1}^{N_{ps}}(A_n^2 + B_n^2)I_n^2$. I_0 is the constant intensity, and one has : $I_n = I_0(1 + C\cos(\phi + \delta_n))$ and $\tan(\varphi) = \frac{\sum_{n=1}^{\mathbf{N_{ps}}} A_n I_n}{\sum_{n=1}^{\mathbf{N_{ps}}} B_n I_n}$.
[23] gives a simplification for this expression in the case of the N_{ps}-buckets algorithm:

$$\delta\varphi \sim \frac{\delta I}{C I_0}\sqrt{\frac{2}{\mathbf{N_{ps}}}} \tag{3.17}$$

where N_{ps} is the number of interferograms taken. So, the precision of the phase calculation scales with the inverse of $\sqrt{N_{ps}}$ and with the inverse of the contrast M: the contrast has a higher effect than the number of frames on the phase accuracy. One can note that, under no other limitation than the shot noise, the precision on the phase is $\propto 1/\sqrt{N_{ps}}$ [98]: in practice however, there are many other limitations than the shot noise.

Intensity noise

The intensity noise δI is dictated by the PMTs: first, there is a noise due to the shot-noise of the photo-electrons. The "Equivalent Noise Input" is the optical power above which the signal is above the noise of the detector: for our PMT (R6357), Hamamatsu estimates it at 1e-15W, which means 1e-15*4.2e5=0.4nA (tube's datasheet [88]) for our wavelength (400nm), and a gain close to maximum, the dependency being in $\sqrt{\text{gain}}$. Since we use the amplifier C7319 at highest gain and bandwidth, the conversion is 10V/μA (amplifier's datasheet [89]) which means a (maximal) final shot noise of 4mV on the image, i.e. a fraction 4e-3/10=4e-4=0.04% of the full range (10V). To that, 2mV RMS = 2.8mV of electrical noise must be added [89].

We can also take into account the current and coupling resistance (thermal noise): $\sqrt{\Delta f(2eI + 4kT/R)}$ $= ((200e3(2 * 1.6\text{e-}19 * 0.01\text{e-}3 + (4 * 1.4\text{e-}23 * 300)/(10e3)))^{0.5} = 1.0$nA where I is the mean current, e is Coulomb's charge, Δ f is the bandwidth, k is the Boltzmann's constant, T the temperature and R the coupling resistance [159]. It leads to $\sim$8mV of noise, but it is unclear if it is already taken into account in the Equivalent Noise Input.

The measured noise on real images also depends on the laser optical stability over time: to measure it, we took several values in different configurations, the results of which are reported in table 3.8, 3rd line. The Intensity noise can be calculated from the total measured noise by subtracting the photoelectron noise and the electrical noise, using a quadratic subtraction [148] (since we are dealing with standard deviations). As stated in reference [148], the signal noise is always dominated by the laser intensity noise rather than the shot noise.

PMT drive [V]	350	500	700	1000
Gain	2e3	4e4	4e5	4e6
Measured noise (fraction of the full 10V range)	0.3%	1.5%	4.8%	13%
Photoelectron shot noise [mV]	0.13	0.4	1.3	4
Intensity noise (laser fluctuations) [mV]	5.5	12	22	36

Table 3.8: Noise of detector (PMT) for different gains.

Final calculation of the precision

Assuming 18 phase-shifts, a signal noise at 2% of the dynamic range, a mean signal at 50% of the dynamic range and M = (2-1)/(2+1) = 0.33 for a 2:1 contrast, an intensity around 32000 counts and 18 frames, $\delta\varphi = \frac{0.02}{0.33*0.5}\sqrt{\frac{2}{18}} = 0.04°$.

As [98] also introduces it, the precision can also be improved by averaging on N_{avg} frames: the factor is $\sqrt{N_{avg}}$. The final expression for the phase precision would be:

$$\delta\varphi \sim \frac{\delta I}{C I_0}\sqrt{\frac{2}{\mathbf{N_{avg}}\mathbf{N_{ps}}}} \Leftrightarrow \boxed{\delta\varphi = \frac{1}{C \times \mathrm{SNR}}\sqrt{\frac{2}{\mathbf{N_{avg}}\mathbf{N_{ps}}}}} \tag{3.18}$$

where SNR is the signal-to-noise ratio.
Considering the "worst-case" scenario of only 9 phase-shifts, SNR = 1.5 only, and a contrast C = 0.1, $\delta\varphi = \frac{1}{0.1*0.5}\sqrt{\frac{2}{9}} = 3°$. Hopefully, as in our study in [9], some numerical filtering can improve the precision on the phase retrieval.

Minimum SNR in collagen for reliable measurements

For reliable measurements in p-SHG, reference [239] states that 2093.75 photons (in total) must be captured to resolve collagen-like structures limited by shot-noise: these calculations can be extended to I-SHG in first approximation. Indeed, both algorithms consist of extracting the argument of a cosine, by a process virtually equivalent of fitting the cosine curve using several experimental points that describe this curve. Here is counted the total number of photons for one pixel, considering all the interferograms, frame average and binning [216]: with 18 phase-shifts (no average, no binning) this means 116 photons per pixel, so the (shot-noise limited) SNR of each interferogram must be at least of $\sqrt{116}$ ~11 in this type of tissue.

In [102], 25 photons are recorded on average at 2 kHz during 30ms for membrane imaging, so 25*2*30=1500 photons in total: this is one order of magnitude more than the minimum required for collagen, justified by the lower SNR in membranes. Also, the use of photon-counting PMTs instead of analog ones seems to increase, in average, the SNR by a factor of 2 and to decrease the variability by a factor of 1.5 [102]. A more detailed analysis shows that a total factor of 4 can be obtained compared to unsynchronized PMTs like in our set-up: the details can be found in appendix A.5.

What can decrease the precision of the phase measurements ?

[193] identifies several factors that can impact an accurate measure of the phase in holography, which also applies here:

1. The absolute phase-shifts introduced by the specimen,
2. Tilt aberrations in the objective [10], misalignment,
3. A beam profile (curvature) mismatch between the reference arm and the sample arm,
4. Any other aberration introduced by the optical elements of the setup.

The $\chi^{(2)}$ has a sign that changes, such that it artificially introduces some π-phase-shifts (this is what is measured). But π phase-shifts between two positions can also be due to the Gouy phase-shift [11], or to a reflection. Careful analysis of the images allows to differentiate between these possibilities.

Moreover, for I-SHG, point $\#1$ is not a problem in most samples, because if the SHG of the sample gets scattered or loses its coherence such that there is no longer any phase information, this is directly translated in the I-SHG images by a loss of contrast [158]. However, it could be considered that some parts of the sample (that are out-of-focus) imply an additional delay on the SHG, large-enough to modify the measured phase, but not sufficiently high to have a noticeable loss of contrast. For instance, delays of several multiples of 2π or below. Imaging thick samples (10μm thick or above) is thus more likely to introduce such artifacts in I-SHG, and may not be used.

Measure of the effect of the number of interferograms

Figure 3.14 shows the calculated phase maps for the PPLN crystal (left) for different numbers of interferograms used for the phase retrieval: no change is really noticeable on the map itself. For a sample of human cornea, however, we see that taking more interferograms does have an averaging effect on the

phase map (similar to when an average is performed over many frames), thus enhancing the precision and reducing the noise. The real differences can be highlighted by considering the width of the phase

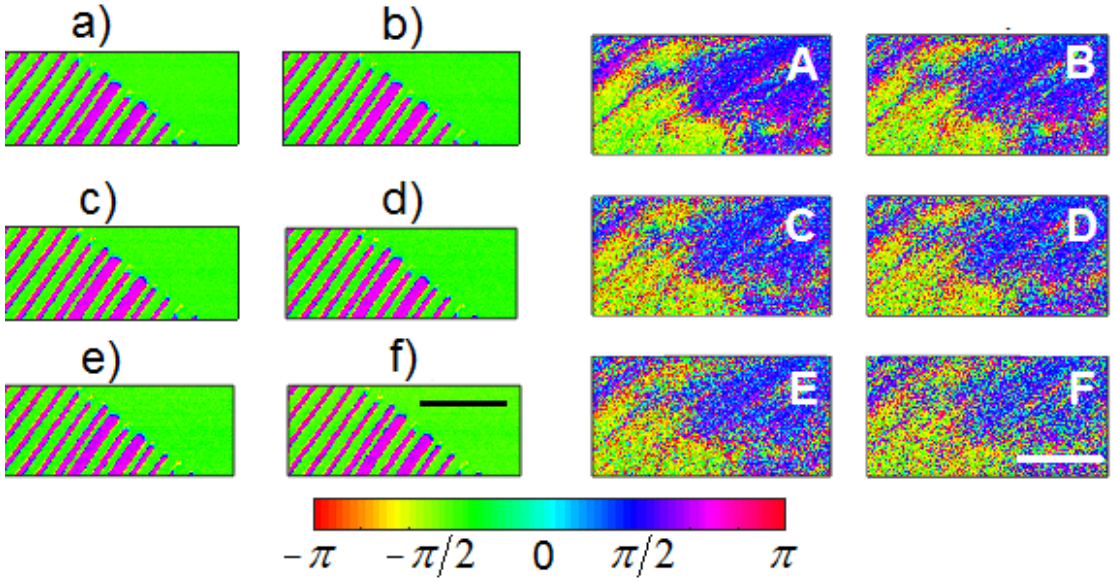

Figure 3.14: (Left) Map of the relative phase of the periodically-poled LiNbO3 domains with (a) 18 (b) 9 c) 6 (d) 5 (e) 4 (f) 3 interferograms used for reconstruction. (Right) Same as (left) but for a sagittal human cornea, with the same number of interferograms for A to E. Scale-bars: 40μm.

distribution: even for the PPLN, it increases when the number of interferograms is reduced, but the phase dispersion is a lot higher for cornea. This is because it is a low-SNR, and more random and disorganized sample than a $LiNbO_3$ crystal.

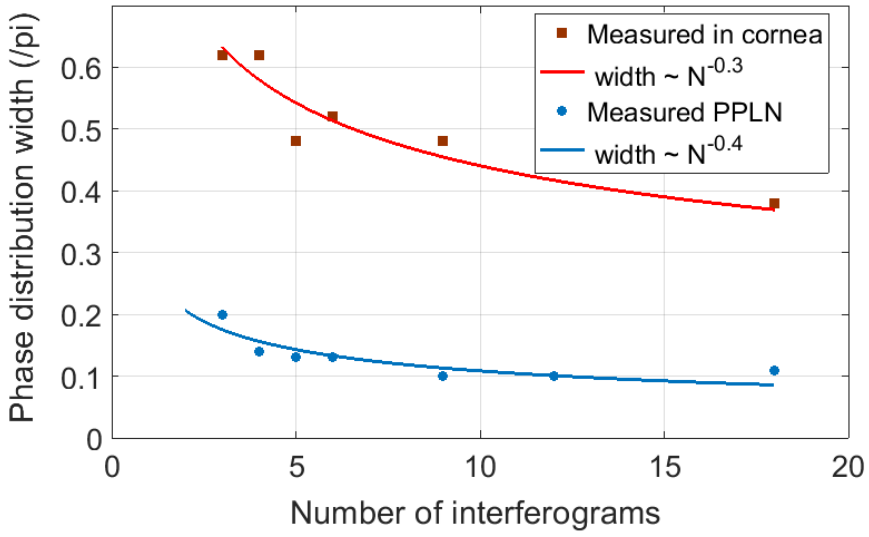

Figure 3.15: Width of the phase distribution (for negative values for instance) for the phase maps of Fig. 3.14 versus the number of interferograms.

We also verify that the dependency is a power law as indicated by equation 3.17 (with a power of -0.5). The calculated exponents are -0.3 for cornea and -0.4 for PPLN, so a higher SNR leads to a power law closer to the one expected. The discrepancy with low-SNR sample (cornea) is however not fully understood.

3.3 Electro-optic phase modulator

This section deals with the details of the electro-optics modulator (EOM) used as a phase-scanner to enhance I-SHG, which is the subject of the article presented in chap. 9. The fundamental and SHG beams are orthogonally polarized, and travel through a rectangular electro-optic crystal that allows, by changing the voltage applied to it, different phase-shifts to be induced in the interferometer. This replaces the standard phase-shifter described in [174] or [10].

3.3.1 Static phase-shifter

This static phase-shifter used for standard I-SHG is a rotating glass plate: it introduces a phase-shift that has a non-linear dependency with the angle of rotation of the plate [207] (cst being a constant):

$$\begin{aligned}\Delta\varphi &= 4\pi\frac{e}{\lambda}\left[\{n_{2\omega}\cos(\arcsin\left(\sin\theta/n_{2\omega}\right))\}-\{n_{\omega}\cos(\arcsin\left(\sin\theta/n_{\omega}\right))\}\right]\\ &= 4\pi\frac{e}{\lambda}\left[\sqrt{n_{2\omega}^2-\sin^2\theta}-\sqrt{n_{\omega}^2-\sin^2\theta}+\text{cst}\right]\end{aligned} \tag{3.19}$$

Figure 3.16(A) shows that the lower the thickness of the glass plate, the higher the glass plate angle must be to achieve the maximum phase-shift of 3π. The incidence angle of the beam on the glass plate must not be too high for optical transmission reasons: the anti-reflection coatings that allow a good transmission are usually made for a 0° AOI, otherwise 45° AOI ones must be used. We fixed the limit at the middle, 22.5° AOI: the minimum thickness of the plate must then be 1mm.

Figure 3.16 (B) shows that to ensure that the walk-off angle (see Fig. 3.16 (C)) is small, the glass plate must be as thin as possible. A thickness of 1mm then seems to be the best option, and a phase-shift of 3π is reached by tilting the plate by 21.5°.

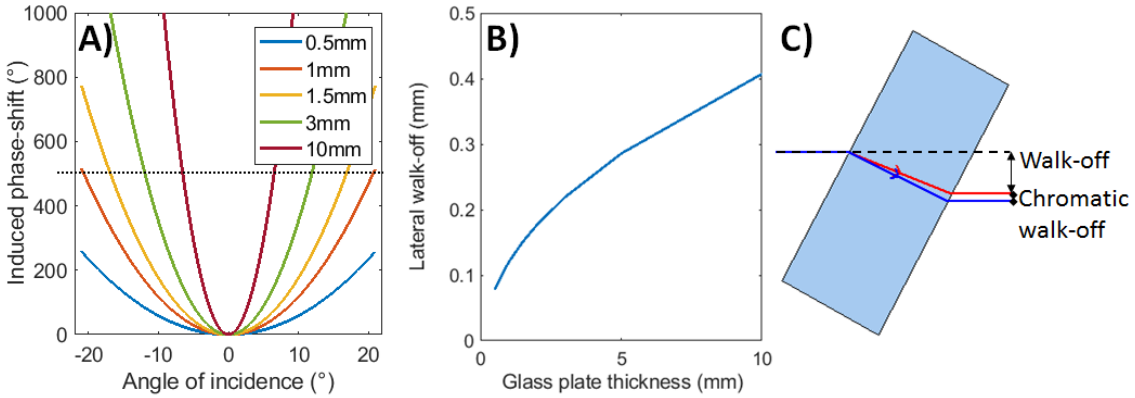

Figure 3.16: (A) Induced phase-shift function of the glass plate thickness: the maximum phase-shift of 3π is indicated with a black doted line. (B) Walk-off angle of the beam as a function of the glass plate thickness, for the rotation angle of the glass plate corresponding to the maximal phase-shift. (C) Geometrical walk-off that the red beam and the blue beam undergo. There is also a chromatic effect due to the difference of wavelength. Effects have been enhanced for clarity.

A walk-off angle will lead to an underfill of the back focal plane of the objective, and to strong spherical aberrations. The walk-off (before the microscope objective) of the wave at xω can be calculated as: $\delta y = e \sin\theta \left[1 - \frac{1}{\sqrt{n_{x\omega}^2 - \sin^2\theta}}\right]$. With a 1mm thick glass plate, we calculated that the maximum walk-off (i.e. between the first and the last phase-shift) is 80μm for the sample scanning, and 320μm for the galvo scanning (due to the additional beam expansion). These values are divided by 3 for the chromatic walk-off. These orders of magnitude of walk-off are not likely to lead to any problem and can be neglected.

3.3.2 Electro-optic effect (Pockels)

The electro-optic modulators exploit the linear variation of the optical index of a material when an external field is applied to it, which is known as Pockels effect. We can define the tensorial impermeability η of a material, which mathematically is the inverse of the permittivity, which itself is the square of the optical index. Then, the electro-optical coefficient with indices i, j when an external field is applied on the k direction is [201]:

$$r_{i,j,k} = \frac{\partial \eta_{ij}}{\partial E_k} \tag{3.20}$$

The index ellipsoid of an anisotropic material is now described by [201]:

$$\left(\frac{1}{n_x^2} + \sum_{k=x,y,z} r_{1k}E_k\right)x^2 + \left(\frac{1}{n_y^2} + \sum_{k=x,y,z} r_{2k}E_k\right)y^2 + \left(\frac{1}{n_z^2} + \sum_{k=x,y,z} r_{3k}E_k\right)z^2 + \sum_{k=x,y,z} 2E_k\left[yzr_{4k} + xzr_{5k} + xyr_{6k}\right] = 1 \tag{3.21}$$

3.3.3 Different crystals

The crystals used in electro-optics belong to three main crystal classes that are summarized in table 3.9:

Crystalline class Symmetry Anisotropy	3m (LiNbO3, BBO) Trigonal Uniaxial	mm2 (KTP, RTP) Orthorhombic Biaxial	$\bar{4}$2m (KD*P, ADP) Tetragonal Uniaxial
Electro-optic tensor	$\begin{pmatrix} 0 & r_{22} & r_{13} \\ 0 & -r_{22} & r_{13} \\ 0 & 0 & r_{33} \\ 0 & r_{42} & 0 \\ r_{42} & 0 & 0 \\ r_{12} & 0 & 0 \end{pmatrix}$	$\begin{pmatrix} 0 & 0 & r_{13} \\ 0 & 0 & r_{23} \\ 0 & 0 & r_{33} \\ 0 & r_{42} & 0 \\ r_{51} & 0 & 0 \\ 0 & 0 & 0 \end{pmatrix}$	$\begin{pmatrix} 0 & 0 & 0 \\ 0 & 0 & 0 \\ 0 & 0 & 0 \\ r_{41} & 0 & 0 \\ 0 & r_{41} & 0 \\ 0 & 0 & r_{63} \end{pmatrix}$
Used coefficients	r_{33} ($+r_{13}$, r_{23})	r_{33} ($+r_{13}$, r_{23})	r_{63} or r_{41}

Table 3.9: Summary of the three main crystal classes used in electro-optics and their properties [185].

3.3.4 Effective optical index

If a crystal of the mm2 class such as RTP is considered, the ellipsoid index (see eq. 3.21) has a simplified description [73]:

$$\begin{bmatrix} 1/n_\alpha^2 + r_{13}E_z & 0 & 0 \\ 0 & 1/n_\beta^2 + r_{23}E_z & 0 \\ 0 & 0 & 1/n_\gamma^2 + r_{33}E_z \end{bmatrix} \tag{3.22}$$

The new principal optical indices in the presence of an external electric field are the eigen values of this matrix, in particular [201]:

$$\frac{1}{n_z^2} = \frac{1}{n_\gamma^2} + r_{33}E_z \Rightarrow n_z \sim n_\gamma - \frac{1}{2}n_\gamma^3 r_{33}E_z \tag{3.23}$$

This approximation is valid if the electro-optic negligibly modifies the optical index, even at the maximum voltage (always the case in "standard" devices). We will verify that this statement is true in our case, for all the derivatives of the optical index considered. We can define the half-wave voltage, i.e. the voltage needed to induce a phase-shift of π, as [161]:

$$\Delta\varphi = \frac{2\pi}{\lambda_0}L\Delta n = \pi \Rightarrow \boxed{V_\pi = \frac{d}{L}\frac{\lambda_0}{n_0^3 r_{\text{eff}}}} \tag{3.24}$$

because $E_z = V/d$ and $\Delta n = n_z - n_\gamma$. The configuration of the modulator used here is longitudinal: it allows us to have lower V_π, as the modulation benefits from the whole crystal length [201]. However, the temperature stability might be a problem.

3.3.5 Verification of the negligible effect of voltage on GDD

Taking the first derivative of the above expression leads to:

$$\frac{dn_z}{d\lambda} = \frac{dn_\gamma}{d\lambda} - \frac{3}{2}\frac{dn_\gamma}{d\lambda} n_\gamma^2 r_{33} \frac{V}{L} \tag{3.25}$$

The second derivative is:

$$\frac{d^2 n_z}{d\lambda^2} = \frac{d^2 n_\gamma}{d\lambda^2} - \frac{3}{2} r_{33} \frac{V}{L} \left[2 n_\gamma \left(\frac{dn_\gamma}{d\lambda} \right)^2 + n_\gamma^2 \frac{d^2 n_\gamma}{d\lambda^2} \right] \tag{3.26}$$

The calculations of group delay and group delay dispersion (see part 3.2.1 for definition) can be done for the minimum and maximum applied voltages. The results are summarized in table 3.10 below, in the first two lines: We see that the effect on the group delay dispersion is only of a fraction of fs^2, which

Material	Lambda (μm)	Voltage range (V)	Group delay in equivalent of calcite	Group delay dispersion (GDD) (fs^2)
RTP	0.81	0-650	Δ = 4 μm	Δ = 0.3
	0.405			Δ = 0.7
	0.81	Fixed	40 mm	10000
	0.405			23000

Table 3.10: Group delay (due to GVM) and group delay dispersion (GDD) variation with the applied voltage on the RTP crystal (first two lines). (Last two lines) Same, but group delay between the two wavelengths, and GDD for both, at a fixed voltage.

would imply a temporal broadening below 1e-7 fs, which is indeed negligible! It can also be seen that 40mm of calcite are needed to compensate for the crystal GVM, and that there is a chirp difference of 23000-10000 = 13000fs^2 introduced between the reference SHG and the fundamental. However, the crystal must be oriented to have the fundamental's polarization parallel to its γ axis, otherwise there is a group delay of 160mm in equivalent of calcite, and the chirp is 54000-6000 = 48000fs^2 ! These conditions would make the crystal not usable for our application.

3.3.6 SHG creation inside the crystal

Only the reference SHG (created before the crystal) and the sample SHG (created after it) should go onto the detector, because their delay, polarization and GDD are controlled and will lead to effective interferences. Any other source of SHG is a source of noise: since the crystal of the EOM is piezoelectric, it can create SHG depending on how it is oriented. For the RTP, the important value of the non-linear susceptibility tensor is $d_{33} = 8.3$pm/V [167]. We can compare the amount of the SHG created in the RTP crystal to the one in the standard quartz plate of the lab. Applying the formula for the intensity of SHG as a function of the material thickness [20, 12], one finds:

$$\frac{P_{2\omega}^{RTP}}{P_{2\omega}^{quartz}} = \frac{\left(d_{eff}^{RTP}\right)^2 n_{2\omega}^{quartz} \left(n_{\omega}^{quartz}\right)^2 \left(w^{quartz}\right)^4}{\left(d_{eff}^{quartz}\right)^2 n_{2\omega}^{RTP} \left(n_{\omega}^{RTP}\right)^2 \left(w^{RTP}\right)^4} \frac{\left(L^{RTP}\,\mathrm{sinc}(L^{RTP}/L_c^{RTP}\,)\right)^2}{\left(L^{quartz}\,\mathrm{sinc}(L^{quartz}/L_c^{quartz}\,)\right)^2} \tag{3.27}$$

where d_{eff} is the effective non-linear coefficient, n the optical index (at fundamental or SHG wavelength), w the size of the smaller beam waist, L the length of the crystal and L_c the SHG coherence length. The beam is collimated through the RTP crystal, but focused through the quartz plate, leading to a beam waist at focus of 0.01mm (after a 50 mm converging lens).

Material	d_{eff} (pm/V)	n_ω	$n_{2\omega}$	w (mm)	L (mm)	L_c (mm)	ratio (%)
y-cut quartz	0.4	1.538	1.56	0.01	0.35	0.021	-
RTP	8.3	1.87	2.0	3	35	3.1	0.05
				0.5			100

Table 3.11: Parameters for the calculation of the SHG generated in RTP, and its ratio compared to the use of a 0.35mm quartz plate instead.

The SH generated by the RTP crystal with these parameters is only 0.05% of the one generated on the reference arm of the interferometer by a quartz plate: thus, it is negligible. However, it should be carefully verified that the beam is not too small when being recollimated after the calcite, and through the EOM: if the beam diameter is below 0.5mm, the signal generated in the crystal becomes comparable with the quartz's one. Indeed, some signal from the RTP crystal has been observed in this condition: it was 30$\times$ higher in the proper polarization (parallel to the γ axis) than the orthogonal one.

3.3.7 Limitation on modulation rate

The length of the crystal used for the EOM must remain under a certain limit to be able to reach the modulation rate required. The modulation rate can be limited by two factors [161]:
(1) the equivalent capacitance of the crystal: considering that two electrodes are separated by the crystal thickness e, and that they each cover the whole length L of it, the capacitance is the same as in two plates and can be written according to the Gauss' law: $C = \varepsilon_0 \varepsilon_r \frac{L \times e}{e}$. Taking $\varepsilon_r = 13$, one finds 4pF, so assuming the load resistance is 50Ω, the response time is limited to RC=50*0.004=0.2ns, which means it has a GHz drive frequency, and thus is not limiting.
(2) the time of transit of the light through the crystal: $\Delta t \approx \frac{c}{n_0 L}$, so 0.23ns for a 35cm long one.
In both cases the same upper bound of 5GHz is found, such that it is not a limitation for our application, which has sub-MHz rates.

3.3.8 Possible limitations

Temporal dispersion

The expression of the inter-pulse delay (GVM) between the fundamental pulse and the reference SHG is given in eq.3.2.1: for 35mm of RTP, it is 18ps (equivalent to 40mm of calcite). The group delay dispersion (GDD) is also usually significant in EO crystals, and will chirp the pulse (see 3.2.2 for theoretical expressions): the values are indicated in table 3.5.

The acoustic ringing

The piezoelectric tensor, which is generally not zero in this kind of crystal, can react to the modulation applied to the crystal creating a ringing effect. More precisely, a high piezoelectric coupling coefficient can modify the value of the electro-optic coefficient from "clamped" to "free" [110]. The higher-order resonances (up to the 15th harmonics) can also be problematic, and the design must be made with this in mind [109]. This effect is negligible however in some crystals, like RTP.

The hygroscopicity

Hygroscopicity - i.e. the ability of a material to attract water - might be problematic [167]. Fortunately, this effect can be largely reduced by using some special coatings.

3.3.9 Crystal performances comparison

Table 3.12 summarizes the different performances of the candidate crystals. The 3m class has the lowest V_π, but leads to a relatively high dispersion effect which would require an important compensation scheme. The 42m class presents the lowest dispersion effects and would not necessitate any dispersion compensation, but presents problems in temperature stability and acoustic resonances, and has a V_π five times higher. The mm2 class lie in-between and, even if it would require a dispersion compensator, has a relatively small V_π and above all an excellent stability in temperature and over resonances.

Crystal class	42m (KD*P, ADP)	mm2 (RTP, KTP)	3m (LiNbO3, LTA)
V_π total [a]	500	200	100
Acoustic ringing (resonances)	High[b]	No	Yes
Optical homogeneity	Excellent	Good	Fair
Purity of modulation	500:1	200:1	100:1
Temperature stability	Problem [c]	Good	Little problems
Hygroscopic	Yes[d]	No	No
Inter-pulse delay (in mm of equivalent calcite)	3	50	140
Pulse broadening ratio [e] 405nm [f]	x1	x1.2	x2.6

Table 3.12: Comparison of different performances for crystal candidates. [a] With a 4mm diameter crystal, 40mm long.
[b] A special configuration with 2 crystals 45deg-cut may mitigate this effect.
[c] among others V_π varies with temperature
[d] might be improved by the use of appropriate coatings
[e] with a 320fs pulse in input.
[f] the ratio at 800nm was always very close to 1. Source: [167], [60].

3.3.10 Comparison of two possibilities

Table 3.13 shows two possible configurations for the same $V_\pi \sim 200$V. The KD*P had uncertainty in its performances with variations of temperature and modulation rate close to the kHz, so it led us toward RTP. This comes at a high cost in term of GVM (requiring much more calcite to compensate), and chirp (3 times more GDD, which is not compensated). However, these values are more attenuated at 1030nm.

Crystal	Crystal length (mm)	V_π	Stability in temperature, resonances ...	Inter-pulse delay (in mm of equivalent calcite)	Difference GDD total fund/SHG nm (fs^2)
KD*P	70	200 (260)	No	2 (-9)	4500 (4000)
RTP	35	220 (250)	Yes	40 (9)	13800 (7500)

Table 3.13: Comparison of two candidate crystal whose lengths are set to have the same half-wave voltage V_π. The values are calculated for a fundamental at 810nm, and for 1030nm between parentheses. Note that the difference of GDD between the fundamental and SHG also takes into account the added calcite to compensate the GVM.

3.3.11 Interferometric contrast with the EOM or not

The phase electro-optic modulator (EOM) introduces some additional chirp to both the fundamental and reference SHG beams. This lowers the interferometric contrast, which is the fringes' contrast measured in I-SHG when the path difference of the interferometer is varied. Figure 3.17 reports some SHG field autocorrelation (see equation 3.11) for various set-up configurations, obtained by recording the I-SHG signal while translating one calcite prism (see Fig. 3.8). (a) shows that a contrast higher than 5:1 is obtained with the stage-scanning configuration and 320fs pulses. This reduces to 3:1 or less if 100fs pulses are used (b), because (for a given chirp), the shorter the pulse, the higher its frequency bandwidth, and thus the higher its temporal broadening. With 320fs pulses, this value is 2:1 when the EOM is inserted in the path (c). Of course, it is very alignment-dependent, and every case presented is expected to have slightly better or lower performances in the lab. The EOM crystal is mainly responsible for the loss of contrast (see table 3.5), such that a change of the following optics gives a similar value of $\sim$2:1 for the contrast every time: 2.5:1 for analog galvos (d) and 2:1 for digital galvos (e). It is complicated to use 100fs pulses, as the contrast is even lower, at e.g. 1.4:1 with digital galvos.

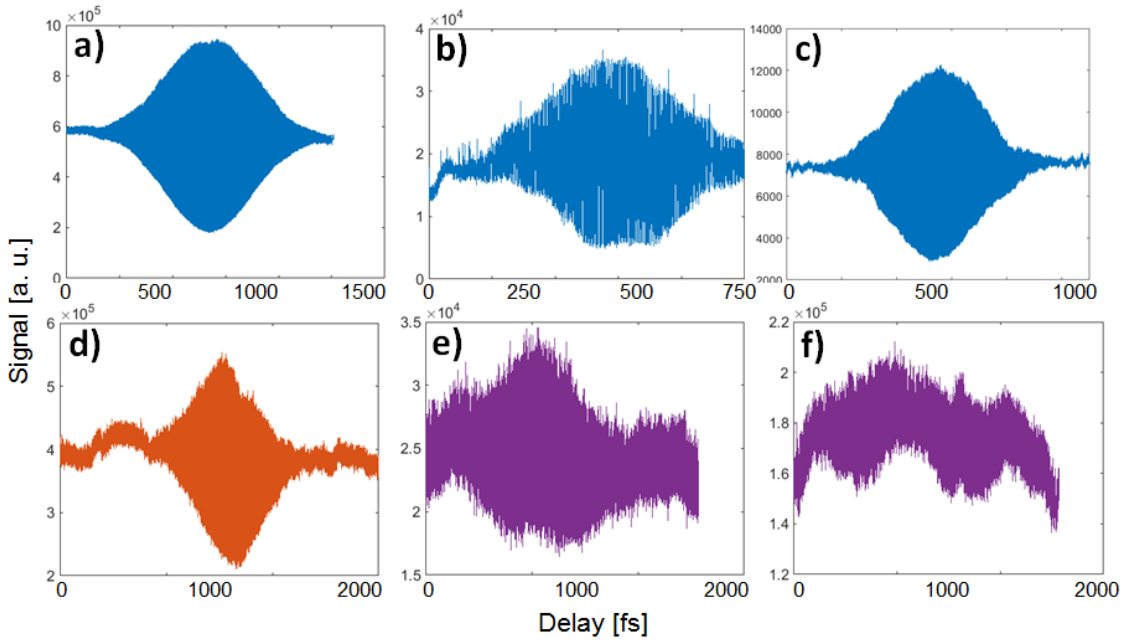

Figure 3.17: Interferometric contrast shown by SHG field autocorrelation for various set-up arrangements. All cases use 320fs pulses except (b) and (f). (a) Stage-scanning, standard I-SHG: contrast > 5:1. (b) Stage-scanning with 100fs pulses, standard I-SHG: contrast < 3:1. (c) Stage-scanning, I-SHG with phase-scanner: contrast >3:1. (d) Analog galvos, I-SHG with phase-scanner: contrast ∼2.5:1. (e) Digital galvos, I-SHG with phase-scanner: contrast ∼2:1. (f) Digital galvos, 100fs pulses, I-SHG with phase-scanner: contrast ∼1.4:1.

3.3.12 Time synchronization of the ramps

The phase EOM allows us to perform single-scan I-SHG (1S-ISHG), by applying the phase-shifts with a voltage ramp at every pixel of a standard SHG image. For this, the duration matching (see eq.(a4) of the article 9) of the voltage ramps is important for the data treatment, as shown in Fig. 3.18 by red lines. If the (chosen) window duration used to split the data into all the phase-shifts is too small, the beginning of the ramps in the windows will progressively become shifted, leading to a non sense reconstruction of the images ((a) and (b)). The window duration has to be equal to the ramp duration + dead-time between ramps (3.18 (c), (d), (e)). If the offset between the beginning of the window and the beginning of the voltage ramp is inside the dead-time (3.18 (c) and (d)), the reconstruction will be able to produce every phase-shift inside the ramp. If the offset is outside the dead-time, the dead-time cannot be separated from the ramp itself: the offset must also be well-controlled.

If a good synchronization is ensured, the interferogram arrays can be filled from the buffer of samples. Figure 3.19 shows that an error on the pixel time (time window) as small as the minimum step to adjust the synchronization (i.e. $1/5\text{MHz} = 0.2\mu\text{s}$) is sufficient to have a progressive shift between the image's lines, leading to a totally wrong reconstruction of the interferogram (a, on a PPLN sample). The pixel

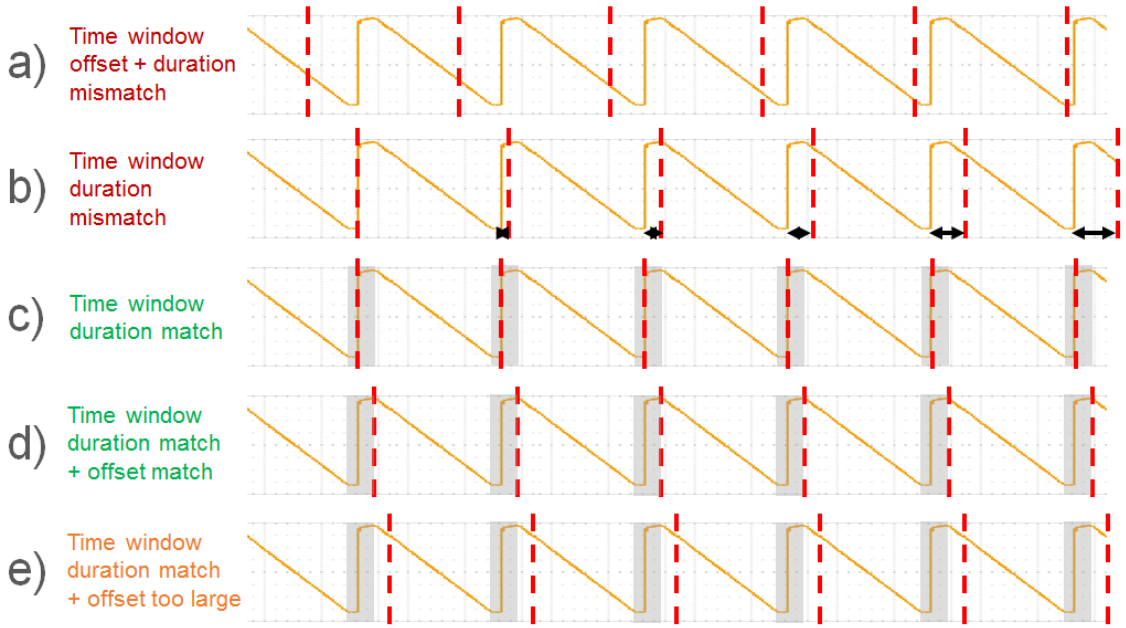

Figure 3.18: Duration match of the voltage ramps for data treatment. (a) The time windows of the data treatment have an offset, and their duration is too small. (b) The time windows have no offset, but are too small, such that their progressive shifts with respect to the beginning of the ramp are clearly visible. (c) The durations of the time windows match, and have no offset. (d) The durations of the time windows match, and their offset can be eliminated in data treatment. (e) The durations of the time windows match, and the offsets cannot be eliminated in data treatment as they are too high.

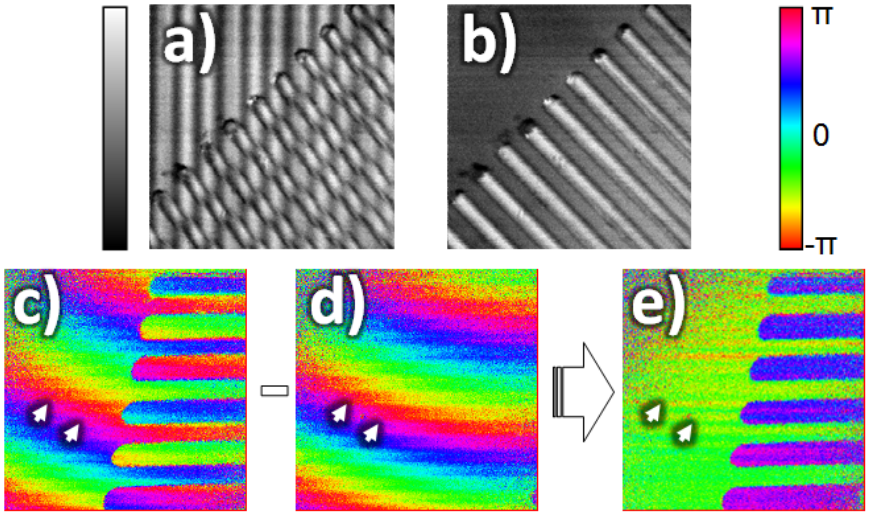

Figure 3.19: Effect of a timing mismatch between the voltage ramps and the pixel time on the reconstructed interferograms. All images are $50\times50\mu m^2$ areas in PPLN. (a) One of the reconstructed interferograms with a pixel time of 22.6 or 23μs. (b) Same, but with the (correct) pixel time (=ramp time) of 22.8μs. (Bottom) Treated phase maps with galvos scanning using line-time measurement for reconstruction: (c) of PPLN raw, (d) of quartz plate and (e) PPLN corrected by the quartz map. Some line shiftings are indicated by white arrows.

time has to be exactly equal to the voltage ramp duration (b) to avoid this. To adjust to any case and to be able to test different timing parameters, it is possible to acquire the whole buffers from the acquisition

card, and to fill the arrays only in post-treatment. The samples are gathered according to which phase-shift they belong to, and the samples acquired during the dead-times of the ramps are ignored. This way of filling the array is so sensitive to timing mismatch that it revealed a slight irregularity for one of the scanning modes of the galvos, which uses the measure of each line-time to reconstruct the image (see section A.4.11): this is shown in Fig. 3.19 (c), where a progressive shift between lines is visible (total ramp time is 22.8μs). Approximately the same shift is visible on the reference map in quartz (Fig. 3.19 d)), but the subtraction of both does not allow us to fully correct this effect (Fig. 3.19 d), some of the irregularities are spotted by white arrows). Thus, the "callback" method (see A.4.9) is preferred for I-SHG using the 20μs ramps of the phase-scanner with galvos-scanning. For 200μs ramps and 2000μs ramps, no real differences are noticeable between callback and linetime measurement methods.

3.3.13 The case of bidirectional scan

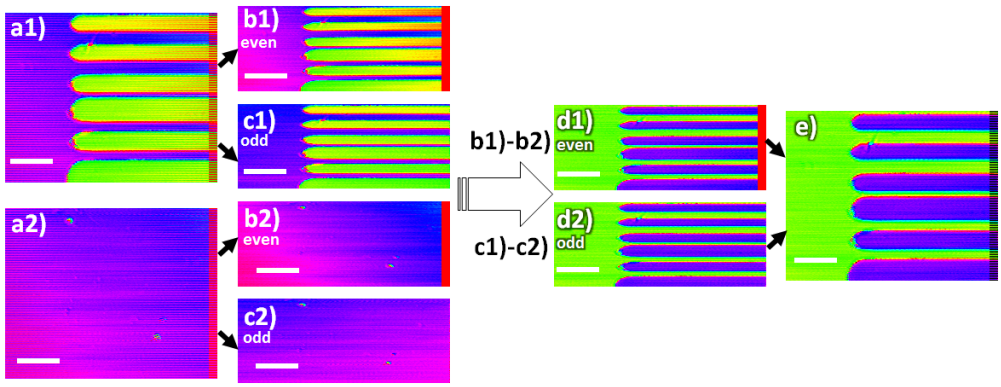

Figure 3.20: Reconstruction of the phase map for stage-scanning with bidirectional mode. Scale-bar: 10μm.

A bidirectional scan (see Fig.A.10) can lead to differences between odd and even lines, as is also described for stage-scanning in A.11. A similar procedure must be done for 1S-ISHG stage-scanning, as shown in Fig. 3.20: the correction (described in Fig.2 of the article in 9) by a calibration (a2) is performed on the even lines (b2 corrects b1) and the odd lines (c2 corrects c1) separately, and the latter are recombined (e). Nevertheless, this problem does not arise with bidirectional scans using digital galvos, but the duration improvement compared to unidirectional is small (10% difference in duration).

3.3.14 Decrease the I-SHG time even more?

In the article of chapt. 9 some techniques to further decrease the acquisition time of I-SHG are mentionned, one of which being the use of the technique of Fig. 2.14 to divide the signal onto multiple detectors. The safest case would be to divide it onto 2 detectors only, to have a minimum of signal losses. However, we have seen in 2.3.3 that a minimum of 3 phase-shifts are needed for the phase reconstruction. This is also visible if eq. 2.23 is considered: the computation of contrast frames removes the constant term, but 2 frames are still needed as there are two unknowns. Nevertheless, since we only probe the polarity in I-SHG, one contrast frame already gives the relative polarity by discriminating the positive and negative parts of the signal: the only solution for inverting the sign of $2\gamma\cos(\varphi+\delta)$ (γ being positive) is to add $\pm\pi$ to δ. Therefore, to discriminate between purely π phase-shifted zones, only two frames leading to one contrast frame are needed. This explains why a lot of information is already visible in such contrast frames compared to the full phase image, see e.g. [9] fig.2, [177] fig.2, [175] fig.3&4. Thus, a very rapid and simple I-SHG would consist of acquiring one interferogram with a low exposure time like 5μs, and dividing its signal into two detectors separated by a beam-splitter (see Fig. 2.14): a contrast frame of 100$\times$100 pixels could then be obtained at a video-rate of 1/(100*100*5e-6)=20Hz. However, such an image would not reflect the full disparities of the phase, and would not allow for the measurement of the interferometric contrast map γ (or "amplitude") that can convey information, as shown in the article 6.

Part II

Articles

Chapter 4

Multimodal nonlinear microscopy applied to meniscus

This chapter reports the multimodal coupling of SHG and p-SHG, in order to investigate a complex biological tissue: the meniscus, a fibrocartilage inside the knee-joint. Multimodal coupling is explained and the structure of the meniscus is exposed, along with the article on this study.

4.1 Need for multimodal imaging

Each nonlinear technique has its own assets and limitations, such that it is usually used to target specific structures in a sample. Thus, to render the full content of a given area, it is preferable to combine several imaging modes. These modes can be recorded either simultaneously or successively: for instance, 2PEF and SHG exploit different contrast mechanisms - and different wavelengths - so they can be used in tandem [256], with two PMTs that collect different wavelength ranges (narrow-band at 400nm for SHG, broadband at 500nm for 2PEF). If it does not result in a too high loss in performances (by using too many PMTs and beam-splitters), 3PEF and THG might also be acquired. After data treatment, images can be combined into a composite one as in [256] or in [146]. CARS images could also be acquired in parallel with the SHG or 2PEF, because the generated wavelength is different. A multimodal scheme that allows CARS to be coupled to SHG and 2PEF was developed in the lab.

Other techniques must be acquired *successively*, because they need to modify a property of the input field that can parasitically impact the other modalities. This is the case of p-SHG, CD-SHG (see C in the appendix) and I-SHG. Acquiring multimodal images thus takes a longer time, and the images are more subjected to spatial drifts in the three directions. Briefly, while I-SHG can measure the polarity of the structures inside the sample, p-SHG allows us to map their *alignment* inside the image plane. It is widely used for various types of samples containing bioproteins like collagen or myosin [182]. CD-SHG aims at using the chirality of a structure to probe its local out-of-plane orientation, but the achiral components of the $\chi^{(2)}$ need to be out of phase with the chiral ones, i.e. their imaginary part needs to be non-zero [75].

4.2 Introduction to a complex tissue: the meniscus

The meniscus is a kind of connective tissue that is suspected to play a major role in joints, and is at the interface between a fibrous tissue and a cartilage: it is sometimes called fibrocartilage [165]. Figure 4.1 shows the position of the two menisci inside the knee joint: they are placed between the femoral and the tibial cartilages (white layers in (b)). They are C-shaped ((a) and (c), especially if viewed in XZ plane), with a decreasing thickness from the outer (convex surface) to the inner border (concave surface, i.e. along X axis) such that a cross-section is triangular (in XY plane, see (b), (d), (e), (f)). Adult menisci can be a few cm large (thickness of the "C"), and a portion of this "C" can be even longer: it is thus necessary to define ROIs inside the tissue to image it in MPM. Globally, there is a revolutionary symmetry that follows the shape of the "C": it seems then logical to cut a slice orthogonal to it (orthogonal to Z, i.e. coronal). For microscopy (or histology), a thin slice is cut (e) and oriented with the femoral part at the top, generally extracted from the body part (also called intermediate, see (c)), but slices in the caudal or cranial part can also be used.

While a newborn mammal has its meniscus fully vascularized, the mature ones have blood vessels constrained to the "red-red" zone (Fig. 4.1 (e), with a "white-white" region without any blood vessels (more proteoglycan-rich) and a "red-white" region in-between [129]. The anatomy of the red-red regions (and to some extent, the red-white) is presented in (f): the tie-fibers form a network that interlace some fascicles of collagen, and at the boundaries of tie-fibers pass some (orthogonal) blood vessels, surrounded by a proteoglycan-rich region.

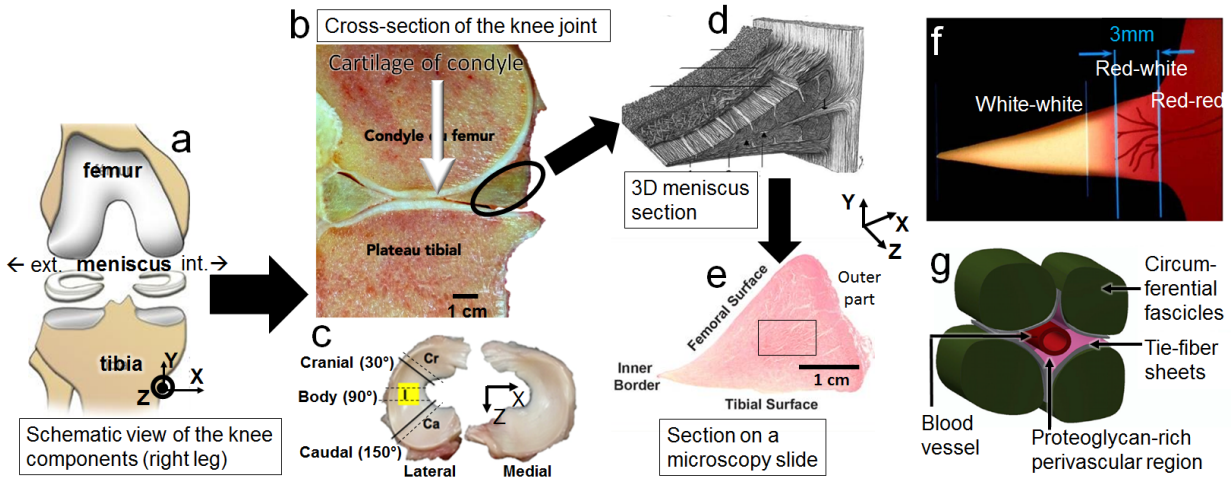

Figure 4.1: Schematic views of the meniscus. (a) Whole knee joint (right leg, viewed in XY plane), with the meniscus between the condyle of the femur and tibial plateau: the two menisci are C-shaped. (b) Cross-section of the joint: bone (red), cartilage layer (white) and meniscus (brown, with the medial one in black circle). (c) The two medial and lateral menisci, viewed from top (XZ plane) with the different parts: cranial, intermediary (or body), and caudal. (d) 3D view of the central part of the medial meniscus (coronal cut), showing the global orientation of fibrils (extracted from [151]). (e) Thin slice ($< 10\mu$m) of (d), for use in histology (H&E staining) or microscopy (XY plane). (f) Schematic view (XY plane) of the different axial zones from the outer to the inner border (see (e)): the red-red (with blood vessels), the white-white (contains more proteoglycans) and the red-white in-between [129] (g) Schematic representation of the main elements in the meniscus: blood vessels surrounded by proteoglycan-rich regions, and tie-fiber sheets. Fascicles are orthogonal to the tie-fibers, in the space between those (extracted from [4]).

Since images are limited to mm in size for MPM, a smaller subdivision of the triangular shape must be made: 5 areas can be defined (Fig. 4.1 e)), the inner or outer borders, the femoral or tibial surfaces and the central part (intrasubstance, black rectangle in (e)). We have reported in Fig. 4.2 the imaging of these different zones for normal (left column) and pathological (with lesions, right column) adults. These are overlays of forward (in red) and backward (in cyan) SHG PMT channels: on the whole, adults with lesions (right) present similar levels of intensity and similar features in forward and backward SHG, whereas in healthy menisci (left) some thick collagen fibers are more visible in the backward direction. Also, damaged tissues show some circular holes with no SHG signal contrary to those of healthy adults. For details on forward and backward SHG, see section 2.1.5.

4.3 Multimodal MPM in the meniscus

We applied multimodal MPM to the study of the complexity of the meniscus: intensity SHG - especially forward and backward - and polarization-resolved SHG (p-SHG) are used, as well as circular dichroism SHG (CD-SHG). CD-SHG is detailed in Appendix C.4, and p-SHG in C. Here we used the simplest

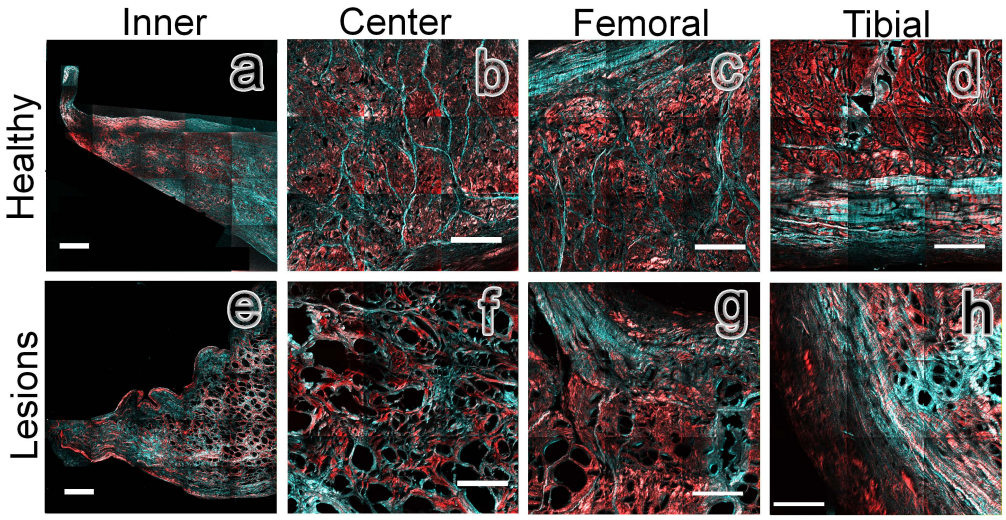

Figure 4.2: Different zones of the meniscus imaged by intensity SHG with mosaic reconstruction, overlay of forward (red) and backward (cyan) channels: (Top) Inner border normal (a) and with lesions (b), (Middle) Center part (intrasubstance) normal (c) and with lesions (d), (Middle) Femoral surface normal (e) and with lesions (f), (Bottom) Tibial surface normal (g) and with lesions (h). Scale-bars: 300μm.

information provided by CD-SHG: its absolute value, because the distinction of positive versus negative values is unclear, but fibrils in-plane will still have low CD signal and the ones out-of-plane a high CD signal (see [189]). Thus, we plotted in Fig. 4.3 (b) the overlay (composite image) of CD-SHG and intensity SHG to test this effect. The sample is an adult meniscus that was macroscopically identified with lesions.

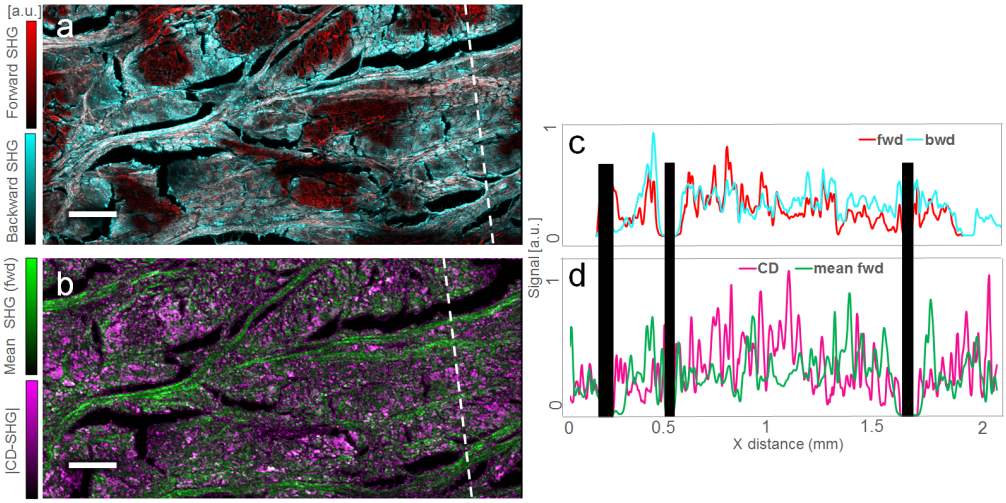

Figure 4.3: Comparison of forward (fwd, red) and backward (bwd, cyan) SHG (a), and |CD-SHG| (magenta) with the average SHG (green, (b)), in a damaged adult meniscus. (a) and (b) are overlays of the two channels. Profile plots along the white dashed line shown on (a) (resp. (b)) can be seen in (c) (resp. (d)). Scale-bars: 200μm.

The plot along the white dashed line (c) confirms that a high |CD| signal (large out-of-plane angle) corresponds to a low SHG intensity, and inversely a low |CD| signal corresponds to a high SHG intensity. An overlay of the forward and backward SHG in the same ROI is also shown in Fig. 4.3 (a): it presents similar observations as Fig. 4.2 in this degenerated tissue. Importantly, the backward SHG does not strictly correspond to |CD-SHG|, as the signal in one area can be high in both forward and backward SHG. Overall, a high forward over backward ratio (F/B) (i.e. a signal mainly forward oriented), which is theoretically consistent with a large out-of-plane angle (see Fig.2.8), is correlated with a large |CD-SHG| value that should also be enhanced by a large out-of-plane angle. Nevertheless, F/B is also dependent on other properties like the diameter of fibril bundles.

4.4 Article on maturation of the meniscus

(EN) Maturation of the Meniscal Collagen Structure Revealed by Polarization-Resolved and Directional Second Harmonic Generation Microscopy

(FR) Maturation de la Structure du Collagène Méniscal Révélée par Microscopie de Génération de Seconde Harmonique Directionnelle et Résolue en Polarisation.

Submitted 11th July 2019; Accepted 12 November 2019; Published 05 December 2019.

Citation: Sc. Rep. 9:18448 (2019)

DOI: 10.1038/s41598-019-54942-0

This study was carried out in collaboration with the veterinary school of St-Hyacinthe, lab of Sheila Laverty who provided the samples and expertise about this tissue. Also, its preliminary part was performed in the L.O.B. (Palaiseau, France) under the supervision of Marie-Claire Schanne-Klein, who also contributed to the design of the study and participate in the writing and revision of the manuscript.

SCIENTIFIC REPORTS
nature research

OPEN

Maturation of the Meniscal Collagen Structure Revealed by Polarization-Resolved and Directional Second Harmonic Generation Microscopy

Maxime Pinsard[1], Sheila Laverty[2*], Hélène Richard[2], Julia Dubuc[2], Marie-Claire Schanne-Klein[3] & François Légaré[1*]

We report Polarization-resolved Second Harmonic Generation (P-SHG) and directional SHG (forward and backward, F/B) measurements of equine foetal and adult collagen in meniscus, over large field-of-views using sample-scanning. Large differences of collagen structure and fibril orientation with maturation are revealed, validating the potential for this novel methodology to track such changes in meniscal structure. The foetal menisci had a non-organized and more random collagen fibrillar structure when compared with adult using P-SHG. For the latter, clusters of homogeneous fibril orientation (inter-fibrillar areas) were revealed, separated by thick fibers. F/B SHG showed numerous different features in adults notably, in thick fibers compared to interfibrillar areas, unlike foetal menisci that showed similar patterns for both directions. This work confirms previous studies and improves the understanding of meniscal collagen structure and its maturation, and makes F/B and P-SHG good candidates for future studies aiming at revealing structural modifications to meniscus due to pathologies.

The meniscus is a semilunar fibrocartilaginous structure interposed between the femoral condyle and the tibial plateau in the knee joint. The meniscus is essential for load transmission across the articular surfaces, for femorotibial joint stability and for long-term joint health[1]. Degradation of the meniscal tissue can increase articular cartilage strain[2], and may lead to cartilage degeneration and osteoarthritis[3]. Knowledge of the complex structure of the meniscal extracellular matrix (ECM) has increased thanks to emerging technologies for *in situ* imaging of intact specimens, such as Optical Projection Tomography (OPT)[4]. In particular the arrangement of meniscal fascicles[4], its tie-fiber organization[5], and the menisco-tibial ligament insertion transition have all recently been revealed by investigation of bovine samples[6].

SHG microscopy is a recent and powerful technique to image the structure of biological specimens as it provides submicron spatial resolution, has low phototoxicity and a high depth selectivity and penetration. In this respect, SHG imaging is similar to multiphoton-excited fluorescence microscopy[7]. However, important differences exist: it is a coherent process sensitive to the phase-matching conditions where the measured signal arises from constructive/destructive interferences, it is also instantaneous and free from photobleaching as the signal conversion is due to a structural arrangement and does not involve electronic transition[8]. SHG microscopy has been used to image fibrillar collagen in specimens including type II collagen in articular cartilage[9–16]. Furthermore, because of its coherent nature, the detection of the signal in the direction of propagation (forward - F) provides different imaging features compared to the backward (B) direction[17]. The F/B ratio increases with the level of homogeneity of noncentrosymmetric structures within the focal volume and has been related to the size of the collagen fibrils for collagen rich tissues[18,19].

[1]Institut National de la Recherche Scientifique, Centre Énergie Matériaux Télécommunications (INRS-EMT); 1650 Boul. Lionel-Boulet, Varennes (QC), J3X 1S2, Canada. [2]Comparative Orthopedic Research Laboratory, Department of Clinical Sciences, Faculté de médecine vétérinaire, Université de Montréal, Saint-Hyacinthe (QC), J2S 2M2, Canada. [3]Laboratoire d'Optique et Biosciences (LOB), École Polytechnique, CNRS, Inserm, Institut Polytechnique de Paris, F-91128, Palaiseau, France. *email: sheila.laverty@umontreal.ca; legare@emt.inrs.ca

The complex noncentrosymmetric structural organization of meniscal collagen has been previously imaged using Second Harmonic Generation (SHG) microscopy[5,20–23]. SHG microscopy has revealed a variety of meniscal structural features including: the fiber bundle organization[24], the arborization of the tie-fibers[5] and the interaction of primary cilia with the ECM[25] in healthy menisci. The effect of degradation on ECM density and cell accumulation[26], of cyclic loading[27] and the meniscal integrity following repair[20] have also been imaged by SHG microscopy. Furthermore large images of the whole joint (cartilage and meniscus) were imaged by multiphoton fluorescence and SHG[28], and even *in-vivo* and minimally processed joints using SHG microendoscopy[29]. SHG and Coherent Anti-Stokes Raman Scattering (CARS) microscopy have also been employed to characterize artificial meniscus-like implants[30]. However, up to now, the local orientation of the meniscal collagen structures has been mainly characterized by OPT, only to a resolution of ~15 µm permitting identification of the collagen fascicles but not of the individual fibers[4]. These fibers were later imaged by SHG microscopy in some areas from bovine samples[5], but their orientation was discussed only in terms of the SHG intensity. The latter is subject to interference due to the coherent nature of the process, that can result in masking the real underlying structure[31] therefore preventing imaging of the fibril orientation and nonlinear tensor properties on its own[32]. Polarization-resolved SHG (P-SHG) was developed to override this limitation, and has been shown to accurately reveal the alignment distribution of collagen fibrils in various tissues such as tail tendon or skin[32–34], but has never been reported in meniscus.

The influence of age on the mechanical response of meniscal connective tissue has been studied at the nanoscale in human menisci using atomic force microscopy[35]. The propagation of collagen II deposition has been investigated in the mouse (using an anti-collagen II bioclone) from the inner to outer border, during meniscal growth from foetus to adult[36]. Furthermore the relative area of meniscus versus articular cartilage has also been characterized during human foetal gestation[37]. In addition, the meniscus has been shown to increasingly develop cartilaginous properties during maturation[38]. A recent study also compared vertical meniscal sections in bovine joints from foetuses and adults[39], and reported that the spacing between circumferential bundles of fibrils is much higher in foetuses than in adults.

Here, we demonstrate the unique potential of SHG and P-SHG to measure the collagen structure in the meniscus, and we use these two techniques together with histology to characterize the structural differences between equine foetal and adult meniscal ECM. Understanding and imaging the meniscal ECM could provide new knowledge to support studies on meniscal degradation events in joint degeneration, and potentially new insights towards meniscal regeneration in the future.

Results

Forward and backward SHG. Representative images of the ECM from the central body of two foetal and adult menisci visualized by standard SHG (using circular polarization) are presented in Figs. 1 and 2 respectively. Only collagen fibrils are visible as they are the only non-centrosymmetric material[5]. Additional images of all foetal and adult menisci can be found in the Supplementary information (respectively Figs. S3 and S4).

The SHG images of Fig. 1 reveal that the collagen of foetal menisci shows similar patterns in both forward and backward SHG directions. Figure 1 shows that F1 (a & b) has aligned horizontal fibrils over the whole region-of-interest (ROI), and that F2 presents numerous different orientations in the ROI (c & d, see also Table S1). For both samples, the visible patterns are similar, and forward and backward SHG images present equivalent features. This is particularly visible on the overlay of the forward and backward channels of Figure S2 (a&b, Supplementary information).

In the case of mature specimens (adults, Fig. 2), the forward images present numerous differences from the backward ones. In the backward direction, thick collagen fibers are visible while the signal between the thick fibers is strongly reduced, or with zero signal (see also Figure S2 c&d). It is worth noting that, here, the retro-reflection of the forward SHG on the backward image seems to be negligible: no pattern from the forward images (a & c) is visible on the backward image (b & d). Thus, the experimental precaution indicated for instance in Légaré *et al.*[40] was not here necessary to obtain a proper backward image.

Polarization-resolved SHG (P-SHG). Collagen fibril orientation in the imaging plane obtained by P-SHG imaging is shown in Fig. 3 for the foetal menisci (exact same zones as in Fig. 1), and in Fig. 4 for the adult ones (exact same zones as in Fig. 2). Images of other foetus and adults can be found in the Supplementary information, Fig. S5 (foetus) and S6 (adult). The foetal meniscal fibrils are either homogeneous in orientation (Fig. 3(a)), or random (Fig. 3(b)), whereas all the adult samples show clusters of homogeneous orientations. On the polar histogram (revealing the overall orientation of the collagen fibrils), the random distribution is seen by an almost circular pattern, whereas an homogeneous distribution leads to a directional double-lobe. These P-SHG images confirm what was shown in the backward SHG images (Figs. 1 and 2): in the adult meniscus (Fig. 4(a),(b)), a complex network arrangement of thick fibers interlaces a rather homogeneous assembly of orthogonal fibril bundles.

Quantitative comparison. The pixel-wise ratio of forward over backward SHG signals (F/B) was averaged first over the whole image in Fig. 5(a), and then by separating the thick fibers from the residual tissue (inter-fibrillar area, see Methods) in Fig. 5(b). The F/B SHG for the thick fibers area are similar for adult vs foetus specimens (not shown), while the remaining tissue (i.e. inter-fibrillar area) shows an F/B around 4.5 for the foetus and around 28 for the adult: this is consistent with what is observed in Figs. 1 and 2. The F/B of the whole image is also significantly different for the adult versus the foetus. In addition, the difference observed in the structure of SHG images was assessed by the ratio of non-fibrous over fibrous areas: as seen in Fig. 5(c), the area without those thick fibers (inter-fibrillar area) is close to 98% for the foetuses whereas it is around 90% for the adult, with a significant statistical difference between both values.

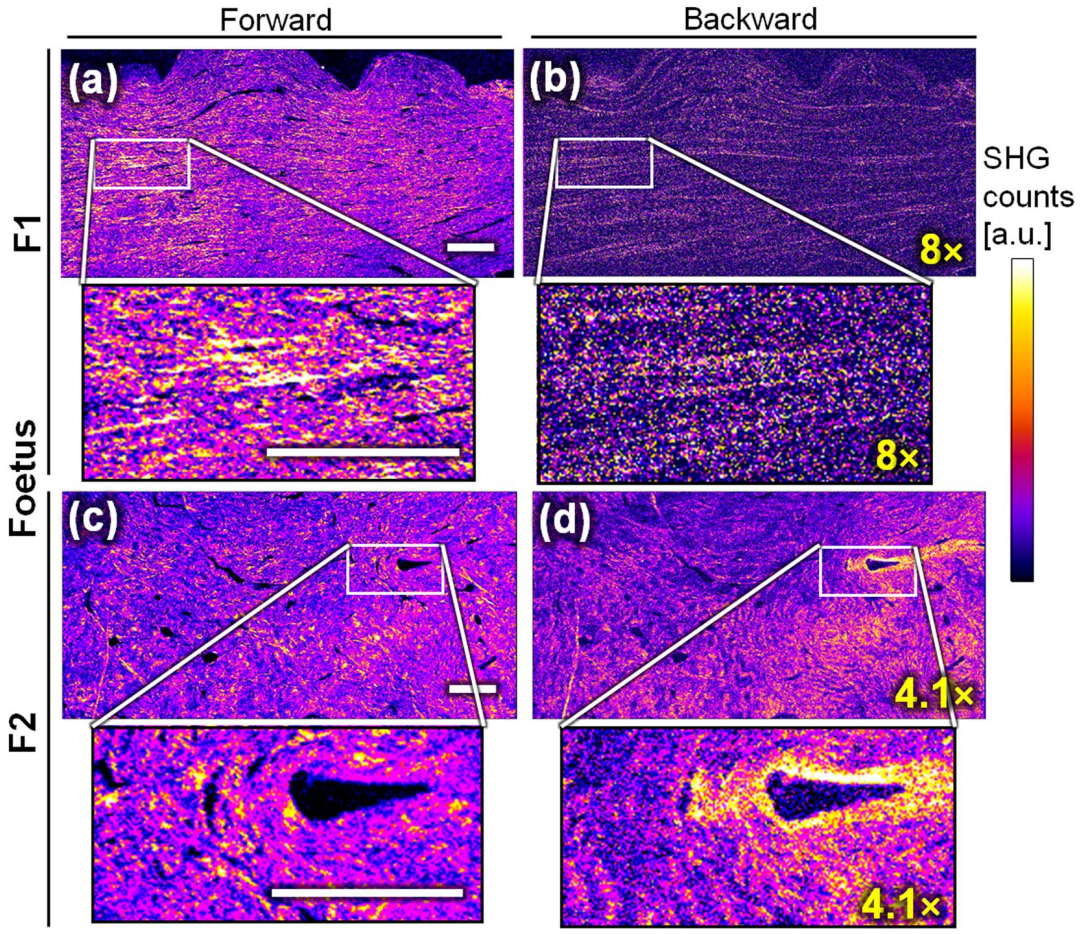

Figure 1. Forward SHG (left, (**a,c**)) and backward SHG (right, (**b,d**)) from two menisci samples from equine foetuses ((**a,b**), F1 and (**c,d**) F2) knee joints). F1 ((**a,b**)) shows a tissue that is mostly homogeneous (horizontal patterns), whereas F2 ((**c,d**)) shows more randomly oriented patterns. Both menisci show similar images in forward and backward directions. The images of the same samples (**a,b or c,d**) are displayed using the same look-up table, but the backward images have been multiplied by a factor indicated in yellow because less signal is physically detected in this direction compared to forward. Scale-bars: 200 μm.

Moreover, the differences between the fibril orientation distributions observed in Figs. 3 and 4 were verified by computing the circular standard deviation (std) of the angle ϕ, for every meniscus imaged in P-SHG. The results are reported in Fig. 5(d). The foetuses are clearly split into two groups, as the difference between the homogeneous and the random fibril orientation is too high to merge them together. Noteworthily, this discrepancy cannot be explained by the age of the foetuses (see Table S1 in the Supplementary information) nor the type of menisci (lateral versus medial). It could rather be partly due to the relatively small site studied, and the difficulty of having all measures at the exact same site in each samples. The two foetal samples with a homogeneous orientation (F1 and F3, see Table S1) do not show a significant difference from the adult group (too few samples), but the group of foetuses having random fibril orientation does show a significant difference. These statistics suggest that some subgroup of foetal samples exhibit different fibril orientation compared to the adults, while the reason to have different subgroups in the foetal samples remains unclear.

Discussion

Collagen, which plays a central role in the architecture of the tissue[41], is the principal component of the adult meniscal ECM (70%), of which 60% is type II and 40% type I[42]. The ordering of the collagen fibrils within the focal volume of excitation (i.e. at the micron-scale) is usually probed by P-SHG using the anisotropy parameter ρ[43] (see Methods section for definition), but this method has been mainly applied to tissues composed of only one type of collagen. Indeed, despite having similar sequences of amino-acids[44], collagen I and II have different properties: they are biochemically different, and their fibrils have different sizes[12]. It is thus a challenge to measure structural parameters such as ρ in such tissues. In previous studies of cartilage tissues, Romijn *et al.*[44] have differentiated collagen I and II but only at some specific pixels, resulting in a ρ mapping with a relatively high level of uncertainty[44]. This discrimination is also challenging because the average ρ in collagen I and II was found to be similar[44].

Moreover, the semilunar and concave form of the meniscus (see Fig. 6 in the Methods), and the 3D arrangement of its collagen results in fibrils pointing out of the image plane: this highly complex structural organization

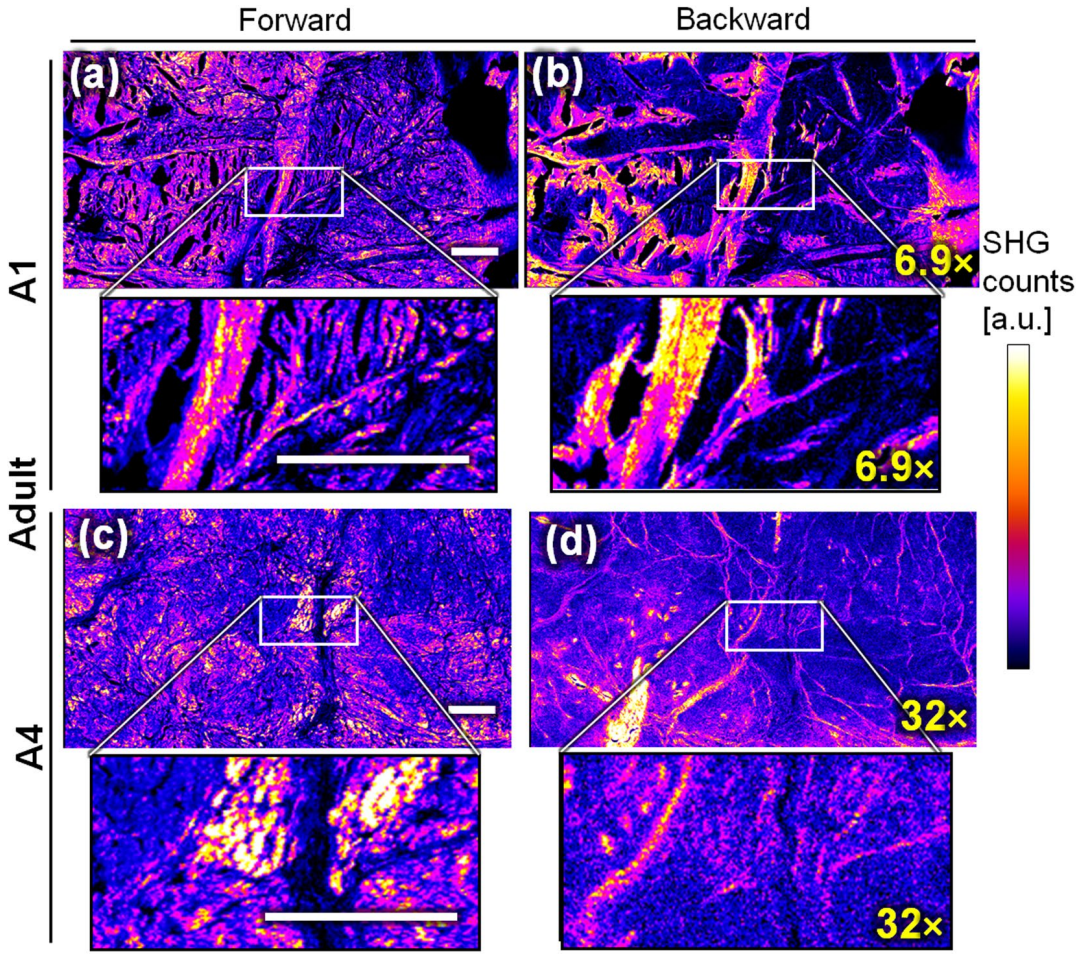

Figure 2. Forward SHG (left, (**a,c**)) and backward SHG (right, (**b,d**)) from two menisci of equine adults (A1 for (**a,b**) and A4 for (**c,d**)) knee joints. Both menisci show different patterns in forward and backward directions: the backward images better highlights the thick structures, mostly identified as fibers. The images of the same samples (**a,b or c,d**) are displayed using the same look-up table, but the backward images have been multiplied by a factor indicated in yellow because less signal is physically detected in this direction compared to forward. Scale-bars: 200 μm.

artificially modifies the measured ρ[44]. As a result, the ρ values averaged over the whole images were undistinguishable between our samples of foetal and adult menisci (not shown here), despite clear different features observable in the images. Overall, the shape and contrast of the polarimetric diagrams extracted at each pixel cannot be exploited due to these complex effects. This comes at a high cost since this is usually the main feature exploited in P-SHG. For instance, this precludes the classification of these tissues by the method previously described by Rouède *et al.*[41], that mainly relies on ρ.

Despite this limitation, P-SHG can be used to measure the in-plane fibrillar orientation ϕ, as it exploits only the average orientation of the polarimetric diagram. The ϕ maps with or without the Kleinman filter condition were similar (data not shown), which shows that these maps are not sensitive to the precise value of the susceptibility tensor components, and that P-SHG's ϕ provides a robust way to measure these orientation maps. The ϕ-map in P-SHG (Figs. 3 and 4) probes the orientation of collagen fibrils at a local scale (pixel resolution, i.e. few μm), while the circular std (see methods section) of Fig. 5(d) measures the global tendency of alignment (at the field-of-view scale, i.e. few mm). A circular std has been chosen because it is a good metric of the dispersion of the ϕ distribution. The collagen fibrillar orientation of the adults (discernible in Fig. 2 and clearly revealed in Fig. 4) seems to confirm what was suggested in Andrews *et al.*[5]: some clusters of fibrils exhibit homogeneous orientation, and are separated by thick fibers. We interpret the clusters as the fascicles and the thick fibers as some parts of the tie-fiber sheets that are described in Andrews *et al.*[5]. The low SHG signal of the inter-fibrillar area observed in backward images is consistent with the fact that the fascicles are perpendicular to the thick fibers in the image plane[5]. Furthermore, the F/B ratio for these zones is higher in average, consistently with what is expected for out-of-plane fibrils[22].

The study of the forward and backward SHG (F/B) provides an analysis on the directionality of the SHG signal. The forward SHG image shows at each pixel the degree of phase-matching, with a selectivity on the ordered structures (within the focal volume), at the size of the SHG wavelength λ_{SHG}. The backward SHG reveals smaller or more

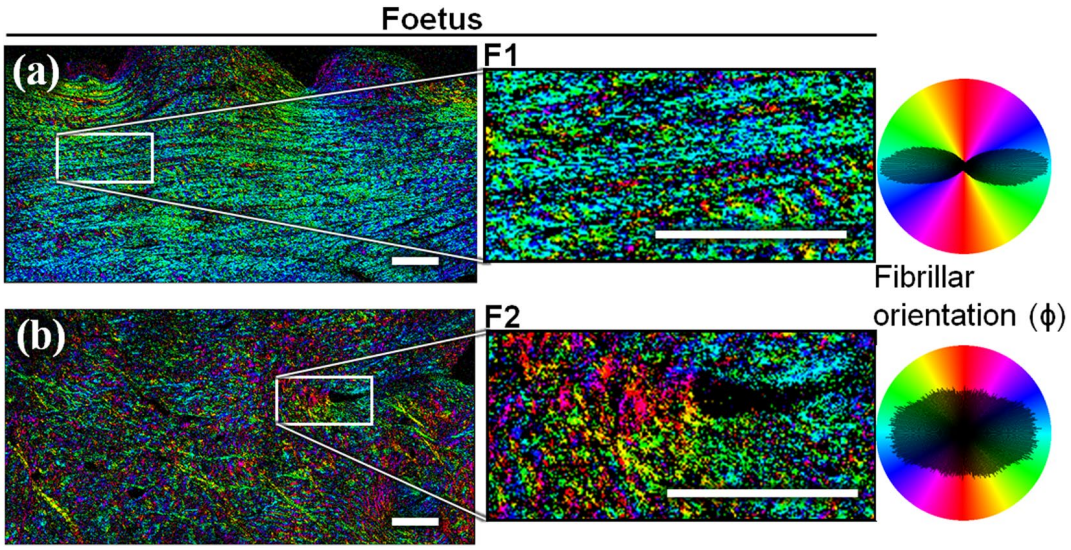

Figure 3. Collagen fibril orientation in the imaging plane (ϕ) measured by P-SHG, for the same foetus specimens (F1 (**a**) and F2 (**b**)) as in Fig. 1. The foetus F1 (**a**) has a homogeneous orientation: the polar histogram reveals two directional lobes. The foetus F2 (**b**) exhibits a random orientation, almost equally scattered over all the angles: the polar histogram is then a low-eccentricity ellipse. Scale-bars: 200 μm.

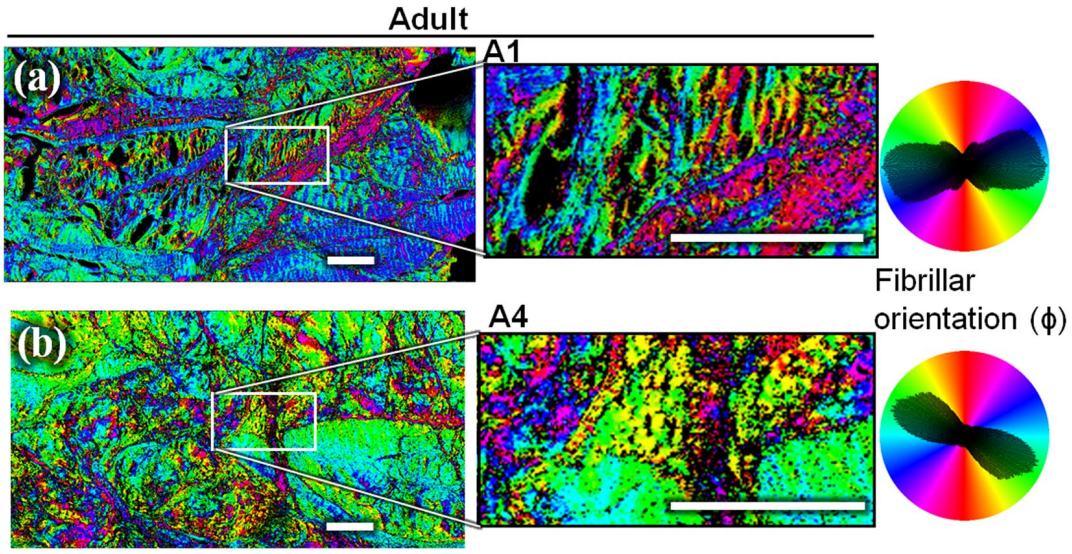

Figure 4. Collagen fibrils orientation in the imaging plane (ϕ) measured by P-SHG, for the same two adults' specimen (A1 (**a**) and A4 (**b**)) as in Fig. 2. These mature menisci have an organized structure, with some thick fibers that clearly delimitate bundles of homogeneous fibrils. On the polar histograms, the orientation shows a principal component coupled with some other components corresponding to the numerous – but still limited – orientations. Scale-bars: 200 μm.

random structures in a complementary way[17]. The F/B ratio is then smaller for the more disorganized structures - or for structures organized on a size smaller than λ_{SHG}[17] - and increases with the fibril diameter, or with the diameter of bundle of fibrils of same polarity[18,45]. This ratio is averaged over the whole field-of-view and thus provides global information on the collagen bundles in terms of size and arangment. Specifically, it is expected to be smaller for type II collagen, which is known to form fibrils with smaller diameters (few tens of nm[46]) than type I collagen (few hundreds of nm)[47,48]. Collagen II is also present in low amounts in foetuses, but increases with age[36,38]. In addition, tie-fibers in mature samples have higher quantities of it compared to the other regions like fascicles[49]. We therefore expect that the tie-fibers exhibit a lower F/B ratio than the rest due to the type II collagen fibrils present in this structure: accordingly, we have observed that the tie-fibers were the main visible patterns in the backward direction. However, the adults that contains more tie-fibers than foetuses would have a smaller global F/B ratio. This confirms that F/B SHG cannot unambiguously discriminate between type I and type II collagen or measure their respective quantities. Nevertheless, it demonstrates that it is a useful structural probe – complementary to histological assessment – sensitive to the different spatial organizations of the collagen (type II or mix type I/II) that varies with age.

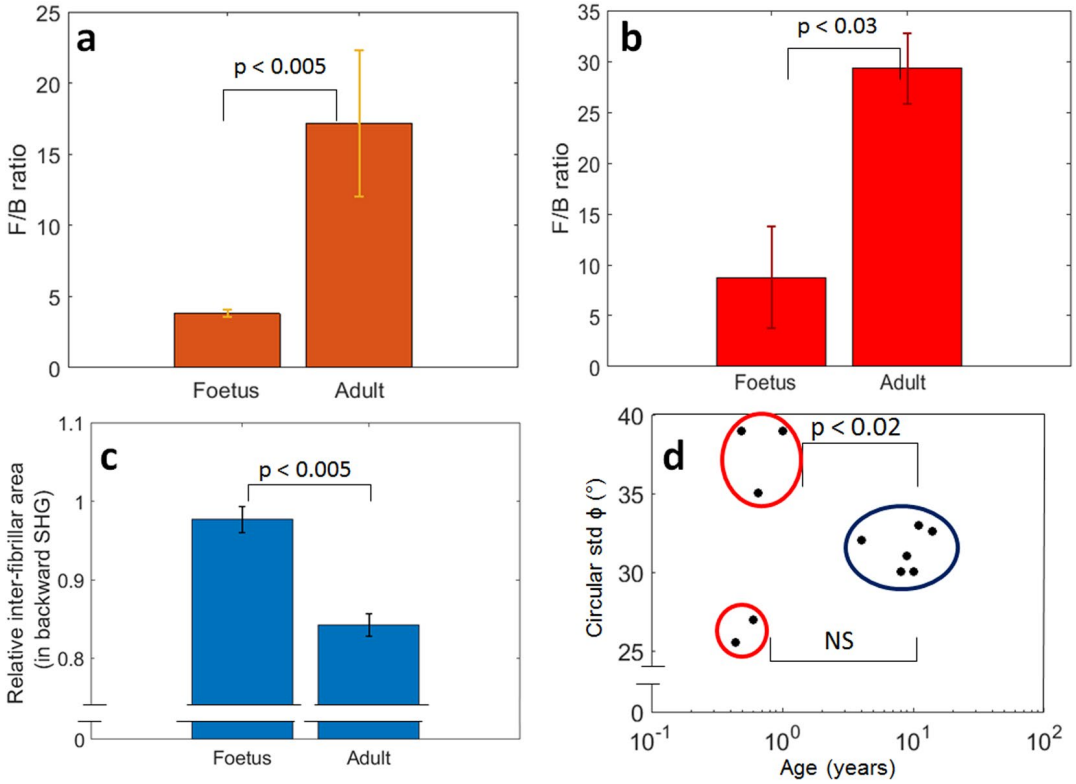

Figure 5. Quantitative results of F/B and P-SHG. Forward over backward ratio (F/B) over the whole image (**a**) or for the inter-fibrillar area (**b**) for all the foetus and adult menisci. (**c**) Relative inter-fibrillar area measured in backward SHG, i.e. the percentage of inter-fibrillar area compared to the whole image. (**d**) Circular standard deviation (std) of the P-SHG fibril orientation in the image plane (ϕ): the adult (in dark blue) have values around 32°, whereas the foetuses (in red) split in two groups: one having a value of ϕ circular std rather low (~26°), the other one a larger value (~37°). In each graph, the mean of the different values was taken, and the error bars indicate the standard error of the mean (SEM) of the serie. The statistical significance (NS: non-significant, $p < 0.05$: significant) was tested using the non-parametric Wilcoxon-Mann-Whitney test. The set of samples consist of $n = 5$ for foetuses and $n = 6$ for adults, which gives an acceptable statistical representation given the difficulty to obtain foetus samples.

Interestingly, the result of Fig. 5(c) confirms what was measured by Qu *et al.*[39] with multimodal multiphoton microscopy (SHG and two-photon fluorescence), using a local thickness measurement: the inter-fibrillar area reduces with maturity in meniscus. However, it is more precise to use P-SHG to circumvent interference pattern artifacts, as mentioned in the introduction. It is also noteworthy that the change from a random collagen meshwork to a more organized arrangement with maturation - that we have observed here in meniscus - has also been demonstrated in developing cartilage[50]. Additionally, cartilage maturation has been shown to be coupled with the apparition of different zones[50,51], which is consistent with the formation of clusters of fibrils in meniscus that we have observed in this study.

To conclude, we report, for the first time to our knowledge, the mapping of the in-plane orientation of the collagen fibrils within the meniscal tissues over large ROIs. The observed structure of the collagen network in adult samples is in agreement with what has been previously reported (with other techniques) in bovine menisci[4,5]: relatively thick tie-fibers oriented radially, interlacing some fascicles oriented circumferentially. Moreover, this organized structure is not identified in the foetal meniscus: the latter is composed of either a random fibril organization, or no network at all with only parallel fibrils. This study confirms the importance of SHG microscopy, especially the F/B as a structural probe for the study of the meniscal – and potentially the cartilage's – ECM, as well as the capacity of P-SHG to map the fibril orientation even with a mix of different collagen types. Both techniques are shown to be automated and applicable within a reasonable acquisition time, enabling large scale studies in the future. They also provide quantitative results which can be significant for further studies of the structure of meniscus at the micron-scale. We anticipate their future use for characterization of degeneration in the meniscus or cartilage, and overall furthering the understanding of such tissues.

Methods

Sample preparation. This project was approved by the Institutional Animal Care and Use Committee (IACUC) of the Faculté de médecine vétérinaire, Université de Montréal. Tissues were obtained from a local slaughterhouse and from horses donated by their owners for research. The age of equine foetuses ($n = 5$) was estimated using crown-rump measurements as previously described[3,52,53]. Adult samples ($n = 6$) were also studied, and had been banked from a previous study. The femorotibial joints were freed of soft tissue, inspected and the

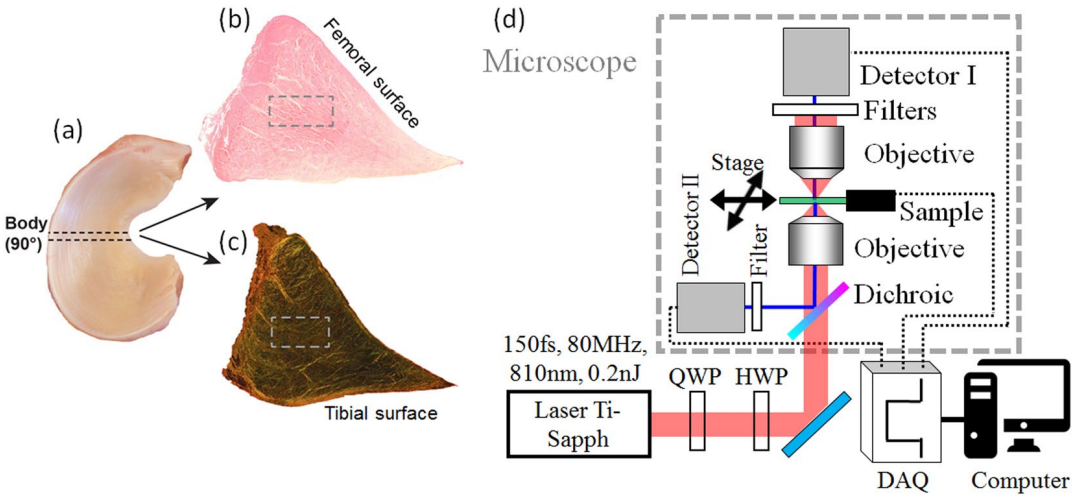

Figure 6. Study design. The meniscus was removed from the equine knee femorotibial stifle (joint) and its body was sectioned at 90° (**a**). The triangular-shaped coronal (circumferential) sections were deposited on a microscope slide. (**b**) HEPS stain for standard histology and (**c**) Picro-sirius red stain for collagen. The rectangle in (**b**) shows the central area of the tissue investigated in SHG and P-SHG microscopy. (**d**) Schematic view of the set-up used for P-SHG and F/B SHG. A femtosecond laser directly excites the sample without being scanned, the image being done by moving the sample laterally with a motorized stage, synchronized to the acquisition by a multifunction card (DAQ). QWP: Quarter-wave plate, HWP: Half-wave plate. In P-SHG, the dichroic mirror can be removed to ensure a better polarization control, as the signal is captured in the forward direction. For F/B measurements, a dichroic filter is inserted before the excitation objective to send the backward SHG to a 2nd detector (II).

menisci harvested. Menisci were included in the study if the macroscopic appearance of all surfaces was normal (no fibrillations or tears) and if the joint of origin was also macroscopically intact (no cartilage erosions or evident pathology). Sample listing can be found on Table S1 of Supplementary information. Each meniscus was then laid over a protractor with the femoral surface uppermost and the cranial border aligned with the angle 0 as described previously[3] (see Fig. 6(b),(c)). A slice orthogonal to the circumferential direction[54], i.e. in the vertical-radial plane[5] was cut in the body of the meniscus. The menisci were placed in 10% formaldehyde for 2 h and then transferred to Ethylenediaminetetraacetic acid (EDTA, to avoid calcification effects on cutting) 20% for 2 weeks prior to paraffin embedding and subsequent sectioning. Five micron sections were cut (Fig. 6(a)) and then placed on a microscope slide (1 mm thick) covered by a thin coverslip (#1.5 H, Thorlabs). The central part of this triangular-shaped tissue (see Fig. 6(b),(c)) was imaged on a microscopy slide oriented upside-down, with the coverslip facing the incoming light since the microscope objective is made to image through a thin coverslip (see Fig. 6(d)). This segment (body) of the meniscus was selected because it is denser in collagen than in proteoglycan, contrary to other sites[1].

Five micron sections were also cut and stained with haematoxylin, eosin, phloxine and saffron (HEPS) as well as Picro-sirius red to illustrate the collagen network architecture under polarized light microscopy (see Supplementary information Figs. S1 and S2). All slides were digitalized with a LeicaDM 4000B microscope and Panoptiq v.1.4.3 computer software. All the images of the ROI of the central part are presented with the same geometry as in Fig. 6(b), with the tibial surface at bottom and the inner border to the right.

SHG microscopy. A mode-locked Ti:Sapph oscillator (Tsunami, Spectra Physics) delivering ~150 fs pulses at 810 nm and 80 MHz rate was used as the laser source. The microscope is a modified commercial laser-scanning setup (iMic, Thermo-Fisher Scientific Munich GmbH), where a plane mirror was inserted before the objective to by-pass the laser-scanning, and send the beam directly to the objective to perform sample-scanning with a translation stage (MLS203, Thorlabs). An achromatic telescope was used to re-size the beam to overfill the back aperture of the objective (UplanSApo 20 ×, strain-free for good polarization control, NA 0.75, air immersion, Olympus). The polarization was controlled by a multi-wavelength half-wave plate (HWP, at 400 and 800 nm), and by an achromatic quarter-wave plate (QWP, 700–2500 nm, B. Halle) placed before the microscope (see Fig. 6(d)). A mechanical motor was used to vertically move the objective to find the proper focus position. Signals were collected in the forward direction using an objective with a numerical aperture of 0.75 (same reference as the excitation one) and detected on a photomultiplier tube (PMT - R6357 amplified with a C7319 unit, Hamamatsu Photonics, Japan) set at 900 V using appropriate spectral filters (two FF01-720/SP-25 and a FF01-405/10, SEMRock, Rochester, NY, USA). Scanning and signal acquisition were synchronized using a custom-written Python (www.python.org) software and a 6110 multichannel I/O acquisition card (National Instruments). Images were recorded using 50 µs pixel dwell-time. The sample-scanning allowed to do rather large scans (2000 × 1000 µm, 2 µm/pixel) in just one acquisition (no mosaic reconstruction) and in a reasonable acquisition time (55 sec), providing that the scan parameters are optimized and the synchronization between the motor and the acquisition DAQ card is controlled. Each image was acquired 3 times to perform an average

measurement. These acquisition parameters were the same for the two techniques F/B SHG and P-SHG. The average power on the sample was adjusted to 20 mW, corresponding to roughly 0.3 nJ/pulse. Raw data visualization was performed with FIJI-ImageJ (NIH[55]) and image processing was performed with MatLab (The MathWorks). All the images are presented with the full imaged areas, and oriented with the femoral surface on top and the outer surface on the left (as in Fig. 6(c)).

Forward and backward SHG measurements (F/B SHG). A circular polarization of excitation was used to image all structures independently of their orientation in the image plane. A long pass dichroic mirror (FF735-Di01-25 × 36, SEMRock) placed at the back-focal plane of the objective was used to reflect the SHG generated in the backward direction (epi). This dichroic mirror is translatable, and was inserted only when backward imaging was performed (using circular polarization), not for linearly polarized excitation. To calibrate the F/B measurements i.e. to take into account that the detection efficiency is different in forward and backward directions, we used the isotropic emission of the two-photon excited fluorescence signal from Coumarin 440 (diluted in ethanol), because its fluorescence (400–460 nm) lies partly in the range of the SHG filters (405 ± 5 nm). The obtained ratio between forward and backward directions was 0.4. The F/B ratio was calculated by an established method[17] by taking the median of the pixel-wise F/B signal in the whole field-of-view, the forward and backward images being the average of the 3 acquired frames.

Polarization-resolved SHG (P-SHG). A perfect linear polarization is needed for P-SHG, so the polarization was calibrated with the routine developed in Romijn *et al.*[56], using a modified version of their MatLab code[57]. This enables to use a varying linear polarization (from 0 to 180°) that stays linear even if the waveplates are placed before the input of the commercial microscope. It is worth noting that the dichroic used in F/B SHG measurements was removed for P-SHG, and that sample-scanning avoids any other source of polarization distortion compared to the standard laser-scanning. As we performed the SHG measurements, images were acquired for 18 polarization states, spaced by steps of 10° so that the full range of [0, 170°] was covered (the rest of the polarizations being redundant).

Theory and data treatment in P-SHG. For a complete description of P-SHG, see Teulon *et al.*[58]. The collagen fibrils are here assumed to have cylindrical symmetry (C_∞ group), and we neglect the chiral components of their nonlinear susceptibility tensor $\chi^{(2)}$. Furthermore, in the case where the fibrils are distributed around the imaging plane (which is reasonable for cartilage-like tissue), the out-of-plane orientation δ should be considered (δ = 0 meaning in the plane)[44]. Even if the Kleinman symmetry should here apply as NIR wavelengths are used to drive the SHG process, thus having energies far from any transition[44], this condition is not assumed a priori to be able to verify it in data treatment. The independent non-zero components of the $\chi^{(2)}$ are then χ_{33}, χ_{31} and χ_{15}. The X axis in the XYZ frame corresponds to the same direction as the x axis in the xyz frame. The simplified expression for the two components of the SHG intensity (X being the direction of propagation) can then be written as[44]:

$$\begin{aligned} I_Z^{2\omega} &\propto |\chi_{15}\cos\delta[A\sin^2(\theta-\phi)+B\cos^2(\theta-\phi)]|^2 \\ I_Y^{2\omega} &\propto |\chi_{15}A\cos\delta\sin(\theta-\phi)\cos(\theta-\phi)|^2 \end{aligned} \quad (1)$$

where θ is the angle of the imposed polarization with respect to the Z-axis of the laboratory frame, and φ the orientation of the collagen fibril with respect to this axis. Also, $A=\chi_{31}/\chi_{15}$ and $B=\chi_{33}/\chi_{15}\cos^2\delta+(2+\chi_{31}/\chi_{15})\sin^2\delta$[44], so that $\rho_0 = B(\delta=0)/A = \chi^{(2)}_{zzz}/\chi^{(2)}_{zyy} = \chi_{33}/\chi_{31}$ is the anisotropy parameter (z being the fibril axis and y the axis orthogonal to X and z). The more standard calculation would assume δ = 0, A = 1 and B = ρ_0, i.e. that the Kleinman condition applies and that the collagen lies in the imaging plane. Here, we process the P-SHG data with or without a filter that imposes abs(A) < 1.1, as in Romijn *et al.*[44] (called the Kleinman filter from now on). We still expect to be close to the Kleinman symmetry (i.e. A ≈ 1) as already mentioned. ρ is in this case the anisotropy parameter in the frame of the tilted fibril, which can be written as $\rho=\rho_0\cos^2\delta+3\sin^2\delta$ where ρ_0 is the anisotropy parameter for no tilt[58]. Summing the above intensities and developing the sine and cosine gives[58]:

$$I_{tot}^{2\omega} = a_0 + a_2\cos 2(\theta-\phi) + a_4\cos 4(\theta-\phi) \quad (2)$$

With

$$\begin{aligned} a_0 &= K/2[1+((\rho-1)/2)^2+2((\rho+1)/2)^2] \\ a_2 &= K(\rho^2-1)/2) \\ a_4 &= K/8(\rho-3)(\rho+1) \end{aligned} \quad (3)$$

and K a constant that gathers different physical parameters. The exact same expression is obtained for the standard case of δ = 0 by substituting ρ_0 to ρ[43]. A custom MatLab routine was then used to extract the relevant information from the P-SHG images. Briefly, a spatial FFT algorithm with respect to the angle θ is used to compute the Fourier transform (variable Ω) of the measured intensity[59]:

$$I_{FFT}(\Omega) = \alpha_0 D(0) + \alpha_2 e^{2i\phi_2} D(2-\Omega) + \alpha_4 e^{4i\phi_4} D(4-\Omega) + c.c. \quad (4)$$

where c.c. is the conjugated complex, and D the Dirac function (Fourier-Transform of cos θ).

The estimation ϕ_2 (resp. ϕ_4) of the relative orientation φ could then be extracted from the first exponential: Ω = 2 (resp. from the second exponential: Ω = 4): $n\phi_n = \mathrm{Arg}[\alpha_n e^{in\phi_n}]$ (n = 2 or 4). Then, $\phi_2 = 0.5\mathrm{atan2}(\alpha_2 e^{2i\phi_2})$

is directly in $[-\pi/2, \pi/2]$ because the 2-arguments arctangent function atan2 casts its result in $]-\pi, \pi]$. For ϕ_4, a simple arctangent must be used to avoid a wrong re-casting[59], ϕ_4 which is then in $[-\pi/8, \pi/8]$. Putting $\beta = \alpha_2^2/(\alpha_2^2 + 4\alpha_4^2)$, it has been shown that the combination $\phi = \beta\phi_2 + (1-\beta)(\phi_4 + m\pi/4)$ gives the most accurate result[59], with m in $\{-2, -1, 0, 1, 2\}$ calculated to minimize the quantity $|\phi_2 - \phi_4|$[59].

Polar histogram for P-SHG. The values of orientation ϕ obtained in P-SHG are circular, so their histograms are better represented on polar plots. The orientation is measured, but the polarity remains unknown so the values of ϕ are obtained in $[-\pi/2, \pi/2]$. To plot the histogram in a full circle, the values of ϕ were thus duplicated by a central symmetry (which makes the polar histograms inherently centrosymmetric). The orientations are color-coded, as indicated on the histograms (e.g. red for vertical and cyan for horizontal orientations). The standard deviation (std) for the values of ϕ must also use a circular calculation, otherwise the boundaries of the distribution are not considered equal and continuous, as an angle should be[60].

Quantitative distributions. The Shapiro-Wilk's test was first used to reject the normality of the distributions, and the difference was then tested using the Wilcoxon-Mann-Whitney test. The significance threshold was set to 0.05. Meniscus shows regions of low SHG signal meaning discontinuities of the visible collagen structure, attributed to either out-of-plane fibrils or zones with no collagen. The relative surface of these inter-fibrillar areas can be calculated in ImageJ: a threshold (ImageJ "Yen white") was first applied to the backward SHG images to discriminate the fibrillated areas from the rest (see the masks in Fig. S7, Supplementary information). Then, the relative area in this binary image was easily calculated.

Data availability

The datasets generated and/or analyzed during the current study are available from the corresponding author on reasonable request.

Received: 11 July 2019; Accepted: 12 November 2019;
Published online: 05 December 2019

References

1. Andrews, S. H. J., Adesida, A. B., Abusara, Z. & Shrive, N. G. Current concepts on structure–function relationships in the menisci. *Connect. Tissue Res.* **58**, 271–281 (2017).
2. Carter, T. E. *et al*. *In vivo* cartilage strain increases following medial meniscal tear and correlates with synovial fluid matrix metalloproteinase activity. *J. Biomech.* **48**, 1461–1468 (2015).
3. Dubuc, J., Girard, C., Richard, H., De Lasalle, J. & Laverty, S. Equine meniscal degeneration is associated with medial femorotibial osteoarthritis. *Equine Vet. J.* **50**, 133–140 (2018).
4. Andrews, S. H. J., Ronsky, J. L., Rattner, J. B., Shrive, N. G. & Jamniczky, H. A. An evaluation of meniscal collagenous structure using optical projection tomography. *BMC Med. Imaging* **13**, 21 (2013).
5. Andrews, S. H. J. *et al*. Tie-fibre structure and organization in the knee menisci. *J. Anat.* **224**, 531–537 (2014).
6. Andrews, S. H. J., Rattner, J. B., Jamniczky, H. A., Shrive, N. G. & Adesida, A. B. The structural and compositional transition of the meniscal roots into the fibrocartilage of the menisci. *J. Anat.* **226**, 169–174 (2015).
7. Denk, W., Strickler, J. H. & Webb, W. Two-photon laser scanning fluorescence microscopy. *Science* **248**, 73–76 (1990).
8. Brown, E. B. *et al*. Dynamic imaging of collagen and its modulation in tumors *in vivo* using second-harmonic generation. *Nat. Med.* **9**, 796–800 (2003).
9. Mansfield, J. *et al*. The elastin network: Its relationship with collagen and cells in articular cartilage as visualized by multiphoton microscopy. *J. Anat.* **215**, 682–691 (2009).
10. Brockbank, K. G. M. *et al*. Quantitative second harmonic generation imaging of cartilage damage. *Cell Tissue Bank.* **9**, 299–307 (2008).
11. Kumar, R. *et al*. Polarization second harmonic generation microscopy provides quantitative enhanced molecular specificity for tissue diagnostics. *J. Biophotonics* **8**, 730–739 (2015).
12. Mansfield, J. C., Winlove, C. P., Moger, J. & Matcher, S. J. Collagen fiber arrangement in normal and diseased cartilage studied by polarization sensitive nonlinear microscopy. *J. Biomed. Opt.* **13**, 044020 (2008).
13. Islam, A., Romijn, E. I., Lilledahl, M. B. & Martinez-Zubiaurre, I. Non-linear optical microscopy as a novel quantitative and label-free imaging modality to improve the assessment of tissue-engineered cartilage. *Osteoarthr. Cartil.* **25**, 1729–1737 (2017).
14. Kiyomatsu, H. *et al*. Quantitative SHG imaging in osteoarthritis model mice, implying a diagnostic application. *Biomed. Opt. Express* **6**, 405 (2015).
15. Matcher, S. J. What can biophotonics tell us about the 3D microstructure of articular cartilage? *Quant. Imaging Med. Surg.* **5**, 143–58 (2015).
16. Finnøy, A., Olstad, K. & Lilledahl, M. B. Non-linear optical microscopy of cartilage canals in the distal femur of young pigs may reveal the cause of articular osteochondrosis. *BMC Vet. Res.* **13**, 1–13 (2017).
17. Chen, X., Nadiarynkh, O., Plotnikov, S. & Campagnola, P. J. Second harmonic generation microscopy for quantitative analysis of collagen fibrillar structure. *Nat. Protoc.* **7**, 654–669 (2012).
18. Brown, C. *et al*. Imaging and modeling collagen architecture from the nano to micro scale. *Biomed. Opt. Express* **5**, 233 (2014).
19. Houle, M. A. *et al*. Analysis of forward and backward Second Harmonic Generation images to probe the nanoscale structure of collagen within bone and cartilage. *J. Biophotonics* **8**, 993–1001 (2015).
20. Koff, M. F. *et al*. Correlation of meniscal T2* with multiphoton microscopy, and change of articular cartilage T2 in an ovine model of meniscal repair. *Osteoarthr. Cartil.* **21**, 1083–1091 (2013).
21. Zhu, X. *et al*. Quantification of collagen distributions in rat hyaline and fibro cartilages based on second harmonic generation imaging. **10024**, 1002424 (2016).
22. Zipfel, W. R. *et al*. Live tissue intrinsic emission microscopy using multiphoton-excited native fluorescence and second harmonic generation. *Proc. Natl. Acad. Sci.* **100**, 7075–7080 (2003).
23. Zhu, X. *et al*. Nonlinear Optical Microscopy Captures High-Resolution Images of Microstructures Within Three Types of Unlabeled Rat Cartilage. *IEEE Photonics J.* **8**, 1–10 (2016).
24. Ignatieva, N. Y. *et al*. Two subsystems of meniscal collagen and their different thermal stabilities. *Dokl. Biochem. Biophys.* **444**, 175–177 (2012).
25. Donnelly, E., Williams, R. & Farnum, C. The primary cilium of connective tissue cells: Imaging by multiphoton microscopy. *Anat. Rec.* **291**, 1062–1073 (2008).

26. Qu, F. *et al*. Repair of dense connective tissues via biomaterial-mediated matrix reprogramming of the wound interface. *Biomaterials* **39**, 85–94 (2015).
27. Cai, H., Hao, Z., Xiao, L., Wan, C. & Tong, L. The collagen microstructural changes of rat menisci and tibiofemoral cartilages under the influence of mechanical loading: An *in vitro* wear test of whole joints. *Technol. Heal. Care* **25**, S207–S217 (2017).
28. Vesuna, S., Torres, R. & Levene, M. J. Multiphoton fluorescence, second harmonic generation, and fluorescence lifetime imaging of whole cleared mouse organs. *J. Biomed. Opt.* **16**, 106009 (2011).
29. Baskey, S. J. *et al*. Pre-Clinical Translation of Second Harmonic Microscopy of Meniscal and Articular Cartilage Using a Prototype Nonlinear Microendoscope. *IEEE J. Transl. Eng. Heal. Med*., 1–10, https://doi.org/10.1109/JTEHM.2018.2889496 (2018).
30. Martínez, H., Brackmann, C., Enejder, A. & Gatenholm, P. Mechanical stimulation of fibroblasts in micro-channeled bacterial cellulose scaffolds enhances production of oriented collagen fibers. *J. Biomed. Mater. Res. - Part A* **100 A**, 948–957 (2012).
31. Rivard, M. *et al*. The structural origin of second harmonic generation in fascia. *Biomed. Opt. Express* **2**, 26 (2011).
32. Stoller, P., Reiser, K. M., Celliers, P. M. & Rubenchik, A. M. Polarization-modulated second harmonic generation in collagen. *Biophys. J.* **82**, 3330–3342 (2002).
33. Erikson, A., Örtegren, J., Hompland, T., de Lange Davies, C. & Lindgren, M. Quantification of the second-order nonlinear susceptibility of collagen I using a laser scanning microscope. *J. Biomed. Opt.* **12**, 044002 (2007).
34. Ducourthial, G. *et al*. Monitoring dynamic collagen reorganization during skin stretching with fast polarization-resolved second harmonic generation imaging. *J. Biophotonics*, 1–9, https://doi.org/10.1002/jbio.201800336 (2019).
35. Kwok, J. *et al*. Atomic force microscopy reveals age-dependent changes in nanomechanical properties of the extracellular matrix of native human menisci: Implications for joint degeneration and osteoarthritis. *Nanomedicine. Nanotechnology, Biol. Med.* **10**, 1777–1785 (2014).
36. Smith, S. M., Shu, C. & Melrose, J. Comparative immunolocalisation of perlecan with collagen II and aggrecan in human foetal, newborn and adult ovine joint tissues demonstrates perlecan as an early developmental chondrogenic marker. *Histochem. Cell Biol.* **134**, 251–263 (2010).
37. Koyuncu, E. *et al*. The morphological anatomy of the menisci of the knee joint in human fetuses. *Balkan Med. J.* **34**, 559–566 (2017).
38. Di Giancamillo, A., Deponti, D., Addis, A., Domeneghini, C. & Peretti, G. M. Meniscus maturation in the swine model: Changes occurring along with anterior to posterior and medial to lateral aspect during growth. *J. Cell. Mol. Med.* **18**, 1964–1974 (2014).
39. Qu, F. *et al*. Maturation State and Matrix Microstructure Regulate Interstitial Cell Migration in Dense Connective Tissues. *Sci. Rep*., **8**, (2018).
40. Légaré, F., Pfeffer, C. & Olsen, B. R. The Role of Backscattering in SHG Tissue Imaging. *Biophys. J.* **93**, 1312–1320 (2007).
41. Rouède, D. *et al*. Determination of extracellular matrix collagen fibril architectures and pathological remodeling by polarization dependent second harmonic microscopy. *Sci. Rep.* **7**, 12197 (2017).
42. Cheung, H. S. Distribution of type I, II, III and v in the pepsin solubilized collagens in bovine menisci. *Connect. Tissue Res.* **16**, 343–356 (1987).
43. Gusachenko, I., Latour, G. & Schanne-Klein, M.-C. Polarization-resolved Second Harmonic microscopy in anisotropic thick tissues. *Opt. Express* **18**, 19339 (2010).
44. Romijn, E. I., Finnøy, A. & Lilledahl, M. B. Analyzing the feasibility of discriminating between collagen types I and II using polarization-resolved second harmonic generation. *J. Biophotonics* **12**, 1–10 (2019).
45. Rivard, M. Imagerie tissulaire par microscopie de seconde harmonique interférométrique - Chap. 5 Microscopie gsh interférométrique. (INRS-EMT, 2015).
46. Notbohm, H. *et al*. Recombinant human type II collagens with low and high levels of hydroxylysine and its glycosylated forms show marked differences in fibrillogenesis *in vitro*. *J. Biol. Chem.* **274**, 8988–8992 (1999).
47. Bai, P., Hardt, T., Cernadas, M. & Brodsky, B. Glycation alters collagen fibril organization. *Connect. Tissue Res.* **28**, 1–12 (1992).
48. Parry, D. A. D., Flint, M. H., Gillard, G. C. & Craig, A. S. A role for glycosaminoglycans in the development of collagen fibrils. *FEBS Lett.* **149**, 1–7 (1982).
49. Kambic, H. E. & McDevitt, C. A. Spatial organization of types I and II collagen in the canine meniscus. *J. Orthop. Res.* **23**, 142–149 (2005).
50. Bland, Y. S. & Ashhurst, D. E. Development and ageing of the articular cartilage of the rabbit knee joint: Distribution of the fibrillar collagens. *Anat. Embryol. (Berl).* **194**, 607–619 (1996).
51. Cluzel, C., Blond, L., Fontaine, P., Olive, J. & Laverty, S. Foetal and postnatal equine articular cartilage development: Magnetic resonance imaging and polarised light microscopy. *Eur. Cells Mater.* **26**, 33–48 (2013).
52. Carthage, W. Developmental horizons and measurements useful for age determination of equine embryos and fetuses. (KANSAS STATE UNIVERSITY, 1968).
53. Fontaine, P. *et al*. Computed tomography and magnetic resonance imaging in the study of joint development in the equine pelvic limb. *Vet. J.* **197**, 103–111 (2013).
54. Coluccino, L. *et al*. Anisotropy in the viscoelastic response of knee meniscus cartilage. *J. Appl. Biomater. Funct. Mater.* **15**, 0–0 (2016).
55. Schindelin, J. *et al*. Fiji: An open-source platform for biological-image analysis. *Nat. Methods* **9**, 676–682 (2012).
56. Romijn, E. I., Finnøy, A., Kumar, R. & Lilledahl, M. B. Automated calibration and control for polarization-resolved second harmonic generation on commercial microscopes. *PLoS One* **13**, 1–13 (2018).
57. Pinsard, M. P-SHG (forked version) GitHub. (2018). Available at: https://github.com/MaxP92/P-SHG. (Accessed: 24th August 2018)
58. Teulon, C., Tidu, A., Portier, F., Mosser, G. & Schanne-Klein, M.-C. Probing the 3D structure of cornea-like collagen liquid crystals with polarization-resolved SHG microscopy. *Opt. Express* **24**, 16084 (2016).
59. Wasik, V., Galland, F., Brasselet, S., Rigneault, H. & Réfrégier, P. Detection of imprecise estimations for polarization-resolved second-harmonic generation microscopy. *J. Opt. Soc. Am. A* **33**, 1353 (2016).
60. Berens, P. CircStat: A MATLAB Toolbox for Circular Statistics. *J. Stat. Softw*., **31**, (2009).

Acknowledgements

The authors acknowledge the financial support from the Canada Foundation for Innovation (CFI) and the Natural Sciences and Engineering Research Council of Canada (NSERC). M.P. acknowledges financial support from the NSERC CREATE/GRK program. S.L. acknowledges funds from the Natural Sciences and Engineering Research Council of Canada (NSERC) and Quebec Network for Cell and Tissue Therapies –ThéCell, a thematic network supported by the Fonds de recherche du Québec–Santé and Fonds de santé équins, Zoetis. S.L. also acknowledges Fonds du Centenaire de la Faculté de médecine Vétérinaire, Université de Montréal. M.P. thanks Nedgine Laurenceau, Margaux Schmeltz and Gaël Latour for experimental and analysis help.

Author contributions

M.P., M.C.S.K., S.L., H.R., J.D. designed the study. M.P., M.C.S.K. and F.L. designed the experiments. S.L., H.R. and J.D. prepared the samples. M.P. performed the experiments and analyzed the data. S.L., H.R. provided the histology data and designed some figures. All authors prepared and revised the manuscript.

Competing interests
The authors declare no competing interests.

Additional information
Supplementary information is available for this paper at https://doi.org/10.1038/s41598-019-54942-0.

Correspondence and requests for materials should be addressed to S.L. or F.L.

Reprints and permissions information is available at www.nature.com/reprints.

Publisher's note Springer Nature remains neutral with regard to jurisdictional claims in published maps and institutional affiliations.

4.5 Extension to cartilage, and perspectives

Forward/backward (F/B) SHG and p-SHG could also be applied to cartilage itself to characterize degeneration and diseases for instance, even if it has already been more studied in the literature. Here we present an inception of such a study: F/B - and p - SHG in the cartilage of condyle extracted from the knee joint of a foal, a juvenile and an adult horse. The associated conference proceeding shows some results, along with some similarities to the results from the meniscus in the previous article. The images were performed in the LOB at Ecole Polytechnique, France, with laser-scanning and mosaic reconstruction.

Differences between foetal and adult meniscus and cartilage revealed by Polarization Second Harmonic Generation Microscopy

Maxime Pinsard[1], Hélène Richard[2], Julia Dubuc[2], Sheila Laverty[2], Marie-Claire Schanne-Klein[3] and François Légaré[1,*]

[1]Institut National de la Recherche Scientifique, Centre Énergie Matériaux et Télécommunications (INRS-EMT), Université du Québec, 1650 boulevard Lionel Boulet, Varennes (QC), J3X 1S2, Canada
[2]Comparative Orthopaedic Research Laboratory, Faculty of Veterinary Medicine, Université de Montréal, QC, Canada
[3]LOB, Ecole Polytechnique, Institut Polytechnique de Paris, CNRS, Inserm, F-91128 Palaiseau, France
legare@emt.inrs.ca

***Abstract*— The characterization of foetal or adult meniscus and cartilage by Polarization Second Harmonic Generation (P-SHG) and standard SHG is presented. Large differences of structure and collagen fibril orientation are revealed. This work can help the understanding of the structure of meniscal fibrocartilage and articular cartilage and their degeneration processes.**

Keywords—non-linear microscopy, meniscus, cartilage

I. Introduction

Polarization Second Harmonic Generation (P-SHG) microscopy combines the specificity for non-centrosymmetric structures of SHG imaging with the orientation sensitivity of standard polarimetry [1]. The meniscus is a complex fibrocartilage whose collagen structure orientation has been previously characterized by SHG but in a limited way [2]. Adult articular cartilage type II collagen has also been studied by P-SHG [3] but only in specific zones and mainly to study osteoarthritis.

Here we present and validate improved imaging of collagen structure and orientation in these important connective tissues.

II. RESULTS

Fig.1 shows on the left the central area of the body part of an equine meniscus cut orthogonally to the circumferential direction in a fetus (a) and adult (b) imaged with Forward (1) and Backward (2) SHG, and P-SHG (3) to reveal the orientation of the collagen fibrils. The Foetal meniscus has a much more random fibril distribution when compared with adult tissues.

In the right panel P-SHG mapping of the collagen fibrils in articular cartilage of a newborn foal (A) is presented with clusters of aligned fibrils, compared with a 4-months-old foal (B) that contains areas of homogeneous collagen II orthogonal and then parallel to the surface. The adult (C) articular cartilage has a more homogeneous collagen orientation close to the articular surface, orthogonal to this surface.

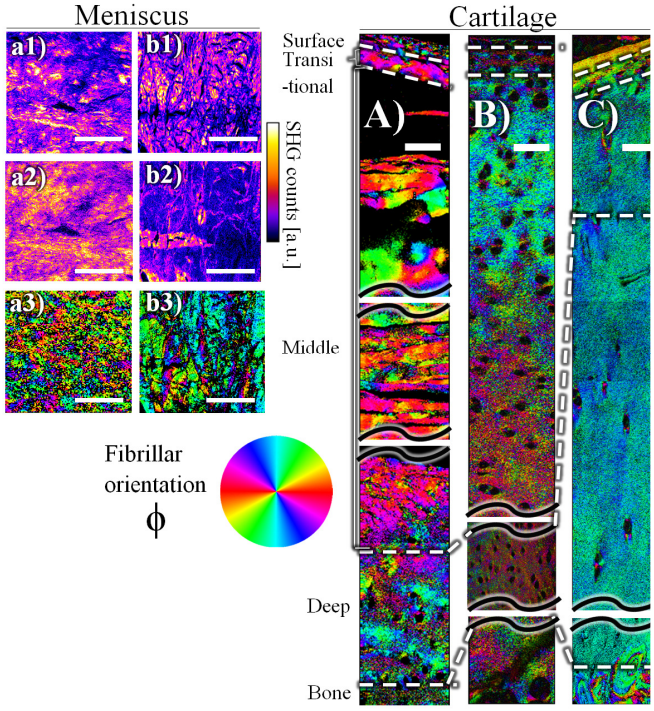

Fig. 1: (Left) Central area of the body of a meniscus cut orthogonally to the circumferential direction in fetus (a) and adult (b) Scale-bars: 200µm. (Right) Articular cartilage from a newborn (A), a juvenile (B) and an adult (C). Scale-bars: 50µm. All are from equine knee-joint.

Conclusion

This work presents a large area imaging of the structures and collagen orientation of meniscus and articular cartilage in a large animal model, and reveals significant differences between immature and adult specimens. Joint tissues undergoing degeneration could be characterized by this approach in the future.

References

[1] A. E. Tuer *et al.*, *J. Phys. Chem. B,* 115(44), pp. 12759-69, 2011.
[2] S. H. J. Andrews *et al.,* J. Anat., 224(5), pp. 531–537, 2014.
[3] J. C. Mansfield *et al.,* J. Biomed. Opt., 13, no. 4, p. 044020, 2008.

Overall, this study shows what multimodal SHG can tell us about the 3D microstructure of articular collagen, specifically in the meniscus. However, such an investigation could benefit from 2PEF coupling, THG, or maybe CARS to probe the chemical nature of all the materials present in such tissues. A study - published in parallel of the article presented here - precisely coupled quantitative SHG with 2PEF and electron microscopy to describe the collagen and elastin structure in 3D in human adult healthy menisci as honeycomb-like compartments in the nano and macro-scale [233]. It could also be interesting to investigate different zones with I-SHG: an example of such image is given in the last figure of the article in chapter 9.

Chapter 5

Gouy phase-shift characterization with I-SHG

This chapter explains the details of the Gouy phase-shift anomaly throughout the focus of a beam, and its possible measurement using I-SHG. The theory of this effect is presented, and the article is shown.

5.1 Article

(EN) Gouy phase shift measurement using interferometric second-harmonic generation.
(FR) Mesure du déphasage de Gouy par Génération de Seconde Harmonique Interférométrique.
Submitted 22nd February 2018; revised 22nd March 2018; accepted 22nd March 2018; published 17 April 2018.
Citation: Optics Letters 43:9(1958), 2018.
DOI: 10.1364/OL.43.001958
This article was done mainly by S. Bancelin and together with Andrew S. Quigley and his team of the Department of Physics and Atmospheric Science of Dalhousie University, who provided the samples. Jarno Van der Kolk of Lora Ramunno's lab (University of Ottawa) provided the numerical simulations, and participated in the writing and revision of the manuscript. I participated in the data analysis, manuscript writing and further experiments on this effect coupled with I-SHG.

Optics Letters

Gouy phase shift measurement using interferometric second-harmonic generation

Stéphane Bancelin,[1] Jarno N. Van der Kolk,[2] Andrew S. Quigley,[3] Maxime Pinsard,[1] Samuel P. Veres,[4] Laurent Kreplak,[3] Lora Ramunno,[2] and François Légaré[1,*]

[1]Institut National de la Recherche Scientifique, Centre Energie Matériaux et Télécommunications (INRS-EMT), Université du Québec, 1650 Boulevard Lionel Boulet, Varennes, Québec J3X 1S2, Canada
[2]Department of Physics and Centre for Research in Photonics, University of Ottawa, Ottawa, Ontario K1N 6N5, Canada
[3]Department of Physics and Atmospheric Science, Dalhousie University, 6310 Coburg Road, Halifax, Nova Scotia B3H 4R2, Canada
[4]Division of Engineering, Saint Mary's University, Halifax, Nova Scotia B3H 3C3, Canada
*Corresponding author: legare@emt.inrs.ca

Received 22 February 2018; revised 22 March 2018; accepted 22 March 2018; posted 23 March 2018 (Doc. ID 323152); published 17 April 2018

We report on a simple way to directly measure the Gouy phase shift of a strongly focused laser beam. This is accomplished by using a recent technique, namely, interferometric second-harmonic generation. We expect that this method will be of interest in a wide range of research fields, from high-harmonic and attosecond pulse generation to femtochemistry and nonlinear microscopy.

OCIS codes: (190.2620) Harmonic generation and mixing; (180.4315) Nonlinear microscopy; (190.4160) Multiharmonic generation; (190.4400) Nonlinear optics, materials.

https://doi.org/10.1364/OL.43.001958

It is well known that, across the focus of a freely propagating Gaussian beam, its phase experiences an additional π-shift compared to a plane wave. This is the so-called axial phase anomaly discovered by Gouy in 1890 [1]. This phase shift has significant consequences in nonlinear optics, since the observation of nonlinear processes requires high peak intensity, thus requiring focus of ultrashort laser pulses. Hence, determining and controlling the phase anomaly is crucial in many fields based on ultrafast light–matter interactions, e.g., THz generation [2,3], femtochemistry [4], and electron acceleration from nanostructures [5,6]. In particular, in attosecond science, few-cycle pulses are used to drive the strong-field processes, and this phase shift creates a spatially dependent carrier envelope phase (CEP) [7–9], which impacts how to design CEP-dependent strong-field experiments, such as the generation of isolated attosecond pulses [10,11]. In coherent nonlinear optical microscopy, the length of interaction is in the range of 1 μm; thus, one expects that phase matching should play no role. However, in processes such second- and third-harmonic generation (SHG and THG, respectively), the electric fields add coherently, and thus the Gouy phase shift strongly affects [12,13] the observed imaging contrast. As a consequence, in the last decade, there have been a number of experimental studies to monitor and map the spatial evolution of this phase anomaly [14–18].

In this Letter, we propose a direct technique to map the axial phase shift under tight focusing conditions using interferometric SHG (I-SHG) microscopy [19,20]. Since SHG is a phase-sensitive non-linear process, the axial phase change as the beam propagates through its focus can be extracted from the measurement of the phase of the signal generated by a point-like source at different positions within the focal volume. To that end, we spatially confined SHG over ~100 nm using the field generated from a single collagen fibril, and measured its interference with a reference SHG beam generated before the microscope.

In this study, we used isolated collagen fibrils extracted and prepared following the protocol established in [21]. SHG imaging was performed using a custom-built laser-scanning microscope as described previously [22,23] (Fig. 1). In short, the laser source was a mode-locked Ti:Sapph oscillator (Tsunami pumped by a 12 W Millenia Pro laser, Spectra Physics) tuned at 810 nm and delivering ~150 fs pulses at 80 MHz. A 5 cm focal lens was used to focus the laser on a 20-μm thick beta-barium borate (BBO) crystal ($\theta = 29.2°$, Eskma Optics) to generate a reference SHG beam whose

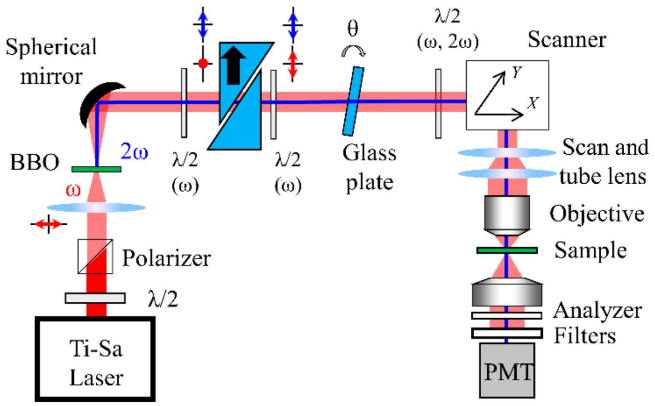

Fig. 1. Schematic of the I-SHG microscope.

intensity was adjusted by moving the crystal closer or farther from the lens focal point. Both the excitation beam (810 nm) and the reference SHG beam (405 nm) were collimated using a metallic spherical mirror. Two calcite wedges were inserted between two half-waveplates at 810 nm and full-waveplates at 405 nm, to introduce a controlled negative delay between the two beams that pre-compensate for the dispersion introduced by all the following optical elements. A 1.5 mm thick BK7 window, placed on a rotating mount, was used to control the phase between the reference and the excitation beam. A last half-wave plate (at 405 nm and 810 nm) was used to adjust the incident linear polarization before entering the microscope. The microscope was built on a telecentric scanner (TillPhotonics GmbH), and the beam was re-sized to overfill the back aperture of a water-dipping objective (Olympus, UplanSApo 40×W3/340, NA 1.1). Mechanical and piezoelectric motors, for coarse and fine adjustments, respectively, were used to vertically move the objective, allowing the acquisition of z-stacks. Signals were collected in the forward direction using a condenser [numerical aperture (NA) 0.55] and detected on a photomultiplier tube (PMT—R6357, Hamamatsu Photonics, Japan) set at 900 V using appropriate spectral filters (two FF01-720/SP-25 and a FF01-405/10, Semrock). Finally, an analyzer was placed just in front of the PMT, and set parallel to the collagen fibril observed. Scanning and signal acquisition were synchronized using a custom-written LabVIEW software and a multichannel I/O board (National Instruments).

20 μm × 40 μm images were recorded in the forward direction, in ∼2 s, using 20 μs pixel dwell time and 100 nm pixel size in order to oversample the fibril structure. The average power on the sample was adjusted to 30 mW, corresponding to 0.4 nJ/pulse. Raw data visualization was performed with ImageJ (NIH) and image processing was performed with MATLAB (The MathWorks) and Origin 10 (OriginLab).

The I-SHG technique aims at retrieving the relative phase of the SHG signal in the sample by measuring its interference with the reference SHG beam (for a complete description of the method, see [19,20]). The intensity measured on the PMT is given by

$$I(\varphi_{\text{ref}}) = I_{\text{ref}} + I_{\text{samp}} + 2\sqrt{I_{\text{ref}} I_{\text{samp}}}\cos(\varphi_{\text{samp}} - \varphi_{\text{ref}}), \quad \textbf{(1)}$$

where φ_{ref} and I_{ref} (respectively, φ_{samp} and I_{samp}) stand for the phase and the intensity of the reference (respectively, sample) SHG beams. The reference phase can be adjusted by rotating the glass window. The relationship between φ_{ref} and the glass-window angle was calibrated using a 350 μm thick y-cut quartz plate as a sample, obtaining the typical interferometric pattern described by Stolle *et al.* [24]. As only the relative phase is relevant here, the zero value for the reference phase was assigned arbitrarily.

This calibration allows, when looking at a collagen fibril, to introduce a control phase shift between the two SHG beams. To isolate the interferometric term, we computed the difference between two raw images acquired with a π phase shift in φ_{ref}:

$$I(\varphi_{\text{ref}}) - I(\varphi_{\text{ref}} + \pi) = 4\sqrt{I_{\text{ref}} I_{\text{samp}}}\cos(\varphi_{\text{samp}} - \varphi_{\text{ref}}). \quad \textbf{(2)}$$

The acquisition of 12 pairs of images, with reference phase varying from 0° to 330° by 30° phase steps and fitting with Eq. (2), allows interpolation of the amplitude and relative phase of the interferometric contrast. For every pixel, we determine the reference phase corresponding to the maximum amplitude, which provides an image of the relative phase in the sample.

Note that the use of a laser-scanning system to scan the incident angle of the beams on the back pupil of the objective led to a change in the optical path, introducing a gradual phase shifting from the center of the interferometric pattern. While this could be calibrated and compensated [25], we choose here to limit our region of interest (ROI) to the very center of the field of view (20 μm × 40 μm).

Using I-SHG microscopy, we measured the phase of the SHG signal from isolated collagen fibrils. The excitation beam is propagating along the *z* axis, and the fibril is lying in the focal plane [*xy* plane, see Fig. 2(a)]. A phase histogram with a single narrow peak corresponds to the phase of the excitation beam [see Eq. (2)]. Since the diameter of collagen fibrils (10–500 nm) [26,27] is commonly well below the axial length of the point spread function (∼1 μm in these conditions), a single fibril acts as a point source. Therefore, acquiring a z-stack of a single collagen fibril is equivalent to scanning a point source within the focal volume, allowing us to probe the phase variation within the focal spot.

Figure 2 displays the Gaussian fit of the phase histogram for five different fibril axial positions within the focal spot. The lateral shift observed in the peak value at increasing depth

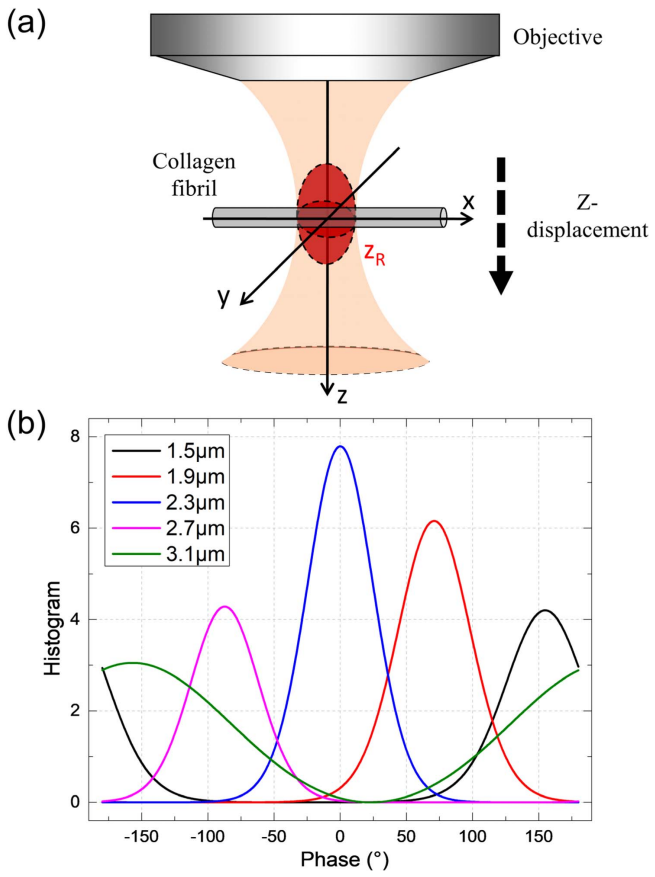

Fig. 2. (a) Schematic of the collagen fibril under laser excitation. (b) Gaussian fitting of the phase histogram measured in the same collagen fibril at different positions within the focal volume. The shift in the peak value reveals the variation of the phase of the excitation beam with focus position.

(Fig. 2) reveals the variation of the phase of the excitation beam with focus position, the so-called Gouy phase shift. Note that the absolute position of the peak is not relevant, as it depends on the choice of the zero reference phase. However, since this zero is defined during the calibration and is kept constant through all experiments, it allows extraction of the variation of phase while adjusting the depth of focus. Therefore, as a convention, we set the origin of the phase at the peak value obtained when the fibril is at the focus of the objective, indicated by the maximal intensity value in the z-stack. In addition, the variation of the peak width observable in Fig. 2 results from the decrease of the SHG signal when the collagen fibril is out of focus, which reduces the signal-to-noise ratio and therefore the accuracy of the phase peak determination.

To accurately measure the Gouy phase shift we displaced the focal volume over 6 μm by 0.15 μm steps and acquired both SHG and I-SHG images at each step. Figure 3 displays the intensity of SHG signal (red squares—top panel) as a function of fibril position within the focal volume together with the evolution of the phase (red squares—bottom panel). It is worth noting that we observe a 2π phase step, since the SHG signal results from the square of the excitation electric field, and therefore the phase shift of the SHG signal is double the one of the excitation beam.

As a first approximation, the phase exhibits the classical arctangent-like behavior of the Gouy phase shift:

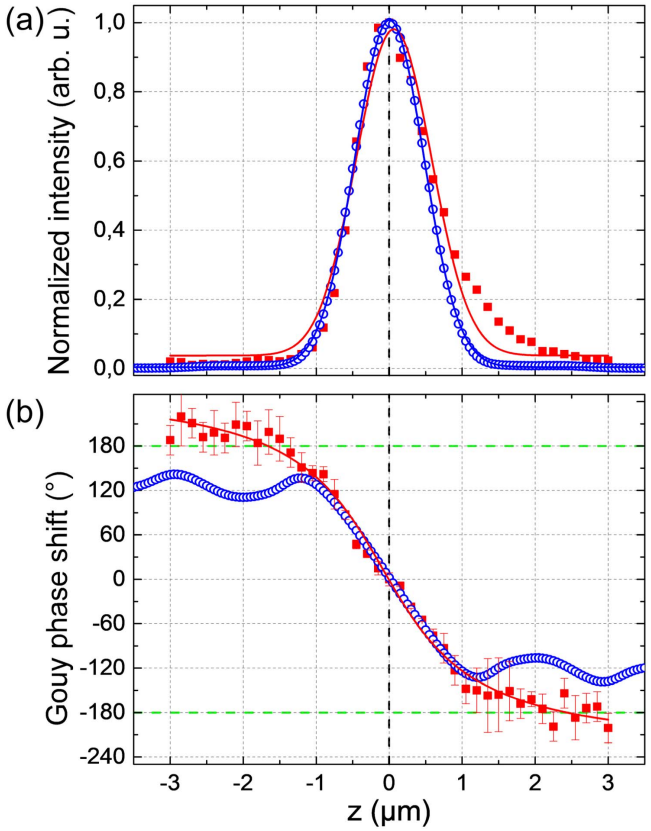

Fig. 3. (a) Intensity profile and (b) Gouy phase shift as a function of fibril position within the focal spot. Red squares indicate experimental measurements, and blue circles represent numerical simulations. Plane lines represent Gaussian fitting in (a) or fitting along Eq. (3) in (b).

$$\varphi_{\text{Gouy}} = -2\arctan\left(\frac{z}{z_R}\right), \tag{3}$$

where z_R is the Rayleigh range of the excitation beam. Fitting the Gouy phase shift using Eq. (3), we obtain a Rayleigh range of 930 ± 80 nm, which is consistent with the one extracted from the intensity profile 1030 ± 40 nm. Note that this corresponds to the theoretical Rayleigh range obtained with a 1.0 NA objective (934 nm), which might indicate a slight under-filling of the back aperture of the objective or result from spherical aberrations.

However, since we are using a tightly focused beam in these experiments, Eq. (3) is not valid anymore, and one has to consider the case of a vector field. In this case, the Gouy phase anomaly is defined as the difference between the actual phase of the wave and the one of a spherical wave [28,29]. Furthermore, in the case of a vector field, the polarization of the beam needs to be considered [30].

To calculate the Gouy phase shift of a tightly focused beam, we used numerical simulations. These simulations were performed by illuminating a 110 nm diameter cylinder, lying in the x direction, with a tightly focused beam [30–32] with a 1.0 NA in a $n = 1.33$ medium, propagating in the z direction. The induced nonlinear polarization (P) is then calculated as

$$\vec{P} = \chi^{(2)} : \vec{E}\,\vec{E}, \tag{4}$$

where $\chi^{(2)}$ is the second-order nonlinear susceptibility tensor for collagen fibrils [33] and E the incident electric field. The far-field emitted electric fields are then calculated using the Green's function approach as in [19], and we determine both the intensity and the phase (blue circles—top and bottom panels, respectively). Note that in the simulations, the Gouy phase shift actually does go from −180° to +180° at longer length scale (Visualization 1, Fig. 4).

In the case of a vector field, one would expect that the Gouy phase shift depends upon the three incident P components, as in [30]. In our simulations, this dependency is accounted for through the tensor nature of $\chi^{(2)}$. This corresponds to our experimental conditions, where the SHG signal is a mix of the contributions of the three incident components of P due to tight focusing.

In conclusion, we have presented a simple technique to measure the Gouy phase anomaly of strongly focused short pulses by means of I-SHG microscopy. The technique allows an accurate measurement of the smooth evolution of the phase through the focus. We expect that this method will be of interest in a wide range of research fields, from high-harmonic and attosecond pulse generation to femtochemistry and nonlinear microscopy.

Funding. Canada Foundation for Innovation (CFI); Natural Sciences and Engineering Research Council of Canada (NSERC); Fonds de Recherche du Québec—Nature et Technologies (FRQNT).

REFERENCES

1. L. G. Gouy, Compt. Rendue Acad. Sci. **110**, 1251 (1890).
2. P. Klarskov, A. C. Strikwerda, K. Iwaszczuk, and P. U. Jepsen, New J. Phys. **15**, 075012 (2013).
3. Y. Bai, L. Song, R. Xu, C. Li, P. Liu, Z. Zeng, Z. Zhang, H. Lu, R. Li, and X. Xu, Phys. Rev. Lett. **108**, 255004 (2012).

4. R. J. Gordon and V. J. Barge, J. Chem. Phys. **127**, 204302 (2007).
5. M. Krüger, M. Schenk, and P. Hommelhoff, Nature **475**, 78 (2011).
6. S. Zherebtsov, T. Fennel, J. Plenge, E. Antonsson, I. Znakovskaya, A. Wirth, O. Herrwerth, F. Süßmann, C. Peltz, I. Ahmad, S. A. Trushin, V. Pervak, S. Karsch, M. J. J. Vrakking, B. Langer, C. Graf, M. I. Stockman, F. Krausz, E. Rühl, and M. F. Kling, Nat. Phys. **7**, 656 (2011).
7. F. Lindner, G. G. Paulus, H. Walther, A. Baltuška, E. Goulielmakis, M. Lezius, and F. Krausz, Phys. Rev. Lett. **92**, 113001 (2004).
8. T. Tritschler, K. D. Hof, M. W. Klein, and M. Wegener, Opt. Lett. **30**, 753 (2005).
9. Y. H. Zhou, H. B. Jiang, and Q. H. Gong, Chin. Phys. Lett. **23**, 110 (2006).
10. M. Hentschel, R. Kienberger, Ch. Spielmann, G. A. Reider, N. Milosevic, T. Brabec, P. Corkum, U. Heinzmann, M. Drescher, and F. Krausz, Nature **414**, 509 (2001).
11. R. Kienberger, E. Goulielmakis, M. Uiberacker, A. Baltuška, V. Yakovlev, F. Bammer, A. Scrinzi, Th. Westerwalbesloh, U. Kleineberg, U. Heinzmann, M. Drescher, and F. Krausz, Nature **427**, 817 (2004).
12. L. Moreaux, O. Sandre, S. Charpak, M. Blanchard-Desce, and J. Mertz, Biophys. J. **80**, 1568 (2001).
13. J. Mertz and L. Moreaux, Opt. Commun. **196**, 325 (2001).
14. J. H. Chow, G. de Vine, M. B. Gray, and D. E. McClelland, Opt. Lett. **29**, 2339 (2004).
15. H. Kandpal, S. Raman, and R. Mehrotra, Opt. Lasers Eng. **45**, 249 (2007).
16. Z. Wang, Z. Zeng, R. Li, and Z. Xu, Chin. Opt. Lett. **5**, S183 (2007).
17. P. Bon, B. Rolly, N. Bonod, J. Wenger, B. Stout, S. Monneret, and H. Rigneault, Opt. Lett. **37**, 3531 (2012).
18. K. J. Kaltenecker, J. C. König-Otto, M. Mittendorff, S. Winnerl, H. Schneider, M. Helm, H. Helm, M. Walther, and B. M. Fischer, Optica **3**, 35 (2016).
19. M. Rivard, K. Popov, C.-A. Couture, M. Laliberté, A. Bertrand-Grenier, F. Martin, H. Pépin, C. P. Pfeffer, C. Brown, L. Ramunno, and F. Légaré, J. Biophoton. **7**, 638 (2013).
20. C.-A. Couture, S. Bancelin, J. Van der Kolk, K. Popov, M. Rivard, K. Légaré, G. Martel, H. Richard, C. Brown, S. Laverty, L. Ramunno, and F. Légaré, Biophys. J. **109**, 2501 (2015).
21. A. Quigley, S. Bancelin, D. Deska-Gauthier, F. Légaré, L. Kreplak, and S. P. Veres, Sci. Rep. **8**, 4409 (2018).
22. M.-A. Houle, C.-A. Couture, S. Bancelin, J. Van der Kolk, E. Auger, C. Brown, K. Popov, L. Ramunno, and F. Légaré, J. Biophoton. **8**, 993 (2015).
23. S. Bancelin, C.-A. Couture, M. Pinsard, M. Rivard, P. Drapeau, and F. Légaré, Sci. Rep. **7**, 6758 (2017).
24. R. Stolle, G. Marowsky, E. Schwarzberg, and G. Berkovic, Appl. Phys. B **63**, 491 (1996).
25. S. Bancelin, C.-A. Couture, K. Légaré, M. Pinsard, M. Rivard, C. Brown, and F. Légaré, Biomed. Opt. Express **7**, 399 (2016).
26. K. E. Kadler, C. Baldock, J. Bella, and R. P. Boot-Handford, J. Cell Sci. **120**, 1955 (2007).
27. D. J. S. Hulmes, J. Struct. Biol. **137**, 2 (2002).
28. M. Born and E. Wolf, *Principles of Optics*, 7th ed. (Cambridge University, 1999).
29. T. D. Visser and E. Wolf, Opt. Commun. **283**, 3371 (2010).
30. P. Xiaoyan, T. D. Visser, and E. Wolf, Opt. Commun. **284**, 5517 (2011).
31. J.-X. Cheng, A. Volkmer, and X. S. Xie, J. Opt. Soc. Am. B **19**, 1363 (2002).
32. B. Richards and E. Wolf, Proc. R. Soc. London A **253**, 358 (1959).
33. A. Erikson, J. Ortegren, T. Hompland, C. de Lange Davies, and M. Lindgren, J. Biomed. Opt. **12**, 044002 (2007).

5.2 Simulations of the Gouy phase-shift

As shown by equation 2.20, a scalar Gaussian beam leads to a simple expression for the Gouy phase-shift anomaly (see section 2.1.4 for the definition). The plot of this Arctan function is shown in Fig.5.1 (b). If the vectorial model of the field is considered instead (see 2.1.3), which is significant if a tight focusing condition is used (2.5), the Gouy phase-shift shows a similar behavior with some differences: the phase (of the fundamental) also experiences a π phase-shift, but the variation is more linear in the focal volume, and shows some oscillations outside of it (Fig. 5.1 c,d). The oscillations depend on the configuration: the optical index of the medium, and N.A. of excitation. They are also present in the more precise simulations of Fig. 3(b) of the article, where Fig. 5.1 a) shows an extended range, which used the Green's function formulation.

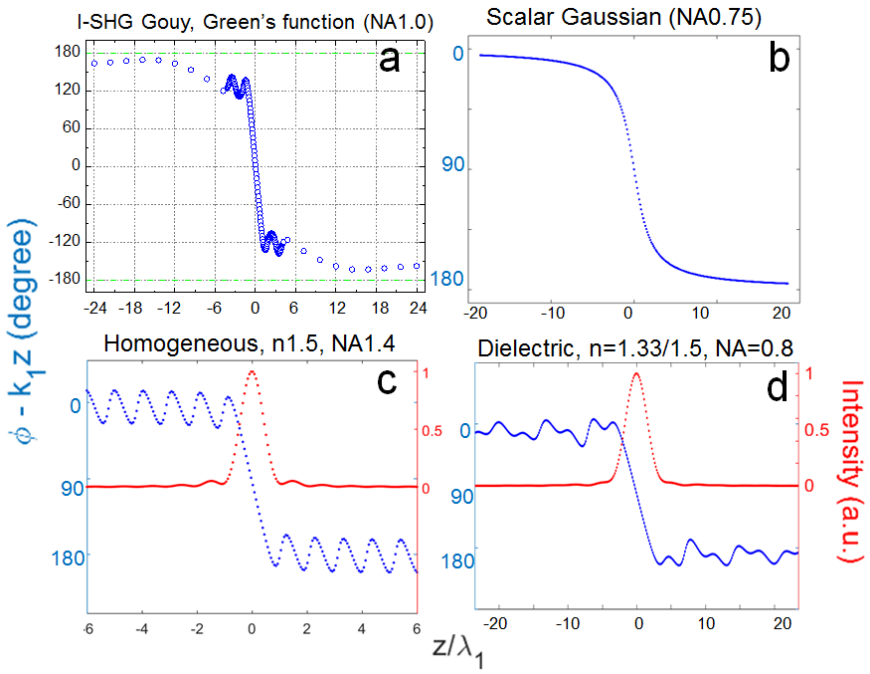

Figure 5.1: Gouy phase-shift anomaly around the focus of a Gaussian beam (fundamental) for different models: scalar Gaussian beam (b) versus vectorial fields (c, d). The medium can be homogeneous with a focusing NA of 1.4 (c) or 0.8 at a dielectric interface n=1.5/1.33 (d). Simulations done in MatLab, using the model of [82] (variation of [37]). (a) is the special case of an extended range of Fig.3(b) in the article: twice the Gouy phase-shift that would be measured in I-SHG. Simulation using Green's function formulation and the tensorial $\chi^{(2)}$ of collagen, coded in C++. λ_1 is the wavelength of the fundamental.

We can calculate the phase measured in I-SHG, by considering the cases where the interferences occur at the sample, or at the detector. In the last case, the propagation must be considered. However, the usual phase term of propagation $\varphi = 2\pi L/\lambda$ - if L is the distance travelled - is compensated for in all cases, because the two waves that interfere have the same wavelength (SHG at 405nm), and

travel the same distance. The phase difference is thus only due to the Gouy phase-shift. The initial phase of the fundamental (at the very beginning of the focus) is noted $\varphi_{0,S}$ and $\varphi_{0,R}$ for the SHG of reference. A Gaussian beam acquires a $\pi/2$ phase-shift through its Rayleigh range (see 2.1.4), i.e. the difference between case (a) and (c) in Fig. 5.2. Also, the SHG from the sample acquires twice the Gouy phase-shift of the fundamental at each position, and no additional term if the propagation to the detector is considered (2nd case). This is because the sample consist of a number of small scatterers (like the collagen fibril used in the article), and their generated SHG is not a Gaussian wave. Yet, it could be different in a homogeneous crystal.

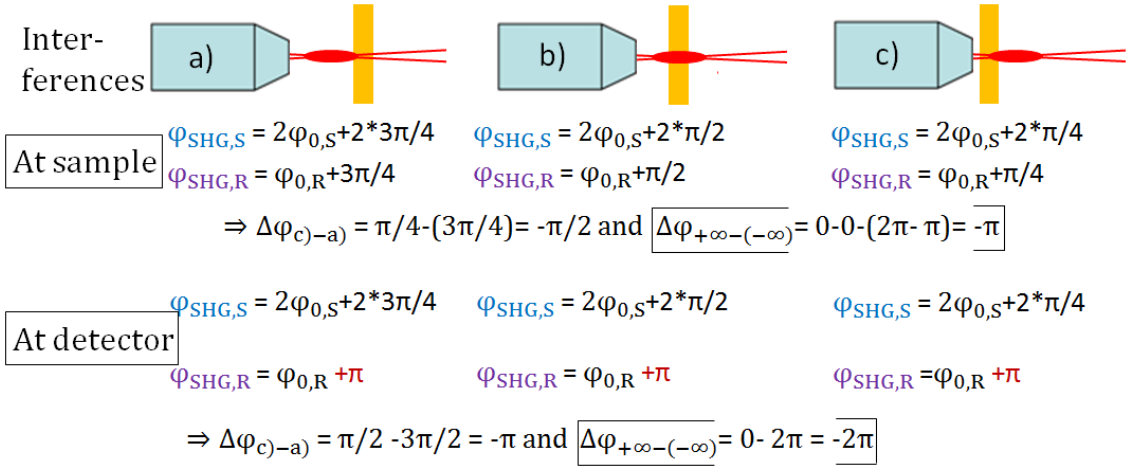

Figure 5.2: Gouy phase-shift calculation in I-SHG. (Top) Schematic view of the focus position in the thin sample. (After) Calculation if the interferences occur at sample (middle) or at detector (bottom).

If the interferences occur only at the sample (Fig. 5.2 top), the total phase difference between the case where the sample is at the beginning of the focus and the case where it is at the end is found to be $-\pi/2$ if the two limit positions are at the edges of the Rayleigh range z_R. It tends to $-\pi$ if $\Delta z \gg z_R$. This is because the Gouy phase-shift of the reference SHG is also considered. By contrast, if the interferences are located at the detector, the reference SHG has experienced its full Gouy phase-shift in any position of the sample (Fig. 5.2 bottom), and thus its variation is 0. Thus, the measured phase difference is doubled in this case: $-\pi$ if $\Delta z{=}\pm z_R$, and -2π if $\Delta z \gg z_R$. This value of 2π is also obtained experimentally in the article (Fig. 3(b), see also Fig.5.2(a)), and the calculated Rayleigh range at $\pm\pi/2$ is in good accordance with the intensity profile. However, the simulations (red in the same figure) would expect a variation of $\sim 3\pi/4$ in the experimental range of $\pm 3\mu$m: they do reach 2π, but within a range where $|z| \sim 10 z_R$, so it is in good accordance with the theoretical condition $\Delta z \gg z_R$. It is thus unclear why the 2π difference is reached so rapidly in the experimental data. Noteworthily, the oscillations in the simulation of Fig. 5.2a) also exist at $|z| > 5\lambda$, but the number of points in this range is too small to

show them. Additionally, more of the collagen fibril is illuminated if the focus is further away from the focal point, and this increases non-linearly: the length of the fibril starts to play a role at some point, such that it is no longer a "point-like source". Also, the simulations need to be adapted to collect the light off-axis, which means using a 2D collector instead of a single point, which is considerably more expensive in computer time. For these reasons, the simulations are precise up to $|z| = 10\lambda$ but beyond that, only a few points taking these effects into account are calculated.

5.3 Implications in SHG

First, since the height of structures is correlated with a change of absolute phase, mapping this absolute phase could reveal the change of height in a sample, with nanostructured domains, for instance.
Second, this phenomenon has various applications in SHG, like the possibility to induce artifacts as a function of the position in depth as described in the following article of chapter 6. Importantly, it implies that if some structures are positioned at different heights spaced by the Rayleigh range or less, they will appear with different phases in I-SHG, even if their polarity is the same. This effect must then be considered in the I-SHG interpretation.

Chapter 6

Artifacts in SHG, and their removal by interferometry

This chapter presents different imaging artifacts that occur in SHG microscopy, when some interfaces between opposite polarities are imaged. The article is presented, as well as some complementary figures and information that did not fit in the publication.

6.1 Effect of the Gouy phase-shift on sarcomeres of myosin

The Gouy phase-shift presented at the previous chapter has a direct effect on the SHG images of various structures: this is e.g. the case for sarcomeres in muscles. Muscles indeed contain a periodic arrangement of actin and myosin (see Fig.1 of the article [158]) that form a sequence of sarcomeres: imaged in SHG, only the myosin is visible [125]. We consider here a stacking of two sequences of sarcomeres in the vertical direction of imaging (the depth Z, parallel to the propagation of light), in Fig. 6.1 where the positive ends are in red, and the negative in blue. There can be a junction between the two rows of sarcomeres (due to constructive interference), if their SHG are in phase. *A priori*, two ends with opposite polarities will not present a junction (A'). However, the Gouy phase-shift of $\pm\pi/4$ at the extremities of the focal volume of the excitation makes their SHG having an additional $\pi/2-(-\pi/2)=\pi$ phase-shift, such that they finally have a phase difference of $\pi+\pi=2\pi$ and constructively interfere. This thus creates a SHG junction between these staggered sarcomeres (A). If the offset Δ between the stacked

sequence of sarcomeres is 0 (or an integer number of the sarcomere's length L, case E of Fig. 6.1), there is also no junction, due to the Gouy phase-shift. The cases in-between (Δ=3L/8 (B), Δ=2L/8 (C) or Δ=L/8 (D)) show that the junctions can be more or less pronounced, depending on Δ. Of course, the spacing in depth between sarcomeres must lead to myosin ends at the extremities of the focal volume for this effect to happen.

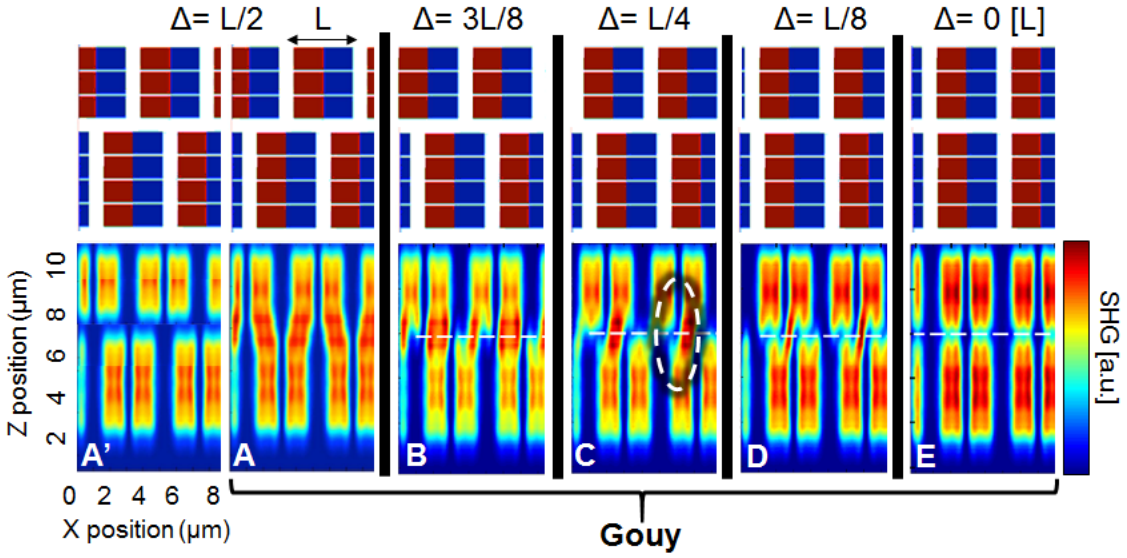

Figure 6.1: Stacking of two sarcomere sequences of myosin in muscles with different offsets, and the consequence on their SHG imaging. (Top) Schematic of the positions, with positive ends in red and negative ends in blue. (Bottom) Simulated SHG from the myosin arrangements of the top. (A)&(A'): with an offset Δ of half the sarcomere's length L, (B) Δ=3L/8, (C) Δ=L/4, (D) Δ=L/8 and (E) Δ is an integer number of L or 0. All cases consider the Gouy phase-shift of the beam (propagation in the vertical direction), except (A'). An example of the focal volume is indicated on (C), bottom. Excitation wavelength: 850nm, NA=0.8 for excitation and 0.55 for collection. Adapted from [52].

In particular, if Δ is close to L/4 (C), the junction between sarcomeres will lead to some signal at the M-band (middle of the white dashed ellipse in (C)), and thus to a periodic signal with only half of the dips (called a single-band pattern). This figure completes the explanation given in the article below, and was explained in previous publications [181, 52].

6.2 Article

(EN) Elimination of imaging artifacts in second harmonic generation microscopy using interferometry.

(FR) Élimination des Artefacts d'Imagerie en Microscopie SHG par Interférométrie.

Submitted 1st Apr. 2019; revised 17th Jun. 2019; accepted 17th Jun. 2019; published 12th Jul. 2019.

Citation: Biomedical Optics Express 10:8(3938), 2019 ; DOI: 10.1364/boe.10.003938

Research Article | Vol. 10, No. 8 | 1 Aug 2019 | BIOMEDICAL OPTICS EXPRESS 3938
Biomedical Optics EXPRESS

Elimination of imaging artifacts in second harmonic generation microscopy using interferometry

MAXIME PINSARD,[1] MARGAUX SCHMELTZ,[2] JARNO VAN DER KOLK,[3] SHUNMOOGUM A PATTEN,[4] HEIDE IBRAHIM,[1] LORA RAMUNNO,[3] MARIE-CLAIRE SCHANNE-KLEIN,[2] AND FRANÇOIS LÉGARÉ[1,*]

[1]*Institut National de la Recherche Scientifique, Centre Énergie Matériaux Télécommunications (INRS-EMT); 1650 Boul. Lionel-Boulet, Varennes (QC), J3X 1S2, Canada*
[2]*Laboratoire d'Optique et Biosciences (LOB), École Polytechnique, CNRS, Inserm, Institut Polytechnique de Paris, F-91128 Palaiseau, France*
[3]*Department of Physics and Centre for Research in Photonics, University of Ottawa, Ottawa (ON), K1N 6N5, Canada*
[4]*INRS-Institut Armand-Frappier, Laval, Québec, Canada, H7V 1B7, Canada*
[*]*legare@emt.inrs.ca*

Abstract: Conventional second harmonic generation (SHG) microscopy might not clearly reveal the structure of complex samples if the interference between all scatterers in the focal volume results in artefactual patterns. We report here the use of interferometric second harmonic generation (I-SHG) microscopy to efficiently remove these artifacts from SHG images. Interfaces between two regions of opposite polarity are considered because they are known to produce imaging artifacts in muscle for instance. As a model system, such interfaces are first studied in periodically-poled lithium niobate (PPLN), where an artefactual incoherent SH signal is obtained because of irregularities at the interfaces, that overshadow the sought-after coherent contribution. Using I-SHG allows to remove the incoherent part completely without any spatial filtering. Second, I-SHG is also proven to resolve the double-band pattern expected in muscle where standard SHG exhibits in some regions artefactual single-band patterns. In addition to removing the artifacts at the interfaces between antiparallel domains in both structures (PPLN and muscle), I-SHG also increases their visibility by up to a factor of 5. This demonstrates that I-SHG is a powerful technique to image biological samples at enhanced contrast while suppressing artifacts.

1. Introduction

Over the last 30 years, Second Harmonic Generation (SHG) microscopy has been gradually confirmed as a powerful tool for high contrast imaging of structures that lack centrosymmetry, in particular some specific biological structures [1–3]. This parametric process generates a single photon at twice the frequency of two incident photons. This, as a multiphoton process, provides the benefit of confining the excitation in the focal volume thus providing intrinsic sub-micron spatial resolution [4]. Furthermore, the use of a near-infrared laser reduces the negative impact of tissue scattering, providing deep-tissue imaging [5]. The SHG signal also scales quadratically with the number of aligned molecules for structures smaller than the focal volume [6,7], and is free of energy losses as no electron is transferred. This considerably reduces phototoxicity and avoids photobleaching [8]. Given its high specificity for non-centrosymmetric media [9], this technique is widely used as a very sensitive and specific structural probe of various biopolymers such as tendon [10,11], cartilage [12], skeletal muscle [13,14] or mitotic spindles [15]. Importantly, this process preserves the coherence of the laser light (spatial and temporal) [6] and is thus able to convey information on the polarity of the scatterers [16,17]. Even though this information is

#363834 https://doi.org/10.1364/BOE.10.003938
Journal © 2019 Received 1 Apr 2019; revised 17 Jun 2019; accepted 17 Jun 2019; published 12 Jul 2019

Biomedical Optics EXPRESS

preserved in conventional SHG microscopy, it requires the interferometric-SHG (I-SHG) method to read it out. I-SHG indeed allows to measure the relative phase of SHG signals from different structures in the sample, and thus to map their relative polarity. It was first applied to non-centrosymmetric crystals [18] and later to biological tissues like muscle [19]. Having revealed the heterogeneous distribution of bundles of fibers in tendon [20], this technique was then used in articular cartilage to discriminate, in zones with low SHG signal, the spots with a random organization of fibrils from those with bundles of fibrils of opposite polarity [21]. Recently, the polarity of microtubules during mitosis was measured [22] after a technological development to increase the speed of the measurement [23]. In this manuscript, we will refer to I-SHG for Interferometric-SHG and to standard or conventional SHG for intensity SHG.

In conventional SHG microscopy, the imaged features are always the result of complex interferences between scatterers exhibiting a non-zero $\chi^{(2)}$, where $\chi^{(2)}$ is the uniform second-order nonlinear optical susceptibility coefficient involved in the interaction that acts as an SHG converter (see [24] for its definition). While these interferences can be seen as a direct link to the real structure in rather simple cases like tail tendon, other patterns are considered as artifacts as the real organization of $\chi^{(2)}$ scatterers is difficult to extract [25,26].

In periodically-poled $LiNbO_3$ crystals (PPLN), there is a periodic alternation of domains of opposite polarity (see Fig. 1(A)). This material is known to have crystal lattice distortions [27], frustration, and defects close to the domain walls [28,29], where the polarity inverts between two homogeneous domains. This leads to a non-negligible change in polarization [28] and refractive index inhomogeneities in this region, which causes light scattering and distortion of the wavefront [30,31].

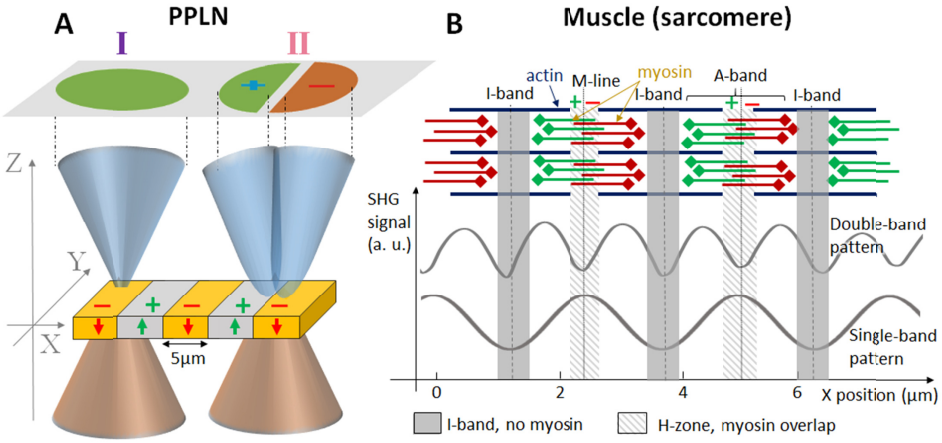

Fig. 1. Schematic structures of Periodically-Poled Lithium Niobate (PPLN, A) and myosin (B), both showing an alternation of domains of opposite polarity. (A) When being imaged by SHG, the excitation beam can be focused inside one PPLN domain (in the bulk, I) or at the interface between two domains (II) leading to a change of the emitted SHG radiation pattern depicted at the top. (B) Structure of myosin inside the sarcomeres of muscles, which consist of A-bands of myosin separated by I-bands (with no myosin). Some thin actin filaments also alternate with certain spacing at the H-zone, located in the middle of the A-band. The symmetry and bipolarity of the myosin filaments lead to alternating maximum and minimum SHG signal, which has two origins. The dips corresponding to the large I-band (dark grey in B)) are always visible because of a lack of myosin (single-band pattern), so no SHG. In addition, the proximity of myosin ends of opposite polarity at the M-line (striped light grey in B)) should lead to measured destructive interferences from π phase-shifted SHG signals, and thus the observation of twice the number of minima, that is the double-band pattern. However, these are sometimes not observed in SHG microscopy.

Skeletal muscles are to some extent similar to PPLN as they also feature an alternation of domains of opposite polarity [19]: the myosin filaments are well-organized inside the sarcomeres with a specific structure depicted in Fig. 1(B)). They are present only in the A-

Biomedical Optics EXPRESS

band, and precisely at its center (called the H-zone or M-line), where the ends of the filaments of opposite polarity overlap. This leads to SHG signals of opposite amplitude (their phase are π phase-shifted). Between two A-bands of myosin is the I-band located, which contains no myosin and therefore does not contribute to the SHG signal. This is well illustrated by the alternation of dips in the SHG signal when imaging the sarcomeres [32,33] and refers to as a single-band pattern (see Fig. 1(B)). However, because some destructive interferences should occur for the signal collected at the M-line, there should be another dip at this position which is indeed observed in some cases [33,34] and is called a double-band pattern (see Fig. 1(B)). This so-called SHG "vernier" has already been observed [33,35,36] and was linked to the proteolysis state of the muscle [32]. Other studies have postulated an effect of damage reparation [36].

While the physical increase of the separation of the two ends of the myosin filaments theoretically leads to a decrease or even the disappearance of the SHG dip at this interface, recent studies state that the single-band pattern originates most of the time from imaging artifacts, which are the result of interferences (and thus of the coherent nature of the SHG light) between adjacent myofibers [25,26].

In this work, we show that SHG artifacts at the interface can have two different origins, either incoherent in the case of PPLN, or coherent for myosin. A strong and scattered second-harmonic signal arises from the nonlinear interaction at the interfaces of the domains in PPLN, which is an artifact since it produces a very high second-harmonic signal that overshadows the real structure. Most of this signal is shown to be eliminated through I-SHG measurements, as it only contributes to the background due to its incoherent nature. We also show that this technique removes the artifacts leading to single-band patterns in muscle, and thus reveals the true nature of the sarcomeres when being imaged by SHG. We show in addition that I-SHG allows to increase the visibility of those interfaces compared to conventional SHG.

2. Materials and methods

2.1 SHG and I-SHG microscopy

For a complete description of the I-SHG method and SHG set-up we refer to [23]. Importantly, an air immersion objective (UplanSApo 20X, NA 0.75, Olympus, Japan)) was used for excitation and the SHG emission was then collected with a 0.8NA objective (LUMPlanFLN, 40X, Olympus) to ensure that the numerical aperture is sufficiently high to collect the whole radiation pattern. The (measured) focal volume of excitation is then of $1x1x4\mu m^3$: the deviation from the theoretical values ($0.4x0.4x1.9\mu m^3$, see [37]) comes from an imperfect collimation and underfilling of the back pupil of the objective, as well as reduced performances from the objective lens. Scanning and signal acquisition were synchronized using a custom-written Python (www.python.org) program for better stability and control.

Standard SHG frames were recorded in the forward direction, in ~3 s, using 20 µs pixel dwell-time and 100 nm pixel size in order to oversample the structure. The average power on the sample was adjusted to 15mW, corresponding to 0.2 nJ/pulse. Raw data visualization was performed with FIJI-ImageJ (NIH [38]) and image processing with MATLAB.

Moreover, a circular iris whose aperture can be gradually decreased down to 5mm diameter was inserted after the collecting objective to allow optional rejection of selected scattered parts of the converted SHG.

2.2 Interferometric contrast and phase in I-SHG

In I-SHG, the phase information is extracted from the interference between the SH generated in the sample and a reference SH beam. The intensity measured at pixel i on an interferogram at phase-shift δ_j can be written as [39,40]:

Biomedical Optics EXPRESS

$$I_i(\delta_j) = A_{ij} + B_{ij} sinc(\Delta/2)\cos(\phi_i + \delta_j) \quad (1)$$

Each interferogram at phase-shift δ_j is subtracted from the one at phase-shift $\delta_j + \pi$:

$$I_i(\delta_j + \pi) - I_i(\delta_j) = 2B_{ij} sinc(\Delta/2)\cos(\phi_i + \delta_j) = b_i \cos(\delta_j) + c_i \sin(\delta_j) \quad (2)$$

where:

$$\begin{aligned} b_i &= 2B_{ij} sinc(\Delta/2)\cos(\phi_i) \\ c_i &= -2B_{ij} sinc(\Delta/2)\sin(\phi_i) \end{aligned} \quad (3)$$

ϕ_i being the relative phase at pixel i. Δ is the integration range of time where the phase-shift varies linearly, which is here zero because the phase-shift is changed by discrete steps and not continuously ($sinc(\Delta/2) = 1$). a_i, b_i and c_i are assumed to be independent on phase-shift variations (i.e. of j), and to only be functions of the pixel position in the image (i.e. of i) [40]. This is usually justified if the laser intensity is maintained constant for all the measurements [39]. The interferometric contrast is then $\gamma_i = \sqrt{b_i^2 + c_i^2}$, where b_i (resp. c_i) is fitted over all δ_j (i.e. the different phase-shifts) for every pixel i. I-SHG allows to measure both the phase ϕ_i and the interferometric contrast γ_i. Similarly, the relative phase ϕ_i can be expressed as: $\tan\phi_i = c_i / b_i$, and is extracted in [–π, π] using the 2-arguments Arctangent function. The real phase-shift induced by the phase-shifter (a rotating glass plate) is non-linear with the glass plate angle and must be first calibrated (see [41]). Also, because the reference and excitation waves both scan the sample by passing through the excitation objective, their retardation varies differently during the scan and some aberrations inevitably appear. A reference correction (as described in [42]) is then applied to the phase and contrast maps to correct it. For more details see [23].

2.3 Periodically-poled lithium niobate (PPLN)

The PPLN is a quasi-phase matching rectangular crystal for SHG conversion at 1064nm (MSHG1064-0.5-xx PPLN, Covesion) with dimensions 10x0.5x0.5mm^3. It consists of a LiNbO3 crystal with a succession of domains of opposite polarity engraved by high voltage. The crystal is imaged in a plane orthogonal to the axis that is normally used for quasi-phase matching (see Fig. 1(A)) by placing it on a microscope coverslip #1.5H (Thorlabs).

2.4 Skeletal muscle – sample preparation

Wild-type zebrafish (*Danio rerio*) of the TL (*Tupfel long fin*) line were bred and maintained according to standard procedure [43]. All experiments were performed in compliance with the guidelines of the Canadian Council for Animal Care and our local animal care committee. Zebrafish (6-months old) and larvae (3 days postfertilization) were fixed in 4% paraformaldehyde. The muscles from 6-months old zebrafish were embedded in paraffin. Sections (6 µm) of paraffin-embedded specimens were deparaffinized in xylene and rehydrated in a graded series of ethanol solutions. The larvae were mounted on slides and their muscles were examined [43].

2.5 Component of the non-linear tensor susceptibility

Considering the propagation along the Z axis in the laboratory frame (X, Y, Z), the SHG response of myosin, due to the C_6 symmetry, is described by the three independent components $d_{11} = \chi^{(2)}_{XXX}$, $d_{12} = \chi^{(2)}_{Xii}$ and $d_{26} = \chi^{(2)}_{iiX} = \chi^{(2)}_{iXi}$, i = Y or Z (or Eq. (4)). In an equivalent way, these components are sometimes referred as d_{33}, d_{31} and d_{15} when inverting

Biomedical Optics EXPRESS

the myosin filament axis and the propagation one. The ratio $d_{11}/ d_{26} = 0.6$ is weaker than d_{12}/ d_{26}, which is close to unity [44]. To have maximum signal, the polarization of the exciting field must then be at 45° of the X and Y axis, in particular at 45° of the myosin filament axis X [44].

$$\begin{bmatrix} P_X^{2\omega} \\ P_Y^{2\omega} \\ P_Z^{2\omega} \end{bmatrix} = \begin{bmatrix} d_{11} & d_{12} & d_{12} & 0 & 0 & 0 \\ 0 & 0 & 0 & 0 & 0 & d_{26} \\ 0 & 0 & 0 & 0 & d_{26} & 0 \end{bmatrix} \begin{bmatrix} E_X^2 \\ E_Y^2 \\ E_Z^2 \\ 2E_Y E_Z \\ 2E_X E_Z \\ 2E_X E_Y \end{bmatrix} \quad (4)$$

For the PPLN, the $\chi^{(2)}$ of LiNbO3 has three independent components due to its 3m crystal class [45] such that its nonlinear susceptibility tensor writes in our coordinates:

$$\begin{bmatrix} 0 & 0 & 0 & 0 & d_{31} & -d_{22} \\ -d_{22} & d_{22} & 0 & d_{31} & 0 & 0 \\ d_{31} & d_{31} & d_{33} & 0 & 0 & 0 \end{bmatrix} \quad (5)$$

When the PPLN is used for quasi-phase matching, the polarization of light is usually set parallel to the Z-axis (the e-axis of the crystal) to access the highest nonlinear components of the $\chi^{(2)}$ (d_{33} and d_{31}). Here, in order to image the domains the propagation of light is set parallel to the Y-axis (see Fig. 1), such that the main excited component is d_{22} (see [46]). The components d_{33} and d_{31} are not excited in the scalar-field approximation, but can contribute due to the distortion of the polarization of the exciting beam occurring at tight focusing regimes according to the vectorial field model [47].

2.6 Numerical simulations

The numerical simulations are all performed using the Green's function approach (as in [20]), with a wavelength of 810nm, a waist of 0.7µm (meaning a spot size of 1.4µm diameter), and an integration volume of 2.8x2.8x10µm^3. The collecting lens is assumed at 3 mm from the focal volume, with a numerical aperture of 0.8. It is worth noting that the Green's function calculation takes into account the tensorial nature of $\chi^{(2)}$ and a vectorial exciting field that becomes significant when focused by a microscope objective [47]. The light is collected in the far-field with a collecting lens with an NA of 0.8 using a Monte Carlo integration with 5,000,000 points.

3. Results and discussion

3.1 Numerical simulations of the theoretical radiation pattern

First, numerical simulations were performed to compute the radiation pattern of the converted SHG signal observed before the collecting lens for two different cases: in the middle of a homogeneous $\chi^{(2)}$ zone (case I) and on an interface between two zones of opposite $\chi^{(2)}$ sign (case II), as indicated in Fig. 1(B). The radiation pattern is in the first case a standard 2D Gaussian (Fig. 2(A.I)) but at an interface it splits into two lobes that are π phase-shifted (Fig. 2(A.II)): in this case their amplitude is indeed of opposite sign. In the case (II) when the two lobes are recombined by a collecting lens (Fig. 2(B)), the detector can be positioned to have a complete (D2), partial (D1) or no (D3) overlap of the lobes on it. Position D1 implies complete destructive interference of both lobes and thus theoretically no signal. Position D3 is the other limit with no interference, such that the measured signal is the incoherent addition of

Biomedical Optics EXPRESS

both lobes. Finally, position D2 lays in between: the destructive interference of the lobes is only partial, such that some signal would be detected.

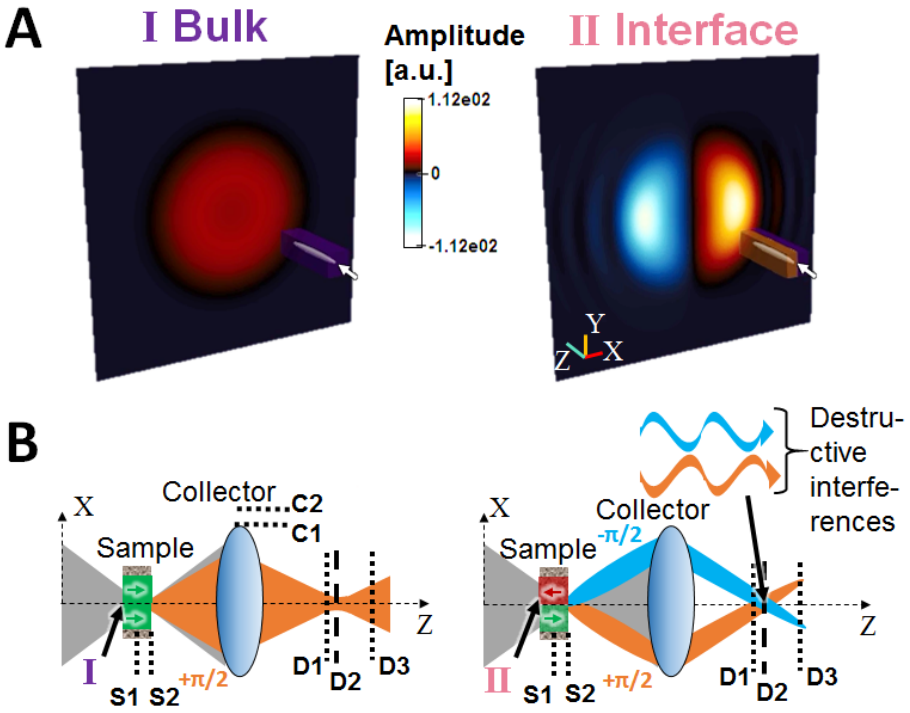

Fig. 2. Theoretical radiation pattern in different configurations of PPLN, and its consequences when being imaged on the detector. (A) Schematic view of the far-field SHG amplitude before the collector of a homogeneous medium and $\chi^{(2)}$ obtained by numerical simulations if the focal volume is located in the bulk (I, left), or if it is located at the interface between two domains with a $\chi^{(2)}$ of opposite sign (II, right). The focal volume is represented by a white oval (pointed by a white arrow), and the far-field pattern is here purposely moved very close to the excitation for the clarity of the illustration (not at scale). For the bulk (I) the shape is a standard 2D Gaussian whereas for the interface (II), the amplitude is spread over two side-lobes of opposite sign, which means their phases are π-phase-shifted. (B) Schematic view of the SH radiation pattern generation and its recombination on the detector by the collector, for the focal volume of excitation being in the bulk (left, I in green) or at an interface between two opposite polarities (right, II, in red and green). The excitation beam is shown in grey, and produces a Gaussian radiation pattern (orange) in case I (left), but two π-phase-shifted lobes (blue and orange) for case II (right). Their respective phases are indicated (-π/2 and π/2). Their subsequent collection leads to a recombination on the detector, which implies a partial (position D1) or total (position D2) overlap of the lobes, or no overlap at all (position D3) depending on the detector position. Since the lobes are π phase-shifted, their overlap will produce partial or complete destructive interference, as indicated by the two out-of-phase sine waves at the top of B. The different focus positions along the sample depth (Z) are indicated by S1 and S2 planes. Also, the collector might be well-aligned with its top at position C1, or misaligned at position C2. The off-axis angle of the lobes on B.II is purposely exaggerated for clarity.

The numerical simulations predict that the total integrated intensity - i.e. the signal measured by the detector during an experiment – is indeed 0 when the lobes overlap in case II (interface, detector at D2) because of destructive interferences. If the detector is misaligned in Z (position D3) such that the two lobes do not overlap at all, they would just sum up incoherently. In this case, the relative intensity is equal to 70% of the intensity detected from bulk (case I), i.e. a ratio $r_I = 0.7:1$.

Biomedical Optics EXPRESS

Overall, the total intensity detected at the interface of the $\chi^{(2)}$ boundaries (II) is always smaller than the one detected in the bulk (I). For further information on the radiation pattern along the transition from the bulk (case I) to the interface (case II), we refer to the videos Visualization 1 and Visualization 2 in the supplementary material. They show numerical simulations of the amplitude of the SHG radiation pattern converted respectively at the surface (position S2 in Fig. 2(B)) or at a depth of Z = 5µm (position S1 in Fig. 2(B)). These two different sample positions S1 and S2 (Fig. 2(B)) also give similar radiation patterns for the interface, and a doughnut-shaped pattern (as already discussed in the literature [16]) is obtained if the excitation is Z = 5µm in depth, unlike the 2D Gaussian obtained when interacting with bulk at its surface. The intensities at Z = 5µm depth also conserve the ratio r_1 = 0.7:1 (see the 2D plots in the videos). Furthermore, the intensity ratios are conserved even with a large misalignment of the collecting lens in lateral position X (see Fig. 5 in the Appendix). If this misalignment is larger than 2mm, the signal decreases because the SHG beams are no longer reaching the detector. This is unrealistic to happen experimentally, as the collecting objective is aligned by maximizing the detected signal with a precision below 1mm. The different normalized integrated intensities of second harmonic signal obtained in the different configurations are summarized in the upper part of Table 1.

Table 1. Intensities at the detector in the bulk or at interfaces obtained by numerical simulations for the different configurations, and their comparison with the experimental values obtained in PPLN.

	Bulk	Interface
Complete overlap of the lobes on the detector	1	0
No overlap of the lobes on the detector	1	0.7
Experiment (PPLN, iris open)	1	2.1
Experiment (PPLN, iris closed to 5mm)	1	0.83

Interestingly, in Fig. 2(A), the individual peak amplitudes of both lobes are much higher than the one of the bulk due to the symmetry breaking, even though the integrated intensity over both lobes is smaller than in the case of the bulk. This can be understood by the absence of signal between the two lobes, and because the pattern associated with the two lobes concentrates the signal in two separated and smaller areas. The bulk pattern on the other hand is spread homogeneously over the whole disk (blue and orange regions in Fig. 2(A)), resulting in a higher number of photons spread over a larger zone.

Furthermore, these simulations have been adapted to the case of myosin and predict a radiation pattern that has the same shape, angle of emission, and relative amplitudes as for PPLN even though they have different $\chi^{(2)}$ symmetry tensors and coefficients. Thus, these results suggest that it is the geometrical property of the interface or the bulk that defines the radiation pattern.

3.2 PPLN: removing incoherent imaging artifacts

On the SHG images of PPLN, stripes occur at the interfaces (bright in Fig. 3(a) and dark for b, c and d) whose spatial thickness is approximately 1µm. This thickness is in good agreement with the expected lateral resolution of ~1µm as mentioned in the method section. The bright stripes in Fig. 3(a) offset the dynamic range of the image as they are 2.1 times higher than the signal in the homogeneous zones of the bulk and thus prevent a good visualization of the structure. This ratio is obtained by taking the average signal from the bright zones divided by the one of the homogeneous zones. Also, the bright stripes in Fig. 3(a) decrease from right to left due to a slight tilt of the sample along Z. It is not the case in the I-SHG image Fig. 3(c)

Biomedical Optics EXPRESS

because I-SHG results from a relative measurement that cancels such an effect. This cancellation is discussed mathematically in Eqs. (1) and (2).

We have discussed in section 3.1 the two limit cases of the effect of the detector position along Z, which show that the detected signal at the interface can theoretically vary between 0 (case D2 in Fig. 2(B.II)) and 0.7 times (case D3 in Fig. 2(B.II)) the signal detected in the bulk (see Table 1). The case in-between (D1 in Fig. 2(B)) corresponds to an experimentally realistic case since a perfect alignment is rarely achieved. Overall, the 2.1 times higher SH signal observed at the interfaces of PPLN in Fig. 3(a) cannot be explained by our numerical simulations, and we suspect that this stronger signal originates from additional sources such as the numerous imperfections and defects present at the involved $\chi^{(2)}$ boundaries, as mentioned before. In other words, these boundaries between two antiparallel noncentrosymmetric domains present strains and perturbations of the refractive index. Additionally, these imperfections are randomly positioned and if they are limited to the nanoscale, they will produce a local-field enhancement as described in [48–50]. This enhancement can be up to 10 times or more [51,52] and leads to "hotspots" that have already been observed even in centrosymmetric materials that present local defects [53]. The emission directionality of these hotspots is not as well-defined as for a conventional SHG signal emitted from an ordered structure, so they are detected as a scattering contribution at the detector. Hence, we expect that this SH signal exhibits a randomly-distributed phase at the detector according to the relation $\varphi = 2\pi L/\lambda$ where L is the optical path and λ is the wavelength. We emphasize that while the SH signal is 2.1 times higher at the interfaces of PPLN compared to the homogeneous zones, the corresponding interferometric contrast is 2.6 times lower (see Fig. 3(c)). This confirms that a significant fraction of the SH signal from the interfaces has a random phase.

To block this undesired intense contribution, an iris in the detection path was closed down to 5 mm, which defines the filtered SHG signal. This iris is positioned close to the imaging plane. However, we found that its precise axial position (Z) is non critical to remove the undesired intense contribution. In this condition, the filtered SHG signal is lower at the interfaces due to destructive interferences as expected from lobes of opposite polarities and predicted by the numerical simulations. More precisely, this SHG signal is reduced by 16% compared to the homogeneous zones (Fig. 3(c)). It is worth noting that closing the iris has no effect on the coherent signal from the homogeneous zones, thus rejecting exclusively the artefactual part. This can be seen on the grey profile plots of Fig. 3(e), as expected since the closed iris diameter is 5mm and the scanned region is only a few tens of μm^2, such that it rejects only the highly scattered part of the signal. This was further verified by measuring the SHG signal from a quartz plate under the same experimental conditions.

Interestingly, despite the fact that the interfaces appear as homogeneous signal stripes on the images, they actually correspond to a spatial average of the signal emitted by the numerous defects whose dimensions are at the nanoscale.

Using I-SHG, we show that there is no real difference in the interferometric contrast γ between the cases when the scattering is rejected or not (Fig. 3(b) and (d). On Fig. 3(e) the profile plots reveal that the case with the iris closed (black dashed line) has slightly less signal in the homogeneous part, and that for both open and closed iris (black continuous and dashed lines) the dip at the interfaces is deeper than in the case of SHG with iris closed (grey dashed line, filtered SHG). We also define the visibility of a certain feature in the image as:

$$Visibility = \frac{I_{max} - I_{min}}{I_{max} + I_{min}} \tag{6}$$

0 meaning no visibility and 1 a perfect one. The visibility of the interfaces in I-SHG is of 0.43 compared to 0.09 for the filtered SHG (iris closed). I-SHG thus enhances this visibility 5 times compared to filtered SHG.

Biomedical Optics EXPRESS

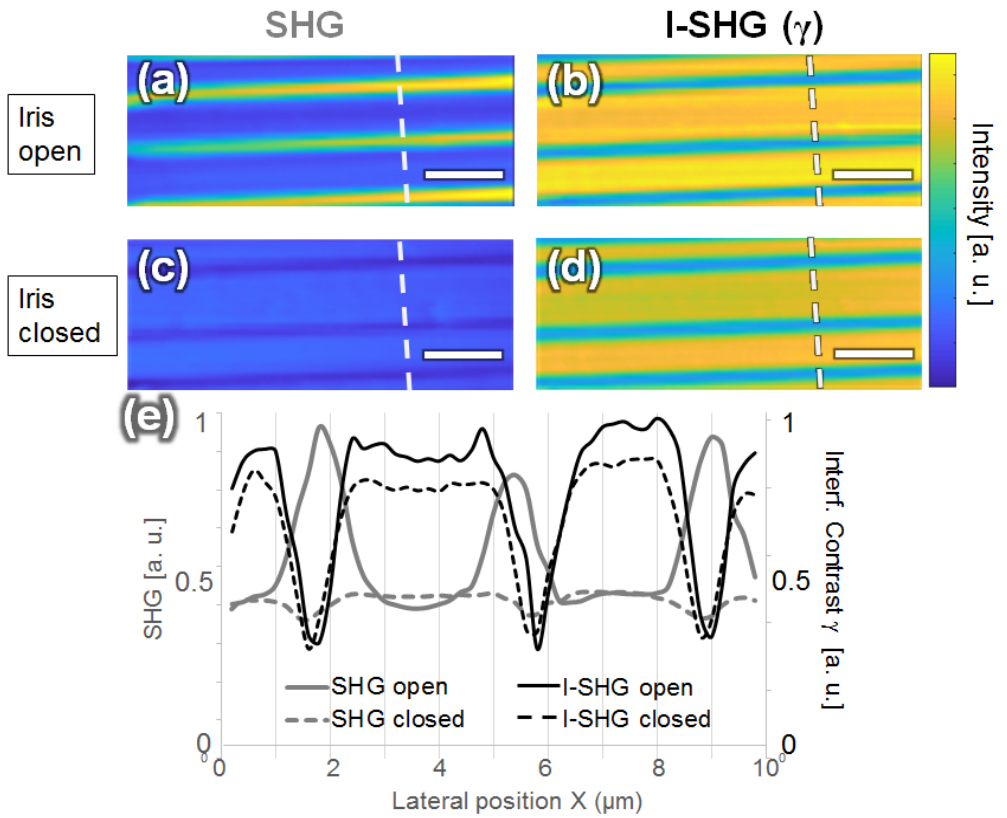

Fig. 3. (Left) Intensity SHG images of PPLN domains, where scattering occurs at the interfaces (a), compared to the same zone imaged with the scattering at the interfaces blocked by an iris (c). (Right) Interferometric contrast γ measured by I-SHG ((b) and (d)) of the same zone and under the same conditions and with same dynamic range as before. No clear differences are visible between these two I-SHG contrast images, showing that the scattering at the interfaces is averaged out by I-SHG. Scale-bars: 5μm. (e) Profile plots along the white dashed lines of the images. With the iris open (grey continuous line), there are intense contributions at the interfaces between domains, which are two times more intense than the homogeneous zones. Closing the iris rejects these contributions and reveals the little dips in SHG signal at the interfaces (grey dashed line) corresponding to destructive interferences (16% lower than the homogeneous contribution), while maintaining the same level of signal for the homogeneous parts. The I-SHG contrast γ is very similar in both cases of open (black continuous line) and closed iris (black dashed line). In the homogeneous zones the closed case has only 10% less signal than the open case. With I-SHG, the interfaces exhibit a high contrast, with a signal drop of more than 50% when going from the homogeneous zones to the interfaces.

These I-SHG images confirm that the very intense SH signal at the interfaces does indeed not exhibit a well-defined phase and thus cannot interfere with the reference beam, and importantly that I-SHG is therefore able to remove this incoherent signal that only acts as a contribution to the background. The imperfect interface in PPLN can thus directly be revealed in I-SHG, while it requires spatial filtering in standard SHG to remove the bright and artefactual interface signal.

3.3 Myosin: removing coherent imaging artifacts

In zebrafish skeletal muscle, similar interfaces as in PPLN are present but they lead to different artifacts: while in all cases alternating structures are present in the samples, they were only sometimes visible as double structures in conventional SHG microscopy. In other cases, the myosin interfaces could not be observed with standard SHG. To begin with, we

Biomedical Optics EXPRESS

present here an SHG image of the sarcomeres from muscles of zebrafish, where the observed patterns are double-band (as mentioned earlier, see Fig. 1(B)). The adjacent sarcomeres appear separated by the I-bands (white arrow-heads in images of Fig. 4) where the SHG signal is minimum, within whom the A-band is split in two by the M-line (where the opposite myosin ends overlap, brown arrows of Fig. 4). This occurs as a dip in SHG signal with slightly more signal than in the I-band (see Fig. 4(a)).

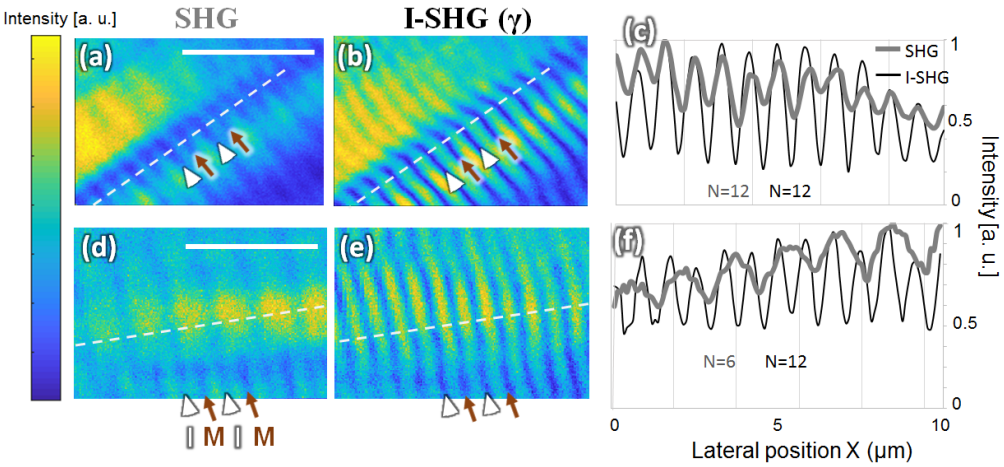

Fig. 4. Myosin inside sarcomeres of skeletal muscle of zebrafish imaged by SHG (left column) and I-SHG (middle column). The I-SHG interferometric contrast enhances the visibility of the myosin pattern compared to the intensity SHG. (a) SHG intensity in 6-months-old zebrafish muscle, showing the expected double-band patterns of myosin. The I-SHG interferometric contrast γ (middle) of the same zones (b) exhibits an enhanced visibility of the sarcomeres pattern compared to the intensity SHG. This is better observed when plotting an intensity projection (right) along the white dashed lines: the visibility of the oscillations is enhanced from 2.5 to 4 times (depending on the zone) for I-SHG (black lines in (c)) compared to SHG (grey lines). (d-f) Same as before, in a larvae zebrafish: the selected zones show a single-band pattern of myosin in intensity SHG (d), while the corresponding interferometric contrast γ in I-SHG (e) reveals the double-band pattern. (f) Profile plots of signals along the white dashed line shown on the images: there are indeed twice the number of peaks for the I-SHG compared to the SHG case, whereas for (a) and (b) their number is similar. Two I-band positions are spotted in each image by white arrow-heads, and two M-lines by brown arrows. Equivalent exposure time is 400μs and 100μs per pixel for the SHG images and I-SHG images, respectively. For SHG images the dynamic range of display is enhanced compared to I-SHG, for clarity. Scale-bars = 5μm for all the images.

When the interferometric contrast γ is measured (by I-SHG), these sarcomeres are revealed more clearly (Fig. 4(b)): the visibility of the "oscillations" (alternation of bulk/interface) is of 0.7 compared to 0.2 for the intensity SHG images (see Fig. 4(c)), so 3 times higher. Interferometric SHG thus greatly enhances the visibility (or imaging contrast) compared to standard intensity SHG. It should be noted that all these images of myosin show no difference whether the iris mentioned earlier was open or closed, because there is no highly scattered SH signal present.

We then show another standard SHG image where the double-band pattern is artifactly hidden in some areas (Fig. 4(d)). Only the I-SHG interferometric contrast γ can reveal it (Fig. 4(e)). On the profile plots (Fig. 4(f)) there are clearly twice the number of dips in the I-SHG signal compared to the SHG one. In the bottom of the image, the double-band pattern is still visible in standard intensity SHG, which shows that this imaging artifact does not occur equally everywhere. It is strongly dependent on the interferences between the SHG converters, and thus on their spatial arrangement. Indeed, the 3D stacking of sarcomeres in muscle can imply artifacts in the axial direction due to the Gouy phase-shift, for some areas in the sample where the sarcomeres' spacing matches a certain phase relation [26]. For example,

Biomedical Optics EXPRESS

in the lateral plane (i.e. XY in Fig. 1(B)) plane, the proximity of shifted sarcomeres in the focal area can result in an SHG signal with similar artefactual connections between the sarcomeres (i.e. a single-band pattern), as extensively discussed before [25,26]. Lastly, the propagation of the SHG wave through the thickness of the muscle (several μm), that is a stacking of sarcomeres, can also be a source of varying phase retardation and thus artifacts in the acquired SHG images. While the detailed origin of the coherent imaging artifacts occurring in the myosin of muscle in conventional SHG microscopy is still under debate, it is assumed that it results from coherent built-up of the SHG signal in a highly complex tissue [25,26]. This is different from the I-SHG case, where the SHG radiation interferes with the reference beam and the I-SHG contrast γ reveals the highest phase modulation. This I-SHG contrast appears to be lower at the M-line than elsewhere in the myosin filament, and thus reveals the destructive interferences occurring at the M-line and uncovers the double-band patterns. Therefore, I-SHG allows to remove a typically observed imaging artifact for such structures, namely the single-band pattern.

3.4 Comparison between PPLN and myosin I-SHG imaging

I-SHG was already used to advance standard SHG microscopy as mentioned in the introduction. Here we focus on the additional advantage of I-SHG being capable of eliminating two different types of imaging artifacts – coherent and incoherent ones.

The converted SHG inside a sample can in general be written as [54]: $I_{SH} = I_{SH}^{ballist} + I_{SH}^{scatter}$, where $I_{SH}^{ballist}$ is the main contribution which has experienced little to no scattering. This conserves the phase relation and thus its coherence. In the case of our example myosin, $I_{SH}^{ballist}$ represents the observed SHG signal. In contrast, the term $I_{SH}^{scatter}$ preserves no coherence and is usually much smaller than the ballistic one. An exception are structures with many randomly-oriented nano-emitters like the PPLN interfaces of our first example, which leads to incoherent imaging artifacts. I-SHG averages this contribution out, as it is an interferometry technique that reveals only the coherent interfering part.

Table 2 summarizes the comparison between PPLN and myosin materials, pointing out the similarity of the expected effects on the SHG at the interfaces and the differences of the artifacts that occur at these interfaces: these structures are analogous, except that the nature of the imaging artifacts is incoherent for PPLN, and coherent for myosin. There are no coherent imaging artifacts in PPLN because, unlike muscle, there is no 3D arrangement of many domains with opposite polarity, but rather a single and well-ordered periodicity, homogeneous in the axial direction (along Z).

Both coherent and incoherent artifacts are fully eliminated in I-SHG microscopy, however in different ways. Coherent artifacts remain visible in the optically collected interferograms but are eliminated in the subsequent image processing (see Fig. 6 of the Appendix, bottom). Incoherent artifacts, on the other hand, already do not show up in the measured interferograms as they only contribute as a constant background for every phase-shift (see Fig. 6, top). Table 2 also points out the two major advantages of I-SHG: it is capable of totally removing artefactual interface structures that appear in some cases in conventional SHG. And even if no artifacts occur, such that structures are correctly imaged by SHG microscopy, the I-SHG technique further increases the visibility of these interfaces by a factor of 3 (in myosin) to 5 (in PPLN). The ability of I-SHG to increase this visibility relies on a reference SHG beam with a well-defined phase. For thick tissues, because of scattering, such phase definition might be partially lost. Yet, this will only reduce the interferometric contrast, so that a phase-modulation could still be extracted to measure the relative polarity of structures.

Biomedical Optics EXPRESS

Table 2. Summary of the differences and similarities between the two samples under study.

	PPLN	Myosin
Periodic domains of opposite polarity	**Yes**	**Yes**
Organization of domains	Single periodic structure	Complex arrangement of multiple periodic structures
Number of interface types	1 with opposite polarities	2 (1 with opposite polarities, 1 without SHG converter)
At interfaces, SHG radiation pattern presents two lobes that interfere destructively, leading to minimum signal	**Yes**	**Yes**
Incoherent signal contribution/artifacts	**Yes**	**No**
SHG ratio at interface/bulk due to hotspots	**× 2.1**	**No hotspots**
Need for iris filtering in standard SHG	**Yes**	**No**
Coherent imaging artifacts in SHG	**No**	**In some cases**
Imaging artifacts removed in I-SHG	**Yes**	**Yes**
Increase of visibility of boundaries by I-SHG	**× 5**	**× 3**

4. Conclusion

The interface between two $\chi^{(2)}$ of opposite polarity leads to an SHG radiation pattern with two lobes whose relative phase is π phase-shifted, which is elucidated in detail by numerical simulations. These lobes normally lead to destructive interferences when being recombined on a detector. However, in some cases of standard SHG, a signal occurs at these interfaces for two different reasons: first, in PPLN the signal is given by an incoherent hotspot contribution due to imperfections, which can be eliminated by optical filtering. Second, in muscle sarcomeres, the signal at these interfaces can produce imaging artifacts due to the coherent nature of the SHG light, which are insensitive to optical filtering. For both examples, it is shown that I-SHG fully eliminates these artifacts, and reveals the destructive interferences at the interfaces without the need of any further processing like spatial filtering. Furthermore, I-SHG even allows to increase the visibility of the interfaces by a factor of 3 to 5. This is of great importance for interpreting correctly the SHG signal produced in various materials, especially in complex biological tissues.

Funding

M.P., F.L. and S.P acknowledges Canada Foundation for Innovation (CFI) and the Natural Sciences and Engineering Research Council of Canada (NSERC). M.P. acknowledges financial support from the NSERC CREATE/GRK program. M.S. acknowledges financial support from the Ecole Doctorale Interface, Univ. Paris-Saclay.

Disclosures

The authors declare that there are no conflicts of interest related to this article.

Biomedical Optics EXPRESS

Appendix: additional numerical simulations

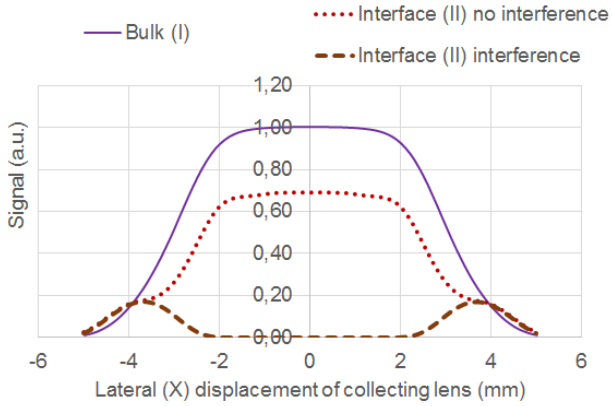

Fig. 5. Numerical simulations of the intensities at the detector when the excitation is in the bulk (I, violet continuous line) or at the interfaces of opposite polarities (II, light and dark red dashed line). The intensity at the interface is 0 when the lobes fully destructively interfere (dark red dashed line), but of 0.7 when they do not overlap on the detector so that there is no interference (light red dotted). In comparison, the intensity for the bulk is 1. These ratios remain the same if the lateral misalignment in X of the collecting objective is below 2 mm. If this misalignment goes over 2 mm, the signal for the bulk and for the interface with no interference decrease as the SHG beams go progressively outside the detector. For the case where the lobes overlap, at high lateral misalignment, the lens does not progressively capture one of the lobes so that the destructive interferences can only partially occur such that the intensity is larger than 0. Over 4 mm of misalignment, all signals decrease to 0. The detector is 45mm^2 placed at 3.3 mm of the collecting lens, whose equivalent diameter is 8 mm.

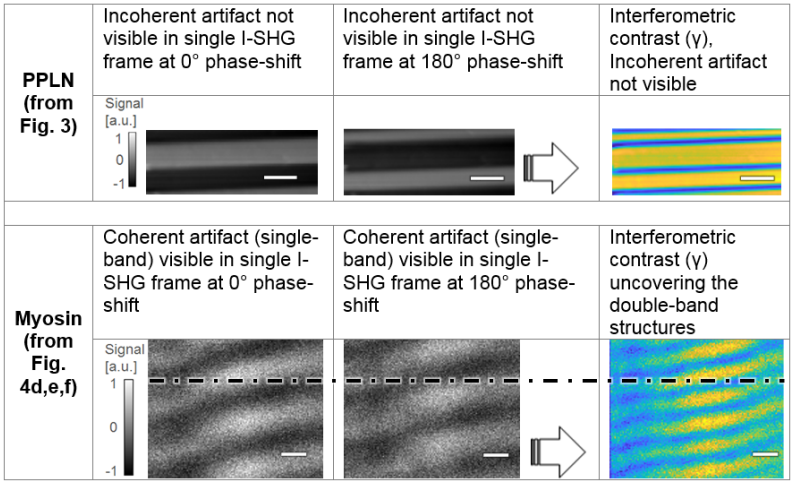

Fig. 6: Comparison of the incoherent and coherent artifacts removal by I-SHG. (Top) PPLN images of Fig. 3, showing the I-SHG contrast γ (right) and two interferograms at 0° (left) and 180° (middle) used to reconstruct the I-SHG image. The incoherent artifacts (bright stripes) are removed from the interferograms directly. Scale-bar: 5μm. (Bottom) Same with myosin images from Fig. 4(e). The coherent artifacts (single-band pattern) are still visible on interferograms (left and middle), but these one are indeed π phase-shifted. The double-band pattern is revealed only in the I-SHG contrast γ (right). A dashed black line guides the eye for comparison between images. Scale-bar: 1μm.

Biomedical Optics EXPRESS

References

1. S. Roth and I. Freund, "Optical second-harmonic scattering in rat-tail tendon," Biopolymers **20**(6), 1271–1290 (1981).
2. P. J. Campagnola, A. C. Millard, M. Terasaki, P. E. Hoppe, C. J. Malone, and W. A. Mohler, "Three-dimensional high-resolution second-harmonic generation imaging of endogenous structural proteins in biological tissues," Biophys. J. **82**(1 Pt 1), 493–508 (2002).
3. A. Zoumi, A. Yeh, and B. J. Tromberg, "Imaging cells and extracellular matrix in vivo by using second-harmonic generation and two-photon excited fluorescence," Proc. Natl. Acad. Sci. U.S.A. **99**(17), 11014–11019 (2002).
4. W. Denk, J. H. Strickler, and W. W. Webb, "Two-photon laser scanning fluorescence microscopy," Science **248**(4951), 73–76 (1990).
5. F. Helmchen and W. Denk, "Deep tissue two-photon microscopy," Nat. Methods **2**(12), 932–940 (2005).
6. P. J. Campagnola and L. M. Loew, "Second-harmonic imaging microscopy for visualizing biomolecular arrays in cells, tissues and organisms," Nat. Biotechnol. **21**(11), 1356–1360 (2003).
7. S. Bancelin, C. Aimé, I. Gusachenko, L. Kowalczuk, G. Latour, T. Coradin, and M.-C. Schanne-Klein, "Determination of collagen fibril size via absolute measurements of second-harmonic generation signals," Nat. Commun. **5**(1), 4920 (2014).
8. A. K. Dunn, V. P. Wallace, M. Coleno, M. W. Berns, and B. J. Tromberg, "Influence of optical properties on two-photon fluorescence imaging in turbid samples," Appl. Opt. **39**(7), 1194–1201 (2000).
9. W. R. Zipfel, R. M. Williams, R. Christie, A. Y. Nikitin, B. T. Hyman, and W. W. Webb, "Live tissue intrinsic emission microscopy using multiphoton-excited native fluorescence and second harmonic generation," Proc. Natl. Acad. Sci. U.S.A. **100**(12), 7075–7080 (2003).
10. A. E. Tuer, M. K. Akens, S. Krouglov, D. Sandkuijl, B. C. Wilson, C. M. Whyne, and V. Barzda, "Hierarchical model of fibrillar collagen organization for interpreting the second-order susceptibility tensors in biological tissue," Biophys. J. **103**(10), 2093–2105 (2012).
11. I. Gusachenko, V. Tran, Y. Goulam Houssen, J. M. Allain, and M.-C. Schanne-Klein, "Polarization-resolved second-harmonic generation in tendon upon mechanical stretching," Biophys. J. **102**(9), 2220–2229 (2012).
12. C. P. Brown, M. A. Houle, M. Chen, A. J. Price, F. Légaré, and H. S. Gill, "Damage initiation and progression in the cartilage surface probed by nonlinear optical microscopy," J. Mech. Behav. Biomed. Mater. **5**(1), 62–70 (2012).
13. S. V. Plotnikov, A. C. Millard, P. J. Campagnola, and W. A. Mohler, "Characterization of the myosin-based source for second-harmonic generation from muscle sarcomeres," Biophys. J. **90**(2), 693–703 (2006).
14. V. Nucciotti, C. Stringari, L. Sacconi, F. Vanzi, L. Fusi, M. Linari, G. Piazzesi, V. Lombardi, and F. S. Pavone, "Probing myosin structural conformation in vivo by second-harmonic generation microscopy," Proc. Natl. Acad. Sci. U.S.A. **107**(17), 7763–7768 (2010).
15. N. Olivier, M. A. Luengo-Oroz, L. Duloquin, E. Faure, T. Savy, I. Veilleux, X. Solinas, D. Débarre, P. Bourgine, A. Santos, N. Peyriéras, and E. Beaurepaire, "Cell Lineage Reconstruction of Early Zebrafish Embryos Using Label-Free Nonlinear Microscopy," Science **329**(5994), 967–971 (2010).
16. M. Rivard, M. Laliberté, A. Bertrand-Grenier, C. Harnagea, C. P. Pfeffer, M. Vallières, Y. St-Pierre, A. Pignolet, M. A. El Khakani, and F. Légaré, "The structural origin of second harmonic generation in fascia," Biomed. Opt. Express **2**(1), 26–36 (2011).
17. R. Lacomb, O. Nadiarnykh, S. S. Townsend, and P. J. Campagnola, "Phase matching considerations in second harmonic generation from tissues: Effects on emission directionality, conversion efficiency and observed morphology," Opt. Commun. **281**(7), 1823–1832 (2008).
18. S. Yazdanfar, L. Laiho, and P. So, "Interferometric second harmonic generation microscopy," Opt. Express **12**(12), 2739–2745 (2004).
19. M. Rivard, C.-A. Couture, A. K. Miri, M. Laliberté, A. Bertrand-Grenier, L. Mongeau, and F. Légaré, "Imaging the bipolarity of myosin filaments with Interferometric Second Harmonic Generation microscopy," Biomed. Opt. Express **4**(10), 2078–2086 (2013).
20. M. Rivard, K. Popov, C. A. Couture, M. Laliberté, A. Bertrand-Grenier, F. Martin, H. Pépin, C. P. Pfeffer, C. Brown, L. Ramunno, and F. Légaré, "Imaging the noncentrosymmetric structural organization of tendon with Interferometric Second Harmonic Generation microscopy," J. Biophotonics **7**(8), 638–646 (2014).
21. C. A. Couture, S. Bancelin, J. Van der Kolk, K. Popov, M. Rivard, K. Légaré, G. Martel, H. Richard, C. Brown, S. Laverty, L. Ramunno, and F. Légaré, "The Impact of Collagen Fibril Polarity on Second Harmonic Generation Microscopy," Biophys. J. **109**(12), 2501–2510 (2015).
22. S. Bancelin, C.-A. Couture, M. Pinsard, M. Rivard, P. Drapeau, and F. Légaré, "Probing microtubules polarity in mitotic spindles in situ using Interferometric Second Harmonic Generation Microscopy," Sci. Rep. **7**(1), 6758 (2017).
23. S. Bancelin, C.-A. C.-A. Couture, K. Légaré, M. Pinsard, M. Rivard, C. Brown, and F. Légaré, "Fast interferometric second harmonic generation microscopy," Biomed. Opt. Express **7**(2), 399–408 (2016).
24. R. W. Boyd, "The Nonlinear Optical Susceptibility," in *Nonlinear Optics, 3rd Edition* (Academic Press, 2008), pp. 3–51.
25. D. Rouède, J.-J. Bellanger, G. Recher, and F. Tiaho, "Study of the effect of myofibrillar misalignment on the sarcomeric SHG intensity pattern," Opt. Express **21**(9), 11404–11414 (2013).

Biomedical Optics EXPRESS

26. W. P. Dempsey, N. O. Hodas, A. Ponti, and P. Pantazis, "Determination of the source of SHG verniers in zebrafish skeletal muscle," Sci. Rep. **5**(1), 18119 (2015).
27. D. Irzhak, D. Roshchupkin, and L. Kokhanchik, "X-ray diffraction on a LiNbO3 crystal with a short period regular domain structure," Ferroelectrics **391**(1 PART 3), 37–41 (2009).
28. V. Gopalan, V. Dierolf, and D. A. Scrymgeour, "Defect–Domain Wall Interactions in Trigonal Ferroelectrics," Annu. Rev. Mater. Res. **37**(1), 449–489 (2007).
29. S. Helmfrid, G. Arvidsson, and J. Webjörn, "Influence of various imperfections on the conversion efficiency of second-harmonic generation in quasi-phase-matching lithium niobate waveguides," J. Opt. Soc. Am. B **10**(2), 222 (1993).
30. F. Zernike and J. E. Midwinter, "4.5 Lithium Niobate," in *Applied Nonlinear Optics* (Wiley Interscience, 1973), pp. 87–88.
31. M. Neradovskiy, E. Neradovskaia, D. Chezganov, E. Vlasov, V. Y. V. Y. A. Shur, H. Tronche, F. Doutre, G. Ayenew, P. Baldi, M. De Micheli, and C. Montes, "Second harmonic generation in periodically poled lithium niobate waveguides with stitching errors," J. Opt. Soc. Am. B **35**(2), 331 (2018).
32. D. Rouède, J.-J. Bellanger, E. Schaub, G. Recher, and F. Tiaho, "Theoretical and experimental SHG angular intensity patterns from healthy and proteolysed muscles," Biophys. J. **104**(9), 1959–1968 (2013).
33. G. Recher, D. Rouède, P. Richard, A. Simon, J.-J. Bellanger, and F. Tiaho, "Three distinct sarcomeric patterns of skeletal muscle revealed by SHG and TPEF microscopy," Opt. Express **17**(22), 19763–19777 (2009).
34. T. Boulesteix, E. Beaurepaire, M.-P. Sauviat, and M.-C. Schanne-Klein, "Second-harmonic microscopy of unstained living cardiac myocytes: measurements of sarcomere length with 20-nm accuracy," Opt. Lett. **29**(17), 2031–2033 (2004).
35. M. Both, M. Vogel, O. Friedrich, F. von Wegner, T. Künsting, R. H. A. Fink, and D. Uttenweiler, "Second harmonic imaging of intrinsic signals in muscle fibers in situ," J. Biomed. Opt. **9**(5), 882–892 (2004).
36. O. Friedrich, M. Both, C. Weber, S. Schürmann, M. D. H. Teichmann, F. von Wegner, R. H. A. Fink, M. Vogel, J. S. Chamberlain, and C. Garbe, "Microarchitecture is severely compromised but motor protein function is preserved in dystrophic mdx skeletal muscle," Biophys. J. **98**(4), 606–616 (2010).
37. W. R. Zipfel, R. M. Williams, and W. W. Webb, "Nonlinear magic: Multiphoton microscopy in the biosciences," Nat. Biotechnol. **21**(11), 1369–1377 (2003).
38. J. Schindelin, I. Arganda-Carreras, E. Frise, V. Kaynig, M. Longair, T. Pietzsch, S. Preibisch, C. Rueden, S. Saalfeld, B. Schmid, J. Y. Tinevez, D. J. White, V. Hartenstein, K. Eliceiri, P. Tomancak, and A. Cardona, "Fiji: An open-source platform for biological-image analysis," Nat. Methods **9**(7), 676–682 (2012).
39. J. E. Greivenkamp, "Generalized data reduction for heterodyne interferometry," Opt. Eng. **23**(4), 350–352 (1984).
40. Z. Wang and B. Han, "Advanced iterative algorithm for phase extraction of randomly phase-shifted interferograms," Opt. Lett. **29**(14), 1671–1673 (2004).
41. R. Stolle, G. Marowsky, E. Schwarzberg, and G. Berkovic, "Phase measurements in nonlinear optics," Appl. Phys. B Laser Opt. **63**(5), 491–498 (1996).
42. T. Colomb, J. Kühn, F. Charrière, C. Depeursinge, P. Marquet, and N. Aspert, "Total aberrations compensation in digital holographic microscopy with a reference conjugated hologram," Opt. Express **14**(10), 4300–4306 (2006).
43. M. Westerfield, *The Zebrafish Book: A Guide for the Laboratory Use of Zebrafish (Danio rerio)* (Eugene University of Oregon Press, 2007).
44. F. Tiaho, G. Recher, and D. Rouède, "Estimation of helical angles of myosin and collagen by second harmonic generation imaging microscopy," Opt. Express **15**(19), 12286–12295 (2007).
45. R. W. Boyd, *Nonlinear Optics* (Academic Press, 2008), **2**(9).
46. M. Odstrcil, P. Baksh, C. Gawith, R. Vrcelj, J. G. Frey, and W. S. Brocklesby, "Nonlinear ptychographic coherent diffractive imaging," Opt. Express **24**(18), 20245–20252 (2016).
47. M. Gu, "Imaging with a High Numerical-Aperture Objective," in *Advanced Optical Imaging Theory* (Springer, 1999), pp. 155–165.
48. A. Bouhelier, M. Beversluis, A. Hartschuh, and L. Novotny, "Near-Field Second-Harmonic Generation Induced by Local Field Enhancement," Phys. Rev. Lett. **90**(1), 013903 (2003).
49. R. W. Boyd, "Local-Field Corrections to the Nonlinear Optical Susceptibility," in *Nonlinear Optics, 3rd Edition* (Academic Press, 2008), pp. 194–195.
50. T. Birr, T. Fischer, A. B. Evlyukhin, U. Zywietz, B. N. Chichkov, and C. Reinhardt, "Phase-Resolved Observation of the Gouy Phase Shift of Surface Plasmon Polaritons," ACS Photonics **4**(4), 905–908 (2017).
51. G. T. Boyd, T. Rasing, J. R. R. Leite, and Y. R. Shen, "Local-field enhancement on rough surfaces of metals, semimetals, and semiconductors with the use of optical second-harmonic generation," Phys. Rev. B Condens. Matter **30**(2), 519–526 (1984).
52. A. V. Zayats, T. Kalkbrenner, V. Sandoghdar, and J. Mlynek, "Second-harmonic generation from individual surface defects under local excitation," Phys. Rev. B Condens. Matter Mater. Phys. **61**(7), 4545–4548 (2000).
53. M. S. Yeganeh, J. Qi, A. G. Yodh, and M. C. Tamargo, "Influence of heterointerface atomic structure and defects on second-harmonic generation," Phys. Rev. Lett. **69**(24), 3579–3582 (1992).
54. J. Martini, V. Andresen, and D. Anselmetti, "Scattering suppression and confocal detection in multifocal multiphoton microscopy," J. Biomed. Opt. **12**(3), 034010 (2007).

This article is the result of the participatory work of several people: Margaux Schmeltz, who has undergone a research collaboration in our lab on this project, and her supervisor Marie-Claire Schanne-Klein, who both participated in the whole study. Jarno Van der Kolk of Lora Ramunno's lab (University of Ottawa) who provided the numerical simulations, and Prof. Kessen Patten of INRS-IAF who provided the samples.

This chapter highlights an unusual aspect of the I-SHG technique: the ability to retrieve the interferometric contrast term, and not only the phase. This was already described in holographic SHG microscopy by Schaffer *et al.* [193] as "amplitude images", and proved to better resolve the weak signals than the intensity SHG. This could partly explain the enhancement of visibility shown in the article below. Indeed, previous studies like [111] showed the visibility of domains in periodically-poled ferroelectrics in intensity SHG only, because they did not recover this interferometric contrast term, but just the phase where the boundary is sometimes not visible.

6.3 Complementary information for the study of artifacts in PPLN and myosin

6.3.1 SHG radiation pattern in a sample with interfaces

The SHG radiation pattern (already discussed in section 2.1.5) is known to change with what is illuminated by the focal volume (see article). Moreover, when the focal volume has different positions in the depth, the SHG radiation pattern is changed from a 2D Gaussian (if at the surface of the sample) to a doughnut shape (if a few μm in depth), as shown by the Fig. 6.2. These results are obtained using the numerical simulations described in section 3.1) of the article, and are actually extracted from the Visualization 1&2 from the Supplementary Material. They also show the progressive change from the two lobes of opposite amplitude, characterizing an interface of opposite polarities, to one pattern of homogeneous amplitude sign when the focus is in a bulk area. When the focal volume is translated in depth in myosin, different patterns are observable in the SHG images shown in Fig. 6.3 (for the description of the sample, see section 2.4 of the article). At some depth (0, 2μm), 4 bright stripes are visible, while at others (4, 9μm) this number is doubled. For a discussion of this effect, the reader is referred to section 3.3 of the article. At 12 and 18μm another artefactual effect can also be seen: the vernier

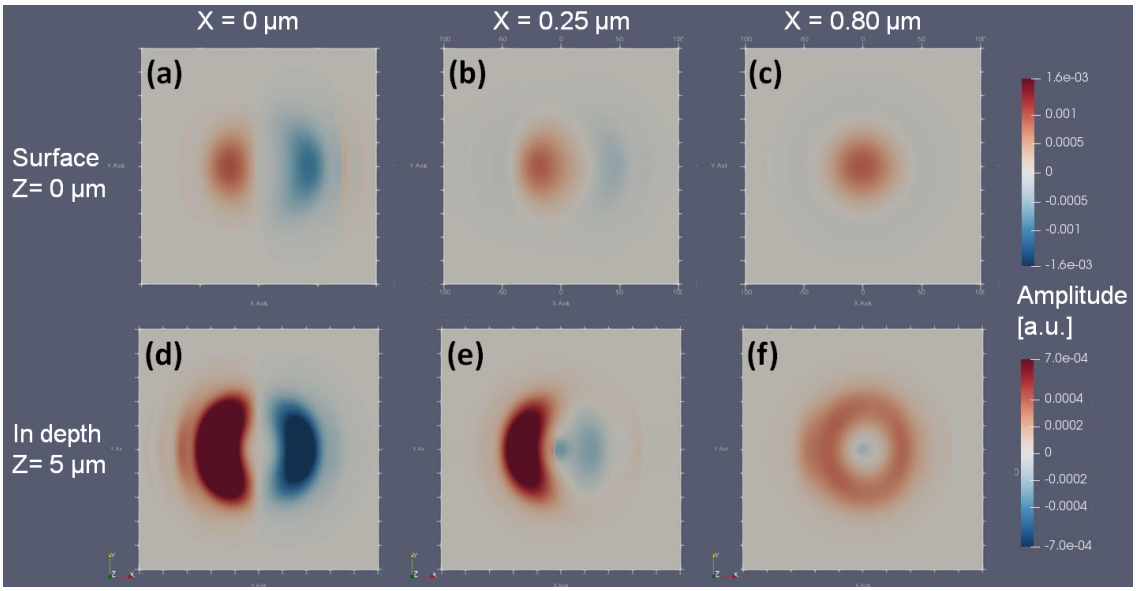

Figure 6.2: Numerical simulations of the SHG radiation pattern (using Green's formulation), the focus of excitation moving from a +/- interface to a homogeneous area. (a-c) The focus is half at the surface of the material (and half in depth). (d-f) The center of the focal volume is at a depth of 5μm from the surface.

link (in the 2D image) already described in [181, 52]. These observations motivated the investigation of these artifacts in myosin, especially the use of I-SHG in it.

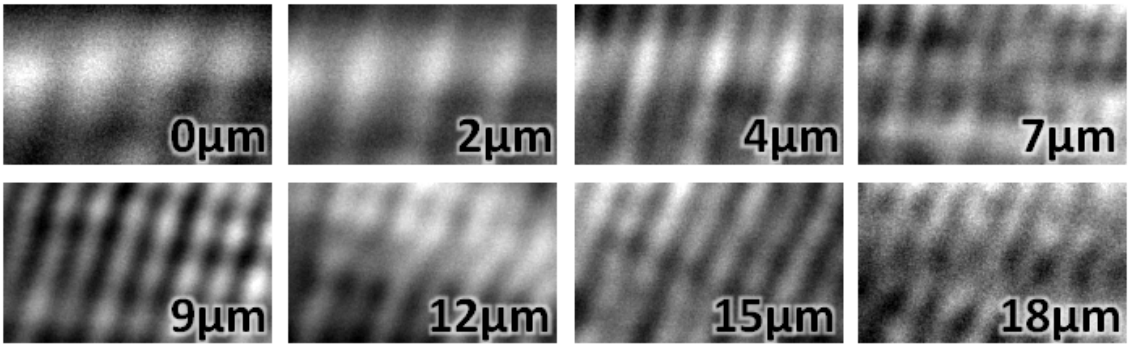

Figure 6.3: Different patterns observed in the SHG images of myosin, at different depth of focus indicated on the frames. The focus depth is indicated on each frame. Scale-bar: 2.5μm

Figure 6.4 is complementary to fig.2 of the article. On top, it can be seen that some incoherent contributions ("side-lobes") are created when the focus is at the focus of the interfaces between PPLN's domain that contains irregularities (b). This is not the case when the focus is in the middle of a bulk area (a). At the bottom, two different frames display the detected pattern when the reference SHG field is added on the optical path, thus forming an interferometer. For two different path differences of the interferometer (c and d), some interferences (rings) are visible in the central pattern, whereas there is

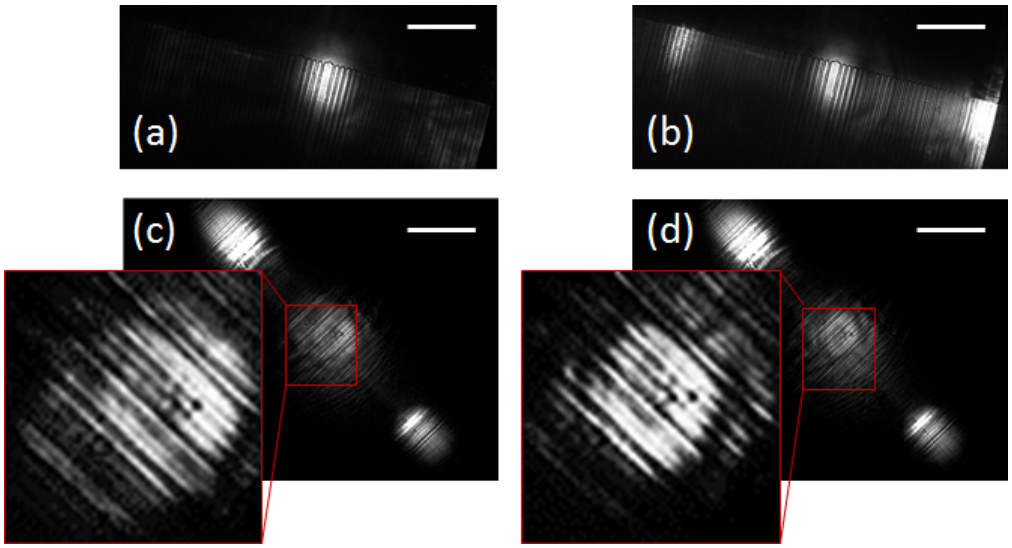

Figure 6.4: SHG signal from PPLN, experimentally recorded by a CCD camera. (Top) When the focus is in the middle of one domain of PPLN, in a bulk area (a), and when it is translated to an interface of opposite polarities showing side-lobes(b). (Bottom) Ring interferences on the central part of the pattern with the zoom on it on insets, for different path difference of the interferometer (c and d). The side-lobes are free of interferences.

none on the scattering part (side-lobes). This further confirms the incoherent nature of the scattering that was already explained in the article.

Chapter 7

Laser-scanning I-SHG with femtosecond pulses

This chapter shows the first article published during my thesis, with the first author being my colleague Stephane Bancelin. It shows how I-SHG - previously performed using a sample-scanning method - can be adapted to standard laser-scanning microscopes. It greatly improves the speed of acquisition by more than one order of magnitude. This paper was a milestone towards the further development of a fast and precise I-SHG.

7.1 Article

(EN) Fast Interferometric Second Harmonic Generation Microscopy

(FR) Imagerie Rapide en Microscopie de Génération de Seconde Harmonique Interférométrique.

Submitted 30 Nov. 2015; revised 5 Jan. 2016; accepted 5 Jan. 2016; published 8 Jan. 2016

Citation: Biomedical Optics Express 7:2(399), 2016.

DOI: 10.1364/BOE.7.000399

I participated in the experiments and in the study of the number of interferograms versus the precision, along with the manuscript writing.

Biomedical Optics EXPRESS

Fast interferometric second harmonic generation microscopy

Stéphane Bancelin,[1] Charles-André Couture,[1] Katherine Légaré,[1] Maxime Pinsard,[1] Maxime Rivard,[1] Cameron Brown,[2] and François Légaré[1,*]

[1]*Institut National de la Recherche Scientifique, Centre Énergie Matériaux Télécommunications (INRS-EMT); 1650 Boul. Lionel-Boulet, Varennes (QC), J3X 1S2, Canada*

[2]*University of Oxford, Botnar Research Center, NDORMS, Windmill Road, Oxford, OX3 7HE, UK*

[*]*legare@emt.inrs.ca*

Abstract: We report the implementation of fast Interferometric Second Harmonic Generation (I-SHG) microscopy to study the polarity of non-centrosymmetric structures in biological tissues. Using a sample quartz plate, we calibrate the spatially varying phase shift introduced by the laser scanning system. Compensating this phase shift allows us to retrieve the correct phase distribution in periodically poled lithium niobate, used as a model sample. Finally, we used fast interferometric second harmonic generation microscopy to acquire phase images in tendon. Our results show that the method exposed here, using a laser scanning system, allows to recover the polarity of collagen fibrils, similarly to standard I-SHG (using a sample scanning system), but with an imaging time about 40 times shorter.

OCIS codes: (180.4315) Nonlinear microscopy; (190.2620) Harmonic generation and mixing; (170.6935) Tissue characterization; (190.4180) Multiphoton processes; (190.4710) Optical nonlinearities in organic materials.

References and links

1. P. J. Campagnola, A. C. Millard, M. Terasaki, P. E. Hoppe, C. J. Malone, and W. A. Mohler, "Three-dimensional high-resolution second-harmonic generation imaging of endogenous structural proteins in biological tissues," Biophys. J. **82**(1), 493–508 (2002).
2. I. Freund and M. Deutsch, "Second-harmonic microscopy of biological tissue," Opt. Lett. **11**(2), 94 (1986).
3. W. R. Zipfel, R. M. Williams, R. Christie, A. Y. Nikitin, B. T. Hyman, and W. W. Webb, "Live tissue intrinsic emission microscopy using multiphoton-excited native fluorescence and second harmonic generation," Proc. Natl. Acad. Sci. U.S.A. **100**(12), 7075–7080 (2003).
4. A. Zoumi, A. Yeh, and B. J. Tromberg, "Imaging cells and extracellular matrix in vivo by using second-harmonic generation and two-photon excited fluorescence," Proc. Natl. Acad. Sci. U.S.A. **99**(17), 11014–11019 (2002).
5. W. Denk, J. H. Strickler, and W. W. Webb, "Two-photon laser scanning fluorescence microscopy," Science **248**(4951), 73–76 (1990).
6. V. E. Centonze and J. G. White, "Multiphoton excitation provides optical sections from deeper within scattering specimens than confocal imaging," Biophys. J. **75**(4), 2015–2024 (1998).
7. A. Deniset-Besseau, J. Duboisset, E. Benichou, F. Hache, P.-F. Brevet, and M.-C. Schanne-Klein, "Measurement of the second-order hyperpolarizability of the collagen triple helix and determination of its physical origin," J. Phys. Chem. B **113**(40), 13437–13445 (2009).
8. S. Bancelin, C. Aimé, I. Gusachenko, L. Kowalczuk, G. Latour, T. Coradin, and M.-C. Schanne-Klein, "Determination of collagen fibril size via absolute measurements of second-harmonic generation signals," Nat. Commun. **5**, 4920 (2014).
9. E. Brown, T. McKee, E. diTomaso, A. Pluen, B. Seed, Y. Boucher, and R. K. Jain, "Dynamic imaging of collagen and its modulation in tumors in vivo using second-harmonic generation," Nat. Med. **9**(6), 796–801 (2003).
10. A. K. Dunn, V. P. Wallace, M. Coleno, M. W. Berns, and B. J. Tromberg, "Influence of optical properties on two-photon fluorescence imaging in turbid samples," Appl. Opt. **39**(7), 1194–1201 (2000).
11. R. LaComb, O. Nadiarnykh, S. S. Townsend, and P. J. Campagnola, "Phase matching considerations in second harmonic generation from tissues: effects on emission directionality, conversion efficiency and observed morphology," Opt. Commun. **281**(7), 1823–1832 (2008).
12. X. Chen, O. Nadiarynkh, S. Plotnikov, and P. J. Campagnola, "Second harmonic generation microscopy for quantitative analysis of collagen fibrillar structure," Nat. Protoc. **7**(4), 654–669 (2012).

#254768 Received 30 Nov 2015; revised 5 Jan 2016; accepted 5 Jan 2016; published 8 Jan 2016

13. S. V. Plotnikov, A. C. Millard, P. J. Campagnola, and W. A. Mohler, "Characterization of the myosin-based source for second-harmonic generation from muscle sarcomeres," Biophys. J. **90**(2), 693–703 (2006).
14. F. Tiaho, G. Recher, and D. Rouède, "Estimation of helical angles of myosin and collagen by second harmonic generation imaging microscopy," Opt. Express **15**(19), 12286–12295 (2007).
15. A. E. Tuer, S. Krouglov, N. Prent, R. Cisek, D. Sandkuijl, K. Yasufuku, B. C. Wilson, and V. Barzda, "Nonlinear optical properties of type I collagen fibers studied by polarization dependent second harmonic generation microscopy," J. Phys. Chem. B **115**(44), 12759–12769 (2011).
16. I. Gusachenko, V. Tran, Y. Goulam Houssen, J.-M. Allain, and M.-C. Schanne-Klein, "Polarization-resolved second-harmonic generation in tendon upon mechanical stretching," Biophys. J. **102**(9), 2220–2229 (2012).
17. S. Roth and I. Freund, "Second harmonic generation in collagen," J. Chem. Phys. **70**(4), 1637 (1979).
18. A. T. Yeh, B. Choi, J. S. Nelson, and B. J. Tromberg, "Reversible dissociation of collagen in tissues," J. Invest. Dermatol. **121**(6), 1332–1335 (2003).
19. G. Latour, I. Gusachenko, L. Kowalczuk, I. Lamarre, and M.-C. Schanne-Klein, "In vivo structural imaging of the cornea by polarization-resolved second harmonic microscopy," Biomed. Opt. Express **3**(1), 1–15 (2012).
20. J. A. Palero, H. S. de Bruijn, A. van der Ploeg-van den Heuvel, H. J. Sterenborg, and H. C. Gerritsen, "In vivo nonlinear spectral imaging in mouse skin," Opt. Express **14**(10), 4395–4402 (2006).
21. S. Bancelin, B. Lynch, C. Bonod-Bidaud, G. Ducourthial, S. Psilodimitrakopoulos, P. Dokládal, J.-M. Allain, M.-C. Schanne-Klein, and F. Ruggiero, "Ex vivo multiscale quantitation of skin biomechanics in wild-type and genetically-modified mice using multiphoton microscopy," Sci. Rep. **5**, 17635 (2015).
22. F. Légaré, C. Pfeffer, and B. R. Olsen, "The role of backscattering in SHG tissue imaging," Biophys. J. **93**(4), 1312–1320 (2007).
23. M. Rivard, M. Laliberté, A. Bertrand-Grenier, C. Harnagea, C. P. Pfeffer, M. Vallières, Y. St-Pierre, A. Pignolet, M. A. El Khakani, and F. Légaré, "The structural origin of second harmonic generation in fascia," Biomed. Opt. Express **2**(1), 26–36 (2011).
24. M.-A. Houle, C.-A. Couture, S. Bancelin, J. Van der Kolk, E. Auger, C. Brown, K. Popov, L. Ramunno, and F. Légaré, "Analysis of forward and backward Second Harmonic Generation images to probe the nanoscale structure of collagen within bone and cartilage," J. Biophotonics **8**(11-12), 993–1001 (2015).
25. J. C. Mansfield, C. P. Winlove, J. Moger, and S. J. Matcher, "Collagen fiber arrangement in normal and diseased cartilage studied by polarization sensitive nonlinear microscopy," J. Biomed. Opt. **13**(4), 044020 (2008).
26. M. Rivard, C.-A. Couture, A. K. Miri, M. Laliberté, A. Bertrand-Grenier, L. Mongeau, and F. Légaré, "Imaging the bipolarity of myosin filaments with Interferometric Second Harmonic Generation microscopy," Biomed. Opt. Express **4**(10), 2078–2086 (2013).
27. D. A. Dombeck, K. A. Kasischke, H. D. Vishwasrao, M. Ingelsson, B. T. Hyman, and W. W. Webb, "Uniform polarity microtubule assemblies imaged in native brain tissue by second-harmonic generation microscopy," Proc. Natl. Acad. Sci. U.S.A. **100**(12), 7081–7086 (2003).
28. A. C. Kwan, D. A. Dombeck, and W. W. Webb, "Polarized microtubule arrays in apical dendrites and axons," Proc. Natl. Acad. Sci. U.S.A. **105**(32), 11370–11375 (2008).
29. N. Olivier, M. A. Luengo-Oroz, L. Duloquin, E. Faure, T. Savy, I. Veilleux, X. Solinas, D. Débarre, P. Bourgine, A. Santos, N. Peyriéras, and E. Beaurepaire, "Cell lineage reconstruction of early zebrafish embryos using label-free nonlinear microscopy," Science **329**(5994), 967–971 (2010).
30. P. Stoller, P. M. Celliers, K. M. Reiser, and A. M. Rubenchik, "Quantitative second-harmonic generation microscopy in collagen," Appl. Opt. **42**(25), 5209–5219 (2003).
31. S. Yazdanfar, L. Laiho, and P. So, "Interferometric second harmonic generation microscopy," Opt. Express **12**(12), 2739–2745 (2004).
32. P. Rechsteiner, J. Hulliger, and M. Flörsheimer, "Phase-sensitive second harmonic microscopy reveals bipolar twinning of markov type molecular crystals," Chem. Mater. **12**(11), 3296–3300 (2000).
33. J. Kaneshiro, Y. Uesu, and T. Fukui, "Visibility of inverted domain structures using the second harmonic generation microscope: comparison of interference and non-interference cases," J. Opt. Soc. Am. B **27**(5), 888–894 (2010).
34. M. Rivard, K. Popov, C.-A. Couture, M. Laliberté, A. Bertrand-Grenier, F. Martin, H. Pépin, C. P. Pfeffer, C. Brown, L. Ramunno, and F. Légaré, "Imaging the noncentrosymmetric structural organization of tendon with Interferometric Second Harmonic Generation microscopy," J. Biophotonics **7**(8), 638–646 (2014).
35. E. Shaffer, C. Moratal, P. Magistretti, P. Marquet, and C. Depeursinge, "Label-free second-harmonic phase imaging of biological specimen by digital holographic microscopy," Opt. Lett. **35**(24), 4102–4104 (2010).
36. O. Masihzadeh, P. Schlup, and R. A. Bartels, "Label-free second harmonic generation holographic microscopy of biological specimens," Opt. Express **18**(10), 9840–9851 (2010).
37. Y. Han, V. Raghunathan, R. R. Feng, H. Maekawa, C. Y. Chung, Y. Feng, E. O. Potma, and N. H. Ge, "Mapping molecular orientation with phase sensitive vibrationally resonant sum-frequency generation microscopy," J. Phys. Chem. B **117**(20), 6149–6156 (2013).
38. C.-A. Couture, S. Bancelin, J. Van der Kolk, K. Popov, M. Rivard, K. Légaré, G. Martel, H. Richard, C. Brown, S. Laverty, L. Ramunno, and F. Légaré, "Impact of collagen fibrils polarity on second harmonic generation microscopy," Biophys. J. **109**(12), 2501–2510 (2015).
39. R. Stolle, G. Marowsky, E. Schwarzberg, and G. Berkovic, "Phase measurements in nonlinear optics," Appl. Phys. B **63**(5), 491–498 (1996).

#254768 Received 30 Nov 2015; revised 5 Jan 2016; accepted 5 Jan 2016; published 8 Jan 2016

1. Introduction

In recent years, Second Harmonic Generation (SHG) microscopy has emerged as a powerful technique to probe non-centrosymmetric structures in biological tissues [1–4]. This type of laser scanning microscopy is characterized by an intrinsic sub-micron spatial resolution, due to the confinement of the excitation in the focal volume, robust upon light scattering which provides a high penetration depth within biological tissues [5,6]. SHG is a coherent process that radiates at exactly half the fundamental wavelength and scales quadratically with the number of aligned molecules [7,8]. Importantly, as SHG does not involve population transfer, it considerably reduces phototoxicity and is free from photobleaching [9,10]. Finally, this technique is highly specific for dense non-centrosymmetric media [3,11]. Therefore, SHG microscopy appears to be a very sensitive and specific structural probe, both *ex vivo* and *in vivo*, of the macro-molecular architecture of a wide variety of tissues [12–15].

Specifically, SHG microscopy has been used to image connective tissues rich in fibrillar collagen such as tendon [16,17], cornea [18,19], skin [20,21], fascia [22,23], cartilage [24,25]. In addition, SHG signals have been obtained from the myosin band in skeletal muscles [14,26] and from tubulin forming the microtubules in cultures of neurons [27,28] or during cell mitosis [1,29]. The common property of these three proteins (fibrillar collagen, myosin and tubulin) is their non-centrosymmetric structure at the macro-molecular scale. Interestingly, if the polarity of these non-centrosymmetric components are opposite relative to each other, the SHG signal emitted would be π phase shifted [30] due to the opposite sign of the achiral component of their second order non-linear susceptibility tensor $\chi^{(2)}$. Therefore, measuring the relative phase of the SHG signal carries important structural information about the observed tissues. Unfortunately, this cannot be done in a standard SHG microscope since it only detects the signal intensity and not the phase.

Interferometric Second Harmonic Generation (I-SHG) microscopy overcomes this limitation and probes the relative polarity of harmonophores in tissues. This technique has been originally proposed to characterize non-centrosymmetric materials such as Beta Barium Borate microcrystals [31], organic crystals [32] or periodically poled crystals [33]. Recently, its potential for tissue imaging has been demonstrated. In particular, I-SHG has been used to investigate the bipolarity of myosin filaments in skeletal muscles [26] and the polarity switch in collagen fascicles in tendon [34]. Note that only few other techniques allow to probe the relative polarity in tissues such as holographic SHG [35,36] or interferometric sum-frequency generation (SFG) [37]. However, in its first implementation, I-SHG suffered from two important drawbacks. First, the picosecond pulses excitation [26,34], used to simplify the interferometric part of the setup, decreased drastically the imaging contrast in tissues because of the smaller excitation peak intensity obtained. In practice, while this low contrast was enough to image highly organized structures such as tendon or muscles, it limited the investigation of more complex architectures such as skin or cartilage. Secondly, images were recorded using a translation stage instead of the more classical laser scanning system, based on galvanometric mirrors, because this latter would modify the relative phase to be measured. The use of a sample scanning system decreases imaging speed considerably, which prevents the investigation of dynamical processes. We recently solved the first issue by implementing a new microscope based on a femtosecond excitation and optimizing the temporal overlap between the two beams by compensating the group velocity delay in the microscope [38].

In the present study, we address the second issue by implementing a fast I-SHG imaging setup using the classical laser scanning system to reconstruct images of the sample. We show that, using a model sample, it is possible to calibrate the variable phase shift introduced by the galvanometric mirrors in order to correct the phase image obtained in biological tissues. Finally, we imaged mice tail tendon, a well characterized collagen-rich tissue, and showed that fast I-SHG microscopy recovers the same phase distribution as sample scanning I-SHG, but with an imaging speed approximately 40 times faster. In addition, analyzing the phase

#254768 Received 30 Nov 2015; revised 5 Jan 2016; accepted 5 Jan 2016; published 8 Jan 2016

distribution as a function of the reference phase step, we optimized the number of images acquired, which allowed us to gain another factor 6 on the imaging time. Altogether, this study validates the use of fast I-SHG in biological tissues and opens avenues for dynamical studies of the relative polarity in a wide range of tissues.

2. Materials and methods

2.1 Experimental setup

Interferometric SHG imaging was performed using a custom-built laser scanning inverted microscope [Fig. 1(a)], based on a femtosecond Titanium-Sapphire laser (Tsunami, Spectra Physics) delivering 150fs pulses at 80MHz repetition rate. The excitation wavelength was set to 810nm. The average power on the sample was adjusted to 30mW, using a half-wave plate and a polarizer. A 5cm focal lens is used to focus the laser on a 20-µm BBO crystal (θ = 29.2°, Eskma Optics) to generate a reference SHG beam outside the microscope. Moving the crystal closer or further from the focal point allowed to adjust the reference SHG intensity. Both the fundamental and the reference SHG were collimated using a metallic spherical mirror. A half-wave plate at 810nm, full-wave plate at 405nm is then used to rotate the fundamental polarization. Two calcite wedges, with optical axis placed in the reference polarization direction, are used to introduce a negative delay between the fundamental and reference beams. This allows to pre-compensate for the group velocity dispersion introduced by all the following optics, especially the microscope objective. A second half-wave plate at 810nm, full-wave plate at 405nm, was used to set the fundamental and reference beam polarization back together. A 1.5mm thick BK7 glass plate, placed on a rotating mount, was used to control the phase between the reference and fundamental beam. Finally, a half-wave plate (at 810nm and 405nm) is used to rotate the incident polarization on the sample. Two galvanometric mirrors (TillPhotonics GmbH) are used to scan the laser on the sample. A telescope increases the beam size to fill the back aperture of the microscope objective (Olympus UAPO, 40xW3/340, water immersion, NA 1.15) providing a typical lateral and axial resolution of 0.35x1.2 µm^2 at 810 nm. Mechanical and piezoelectric motors, for coarse and fine adjustments respectively, were used to vertically move the objective, allowing acquisition of z-stacks in the sample. Finally, signals were collected in the forward direction using a condenser (NA 0.55) and detected on a photomultiplier tube (R6357, Hamamatsu Photonics) set at 550V for crystal experiments and at 800V for tissue imaging. The SHG signal was selected using appropriate spectral filters (two FF01-720/SP-25 and a FF01-405/10-25, Semrock). An analyzer was placed before the detector. Images were recorded in the forward direction using 10µs pixel dwell-time and typically 300 nm pixels size.

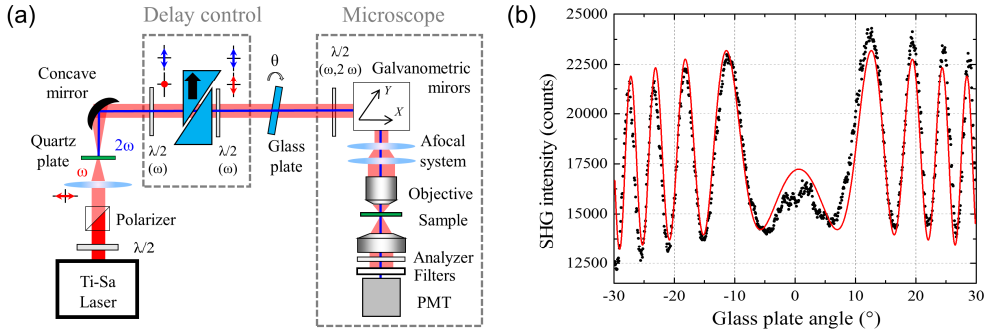

Fig. 1. Experimental setup used for fast I-SHG microscopy. a) Experimental setup and b) characterization of the glass plate used to extract the relative phase.

#254768 Received 30 Nov 2015; revised 5 Jan 2016; accepted 5 Jan 2016; published 8 Jan 2016

2.2 Phase extraction

I-SHG technique retrieves, pixel by pixel, the relative phase of the SHG signal in the sample by measuring its interference with a reference SHG beam.

The three conditions required to optimize interferences are spatial overlap, temporal overlap, and identical polarization. In this setup, the use of a collinear geometry ensures the spatial overlap of the reference SHG with the sample SHG signal. Also, the two calcite wedges allow to correct for the group velocity dispersion introduced by the microscope and therefore provide the temporal overlap between the fundamental pulses at ω and the reference pulses at 2ω. Finally, the analyzer ensures that only the SHG with a specific polarization is detected on the photomultiplier tube. As a consequence, the modulation between the sample and the reference SHG beams is maximized compared to the background SHG signal, which ensures a high interferometric contrast.

To extract the interferometric term from the raw SHG images acquired with I-SHG setup, we subtract two raw images taken at π shifted reference phases:

$$I\left(\varphi_{ref}\right) - I\left(\varphi_{ref} + \pi\right) = 4\sqrt{I_{ref} I_{\text{samp}}}\cos\left(\varphi_{\text{samp}} - \varphi_{ref}\right) \quad (1)$$

where I_{ref} and I_{samp} are the reference and sample SHG intensities respectively and φ_{ref} and φ_{samp} their phases. This eliminates the background SHG signals ($I_{ref} + I_{samp}$), independent from the reference phase, and doubles the interferometric contrast. The acquisition of 24 pairs of images, with reference phase varying from 0° to 345° by 15° phase step, allows to interpolate the amplitude and relative phase of the interferometric contrast. For every pixel, we determine the reference phase corresponding to the maximum amplitude, which provides an image of the relative phase in the sample. As a convention, a red (resp. green) color will be assigned to the negative (resp. positive) phase values in all the following images.

The reference phase (φ_{ref}) is controlled by rotating the BK7 glass window. However, this requires to calibrate the nonlinear relationship between the glass plate angle and the resulting φ_{ref} values. To that end, we set another y-cut quartz plate in place of the sample in the focus of the objective. As only the relative phase is relevant here, the zero value for the reference phase was assigned to an arbitrary value. Rotating the glass plate allows to retrieve the typical interferometric pattern [Fig. 1(b)] as described by Stolle *et al.* [39], which provides the relative value of φ_{ref} for any glass plate angle.

2.3 Sample preparation

Samples were obtained from 8 weeks old male C57/Bl6 mice. The tails were harvested and fixed in 4% PFA for 6 to 8 hours at 4°C. Using a surgical scalpel, samples were cut in few mm pieces and tail tendon compartments were opened and exposed under a Nikon dissection scope with 0.7-83 zoom lens. After harvesting, tail tendons were embedded in OCT-compounds Tissue-Tek (Electron Microscopy Sciences, Hatfield, PA) and 10 µm section was cut using a Leica cryostat CM3000 (Leica Microsystems, Wetzlar, Germany). The sections were transferred onto a 150-µm thick coverslips (VWR International, West Chester, PA; 25_60 mm, No. 1) treated with 3-aminopropyltriethoxysilane or gelatin-chromium potassium sulfate solution (gelatin type A, and chromium potassium sulfate; both Sigma, St. Louis, MO) for optimal tissue adhesion.

3. Results

3.1 Fast I-SHG in periodically poled lithium niobate

To validate our measurements, we used Periodically-Polled Lithium Niobate (PPLN) crystal as a model sample. Figure 2 shows the 24 subtraction images acquired. As expected, we directly observe different phases (represented in red and green), corresponding to the $\chi^{(2)}$

#254768 Received 30 Nov 2015; revised 5 Jan 2016; accepted 5 Jan 2016; published 8 Jan 2016

domains in PPLN. However, we also observed a circular pattern indicating variations of the relative phase within the field of view.

This circular pattern is attributed to the dispersion introduced by the microscope objective. Indeed, using two galvanometric mirrors to acquire the image, we change the incident angle of the excitation beam on the back pupil of the objective. This changes the optical path within the microscope, in particular the objective, which is virtually equivalent to the rotation of the glass plate used to scan the phase. Therefore, when scanning the laser beam in the microscope, the phase shift between the reference and the sample beams varies from one pixel to another. This explain the circular pattern observed in Fig. 2 since a given incident angle corresponds to a constant dispersion. For a fixed φ_{ref}, the reference and pump beams are gradually phase shifted as we progress further from the center of the interferometric pattern, which eventually leads to destructive interferences appearing as black circles in Fig. 2.

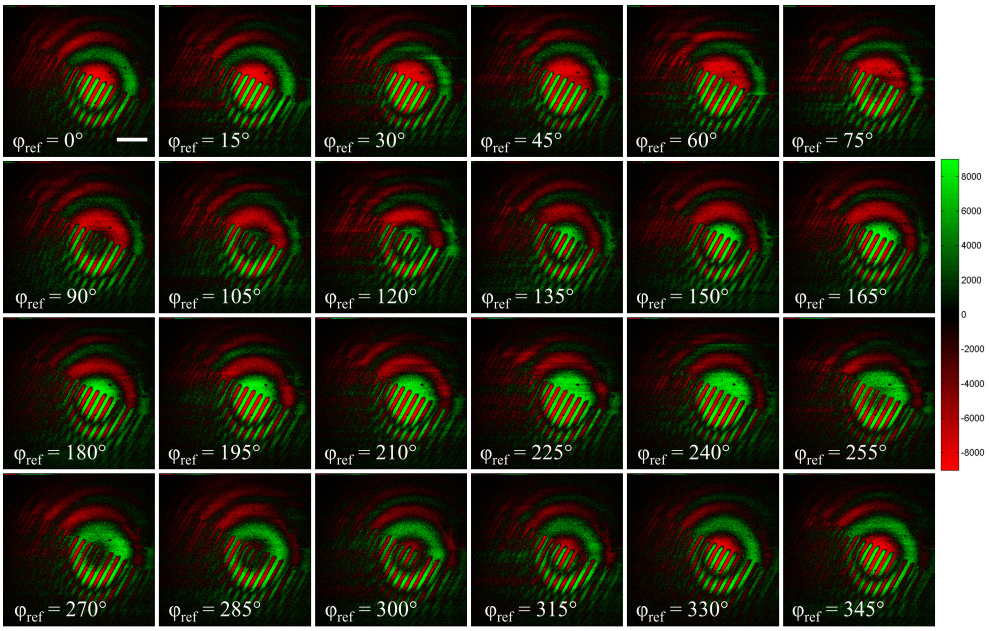

Fig. 2. Subtraction stack obtained in PPLN sample. Red and green colors stand respectively for negative and positive values after the subtraction. Therefore, red and green colors reflect the sign of the cosine term in Eq. (1) and denote π phase shifted sample phase. Scale bar: 50µm.

Interestingly, the phase shift introduced by the microscope depends only on the excitation geometry and not on the sample used. Therefore, using a known sample, it is possible to calibrate this effect and correct it in the phase image. This is achieved using another 350 µm y-cut quartz plate as a sample, the same configuration previously used for the calibration of the glass plate. Measuring the interference obtained between the signal generated in the reference and the sample quartz, we directly image the phase shift introduced during the laser scanning. Figures 3(a) and 3(b) show the resulting phase image and the corresponding phase histogram. In particular, Fig. 3(b) shows a very broad phase distribution, while an unbiased phase measurement would have showed a very narrow peak in such a crystalline sample. Figure 3(c) shows the profiles within the subtracted images, along the black dashed line in Fig. 3(a), for different reference phases (*i.e.* different positions of the glass plate). These profiles are very similar to the one shown in Fig. 1(b), which confirmed that changing the angle of the laser beam on the back pupil of the objective has a similar effect than the rotation of the glass window outside the microscope. All in all, the zero phase value in Fig. 1(b), chosen while calibrating the glass plate angle, can only recover the sample relative phase correctly in the center of the circular fringes in Fig. 3(a).

#254768 Received 30 Nov 2015; revised 5 Jan 2016; accepted 5 Jan 2016; published 8 Jan 2016

In addition, Fig. 3(c) shows a decrease of the interferometric contrast as we progress further from the center of the circular pattern. This is due to the delay introduced by the microscope objective between the fundamental beam and the reference SHG. Importantly, the calcite wedges used to pre-compensate for the delay brought by the microscope, which optimizes the temporal overlap between fundamental and reference pulses, introduce the same correction in the whole field of view. This results in a maximum contrast in the center of the circular pattern, where the temporal overlap is optimized, as observable in Fig. 3(c), but a drastically decreased contrast in the border.

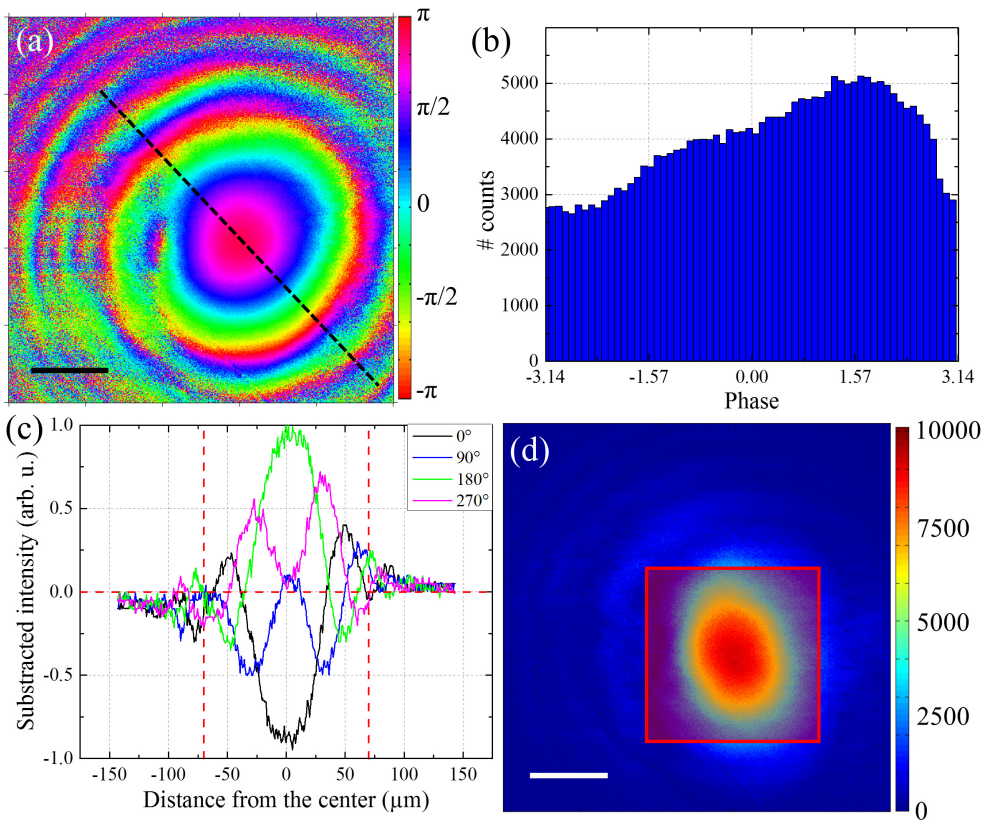

Fig. 3. Impact of the sample scanning in phase measurement. a) Phase calibration in a sample quartz plate. b) Histogram of the relative phase measured in the sample quartz plate. c) Profile of the subtracted images, calculated along the black dashed line in (a), as a function of the distance from the center of the circular pattern, for various reference phases. d) Interferometric contrast in the field of view. Scale bars: 50µm.

Figure 3(d) shows an image of the interferometric contrast (amplitude of the cosine modulation following Eq. (1) obtained in the sample quartz. As the contrast very rapidly decreases in the border of the image, it appears that only a small portion of the field of view can be effectively used to perform I-SHG. The size of the exploitable part of the image depends on the sample imaged. Indeed, in PPLN, the very well organized crystalline domains result in a very high interferometric contrast, which remains sufficient to extract the relative phase in a large field of view (approximately 200x200µm^2). On the contrary, in biological tissues, the contrast is usually lower which imposes a sharper limit (typically 100x100µm^2). Interestingly, the interferometric contrast obtained in the center of the image is similar to the one reported previously [38] using the sample scanning system. Therefore, this approach will be applicable in disorganized collagen structures such as skin or cartilage, but with a limited field of view. Finally, it is worth noting that the slightly elliptical shape observed in Fig. 3(d)

#254768 Received 30 Nov 2015; revised 5 Jan 2016; accepted 5 Jan 2016; published 8 Jan 2016

is attributed to the chromatic aberrations introduced by the microscope objective, which results in a small spatial shift between the reference and the fundamental beam. Note that this spatial shift is likely to contribute to the decrease of contrast in the edge of the field of view.

3.2 Phase correction

Measuring the phase introduced by the microscope allows to correct the phase images obtained with the laser scanning system. In all the following images, we limit our field of view to 100x100µm^2, where the interferometric contrast is sufficient to accurately extract the relative sample phase. Figures 4(a) and 4(b) show respectively the phase image and histogram obtained in PPLN. After a subtraction of the phase introduced by the microscope, we obtained the corrected phase image and histogram shown in Figs. 4(c) and 4(d). As the phase extracted is only relative, the actual position of the peaks is not relevant as it depends on the choice of the zero reference phase. However, the peak width is very important as it has been shown to provide information about the polarity of non-centrosymmetric structures in the sample [26,34]. Therefore, in all the following phase distribution, the origin of the phase was chosen to ensure that the two peaks are located at ± π/2. Using a bi-Gaussian fitting of the phase distribution in Fig. 4(d) we found the two peaks width to be σ = 0.063π ± 0.005π and σ = 0.059π ± 0.001π respectively.

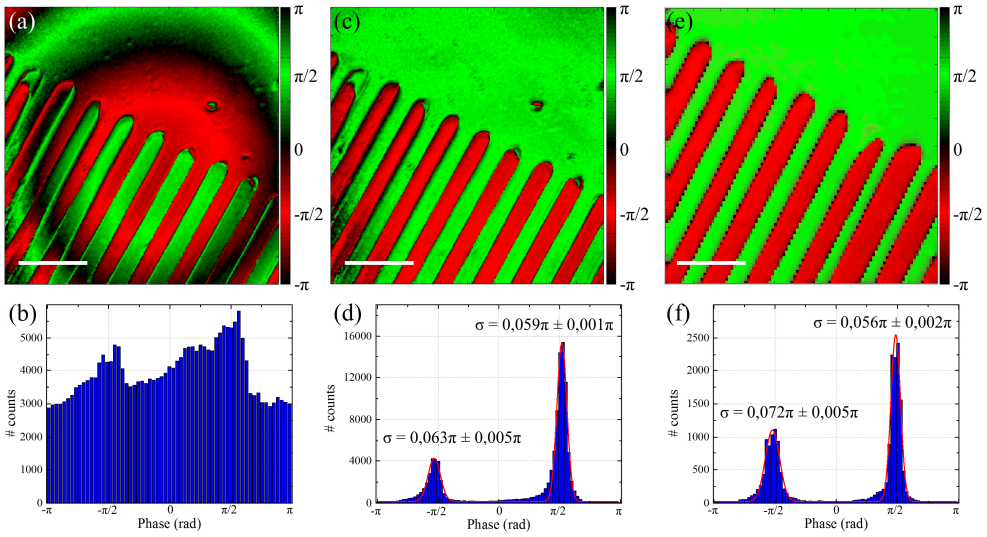

Fig. 4. Phase correction in PPLN. Phase a) image and b) histogram measured in PLLN sample before correction. Phase c) image and d) histogram after correction of the phase shift introduced by the microscope. Phase e) image and f) histogram measured in PPLN sample using the former sample scanning I-SHG setup. The red straight lines in d) and f) are bi-Gaussian fittings of the phase distributions used to retrieve the peaks width σ. Scale bars: 25µm.

To validate our phase correction, we compared our results to the ones obtained previously using the sample scanning I-SHG microscope [34]. Figures 4(e) and 4(f) show the phase image and histogram of the same PPLN sample (but not the exact same ROI) acquired with sample scanning instead of laser scanning. We obtained very similar results, especially for the peaks width σ = 0.072π ± 0.005π and σ = 0.056π ± 0.002π respectively. This demonstrates that the phase correction used with laser scanning allows to recover the exact phase distribution in the sample.

#254768 Received 30 Nov 2015; revised 5 Jan 2016; accepted 5 Jan 2016; published 8 Jan 2016

3.4 Fast I-SHG in tendon

To validate our approach in biological tissues, we measured the phase distribution in tendon. Using the sample scanning set-up, I-SHG microscopy has previously shown that in tendon the SHG phase is preserved over long distances in the fibril direction and switches very rapidly in the transverse direction [34]. Figure 5(a) shows the uncorrected phase image, obtained with the laser scanning system, in which the phase shift introduced by the microscope is directly observable. In particular we observe a sharp switch of the phase from $-\pi/2$ to $\pi/2$ (or vice versa) along the fibrils, which is in contradiction with the previous observation. Again, the region of interest is limited to $100\text{x}100\mu\text{m}^2$ to maintain a high interferometric contrast in the whole image. Figure 5(b) shows the phase after correction. It shows that the correction allows to recover the expected behavior in the tendon images and therefore to extract the relative phase information in the whole image. It is worth noting that, since the phase correction to apply is determined in a crystalline sample, the accuracy of the relative phase measurement is not significantly modified compared to the former sample scanning.

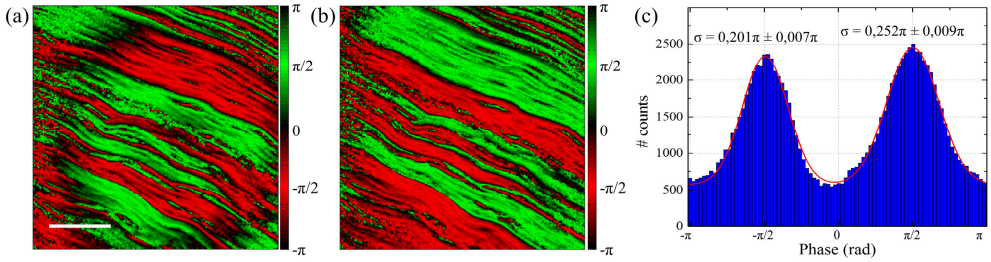

Fig. 5. Fast I-SHG imaging of a mice tail tendon. a) and b) Phase images before and after correction respectively. c) Corrected phase distribution obtained in tendon. Red straight line is the bi-Gaussian fitting used to retrieve the peaks width σ.

Finally, Fig. 5(c) shows the phase distribution in the corrected image. It is worth noting that this distribution is remarkably similar to the one obtained with sample scanning [34]. In particular, the bi-Gaussian fitting of the phase distribution provides the width of the two peaks $\sigma = 0.218\pi \pm 0.003\pi$ and $\sigma = 0.247\pi \pm 0.003\pi$, which are in very good agreement with the previously reported values [34].

Importantly, images obtained with the galvanometric mirrors were acquired at 5s/frame, while, for the exact same field of view and pixel size, images were acquired at 195s/frame with the sample scanning system. Since image acquisition is 39 times faster with laser scanning than with sample scanning, the implementation of a laser scanning capable of retrieving an accurate phase in the sample is a significant improvement for I-SHG microscopy. Altogether, since we acquired here 36 images to extract the phase, the phase image in Fig. 4(c) was acquired in 180 seconds whereas the phase image in Fig. 4(e) was acquired in about 2 hours.

3.5 Optimization of the phase step

In addition, to reduce even more the imaging time, the number of images acquired can be significantly reduced. Indeed, Fig. 4(c) and e has been acquired using 15° reference phase step, which corresponds to 36 images. Increasing the phase step would reduce the number of images and therefore significantly decrease the imaging time. However, this might result in a decrease of the phase determination accuracy. To evaluate this effect we measured the width of the two peaks of the phase distribution from tendon sample as a function of the phase step. Results are displayed in Fig. 6(a), showing that the peak width does not change significantly, even with a phase step of 90° corresponding to only 6 images acquired.

#254768 Received 30 Nov 2015; revised 5 Jan 2016; accepted 5 Jan 2016; published 8 Jan 2016

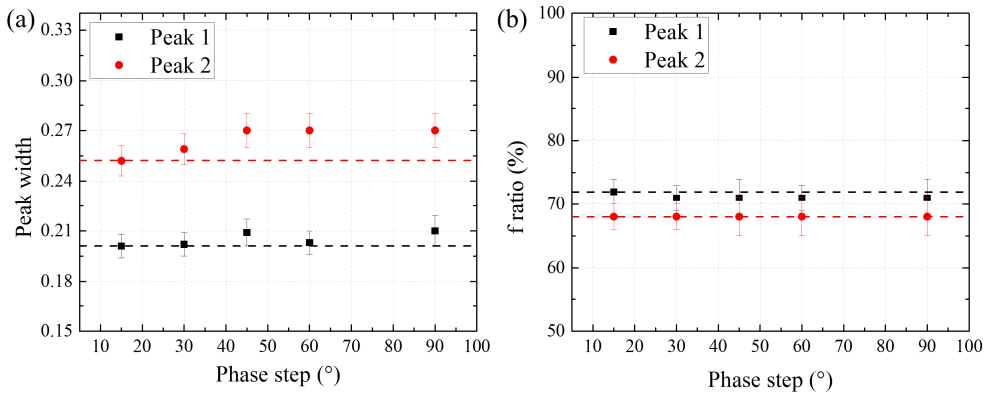

Fig. 6. Impact of the reference phase step on the peak width determination. a) Peak width measured in tendon as a function of the reference phase step used for the image acquisition. b) Ratio of fibrils pointing in opposite direction (f ratio) as a function of the reference phase step. Black squares and red circles correspond to the first peak (centered at $-\pi/2$) and the second peak (centered at $\pi/2$) respectively. Red and black straight lines indicate the more precise value obtained with a 15° reference phase step.

Finally, the peak widths measured in Fig. 6(a) allow to extract the ratio of fibrils pointing in opposite direction [34,38].

$$f = \frac{N\left(+\chi^{(2)}\right)}{N\left(+\chi^{(2)}\right)+N\left(-\chi^{(2)}\right)} \tag{2}$$

where $N(+ \chi^{(2)})$, resp. $N(-\chi^{(2)})$, stands for the number of collagen fibrils having a positive, resp. negative, nonlinear susceptibility. Indeed, previous work has demonstrated that the f ratio is directly related with the width of the phase distribution. It is worth noting that the value of the f ratio extracted does not significantly change with the reference phase step, as shown in Fig. 6(b). Therefore, at least in tendon, only 6 images are required to probe efficiently the phase distribution, which, using the laser scanning and the phase correction, limits the imaging time to 30s.

5. Conclusion

We reported here the first implementation of fast I-SHG microscopy using a scanning system based on galvanometric mirrors. To that end, we calibrated the phase shift introduced by the scanning system in the microscope. As a proof of concept, we imaged the phase in periodically poled lithium niobate and showed that the phase correction allows to retrieve the expected phase distribution, in particular the peaks width. Finally, we successfully imaged the phase distribution in mice tail tendons which demonstrates that this set-up allows to probe efficiently the distribution of polarity in tissues with an imaging speed 39 times faster than the sample scanning. This imaging time improvement can be even push further to 234 by reducing the number of images acquired, without significant loss of precision. We anticipate that this improvement will serve as a significant enhancement to current I-SHG microscopy, allowing to image the phase variations in dynamical processes.

Acknowledgments

The authors acknowledge the financial support from the Canada Foundation for Innovation (CFI), the Natural Sciences and Engineering Research Council of Canada (NSERC), le Fond Québécois de la Recherche sur la Nature et les Technologies (FQRNT) and the Conseil de Recherches en Sciences Naturelles et en Génie du Canada (CRSNG).

7.2 Comments

The polarization of excitation is set parallel to the PPLN domains, and changed to be parallel to the fibers in tendon.

Figure 3(a) and (d) of the article shows that the I-SHG interferometric contrast decreases sharply beyond a FOV of 100×100μm^2 in galvos-scanning. The beam scanning through the objective was blamed, but two effects could actually be involved:

(a) the *spatial* overlap of the sample SHG and the reference SHG when the beam is scanned off-axis, as both can have different aberrations through the scanning head (galvos + telescope), or be focused differently at large scanning angles (deformed focal point, see section 3.1.3 or 3.3). It is also possible that only one of these fields is deformed, still leading to a poor overlap of both fields at the detector. In all cases, this is a sort of enhancement of the vignetting effect previously encountered (3.1.3).

(b) the same effect as (a), but in the *temporal* domain: the beam travels through slightly more glass in the galvos' telescope and microscope objective, which increases the GVM (3.2.1) at edges.

According to the equation of GVM 3.2, the maximum deflection angle α for a 200×200μm^2 scan is $\tan\alpha$=20*0.2/(2*50) = 0.04 (objective 20X and scan lens of 50mm). We can calculate that the 20X objective has the equivalent of 45mm of BK7 glass, such that at the edges 45*0.04 = 1.8mm more BK7 is crossed. According to equation 3.5, this means a delay of 1.8/1000*(1/1.97e8-1/1.90e8)*1e15 = 337fs. This approximately represents the maximum spacing beyond which two 150fs pulses no longer overlap, and is thus consistent with a substantial loss of contrast in the edges of the image. The point (a) (spatial effect) could also play a role, but is difficult to estimate how much of an effect it has as the aberrations of the two lenses in the galvos' telescope, and the objective's, must be estimated. Also, this effect alone is responsible for a vignetting much smaller in standard SHG images (3.1.3), such that it is considered smaller than (b). Finally, this hypothesis is reinforced by the much less significant loss of contrast in galvos using ps pulses (Fig 9.5 C).

The speed difference of laser-scanning versus sample-scanning mentioned in the article was later reduced by improving the control of the motorized stage (see section A.3). Also, the number of phase-shifts required for the phase extraction is studied in section 3.2.4. Finally, the "fast I-SHG" was sped up by another order of magnitude with the single-frame I-SHG of chapter 9. However, this arrangement was still sufficient to probe a relatively fast process: microtubules in spindles during mitosis, which is the subject of the article of the next chapter (8).

Chapter 8

I-SHG in microtubules

This chapter shows an application of the findings in chapter 7: using fast I-SHG to image the relative phase of microtubules inside mitotic spindles. The article, with my colleague Stephane Bancelin as the first author, has been inserted. This work showed the potential of I-SHG to image dynamic processes, and its limitations for dealing with moving samples. It later motivated the development of a single-scan I-SHG to enhance the precision of measurement.

8.1 Article

(EN) Probing microtubules polarity in mitotic spindles *in-situ* using Interferometric Second Harmonic Generation Microscopy.

(FR) Mesure de la Polarité des Microtubules dans des Fuseaux Mitotiques *in situ* par Microscopie de Génération de Seconde Harmonique Interférométrique.

Submitted: 20th February 2017; Revised 14th April 2017; Accepted: 15th June 2017; Published online: 28th July 2017.

Citation: Scientific Reports, 7:1(6758), 2017.

DOI: 10.1038/s41598-017-06648-4

SCIENTIFIC REPORTS

OPEN

Probing microtubules polarity in mitotic spindles *in situ* using Interferometric Second Harmonic Generation Microscopy

Received: 20 February 2017
Accepted: 15 June 2017
Published online: 28 July 2017

S. Bancelin[1], C.-A. Couture[1], M. Pinsard[1], M. Rivard[1], P. Drapeau[2] & F. Légaré[1]

The polarity of microtubules is thought to be involved in spindle assembly, cytokinesis or active molecular transport. However, its exact role remains poorly understood, mainly because of the challenge to measure microtubule polarity in intact cells. We report here the use of fast Interferometric Second Harmonic Generation microscopy to study the polarity of microtubules forming the mitotic spindles in a zebrafish embryo. This technique provides a powerful tool to study mitotic spindle formation and may be directly transferable for investigating the kinetics and function of microtubule polarity in other aspects of subcellular motility or in native tissues.

Over the years, Second Harmonic Generation (SHG) microscopy has emerged as an effective tool in biology[1–3]. Like in two-photon excited fluorescence (2P), this type of laser scanning microscopy is characterized by an intrinsic 3D sub-micron resolution that is robust upon light scattering and which allows for higher image depth when compared to confocal microscopy[4,5]. SHG is a nonlinear optical process in which highly polarizable and non-centrosymmetric structures emit photons at exactly half the excitation wavelength[6]. Since SHG does not involve population transfer, it significantly reduces phototoxicity and is photobleaching-free[7]. The emitted light results from the coherent sum of the electromagnetic field generated by every single SHG emitter and thus scales quadratically with the number of aligned molecules sharing the same polarity[8]. Indeed, adjacent molecules of the same polarity will emit strong SHG signals due to constructive interference while the SHG signal will almost vanish in the case of adjacent molecules of opposite polarity[9].

Over the years, many groups have demonstrated that exploiting the intrinsic nonlinear optical properties of the sample is a valuable, although challenging approach. In the case of SHG, since the signal is highly specific for dense non-centrosymmetric media[3], only few biological molecules produce detectable SHG signals[1,10–12]. SHG microscopy has been used to image collagen-rich tissues such as tendon[13], cornea[14], skin[15], fascia[16] and cartilage[17]. Furthermore, SHG signals have been obtained from the myosin band in skeletal muscles[1,12]. Lastly, SHG signal have been reported in microtubules (MTs)[1,11].

MTs are a key component of the cell cytoskeleton, involved in structural support and intracellular transport. Formed as a lattice of tubulin heterodimers, having two different ends, MTs exhibit an intrinsic polarity. This polarity has important biological consequences since it determines the dynamics of polymerization and the directionality of molecular motor movement[18,19] and plays a role in the organization and function of various cell type[20–22]. The polarity of MTs has long been thought to be involved in the assembly of mitotic spindles[23], responsible for the segregation of chromosomes during cell division. Indeed, near the centrosomes, the MTs exhibits the same polarity while in the center MTs are antiparallel[24,25]. However, the relationship between MTs polarity and spindle dynamics during mitosis remains poorly understood, mainly because of the huge challenge to measure MTs polarity in spindles.

Several methods have been used to record the polarity of MTs. Currently, the gold standard remains the hook method[26], based on electron microscopy to directly visualize individual MTs. However, this technique requires thin and fixed sections and has been so far limited to study few tissue preparations[27,28]. Fluorescently labelled

[1]Institut National de la Recherche Scientifique, Centre Energie Matériaux Télécommunications (INRS-EMT), Université du Québec, 1650 boulevard Lionel-Boulet, Varennes, QC, J3X 1S2, Canada. [2]Département de Neurosciences, Centre de Recherche, Centre Hospitalier de l'Université de Montréal, Montreal (QC), 900 rue Saint-Denis, Pavillon R, H2X 0A9, Canada. Correspondence and requests for materials should be addressed to F.L. (email: legare@emt.inrs.ca)

plus-end tracking proteins[29] and laser ablation[30] provide information about MT polarity, but the quantification remains indirect and these techniques are invasive. More recently, SHG microscopy has been proposed as an alternative method to probe, non-invasively, the polarity of MTs in thick living tissues. Individually, MTs are very weak SHG emitters. However, the constructive interference in MTs arrays that have the same polarity results in detectable signals that have been used to visualize MTs in neurons[31,32], cilia[12], astroglial filaments[33] and mitotic spindles[1,34–36]. Kwan *et al.* demonstrated that the polarity of MTs can be extracted from the ratio of forward and backward SHG signals[32] with a limitation in disordered MTs arrays, such as the mitotic spindle. Lastly, Yu *et al.* established a very elegant method to measure MT polarity in spindles, based on a combination of SHG and 2 P images of fluorescently labelled MTs[36].

Here, we use interferometric SHG (I-SHG) to measure the polarity of MTs in mitotic spindles without requiring any exogenous labelling. Originally developed to characterize non-centrosymmetric crystals[37,38], I-SHG is based on the measurement of the phase of the SHG signal. In the past years, its potential for tissue imaging has been demonstrated with different proteins, such as myosin from skeletal muscle[39] and collagen from tendon and cartilage[40,41]. Having recently solved one of the main drawbacks of I-SHG[42], namely the long imaging time, we demonstrate here the possibility to use I-SHG to record the dynamical evolution of MT polarity in mitotic spindles from live zebrafish embryos.

Materials and Methods

Experimental setup. I-SHG imaging was performed using a custom-built laser-scanning microscope (for a complete description of the setup see ref. 42). In short, the excitation source was a mode-locked Ti:Sapph laser (810 nm wavelength, 80 MHz repetition rate, ~150 fs pulses width, Tsunami, Spectra Physics) pumped by a 12 W Millenia Pro laser (Spectra Physics). Beam intensity was controlled using a half-waveplate and a Glan-Thompson polarizer. A 5 cm focal lens was used to focus the laser on a 20-µm BBO crystal ($\theta = 29.2°$, Eskma Optics) to generate a reference SHG beam outside the microscope whose intensity was adjusted by moving the crystal closer or further from the focal point. Both the excitation (810 nm) and the reference SHG (405 nm) were collimated using a metallic spherical mirror. To pre-compensate the group delay introduced by the optical components downstream, two calcite wedges were inserted between two half-wave plates at 810 nm and a full-wave plate at 405 nm. A 1.5 mm thick BK7 glass plate was placed on a rotating mount to control the phase between the reference and the excitation beam. A half-wave plate (at 405 nm and 810 nm) was inserted in front of the scanner to control the incident polarization. The microscope incorporated two galvanometer-mounted mirrors (TillPhotonics GmbH), a telescope to overfill the back aperture of the z-motorized water-immersion objective (40x, NA 1.15, Olympus), appropriate spectral filters (two FF01-720/SP-25 and a FF01-405/10–25, Semrock) and a photomultiplier tube (R6357, Hamamatsu Photonics) set at 1050 V. Scanning and signal acquisition were synchronized using a custom-written LabView software and a multichannel I/O board (National Instruments). $50 \times 50\,\mu m^2$ images were recorded in the forward direction, in about 2 s, using 30 µs pixel dwell-time and typically 200 nm pixel size. The average power after the objective was typically 100–150 mW. Raw data visualization was performed with ImageJ (NIH, USA) and image processing was performed with MATLAB (The MathWorks) and Origin 10 (OriginLab) as described below.

Phase extraction. I-SHG is based on the interference of the SHG with the reference beam to extract the phase of the signal generated in the sample (for a complete description of the method see refs 41 and 42). Briefly, the nonlinear relationship between the glass-window angle and the phase shift introduced was calibrated with a 350 µm thick y-cut quartz plate used as a sample. This allowed, when looking at biological samples, to introduce a control phase shift between the two SHG beams. Then, we acquired 9 images, with reference phase varying from 0° to 480° by 60° phase steps. Subtracting two-by-two the images, taken with a 180°-phase shift (0°–180°; 60°–240°; 120°–300°…), allowed us to extract the interferometric term and to interpolate both the amplitude and the relative phase following eq. 1:

$$I(\varphi_{ref}) - I(\varphi_{ref} + \pi) = 4\sqrt{I_{ref} I_{\mathrm{samp}}}\,\cos(\varphi_{\mathrm{samp}} - \varphi_{ref}) \quad (1)$$

where φ_{ref} and I_{ref} (respectively φ_{exp} and I_{exp}) stand for the phase and the intensity of the reference (respectively sample) SHG beams. Finally, the phase image was reconstructed by determining, in every pixel, the reference phase that corresponds to the maximum amplitude. Note that the rotation of the glass plate, used to scan the reference phase, imposed a dead-time between images and that the manual adjustment of the incident polarization and the depth of focus between phase-stack recording, to correct for the slight movement of the spindles result in about 45 s of temporal resolution.

Phase correction. The use of two galvanometric mirrors to scan the incident angle of the excitation beam on the back pupil of the objective led to a change in the optical path, which is virtually equivalent to rotating the glass plate. Therefore, when scanning the laser to acquire images, the phase difference between the reference and the sample SHG is gradually shifted as we progress further from the center of the interferometric pattern. However, since this phase shift depends only on the excitation geometry, it is possible to calibrate this effect[42]. This was achieved using again a y-cut quartz plate as a sample to directly image the phase shift introduced in the microscope. Nevertheless, since the calcite wedges used to pre-compensate for the group delay dispersion brought by the microscope introduced the same correction in the whole field of view, we observed a sharp decrease in interferometric contrast as we progressed further from the center (see ref. 42 for further discussion of this effect). Therefore, it appeared that only a small portion ($\sim 100 \times 100\,\mu m^2$) of the field of view could be effectively used to perform I-SHG with laser scanning acquisition. While an important limitation to image biological tissues, this was sufficient to measure the phase of SHG signal from mitotic spindles.

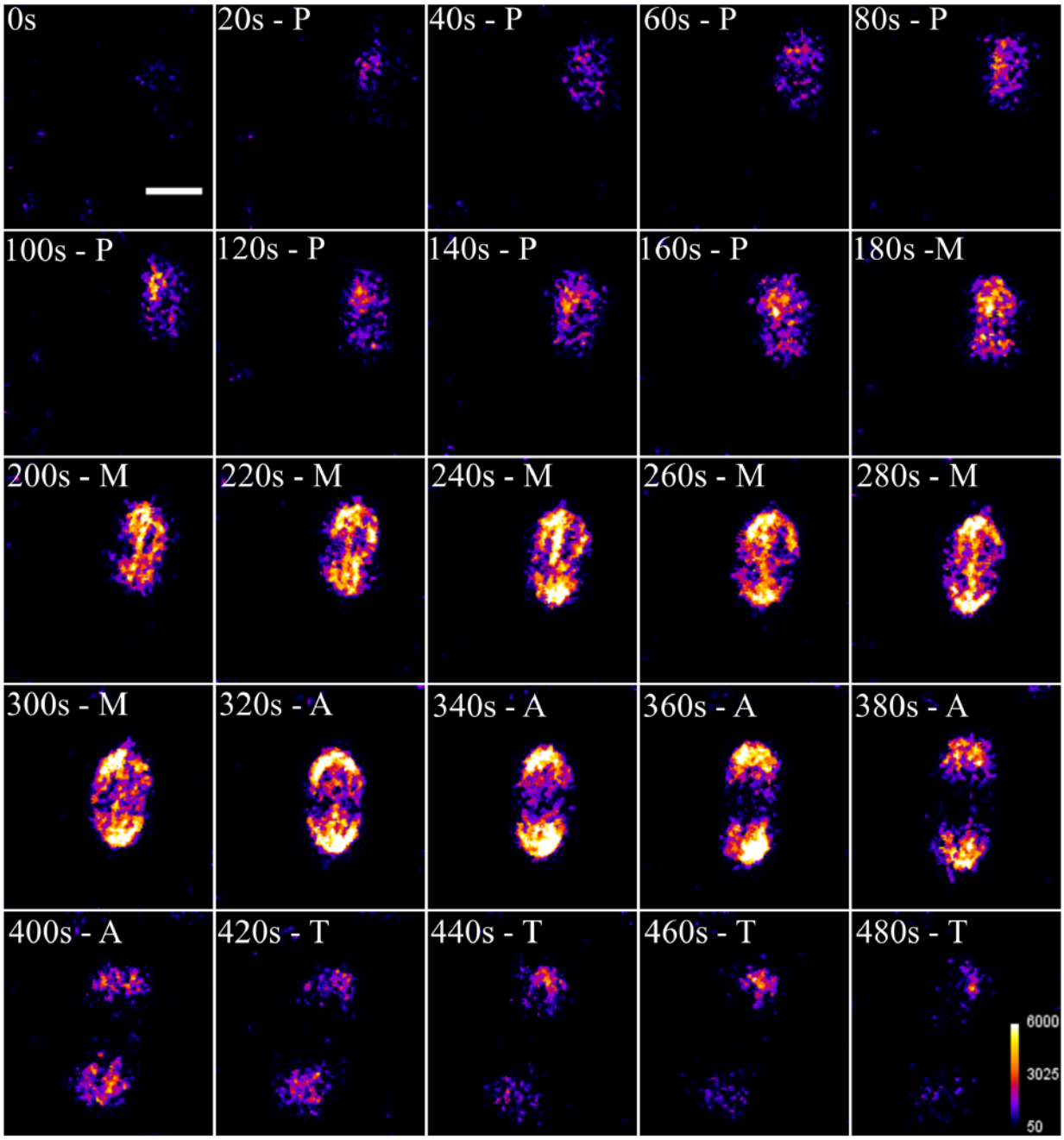

Figure 1. Time-lapse SHG imaging of mitotic spindles during mitotic division of a zebrafish embryo. Prometaphase (P; 20–160 s), metaphase (M; 180–300 s), anaphase (320–400 s) and telophase (420–480 s). Average power at focus: 150 mW, photomultiplier tube set at 1100 V. Scale bar: 10 µm.

Sample preparation. Wild-type zebrafish (*Danio rerio*) of the TL line were bred and maintained according to standard procedures[43]. All experiments were performed in compliance with the guidelines of the Canadian Council for Animal Care and conducted at the *Centre de Recherche du Centre Hospitalier de l'Université de Montréal* (CRCHUM). All protocols were approved by the animal care committee of CR-CHUM (agreement number: N15018PMDz). Embryos were mounted in a 3 cm Petri dish with a 1 cm hole at the bottom sealed with a 170 µm-thick coverslip. Another coverslip was set on top to minimize sample motion during imaging. Temperature in the room was about 20 °C, which slows down the development compared to the standard developmental table[44]. Embryos were imaged within 4 h after fertilization.

Results

Using time-lapse SHG microscopy, we imaged the mitotic divisions of a zebrafish embryo within 4 h after fertilization to record the dynamical behavior of mitotic spindles (Fig. 1). The SHG signal appeared during the prometaphase, when the MTs elongate to form the mitotic spindles (20–160 s). Then, the flattening and broadening

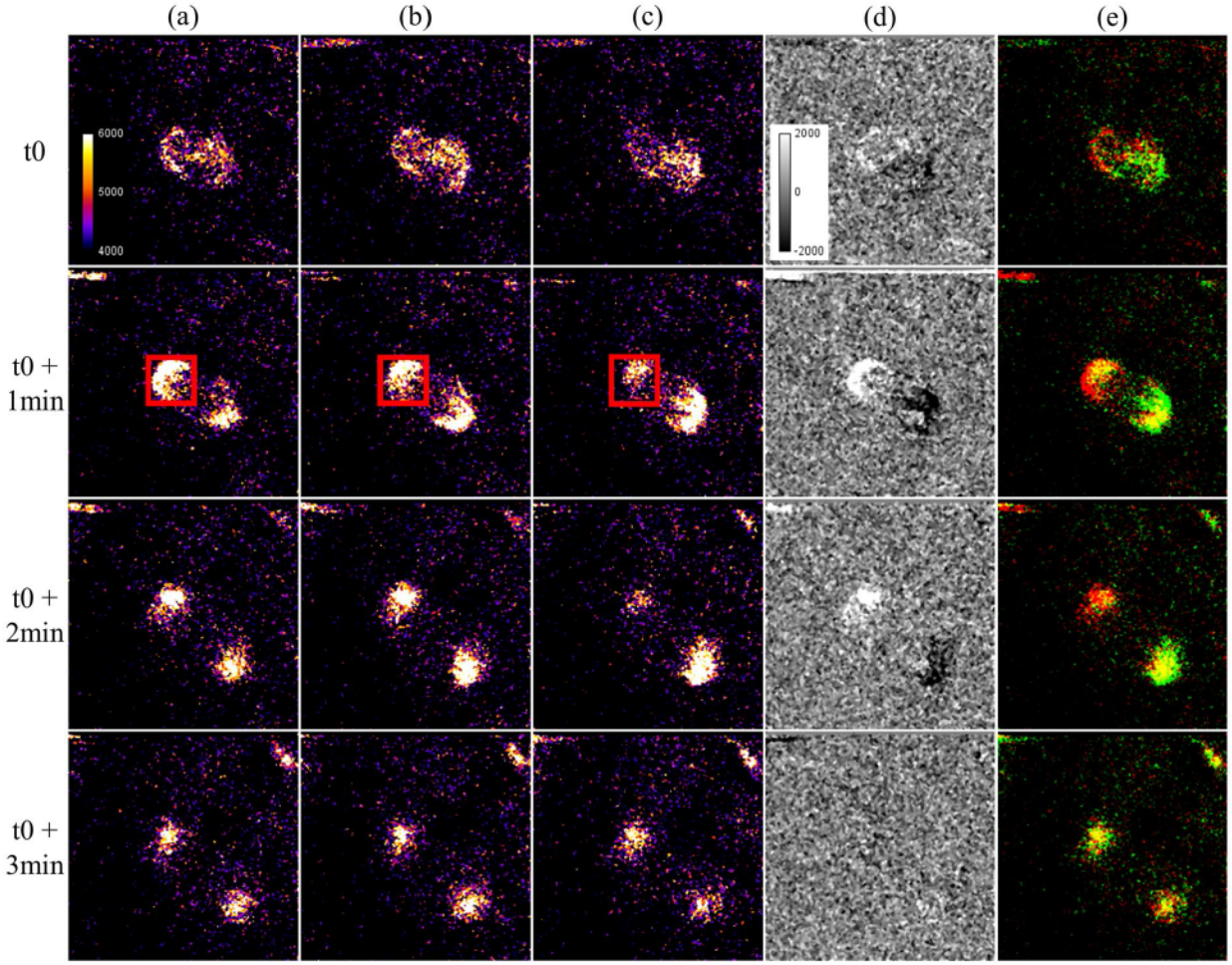

Figure 2. I-SHG of mitotic spindles in a zebrafish embryo. (**a**–**c**) Images acquired with different reference phases (0°, 90° and 180° respectively). Constructive and destructive interference occurs in opposite poles at 0° and 180° while no variations are observable at 90°. (**d**) Subtraction of the images (**a**,**c**) showing the interferometric contrast in the two poles. (**e**) 2-colors merge of the images acquired at 0° (in red) and 180° (in green). Average power at focus: 100 mW, photomultiplier tube set at 1050 V. Field of view: $50 \times 50\,\mu m^2$.

of the MTs resulted in an increase in the SHG signal and revealed the alignment of the chromosomes between the centrosome during the metaphase (180–300 s). The migration of the chromosomes occurs in the anaphase (320–400 s) and SHG microscopy allowed us to clearly monitor the separation of mitotic spindles. Finally, the endogenous SHG signal gradually vanished during telophase while the mitotic spindles uncondensed and the MTs dispersed into the cell (420–480 s). Note that, during the metaphase, SHG from the middle region always appeared dimmer, as previously reported[1,20], which is due to an antiparallel alignment of MTs (see further in the Discussion).

We then used I-SHG to visualize the change in spindle polarity throughout the course of mitosis. To that end, we acquired phase-stacks at two different times in metaphase and in anaphase (Fig. 2a–c). A median filter was applied to remove the noise. Note, the remaining background was not due to noise, but to the reference signal used in I-SHG. While varying the reference from 0° (a) to 180° (c), we could directly observe that the SHG intensity from pole varied. This is highlighted in the red rectangle, where the intensity was maximal at 0° of reference phase, due to constructive interference, diminished at 90° and was minimal at 180° since the reference and sample SHG interfered destructively. It is worth noting that the other pole exhibited the inverse behaviour, which highlights the interferometric nature of this variation.

To better visualize these variations of intensity, Fig. 2d and e display respectively the subtraction and the merged colors of the corresponding images (a and c). Notably, the variations of contrast upon the progress of mitosis in Fig. 2d indicates different degrees of polarity from the beginning of the metaphase to the end of anaphase. Furthermore, the different colors observed in the two poles in Fig. 2e revealed the presence of two opposite polarities. Note that no prior knowledge of the MTs orientation is required here since the optimization of the SHG intensity from the spindles (for a fixed reference phase) allows to match the laser polarization with the average MTs orientation.

From the reference phase stack, I-SHG allowed us to reconstruct the image of the phase in the sample and to extract the phase histogram (Fig. 3). The green and red pixels correspond to π-phase shifted signals, revealing

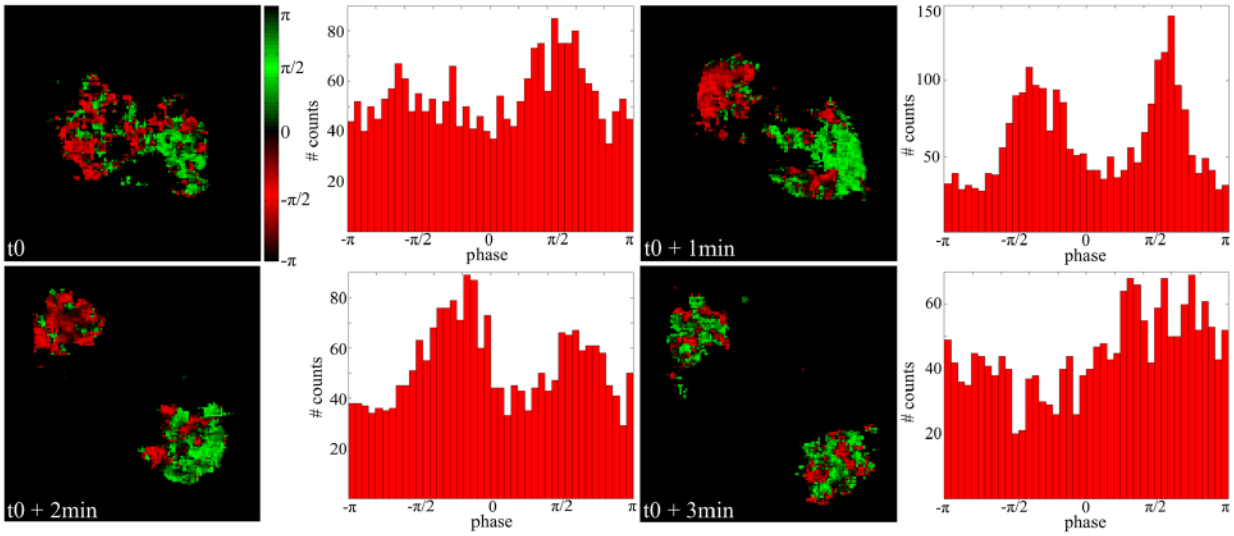

Figure 3. Image and histogram of the phase of the SHG signal generated in the spindles during mitosis. Field of view: $29 \times 29\,\mu m^2$.

opposite polarities of spindles. One can directly see that at the beginning of the metaphase (t_0) the red and green pixels started to segregate, while the phase histogram showed two broad peaks, revealing the opposite polarities in the two poles. Then, at the end of metaphase ($t_0 + 1$ min) and the beginning of the anaphase ($t_0 + 2$ min), the spindles clearly had opposite polarities in the two poles, and the histograms show two narrower peaks. Lastly, at the end of the anaphase ($t_0 + 3$ min), when the spindle uncondensed and the MTs disperse, the polarity was almost random around the two poles and the phase histogram is almost flat.

Discussion

The SHG intensity is a good qualitative indicator of structural organization, since its quadratic dependency with oriented molecules[8] makes it very sensitive of slight change in polarity. Yet, since SHG signals from MTs are rather weak and depend on a wide range of experimental parameters, quantification of structural changes based only on the signal intensity would be subjected to very large uncertainties. Figure 4a displays the superposition of the bi-Gaussian fitting of the phase histograms at different time points. At $t_0 + 1$ min and $t_0 + 2$ min, the phase distribution appears narrower, revealing a higher degree of polarity alignment of the MTs. In parallel, Fig. 4b shows the evolution of the average SHG intensity over time. Note that there is no reference signal in this case.

Altogether, Fig. 4a and b highlight the correlation between the SHG intensity and phase distribution. Indeed, almost flat phase distributions (t_0 and $t_0 + 3$ min) correspond to low SHG signal (around 200 s and 380 s), while peaked distributions ($t_0 + 1$ min and $t_0 + 2$ min) are associated with higher intensities (around 260 s and 320 s). As previously shown[40,41], one can quantify this effect, since the width of the phase peaks is related to the ratio of MTs with opposite polarities:

$$f = \frac{N(+\beta^{(2)})}{N(+\beta^{(2)}) + N(-\beta^{(2)})} \tag{2}$$

where $N(+\beta^{(2)})$ and $N(-\beta^{(2)})$ are respectively the number of MTs with a positive and negative nonlinear susceptibility, or equivalently with one polarity or the other. Therefore, $f = 0$ or 1 when all the MTs are pointing in the same direction, while $f = 0.5$ when the MTs are randomly polarized in the focal volume. Note that there is an ambiguity in the definition of the f ratio, which reflects the ambiguity in the sign of the measured polarity. By convention, we attributed the f ratio below 0.5 to the negative phase peak (centered at $-\pi/2$) and the f ratio above 0.5 to the positive phase peak (centered at $\pi/2$). Determining the absolute sign of the polarity would require measuring the phase of the SHG signal in a reference sample.

Figure 4c displays the evolution of the f ratios calculated from the phase distribution over different time points. As expected, f is closer to 0.5 at the beginning of the metaphase (t_0) and the end of anaphase ($t_0 + 3$ min), since the MTs are arranged in a more disorganized array. In turn, at the end of the metaphase ($t_0 + 1$ min) and the beginning of the anaphase ($t_0 + 2$ min), f departs from 0.5, revealing the same polarity of MTs within highly aligned mitotic spindles.

The physics of SHG is well known[6] and several studies have derived the theory of signal generation by a focused laser in biopolymers[8,9,36]. Assuming that all individual MTs generate equal signals, the SHG is directly proportional to the coherent sum of all the elementary responses. Thus, SHG intensity (I_{SHG}) depends on intrinsic properties of the MTs as well as on their macromolecular arrangement (density and polarity):

$$I_{SHG} \propto \left|\beta^{(2)}\right|^2 N^2 (f - 0.5)^2 \tag{3}$$

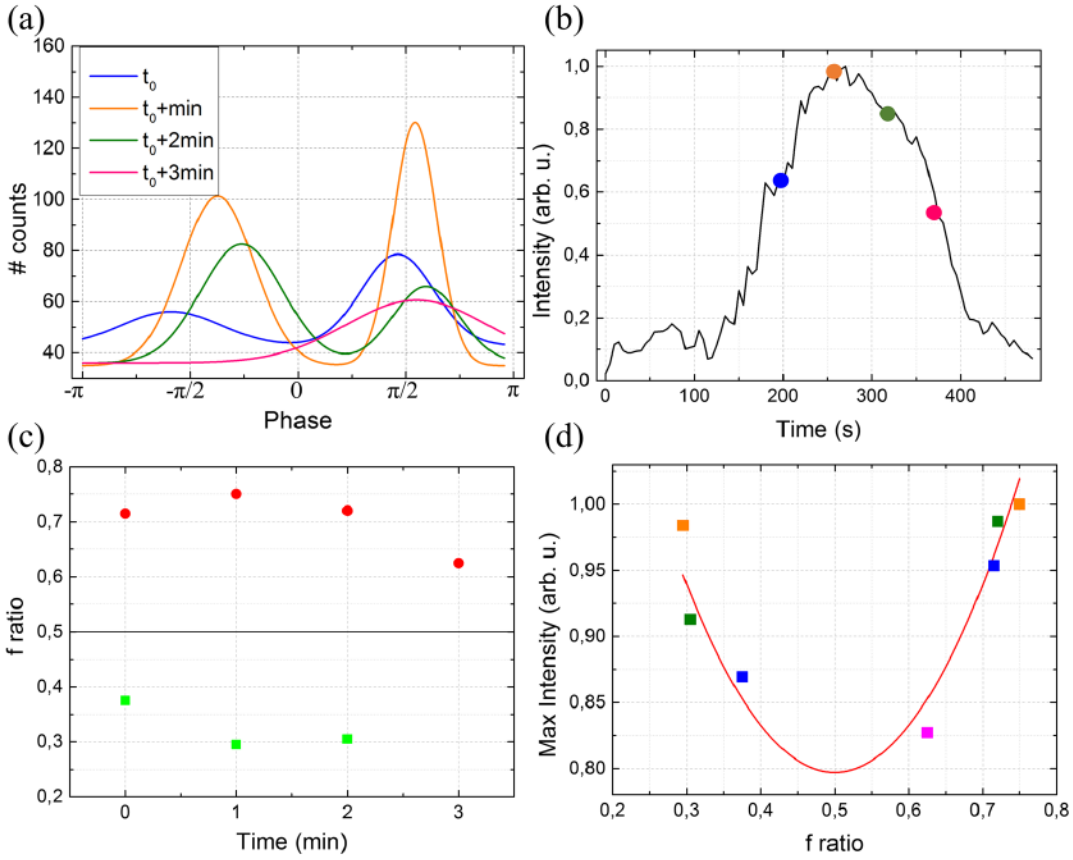

Figure 4. (**a**) Phase histogram at different time points highlighting the narrowing of the peak after 1 and 2 min. (**b**) Average intensity in the field of view (from Fig. 1) versus time. Colored circles correspond approximately to the time points in a. (**c**) Evolution of the f ratio with time. There is only one point at 3 min since only one peak (centered at $\pi/2$) is observable in the phase histogram at this time, due to quasi-random MTs polarity at this time. (**d**) Correlation between the maximum SHG intensity and the f ratio. The colored squared display the data extracted from (**a**) and the red line is the theoretical dependency (Eq. 3).

where $\beta^{(2)}$ is the hyperpolarizability and N the total number of MTs in the focal spot. This equation shows that the SHG signal scales quadratically with the excess number of MTs in one direction. Extracting the *f* ratio from the phase histogram (in Fig. 4a) while simultaneously measuring the SHG intensity (with the reference signal) stands to verify this correlation. As shown in Fig. 4d, we observed an excellent correlation between the experimental measurements (colored squares) and the theoretical quadratic dependency (Eq. 3). Note that since SHG signal scales with the square of f-0.5, it cannot discriminate between a perfectly antiparallel network of MTs (f = 0.5) and the simple absence of MT. However, even a slight asymmetry (f = 0.55) in the MTs polarity distribution allows to detect the phase of the signal[41].

Conclusion

Since SHG microscopy does not require external perturbation, such as fixation or exogenous labelling, it can be applied in native tissues. Therefore, I-SHG microscopy offers a direct and dynamical method to quantify the degree of polarity of MT arrays in cells. We report here its first use in live cell imaging and show that I-SHG allows measurement of the evolution of MT polarity in mitotic spindles during the first divisions of a zebrafish embryo. It has long been proposed that this polarity plays a role in many cell processes and behaviors such as force transmission, cell migration, protein localization and transport. However, up to now, it has remained highly challenging to image MTs polarity *in situ*, impeding a proper investigation of these effects. Note that this method is not limited to imaging mitotic spindles but should be directly transferable to offer new insights into MT polarity in other systems such as dendrites[11] or neuronal processes[28].

References

1. Campagnola, P. J. *et al.* Three-dimensional high-resolution second-harmonic generation imaging of endogenous structural proteins in biological tissues. *Biophys. J.* **81**, 493–508 (2002).
2. Zoumi, A., Yeh, A. & Tromberg, B. J. Imaging cells and extracellular matrix *in vivo* by using second-harmonic generation and two-photon excited fluorescence. *Proc. Natl. Acad. Sci. USA* **99**, 11014–11019 (2002).
3. Zipfel, W. R. *et al.* Live tissue intrinsic emission microscopy using multiphoton-excited native fluorescence and second harmonic generation. *Proc. Natl. Acad. Sci. USA* **100**, 7075–7080 (2003).
4. Denk, W., Strickler, J. H. & Webb, W. W. Two-photon laser scanning fluorescence microscopy. *Science* **248**, 73–76 (1990).

5. Centonze, V. E. & White, J. G. Multiphoton excitation provides optical sections from deeper within scattering specimens than confocal imaging. *Biophys. J.* 75(4), 2012–2024 (1998).
6. Boyd, R. W. *Nonlinear Optics* 3rd Edition, Academic Press (2008).
7. Brown, E. *et al.* Dynamic imaging of collagen and its modulation in tumors *in vivo* using second-harmonic generation. *Nat. Med.* **9**, 796–800 (2003).
8. Bancelin, S. *et al.* Determination of collagen fibril size via absolute measurements of second-harmonic generation signals. *Nat. Commun.* **5**, 4920 (2014).
9. Moreaux, L., Sandre, O., Blanchard-Desce, M. & Mertz, J. Membrane imaging by simultaneous second-harmonic generation and two-photon microscopy: errata. *Opt. Lett.* **25**, 678 (2000).
10. Campagnola, P. J. & Loew, L. M. Second-harmonic imaging microscopy for visualizing biomolecular arrays in cells, tissues and organisms. *Nat. Biotechnol.* **21**, 1356–1360 (2003).
11. Dombeck, D. A. *et al.* Uniform polarity microtubule assemblies imaged in native brain tissue by second-harmonic generation microscopy. *Proc. Natl. Acad. Sci. USA* **100**, 7081–7086 (2003).
12. Tiaho, F., Recher, G. & Rouède, D. Estimation of helical angles of myosin and collagen by second harmonic generation imaging microscopy. *Opt. Express* **15**, 12286–12295 (2007).
13. Stoller, P., Celliers, P. M., Reiser, K. M. & Rubenchik, A. M. Quantitative second-harmonic generation microscopy in collagen. *Appl. Opt.* **42**, 5209–5219 (2003).
14. Yeh, A. T., Choi, B., Nelson, J. S. & Tromberg, B. J. Reversible dissociation of collagen in tissues. *J. Invest. Dermatol.* **121**, 1332–1335 (2003).
15. Bancelin, S. *et al. Ex vivo* multiscale quantitation of skin biomechanics in wild-type and genetically-modified mice using multiphoton microscopy. *Sci. Rep.* **5**, 17635 (2015).
16. Légaré, F., Pfeffer, C. & Olsen, B. R. The role of backscattering in SHG tissue imaging. *Biophys. J.* **93**, 1312–1320 (2007).
17. Houle, M.-A. *et al.* Analysis of forward and backward second harmonic generation images to probe the nanoscale structure of collagen within bone and cartilage. *J. Biophotonics* **9**, 993–1001 (2015).
18. Desai, A. & Mitchison, T. J. Microtubule polymerization dynamics. *Annu. Rev. Cell Dev. Biol.* **13**(1), 83–117 (1997).
19. Hirokawa, N. Kinesin and dynein superfamily proteins and the mechanism of organelle transport. *Science* **279**(5350), 519–526 (1998).
20. Baas, P. W. & Lin, S. Hooks and comets: the story of microtubule polarity orientation in the neuron. *Dev. Neurobiol.* **71**(6), 403–418 (2011).
21. Viktorinova, L. & Dahmann, C. Microtubule polarity predicts direction of egg chamber rotation in Drosophila. *Curr. Biol.* **23**(15), 1472–1477 (2013).
22. Harumoto, T. *et al.* Atypical cadherins dachsous and fat control dynamics of noncentrosomal microtubules in planar cell polarity. *Dev. Cell.* **19**(3), 389–401 (2010).
23. Wittmann, T., Hyman, A. & Desai, A. The spindle: a dynamic assembly of microtubules and motors. *Nat. Cell Biol.* **3**(1), E28–E34 (2001).
24. Haimo, L. T. Microtubule polarity in taxol-treated isolated spindles. *Can. J. Biochem. Cell B.* **63**(6), 519–532 (1985).
25. Mohler, W., Millard, A. C. & Campagnola, P. J. Second harmonic generation imaging of endogenous structural proteins. *Methods* **29**(1), 97–109 (2003).
26. Heidemann, S. R. & Mcintosh, J. R. Visualization of the structural polarity of microtubules. *Nature* **286**(5772), 517–519 (1980).
27. Baas, P. W., Deitch, J. S. & Black, M. M. & Banker, G. A. Polarity orientation of microtubules in hippocampal neurons: uniformity in the axon and nonuniformity in the dendrite. *Proc Natl Acad Sci USA* **85**(21), 8335–8339 (1988).
28. Rakic, P., Knyihar-Csillik, E. & Csillik, B. Polarity of microtubule assemblies during neuronal cell migration. *Proc Natl Acad Sci USA* **93**(17), 9218–9222 (1996).
29. Rolls, M. M. *et al.* Polarity and intracellular compartmentalization of *Drosophila* neurons. *Neural Dev.* **2**(1), 7 (2007).
30. Brugués, J., Nuzzo, V., Mazur, E. & Needleman, D. J. Nucleation and transport organize microtubules in metaphase spindles. *Cell* **149**(3), 554–564 (2012).
31. Stoothoff, W. H., Bacskai, B. J. & Hyman, B. T. Monitoring tau-tubulin interactions utilizing second harmonic generation in living neurons. *J. Biomed. Opt.* **13**, 64039 (2008).
32. Kwan, A. C., Dombeck, D. A. & Webb, W. W. Polarized microtubule arrays in apical dendrites and axons. *Proc. Natl. Acad. Sci. USA* **105**, 11370–11375 (2008).
33. Fu, Y., Wang, H., Shi, R. & Cheng, J. Second harmonic and sum frequency generation imaging of fibrous astroglial filaments in *ex vivo* spinal tissues. *Biophys. J.* **92**, 3251–3259 (2007).
34. Barad, Y., Eisenberg, H., Horowitz, M. & Silberberg, Y. Nonlinear scanning laser microscopy by third harmonic generation. *Appl. Phys. Lett.* **70**, 922 (1997).
35. Olivier, N. *et al.* Cell lineage reconstruction of early zebrafish embryos using label-free nonlinear microscopy. *Science* **329**, 967–971 (2010).
36. Yu, C. *et al.* Measuring microtubule polarity in spindles with second-harmonic generation. *BPJ* **106**, 1578–1587 (2014).
37. Rechsteiner, P., Hulliger, J. & Flörsheimer, M. Phase-sensitive second harmonic microscopy reveals bipolar twinning of markov type molecular crystals. *Chem. of Mat.* **12**, 3296–3300 (2000).
38. Yazdanfar, S., Laiho, L. H. & So, P. T. C. Interferometric second harmonic generation microscopy. *Opt. Express* **12**, 2739 (2004).
39. Rivard, M. *et al.* Imaging the bipolarity of myosin filaments with interferometric second harmonic generation microscopy. *Biomed. Opt. Express* **4**, 2078–2086 (2013).
40. Rivard, M. *et al.* Imaging the noncentrosymmetric structural organization of tendon with interferometric second harmonic generation microscopy. *J. Biophotonics* **7**, 638–646 (2013).
41. Couture, C.-A. *et al.* The impact of collagen fibril polarity on second harmonic generation microscopy. *Biophys. J.* **109**, 2501–2510 (2015).
42. Bancelin, S. *et al.* Fast interferometric second harmonic generation microscopy. *Biomed. Opt. Express* **7**, 399 (2016).
43. Westerfield M. *The zebrafish book: a guide for the laboratory use of zebrafish* (*Danio rerio*) University of Oregon press (2000).
44. Oates, A. C., Gorfinkiel, N., González-Gaitán, M. & Heisenberg, C. P. Quantitative approaches in developmental biology. *Nat. Rev. Genet.* **10**(8), 517–530 (2009).

Acknowledgements

We thank Mr. Guy Laliberté for animal husbandry. PD was supported by the Canadian Institutes of Health Research. FL thanks the Canada Foundation for Innovation (CFI), the Conseil de Recherche en Sciences Naturelles et en Génie du Canada (CRSNG) and the Fond Québécois de la Recherche sur la Nature et les Technologies (FQRNT) for financial support.

Author Contributions

S.B., C.-A.C. and M.P. performed the experiments, processed the data and wrote the manuscript. M.R. contributed to the design of the experiments. P.D. provided the zebrafish samples and help interpreted the results. F.L. conceived the idea and supervised the project. All authors reviewed the manuscript.

Additional Information

Competing Interests: The authors declare that they have no competing interests.

Publisher's note: Springer Nature remains neutral with regard to jurisdictional claims in published maps and institutional affiliations.

This article was done through a collaboration with Pierre Drapeau of the Département de Neurosciences of CHUM Montréal who provided the samples. I participate in set-up designing and manuscript writing.

8.2 Further discussion and perspective

The main limitation of this study is the resolution of the images, as well as the relatively low SHG signal from microtubules that require a quite high exciting power above 100mW, that showed to damage the embryo in some cases, forced to use the 20X objective instead of the 40X, and put the standard laser-scanning I-SHG at its limits.

Microtubules in *meiotic* spindles could also be imaged by SHG in the 1st or 2nd phase of the meiosis, not only mitosis. A very recent work [231] showed that SHG in microtubules can be produced when microtubules have a non-uniform polarity, and thus the cell's tubulin can be imaged - under certain conditions - not only in spindles during mitosis: in e.g. fibroblasts, there is a SH signal originating from areas where microtubules are constricted and tubulin are parallel to each other [231]. Furthermore, in dendrites (neurons) the uniform polarity of microtubules is not sufficient for SHG, as they also need to have a certain organization [231]. Single-scan I-SHG (presented in the article of chapter 9) could investigate the polarity in dendrites to better elucidate this statement.

Chapter 9

Single-scan I-SHG by fast phase-shifting

This chapter presents the single-scan I-SHG (1S-ISHG) implementation. It shows the article, and complementary information. The phase-scanner is a genuine advance in I-SHG acquisition, as the speed is increased by more than one order of magnitude. It also allows I-SHG to be performed without reducing the number of phase-shifts and risking a decrease of the precision (see eq. 3.18), as the interferograms are extracted from a buffer such that their number is adjustable in the data treatment.

9.1 Article

(FR) Microscopie de Génération de Seconde Harmonique Interférométrique à mono-acquisition avec un modulateur de phase kHz.

Received 30 Oct 2019; revised&accepted 25 Nov 2019; published 18 Dec 2019

Citation: Optics Express 27(26):38435 (2019).

DOI: 10.1364/OE.27.038435

This work is the result of a collaboration with Axis Photonics Inc.: Christian-Yves Coté, Lee-Pierre Belley and Jean-Marc Piau, with whom we made the phase-scanner.

Research Article | Vol. 27, No. 26 / 23 December 2019 / Optics Express 38435

Optics EXPRESS

Single-scan interferometric second harmonic generation microscopy using a kHz phase-scanner

MAXIME PINSARD,[1] LEE-PIERRE BELLEY,[2] JEAN-MARC PIAU,[2] CHRISTIAN-YVES COTÉ,[2] HEIDE IBRAHIM,[1] AND FRANÇOIS LÉGARÉ[1,*]

[1] *Institut National de la Recherche Scientifique, Centre Énergie Matériaux Télécommunications (INRS-EMT); 1650 Boul. Lionel-Boulet, Varennes (QC), J3X 1S2, Canada*
[2] *Axis Photonique Inc., 1650 Boul. Lionel-Boulet, Varennes (QC), J3X 1S2, Canada*
[*] *legare@emt.inrs.ca*

Abstract: In conventional laser-scanning microscopy, images are formed by acquiring the signal from pixel to pixel. Here, we report more than one order of magnitude reduction in acquisition time of Interferometric Second Harmonic Generation (I-SHG) by scanning the phase within each pixel, to characterize the relative polarity of various samples. Using an electro-optic phase-scanner, we show that the phase-shift patterns required for interferometry can be applied at each pixel during the scanning of the sample, allowing single-scan I-SHG (1S-ISHG) measurements. Requiring exposure times comparable to standard SHG intensity images, the additional phase information of the signal can thus be retrieved in parallel to its amplitude at the time-scale of seconds. Moreover, slower modulations can be used to enhance the precision of the phase measurement, without any spatial or temporal shift between interferograms, in contrast to conventional frame phase-shifting I-SHG (standard I-SHG). This continues to extend I-SHG to dynamical processes, and opens it to large-scale studies, as well as to imaging samples where the signal-to-noise ratio is an issue.

1. Introduction

Over the last 30 years, Second Harmonic Generation (SHG) microscopy has been gradually confirmed as a valuable method to characterize non-centrosymmetric structures, in particular certain biological tissues [1]. This type of scanning microscopy uses a near-infrared laser for excitation that limits scattering inside tissues, thus allowing a high penetration depth [2]. The 3D confinement of the focal volume of excitation also enables a sub-micron spatial resolution [3]. SHG is endogenous, with no need of marker or staining which makes it minimally invasive. Being a parametric process that converts two exciting photons into a single photon at twice the frequency, it also does not involve any electronic excitation. It is therefore free from photobleaching, and greatly reduces phototoxicity compared to other two-photon processes, such as two-photon excited fluorescence (2PEF) [4]. Secondly, it is a coherent process which involves a relationship between the excitation and the converted SHG in terms of phase: this restricts the generation to non-centrosymmetric media and makes it intrinsically background-free. Thus, SHG microscopy has been shown to be very sensitive and highly specific to a wide variety of structural proteins [1,5] or carbohydrates [6]. It was also used to characterize ferroelectrics [7,8], especially to reveal phase transitions [9]. Magnetic structure of materials that can be centrosymmetric in their crystallographic structure but exhibiting an electrical quadrupole or a magnetic order (thus breaking the time-inversion symmetry) [10,11], as well as strongly correlated materials [12] were moreover studied by SHG.

#381493 https://doi.org/10.1364/OE.27.038435
Journal © 2019 Received 30 Oct 2019; revised 25 Nov 2019; accepted 25 Nov 2019; published 18 Dec 2019

Optics EXPRESS

The coherence of the SHG process also conserves the phase of the excitation field. This means that not only the intensity of the signal carries information, but also its phase, which adds an additional mode of contrast. Unfortunately, this phase information cannot be extracted with a standard SHG microscope, since it would require a detector with a bandwidth higher than the optical frequency (~300THz), which is several orders of magnitude over the limit of usual detectors (few GHz). Interferometry is the usual indirect way of retrieving the phase information, and the so-called Interferometric-SHG (I-SHG) was first applied to characterize ferroelectrics [8]. It was later transferred to the imaging of biological tissues like muscle [13,14], tendon [15] and cartilage [16]. Since the acquisition speed was quite low (~1-2h to acquire a standard I-SHG map), the technique was further improved, and confirmed its compatibility with standard scanning microscopy set-ups, featuring: (1) a laser-scanning system to enable frame acquisition within seconds [17], and (2) a femtosecond excitation that provides a high signal-to-noise ratio (SNR) and a reduced exposition to laser light [18]. These improvements recently allowed us to probe dynamical processes like the evolution of the polarity of microtubules during mitosis [19]. However, this frame phase-shifting I-SHG measurement implied the acquisition of 9 interferograms, with a dead-time of ~1sec between them to shift the relative phase. In this case, it was additionally necessary to manually adjust the polarization and the depth of focus to follow the 3D movement of the microtubules. Altogether, the temporal resolution was limited to 45sec, even if each single interferogram was recorded in 2sec [14]. This is more than twice the theoretical time of 9×2 = 18sec [14], and very close to the acceptable limit of 1min – the duration of some phases of the mitosis – after which the microtubular spindles change their arrangement and loose their centrosymmetry. Moreover, the fact that subsequent interferograms are separated by a few seconds can lower the precision of the phase measurement, especially in moving samples. In addition, laser-scanning I-SHG comes with trade-offs compared to sample-scanning, which e.g. enables scans of large areas without any mosaic reconstruction [13,20].

In this work, we address and optimize these time - and imaging quality - affecting issues by implementing single-scan I-SHG (1S-ISHG) using a kHz electro-optic phase-scanner. We show that its fastest mode considerably increases the speed of I-SHG imaging by more than one order of magnitude with only a slight loss in precision. If required, a precision equivalent to standard I-SHG can be achieved with a slow mode of 1S-ISHG that is still twice as fast, and the different pixels of the interferograms are separated in time by only 200µs maximum, instead of a few seconds. Finally, we apply this technique to image samples exhibiting a relatively low signal-to-noise ratio (SNR): mice-tail tendon and horse's meniscus from knee joint. The fastest mode of the phase-scanner leads to a noisier and less accurate I-SHG map in these bio-samples, but still enables full phase retrieval. Altogether, the increased speed is promising for future probing of relative polarity in dynamical processes and large-scale studies of various tissues or crystals, notably the aforementioned study of phase transition in condensed matter [21]. The improved accuracy of the slow mode also opens up the possibility of dealing with samples that exhibit a low SHG signal.

2. Material and methods

2.1. General principle

Single-scan I-SHG capitalizes on the MHz speed of electronic acquisition cards to split each pixel of a standard image in many subpixels, thus acquiring all interferograms almost simultaneously (by contrast to successive acquisitions of many images) and providing an increase of speed more than one order of magnitude compared to previously reported I-SHG measurements.

2.2. Experimental set-up

320fs pulses at 810nm and 80MHz repetition rate were used for SHG, altogether with galvanometric (galvos) mirrors from Cambridge Technology (model 6220H) coupled with achromatic doublets

Optics EXPRESS

as scan lens and tube lens. This maximizes the throughput at 405nm and the scanned field-of-view, while minimizing the amount of dispersive material in the excitation and reference beams such that only a small amount of calcite is needed to compensate for the group delay (see [2] for explanations). Figure 1(a) shows the full set-up used for the different modes of I-SHG: an air immersion objective (UplanSApo 20X, NA 0.75, Olympus, Japan) was used for illumination and the SHG emission was then collected with a condenser (NA = 0.55). The (measured) focal volume of excitation is $1\times1\times4\mu m^3$: the deviation from the theoretical values ($0.4\times0.4\times1.9\mu m^3$, see [22]) comes from an imperfect collimation and underfilling of the back pupil of the objective, as well as from a reduced performance of the objective lens. Scanning and signal acquisition were synchronized using a custom-written Python program for stability and control. The average power on the sample was adjusted to 25mW, corresponding to 0.31 nJ/pulse. Raw data visualization was performed with FIJI-ImageJ (NIH, [23]), and image processing with a custom-made GUI in MATLAB that allows batch processing of the data and rendering.

The setup is designed in a modular way to choose between different pathways for image acquisition: P1 for sample-scanning with a motorized stage and P2 for laser-scanning using galvos (Fig. 1(a)). In this article, we will now refer to "stage-scanning" for the sample-scanning, and to "galvos-scanning" for the laser-scanning method. For a complete description of the I-SHG method and set-up we refer to [24] for galvos-scanning and to [13] for stage-scanning. Both galvos and stage use unidirectional raster scanning, which scans the X direction at every step of the Y direction (see Fig. 1(b)).

In our previous study [2], we reported a 40 times speed improvement for laser-scanning, compared to stage-scanning I-SHG. However, the stage-scanning was based on a non-optimized LabView code, which we have later improved by controlling the scan with a Python software. This enabled a flexible choice of every scan parameter, to further optimize the scan duration. E.g. using a smooth scanning profile, we could reduce the imaging time by a factor of 1.4. If the resolution of the scan is set above 0.5µm, a faster velocity profile [25] can be employed which reduces the duration by another factor of 5. Since the acceleration of the stage is limited to $2000mm/s^2$ [25], each scan size has its optimal pixel exposure time, related to the optimal speed calculated with the accelerations and decelerations at each line of the scan. The pixel exposure time can still be set to a different value, at the cost of a slight increase of acquisition time. Overall, taking into account the moving time of the static phase-shifter, we calculated that the scan time in I-SHG can be reduced by a factor of 8 to 35 using galvos-scanning compared to an optimized stage-scanning.

We also introduce here different modes for I-SHG: single-scan I-SHG (1S-ISHG) utilizing a phase-scanner, unlike conventional I-SHG that is based on a rotatable glass plate (see [2]). For general I-SHG phase extraction and data treatment, we refer to [14]. The special case of contrast enhancement achieved with 30 phase-shifts is detailed in the Appendix A.1.

2.3. Phase scanner

The phase scanner (developed in collaboration with Axis Photonique Inc, Canada) is a system that includes a transverse electro-optic phase modulator (EOM), a high-voltage kHz driver, its control electronics and software interface. The EOM uses a $3\times3\times35$ mm^3 RTP crystal (Y-cut, custom made by Raicol Crystals Ltd, see [26] for details). Such crystals are known for their stability and have already been utilized for high precision interferometers [27]. The required voltage to apply a π phase-shift between a pulse at 810nm (the wavelength of excitation) and its SHG at 405nm is ~250V (measured). The high-voltage driver is set to work from 0 to 1300V, providing up to 5π phase-shift (see Appendix A.1 for the need of 5π). Linear voltage ramps (i.e. a sawtooth waveform) are generated to continuously change the phase-shift inside every pixel of the image (performing an intra-pixels phase scan), during the scans in X direction (see Fig. 1(b)): pixel time (i.e. ramp, see Fig. 1(c)) can be set to 20, 200 or 2000µs. These pixels

Optics EXPRESS

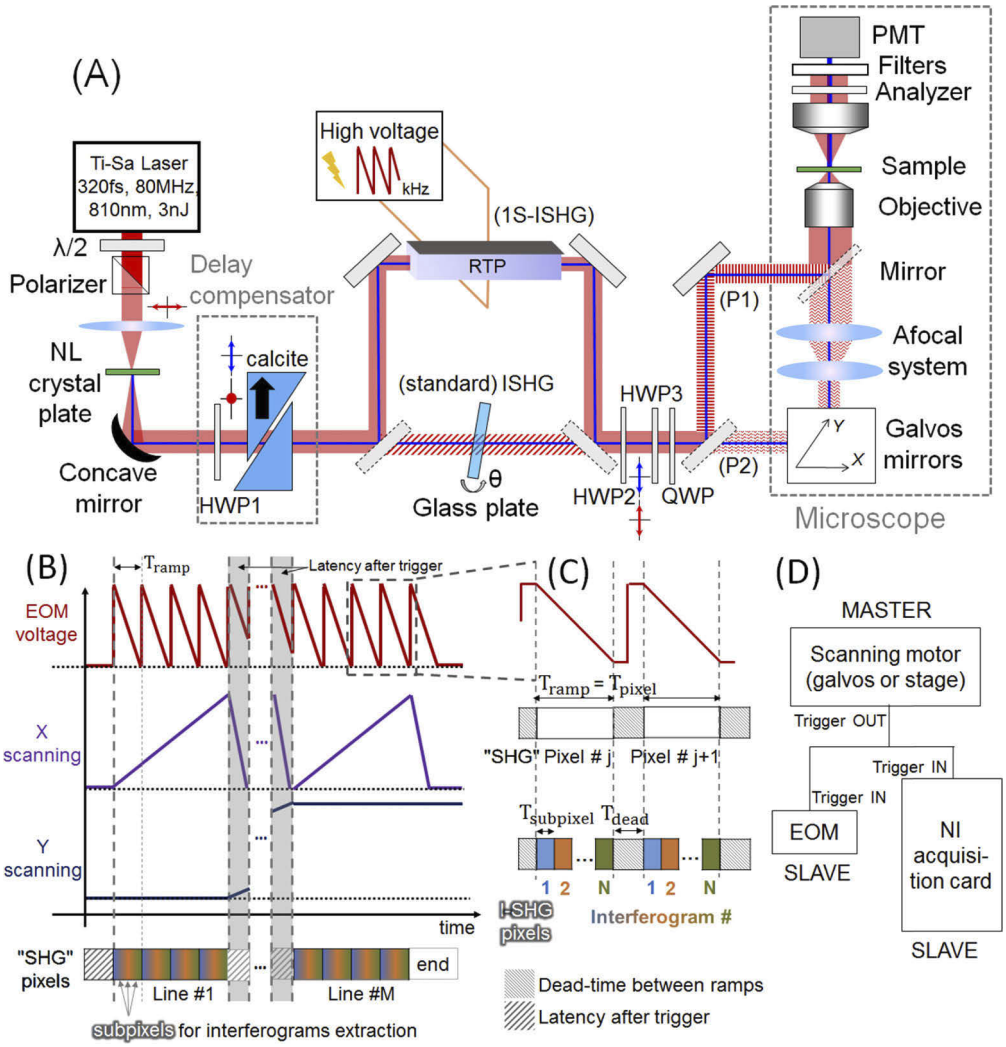

Fig. 1. (a) Schematic view of the set-up used for I-SHG. The standard phase-shifter (a rotatable glass plate) can be by-passed to have the common-path interferometer pass in the phase-scanner (EOM). The beams are sent to galvos for standard laser-scanning (P2). They can also be by-passed using plane mirrors to directly send the beams into the objective (P1). The scan is then performed by a motorized stage (stage-scanning). The flat mirrors are represented by grey rectangles, with dotted outline if put on a flip mount. HWP1&2: half-wave plate at 810nm, full wave-plate at 405nm. HWP3: dual half-wave plate at 810nm and 405nm, QWP: quarter-wave plate at same wavelengths. (b) Simplified version of the ramp waveform used for the phase scanner, and its synchronization with the X and Y scanning of the scanning motor. (c) Zoom of (b) on two voltage ramps, showing how standard pixels are divided into N subpixels that correspond to N interferograms. (d) Description of the hierarchy between the motor (master) which triggers the timing of the EOM and the acquisition card (slaves).

Optics EXPRESS

form the standard microscopy image and are noted "SHG pixel", while the subpixels of the interferograms are noted "I-SHG pixel" (Figs. 1(b) and 1(c), see also section 2.3). Because the scan is unidirectional and the acceleration of the moving part is limited to a finite value, there is a flyback time between the X scans [28] and some moving time for the Y direction in parallel. This leads to an overall latency time at the beginning of each image line (see Fig. 1(b)). The voltage ramps (phase scans) are thus re-synchronized at each line of the image to account for this latency, using a trigger between the EOM and both the acquisition card and the scanning motor (master/slave configuration, see Fig. 1(d)).

The polarization of the fundamental beam is vertical and set parallel to the γ-axis (i.e. the electrode axis) of the RTP crystal, while the polarization of the reference SHG beam is set horizontal. This configuration leads to a different electro-optic modulation for the two beams, and thus to a relative phase-shift. Instead of intra-pixels, the phase-shift can also be changed frame-by-frame using a rotating glass plate (see Fig. 1(a)), according to the conventional I-SHG reported previously [13,24,29].

2.4. Buffer synchronization and filling of the interferograms

Figure 1(c) zooms on two ramps of Fig. 1(b): the "SHG" pixels are divided into N subpixels, which will serve to construct the N interferograms. There is also a dead-time (grey) between ramps due to the electronics, which is discarded (exaggeratedly illustrated for clarity): the complete process of subpixels extraction is described in A.2 in the Appendix, with Table 2 in particular showing the different exposure times of the interferograms, for the different modes.

While the exposure time in multiphoton microscopy is usually around 5-20µs, the 20µs 1S-ISHG phase-scanning needs to cope with less than 1µs per subpixel (Table 2). This is compensated by the fact that in I-SHG, the phase contrast is computed by taking successive interferogram frames, effectively leading to a much higher number of detected photons compared to those collected during a subpixel time (down to 0.6µs, see Table 2). It is also worth noting that a true pixel integrator synchronized with the laser pulse rate could be used to improve the detection sensitivity [17] without increasing the exposure time, since it avoids correlation between adjacent pixels and lowers the image noise. To further improve this aspect, a digital photon counter could also be implemented instead of the analog PMT, but this would require advanced synchronization, with an external clock at the subpixels frequency to extract the different interferograms (not implemented here).

2.5. Correction of the interpulse delay

The reference and excitation beams are collinear (common-path interferometer), and thus travel through the same amount of optical medium. The 1st order normal dispersion of the different optics (microscope objective, lenses, RTP crystal) leads to group velocity mismatch (GVM, or temporal walk-off) between the pulses of these two beams. This resulting group delay is here compensated using a calcite prism pair ("delay compensator", see [16]). Each optical configuration of the interferometer leads to a different group delay: they are all reported in Table 1.

Table 1. Group delays for different configurations in I-SHG, at 810nm fundamental wavelength.

	Group delay due to GVM between fundamental and reference SHG [ps]	Corresponding amount of calcite [mm]	Group delay dispersion (GDD) difference between fundamental and reference SHG [fs^2]
I-SHG stage (standard)	10	22	5000
I-SHG galvos (standard)	23	51	10000
1S-ISHG stage	32	72	20000
1S-ISHG galvos	41	91	25000

Optics EXPRESS

The last column of Table 1 indicates the difference of group delay dispersion (GDD) between the two pulses of the interferometer, which plays a significant role on the observed image contrast. A different GDD will imply a different frequency chirp on the two pulses. Because their central frequency is also different, one pulse (the reference SHG) will inevitably be wider in time than the other: the non-overlapping part of the reference pulse will thus not interfere, leading to a decrease of the interference contrast C (see Appendix A.3 for the equation). With the EOM's crystal, the chirp difference is increased even more by the additional calcite amount needed for the GVM correction. For pulse durations of 120fs (10nm bandwidth), GDD values above 20000fs^2 would lead to a too strong temporal broadening. We measured a reduction in interference contrast C to 1.5:1 with 120fs pulses (not shown here), compared to a contrast C of 2.8:1 for 300fs pulses. For this reason, pulses at 320fs were preferred, which limits the difference in duration between the fundamental and the reference SHG beam to around ~100fs, for both the stage and galvos configurations. The high GDD difference between the 405 and 810nm beams (~14000fs^2) is mainly due to the highly dispersive RTP crystal: this problem could be reduced by using a KD*P crystal instead. We have calculated that a two times longer KD*P crystal would have the same half-wave voltage of 260V, with a GDD difference of only ~4000fs^2. This could theoretically enable the use of shorter pulses, close to 120fs.

In our configuration, to efficiently correct the chirp difference between both beams, a pulse compressor providing a certain amount of negative GDD at 810nm and twice this amount at 405nm is required. As conventional compression systems (prism or grating pair, chirped mirrors...) do not provide such feature, two different compressors for each wavelength 405 and 810nm would be required. This would however change the common-path geometry of the interferometer which ensures a good stability and ease of alignment. To nevertheless keep an optimal level of signal at the focus of the microscope, the GDD of the fundamental beam has been pre-compensated before the interferometer using a chirped mirrors pair (used with 32 bounces, −500fs^2 per bounce, 0°, Ultrafast Innovations GmbH).

2.6. Calibration of the polarization

The polarizations of the fundamental and reference SHG beam are controlled by a HWP and a QWP placed before the microscope, both designed to work at 405 and 810nm (see Fig. 1(a)). They are carefully calibrated with a modified version [30] of the routine developed in [31]. This enables to control the orientation of both input polarizations, to ensure that they are maximally linear and parallel to each other, even if the waveplates are placed before the input of the commercial microscope.

2.7. Sample preparation

Tendon samples were obtained from an 8 weeks old male C57/Bl6 mice, whose tail was harvested and fixed, and later embedded in OCT compound to be cut using a cryostat (Leica). The meniscus was banked from a previous study: it consists of a medial meniscus from the knee joint of an adult horse, where a slice orthogonal to the circumferential direction [32] was cut in the body part (middle one). It was then placed in 10% formaldehyde for 2h and later transferred to Ethylenediaminetetraacetic acid (EDTA) 20% for 2 weeks prior to paraffin embedding and subsequent sectioning (see [33] for details). For both samples, a five-µm thick section was cut, and then placed on a microscope slide (1mm thick) covered by a coverslip (#1.5H, Thorlabs).

2.8. Phase maps and polar histogram for I-SHG

The values of orientation φ obtained in I-SHG are circular, so their histograms are better represented with polar plots. To clearly see the differences between images and the distribution of φ, its values are not fitted to separate between positive and negative polarities as usual, but rather represented using a circular HSV (Hue, Saturation, Value) colormap.

Optics EXPRESS

3. Results

3.1. 1S-ISHG in Periodically Poled Lithium Niobate (PPLN)

We first validated our method in a model sample, Periodically Poled Lithium Niobate (PPLN, see [14] for details about the structure). Figure 2 shows the phase maps obtained with the different I-SHG methods, the first line showing the acquisitions with stage-scanning, and the second line the acquisitions with galvos-scanning. It is worth noting that different zones of PPLN with different domain size are imaged in each case, which explains the difference in size of observable patterns.

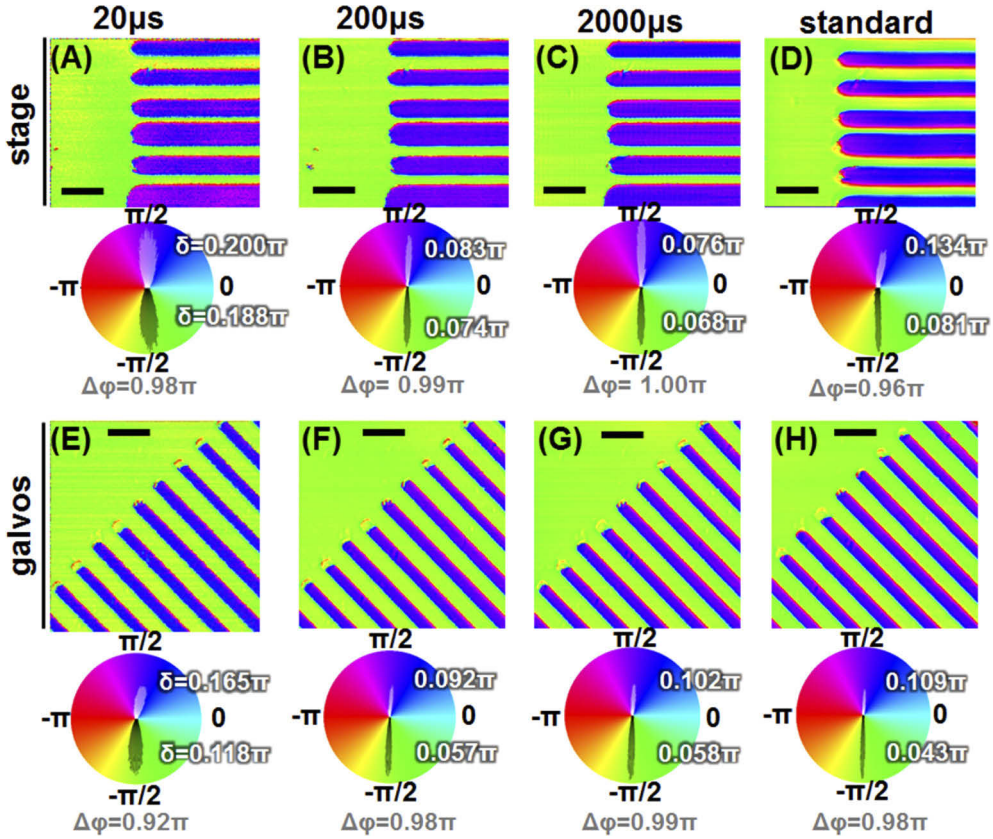

Fig. 2. Map of the relative phase of PPLN obtained by I-SHG, with the different methods. First line: stage-scanning ($50\times40\mu m^2$, 0.2µm step), second line: galvos-scanning ($50\times50\mu m^2$, 0.125µm step). (a)&(e) 1S-ISHG with the 20µs phase scan, (b)&(f) with the 200µs phase scan, (c)&(g) with the 2000µs phase scan. (d)&(h) Standard I-SHG with the standard phase-shifter (a rotatable glass plate). Polar histograms of a croped part of the phase images (to have similar peaks height, for clarity) are inserted below each map (see section 2.7), and the upper part is in white for visibility. The precision on $\Delta\varphi$ are $\approx \pm0.003\pi$, and $\pm\,0.005\pi$ for the peak widths δ. Acquisition times are: 70sec (a) and 5sec (e) ; 70sec (b) and 65sec (f) ; 156sec = 2.6min (c) and 450sec = 7.5min (g) ; $18\times(68+1) = 1242$sec = 21min (d) and $18\times(5+1) = 110$sec~2min (h). Scale-bars: 10µm.

Despite having different number of interferograms and exposure times, the phase distributions (indicated as a histogram below each sub-plot) of the 200µs (Figs. 2(b) and 2(f)) and 2000µs phase scan modes (Figs. 2(c) and (g)) are similar to the standard I-SHG (Figs. 2(d) and 2(h)): two peaks at $-\pi/2$ and $\pi/2$, with a distribution width of $\approx 0.060 \pm 0.004\pi$ and $0.100\pi\pm0.004\pi$.

Optics EXPRESS

The phase distribution is much wider with the 20µs phase scan (peaks are spaced by 0.92π with a width of $0.118 \pm 0.005\pi$ and $0.165 \pm 0.05\pi$), because the number of photons detected for each interferogram is lower (see Eq. (a5) in the Appendix). Also, with 20µs phase scan, the temporal fluctuations of the laser source are not averaged out because the pixel time of the interferograms corresponds to a rate over 500 kHz (see Appendix A.2), resulting in a signal variation from line to line (Figs. 2(a) and 2(e)). This might also broaden the phase histogram.

3.2. Phase correction

Because the ramp time calculated by the acquisition process is precise only at τ_R=0.2µs (see A.2 in the Appendix), there might be a small residual difference compared to the real duration of the phase scan fixed by the phase-scanner. To correct this effect, a calibration of the phase-shift can be performed, even if the stage-scanning mode is normally calibration-free with standard I-SHG [13]. Galvos I-SHG requires in any case a calibration to correct the aberration effect of the objective [24]: this is performed via I-SHG on a homogeneous sample like a quartz plate [16], which corrects for both effects. Since it is alignment-dependent, this calibration must be repeated for every change in scan size and every set of experiment to be accurate. The need for a phase correction due to the phase-scanner however only depends on the timing parameters (duration of the voltage ramps, hardware-coded timings), which are supposed to be constant. Thus, these calibrations for stage-scanning need to be performed only once for each setting.

Figure 3(a) shows one example of such a calibration: since the voltage is scanned along the X direction, the phase correction remains constant along Y and consists in a linear variation in X only. In comparison, a galvo scanning uses a 2D parabola fit (Fig. 3(b)). The phase could also be calibrated by the measured quartz phase itself as in our previous work [2], but we found that correcting by a fit instead avoids the influence of imperfections or noise that might be present in the calibration phase map of quartz.

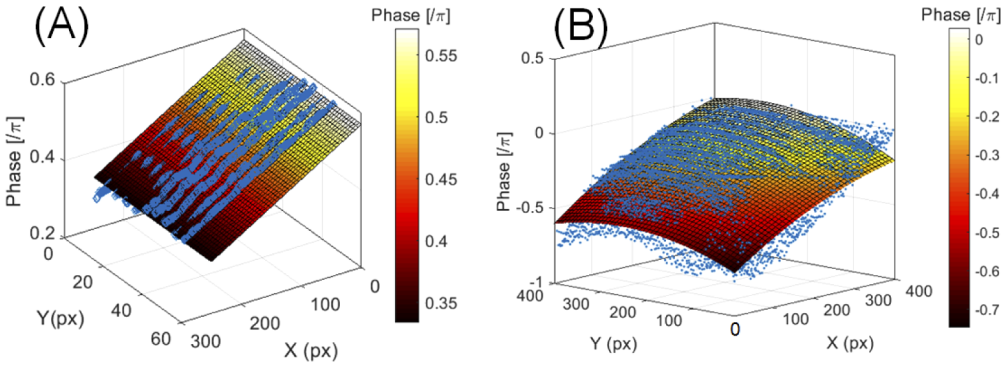

Fig. 3. (a) Example of a calibration in quartz for a stage-scanning of 40×10µm^2, step 0.2µm, 20µs phase scan (3D dot plot), along with a linear surface fit of the calibration, color-coded in phase. (b) Same with a galvos-scanning 50×50µm^2, step 0.125µm and 200µs phase scan: the fit is a 2D parabola.

For more details and an example about the correction of the aberrations induced by the galvos-scanning across the imaging objective, we refer to [2].

3.3. 1S-ISHG in biological tissues

Figure 4 refers to the I-SHG maps in tendon using galvos-scanning, after correction by the calibration map acquired in a quartz plate. As previously reported [15,24], there are two peaks in the phase distribution spaced by π. The bi-Gaussian fitting of the phase histograms for

Optics EXPRESS

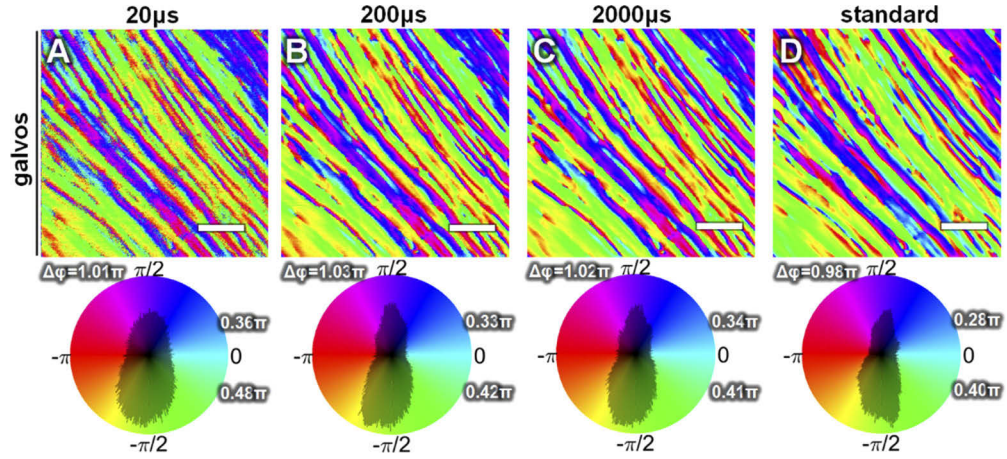

Fig. 4. I-SHG phase-map of mice-tail tendon ($50\times50\mu m^2$, 0.125µm step). 1S-ISHG with: (a) 20µs phase scan acquired in 5sec, (b) 200µs phase scan acquired in 65sec, (c) 2000µs phase scan acquired in 450sec = 7.5min. (d) Standard I-SHG acquired in $18\times(5+1) = 110$sec~2min. The precision on $\Delta\varphi$ are $\pm\,0.01\pi$, and 0.015π for the peak widths. Scale-bars: 10µm.

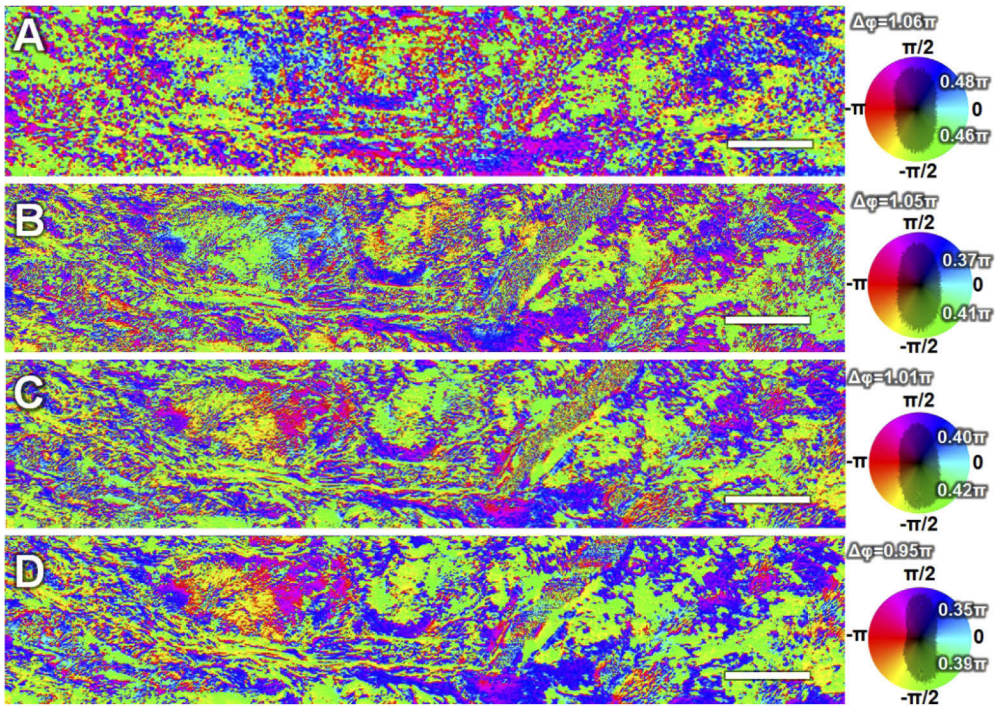

Fig. 5. I-SHG phase-map of the central part of an adult horse meniscus ($500\times100\mu m^2$, 0.5µm step) by stage-scanning. 1S-ISHG with : (a) 20µs phase scan acquired in 25sec, (b) 200µs phase scan acquired in 126sec, (c) 2000µs phase scan acquired in 495sec = 8.3min. (d) Standard I-SHG with the standard phase-shifter acquired in $18\times(106+1) = 1926$sec~32min. The precision on $\Delta\varphi$ are $\pm\,0.01\pi$, and 0.01π for the peak widths. Scale-bars: 50µm.

standard I-SHG scan leads to FWHM distribution's around $0.34 \pm 0.01\pi$, slightly better than the

Optics EXPRESS

$0.37 \pm 0.01\pi$ measured for 1S-ISHG using a 2000µs or 200µs phase-scan, and in good agreement with our value previously reported [15]. This increases to $0.42 \pm 0.015\pi$ for 20µs phase scans: it shows well that a diminution of exposure time (and thus of the number of photons) used to reconstruct the phase map is translated into a higher uncertainty on the phase determination, as the imaged area remains rigorously constant for each case.

To show the full benefits of the stage-scanning mode, i.e. the ability to scan a large ROI at once without any need for mosaic reconstruction, we performed I-SHG measurements in a $0.5\times0.1\text{mm}^2$ ROI in meniscus. This scan size is 5 times higher (in X) than the maximum acceptable scan that can be performed with galvos-scanning, while ensuring a sufficient I-SHG contrast C over the whole ROI in this biological sample with low SNR. As can be seen in Fig. 5, the relative polarity of this tissue is again characterized by two π phase-shifted peaks. The 20µs mode (Fig. 5(a)) is acquired in 25sec only, but needs a smoothing average to display a correct phase map. The 2000µs mode (Fig. 5(c)) shows very similar patterns and phase distribution compared to the reference (Fig. 5(d)), with the benefit of an acquisition time divided by $32/8 = 4$. Finally the 200µs mode (Fig. 5(b)) shows a result closer to reference than the 20µs one, but still exhibit some slight phase errors. This confirms that large exposure times are required to retrieve with full accuracy the phase from such a low SNR sample.

The interferometric contrast (or "amplitude") that provides an enhanced intensity map of the sample can also be extracted from the acquired interferograms (see [14]), in parallel of the phase (not shown here).

4. Discussion

4.1. Subpixels shift and synchronization

Because the phase-shift is changed while the motor is scanning, there might be a spatial shift between the interferogram pixels, especially between the first and the last ones. However, if the Nyquist criterion is respected - and the step size of the image is set below the lateral resolution of the microscope (here ~1µm) - this effect becomes negligible. If the parameters do not match this criterion, the measurement will be distorted by a so-called motion artifact [34]. This artifact however would show up identically in any sample (such as the calibration one) and can thus be compensated by the correction described in section 3.2. It is worth noting that a motion artifact can also exist in conventional I-SHG as the laser beam or the sample can move during different phase-shifts, as described earlier. A single-scan approach reduces this artifact. Notably, a scan free of any motion artifact would require a piezo whose driving voltage is increased at every image pixels (no acceleration or deceleration, only steps), but the response time would need to follow the ~ 50kHz pixel rate while piezos are usually limited to under kHz.

The imaging precision could be improved by the use of a more sensitive detector, as discussed in section 2.3. Alternatively, one could utilize beam-splitters to obtain 2 interferograms with a phase separation of 180° at half the incident amplitude, that can be measured on 2 different detectors: some setups extend this scheme to the simultaneous recording of 4 interferograms on 4 detectors [35]. Such approaches could reduce the number of interferograms extracted from the phase-scan by a factor of 2 to 4, and thus avoid potential motion artifacts. However, the 2 to 4 gain in exposure time does not relate to a higher number of photons per interferogram, as the beam splitting process distributes the photons on the different detectors, and is subjected to potential losses. Also, such a set-up is very sensitive to the output polarizations of the two beams of the interferometer, as a slight tilt in polarization can unbalance the different paths of detection.

Importantly, some setups of polarization-resolved SHG (p-SHG) using an EOM have been reported, with the difference that they modulate the polarization rather than the phase. Stoller *et al.* [36] used an EOM which was - similarly to ours - driven by a kHz sawtooth waveform, but however required a lock-in detection. In our setup, the EOM acts as the master clock and trigger, which removes the need of lock-in detection. More recently, Tanaka *et al.* [34] and DeWalt *et al.*

Optics EXPRESS

[37] showed another way to diminish motion artifacts by the use of an EOM to switch between two polarization states at each pixel, and a single-scan p-SHG by recording 3 polarizations on 3 different detectors using analyzers (no modulation of the polarization) has also been reported [38]. Yet, they are not applicable for phase-shifting.

4.2. Comparison with static phase-shifter I-SHG

In standard I-SHG with a static phase-shifter, the different interferograms used for phase reconstruction are separated in time by a few seconds, which limits the precision of the measurement for various reasons: (1) 3D position: the position of the sample in the focal volume may slightly vary because of external vibrations. For living samples like mitotic spindle exhibiting natural movements, this position is expected to vary even more (outside the focal volume) within a time-scale of a few seconds or below. Such change in depth position will directly affect the measured phase due to the variation of the Gouy phase-shift in the focal volume, as explained in our previous work [39]. Any drift in the two other dimensions (lateral plane) has to be corrected in the image treatment (automatically if the SNR is sufficient, otherwise manually) to avoid substantial errors on the final result. These problems do not apply to 1S-ISHG, because the interferogram pixels are temporally separated by at most the phase-scan time.

Additionally, phase-scans of 200 and 2000µs lead to a longer exposure time, and thus a higher risk to cause phototoxicity due to laser damage on the sample. To attenuate this problem, a kHz shutter could be used to block the irradiance during the flyback of the motor [28], which accounts for ~20% of the galvos-scanning time.

Switching from stage to galvos-scanning allowed us in [24] to increase the I-SHG acquisition speed by 1 to 1.5 orders of magnitude (from the hour scale to the minute scale), see abscissa of Fig. 6. Here, going from standard phase-shifting to the fastest single-scan mode (20µs) further increases this speed by another order of magnitude (from the minute scale to the second scale,

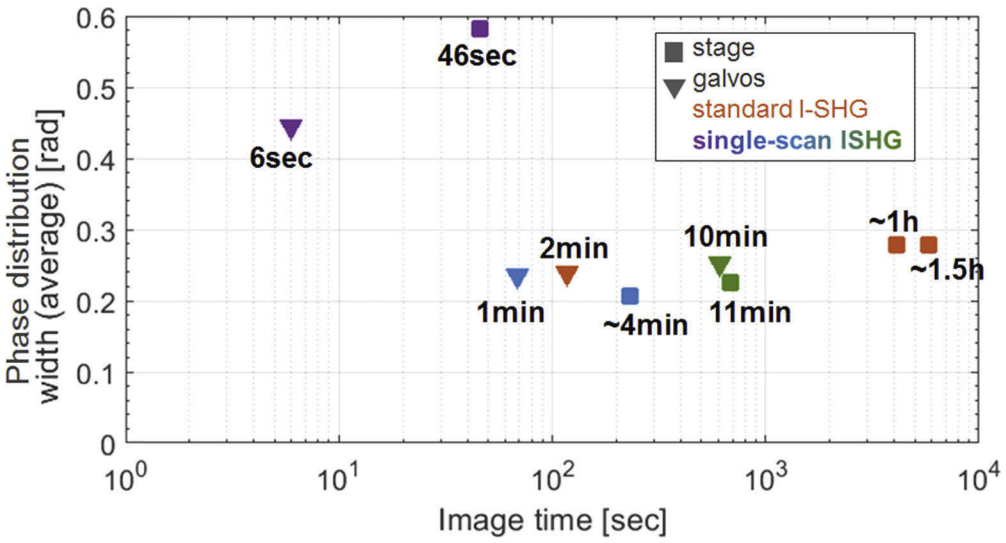

Fig. 6. Comparison of image time in I-SHG for a 250×250µm^2, 0.5µm step scan (abscissa, in log-scale) versus the phase distribution width, averaged on the two phase peaks of the model sample PPLN of Fig. 2. Orange = static phase-shifter, green = 2000µs phase scan, blue = 200µs, violet = 20µs. The duration corresponding to stage-scanning (resp. galvos-scanning) are indicated by square (resp. triangle) markers. The duration of standard I-SHG with stage-scanning used in [24] is also indicated (1.5h).

Optics EXPRESS

here a 20× factor). This comes with a trade-off in precision of the phase retrieval – measured with the average width of the phase distribution in PPLN of Fig. 2 – of ~ ×2 as shown in the ordinates of Fig. 6: the phase peaks are approximately two times wider. However, 1S-ISHG is shown to be similar in precision to standard I-SHG for the 200 and 2000µs phase-scans, with an acquisition time more than 10 times shorter for stage-scanning, and still 2 times shorter for galvos-scanning. A phase-scan time between 20 and 200µs could also be implemented to ensure a precision close to the 200µs mode with a scan speed slightly lower than the 20µs one. Noteworthily, the 20µs 1S-ISHG mode still performs well at retrieving the relative polarity inside any of the presented samples, i.e. discriminating π phase-shifted zones within them, as was presented in our other works [13,15,16,24] with a Red (for minus sign) and Green (for plus sign) colormap instead of HSV.

5. Conclusion

In this work, we have demonstrated, for the first time, the possibility of single-scan acquisition in I-SHG microscopy (1S-ISHG) based on an electro-optic phase-scanner. The scan of phase-shifts is performed for each pixel of the I-SHG image being acquired, which corresponds to a total acquisition of only a few seconds. For comparison, standard I-SHG implied the acquisition of 9 or more frames, which lasted few minutes or more: the speed is increased 20 times, while the phase precision is decreased by only a factor 2, which is still sufficient to accurately discriminate opposite polarities. This opens the possibility of measuring - in a minimally invasive way - the relative polarity in many biophysical systems undergoing fast dynamics, e.g. in microtubules in various stages of the mitosis, living bio-samples, or tissues submitted to dynamic traction assays, with an enhanced time resolution. It also opens I-SHG to large scale studies, where a large bank of samples need to be imaged and characterized in a reasonable time, for instance in biology [40]. Even at a precision equivalent to standard I-SHG, using a slower phase-scan, the corresponding imaging time is reduced by a factor of two. Lastly, a high exposure time can be used to characterize samples with low SNR, without the need to average several frames that are potentially exposed to 3D motion. 1S-ISHG can also scan large areas without mosaic reconstruction using stage-scanning, in a time which is more than one order of magnitude smaller than for standard I-SHG. As the phase-scanner is set to work as a slave of the scanning motor, and because the complete interferometer only consists of optics and electronics set separated from the microscope, this phase-scanner can be quite straightforwardly implemented into existing multiphoton imaging systems with only a slight modification in the code used to construct the images. This technology can also be applied to other SHG enhancements such as polarization-resolved SHG (p-SHG), resulting in a similar speed improvement.

Appendix

A.1 Phase extraction

The intensity measured at pixel i on an interferogram at phase-shift δ_j can be written as [14,41,42]:

$$I_i(\delta_j) = A_{ij} + B_{ij}\mathrm{sinc}(\Delta/2)\cos(\varphi_i + \delta_j) = a_i + b_i\cos(\delta_j) + c_i\sin(\delta_j) \quad \text{(a0)}$$

φ_i being the relative phase at pixel i and Δ the integration range of time where the phase-shift varies linearly, the background intensity a_i and the modulation amplitude $B_{ij} = B_i$ depending on i only as they are assumed to not vary with phase-shift [42]. Also, the phase-shifts are regularly spaced: $\delta_j = j \times \delta$ where δ is constant. The contrast frames are obtained by subtracting two π

Optics EXPRESS

phase-shifted interferograms:

$$\begin{cases} D(0) = I_i(\delta_j) - I_i(\delta_j + \pi) = 2B_i \mathrm{sinc}(\Delta/2)\cos(\varphi_i + \delta_j) \\ D(\pi) = I_i(\delta_j + \pi) - I_i(\delta_j + 2\pi) = -2B_i \mathrm{sinc}(\Delta/2)\cos(\varphi_i + \delta_j) \\ D(2\pi) = I_i(\delta_j + 2\pi) - I_i(\delta_j + 3\pi) = 2B_i \mathrm{sinc}(\Delta/2)\cos(\varphi_i + \delta_j) \\ D(3\pi) = I_i(\delta_j + 3\pi) - I_i(\delta_j + 4\pi) = -2B_i \mathrm{sinc}(\Delta/2)\cos(\varphi_i + \delta_j) \end{cases} \quad \text{(a1)}$$

This process can be iterated several times to increase even more the interferometric contrast γ_i:

$$\Rightarrow \begin{cases} D(0) - D(\pi) = 4B_i\,\mathrm{sinc}(\Delta/2)\cos(\varphi_i + \delta_j) \\ D(3\pi) - D(2\pi) = -4B_i\,\mathrm{sinc}(\Delta/2)\cos(\varphi_i + \delta_j) \end{cases} \quad \text{(a2)}$$

$$\Rightarrow [D(0) - D(\pi)] - [D(3\pi) - D(2\pi)] = 8B_i\,\mathrm{sinc}(\Delta/2)\cos(\varphi_i + \delta_j) = \gamma_i \cos(\varphi_i + \delta_j) \quad \text{(a3)}$$

where $\gamma_i = 8B_i\,\mathrm{sinc}(\Delta/2)$. In the general case, if the subtraction is performed n times, N=(360/δ*(n + 2)/2) interferograms are needed, and γ_i will be multiplied by 2^n. In our example n = 3, so γ_i is multiplied by 8, and N = 360/30*(3 + 2)/2 = 30 phase-shifts are required if the base phase-shift step is δ=30°.

With the standard I-SHG, the phase-shift is changed by discrete steps such that sinc(Δ/2) = 1. Considering that the relative phase is obtained by $\tan\varphi_i = c_i/b_i$, one has $\varphi_i(\Delta = 0) = \varphi_i(\Delta \neq 0)$: the relative phase is independent of Δ. The interferometric contrast $\gamma_i = \sqrt{{b_i}^2 + {c_i}^2}$ implies $\gamma_i(\Delta \neq 0) = \gamma_i(\Delta = 0)\mathrm{sinc}(\Delta/2)$, i.e. just a constant multiplicative factor, because Δ (the ramp time) is constant.

A.2 Detail of the extraction of the interferograms from the buffer synchronized by the phase scans

In Fig. 7, we explain how the pixels of the interferograms are extracted from the buffers normally used to compute the pixels of the standard image. To measure the signal from the PMT (R6357, Hamamatsu Photonics, Japan), the signal is oversampled by an Analog-to-Digital acquisition card (PCI-6110, National Instruments, Austin, USA) at f_{sample}= several MHz (settable), which is much higher than the pixel rate f_{pixel}, usually in the range 1-100kHz. This oversampling allows to split each pixel into up to N=f_{sample}/f_{pixel} ~ 5-1000 subpixels. The number N of subpixels is equal to the imposed number of interferograms. Between ramps, the high-voltage must be reset (see Fig. 1(c) or Fig. 7) which leads to dead-times (=T_{dead}) that have to be taken into account such that:

$$\text{Pixel time} = \frac{1}{f_{pixel}} = T_{ramp} = T_{dead} + \sum_{j=1}^{N} T_{subpixel}(i) \quad \text{(a4)}$$

Because the maximum rate of the acquisition card f_{sample} is limited to 5MHz [43], the smallest accessible time interval is $\tau_R = 1/5 = 0.2\mu s$. Also, the acquisition rate is always a sub-multiple of the 20MHz master time-base rate [43], which means this time resolution can be adjusted by steps down to $\Delta\tau_R = 1/20 = 0.05\mu s$ only. This implies that T_{ramp}, $T_{subpixel}$ (i) and T_{dead} have to be multiples of τ_R, and can be adjusted by steps of $\Delta\tau_R$ only.

Table 2 shows the subpixel times (i.e. the pixel time of the I-SHG interferograms) corresponding to the different phase-scan modes: a certain number of samples from the buffer are averaged to compute the subpixels, and some other are discarded because they correspond to the dead-time between the ramps.

Optics EXPRESS

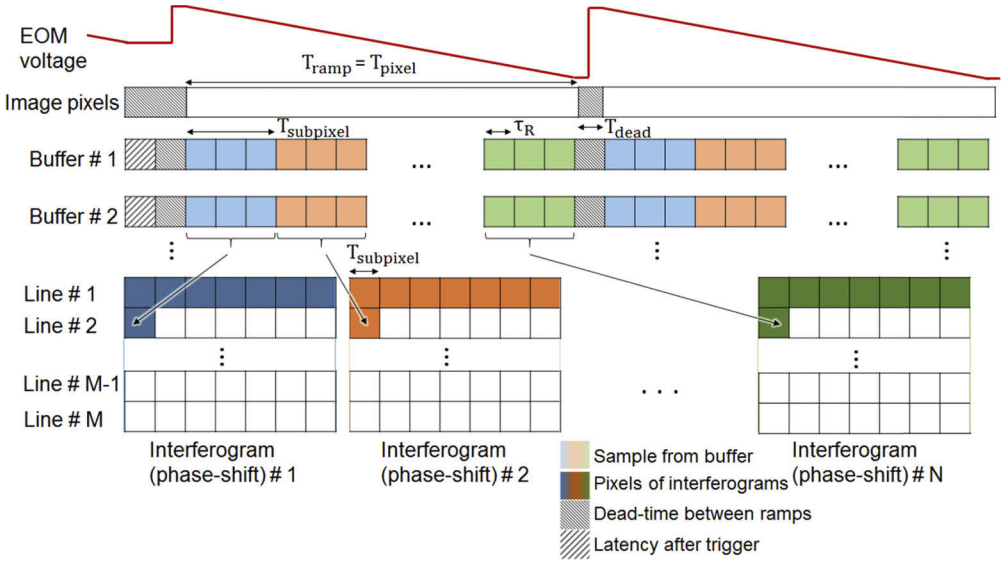

Fig. 7. Detail of the filling of the interferogram arrays, from the acquired buffer. One ramp corresponds to one pixel of the standard image, but the oversampling of these pixels allows to split them into several subpixels. Samples from the buffer are averaged by packet and form each subpixel, i.e. the pixels of the N different interferograms. There are some dead-times between ramps indicated in grey, and a latency at the beginning of each line indicated by striations.

Table 2. Timing used for the different ramp times of the phase scanner: pixel time of the 30 interferograms, and corresponding number of samples used to form these pixels.

With a set of 30 phase-shifts, at 5MHz / Ramp time T_{ramp}	Subpixel time (interferograms dwell time) $T_{subpixel}$ (µs)	Number of buffer samples averaged into one subpixel	Number of buffer samples in dead-times
20 µs	0.6	3	10
200 µs	7.4	37	140
2000 µs	67.2	42	115

A.3 Equation of the precision of the phase measurement

If C is the level of interference contrast and N the number of interferograms, the precision $\delta\varphi$ of the phase calculated by our method (see [41]) is estimated by [44]:

$$\delta\varphi \sim \frac{1}{C \times SNR}\sqrt{\frac{2}{N}} \tag{a5}$$

The SNR is a sum of various terms: the electronical noise, the laser's fluctuations and the photon shot noise $SNR_{shot} \sim \sqrt{n_{photons}}$. The number $n_{photons}$ of collected photons is also assumed proportional to the exposure time.

Funding

Canada Foundation for Innovation; Natural Sciences and Engineering Research Council of Canada; Fonds de Recherche du Québec - Nature et Technologies.

Optics EXPRESS

Acknowledgments

M.P. thanks the company Raicol Crystals for technical discussions, the CREATE/GRK program for scholarship, and Antoine Laramée for implementation help. M.P. also acknowledges Sheila Laverty from St-Hyacinthe veterinary school for meniscus samples, and Magali Millecamps & Laura Stone from McGill's Edwards Centre for Research on Pain for tendon samples.

Disclosures

The authors declare that there are no conflicts of interest related to this article.

References

1. S. Roth and I. Freund, "Optical second-harmonic scattering in rat-tail tendon," Biopolymers **20**(6), 1271–1290 (1981).
2. F. Helmchen and W. Denk, "Deep tissue two-photon microscopy," Nat. Methods **2**(12), 932–940 (2005).
3. W. Denk, J. H. Strickler, and W. W. Webb, "Two-photon laser scanning fluorescence microscopy," Science **248**(4951), 73–76 (1990).
4. P. J. Campagnola, A. C. Millard, M. Terasaki, P. E. Hoppe, C. J. Malone, and W. A. Mohler, "Three-dimensional high-resolution second-harmonic generation imaging of endogenous structural proteins in biological tissues," Biophys. J. **82**(1), 493–508 (2002).
5. A. Zoumi, A. Yeh, and B. J. Tromberg, "Imaging cells and extracellular matrix in vivo by using second-harmonic generation and two-photon excited fluorescence," Proc. Natl. Acad. Sci. U. S. A. **99**(17), 11014–11019 (2002).
6. J. R. M. Brown, A. C. Millard, and P. J. Campagnola, "Macromolecular structure of cellulose studied by second-harmonic generation imaging microscopy," Opt. Lett. **28**(22), 2207–2209 (2003).
7. K. J. Choi, M. Biegalski, Y. L. Li, A. Sharan, J. Schubert, R. Uecker, P. Reiche, Y. B. Chen, X. Q. Pan, V. Gopalan, L. Q. Che, D. C. Schlom, and C. B. Eom, "Enhancement of ferroelectricity in strained BaTiO3 thin films," Science **306**(5698), 1005–1009 (2004).
8. S. Yazdanfar, L. Laiho, and P. T. C. So, "Interferometric second harmonic generation microscopy," Opt. Express **12**(12), 2739–2745 (2004).
9. M. Fiebig, T. Lottermoser, D. Meier, and M. Trassin, "The evolution of multiferroics," Nat. Rev. Mater. **1**(8), 16046 (2016).
10. M. Fiebig, V. V. Pavlov, and R. V. Pisarev, "Second-harmonic generation as a tool for studying electronic and magnetic structures of crystals: review," J. Opt. Soc. Am. B **22**(1), 96–118 (2005).
11. M. Fiebig, T. Lottermoser, D. Fröhlich, A. V. Goltsev, and R. V. Pisarev, "Observation of coupled magnetic and electric domains," Nature **419**(6909), 818–820 (2002).
12. M. Fiebig, D. Fröhlich, T. Lottermoser, V. V. Pavlov, R. V. Pisarev, and H. J. Weber, "Second harmonic generation in the centrosymmetric antiferromagnet NiO," Phys. Rev. Lett. **87**(13), 137202 (2001).
13. M. Rivard, C.-A. Couture, A. K. Miri, M. Laliberté, A. Bertrand-Grenier, L. Mongeau, and F. Légaré, "Imaging the bipolarity of myosin filaments with Interferometric Second Harmonic Generation microscopy," Biomed. Opt. Express **4**(10), 2078–2086 (2013).
14. M. Pinsard, M. Schmeltz, J. van der Kolk, S. A. Patten, H. Ibrahim, L. Ramunno, M.-C. Schanne-Klein, and F. Légaré, "Elimination of imaging artifacts in second harmonic generation microscopy using interferometry," Biomed. Opt. Express **10**(8), 3938 (2019).
15. M. Rivard, K. Popov, C.-A. Couture, M. Laliberté, A. Bertrand-Grenier, F. Martin, H. Pépin, C. P. Pfeffer, C. Brown, L. Ramunno, and F. Légaré, "Imaging the noncentrosymmetric structural organization of tendon with Interferometric Second Harmonic Generation microscopy," J. Biophotonics **7**(8), 638–646 (2014).
16. C.-A. Couture, S. Bancelin, J. N. van der Kolk, K. Popov, M. Rivard, K. Légaré, G. Martel, H. Richard, C. Brown, S. Laverty, L. Ramunno, and F. Légaré, "The Impact of Collagen Fibril Polarity on Second Harmonic Generation Microscopy," Biophys. J. **109**(12), 2501–2510 (2015).
17. Q. Nguyen, J. Driscoll, E. M. Dolnick, and D. Kleinfeld, "MPScope 2.0. A Computer System for Two-Photon Laser Scanning Microscopy with Concurrent Plasma-Mediated Ablation and Electrophysiology," in *In Vivo Optical Imaging of Brain function*, Second Edition (Taylor & Francis, 2009), pp. 117–142.
18. S. Tang, T. B. Krasieva, Z. Chen, G. Tempea, and B. J. Tromberg, "Effect of pulse duration on two-photon excited fluorescence and second harmonic generation in nonlinear," J. Biomed. Opt. **11**(2), 020501 (2006).
19. S. Bancelin, C. A. Couture, M. Pinsard, M. Rivard, P. Drapeau, and F. Légaré, "Probing microtubules polarity in mitotic spindles in situ using Interferometric Second Harmonic Generation Microscopy," Sci. Rep. **7**(1), 6758 (2017).
20. Y. Fu, T. B. Huff, H.-W. Wang, J.-X. Cheng, and H. Wang, "Ex vivo and in vivo imaging of myelin fibers in mouse brain by coherent anti-Stokes Raman scattering microscopy," Opt. Express **16**(24), 19396 (2008).
21. D. H. Torchinsky and D. Hsieh, "Rotational anisotropy nonlinear harmonic generation," in *Magnetic Characterization Techniques for Nanomaterials* (Springer Berlin Heidelberg, 2017), pp. 1–49.
22. W. R. Zipfel, R. M. Williams, and W. W. Webb, "Nonlinear magic: Multiphoton microscopy in the biosciences," Nat. Biotechnol. **21**(11), 1369–1377 (2003).

Optics EXPRESS

23. J. Schindelin, I. Arganda-Carreras, E. Frise, V. Kaynig, M. Longair, T. Pietzsch, S. Preibisch, C. Rueden, S. Saalfeld, B. Schmid, J. Y. Tinevez, D. J. White, V. Hartenstein, K. Eliceiri, P. Tomancak, and A. Cardona, "Fiji: An open-source platform for biological-image analysis," Nat. Methods **9**(7), 676–682 (2012).
24. S. Bancelin, C.-A. Couture, K. Légaré, M. Pinsard, M. Rivard, C. Brown, and F. Légaré, "Fast interferometric second harmonic generation microscopy," Biomed. Opt. Express **7**(2), 399–408 (2016).
25. Thorlabs, *BBD102 and BBD103 Brushless DC Servo Controllers - User Guide* (2012).
26. M. Roth, E. Samoka, E. Mojaev, and M. Tseitlin, "Rtp Crystals for Electro-Optic Q-Switching," Univ. Jerusalem **6**, 205–212 (2007).
27. M. T. Hartman, V. Quetschke, D. B. Tanner, D. H. Reitze, and G. Mueller, "Parallel phase modulation scheme for interferometric gravitational-wave detectors," Opt. Express **22**(23), 28327–28337 (2014).
28. V. Nikolenko, B. Nemet, and R. Yuste, "A two-photon and second-harmonic microscope," Methods **30**(1), 3–15 (2003).
29. R. Stolle, G. Marowsky, E. Schwarzberg, and G. Berkovic, "Phase measurements in nonlinear optics," Appl. Phys. B: Lasers Opt. **63**(5), 491–498 (1996).
30. M. Pinsard, "P-SHG (forked version) GitHub," https://github.com/MaxP92/P-SHG.
31. E. I. Romijn, A. Finnøy, R. Kumar, and M. B. Lilledahl, "Automated calibration and control for polarization-resolved second harmonic generation on commercial microscopes," PLoS One **13**(4), e0195027 (2018).
32. L. Coluccino, C. Peres, R. Gottardi, P. Bianchini, A. Diaspro, and L. Ceseracciu, "Anisotropy in the viscoelastic response of knee meniscus cartilage," J. Appl. Biomater. Funct. Mater. **15**(1), e77–e83 (2017).
33. J. Dubuc, C. Girard, H. Richard, J. De Lasalle, and S. Laverty, "Equine meniscal degeneration is associated with medial femorotibial osteoarthritis," Equine Vet. J. **50**(1), 133–140 (2018).
34. Y. Tanaka, E. Hase, S. Fukushima, Y. Ogura, T. Yamashita, T. Hirao, T. Araki, and T. Yasui, "Motion-artifact-robust, polarization-resolved second-harmonic-generation microscopy based on rapid polarization switching with electro-optic Pockells cell and its application to in vivo visualization of collagen fiber orientation in human facial skin," Biomed. Opt. Express **5**(4), 1099–1113 (2014).
35. C. L. Koliopoulos, "Simultaneous phase shift interferometer," Proc. SPIE **1531**, 119–127 (1991).
36. P. Stoller, K. M. Reiser, P. M. Celliers, and A. M. Rubenchik, "Polarization-modulated second harmonic generation in collagen," Biophys. J. **82**(6), 3330–3342 (2002).
37. E. L. Dewalt, S. Z. Sullivan, P. D. Schmitt, R. D. Muir, and G. J. Simpson, "Polarization-modulated second harmonic generation ellipsometric microscopy at video rate," Anal. Chem. **86**(16), 8448–8456 (2014).
38. S. Psilodimitrakopoulos, P. Loza-Alvarez, and D. Artigas, "Fast monitoring of in-vivo conformational changes in myosin using single scan polarization-SHG microscopy," Biomed. Opt. Express **5**(12), 4362–4373 (2014).
39. S. Bancelin, J. N. Van der Kolk, A. S. Quigley, M. Pinsard, S. P. Veres, L. Kreplak, L. Ramunno, and F. Légaré, "Gouy phase shift measurement using interferometric second-harmonic generation," Opt. Lett. **43**(9), 1958–1961 (2018).
40. B. Lynch, C. Bonod-Bidaud, G. Ducourthial, J. S. Affagard, S. Bancelin, S. Psilodimitrakopoulos, F. Ruggiero, J. M. Allain, and M. C. Schanne-Klein, "How aging impacts skin biomechanics: A multiscale study in mice," Sci. Rep. **7**(1), 1–10 (2017).
41. J. E. Greivenkamp, "Generalized data reduction for heterodyne interferometry," Opt. Eng. **23**(4), 350–352 (1984).
42. Z. Wang and B. Han, "Advanced iterative algorithm for phase extraction of randomly phase-shifted interferograms," Opt. Lett. **29**(14), 1671–1673 (2004).
43. National Instruments, *NI PCI-6110/6111 User Manual* (2003).
44. C. P. Brophy, "Effect of intensity error correlation on the computed phase of phase-shifting interferometry," J. Opt. Soc. Am. A **7**(4), 537–541 (1990).

9.2 Further information on the phase scanner

The high voltage of the EOM can be calibrated by acquiring a single line of pixels, using the 2000μs voltage ramp (Fig. 9.1). The line is divided into 150 pixels which means 15μs exposure time. One ramp is sufficient as it scans the entire range of the EOM. It is acquired almost instantaneously, in 2000μs=0.2ms. Otherwise, the calibration can also be done with the DC mode, by successively changing the voltage by steps of e.g. 10V. But this mode is not optimized for speed: the total acquisition time will be around 10 mins. Note that this DC mode could also replace the rotatable glass plate as a static phase-shifter. The first method (AC) has the advantage being able to be done routinely, in a snapshot, to check the calibration before measurements. The fitting curve (red) confirms that the dependence of the phase-shift with respect to the applied voltage is indeed linear, as the experimental points indeed follow the cosine curve: there seems to not be any noticeable Kerr effect, which would add a quadratic dependence.

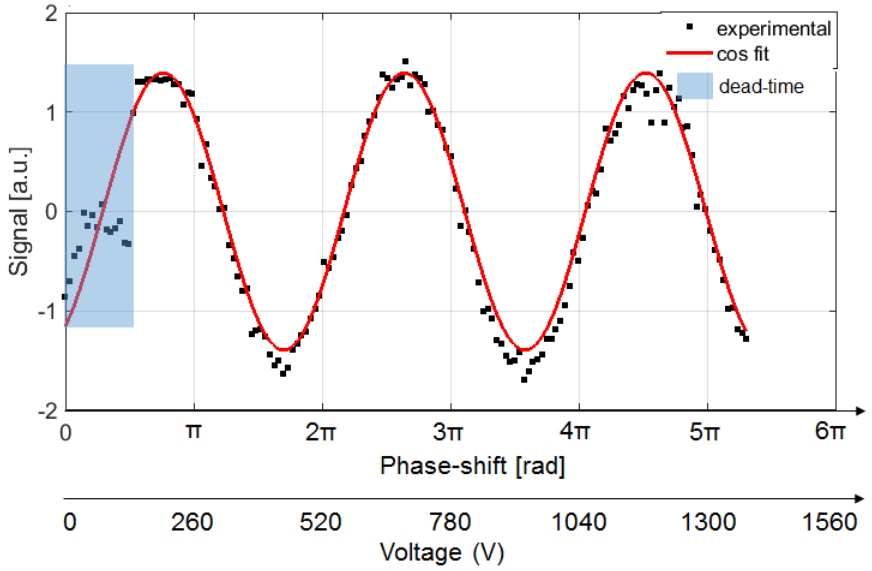

Figure 9.1: Calibration of the high voltage of the EOM (using the 2000μs voltage ramp). Exposure time by point: 15μs.

The calibration of the polarization at the excitation and reference SHG wavelengths is also important: Fig. 3.6 in section 3.2.1, complementary to part 2.4) of the article, shows the possibilities of using one or two waveplates.

When an interferogram is recorded at an unusually low exposure time (e.g. with the 20μs voltage ramps), the obtained images can reveal fluctuations happening at a lower time-scale, because they are no longer averaged compared to higher exposure times. It is visible in the phase map of a tendon acquired with the 20μs voltage ramps (Fig. 9.2), where the laser fluctuations (some are pointed to by white arrows)

are degrading the image quality. These fluctuations are invisible in the phase map with 200μs voltage ramps, even if acquired just after the first one under the same experimental conditions. This is because a higher exposure time averages the temporal fluctuations. The user must therefore ensure that the temporal stability of the laser is good before performing single frame I-SHG acquisitions. A photodiode can reveal these fluctuations, down to the nanosecond time-scale.

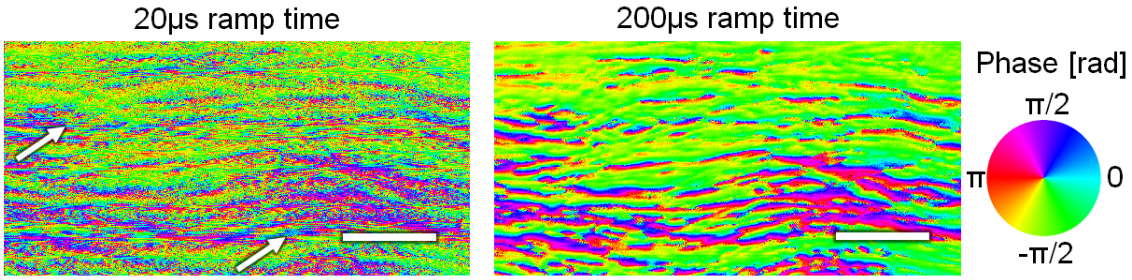

Figure 9.2: Temporal fluctuations of the laser source under the μs time-scale. (a) Phase map of a tendon (see article for description), obtained by I-SHG with the 20μs voltage ramp (stage-scanning). Fluctuations are visible, and white arrows point to some of them. (b) Same, but acquired with more time per pixel (200μs ramp) which will average the fluctuations. Scale-bar: 20μm.

In addition, we illustrate here (Fig. 9.3) the possibility of discriminating the local relative polarity for all 1S-ISHG modes, despite the reduction of precision if the speed of the mode is increased. The images are the same phase map of a meniscus presented in fig.5 of the article. The red (negative polarity) or green (positive polarity) zones are indeed similar in all the images, from 20μs (A) to 2000μs (C) and standard I-SHG (D). The red/green colormaps were computed by fitting the phase histograms (indicated on the right of the image), meaning that the colormaps reflect the distributions of phase, and that any black pixel does not belong to one of the two peaks at $\pi/2$ or -$\pi/2$. The Gaussian fitting used to compute the colormaps are indicated in yellow on the colorwheels at the right. The polarization used here is linear and oriented horizontally (in the image plane), but a circular I-SHG could be implemented to equally excite all the fibrils in this complex tissue. Figure 9.4 presents phase-maps of PPLN obtained by single-scan I-SHG technique with 120fs pulses and analog new galvos. Compared to the article, where 320fs pulses are used, the phase distributions are less narrow which shows a decreased precision due to lower contrast.

Moreover, the phase-scanner was tested at a wavelength close to 1μm (1064nm), and showed a half-wave voltage of $\sim$280V, as compared to 250V at 810nm. With a 1400V range, 5π of phase-shift can still be reached (see Fig. 9.5 (A)). However, we used the laser presented in [174] that was previously utilized for I-SHG (Vanguard), featuring 12ps pulses: such pulses have much less spectral bandwidth ($10/0.13\sim 100$ times less), and the temporal effects are thus attenuated. With the basic I-SHG elements,

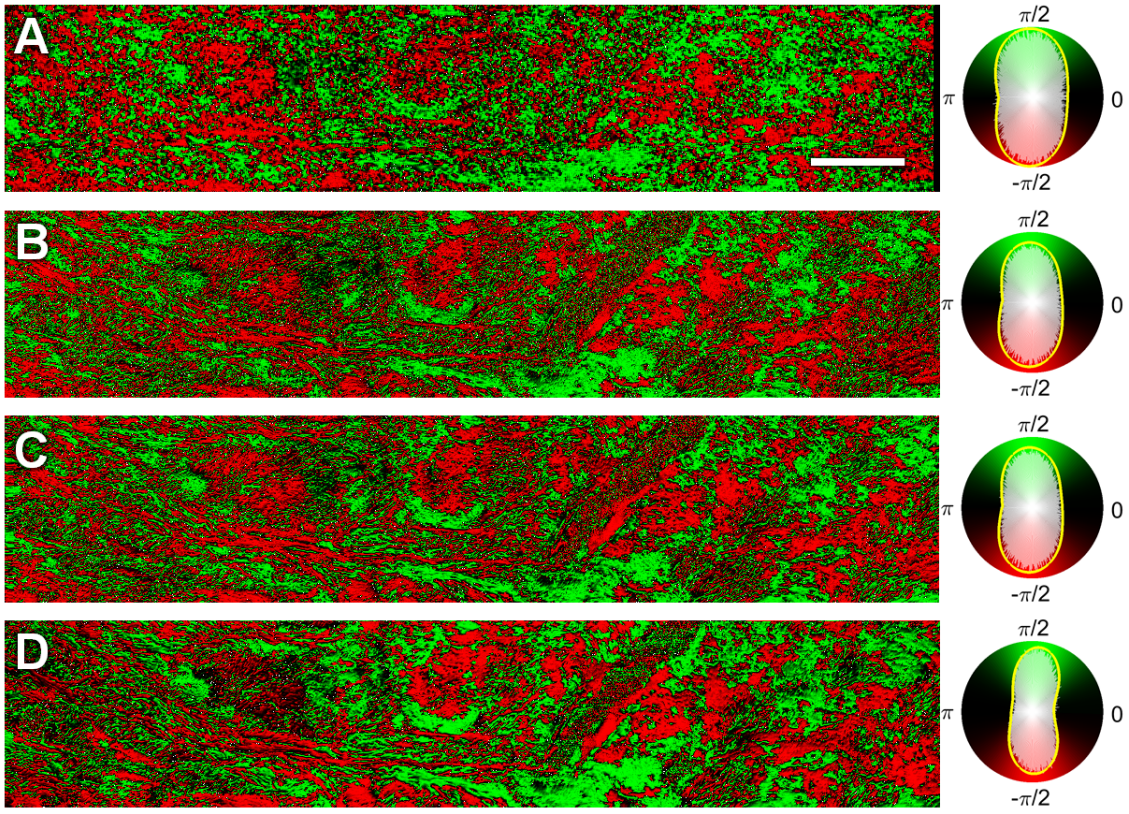

Figure 9.3: 1S-ISHG phase map inside meniscus (central zone), seen with a colormap highlighting the two different polarities (complementary to fig.5 of the article). (A) 20μs, (B) 200μs and (C) 2000μs modes, compared to (D) standard static I-SHG. The phase histograms are indicated on the right, on the colorwheels that were built from the Gaussian fit of the phase peaks, indicated in yellow on the histograms. Scale-bar: 50μm.

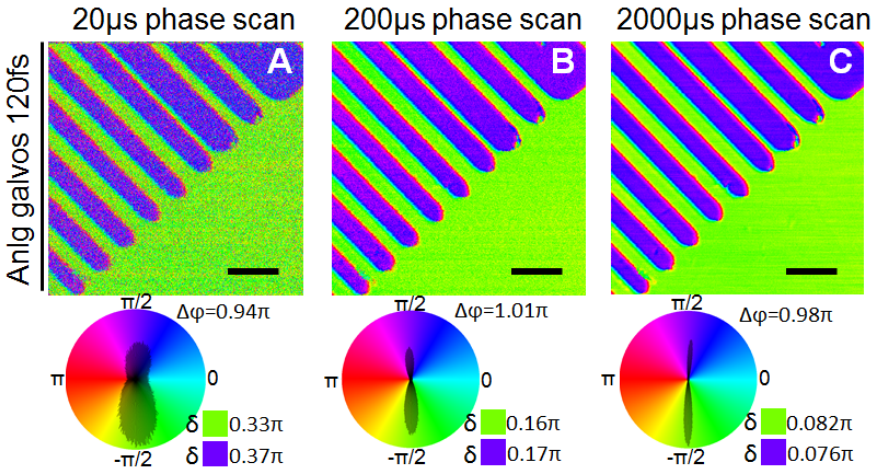

Figure 9.4: Single-frame I-SHG images (phase) of PPLN using different phase-scan speed, acquired with 120fs pulses (and analog galvos): (A) 20μs, (B) 200μs, (C) 2000μs. Scale-bar: 10μm.

the group delay due to GVM is slightly below 6ps, which is acceptable, but it increases to 18ps with the phase-scanner: ∼36mm of calcite is still needed to compensate for it, which corresponds to one

roundtrip in our prisms set at the minimum width. However, as seen in the field autocorrelation (see section 3.2.2) in Fig. 9.5 (B), there is a large tuning range for the GVM compensation contrary to fs pulses, and the GDD due to the dispersive elements still exists, though it has no noticeable effect with ps pulses.

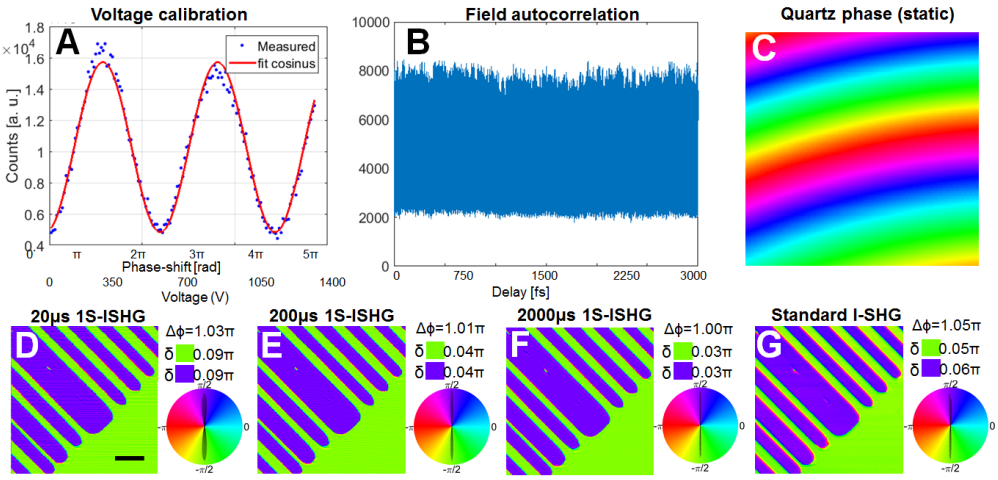

Figure 9.5: I-SHG in PPLN (50×50μm) using a 1064nm wavelength and picosecond pulses, with the new analog galvos. (A) Calibration of the high voltage and the phase-shift it induces. (B) Interferometric contrast and fringes seen by field autocorrelation. (C) Phase-map acquired in quartz, with standard I-SHG. (Bottom) PPLN phase-map with 1S-ISHG and the modes: (D) 20μs, (E) 200μs, (F) 2000μs.(G) With standard I-SHG. The average power on sample is $\sim$ 80mW, compared to 15mW with fs pulses. Scale-bars: 10μm.

The interferometric contrast thus depends only on spatial effects, not temporal: Fig. 9.5(B) shows a contrast of 4:1, because the alignment was imperfect. It can be seen in Fig. 9.5(C), as the I-SHG interference pattern (acquired in quartz) is not centered. Yet, the contrast is relatively high, even at an off-centered position, thanks to the ps pulses: with fs pulses instead, it was shown that the contrast decreases quickly at a few tens of μm from the center of the pattern [10]. The sample phase map (of PPLN) can then be corrected using this calibration, and the maps (D) to (G) are obtained. The phase distributions are narrower than e.g. fig.2 of the article, which used fs pulses. Importantly, the longest phase-scan of 1S-ISHG (acquired in 380secs) is confirmed as the most precise mode, with a distance between phase peaks exactly equal to π, and the narrowest peak widths (even smaller than standard I-SHG).

Figure 9.6 and 9.7 show backward I-SHG images for the first time. Instead of using a full transmission dichroic mirror, a 50:50 beam-splitter in the visible range is used instead. It will therefore reflect 50% of the backward SHG signal to the PMT, and 0.5*0.5 = 25% of the reference SHG. This loss of power could be reduced by dividing the reference and sample arms in the interferometer, and by illuminating

the sample from the collective objective with the reference SHG such that both SHG travel in the same direction (backward), and get totally reflected by the dichroic. However, relatively thin samples would be required so as not to affect the reference SHG too much when it travels through the sample.

PPLN phase-maps are quite similar in intensity SHG in both directions (Fig. 9.6 A and B), but the boundaries seem to be enhanced in backward (as seen in forward SHG in chap. 6). Stage-scanning using the 2000μs phase-scan speed shows a much noisier phase-map in backward (B') compared to forward (B). Figure 9.6 C however proves that the precision on the phase can be improved. The 200μs phase-scan speed gives a lower SNR implying a higher uncertainty on the phase measurement (Fig. 9.6 D): the phase distribution still presents two peaks, but poorly distinguishable. Notably, the phase-map values in B' and D are inverted, which is just a display convention as the phase measured in I-SHG is always relative.

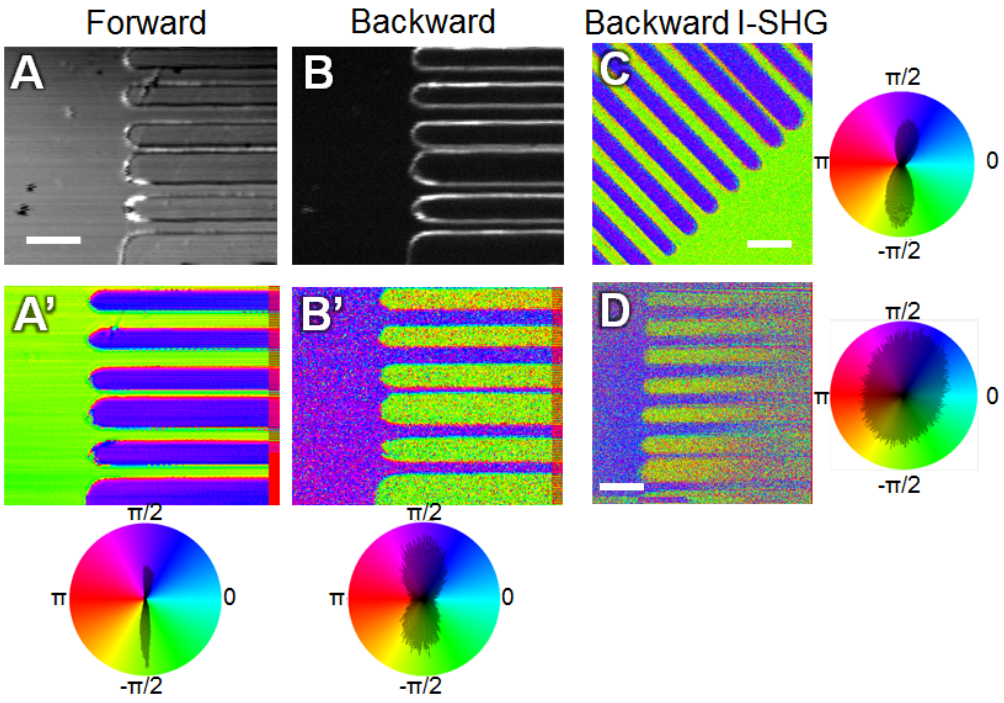

Figure 9.6: Backward I-SHG acquired in PPLN, and its comparison with forward for different scan modes. (Left): stage-scanning acquired with 1S-ISHG using the 2000μs phase-scan speed, forward (A for intensity SHG, A' for phase I-SHG) and backward (B for intensity SHG, B' for phase I-SHG). (Right): Backward 1S-ISHG phase-maps, with analog galvos scanning and 2000μs phase-scan speed (C), with digital galvos scanning and 200μs phase-scan speed (D). Scale-bars: 10μm.

In backward images of tendon, the visible features are substantially different than in forward because the coherence length is much smaller (see section 2.1.5), as shown in Fig. 9.7, first line. This is again interpreted as a decrease in precision on the phase measurement, coupled with the difficulty of distinguishing patterns from the sample itself. For some examples, the phase is very noisy (Fig. 9.7 D'),

but for others small patterns appear (Fig. 9.7 B'). These two I-SHG phase maps were acquired with the 2000μs phase-scan speed, because the slower ones (20 and 200μs) had too low of exposure times to permit a sufficient SNR for a good phase retrieval. In Fig. 9.7 F', it seems that the backscattering of the forward on the backward direction (see [119]) is the main visible feature, as the recognizable patterns are quite similar to the forward SHG intensity image, and not "speckle-like", as is usually found in the backward direction. Overall, backward I-SHG is interesting since forward detection is not always

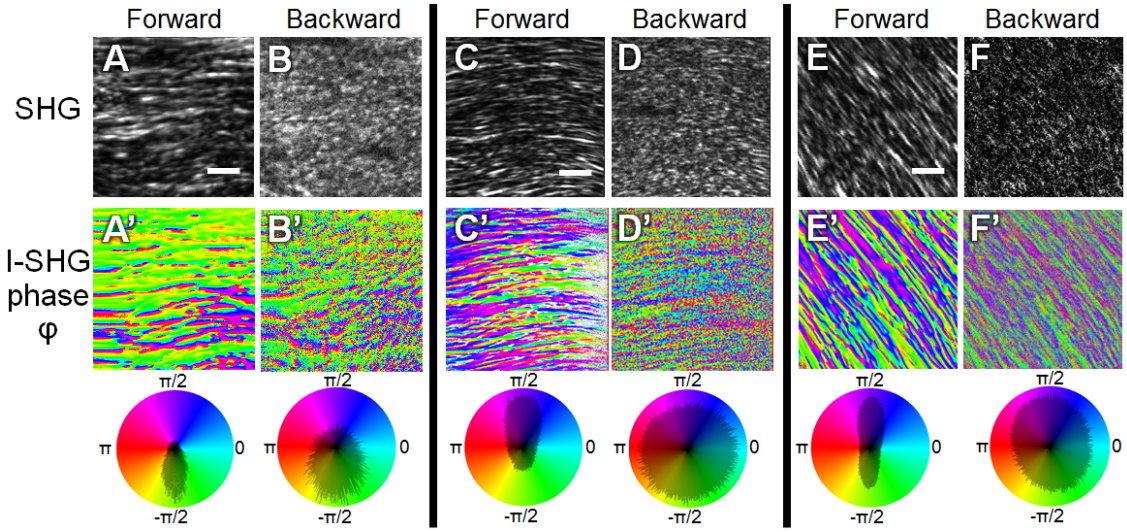

Figure 9.7: Backward I-SHG acquired in tendon, and its comparison with forward for different scan modes. The first line (with grey scales) shows the intensity SHG images, the second line (with HSV colormap) is for the I-SHG phase-maps. 3 different scan-modes separated by thick black lines show the SHG and I-SHG for forward and backward directions. (Left): stage-scanning acquired with 1S-ISHG using the 2000μs phase-scan speed, forward (A&A') and backward (B&B'). (Middle): digital galvos with standard I-SHG, forward (C&C') and backward (D&D'). (Middle): analog galvos with standard I-SHG, forward (E&E') and backward (F&F'). Scale-bars: 10μm.

possible, as it is limited to thin and relatively transparent samples. However, lower signal is usually collected from this direction, and the lower coherence compared to forward direction also greatly reduces I-SHG performances in backward direction.

Conclusion and perspectives

9.3 Most significant findings and contributions

This thesis was mainly focused on coupling Interferometric Second Harmonic Generation microscopy (I-SHG) to a global multiphoton imaging paradigm involving other microscopy techniques, and on improving the compatibility of I-SHG with them. We started by showing the different mechanisms that influence second harmonic generation, in order to be able to correctly interpret the images acquired with this technique. In addition, I-SHG was presented in detail, along with its limitations: among others, the fact that the measured signal is the result of complex interferences. To overcome these limitations, it was necessary to focus on the details of the microscopy assembly, from the production of the laser signal to the acquisition of images, and through the electronic and software control of the various instruments. In particular, the geometry of the optical assembly and its components have been redesigned to make I-SHG more versatile (notably its use with a laser-scanning or an electro-optical modulator, EOM), and to integrate other modes of contrast such as CARS (and its frequency-modulated variant, FM-CARS), 2-photon fluorescence (2PEF), polarization-resolved SHG (p-SHG) or circular dichroism SHG (CD-SHG). In addition, a new galvanometric laser-scanning system has been implemented at the hardware and software level, to be more compatible with I-SHG and SHG microscopy in general. Finally, the translation plate used for scanning the sample has been completely reprogrammed to change the acquisition parameters, avoid certain deformations and reduce the imaging time. This modality is, indeed, always useful for visualizing structures requiring a large field-of-view.

The second objective was to apply this implementation of several imaging modalities and large field-of-view to the study of the meniscus of the knee joint, which has a much more complex collagen arrangement than most tissues containing this biopolymer. In particular, "directional" SHG microscopy

(forward and backward) made it possible to differentiate several arrangements of collagen fibrils in this tissue: some fibrils are grouped as thick fibers called "tie-fibers", and others form bundles in the perpendicular direction called "fascicles". In addition, the maturation of this tissue has also been studied through the alignment of collagen fibrils in the imaging plane by polarization-resolved SHG (p-SHG) microscopy. This technique has e.g. shown that immature menisci exhibit a fairly random alignment of collagen, with some samples, by contrast, having a uniform arrangement. In more mature tissues (adult) one finds rather homogeneously aligned clusters (orthogonal fascicles), delimited by thick fibers (sections of "tie-fibers sheets"), according to the model proposed in another study on bovine samples [4].

In addition, the thesis also aimed at studying advanced aspects of SHG microscopy, which could partly explain the complexity of the formation of the images. One of them is the Gouy phase-shift that a beam undergoes while crossing its focus, and which therefore implies a variation of the phase in the vicinity of the focal volume: it is then not only a very important aspect for I-SHG, but also in standard SHG. It has been shown that this phase-shift can be directly characterized by I-SHG measurements, with a sample whose thickness is small compared to the focal volume. It also means that it will act on any phase imaged by I-SHG, where structures of the same polarity but slightly shifted in depth will present a variation in phase.

This effect is also artefactual in standard SHG microscopy, and in some arrangements it is likely to have a significant impact. For example, we have seen that in muscle sarcomeres, myosin filament alternations could be arranged in 3D such that it produces coherent artifacts (single-band), partly due to the Gouy phase-shift. Aiming at studying a model sample that similarly presents series of interfaces between two opposite polarities (the PPLN), we showed that it did not have coherent artifacts, but rather that defects created a large scattering contribution. This was a good opportunity to study the radiation pattern at these interfaces by numerical simulations, and thus to clarify this point which was little discussed in the literature: the SHG converted at an interface of opposite polarities always takes the form of two lobes delimited by the interface, of opposite amplitudes (i.e. π phase-shifted). These lobes are therefore supposed to interfere destructively once recombined on the detector. We have shown that I-SHG allowed us to recover these destructive interferences (i.e. zero signal) at the interfaces presenting these artifacts, and to increase the visibility of those which do not present artifacts by a factor 3 to 5.

Finally, the last objective was to benefit from the aforementioned improvements to make I-SHG more versatile and rapid. The control of the scanning methods was decisive, as was the complete development

of a new software to operate the microscope, capture images, and process and format data. The imaging of a dynamic process (cellular mitosis) allowed us to prove that femtosecond I-SHG by laser scanning worked in such studies, but also showed its experimental limits: for example, the need of adjustments during acquisition, as well as its limited precision due to a low SNR in such a sample, and thus the need to work with a faster method.

We have seen the possibility of using the electro-optic effect to apply the phase-shift required in I-SHG at a rate up to the one used to form the images ($\sim$ 50kHz), even with an interferometer with one arm, thus acting on two different wavelengths. However, it was necessary to study precisely the mechanisms that govern the interferometric contrast: it involves not only the spatial overlap of the beams, but more importantly their temporal overlap, which must be optimized and corrected for first-order and second-order dispersions that impact femtosecond pulses. These advances later allowed us to apply the phase-shifts during pixels acquisition, rather than between each interferogram, which converted I-SHG into a single-scan acquisition (1S-ISHG). With the PPLN model sample, mouse tail tendon and equine meniscus samples, it was shown that this acquisition mode actually gave similar results to the normal method, provided that the number of collected photons was equivalent. The 1S-ISHG also allows us to obtain I-SHG (phase and amplitude) images in a time equal to that of a standard SHG image, if the fast mode is used. Since less photons are collected, the accuracy on the phase is reduced but we can still find the correct polarity at each pixel (because it just means to discriminate whether the phase is around $\pi/2$ or -$\pi/2$).

All these improvements thus make it possible to produce more precise I-SHG images with less experimental and computational efforts. In addition, we have also successfully integrated I-SHG into a more general paradigm, which encompasses other variants of SHG, and multiphoton microscopy on the whole. Nevertheless, there is still some potential to push this integration even further.

9.4 Perspectives

Overall, I-SHG has the advantages of SHG microscopy (high specificity and low invasiveness), while also removing imaging artifacts: if confirmed in other samples, this opens up I-SHG as a paradigm to not only determine the polarity, but also obtain images of structures with higher contrast.
Experiment of single-scan I-SHG are rather simple and fast to perform, as is the data treatment too: a

"black box" containing the I-SHG optical components could be built as an add-on to place before any scanning microscope, to upgrade it to the I-SHG modality.

The 1S-ISHG speed improvement by more than one order of magnitude could be used to characterize dynamic processes in the future: it could be a great benefit for microtubule imaging in particular, at first to improve the resolution in mitosis imaging, and meiosis division could also be invetigated. Most importantly, it could serve to elucidate the ongoing debate on local and global polarity of these proteins in the dendrites of neurons [231], or fibroblasts. This could also be applied to large-scale and systematic studies, to characterize a high number of samples and have better statistics for biology studies.

I-SHG could also be further developed, using circular polarization in input or the backward SHG signal, as encouraged by the last proof-of-concepts shown in the last chapter. I foresee possible removal of artifacts in samples other than muscles or PPLN, and the use of the height dependence with the phase to perform profilometry by I-SHG as well. The new microscope program and its multimodal coupling will also be of great value for the study of future biological samples or optically nonlinear materials, which readily opens up an efficient use of enhanced SHGs (I-SHG, P-SHG, CD-SHG, and F/B SHG) in tandem with other nonlinear microscopies, and showed their usefulness in understanding the hyperstructure of collagen in 3D.

Finally, pathologies in muscles like dislocations could be further investigated using the set-up. The meniscus structure is also still not well understood, and could benefit from the multimodal imaging coupled to improved I-SHG: using efficient stage-scanning, a multiscale study with image sizes from the 10mm to the 100μm scale, or under traction assay, could be highly interesting and valuable for studies of the knee joint.

Bibliography

[1] S. Akturk, X. Gu, M. Kimmel & R. Trebino, 2006, 'Extremely simple single-prism ultrashort- pulse compressor'. *Optics Express*, **14**(21):p. 10101, doi:10.1364/OE.14.010101

[2] B. Alberts, Q. Johnson & W. Peter, *Molecular Biology of the Cell* (Garland Science, 2007)

[3] R. Ambekar Ramachandra Rao, M. R. Mehta, S. Leithem & J. Toussaint, 2010, 'Fourier Transform-Second-Harmonic Generation Imaging of Collagen Fibers in Biological Tissues - OSA Technical Digest (CD)'. *Biomedical Optics*, p. BSuD63

[4] S. H. Andrews, J. B. Rattner, Z. Abusara, A. B. Adesida, N. G. Shrive & J. L. Ronsky, 2014, 'Tie-fibre structure and organization in the knee menisci'. *Journal of Anatomy*, **224**(5):pp. 531–537, doi:10.1111/joa.12170

[5] Z. Ansari, Y. Gu, M. Tziraki, R. Jones, P. M. French, D. D. Nolte & M. R. Melloch, 2001, 'Elimination of beam walk-off in low-coherence off-axis photorefractive holography.' *Optics letters*, **26**(6):pp. 334–6, doi:10.1364/OL.26.000334

[6] J. Art, 'Photon Detectors for Confocal Microscopy', in 'Handbook Of Biological Confocal Microscopy SE - 12', pp. 251–264 (Springer, 2006), ISBN 978-0-387-25921-5

[7] P. W. Baas, J. S. Deitch, M. M. Black & G. A. Banker, 1988, 'Polarity orientation of microtubules in hippocampal neurons: Uniformity in the axon and nonuniformity in the dendrite'. *Proceedings of the National Academy of Sciences of the United States of America*, **85**(21):pp. 8335–8339, doi:10.1073/pnas.85.21.8335

[8] R. Bagnell, 2012, 'Pathology 464 - Light Microscopy Chap. 7 - Lenses', Tech. rep., Microscopy Services Laboratory, UNC School of medicine, Chapell Hill, NC, USA

[9] S. Bancelin, C.-A. Couture, M. Pinsard, M. Rivard, P. Drapeau & F. Légaré, 2017, 'Probing microtubules polarity in mitotic spindles in situ using Interferometric Second Harmonic Generation Microscopy'. *Scientific Reports*, **7**(1):p. 6758, doi:10.1038/s41598-017-06648-4

[10] S. Bancelin, C.-A. C.-A. Couture, K. Légaré, M. Pinsard, M. Rivard, C. Brown & F. Légaré, 2016, 'Fast interferometric second harmonic generation microscopy'. *Biomedical Optics Express*, **7**(2):p. 399, doi:10.1364/BOE.7.000399

[11] S. Bancelin, J. N. van der Kolk, A. S. Quigley, M. Pinsard, S. P. Veres, L. Kreplak, L. Ramunno & F. Légaré, 2018, 'Gouy phase shift measurement using interferometric second-harmonic generation'. *Optics Letters*, **43**(9):p. 1958, doi:10.1364/OL.43.001958

[12] S. Bancelin, S. Vigne, N. Hossain, M. Chaker & F. Légaré, 2016, 'Nonlinear optical properties of calcium barium niobate epitaxial thin films'. *Optics Express*, **24**(15):p. 17497, doi:10.1364/oe.24.017497

[13] S. Behnel, R. Bradshaw, C. Citro, L. Dalcin, D. Seljebotn & K. Smith, 2011, 'Cython: The Best of Both Worlds'. *Computing in Science Engineering*, **13**(2):pp. 31 –39, doi:10.1109/MCSE.2010.118

[14] D. P. Biss & T. G. Brown, 2003, 'Polarization-vortex-driven second-harmonic generation'. *Optics Letters*, **28**(11):p. 923, doi:10.1364/OL.28.000923

[15] F. Blanchard, G. Sharma, L. Razzari, X. Ropagnol, H.-C. Bandulet, F. Vidal, R. Morandotti, J.-C. Kieffer, T. Ozaki, H. Tiedje, H. Haugen, M. Reid & F. Hegmann, 2011, 'Generation of Intense Terahertz Radiation via Optical Methods'. *IEEE Journal of Selected Topics in Quantum Electronics*, **17**(1):pp. 5–16, doi:10.1109/JSTQE.2010.2047715

[16] N. Bobroff, 1986, 'Position measurement with a resolution and noise-limited instrument'. *Review of Scientific Instruments*, **57**(6):pp. 1152–1157, doi:10.1063/1.1138619

[17] J. Borbely, 'MSL-LoadLib', `https://pypi.org/project/msl-loadlib`, 2017

[18] R. W. Boyd, 'Descriptions of Nonlinear Optical Processes', in 'Nonlinear Optics', p. 7 (Academic Press, 2007)

[19] R. W. Boyd, 'The Nonlinear Optical Susceptibility', in 'Nonlinear Optics', pp. 3–51 (Academic Press, 2007)

[20] R. W. Boyd, *Nonlinear optics*, vol. 2 (Elsevier, 2008), ISBN 3540669183, doi:10.1002/adma.19900020919

[21] R. W. Boyd, 'Second- and Higher-Order Harmonic Generation', in 'Handbook of Biomedical Nonlinear Optical Microscopy', pp. 158–163 (Oxford University Press, 2008)

[22] J. S. Bredfeldt, Y. Liu, C. A. Pehlke, M. W. Conklin, J. M. Szulczewski, D. R. Inman, P. J. Keely, R. D. Nowak, T. R. Mackie & K. W. Eliceiri, 2014, 'Computational segmentation of collagen fibers from second-harmonic generation images of breast cancer'. *Journal of Biomedical Optics*, **19**(1):p. 016007, doi:10.1117/1.JBO.19.1.016007

[23] C. P. Brophy, 1990, 'Effect of intensity error correlation on the computed phase of phase-shifting interferometry'. *Journal of the Optical Society of America A*, **7**(4):p. 537, doi:10.1364/JOSAA.7.000537

[24] J. H. Bruning, D. R. Herriott, J. E. Gallagher, D. P. Rosenfeld, A. D. White & D. J. Brangaccio, 1974, 'Digital Wavefront Measuring Interferometer for Testing Optical Surfaces and Lenses'. *Applied Optics*, **13**(11):p. 2693, doi:10.1364/AO.13.002693

[25] J. M. Bueno, F. J. Avila & P. Artal, 2017, 'Comparison of second harmonic microscopy images of collagen-based ocular tissues with 800 and 1045 nm'. *Biomedical Optics Express*, **8**(11):pp. 1377–1386, doi:10.1364/BOE.8.005065

[26] Cambridge Technology Inc ., 2004, 'Cambridge Technology Inc . Raster / Cycloid Retrace Waveform Generation', Tech. Rep. 617, Cambridge Technology

[27] P. J. Campagnola & L. M. Loew, 2003, 'Second-harmonic imaging microscopy for visualizing biomolecular arrays in cells, tissues and organisms'. *Nature Biotechnology*, **21**(11):pp. 1356–1360, doi:10.1038/nbt894

[28] P. J. Campagnola, M. D. Wei, A. Lewis & L. M. Loew, 1999, 'High-resolution nonlinear optical imaging of live cells by second harmonic generation'. *Biophysical Journal*, **77**(6):pp. 3341–3349, doi:10.1016/S0006-3495(99)77165-1

[29] Cargille, 'Refractive Index (Matching) Liquids', `http://www.cargille.com/refractivestandards.shtml`, 2003

[30] R. K. Chang, J. Ducuing & N. Bloembergen, 1965, 'Relative phase measurement between fundamental and second-harmonic light'. *Physical Review Letters*, **15**(1):pp. 6–8, doi:10.1103/PhysRevLett.15.6

[31] Y. Chang, C. Chen, J. Chen, Y. Jin & X. Deng, 2009, 'Theoretical simulation study of linearly polarized light on microscopic second-harmonic generation in collagen type I'. *Journal of Biomedical Optics*, **14**(4):p. 044016, doi:10.1117/1.3174427

[32] K. Charan, B. Li, M. Wang, C. P. Lin & C. Xu, 2018, 'Fiber-based tunable repetition rate source for deep tissue two-photon fluorescence microscopy'. *Biomedical Optics Express*, **9**(5):p. 2304, doi:10.1364/BOE.9.002304

[33] S.-Y. Chen & C.-K. Sun, 'Combined SHG/THG Imaging', in 'Second Harmonic Generation Imaging', (CRC Press/Taylor & Francis, 2013), ISBN 978-1-4398-4914-9, doi:10.1201/b15039-18

[34] X. Chen & P. J. Campagnola, 'SHG Microscopy and Its Comparison with THG, CARS, and Multiphoton Excited Fluorescence Imaging', in 'Second Harmonic Generation Imaging', p. 465 (Taylor and Francis, 2014)

[35] X. Chen, O. Nadiarynkh, S. Plotnikov & P. J. Campagnola, 2012, 'Second harmonic generation microscopy for quantitative analysis of collagen fibrillar structure'. *Nature Protocols*, **7**(4):pp. 654–669, doi:10.1038/nprot.2012.009

[36] J. Cheng & X. Xie, 2004, 'Coherent Anti-Stokes Raman Scattering Microscopy: Instrumentation, Theory, and Applications'. *J. Phys. Chem. B*, **108**(1):pp. 827–840, doi:10.1039/c3cc45319g

[37] J.-x. Cheng & X. S. Xie, 2002, 'Green's function formulation for third-harmonic generation microscopy'. *JOSAB*, **19**(7):pp. 1604–1610

[38] S.-w. Chu, T.-m. Liu, C.-k. Sun, C.-y. Lin & H.-j. Tsai, 2003, 'Real-time second-harmonic-generation microscopy based on a 2-GHz repetition rate Ti:sapphire laser.' *Optics express*, **11**(8):pp. 933–938, doi:10.1364/OE.11.000933

[39] W. Chun, D. Do & D. G. Gweon, 2013, 'Design and demonstration of multimodal optical scanning microscopy for confocal and two-photon imaging'. *Review of Scientific Instruments*, **84**(1), doi:10.1063/1.4773232

[40] R. Cicchi, L. Sacconi, F. Vanzi & F. Pavone, 'How to Build an SHG Apparatus', in 'Second Harmonic Generation Imaging', pp. 21–50 (Taylor and Francis, 2013), ISBN 978-1-4398-4914-9, doi:10.1201/b15039-4

[41] B. Clancy & J. Salafsky, 2017, 'Second-harmonic phase determination by real-time in situ interferometry'. *Phys. Chem. Chem. Phys.*, **19**(5):pp. 3722–3728, doi:10.1039/C6CP07708K

[42] T. Colomb, E. Cuche, F. Charrière, J. Kühn, N. Aspert, F. Montfort, P. Marquet & C. Depeursinge, 2006, 'Automatic procedure for aberration compensation in digital holographic microscopy and applications to specimen shape compensation.' *Applied optics*, **45**(5):pp. 851–863, doi:10.1364/AO.45.000851

[43] T. Colomb, J. Kühn, F. Charrière & C. Depeursinge, 2006, 'Total aberrations compensation in digital holographic microscopy with a reference conjugated hologram'. *Optics Express*, **14**(10):pp. 1035–1041, doi:10.1364/OE.14.004300

[44] Y. Cortial, 'Interférences à 2 ondes (2018-03-07)', `http://web.cortial.net/bibliohtml/2ondes.html`, 2012

[45] C. Couture, 2014, *Imagerie Des Tissus De Collagene Par Generation De Seconde Harmonique Interferometrique*, Master's thesis, INRS-EMT

[46] C. A. Couture, S. Bancelin, J. N. van der Kolk, K. Popov, M. Rivard, K. Légaré, G. Martel, H. Richard, C. Brown, S. Laverty, L. Ramunno & F. Légaré, 2015, 'The Impact of Collagen Fibril Polarity on Second Harmonic Generation Microscopy'. *Biophysical Journal*, **109**(12):pp. 2501–2510, doi:10.1016/j.bpj.2015.10.040

[47] K. Creath, 1988, 'V Phase-Measurement Interferometry Techniques'. *Progress in Optics*, **26**(C):pp. 349–393, doi:10.1016/S0079-6638(08)70178-1

[48] E. Cuche, P. Marquet & C. Depeursinge, 1999, 'Simultaneous amplitude-contrast and quantitative phase-contrast microscopy by numerical reconstruction of Fresnel off-axis holograms.' *Applied optics*, **38**(34):pp. 6994–7001, doi:10.1364/AO.38.006994

[49] P. Davidovits & M. D. EGGER, 1969, 'Scanning Laser Microscope'. *Nature*, **223**(5208):p. 831, doi:10.1038/223831a0

[50] H. B. De Aguiar, S. Gigan & S. Brasselet, 2017, 'Polarization recovery through scattering media'. *Science Advances*, **3**(9):pp. 1–8, doi:10.1126/sciadv.1600743

[51] D. Débarre, W. Supatto, A. M. Pena, A. Fabre, T. Tordjmann, L. Combettes, M. C. Schanne-Klein & E. Beaurepaire, 2006, 'Imaging lipid bodies in cells and tissues using third-harmonic generation microscopy'. *Nature Methods*, **3**(1):pp. 47–53, doi:10.1038/nmeth813

[52] W. P. Dempsey, N. O. Hodas, A. Ponti & P. Pantazis, 2015, 'Determination of the source of SHG verniers in zebrafish skeletal muscle'. *Scientific Reports*, **5**, doi:10.1038/srep18119

[53] W. Denk, W., Strickler, JH and Webb, 1990, 'Two-photon laser scanning fluorescence microscopy.' *Science (New York, N.Y.)*, **248**(4951):pp. 73–76

[54] J. C. Diels, J. J. Fontaine, I. C. McMichael & F. Simoni, 1985, 'Control and measurement of ultrashort pulse shapes (in amplitude and phase) with femtosecond accuracy.' *Applied optics*, **24**(9):p. 1270

[55] C. Ding, J. R. Ulcickas, F. Deng & G. J. Simpson, 2017, 'Second Harmonic Generation of Unpolarized Light'. *Physical Review Letters*, **119**(19), doi:10.1103/PhysRevLett.119.193901

[56] X. Y. Dow, E. L. DeWalt, S. Z. Sullivan, P. D. Schmitt & G. J. Simpson, 2016, 'Imaging the Nonlinear Susceptibility Tensors of Collagen by Nonlinear Optical Stokes Ellipsometric Microscopy'. *Biophysical Journal*, **1**(7):pp. 1361–1374, doi:10.1117/12.2212944

[57] C. R. Drifka, A. G. Loeffler, K. Mathewson, G. Mehta, A. Keikhosravi, Y. Liu, S. Lemancik, W. A. Ricke, S. M. Weber, W. J. Kao & K. W. Eliceiri, 2016, 'Comparison of Picrosirius Red Staining With Second Harmonic Generation Imaging for the Quantification of Clinically Relevant Collagen Fiber Features in Histopathology Samples'. *Journal of Histochemistry and Cytochemistry*, **64**(9):pp. 519–529, doi:10.1369/0022155416659249

[58] M. Dubreuil, S. Rivet & Y. Le Grand, 2017, 'Snapshot second-harmonic generation polarimeter based on spectral analysis'. *Optics Letters*, **42**(22):p. 4639, doi:10.1364/ol.42.004639

[59] M. D. Duncan, J. Reintjes & T. J. Manuccia, 1982, 'Scanning coherent anti-Stokes Raman microscope'. *Optics Letters*, **7**(8):p. 350, doi:10.1364/ol.7.000350

[60] Ebook, '4.4 Dielectrics and Electroopics', in 'Handbook of Condensed Matter', vol. 178, pp. 228–229 (Springer, 1956), doi:10.1038/178228a0

[61] A. D. Edelstein, M. A. Tsuchida, N. Amodaj, H. Pinkard, R. D. Vale & N. Stuurman, 2014, 'Advanced methods of microscope control using μManager software'. *Journal of Biological Methods*, **1**(2):p. 10, doi:10.14440/jbm.2014.36

[62] K. W. Eliceiri, M. R. Berthold, I. G. Goldberg, L. Ibáñez, B. S. Manjunath, M. E. Martone, R. F. Murphy, H. Peng, A. L. Plant, B. Roysam, N. Stuurmann, J. R. Swedlow, P. Tomancak & A. E. Carpenter, 2012, 'Biological imaging software tools'. *Nature Methods*, **9**(7):pp. 697–710, doi:10.1038/nmeth.2084

[63] A. Erikson, J. Ortegren, T. Hompland, C. de Lange Davies & M. Lindgren, 2007, 'Quantification of the second-order nonlinear susceptibility of collagen I using a laser scanning microscope'. *Journal of Biomedical Optics*, **12**(August 2007):p. 044002, doi:10.1117/1.2772311

[64] Eskma, 2010, 'Eskma Optics, Ultrathin non-linear crystals (notes)', Tech. rep., Eskma Inc.

[65] C. L. Evans, E. O. Potma, M. Puoris'haag, D. Côté, C. P. Lin & X. S. Xie, 2005, 'Chemical imaging of tissue in vivo with video-rate coherent anti-Stokes Raman scattering microscopy.' *Proceedings of the National Academy of Sciences of the United States of America*, **102**(46):pp. 16807–16812, doi:10.1073/pnas.0508282102

[66] Femtolasers, 2007, 'Femtometer - Dispersion Minimized Autocorrelator', Tech. rep., Femtolasers

[67] P. A. Franken, A. E. Hill, C. W. Peters & G. Weinreich, 1961, 'Generation of optical harmonics'. *Physical Review Letters*, **7**(4):pp. 118–119, doi:10.1103/PhysRevLett.7.118

[68] I. Freund, M. Deutsch & A. Sprecher, 1986, 'Connective tissue polarity. Optical second-harmonic microscopy, crossed-beam summation, and small-angle scattering in rat-tail tendon'. *Biophysical Journal*, **50**(4):pp. 693–712, doi:10.1016/S0006-3495(86)83510-X

[69] O. Friedrich, M. Both, C. Weber, S. Schürmann, M. D. Teichmann, F. Von Wegner, R. H. Fink, M. Vogel, J. S. Chamberlain & C. Garbe, 2010, 'Microarchitecture is severely compromised but motor protein function is preserved in dystrophic mdx skeletal muscle'. *Biophysical Journal*, **98**(4):pp. 606–616, doi:10.1016/j.bpj.2009.11.005

[70] K. L. B. Fung, M. Samim, A. Gribble, V. Barzda & I. A. Vitkin, 2018, 'Monte Carlo simulation of polarization-sensitive second-harmonic generation and propagation in biological tissue'. *Journal of Biophotonics*, p. e201800036, doi:10.1002/jbio.201800036

[71] Y. Gao, A. J. Goodman, P. C. Shen, J. Kong & W. A. Tisdale, 2018, 'Phase-Modulated Degenerate Parametric Amplification Microscopy'. *Nano Letters*, **18**(8):pp. 5001–5006, doi:10.1021/acs.nanolett.8b01827

[72] A. Gasecka, A. Daradich, H. Dehez, M. Piché & D. Côté, 2013, 'Resolution and contrast enhancement in coherent anti-Stokes Raman-scattering microscopy'. *Optics Letters*, **38**(21):p. 4510, doi:10.1364/OL.38.004510

[73] O. Gobert, N. Fedorov, G. Mennerat, D. Lupinski, D. Guillaumet, M. Perdrix, A. Bourgeade & M. Comte, 2012, 'Wavelength dispersion measurement of electro-optic coefficients in the range of 520 to 930 nm in rubidium titanyl phosphate using spectral interferometry'. *Applied Optics*, **51**(5):p. 594, doi:10.1364/AO.51.000594

[74] M. Goeppert-Mayer, 1931, 'Über Elementarakte mit zwei Quantensprüngen'. *Annalen der Physik*, **401**(3):pp. 273–294

[75] A. Golaraei, L. Kontenis, K. Mirsanaye, S. Kro, M. K. Akens, B. C. Wilson, V. Barzda, S. Krouglov, M. K. Akens, B. C. Wilson & V. Barzda, 2019, 'Complex Susceptibilities and Chiroptical Effects of Collagen Measured with Polarimetric Second-Harmonic Generation Microscopy'. *Scientific Reports*, **9**(1):p. 12488, doi:10.1038/s41598-019-48636-w

[76] A. Golaraei, K. Mirsanaye, Y. Ro, S. Krouglov, M. K. Akens, B. C. Wilson & V. Barzda, 2019, 'Collagen chirality and three-dimensional orientation studied with polarimetric second-harmonic generation microscopy'. *Journal of Biophotonics*, **12**(1):pp. 1–9, doi:10.1002/jbio.201800241

[77] A. J. Goodman & W. A. Tisdale, 2015, 'Enhancement of second-order nonlinear-optical signals by optical stimulation'. *Physical Review Letters*, **114**(18):pp. 1–5, doi:10.1103/PhysRevLett.114.183902

[78] N. H. Green, R. M. Delaine-Smith, H. J. Askew, R. Byers, G. C. Reilly & S. J. Matcher, 2017, 'A new mode of contrast in biological second harmonic generation microscopy'. *Scientific Reports*, **7**(1):p. 13331, doi:10.1038/s41598-017-13752-y

[79] J. E. Greivenkamp, 1984, 'Generalized data reduction for heterodyne interferometry'. *Optical Engineering*, **23**(4):pp. 350–352, doi:10.1117/12.7973298

[80] B. A. Grubbs, N. P. Etter, W. E. Slaughter, A. M. Pittsford, C. R. Smith & P. D. Schmitt, 2019, 'A Low-cost Beam Scanning Second Harmonic Generation Microscope with Application for Agrochemical Development and Testing'. *Analytical Chemistry*, p. acs.analchem.9b02304, doi:10.1021/acs.analchem.9b02304

[81] M. Gu, *Advanced Optical Imaging Theory* (Springer, 1999), ISBN 9783540008590

[82] M. Gu, 'Imaging with a High Numerical-Aperture Objective', in 'Advanced Optical Imaging Theory', chap. 6, pp. 155–165 (Springer, 1999), ISBN 9783540008590

[83] I. Gusachenko, 2012, *Polarization-resolved Second Harmonic Microscopy in collagenous tissues : theoretical and experimental developments , and application to microstructural imaging during biomechanical assays in tendon .*, Ph.D. thesis, Ecole Polytechnique X

[84] I. Gusachenko, G. Latour & M.-C. Schanne-Klein, 2010, 'Polarization-resolved Second Harmonic microscopy in anisotropic thick tissues'. *Optics Express*, **18**(18):p. 19339, doi:10.1364/OE.18.019339

[85] I. Gusachenko & M. C. Schanne-Klein, 2013, 'Numerical simulation of polarization-resolved second-harmonic microscopy in birefringent media'. *Physical Review A - Atomic, Molecular, and Optical Physics*, **88**(5):pp. 1–15, doi:10.1103/PhysRevA.88.053811

[86] I. Gusachenko, V. Tran, Y. G. Houssen, J. M. Allain & M. C. Schanne-Klein, 2012, 'Polarization-resolved second-harmonic generation in tendon upon mechanical stretching'. *Biophysical Journal*, **102**(9):pp. 2220–2229, doi:10.1016/j.bpj.2012.03.068

[87] P. S. Halasyamani & K. R. Poeppelmeier, 1998, 'Noncentrosymmetric Oxides'. *Chemistry of Materials*, **10**(10):pp. 2753–2769, doi:10.1021/cm980140w

[88] Hammamatsu, 2005, 'Hammamatsu PMT datasheet : R6357 Tube, 2005', Tech. rep., Hammamatsu

[89] Hammamatsu, 2011, 'Hammamatsu PMT datasheet : C7319 Amplifier Unit, 2011', Tech. rep., Hammamatsu

[90] Y. Han, J. Hsu, N. H. Ge & E. O. Potma, 2015, 'Polarization-sensitive sum-frequency generation microscopy of collagen fibers'. *Journal of Physical Chemistry B*, **119**(8):pp. 3356–3365, doi:10.1021/jp511058b

[91] Y. Han, V. Raghunathan, R. R. Feng, H. Maekawa, C. Y. Chung, Y. Feng, E. O. Potma & N. H. Ge, 2013, 'Mapping molecular orientation with phase sensitive vibrationally resonant sum-frequency generation microscopy'. *Journal of Physical Chemistry B*, **117**(20):pp. 6149–6156, doi:10.1021/jp4022147

[92] A. Hanninen, M. W. Shu & E. O. Potma, 2017, 'Hyperspectral imaging with laser-scanning sum-frequency generation microscopy'. *Biomedical Optics Express*, **8**(9):p. 4230, doi:10.1364/BOE.8.004230

[93] B. Hao & J. Leger, 2007, 'Experimental measurement of longitudinal component in the vicinity of focused radially polarized beam'. *Optics Express*, **15**(6):pp. 3550–3556

[94] P. Hariharan, *Optical Interferomety* (Academic Press, 2003)

[95] K. Hibino, 1997, 'Susceptibility of systematic error-compensating algorithms to random noise in phase-shifting interferometry.' *Applied optics*, **36**(10):pp. 2084–93, doi:10.1364/AO.36.002084

[96] E. E. Hoover, J. J. Field, D. G. Winters, M. D. Young, E. V. Chandler, J. C. Speirs, J. T. Lapenna, S. M. Kim, S. Y. Ding, R. A. Bartels, J. W. Wang & J. A. Squier, 2012, 'Eliminating the scattering ambiguity in multifocal, multimodal, multiphoton imaging systems'. *Journal of Biophotonics*, **5**(5-6):pp. 425–436, doi:10.1002/jbio.201100139

[97] E. E. Hoover & J. A. Squier, 2013, 'Advances in multiphoton microscopy technology'. *Nature Photonics*, **7**(2):pp. 93–101, doi:10.1038/nphoton.2012.361

[98] P. Hosseini, R. Zhou, Y.-H. Kim, C. Peres, A. Diaspro, C. Kuang, Z. Yaqoob & P. T. C. So, 2016, 'Pushing phase and amplitude sensitivity limits in interferometric microscopy'. *Optics Letters*, **41**(7):p. 1656, doi:10.1364/OL.41.001656

[99] R. Hristu, S. G. Stanciu, D. E. Tranca & G. A. Stanciu, 2016, 'Improved quantification of collagen anisotropy with polarization-resolved second harmonic generation microscopy'. *Journal of Biophotonics*, **9**:pp. 1–9, doi:10.1002/jbio.201600197

[100] T. Hutchinson, *Essentials of statistical methods, in 41 pages* (Rumsby Scientific Pub., 1993)

[101] Y. Jeon, H. Min & D. Kim, 2005, 'Determination of the Crystalline x -Axis of Quartz by Second-Harmonic Phase Measurement'. *Journal of the Korean Physical Society*, **46**(June):pp. 159–162

[102] J. Jiang & R. Yuste, 2008, 'Second-Harmonic Generation Imaging of Membrane Potential with Photon Counting'. *Microscopy and Microanalysis*, **14**(06):pp. 526–531, doi:10.1017/S1431927608080811

[103] Y. Jiang, I. Tomov, Y. Wang & Z. Chen, 2004, 'Second-harmonic optical coherence tomography'. *Optics Letters*, **29**(10):p. 1090, doi:10.1364/OL.29.001090

[104] R. C. Johnson & J. T. Hupp, 'Nonlinear Optical Properties of Metal Nanoparticles', in 'Metal Nanoparticles: Synthesis, characterization and applications', pp. 141–143 (Marcel Dekker, Inc, 2002)

[105] R. Jones, C. J. Oliver & E. R. Pike, 1971, 'Experimental and Theoretical Comparison of Photon-Counting and Current Measurements of Light Intensity'. *Applied optics*, **10**(7):pp. 1673–1680

[106] P. A. A. M. Junior, P. S. Neto & C. S. De Barcellos, 2011, 'Generalization of Carré equation'. *Optik*, **122**(6):pp. 475–489, doi:10.1016/j.ijleo.2010.03.009

[107] K. E. Kadler, C. Baldock, J. Bella & R. P. Boot-Handford, 2007, 'Collagens at a glance'. *Journal of Cell Science*, **120**(12):pp. 1955–1958, doi:10.1242/jcs.03453

[108] W. Kaiser & C. G. B. Garrett, 1961, 'Two-photon excitation in CaF2: Eu2+'. *Physical Review Letters*, **7**(6):pp. 229–231, doi:10.1103/PhysRevLett.7.229

[109] I. P. Kaminow, 1966, 'Barium titanate light modulator. II'. *Applied Physics Letters*, **8**(11):pp. 305–307, doi:10.1063/1.1754450

[110] I. P. Kaminow & E. H. Turner, 1971, 'Electro-optic light modulators'. *Kristall und Technik*, **6**(4):pp. 563–572, doi:10.1002/crat.19710060414

[111] J. Kaneshiro, Y. Uesu & T. Fukui, 2010, 'Visibility of inverted domain structures using the second harmonic generation microscope: Comparison of interference and non-interference cases'. *Journal of the Optical Society of America B*, **27**(5):p. 888, doi:10.1364/JOSAB.27.000888

[112] H. Kang, B. Jia & M. Gu, 2010, 'Polarization characterization in the focal volume of high numerical aperture objectives.' *Optics express*, **18**(10):pp. 10813–10821, doi:10.1364/OE.18.010813

[113] U. Keller & L. Gallmann, 2010, 'Ultrafast Laser Physics', Tech. rep., ETH Zurich

[114] C. L. Koliopoulos, 1991, 'Simultaneous phase shift interferometer'. *Advanced Optical Manufacturing and Testing II*, **1531**:pp. 119–127

[115] S. Kujala, A. Mannila, L. Karvonen, K. Kieu & Z. Sun, 2016, 'Natural Silk as a Photonics Component: A Study on Its Light Guiding and Nonlinear Optical Properties'. *Scientific Reports*, **6**(October 2015):pp. 1–9, doi:10.1038/srep22358

[116] K. G. Larkin, B. R. Oreb, K. G. Larkin, B. F. Oreb & C. Scientific, 1992, 'Design and assessment of symmetrical phase-shifting algorithms'. *Journal of the Optical Society of America A*, **9**(10):pp. 1740–1748

[117] G. Latour, J.-P. Echard, M. Didier & M.-C. Schanne-Klein, 2012, 'In situ 3D characterization of historical coatings and wood using multimodal nonlinear optical microscopy'. *Optics Express*, **20**(22):p. 24623, doi:10.1364/oe.20.024623

[118] H. Lee, M. J. Huttunen, K.-J. Hsu, M. Partanen, G.-Y. Zhuo, M. Kauranen & S.-W. Chu, 2013, 'Chiral imaging of collagen by second-harmonic generation circular dichroism'. *Biomedical Optics Express*, **4**(6):p. 909, doi:10.1364/BOE.4.000909

[119] F. Légaré, C. Pfeffer & B. R. Olsen, 2007, 'The Role of Backscattering in SHG Tissue Imaging'. *Biophysical Journal*, **93**(4):pp. 1312–1320, doi:10.1529/biophysj.106.100586

[120] Leica Microsystems CMS GmbH, 2009, 'Water Immersion Micro Dispenser', Tech. rep., Leica

[121] S. Leute, T. Lottermoser & D. Fröhlich, 1999, 'Nonlinear spatially resolved phase spectroscopy'. *Optics Letters*, **24**(21):p. 1520, doi:10.1364/OL.24.001520

[122] Lightcon.com, 'Gaussian beam propagation', `http://toolbox.lightcon.com/tools/gaussianbeampropagation`, 2016

[123] Q. Liu, Y. Wang, J. He & F. Ji, 2015, 'Modified three-step iterative algorithm for phase-shifting interferometry in the presence of vibration'. *Applied Optics*, **54**(18):pp. 5833–5841, doi:10.1364/AO.54.005833

[124] Q. Liu, Y. Wang, J. He & F. Ji, 2015, 'Phase shift extraction and wavefront retrieval from interferograms with background and contrast fluctuations'. *Journal of Optics*, **17**(2):p. 025704, doi:10.1088/2040-8978/17/2/025704

[125] M. E. Llewellyn, R. P. Barretto, S. L. Delp & M. J. Schnitzer, 2008, 'Minimally invasive high-speed imaging of sarcomere contractile dynamics in mice and humans'. *Nature*, **454**(7205):pp. 784–788, doi:10.1038/nature07104

[126] G. D. Luca, R. Breedijk, R. Hoebe, S. W. Hell, S. J. Sahl, M. Bates, A. Alberti, C. Robens, W. Alt, P. Hemmer, J. S. Ben-benjamin, M. J. Huttunen, A. Abbas, J. Upham & R. W. Boyd, 2017, 'sensitivity Label-free super-resolution with coherent nonlinear structured-illumination microscopy'. *Journal of Optics*, **19**, doi:10.1088/2040-8986/aa792d

[127] C. Macias-Romero, M. E. P. Didier, P. Jourdain, P. Marquet, P. Magistretti, O. B. Tarun, V. Zubkovs, A. Radenovic & S. Roke, 2014, 'High throughput second harmonic imaging for label-free biological applications.' *Optics express*, **22**(25):pp. 31102–12, doi:10.1364/OE.22.031102

[128] J. J. Maki, M. Kauranen & A. Persoons, 1995, 'Surface second-harmonic generation from chiral materials'. *Physical Review B*, **51**(3):pp. 1425–1434, doi:10.1103/PhysRevB.51.1425

[129] E. A. Makris, P. Hadidi & K. A. Athanasiou, 2011, 'The knee meniscus: Structure-function, pathophysiology, current repair techniques, and prospects for regeneration'. *Biomaterials*, **32**(30):pp. 7411–7431, doi:10.1016/j.biomaterials.2011.06.037

[130] D. Malacara, H. Schreiber & J. H. Bruning, *Optical Shop Testing: Third Edition* (Wiley-Interscience, 2006), ISBN 9780470135976, doi:10.1002/9780470135976.ch14

[131] G. F. Marshall & G. E. Stutz, *Handbook of optical and laser scanning (second edition)* (CRC Press, 2012), ISBN 9781439808801

[132] A. A. Maznev, T. F. Crimmins & K. A. Nelson, 1998, 'How to make femtosecond pulses overlap'. *Optics Letters*, **23**(17):p. 1378, doi:10.1364/OL.23.001378

[133] L. Moreaux, O. Sandre, S. Charpak, M. Blanchard-Desce & J. Mertz, 2001, 'Coherent scattering in multi-harmonic light microscopy'. *Biophysical Journal*, **80**(3):pp. 1568–1574, doi:10.1016/S0006-3495(01)76129-2

[134] I. National Instruments, 2012, 'NI-DAQ 6259 manual', Tech. rep., National Instruments

[135] I. National Instruments, 2016, 'Measurement Accuracy of a Data Acquisition Board (white paper)'

[136] I. National Instruments, 2018, 'Calculating Absolute Accuracy or System Accuracy (white paper)'

[137] A. Negrean & H. D. Mansvelder, 2014, 'Optimal lens design and use in laser-scanning microscopy'. *Biomedical Optics Express*, **5**(5):p. 1588, doi:10.1364/BOE.5.001588

[138] E. B. Neufeld, B. M. Lucotte & R. S. Balaban, 'Multiphoton Excitation Imaging of the Arterial Vascular Bed', in 'Second Harmonic Generation Imaging', p. 291 (Taylor and Francis, 2014)

[139] G. New, *Introduction to nonlinear optics*, vol. 9780521877015 (Cambridge University Press, 2011), ISBN 9780511975851, doi:10.1017/CBO9780511975851

[140] I. Newport, 2006, 'Prism Compressor for Ultrashort Laser Pulses App-Note 29', Tech. rep., Newport

[141] Q. T. Nguyen, N. Callamaras, C. Hsieh & I. Parker, 2001, 'Construction of a two-photon microscope for video-rate Ca2+imaging'. *Cell Calcium*, **30**(6):pp. 383–393, doi:10.1054/ceca.2001.0246

[142] Q.-t. Nguyen, J. Driscoll, E. M. Dolnick & D. Kleinfeld, 'MPScope 2.0. A Computer System for Two-Photon Laser Scanning Microscopy with Concurrent Plasma-Mediated Ablation and Electrophysiology', in 'In Vivo Optical Imaging of Brain Function, Second Edition', pp. 117–142 (CRC Press/Taylor & Francis, 2009)

[143] Q.-t. Nguyen, P. S. Tsai & D. Kleinfeld, 2006, 'MPScope : A versatile software suite for multiphoton microscopy'. *Journal of Neuroscience Methods*, pp. 1–9, doi:10.1016/j.jneumeth.2006.03.001

[144] L. Novotny & B. Hecht, *Principles of nano-optics* (Cambridge University Press, 2006), ISBN 0521832241

[145] V. Ntziachristos, 2010, 'Going deeper than microscopy: The optical imaging frontier in biology'. *Nature Methods*, **7**(8):pp. 603–614, doi:10.1038/nmeth.1483

[146] N. Olivier, M. A. Luengo-Oroz, L. Duloquin, E. Faure, T. Savy, I. Veilleux, X. Solinas, D. Débarre, P. Bourgine, A. Santos, N. Peyriéras & E. Beaurepaire, 2010, 'Cell lineage reconstruction of early zebrafish embryos using label-free nonlinear microscopy'. *Science*, **329**(5994):pp. 967–971, doi:10.1126/science.1189428

[147] D. Oron & Y. Silberberg, 2015, 'Temporal focusing microscopy'. *Cold Spring Harbor Protocols*, **2015**(2):pp. 145–151, doi:10.1101/pdb.top085928

[148] Y. Ozeki, F. Dake, S. Kajiyama, K. Fukui & K. Itoh, 2009, 'Analysis and experimental assessment of the sensitivity of stimulated Raman scattering microscopy'. *Optics Express*, **17**(5):p. 3651, doi:10.1364/oe.17.003651

[149] X. Pang, T. D. Visser & E. Wolf, 2011, 'Phase anomaly and phase singularities of the field in the focal region of high-numerical aperture systems'. *Optics Communications*, **284**(24):pp. 5517–5522, doi:10.1016/j.optcom.2011.08.021

[150] F. S. Pavone & P. J. Campagnola, *Second Harmonic Generation Imaging* (CRC Press/Taylor & Francis, 2016), ISBN 9781439849156

[151] W. Petersen & B. Tillmann, 1998, 'Collagenous fibril texture of the human knee joint menisci'. *Anatomy and Embryology*, **197**(4):pp. 317–324, doi:10.1007/s004290050141

[152] M. D. Peterson, P. L. Hayes, I. S. Martinez, L. C. Cass, J. L. Achtyl, E. a. Weiss & F. M. Geiger, 2011, 'Second harmonic generation imaging with a kHz amplifier [Invited]'. *Optical Materials Express*, **1**(1):p. 57, doi:10.1364/OME.1.000057

[153] T. Petralli-Mallow, T. M. Wong, J. D. Byers, H. I. Yee & J. M. Hicks, 1993, 'Circular dichroism spectroscopy at interfaces: A surface second harmonic generation study'. *Journal of Physical Chemistry*, **97**(7):pp. 1383–1388, doi:10.1021/j100109a022

[154] C. P. Pfeffer, B. R. Olsen & F. Légaré, 2007, 'Second harmonic generation imaging of fascia within thick tissue block'. *Optics Express*, **15**(12):p. 7296, doi:10.1364/oe.15.007296

[155] M. Pinsard, 'python-Tsunami-Vanguard', `https://github.com/MaxP92/python-Tsunami-Vanguard`, 2017

[156] M. Pinsard, 'thorlabs python low-level', `https://github.com/MaxP92/thorlabs{_}python{_}low-level`, 2017

[157] M. Pinsard, 'P-SHG (forked version) GitHub', `https://github.com/MaxP92/P-SHG`, 2018

[158] M. Pinsard, M. Schmeltz, J. van der Kolk, S. A. Patten, H. Ibrahim, L. Ramunno, M.-C. Schanne-Klein & F. Légaré, 2019, 'Elimination of imaging artifacts in second harmonic generation microscopy using interferometry'. *Biomedical Optics Express*, **10**(8):p. 3938, doi:10.1364/boe.10.003938

[159] PMTs, 2010, 'Technical reprint reducing noise from photomultipliers', Tech. rep., Unknown

[160] T. A. Pologruto, B. L. Sabatini & K. Svoboda, 2003, 'ScanImage: flexible software for operating laser scanning microscopes'. *Biomed Eng Online*, **2**:p. 13

[161] T. H. K. P. U. PolyU, 'FOC MSc -Chapter 5 Modulation of Light'

[162] K. I. Popov, A. F. Pegoraro, A. Stolow & L. Ramunno, 2012, 'Image formation in CARS and SRS: effect of an inhomogeneous nonresonant background medium'. *Optics Letters*, **37**(4):p. 473, doi:10.1364/OL.37.000473

[163] E. O. Potma, C. L. Evans & X. S. Xie, 2006, 'Heterodyne coherent anti-Stokes Raman scattering (CARS) imaging'. *Optics Letters*, **31**(2):p. 241, doi:10.1364/ol.31.000241

[164] S. Psilodimitrakopoulos, I. Amat-Roldan, P. Loza-Alvarez & D. Artigas, 2010, 'Estimating the helical pitch angle of amylopectin in Starch using polarization second harmonic generation microscopy'. *Journal of Optics*, **12**(8), doi:10.1088/2040-8978/12/8/084007

[165] F. Qu, Q. Li, X. Wang, X. Cao, M. H. Zgonis, J. L. Esterhai, V. B. Shenoy, L. Han & R. L. Mauck, 2018, 'Maturation State and Matrix Microstructure Regulate Interstitial Cell Migration in Dense Connective Tissues'. *Scientific Reports*, **8**(1), doi:10.1038/s41598-018-21212-4

[166] F. Radaelli, L. D'Alfonso, M. Collini, F. Mingozzi, L. Marongiu, F. Granucci, I. Zanoni, G. Chirico & L. Sironi, 2017, 'μmAPPS: A novel phasor approach to second harmonic analysis for in vitro-in vivo investigation of collagen microstructure'. *Scientific Reports*, **7**(1), doi:10.1038/s41598-017-17726-y

[167] I. Raicol, 2016, 'Raicol crystal catalog', Tech. rep., Raicol

[168] P. Rastogi, *Holographic Interferomety* (Springer, 1994)

[169] G. Recher, D. Rouède, P. Richard, A. Simon, J.-J. Bellanger & F. Tiaho, 2009, 'Three distinct sarcomeric patterns of skeletal muscle revealed by SHG and TPEF microscopy.' *Optics express*, **17**(22):pp. 19763–19777, doi:10.1364/OE.17.019763

[170] A. C. Ribes, S. Damaskinos & A. Dixon, 2000, 'Inexpensive , High-Quality Optical Relay for Use in Confocal Scanning Beam Imaging'. *Scanning*, **22**:pp. 282–287, doi:10.1002/sca.4950220502

[171] B. Richards & E. Wolf, 1959, 'Electromagnetic diffraction in optical systems II. Structure of the image field in an aplanatic system'. *Proceedings of the Royal Society of London Series a-Mathematical and Physical Sciences*, **253**(1274):p. 3580379, doi:10.1098/rspa.1959.0200

[172] R. Richards-Kortum & E. Sevick-Muraca, 1996, 'Quantitative Optical Spectroscopy for Tissue Diagnosis'. *Annual Review of Physical Chemistry*, **47**(1):pp. 555–606, doi:10.1146/annurev.physchem.47.1.555

[173] J. Riporto, A. Demierre, V. Kilin, T. Balciunas, C. Schmidt, G. Campargue, M. Urbain, A. Baltuska, R. Le Dantec, J. P. Wolf, Y. Mugnier & L. Bonacina, 2018, 'Bismuth ferrite dielectric nanoparticles excited at telecom wavelengths as multicolor sources by second, third, and fourth harmonic generation'. *Nanoscale*, **10**(17):pp. 8146–8152, doi:10.1039/c7nr08102b

[174] M. Rivard, 2015, *Imagerie tissulaire par microscopie de seconde harmonique interférométrique*, Ph.D. thesis, INRS EMT

[175] M. Rivard, C.-A. Couture, A. K. Miri, M. Laliberté, A. Bertrand-Grenier, L. Mongeau & F. Légaré, 2013, 'Imaging the bipolarity of myosin filaments with Interferometric Second Harmonic Generation microscopy'. *Biomedical Optics Express*, **4**(10):p. 2078, doi:10.1364/BOE.4.002078

[176] M. Rivard, M. Laliberté, A. Bertrand-Grenier, C. Harnagea, C. P. Pfeffer, M. Vallières, Y. St-Pierre, A. Pignolet, M. A. El Khakani & F. Légaré, 2011, 'The structural origin of second harmonic generation in fascia'. *Biomedical Optics Express*, **2**(1):p. 26, doi:10.1364/BOE.2.000026

[177] M. Rivard, K. Popov, C. A. Couture, M. Laliberté, A. Bertrand-Grenier, F. Martin, H. Pépin, C. P. Pfeffer, C. Brown, L. Ramunno & F. Légaré, 2014, 'Imaging the noncentrosymmetric structural organization of tendon with Interferometric Second Harmonic Generation microscopy'. *Journal of Biophotonics*, **7**(8):pp. 638–646, doi:10.1002/jbio.201300036

[178] E. I. Romijn, A. Finnøy, R. Kumar & M. B. Lilledahl, 2018, 'Automated calibration and control for polarization-resolved second harmonic generation on commercial microscopes'. *PLoS ONE*, **13**(4):pp. 1–13, doi:10.1371/journal.pone.0195027

[179] D. G. Rosenegger, C. H. T. Tran, J. LeDue, N. Zhou & G. R. Gordon, 2014, 'A high performance, cost-effective, open-source microscope for scanning two-photon microscopy that is modular and readily adaptable'. *PLoS ONE*, **9**(10), doi:10.1371/journal.pone.0110475

[180] S. Roth & I. Freund, 1979, 'Second harmonic generation in collagen'. *J. Chem. Phys*, **60**(1637), doi:10.1063/1.437677

[181] D. Rouède, J.-J. Bellanger, G. Recher & F. Tiaho, 2013, 'Study of the effect of myofibrillar misalignment on the sarcomeric SHG intensity pattern'. *Optics Express*, **21**(9):p. 11404, doi:10.1364/OE.21.011404

[182] D. Rouède, E. Schaub, J.-J. Bellanger, F. Ezan, J.-C. Scimeca, G. Baffet & F. Tiaho, 2017, 'Determination of extracellular matrix collagen fibril architectures and pathological remodeling by polarization dependent second harmonic microscopy'. *Scientific Reports*, **7**(1):p. 12197, doi:10.1038/s41598-017-12398-0

[183] D. Sage, 'OrientationJ. ImageJ's plugin for directional analysis in images', `http://bigwww.epfl.ch/demo/orientation/index.html?image=4`, 2012

[184] S. J. Sahl, S. W. Hell & S. Jakobs, 2017, 'Fluorescence nanoscopy in cell biology'. *Nature Reviews Molecular Cell Biology*, **18**(11):pp. 685–701, doi:10.1038/nrm.2017.71

[185] B. E. Saleh & M. C. Teich, 'Electro-Optics', in 'Fundamentals of Photonics', vol. 5, pp. 696–736 (New York: Wiley, 1991), ISBN 0471839655, doi:10.1002/0471213748.ch18

[186] D. Sandkuijl, L. Kontenis, N. M. Coelho, C. McCulloch & V. Barzda, 2014, 'Interferometric backward third harmonic generation microscopy for axial imaging with accuracy beyond the diffraction limit'. *PLoS ONE*, **9**(4):pp. 9–14, doi:10.1371/journal.pone.0094458

[187] Sbyrnes321, 'Electron asymmetric motion animation [CC0]', `https://commons.wikimedia.org/wiki/File:Electron_asymmetric_motion_animation.gif`, 2014

[188] M.-C. Schanne-Klein, 'Chapter 15: SHG Imaging of Collagen and Application to Fibrosis Quantization', in 'Second Harmonic Generation Imaging', pp. 349–371 (CRC Press, 2013), ISBN 978-1-4398-4914-9, doi:10.1201/b15039-19

[189] M. Schmeltz, C. Teulon, G. Latour, D. Ghoubay, V. Borderie, C. Aimé & M.-C. Schanne-Klein, 2019, 'Implementation of artifact-free circular dichroism SHG imaging of collagen'. *Optics Express*, **27**(16):p. 22685, doi:10.1364/oe.27.022685

[190] M. Schmeltz, C. Teulon, M. Pinsard, U. Hansen, M. Alnawaiseh, D. Ghoubay, V. Borderie, G. Mosser, C. Aimé, F. Légaré, G. Latour & M.-C. Schanne-Klein, 2020, 'Probing the polarity distribution of collagen fibrils with CD-SHG microscopy (in review)'. *Nature Communications*

[191] C. Seebacher & R. Uhl, 'Colibri-open source software for laser scanning microscopy', in 'Conf. proc.', vol. 6630, p. 82152 (2006)

[192] S. A. Self, 1983, 'Focusing of spherical Gaussian beams'. *Applied Optics*, **22**(5):p. 658, doi:10.1364/AO.22.000658

[193] E. Shaffer & C. Depeursinge, 'Holographic SHG Imaging', in 'Second Harmonic Generation Imaging', pp. 191–228 (Taylor and Francis, 2013), ISBN 978-1-4398-4914-9, doi:10.1201/b15039-12

[194] E. Shaffer, P. Marquet & C. Depeursinge, 2010, 'Real time, nanometric 3D-tracking of nanoparticles made possible by second harmonic generation digital holographic microscopy'. *Optics Express*, **18**(16):p. 17392, doi:10.1364/OE.18.017392

[195] E. Shaffer, P. Marquet & C. Depeursinge, 2011, 'Second harmonic phase microscopy of collagen fibers'. *Multiphoton Microscopy in the Biomedical Sciences XI*, **7903**:p. 79030G, doi:10.1117/12.874538

[196] E. Shaffer, C. Moratal, P. Magistretti, P. Marquet & C. Depeursinge, 2010, 'Label-free second-harmonic phase imaging of biological specimen by digital holographic microscopy'. *Optics Letters*, **35**(24):p. 4102, doi:10.1364/ol.35.004102

[197] J. Sharpe, 2009, 'Optical projection tomography'. *Advanced Imaging in Biology and Medicine: Technology, Software Environments, Applications*, pp. 199–224, doi:10.1007/978-3-540-68993-5

[198] S. Sioncke, S. V. Elshocht, T. Verbiest, M. Kauranen & K. E. S. Phillips, 2001, 'Circular-difference effects in second-harmonic generation from thin films'. *Synthetic Metals*, **124**:p. 3

[199] S. Sioncke, S. Van Elshocht, T. Verbiest, A. Persoons, M. Kauranen, K. E. Phillips & T. J. Katz, 2000, 'Optical activity effects in second harmonic generation from anisotropic chiral thin films'. *Journal of Chemical Physics*, **113**(17):pp. 7578–7581, doi:10.1063/1.1311977

[200] M. Sivaguru, M. M. Kabir, M. R. Gartia, D. S. C. Biggs, B. S. Sivaguru, V. A. Sivaguru, G. A. Fried, G. L. Liu, S. Sadayappan & K. C. Toussaint, 2017, 'Application of an advanced maximum likelihood estimation restoration method for enhanced-resolution and contrast in second-harmonic generation microscopy'. *Journal of Microscopy*, **267**(3):pp. 397–408, doi:10.1111/jmi.12579

[201] Y. Sortais & J.-M. Jonathan, 2015, 'Course: Effets & Composants Électro-Optiques'

[202] K. R. Spring & M. W. Davidson, 2010, '[MicroscopyU] Properties of Microscope Objectives'

[203] K. R. Spring, B. O. Flynn, J. C. Long & M. W. Davidson, 2015, 'Spatial Resolution in Digital Imaging (tutorial)', Tech. rep., Nikon

[204] S. G. Stanciu, F. J. Ávila, R. Hristu & J. M. Bueno, 2017, 'A Study on Image Quality in Polarization-Resolved Second Harmonic Generation Microscopy'. *Scientific Reports*, **7**(1):p. 15476, doi:10.1038/s41598-017-15257-0

[205] E. H. Stelzer, 2006, 'The intermediate optical system of laser-scanning confocal microscopes'. *Handbook of Biological Confocal Microscopy: Third Edition*, pp. 207–220

[206] G. Stibenz & G. Steinmeyer, 2005, 'Interferometric frequency-resolved optical gating'. *Optics Express*, **13**(7):p. 2617, doi:10.1364/opex.13.002617

[207] R. Stolle, G. Marowsky, E. Schwarzberg & G. Berkovic, 1996, 'Phase measurements in nonlinear optics'. *Applied Physics B Laser and Optics*, **63**(5):pp. 491–498, doi:10.1007/BF01828946

[208] P. Stoller, P. M. Celliers, K. M. Reiser & A. M. Rubenchik, 2003, 'Quantitative second-harmonic generation microscopy in collagen.' *Applied optics*, **42**(25):pp. 5209–5219, doi:10.1364/AO.42.005209

[209] Y. Surrel, 1996, 'Measurements By the Use of Phase Stepping'. *Applied optics*, **35**(1):pp. 51–60

[210] R. L. Sutherland, *Handbook of Nonlinear Optics, Second Edition, Revised and Expanded* (Marcel Dekker, 2003), ISBN 0-8247-4243-5, doi:10.1117/1.601248

[211] R. L. Sutherland, 'Nonlinear Index of Refraction', in 'Handbook of Nonlinear Optics - Second Edition, Revised and Expanded', p. 369 (Marcel Dekker, Inc, 2003), ISBN 0-8247-4243-5

[212] N. A. Talaikova, A. A. Grebenyuk, A. L. Kalyanov & V. P. Ryabukho, 2016, 'Numerical focusing in diffraction phase microscopy'. *Progress in Biomedical Optics and Imaging - Proceedings of SPIE*, **9917**:p. 99171V, doi:10.1117/12.2229881

[213] Technion, 'Phase-matching bandwidth, and Group velocity mismatch (GVM) Phase-matching in Second-Harmonic Generation', `http://phelafel.technion.ac.il/{~}smoise/poster4.pdf`, 2010

[214] V. Technologies, 2015, 'Physical Scanner Considerations (r3.8) - Thermal Limits', Tech. rep., Vidrio Technologies

[215] C. Technology, 2008, 'MicroMax 673 Series - BOARD LEVEL DUAL AXIS DRIVER ELECTRONICS Rev3.4', Tech. rep., Cambridge Technology

[216] C. Teulon, 2017, *Imagerie quantitative de biopolymères par génération de second harmonique résolue en polarisation*, Ph.D. thesis, Paris-Saclay - LOB

[217] B. J. Thompson, R. Sirohi & F. S. Chau, *Optical methods of measurement - wide-field technique* (Marcel Dekker, Inc, 1999), ISBN 0824760034

[218] R. E. Thompson, D. R. Larson & W. W. Webb, 2002, 'Precise nanometer localization analysis for individual fluorescent probes.' *Biophysical journal*, **82**(5):pp. 2775–83, doi:10.1016/S0006-3495(02)75618-X

[219] Thorlabs, 'Private communications with Thorlabs, Inc.', 2017

[220] Thorlabs, 2018, 'Scan Lenses for Laser Scanning Microscopy - Application info', Tech. rep., Thorlabs

[221] I. Thorlabs, 2012, 'BBD102 and BBD103 Brushless DC Servo Controllers - User Guide', Tech. rep., Thorlabs

[222] I. Thorlabs, 2012, 'Thorlabs APT Controllers Host-Controller Communications Protocol Rev.3', Tech. rep., Thorlabs

[223] F. Tiaho, G. Recher & D. Rouède, 2007, 'Estimation of helical angles of myosin and collagen by second harmonic generation imaging microscopy.' *Optics express*, **15**(19):pp. 12286–12295, doi:10.1364/OE.15.012286

[224] N. Tian, L. Fu & M. Gu, 2015, 'Resolution and contrast enhancement of subtractive second harmonic generation microscopy with a circularly polarized vortex beam'. *Scientific Reports*, **5**(September):p. 13580, doi:10.1038/srep13580

[225] J. Tichý, J. Erhart, E. Kittinger, J. Přívratská, J. Tichý*, J. Erhart, E. Kittinger* & J. Přívratská, 'Piezoelectric Properties', in 'Fundamentals of Piezoelectric Sensorics', p. 73 (Springer Berlin Heidelberg, Berlin, Heidelberg, 2010), doi:10.1007/978-3-540-68427-5_5

[226] H. Tomizawa, H. Dewa, A. Mizuno, T. Taniuchi & H. Hanaki, 'First Emission of Novel Photocathode Gun Gated by Z-polarized Laser Pulse', in 'Conf. Proc.', IPAC-2010-THPEC025, p. THPEC025 (2010)

[227] R. Trebino & I. Conoptics, 2010, 'Dispersion and how to control it', Tech. rep., Conoptics

[228] P. S. Tsai, C. Mateo, J. J. Field, C. B. Schaffer, M. E. Anderson & D. Kleinfeld, 2015, 'Ultra-large field-of-view two-photon microscopy'. *Optics Express*, **23**(11):p. 13833, doi:10.1364/OE.23.013833

[229] Y. Uesu, S. Kurimura & Y. Yamamoto, 1995, 'Optical second harmonic images of 90Â° domain structure in BaTiO3 and periodically inverted antiparallel domains in LiTaO3'. *Applied Physics Letters*, **66**(17):pp. 2165–2167, doi:10.1063/1.113934

[230] B. E. Urban, B. Dong, X. Zhang, H. Yang & H. F. Zhang, 2018, 'Patterned-illumination second harmonic generation microscopy of collagen fibrils in rat scleras'. *Optics Letters*, **43**(21):p. 5190, doi:10.1364/OL.43.005190

[231] V. Van Steenbergen, W. Boesmans, Z. Li, Y. de Coene, K. Vints, P. Baatsen, I. Dewachter, M. Ameloot, K. Clays & P. Vanden Berghe, 2019, 'Molecular understanding of label-free second harmonic imaging of microtubules'. *Nature Communications*, **10**(1):pp. 1–14, doi:10.1038/s41467-019-11463-8

[232] K. Veenstra, A. Petukhov, A. de Boer & T. Rasing, 1998, 'Phase-sensitive detection technique for surface nonlinear optics'. *Physical Review B - Condensed Matter and Materials Physics*, **58**(24):pp. R16020–R16023, doi:10.1103/PhysRevB.58.R16020

[233] V. Vetri, K. Dragnevski, M. Tkaczyk, M. Zingales, G. Marchiori, N. F. Lopomo, S. Zaffagnini, A. Bondi, J. A. Kennedy, D. W. Murray & O. Barrera, 2019, 'Advanced microscopy analysis of the micro-nanoscale architecture of human menisci'. *Scientific Reports*, **9**(1):p. 18732, doi:10.1038/s41598-019-55243-2

[234] A. Vogel, J. Noack, G. Hüttmann & G. Paltauf, 2002, 'Femtosecond-laser-produced low-density plasmas in transparent biological media: a tool for the creation of chemical, thermal, and thermomechanical effects below the optical breakdown threshold'. *Commercial and Biological Applications of Ultrafast LAsers IV*, **4633A**:pp. 23–37, doi:10.1117/12.461385

[235] L. V. Wang & H.-i. Wu, '9 Optical Coherence Tomography - Time Domain OCT', in 'Biomedical Optics - Principles and Imaging', pp. 184–209 (Wiley, 2007)

[236] X. Wang, S. Fardad, S. Das, A. Salandrino & R. Hui, 2016, 'Direct observation of bulk second-harmonic generation inside a glass slide with tightly focused optical fields'. *Physical Review B*, **93**(16):pp. 1–5, doi:10.1103/PhysRevB.93.161109

[237] X. H. Wang, L. Lin, S. J. Chang, H. Zhang & S. J. Hao, 2008, 'Examination of validity of paraxial approximation in second harmonic generation microscopy under low numerical aperture'. *Chinese Physics Letters*, **25**(8):pp. 2884–2887, doi:10.1088/0256-307X/25/8/042

[238] Z. Wang & B. Han, 2004, 'Advanced iterative algorithm for phase extraction of randomly phase-shifted interferograms.' *Optics letters*, **29**(14):pp. 1671–1673, doi:10.1364/OL.29.001671

[239] V. Wasik, P. Réfrégier, M. Roche & S. Brasselet, 2015, 'Precision of polarization-resolved second harmonic generation microscopy limited by photon noise for samples with cylindrical symmetry'. *Journal of the Optical Society of America A*, **32**(8):p. 1437, doi:10.1364/JOSAA.32.001437

[240] Wikipedia, 'Standard error', https://en.wikipedia.org/wiki/Standard_error#Using_a_sample_to_estimate_the_standard_error, 2015

[241] R. M. Williams, W. R. Zipfel & W. W. Webb, 'Multiphoton microscopy in biological research', in 'Current Opinion in Chemical Biology', vol. 5, pp. 603–608 (Elsevier Current Trends, 2001), ISBN 1367-5931, doi:10.1016/S1367-5931(00)00241-6

[242] P. T. Wilson, Y. Jiang, O. A. Aktsipetrov, E. D. Mishina & M. C. Downer, 1999, 'Frequency-domain interferometric second-harmonic spectroscopy'. *Optics Letters*, **24**(7):p. 496, doi:10.1364/OL.24.000496

[243] P. T. Wilson, Y. Jiang, R. Carriles & M. C. Downer, 2003, 'Second-harmonic amplitude and phase spectroscopy by use of broad-bandwidth femtosecond pulses'. *Journal of the Optical Society of America B*, **20**(12):p. 2548, doi:10.1364/JOSAB.20.002548

[244] J.-P. Wu, B. J. Swift, T. Becker, A. Squelch, A. Wang, Y.-C. Zheng, X. Zhao, J. Xu, W. E. I. Xue, M. Zheng, D. G. Lloyd & T. B. Kirk, 2017, 'High-resolution study of the 3D collagen fibrillary matrix of Achilles tendons without tissue labelling and dehydrating'. *Journal of Microscopy*, **00**(0):pp. n/a–n/a, doi:10.1111/jmi.12537

[245] S. Yazdanfar, L. Laiho & P. T. C. So, 2004, 'Interferometric second harmonic generation microscopy.' *Optics express*, **12**(12):pp. 2739–2745, doi:10.1364/OPEX.12.002739

[246] C.-H. Yeh, C.-Z. Tan, C.-h. A. Cheng, J.-T. Hung & S.-Y. Chen, 2018, 'Improving resolution of second harmonic generation microscopy via scanning structured illumination'. *Biomedical Optics Express*, **9**(12):p. 6081, doi:10.1364/BOE.9.006081

[247] E. Yew & C. Sheppard, 2006, 'Effects of axial field components on second harmonic generation microscopy'. *Optics Express*, **14**(3):pp. 1167–1174, doi:10.1364/OE.14.001167

[248] E. Y. S. Yew & C. J. R. Sheppard, 2007, 'Second harmonic generation polarization microscopy with tightly focused linearly and radially polarized beams'. *Optics Communications*, **275**:pp. 453–457, doi:10.1016/j.optcom.2007.03.065

[249] H. Yokota, J. Kaneshiro & Y. Uesu, 2012, 'Optical second harmonic generation microscopy as a tool of material diagnosis'. *Physics Research International*, **2012**, doi:10.1155/2012/704634

[250] M. D. Young, J. J. Field, K. E. Sheetz, R. A. Bartels & J. Squier, 2014, 'A pragmatic guide to multiphoton microscope design'. *Advances in Optics and Photonics*, **6**:pp. 293–339, doi:10.1364/AOP

[251] S. Yue, M. Slipchenko & J.-X. Cheng, 2011, 'Multimodal nonlinear optical microscopy'. *Laser & Photonics Reviews*, **5**(4):pp. 496–512, doi:10.1002/lpor.201000027

[252] F. Zernike, 1935, 'Phase contrast'. *pdfs.semanticscholar.org*

[253] H. Zhao, R. Cisek, A. Karunendiran, D. Tokarz, B. A. Stewart & V. Barzda, 2019, 'Live imaging of contracting muscles with wide-field second harmonic generation microscopy using a high power laser'. *Biomedical Optics Express*, **10**(10):p. 5130, doi:10.1364/boe.10.005130

[254] W. R. Zipfel, R. M. Williams, R. Christie, A. Y. Nikitin, B. T. Hyman & W. W. Webb, 2003, 'Live tissue intrinsic emission microscopy using multiphoton-excited native fluorescence and second harmonic generation'. *Proceedings of the National Academy of Sciences*, **100**(12):pp. 7075–7080, doi:10.1073/pnas.0832308100

[255] W. R. Zipfel, R. M. Williams & W. W. Webb, 2003, 'Nonlinear magic: multiphoton microscopy in the biosciences.' *Nature biotechnology*, **21**(11):pp. 1369–1377, doi:10.1038/nbt899

[256] A. Zoumi, A. Yeh & B. J. Tromberg, 2002, 'Imaging cells and extracellular matrix in vivo by using second-harmonic generation and two-photon excited fluorescence.' *Proceedings of the National Academy of Sciences of the United States of America*, **99**(17):pp. 11014–9, doi:10.1073/pnas.172368799

[257] A. Zumbusch, 'CARS Microscopy', in 'Handbook of Biophotonics, Part 2. Photonics for Health Care, 2. Pathology', pp. 1–20 (Wiley-VCH Verlag GmbH & Co. KGaA, Weinheim, Germany, 2010), ISBN 9783527643981, doi:10.1002/9783527643981.bphot023

Appendix A

Python software for microscopy acquisition

A.1 Microscopy softwares/libraries used in other labs

Many manufacturers have their own microscopy softwares for image acquisition and visualization: NIS or FluoView (Nikon), cellSens (Olympus) or ThorImage (Thorlabs). Besides costing sometimes 1000+$, these softwares are often "closed" and cannot really be modified to be integrated with elements of other brands, or carry out a custom functionality. In particular, our lab is equipped with an iMic microscope (Till Photonics, now Thermo-Fischer GmbH), and a "Live Acquisition Software" exist but can only be used for very specific applications.

For these reasons, some alternatives have emerged. They are sometimes cost-free and sometimes not, and include support for many devices, which is constantly growing if a good community of developers remain active on the project. One of them is MicroManager (or μManager), an open-source project (in Java) coupled to ImageJ [61] but is unfortunately designed for wide-field microscopy [62].

Other projects are more adapted to laser scanning microscopy like ScanImage [160] (coded in MatLab), e-Maging (for fast scanning with resonant mirror [141]), or MPScope 2.0 [143] (coded in Pascal), with the problem that iMic microscope usually have little support among the communities. It is worth noting that a LabView code was developed by C. Seebacher before 2006 [191] under the name "Colibri project", and has been used in our lab since then (with a modified version). LabView is a non-free platform that exploits visual objects and blocks interconnected with each other. It is hard to apprehend for someone that has always coded with written scripts. It is in general complicated to modify an already existed "block diagram", because the underlying logic of it needs to be first assimilated, and because simple operations required extended block arrangements (in that case, a DLL written in C++ can be used instead). Python (Python Software Foundation, https://www.python.org/), on the contrary, obeys to a relatively homogeneous paradigm (things are "pythonic" or not) and emphasizes the simplicity by reducing the number of code lines as much as possible. It is also a more "low-level"[1] language than LabView, which makes it for some aspect longer to apprehend, but - once the knowledge is acquired

[1] a language is "low-level" when it is closer to the hardware it controls, and more "high-level" when it has more abstractions (e.g. graphical commands instead of script)

- the user can easily understand the reality of the hardware he is using, and access to more complex functionalities or parameters.

The previously cited freeware alternatives are nice project to allow compatibility and performances at a low-cost, but the complexity of the code can be discouraging for a non-trained person. Furthermore, you need knowledge on their specific language to be able to shape the software to meet your needs: MPScope is coded in Pascal (for performances), which is not among the basic languages that students usually know. ScanImage is coded in Matlab, a simpler language, but with decreased peformances, while Python is being increasingly popular, and learnt at school.

In conclusion, Python appears as a good trade-off between efficiency (execution speed) and simplicity (to modify and further develop the code).

A.1.1 Microscopy libraries in Python

Because many types of microscopy exist, many Python codes have been developed for them. To the best of my knowledge I can cite :
- PYME (for wide-field microscopy, uses WX visual toolbox)
- POSSM (for tunneling microscopy)
- MicroscoPy (uses TKinter visual toolbox)
- Acq4 (for neurophysiology research)

Even if these codes are freely available online, they have little documentation which makes it difficult to adapt them for other purposes. Furthermore, our set-up has specific instruments, and specific working modes like e.g. stage-scanning that need to be coded and adapted in the new environment. For these reasons, it was chosen to start a whole new program from scratch, that would thus be purely in Python. Building such a program is long, but it was rewarding as it allows a full understanding of the different instruments of the set-up, and thus opens the way to improvements, and the implementation of new scanning mirrors (see after, section A.4) or of a fast stage-scanning (see after, section A.3) for instance. Above all, it was very useful for the development of the single-scan ISHG (chapter 9) that requires a full understanding of the image formation process.

A.2 GUI for scanning microscopy

A.2.1 Parallel tasks in Python and the Global Interpreter Lock (GIL)

Keeping a GUI responsive

Usually, a GUI is made to provide a direct and easy access of the code execution to the user, and to be able to execute many tasks in parallel. The classic and basic execution of a code is indeed from top to bottom, each line being interpreted and executing *consecutively*. In a GUI, the interface (buttons, text areas ...) needs to keep its responsive behavior, even more when executing a time-consuming function. In other words, it needs to perform some task *simultaneously*. This is automatically the case in MatLab for instance (which is therefore made very "user-friendly"), but in other languages (often more "low-level")

like Python, this has to be explicitly commanded. For this reason, the so-called "threads" exist and a simple syntax like :

```
worker_motor = Worker_motor(arg1, arg2)
thread_motor = QThread()
worker_motor.moveToThread(thread_motor)
```

allows to create the worker "`worker_motor`" (which is a Class where the task will be performed in parallel), and put it in the independent thread "`thread_motor`".

True parallelism (processes)

If the previous example is fine to keep the GUI responsive, it is actually not performing the tasks in different processors, so cannot be called *true parallelism*. In short, this is because Python prevents this for safety reasons (with the "Global Interpreter Lock", GIL). This becomes a problem if some CPU-intensive tasks have to be performed in parallel (and the calculations have to be done simultaneously for time saving). It is also problematic in our case when a motor has to be controlled (scanning the laser), in parallel of the calculations on an array (reshaping raw data, averaging them), and in parallel of the image display:
- if the scanning motor is told to move at each new buffer of data, non-simultaneous tasks would result in dead-times in image acquisition. In addition to a high loss of time, some possible changes of the sample between buffers (drifts, change of properties ...) could also occur. The live display could then be sacrificed, which is a loss of ergonomicity for the acquisition GUI.
- if the scan motor is told to start and not controlled until the end of the acquisition, the tasks (data treatment + display) would lead to a delayed display, which can imply a latency between the successive acquisitions.
Fortunately true parallelism can be achieved by either:
(1) using others Python's superset like Cython [13]
(2) using Processes (package "multiprocess")
(3) probably other ways

I have only tried the second option, mainly because I did not know the existence of the first one at the beginning! It still requires a little trick to work correctly. A "Process" is indeed different from a "Thread" by nature, as it cannot receive any direct order if they are already running (nor pyQtSignals), and does not accept all variables. A good way is to communicate with them by "Queues".

The Queues are some First-Input-First-Output (FIFO) communication pipes between Processes, and allow to send any Python object. Since an already-started Process cannot receive orders, it has to *listen* to new elements in the communication Queue all the time, and send results/orders back to the main GUI by another Queue, or the same Queue. This can be done using an infinite loop, and a blocking "Listen" function.

Figure A.1 shows the different "Thread" used in the Python program: the main instance controls several instruments, all in QThread such that their execution is totally independent from each other. It includes: the scanning motor in XY (Thorlabs, for sample-scanning and positioning), the 2 or 3 motors controlled by the "APT" library (Thorlabs, for rotation of waveplates...), the "iMic" (objective change, coarse Z), the piezo PI (fine move in Z), the spectrometer (Ocean Optics, records the spectrum in

real-time), the shutter (Thorlabs, controls the laser exposition), the phase EOM (see chapter 9) and the Thread for the scan (static acquisition, and galvos-scanning). Some "Process" are only used in the scan Thread, and represented with a colored fill.

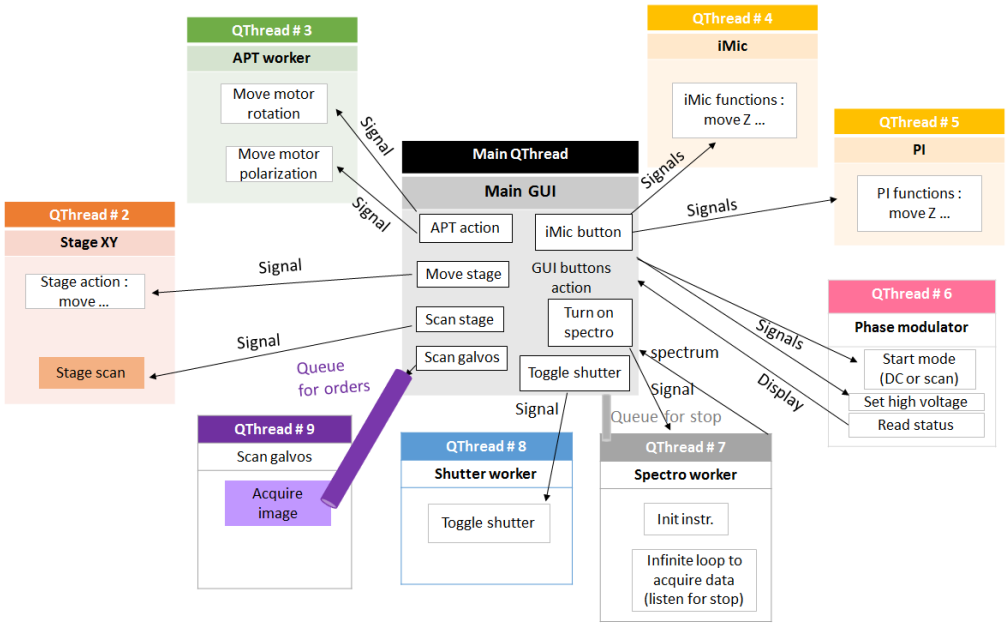

Figure A.1: Schematic of the Python QThreads that communicate with the GUI. The Processes are indicated in colored fill.

A.2.2 Other specificities

Calling 32-bits libraries from a 64 bits application - memory usage

On Windows 64bits platforms, 2GB of RAM are allocated to a 32 bits application. For our program, this limits the memory available to store variables, such as images. For instance, our Python 32 bits was not able to allocate an array with more than 10e6 elements (with 64 bits precision). At the average acquisition rate of 1MHz, it means only 10sec of continuous acquisition. Of course, it can be (partially) circumvented by: a clever management of variables (like doing averaging), clearing unused data or saving them on the disk (and reload it later). Yet, this limitation might force the programmer to do too many compromises to keep the memory sane.

The solution is to switch to Python 64bits, but some foreign libraries usually prevent doing so, because they are coded only in 32 bits if the instrument is quite old (e.g. the iMic library controlling the microscope in our case). Fortunately, inter-process communications exist: the principle is to use server32.exe to communicate orders and some basic variable using a standard Client/Server architecture as illustrated on Fig. A.2. The server Class contains the 32 bit library calling, and all the functions to communicate with it. The client Class that is the "real" object used by Python 64 bits just contains mirror functions, that call the corresponding ones in the server Class, passing by server32.exe (a Windows tool): for instance, "move_motor" is a mirror of "move_motor32" (Fig. A.2).

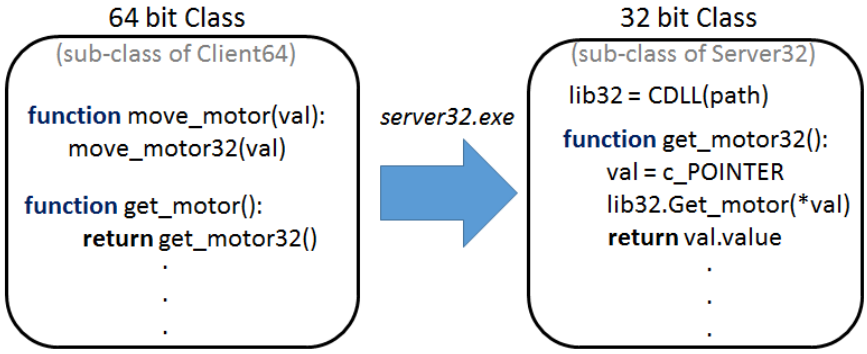

Figure A.2: Schematic of the two Python Classes used: a client (sub-class of Client64) that contains the basic orders, and that send them by server32.exe to the server Class (sub-class of Server32). The latter contains all the library definition, pointers, arrays (by *ctypes*), in 32 bits.

This protocol has been implemented by Joseph Borbely and shared through the "msl-loadlib" package [17], which I thank a lot for his work. I later re-implemented some custom server/client Classes to suit my needs.

64 bits applications have a RAM limitation corresponding to the PC specifications, which is nowadays 16GB in average. When working in Python 64bits, a test showed that a 64 bits precision array can be successfully allocated with up to 1e9 elements, which means a factor of 100 improvement compared to the 32 bits version. The programmer - using the protocol to manage 32 bits libraries on Python 64 bits - can now limit the variables usage by putting the maximum at e.g. the standards of the 32bits version, while being sure that the memory will never overflow thanks to the factor of 100 in dynamic range.

A.3 Sample scanning with a motorized high-speed stage

A.3.1 Simple method to implement a motorized sample scanning, and its limitations

A motorized stage is different from the piezo stepper because it does not perform the scan pixel-by-pixel, but line-by-line: this is due to the acceleration and then deceleration that the motor needs to do to reach a given position, possibly reaching a constant velocity phase if the move is long enough (see Fig. A.3 a)[1]. If the scan was designed pixel-by-pixel, the total imaging time for the considered scan in table 3.3

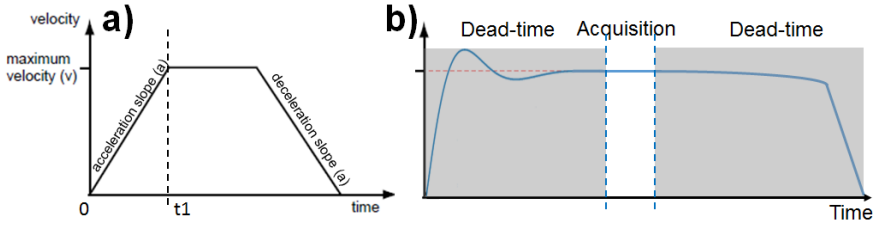

Figure A.3: a) Velocity of the motor vs time for a trapez profiled move. Adapted from [221]. b) Velocity of the motor vs time for real profiled move. The grey areas represent dead-times (no acquisition point are recorded).

[1]this is not the case for a piezo motor, where the position steps are performed by a tension change (the only limitation is then the maximal frequency of the driving signal

(400×400 pixels) would be at least 640 secs [2] ! A line-by-line scan decreases this value below 80sec, so this option is preferable. A more detailed study of the real acceleration time and deceleration will be explained after, but we can keep in mind for now that this simple model of move profile is not directly applicable to a real motor (like the Thorlabs' one). This implies that the acceleration and deceleration time required to perform a given scan cannot be directly calculated by a simple and unique formula.
The easiest way of implementing a line-by-line scan is thus to determine empirically a "dead-time zone" before and after the acquisition of the line, where there is no data recording to let the motor stabilizing its velocity. This "dead distance" must be large enough to be adapted to short and long line scan. However, the exposure time (depending on the motor speed) should not be changed to ensure the acceleration time remains the same.

This method was implemented with success in our lab under a LabView control. Unfortunately, a bidirectional (see Fig. A.10B) scan cannot be properly implemented, as the real acceleration time is different from the deceleration time (which would imply a shift between odd and even lines), not to mention that the dead-time zones potentially increase the scan duration by a large amount (see Fig. A.3 b). Above all, some shifts leading to an image deformation where observed when a pixel size under 0.5μm was used (see Fig. A.4).

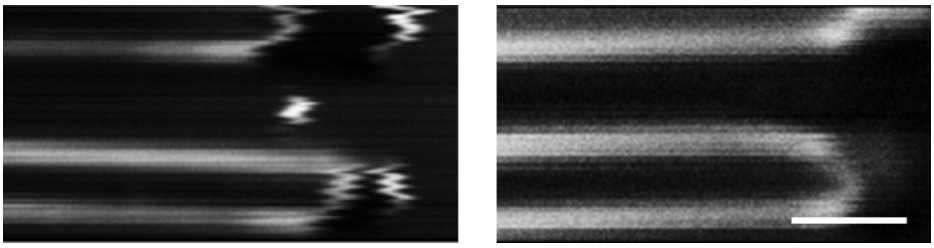

Figure A.4: (Left) Image of PPLN crystal by stage scan with the non-synchronized method (in LabView). (Right) Similar scan with the synchronized method (for comparison). Scale-bar: 4μm

A.3.2 Implementation of a synchronized scan : theory

The main conclusion from the limitations of the "easy" unsynchronized method is that a trigger must tell the acquisition that the acceleration is over, and another one that the deceleration begins (which would demarcate clearly the acquisition time).

Trapezoidal scan

Taking into account the schematic of Fig. A.3a, the acceleration (e.g. over x direction) is performed at a constant value a_0 so $\frac{dx}{dt} = a_0 t$ and the max velocity attained after the acceleration time τ_{acc} is: $v_{\max} = a_0 \tau_{acc}$. Also, $x(t) = a_0 \frac{t^2}{2}$ and the distance travelled during the acceleration is :

$$x_1 = a_0 \frac{{\tau_{acc}}^2}{2} = \frac{1}{2} \frac{{v_{\max}}^2}{a_0} \tag{A.1}$$

[2] Considering 1ms of acceleration+deceleration + 1ms of move + 1ms of stabilization/data transfer

S-curve scan

Here, the Fig. A.5 is considered. The acceleration are different regarding the instant considered along

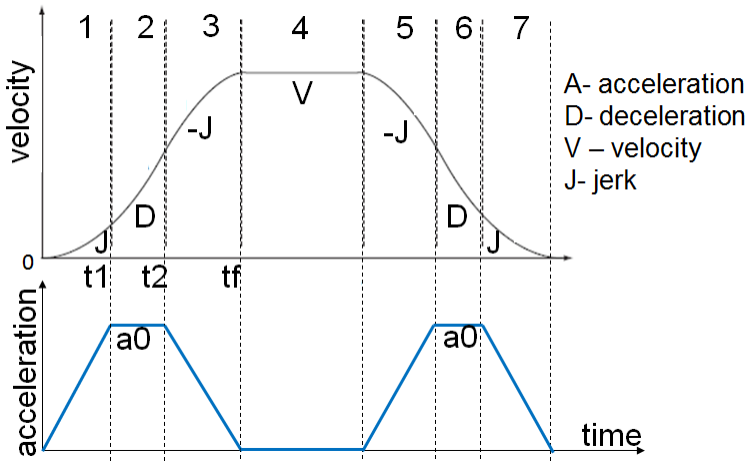

Figure A.5: (Top) Velocity of the motor vs time for a S-curve profiled move. (Bottom) Motor's acceleration vs time for the same move. Adapted from [221].

the acceleration profile :

$$\dddot{x}(t_1) = a_0 = Jt_1 \quad \text{and} \quad \dddot{x}(t_2) = a_0 = -J(t_2 - t_f) \tag{A.2}$$

Between t_1 and t_2, the acceleration is constant, and between t_2 and t_f it is decreasing linearly, such that $\dddot{x}_{t_2,t_f} = -Jt + \text{cst}$ with 'cst' a constant to determine.
It is also known that $t_1 = a_0/J$ and $t_f - t_2 = a_0/J$ and $\ddot{x}(t_f) = 0$, so that $\text{cst} = J\left(\frac{v}{a_0} + \frac{a_0}{J}\right)$.
Thus the maximum velocity reached is $v_{\max} = \dot{x}(t_f) = \int_{t_0}^{t_f} \dot{x}(t)dt$, whose integral's has to be decomposed over all the different part:

[a,b]=	0,t_1	t_1,t_2	t_2,t_f
$\int_a^b \dddot{x}(t)dt$=	$\frac{1}{2}Jt_1{}^2$	$a_0(t_2 - t_1)$	$\frac{1}{2}J({t_f}^2 - {t_2}^2) + \text{cst}(t_f - t_2) + \text{cst2}$

(A.3)

We then have:

t in	$[0, t_1]$	$[t_1, t_2]$	$[t_2, t_f]$
$\dot{x}(t)$	$\frac{1}{2}Jt^2$	$a_0 t - \frac{{a_0}^2}{2J}$	$-\frac{Jt^2}{2} + J\left(\frac{v_{\max}}{a_0} + \frac{a_0}{J}\right)t + \text{cst2}$

(A.4)

Taking into account the equality $\dot{x}(t_f) = v_{\max}$, we have $\text{cst2} = v_{\max} - \frac{J}{2}\left(\frac{v_{\max}}{a_0} + \frac{a_0}{J}\right)^2$.
We can already determine the required time for a complete acceleration : $t_f = v_{\max}/a_0 + a_0/J$.
The velocities have to be integrated one last time to find the positions:

t in	$[0, t_1]$	$[t_1, t_2]$	$[t_2, t_f]$
x(t)	$\frac{1}{6}Jt^3$	$a_0\frac{t^2}{2} - \frac{{a_0}^2}{2J}t + \text{cst3}$	$-\frac{Jt^3}{6} + J\left(\frac{v_{\max}}{a_0} + \frac{a_0}{J}\right)\frac{t^2}{2} + \text{cst2} \times t + \text{cst4}$

(A.5)

Considering the value of x at t1 in the first and the second part, $\text{cst3} = a_0^3/6J^2$. Doing the same for t2 and tf, $\text{cst4} = \frac{-J{v_{\max}}^3}{6{a_0}^3} + \frac{v_{\max}}{a_0}\left(v_{\max} - J\left(\frac{a_0}{J} + \frac{v_{\max}}{a_0}\right)^2\right)\frac{t^2}{2} + \frac{J{v_{\max}}^2}{2{a_0}^2}\left(\frac{a_0}{J} + \frac{v_{\max}}{a_0}\right)$.
Hopefully, when calculating the value of interest (i.e. the distance needed for a complete acceleration),

this nicely reduces to:

$$x(t_f) = \frac{v_{\max}}{2}\left(\frac{v_{\max}}{a_0} + \frac{a_0}{J}\right) \tag{A.6}$$

Line time calculation

We want to have the duration of one scan line as small as possible, with $t_{line} = \frac{d}{v_{\max}} + 2t_{acc}$ where t_{acc} is the time necessary to accelerate (or decelerate). Taking the derivative of this expression allows to find the extrema, here the minimum. Then for a trapezoidal profile, a0 must be as large as possible, and $v_{\max,trapez} = \sqrt{da_0/2}$.
For a S-curve profile, it's a bit more tricky. The quantity to minimize is $\min_{v,a0}\left[\frac{d}{v_{\max}} + 2\left(\frac{v_{\max}}{a_0} + \frac{a_0}{J}\right)\right]$. Taking the derivative *w.r.t.* $v_{\max}$ leads to the same expression as the trapezoidal mode: $v_{\max,opt} = \sqrt{da_0/2}$. This expression is useful if $a_0 \neq a_{Scurve,opt}$. If $a_0 = a_{Scurve,opt}$, the velocity can be calculated by taking the derivative *w.r.t.* a0 to get: $a_{Scurve,opt} = \sqrt{Jv}$. Then $v_{max,Scurve,opt}$ and $a_{0,Scurve,opt}$ can be obtained in that case: table below shows all the different expressions for the different scan modes.

	Trapez	Scurve (non-optimal acceleration)	Scurve (optimal acceleration)
Optimal acceleration	$a_0 = a_{max}$	$a_0 \neq a_{Scurve,opt}$	$a_{Scurve,opt} = \left(J^2 d/2\right)^{1/3}$
Optimal velocity		$\sqrt{da_0/2}$	$v_{max,Scurve,opt} = \left(Jd^2/4\right)^{1/3}$

A.3.3 Synchronized scan with triggers

Move trigger

The BBD102 (and BBD202) has three types of trigger: while in motion (trigger to logical level HIGH when the motor is moving), when the move is complete (the opposite), and *as long as* the velocity is the maximum velocity (i.e. as long as the velocity is constant). Every one of these could be used, but the most evident seems the last one as we want to acquire data only when the motor has a constant velocity, to avoid distortions of the image.

Control in Python

For this types of custom control, Thorlabs offers APT.dll for all its motors. Unfortunately - at least as far as 2017 - no possibility to control the trigger properly has been implemented. A low-level control must therefore be coded, by-passing the DLL. This consist of sending directly strings of hexadecimal numbers to the control unit. For instance:

```
'x43\x04\x01\x00\x21\x01'
```

is used to home the motor in the X direction. This hexadecimal string follows a regular pattern: the two first number are for the command ('x43\ x04' is 'homing'), the two after are always set to 'x01\ x00'

for a BBD102 controller, 'x21' assign the destination (i.e. channel # 1), and the last 'x01' assign the emitter of the command (here the PC motherboard). I uploaded a detailed library and an example code on GitHub at `https://github.com/MaxP92/thorlabs_python_low-level` [156]. This code is based on the thorlabs low-level guide [222]. The communications with the unit are ensured by the package "pySerial", but could also be controlled by "pyFtdi" (see the GitHub code [156] for details).

Note that other Thorlabs Python codes have been shared by other people, like "thorpy" or "pyThorAPT" for low-levels communications, and "thorlabs_apt" or "PyAPT" for more classic use through APT.dll: they all can be found on GitHub. It is worth noting that a low-level commands allows to control many Thorlabs instrument in parallel and *independently*, contrary to APT.dll that can be utilized by one instrument at a time (then, the orders of control must be sent successively).

Parallel processes and communications for the scan

The sample scanning, although requiring slower commands than a laser scanning, still needs some parallel Processes to avoid increasing the acquisition time (already quite long). The acquisition must indeed listen to the Start Trigger when the move starts, and the motor should not go to the next line without being sure that the reading of samples from the detector is ready. To achieve that, a simple two-sides communication between the Worker for the move of the motor and the Worker for the data reading can be implemented: the motor Worker tells the reading Worker that it is ready, and when the latter replies the same message it moves one line of the scan. This ensures the reading Worker to listen to the Start and End triggers exactly when it should. The whole implementation is described on Fig. A.6. When the

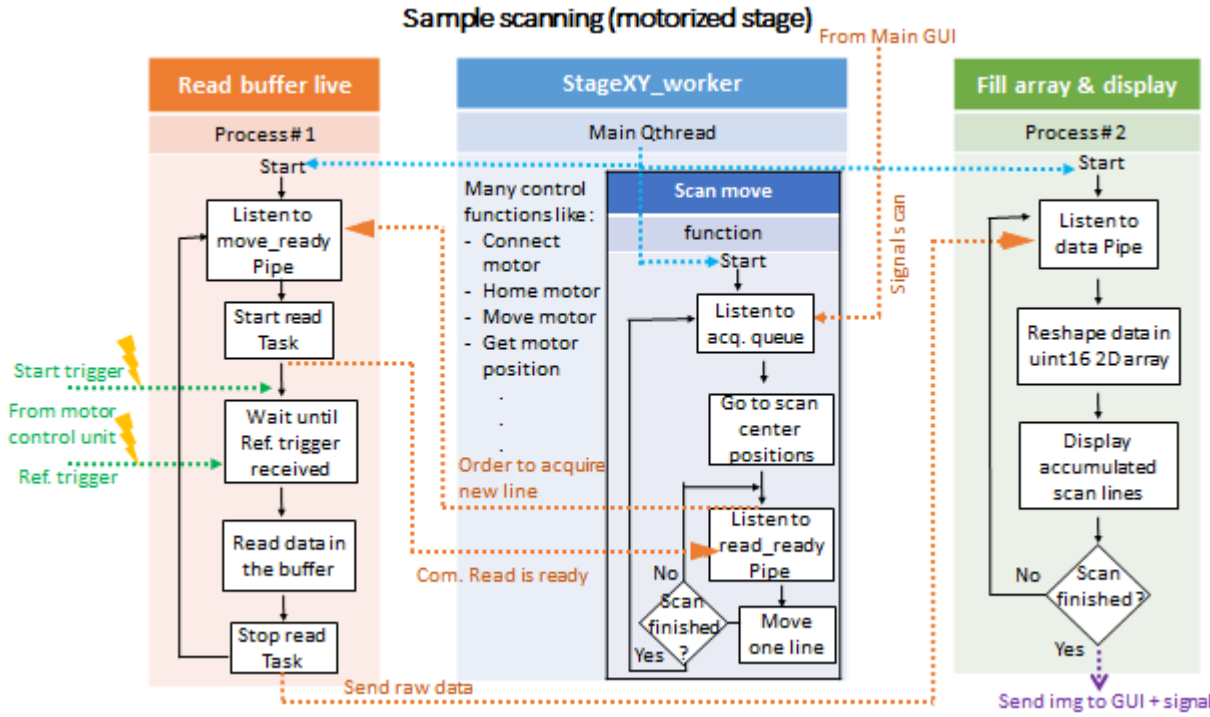

Figure A.6: Sample scanning code (with motorized stage) explained by blocks. For clarity, only the main features have been represented (in particular, the end of the scan and later communications between processes have been hidden). Orange arrows show communications by Queues, where the listen command are always blocking.

image is finished, the motor Worker simply return in the blocking command that listen for new orders from the GUI (take another new image, or quit the Thread).

Real values for acceleration and deceleration dead-zones

We previously saw that the motor needs to accelerate and decelerate, so that to perform, say, 10μm at a constant speed, the user cannot just tell the motor to move by this distance. He must rather tell it to travel a certain distance *before* the required start point (acceleration)[1], and to target a final position *further* than the required ending point (deceleration). The values of these offsets have been previously calculated for the case of a trapezoidal move profile or a S-curve one. The result of a scan with these theoretical values is shown on the Fig. A.7. We see that the scan is performed with a horizontal velocity

Figure A.7: Comparison of scan images of circular holes in a LiNbO3 crystal (fast direction is the horizontal). (a) With a trapezoidal scan and theoretical values of offset. (b) With a corrected scan. Scale-bar 40μm.

not exactly constant: the distortion of the circular hole (see right (b) image for comparison) seems to decrease from left to right which is a clear indicator of a slight deceleration at the beginning of the move.

This is because the start trigger of the motor is raised as soon as the required velocity is reached, without waiting for the velocity to stabilize. As this stabilization is ensured by a PID feedback loop, it cannot adapt to every case of velocity and travel distance (this would require a real-time correction of the PID parameters, which might be done by a more expensive control unit). Figure A.8 shows an

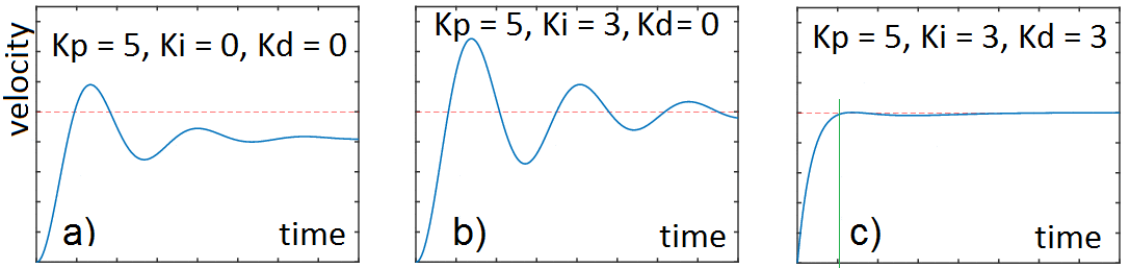

Figure A.8: Example of PID parameters tuning of a hypothetical acceleration curve. The red line indicates the steady-state value (to reach), and the green vertical one shows the settling time. (a) The imposed value is not reached, because there is no integral and derivative term. (b) The imposed value is reached, but after many oscillations. (c) Adding a derivative term reduces the oscillations.

example of PID tuning, on what can be the acceleration profile: the gain Kp is increased to allow the motor to actually reach the desired velocity value. At some point, the integral term Ki must be increased to fully remove the steady-state error (b). It comes with the cost of a high overshoot and oscillations before stabilization, and the derivative term Kd is then slightly increased to limit this effect (c), and leads to an optimal settling time.

Considering the previous deformed image, in trapezoidal mode the curve is certainly similar to the one of Fig. A.8a, with a smaller overshoot though, at least for the used scan parameters. Some tests

[1] thus the initial position must be offset by this distance

were performed, and the PID parameters were slightly optimized for a bunch of "standard scans". But it should be mentioned that these optimal parameters also depend on the weight of the body (sample holder + sample). The weight considered for the tests was a 'classic' microscopy slide 26x76x1 mm.

For small scan sizes, it was necessary to increase the acceleration by a certain offset to get no image deformation. This mode (trapezoidal profile) can nevertheless be used for images that are not conserved after experiment: the one acquired to find the good XY position, the good focus, and to set everything up before acquiring a real experiment (which can actually represent a lot of images, so a lot of time is saved). It can also be very useful for images whose resolution is coarse, 1μm or over.

By using the S-curve profile, the maximum change rate of the acceleration (called the "jerk") is limited to small values, such that the maximum velocity is approached smoothly. This implies a higher acceleration time (meaning a higher total acquisition time), but advantageously shows no stabilization problem: the result of this type of profile is shown in Fig. A.7(b).

Use of a Reference trigger for end of move

We have seen that the mathematical values of the acceleration offsets are sometimes not sufficient to ensure a scan with no deformations: as a result, the user is tempted to utilize higher offsets. But because the effect of the PID settings on the acceleration time are difficult to predict, the imposed offset could not be sufficient in some cases.

Figure A.9A) shows an example where the acceleration offset is too small compared to the needed one, which leads to a phase of constant speed smaller than the size of the image. Note that there is also an offset that can be imposed in data acquisition ("Read offset"), by simply shifting the indices in the image array. The scan still starts when the speed is constant if this Read offset is large (as in case A)), but because the travelled distance at a constant velocity is smaller than the required one, the scan is not performed entirely. This is because an "end" trigger has been introduced to the process: for this, we use a "Reference trigger" (stop) that is considered only when "NbPreTriggerSamps_min" points have been acquired. Its source is the same source as the start trigger, such that when the velocity is not constant anymore, the acquisition is ended. If the offset for acceleration (and deceleration) is set higher than the required one, this will just increase the acquisition time, but the whole scan will be acquired. However, if the Read offset (in reading data) is too high, the acquired data are then shifted regarding the normal spatial position (Fig. A.9B, bottom), and the acquisition will be incomplete.
This types of diagram could be drawn for every possible cases, but I believe that these two ones clearly show what problem can be encountered if the offsets parameters are not well set.

Tuning of the S-curve mode

The jerk is the variation of the acceleration in time (in mm/s^3). Regarding the equation, it should be set to the highest value to minimize the scan duration. However, if it is set to its maximum value, the scan has actually a trapezoidal profile. Moreover, a high jerk was shown to result in some deformations on the images. A too low value, on the contrary, makes the scan very long to complete: this parameter could probably be adjusted for every scan, but fixing it at 10000mm/s^3 seems to be a good reference.

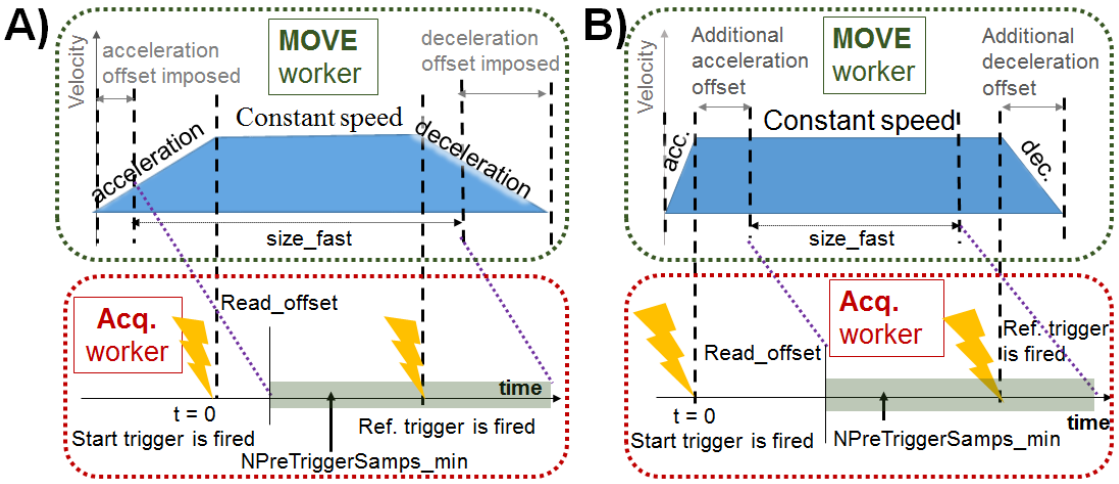

Figure A.9: Schematic explanation of the case where the imposed acceleration offset is too small (A) or too high (B). (Top) Speed of the motor vs time. The size of the line to achieve is limited by the dotted double-headed arrow. This length is reported on the bottom by a green area. (Bottom) Timeline of the reader worker, the start and stop triggers are showed with a yellow lightning. The data acquisition is considered only after the read offset. (A) The green area is not completely acquired before the Reference trigger is fired, because the real scan time is too short. (B) Same, but because the Read offset is too long.

Real duration of the scan

The total duration of the scan is supposed to be:

$$t_{acq.} = \left(\frac{d}{v_{\max}} + 2t_{acc} + \tau_{slow} \right) N_{slow} \tag{A.7}$$

with t_{acc} the time required to accelerate/decelerate (see before), N_{slow} the number of lines in the slow direction (usually the vertical), and τ_{slow} the time to perform the incremental change of line in the slow direction (generally 10ms). For a classic scan of 400×40pixels, this calculation leads to 2.25 sec, whereas the observed total time is close to 8sec ! Further investigation showed that each transition between two moves needs an additional 25ms. This might be mostly due to the PID settling time, and a bit to the USB transfer delay.

I also noticed that in an unidirectional scan (see Fig. A.10 B), the return at the beginning of the line can be performed simultaneously with the incremental move in the slow direction, to save time. Usually, the slow move is way faster than the line "flyback" (return of the motor to origin), such that the unidirectional time is approximately twice the bidirectional one.

Not waiting for move completion at each step

An even faster solution can be implemented, but it was not chosen at first, because it is intrinsically less safe. The idea is to benefit from the dead-time at acceleration (resp. deceleration) of one motor to perform the deceleration (resp. acceleration) of the other motor in parallel. The motor no longer waits that each move is effectively completed ("non-blocking mode"). Figure A.10 explains the two cases: in "blocking mode", the Slow move starts after the Fast is immobilized. In the "non-blocking mode", the

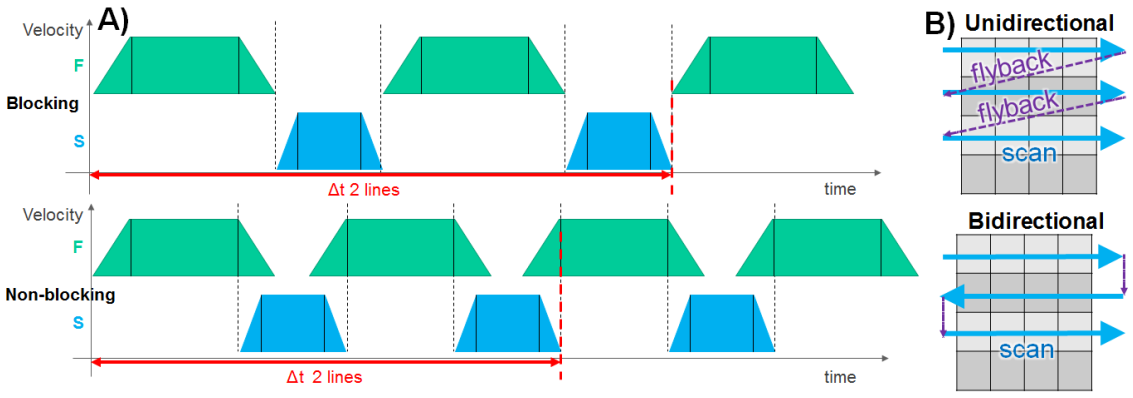

Figure A.10: A) Differences of blocking and non-blocking methods explained with the move of the motor Fast (green) and Slow (blue). The trapezoidal forms represent the different phases of acceleration - constant speed - deceleration. If blocking option, the Slow move starts after the Fast is immobilized. If non-blocking, the Slow move starts when the recording of the image line is finished (when Fast starts to decelerate). The Fast starts also earlier, so that it reaches its constant acceleration when the Slow is finished. The bidirectional trapezoidal case is considered here. B) Explanation of unidirectional versus bidirectional scan.

Slow move starts as soon as the recording of the image line is finished (i.e. when the motor Fast starts to decelerate). The motor Fast starts also earlier, so that it reaches its constant acceleration when the Slow one has finished. This is possible because two different triggers are sent whether the speed of the motor Fast enters or leaves its phase of constant speed. This method ensures that, when the image line is being recorded, the Slow motor is well immobilized. The most significant time saving is in bidirectional mode (Fig. A.10B), as in unidirectional the flyback can be performed only when the motor is immobilized, to then start again in the opposite direction. But some time is still saved, probably because of reduced communication latencies with the controller. Unfortunately, the non-blocking strategy could not be used with S-curve profiles in practice, but only with trapez ones.

A.3.4 Image registration for bidirectional scan

Using 2D cross-correlation of the even lines and odd lines images, it is possible to correct for the shifts ("DIPimage" in MatLab) between even (direct) and odd (reverse direction) of bidirectional scans: the Fig. A.11 shows an example of such a correction. The shift is clearly visible when odd and even lines are separated (2). The recombined image (4) is corrected for the 296pixels shift (exaggerated for clarity).

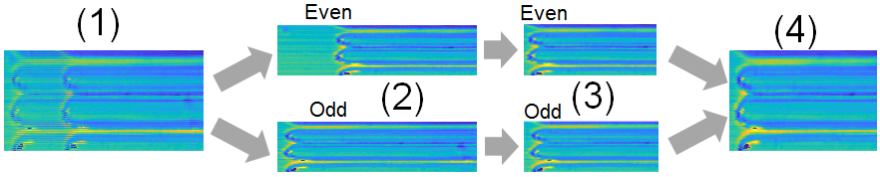

Figure A.11: Image correction using Dipimage. Example of a bidirectional stage-scanning: shifts between lines exist in raw image (1). (2) divided into even (top) and odd (bottom) lines, the shift is calculated by cross-correlation and corrected (3), then the images are recombined (4).

A.3.5 Conclusion

To conclude, the move profiles, along with the PID parameters for velocity stabilization, were investigated. To increase the stability, an "end" trigger was also used to be sure that all the acquired points were recorded only when the velocity of the motor was constant. The required offsets to have a certain distance travelled at a constant velocity can be calculated with the laws of motion, but are in practice verified only when the maximum velocity is set smoothly (S-curve profile). Table A.1 below compares the different features of the scan mode that can be used. It should be noted that the S-curve mode

Method			T scan (s)	Commentary
Unsynchronized			**519** (779)	Slow, unstable, not adaptable
Synchronized	**blocking**	**S-curve**	**198** (346)	No effects observed
		Trapez	**99** (194)	deformations at image edges (some cases)
	non-blocking	**S-curve**	unknown	No effects observed
		Trapez	**52** (103)	deformations at image edges (some cases)
Ideal motor (acc. 2000mm/s^2)			45	(theory)
Ideal motor (acc. infinite)			22	(theory)
Galvo scan at fast rate (20μs/pixel)			10	(theory)

Table A.1: Comparison of the features for different stage scan. With a scan of 1000x500 pixels, 2μm/pixel. The acceleration was set to 1500mm/s^2 and the optimal velocity is then 38.7mm/s for trapezoidal scan. The parameters that lead to the lowest acquisition time were used in every case.

can be safely employed with no deformations, but some cases of bidirectional scan require to manually impose an offset between the even (done from left to right) and the odd (done from right to left) lines. For trapez profiles (supposedly the fastest mode), the PID stabilization dominates the timing of the move, except when the resolution is coarse ($> 1\mu$m per pixel). Even when this mode is not safe for the edges of the image, it can still be used for routine images, that do not require high quality. The overall move speed is limited by an additional dead-time that cannot be explained by the manufacturer Thorlabs: it might partly be due to the PID settling time, and the transfer time via USB. To achieve all these controls, a low-level communications protocol was done, because the DLL provided is not exhaustive (this problem was also unknown to Thorlabs)[219]. The fastest set of parameters is with the non-blocking mode, using trapez and bidirectional options, as can be seen in Fig. 3.5. This scan is up to 7 times faster than in the case of a non-synchronized unidirectional scan. Thus, compared to the case of an infinite acceleration (true for a galvo scan at good approximation), I conclude that a stage scan can be only 2.4 times (at same exposure time) to 5 times (at normal exposure time) slower than the galvo scan, when well-optimized. Of course, the speed comparison depends a lot on the size of the scan.

A.4 Laser-scanning by galvanometric mirrors

A.4.1 Principles of galvanometric mirrors

Galvanometric (or galvos) mirrors use an electric current to create a electro-magnet which, coupled to a permanent magnet, will deflect a mirror by a small angle and thus produce a scan of an input beam. Two mirrors with one galvo head each can produce a 2D raster scan [131].

A.4.2 Optical arrangement

This appendix is just a complementary of section 3.1.6 in chapter 3.

A.4.3 Heatsinking

The maximum RMS current of the scanner is 1.6A on each channel with 0.2A for the board: 3.4A in total at 24V, so 82W. Approximately 16W are dissipated in the scanner, so an additional 66W will be converted to heat. The junction temperature is 40° C above the case of the controller, and must remain under 100° C. So 66W must be dissipated with a rise of temperature lower than 100-(20+40) = 40° C [215]. In practice, we observed that a 15×10×3cm chunk of aluminum (sticked with thermal grease) is not sufficient to ensure a perfect dissipation. For that reason, we chose to use a water cooling system with a chiller.

A certain heating can also be problematic on the mirrors themselves, as related on [214]. This is especially true if an unidirectional scan (Fig. A.10B) is used, because it is more current-demanding. For our set-up, this effect is limited by the use a metallic box in contact of the galvo base that will passively dissipate the heat in the air.

A.4.4 Galvo performances

The galvos mirrors are controlled in a very different way with respect to a motorized stage for instance: their velocity cannot be directly controlled (which would be useful to set a specific exposure time). Instead, the galvos can go from one position to another within a limited time. If the step (in mechanical angle) is small enough to be considered as a "small step" (usually 0.1° or under), the speed is limited by the "small angle step response". If the step is larger, the galvo will behave somewhat proportionally to the size of the step (with respect to a small angle step), but will reach a threshold where the bandwidth at full scale - i.e. the maximum rate the galvo can sustain to move the mirrors at full range - will be limiting. The bandwidth at small angle is only limiting if the galvo reverse the mirror direction at each small steps (which is harder to maintain than many steps in the same direction). Overall, we can define an approximate minimum line duration, i.e. the average amount of time required between two inversion of the direction of the mirror:

$$lineMin = \max\left(\text{lineMinBW},\ \text{angleRange}/\text{limitSmallStep} \times \text{smallAngleStepResponse}\right) \qquad \text{(A.8)}$$

where $lineMinBW = \max\left(\text{smallAngleStepResponse}, \frac{\text{ratioFullScale}}{\text{BWFullScale}}, \frac{\text{smallAngleStep}}{\text{BWSmallSteps}}\right)$. Therefore, the galvo must be asked to move by a certain step at a rate faster than $1/\text{smallAngleStepResponse}$, otherwise there is a break in the galvo movement, and the velocity is not constant during the scan (the profile is a "staircase" and not a ramp, see Fig. A.12(a) vs (b)).

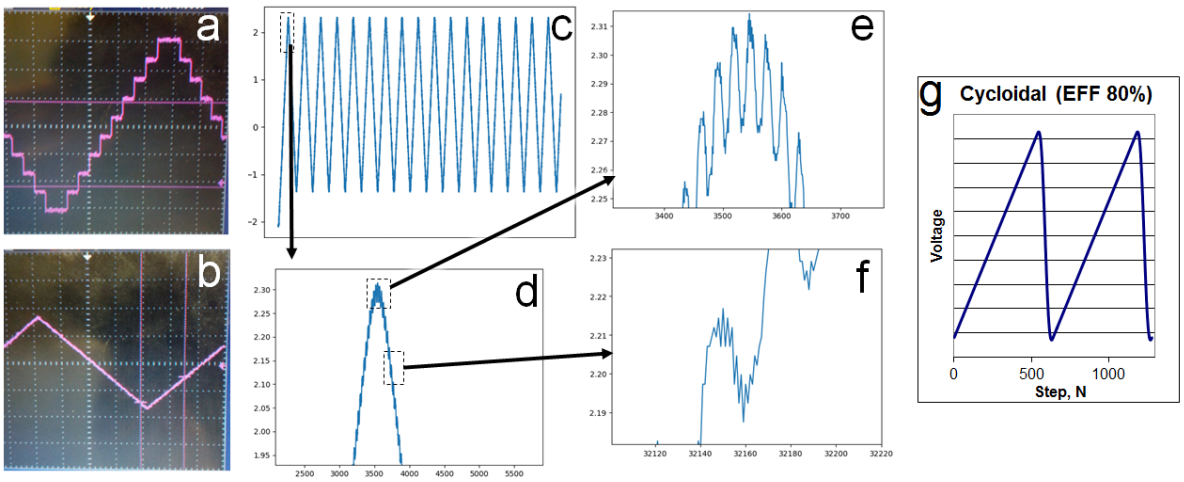

Figure A.12: (Left) Scope trace of the position of the galvo mirror with a command rate not high enough (100Hz) to avoid the galvo to pause (a), and high enough (5kHz) to avoid the steps and have a linear velocity (b). Horizontal scale = 1div <-> 250ms, line-time = 0.1s. (Middle) Visible resonances on the position control signal if a simple sawtooth (or triangle) waveform is used. (d) is a zoom of (c), and (e) a zoom of the peak of (d), (f) of the decrease of (d). (Right) Example of a proper cycloidal waveform with a 80% efficiency (g).

The number of angle positions to send to the galvo is then Npts = lineTime × rateCommand where the rate is :

$$\text{rateCommand} = \max\left(\frac{1}{\text{smallAngleStepResponse}}; \frac{\text{angleRange}}{\text{smallAngleStep}} \times \frac{1}{\text{lineTime}}\right) \tag{A.9}$$

Setting the command rate faster than this is useless, and will just result in larger arrays of command. The maximum line time is however limited by this rate, because a smaller rate will result in a "stepping" behavior (Fig. A.12, left). This is true if the whole scan - or each scan-line - is pre-written in the buffer before starting the scan. If the positions are written in live, there is no really any limitations. If a pre-set array is used, the "stepping" might even be tolerable, as it concerns cases where the galvos is moving very slowly (line time higher than 40sec). See section A.4.6 for more details.

Table A.2 lists the different important timing parameters used for analog galvos scan.

smallAngleStep (°)	limitSmallStep (°)	1/Small angle step response (Hz)	BWSmallSteps (Hz)	BWFullScale (Hz)
0.1	0.8	5000	1000	200

Table A.2: Time performances of the galvos mirrors

A.4.5 An efficient waveform to avoid resonances: cycloid

If a simple triangle (or sawtooth) command waveform is used to drive the galvo, some unwanted resonances might be excited, because the transition between lines is too sharp (see Fig. A.12, right). To avoid this problem, a cycloidal waveform (see Fig. A.12g) can be employed instead [26]. The linear part (to have a constant velocity) is still a ramp, but the flyback portion (to allow the galvo to return to the initial position) is a cycloid of the form [26]:

$$s(t) = \frac{A}{2\pi}\left[\frac{2\pi}{T}t - \sin\left(\frac{2\pi}{T}t\right)\right] \tag{A.10}$$

This waveform has the advantage of allowing the galvo to decelerate and accelerate in a smooth way. The time allocated for the cycloidal flyback can be calculated as: $t_{\text{flyback}} = (100/EFF - 1) \times t_{\text{line}}$ where EFF is the efficiency of the waveform (in %). Evidently, the scan is faster if EFF is closer to 100 %, but at some point the galvo is not able to follow the required rate. Generally, EFF is under 80 % for unidirectional scans [26].

A.4.6 Writing of the samples

There are different strategies to write the scan command samples:
- writing the whole scan before, line-by-line. This is the easiest, because the scan is written before launching the scan, and there is also no possibility of latency of the writing. This allows to have a scan limited by the buffer size of the DAQ card only, and not by the maximum RAM available in the PC.
- writing the whole scan before, each sample at a time: useful if the scan profile has no simple definition in only one function. However, the writing to the DAQ's buffer is long: 3 seconds to write a 4sec scan (40000 samples).
- writing the scan in live, with a small part of it pre-written in the buffer. This implies a parallel Process to write, as the main scan Process is already reading the acquired samples during the scan. The advantage is that the scan duration is not limited by the writing process, and only a small part of the memory of the DAQ card is occupied at any time.

The writing of the whole scan before, line-by-line is implemented by default. The writing of the scan in live is also implemented as a possible option, if the scan is longer than a time equivalent to 20E6 samples.

A.4.7 Trigger

To synchronize the pixels of the image with the movement of the galvos, different methods could be used:
(1) Acquire the image in blocks and, because the timing of the galvo is well-controlled and repeatable, put the acquired samples in the final array, by shifting them if needed. This method is used to control the old digital galvos.
(2) Acquire the position of the galvos in parallel of the samples, and use it to correct the position of the samples in the final array.
(3) Use a trigger from the galvos to tell the acquisition when a line is finished and when a new one starts.
We chose to go with the last option (best in precision). The controller (Micromax 673) gives access to

three signals that could be used as trigger : the position of the galvo mirror, its velocity, or the current applied to the galvo to make it tilt (all of this in real-time). Figure A.13 represents the different signals that have been measured for a bidirectional scan: the velocity is constant when the position moves linearly, and transition rapidly to the new value when the velocity reverses its sign. The acquisition could be paused when the velocity value enters in the transition region. However, its value is arbitrarily set in function of the actual velocity, so this signal is a bit tricky to predict. The "current monitor" is

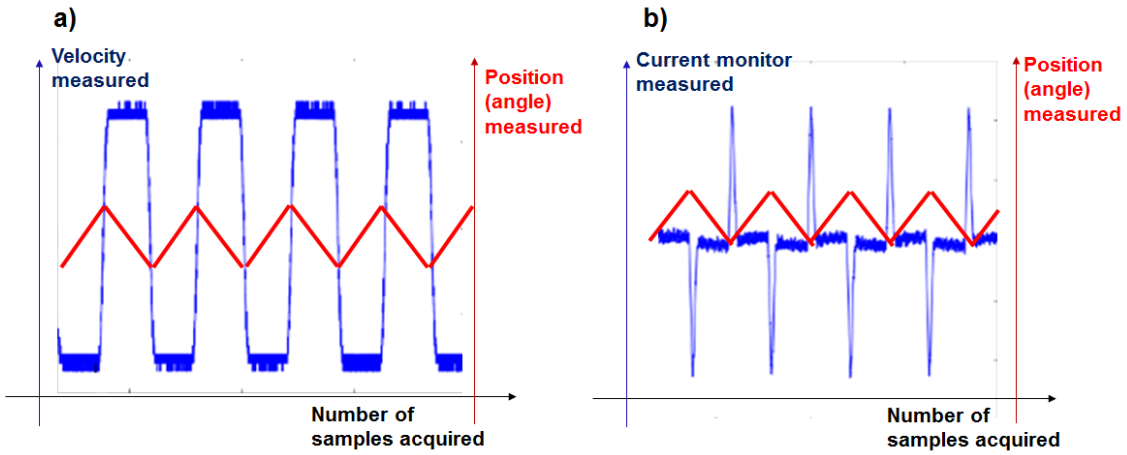

Figure A.13: Possible trigger signals output by the controller of the galvos. (a) The velocity signal, which is constant when the galvo is moving linearly. (b) The current signal applied to the galvo to move it: close to zero, unless a flyback is imposed. For comparison the position signal has also been plotted in red. Both curves represent a bidirectional scan.

around zero when the velocity is constant, but reaches high peaks when it is transitioning. Again, the acquisition could be paused when the signal is outside a certain window, however the value of current with respect to the used parameters is unknown.

A.4.8 Two different acquisition cards

The two possible DAQ cards have some similarities, but differ in many other properties: the 6110 performs simultaneous sampling in up to four channels (in input) with a 12 bit resolution, so it means that four channels can be exploited at the maximum acquisition rate of 5MHz. However, this rate must be no smaller than 0.1MHz. In the 6259, the sampling of the channels is done by one ADC (the channels all aggregate to it). It means a larger number of channels can be used (up to 32), at any acquisition rate (no minimum), providing the global ADC rate is under 1MHz (so the rate of one channel is $1/nb_{\text{channel}}$ MHz maximum). The 6259 also has a higher read resolution (16 bits) and accuracy. The compared properties are enumerated in table A.3. Thus, the best resolution for an analog trigger is obtained on the 6259 card, using a "Read" channel. However, this mode prevents using other channels for acquisition, and another card must be used in parallel.

DAQ card	6110	6259
Read resolution	12 bits	16 bits
Nb of channel	4 (- analog trigger)	32
Max rate read (MHz)	5 (simultaneous)	1/nb_channel (aggregate)
Min rate read (MHz)	0.1	0
Min reading range (mV)	+-0.2	+-0.1
Abs. accuracy	-	10x better
Analog trigger resolution	8bits	10 bits
Analog trigger channel	1 of any 4 channels	1 channel or APFI0
Write accuracy	+-8mV	+- 2mV

Table A.3: Comparison of the two DAQ cards.

Specifications, limitations

The maximum duration of the scan can be *a priori* limited by various parameters. First, a slow scan requires to write a lot of command of position: the maximum size that can be allocated on each DAQ card is 252E6 elements, so the memory must be split between 2 channels for writing, and at least one channel for reading. Also, an array must first be allocated by the RAM of the PC, i.e. in the Python acquisition program. The maximum (measured) size for this array is approximately 4E6 elements, which is limiting compared to the $252E6/4$ elements of the DAQ card. Considering the samples are written at a 5kHz rate (see before), this means 42sec per line [1] maximum (considering the whole scan is written once in the buffer, this value is higher if each scan line is written in live).

Moreover, the acquisition is made line-by-line and limits also their duration: the size of the array that will temporarily contain the acquired samples is limited by the same 4E6 elements. The maximum duration of a line is then $2/\text{nb}_{\text{channel}}/\text{rate}$ sec: for an acquisition rate of 1MHz and 2 channels, the limit is 2 secs per line (exposure time of 5ms with 400 pixels). This value is not very likely to be reached, and even then the acquisition rate could be easily reduced, to avoid acquiring too many samples.

A.4.9 Synchronization with triggers

Ideally, the program would read the acquired samples during one line of the scan when the latter is finished, i.e. when the trigger is received. In practice, several options are possible:
(1) to ask the program to read after having wait a certain time (corresponding to the line time). The challenge is to know the exact duration of one line, and to be able to wait a short-enough time with a software command: on Windows OS, the minimum wait time is limited to 20ms, whereas a scan line can be shorter than 2 ms.
(2) to use the "timeout" option of the Read command: it utilizes the internal clock of the DAQ card, but does not work well for acquisition rates $>$ 100 kHz (tested).
(3) to assume that the line time will stay constant, and read each time a fixed number of samples (corresponding to the line time): the problem is to discriminate the samples that have not been read and that will remain in the buffer of the DAQ card. These samples will be considered as a part of the next line, and this repeated effect will progressively shift the successive lines.
(4) to measure the duration of each line using a counter that receive the result of the analog trigger

[1] for a typical image of 400 lines

processing, and use this information to separate each line in the buffer in post-processing.
(5) to implement a function ("callback") that will do an action when receiving the trigger that indicates the end of the line. This action will software-triggers the reading of the samples.

The last option is the most desirable and can be implemented in the program using DAQ signals that will register a callback function. This function will then read the corresponding samples. The possible actions available on the DAQ cards have been tested:
- an independent Task is created to read the analog trigger of the main Read Task as a Digital input waveform. When the Task detects a change in the input, it raises a signal.
- an independent Task is used only to detect the trigger from the galvos, and this trigger is employed as the sample clock for this Task. When a sample is available, a signal can be connected to the callback function.
- a Counter Task can be used to count each time the trigger signal from the main Read Task issues a "pulse", i.e. goes in a state that is different from its normal one. The advantage is that the Task can be told to recognize pulses that have a minimum pulse width, to avoid fluctuations around the trigger threshold being recognized as a real trigger ("false triggering").

The first method works well, but is only possible on the 6259 card. The second one leads to a higher variation on the number of samples acquired per line. The last one works well on both cards, it is thus preferred. Figure A.15 shows the voltage (the galvo position) used by the DAQ card to trig the reading

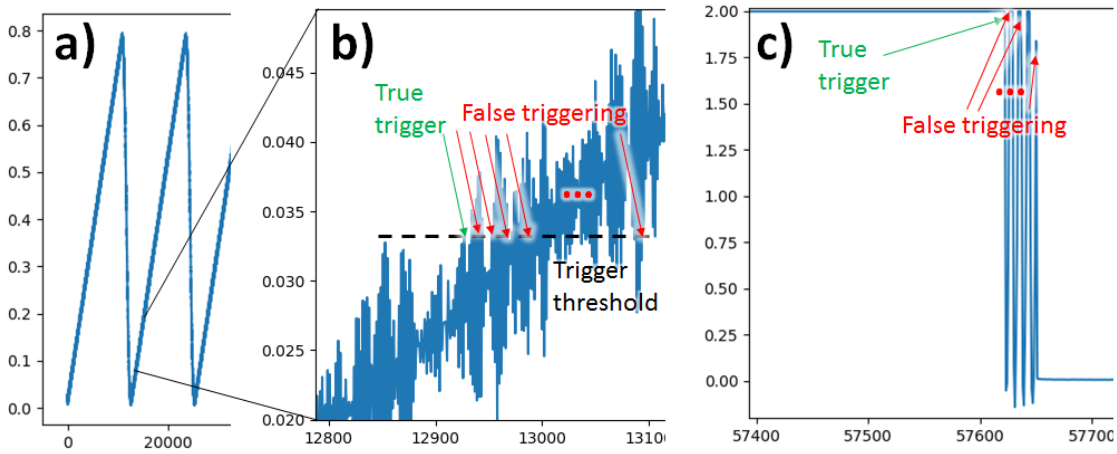

Figure A.14: Profile example showing why false triggering may occur: some fluctuations on the trigger signal ((a) and zoomed in (b)) make it going below and above the threshold in short periods of time, some of which being sufficiently high to be considered as a trigger event (false positive) (c).

of the samples. When it is outside a certain window of voltage, the trigger goes from its HIGH state to the LOW one, and the acquisition is in pause. The curve on the bottom is the "Analog Comparison Event", i.e. a digital signal that represents the trigger state in live. The scan waveform is different whether a bidirectional (Fig.A.15 a) or an unidirectional (b) scanning is chosen. For unidirectional, if the pause trigger is a window trigger (b), (i)) like in bidirectional, the flyback (see Fig. A.10B) raises a short trigger pulse in addition to the main one. If it is set to an analog level with hysteresis (b), (ii)), the flyback levels are not considered because their slope is the inverse of the direct move. Here, a 50% efficiency waveform is plotted for clarity (meaning the flyback takes 50% of the direct move time), but in practice, efficiencies up to 80% can be attained, allowing a faster scan. The summary of the routine for the galvo scanning using the callback method, illustrated by a block diagram, can be found in Fig. A.16.

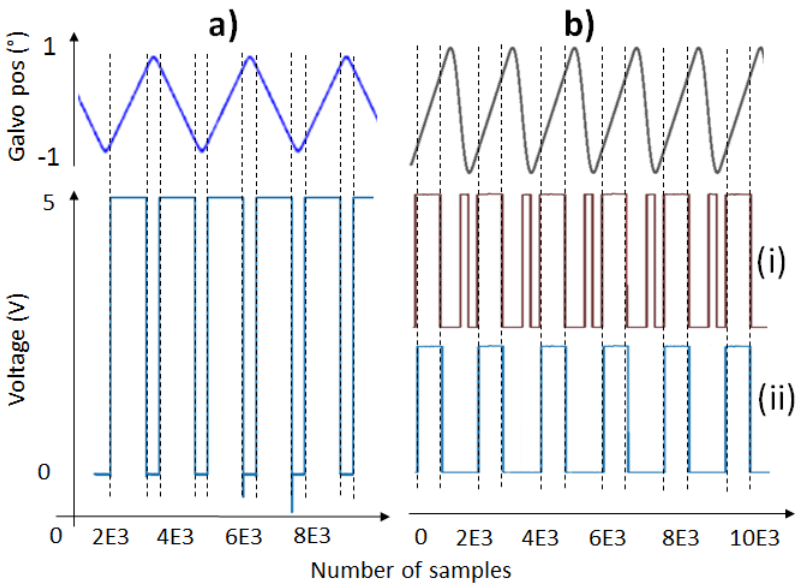

Figure A.15: Trigger with the galvo position. a) Bidirectional scan done by a triangle waveform. b) Unidirectional scan with a cycloidal waveform, at 50% efficiency. (Top) Position of the first galvo mirror function of time. (Bottom) Corresponding Pause Trigger of the DAQ, which is in the LOW state when the galvo position is higher or lower a certain voltage level. The bidirectional is preferable in theory for speed maximization, but can lead to shifts between lines in practice. If unidirectional, the form depends on the efficiency: 100% a perfect sawtooth and 0% a symmetrical triangle. If the pause trigger is a window trigger as for a), the flyback also raises a short trigger pulse (i). If it is set to an analog level with hysteresis, the flyback does not interfere (ii).

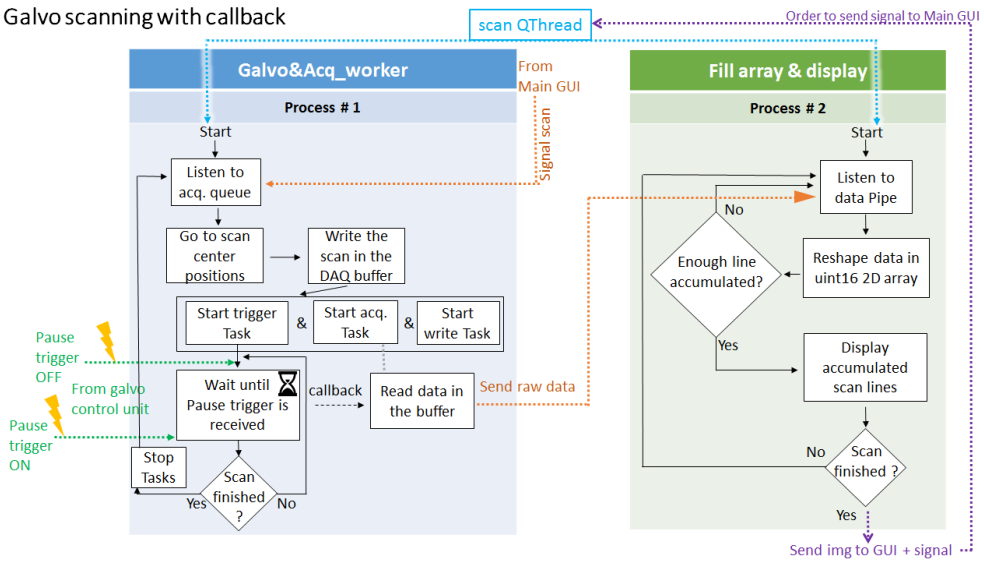

Figure A.16: Block diagram for the galvo scan routine with callbacks: one Process is used to handle the different NI-DAQ Tasks, while the other one works in parallel to treat the raw data and display the image. The synchronization is ensured by a Pause trigger, the analog position signal of the galvo mirror on the X axis: each time the trigger is received (at each line), the routine enters in the callback function to read the data samples from the buffer.

A.4.10 Avoid latencies for display of image part

A new set of data is acquired at each lines, which means that the data must be treated in 2ms or less. The several necessary actions to do it can be problematic: first, the data must be read from the buffer of the DAQ card to the RAM of the PC. Then, the data must be stored in an array, and sent to an independent Process that will treat it (average ...), and finally the final part of image is sent to a function that plots it in real-time. After the acquisition of one line, if this whole treatment takes more time than the acquisition of the next line, there will be latencies in the scan process. One possibility is to accumulate several lines, in other words to treat not just one line at a time, but a packet of it. Figure A.17 shows the different possibilities on an axis: on the left, the data treatment is set at a high rate, but the speed of the treatment might not be sufficient to follow this rate. Accumulating some data is

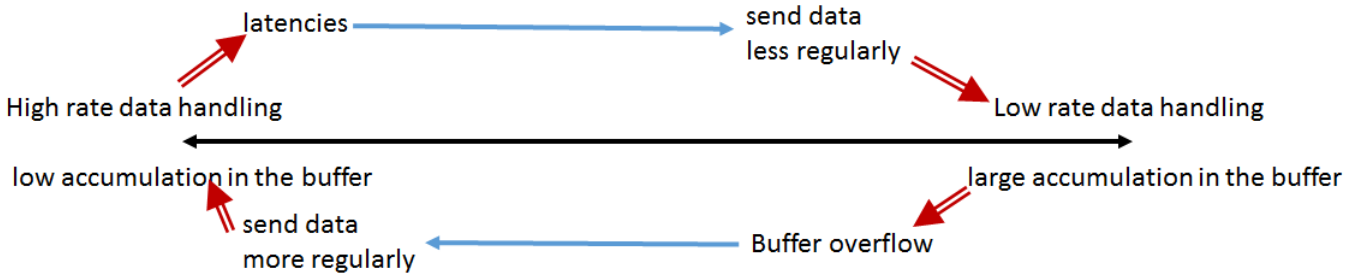

Figure A.17: Schematic of the data handling by the acquisition process: treating data at the maximum rate might induce some latencies, so the data can be accumulated instead. If the accumulation is too high, the buffer will however overflow.

the solution, but a too high accumulation can lead to an overflow of the memory. In practice the data could be stored in many locations :
- in the buffer of the DAQ card (providing the read position of the different lines is stored somewhere, to latter de-correlate the lines). This is used if the read of the samples is the slowest action.
- in the RAM of the PC, in an array of raw data (kept in the Acquisition Process). This is employed if the transfer of the data to the other Process is the limiting task, or if the data treatment is the limiting one.
- in the treatment Process, inside an image array (also in the RAM of the PC). Useful if the display of the image is the limiting task.

If the data assignment is the limiting task, the data must be sent as frequently as possible directly to the treatment Process, without being assigned to an array. Some speed test showed that the data assignment can be slow if the array is not pre-allocated, and that the data transfer can be a bit limiting. The display of the data can be easily made by blocks of several lines, to avoid latencies. In practice, the Read is performed by packets, such that a bit of the sample are kept in the buffer of the DAQ card. Also, the data is transferred directly through the Processes, to be displayed.

A.4.11 Limitation of the callback method

The described method (with callback) was successfully implemented, but it was working well for one basic test example. Later, I realized it was in fact running close to its maximum capacities. This is because the Read of samples at every lines MUST be finished before new samples corresponding to a new line arrive in the buffer. Unfortunately, the reading is not instantaneous, as some time is lost by:

- each time the code is told to enter in the callback function
- the read process itself
- the transfer into a suitable Python array
- the transfer to the Process that will treat the data

If the scan is bidirectional, the time to perform all of this is short (can be down to 40μs), because it contains only the change of direction. If a unidirectional scan is used, there is an additional flyback time, and the available time can grow above 1ms. But the maximum speed that the callback can endure was precisely around 10kHz. For this reason, the code was adapted to use the method (4) aforementioned (i.e. with a acquisition of each line duration), in replacement of the (5). The read is performed by packet of a few lines (generally every 0.3 sec or less), and the duration of each line measured by the counter is used later in the data treatment, to put the samples at the right place. Figure A.18 summarizes this method incorporated in the galvo scan routine, that has two parallel Processes. Fortunately, the callback

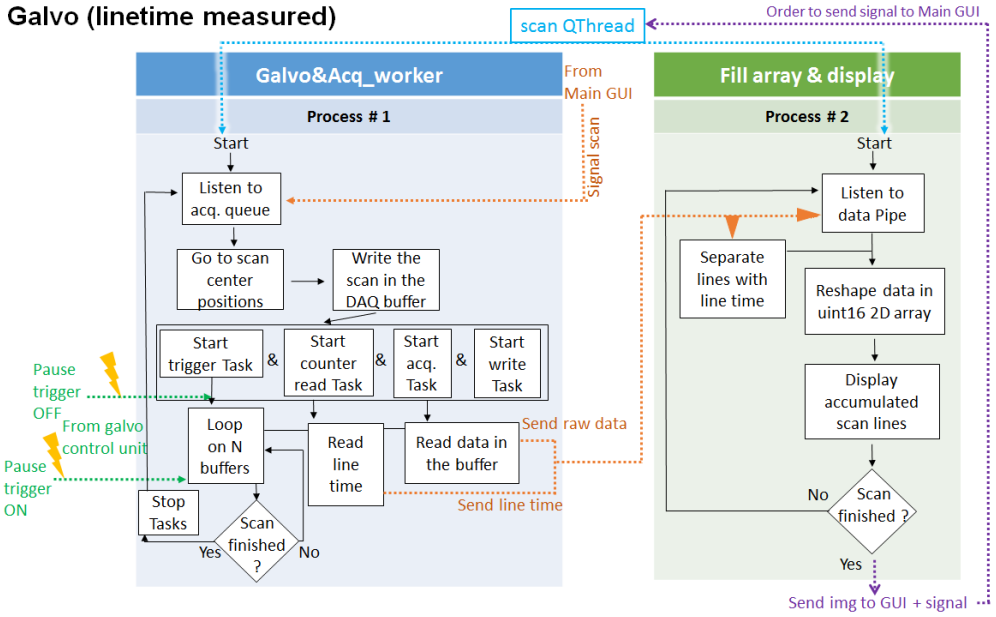

Figure A.18: Block diagram for the galvo scan routine with measurement of line duration: one Process is used to handle the different NI-DAQ Tasks, while the other one works in parallel to treat the raw data, and display the image. The synchronization is ensured by a Pause trigger, i.e. the analog position signal of the galvo mirror on the X axis.

method was shown to work well for all the "standard" scans performed with the galvos, thanks also to the restriction to unidirectional scans. Both methods can thus generally be employed, and the (4) is preferred for precise scans.

A.4.12 Comparison between the two galvos

On table A.4 are listed the different features for comparing the old galvos (digital), and the new ones (analog).

Feature	Digital galvos	Analog galvos
Small scan	down to 1μm	down to 5μm
Large scan electronically optically	900x900μm lower FOV	1200x1200μm higher FOV
Max offset with 200x200μm FOV (X&Y)	1&1mm	0.5&0.5mm
Scan modes	Bidirectional unidirectional efficiency 85%	* Unidirectional efficiency <70%
Fast scan (min line time)	1ms for small, 2ms for standard	1ms, 2ms for standard
Maximum line time	1sec for small scan, several seconds for full FOV	0.7sec for small scan, few seconds for full FOV
Entrance beam ⌀(max)	4mm	10mm
Control of position	With scan	Yes
Polarization distortion	high	low
Transmission around 400nm	low	high
Equivalent thickness of BK7	71mm	42mm

Table A.4: Comparison of the performances of the two types of galvos. *bidirectional mode could potentially be implemented.

A.5 PMT detection

A.5.1 Pixel integration

The SHG is created at the laser rate (the process being ∼instantaneous) i.e. 80MHz, but the exposure time of an image pixel is usually much longer, leading to acquisition rates ranging from 200kHz to below 50kHz. The signal recorded during a pixel time thus needs to be averaged: it can be easily done by over-sampling one pixel time, and averaging the resulting samples [142]. However, there is about 2% or higher cross-correlation between pixels, even if the time constant of the amplifier (that also acts as a low-pass filter) is set at the standard value of 1/4 the pixel dwell time [6]. This can be seen on Fig. A.19, A: the non-standardized (unsynchronized) analog integration leads to a random sample picking for pixel integration, and inevitably to correlation between adjacent pixels. This problem can be solved by using a "true pixel integrator" as a pre-amplifier/low-pass filter that will output a TTL clock that represents the timing of the integration (i.e. the charge/discharge of its capacitance) [142]. This clock can be used by the digital acquisition to synchronize the digital averaging occurring at each pixel with this integration: there are no more cross-correlation between pixels, as shown in Fig. A.19B. It is also possible to decrease the sampling rate, thus allowing to use less computer memory, and to deal with situations where the sampling rate is limiting.

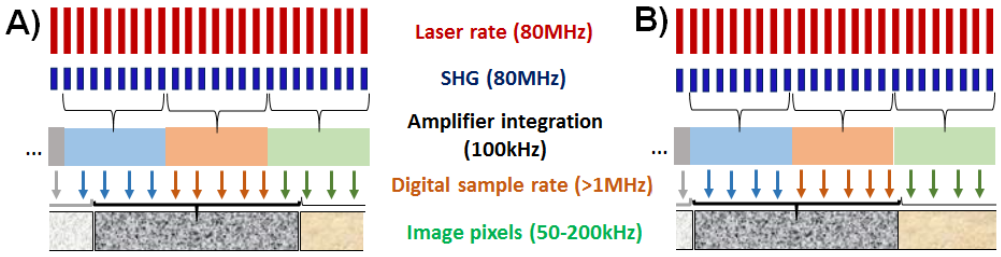

Figure A.19: Schematic of the different sampling and integration that occurs during the acquisition of pixels, for unsynchronized (A) and synchronized modes (B). (A) The pre-amplifier integrates the SHG rate (80MHz) at 100kHz, but is a non-standardized analog integration, such that it is not synchronized with the laser rate, nor the pixel time. This results in obvious correlation between pixels, as two adjacent pixels both contain a part of the same integration. (B) Same, but synchronization with the digital sampling allows to avoid pixel correlation. Different rates are not to scale for clarity.

Furthermore, the relative variance of the pixels shows that the accuracy level with a synchronized scheme can be up to 2 times higher compared to non-synchronized [105]. The results are listed in table A.5, where q is the output charge of the electron multiplier, $\overline{n}$ is the mean number of count per second, and T is the integration time. If a digital integration scheme is used instead, a synchronized integration

Storage	Method	Relative variance of pixels
Capacitance	Non-sync	$\frac{2}{\overline{n}T}\left(1+\frac{Var(q)}{\overline{q}^2}\right)$
	Analog detection scheme	$\frac{2}{\overline{n}T}$
Digital	Non-sync	$\frac{1}{\overline{n}T}\left(1+\frac{Var(q)}{\overline{q}^2}\right)$
	Photon-counting	$\frac{1}{\overline{n}T}$

Table A.5: Pixel variance in function of the method used for averaging (extracted from [105]).

(i.e. a photon-counting method) can lead to an accuracy 4 times better than the analog unsynchronized one. In other words, the same level of accuracy can be obtained using a pixel exposure time 4 times smaller [6]. In that case, because true photon counts are measured, an averaging is not necessary, and the sampling rate could also be set at the pixel rate (meaning one sample per integration of counts, so one arrow per pixel in Fig. A.19B).

A.6 Precision on digital reading

A.6.1 Relative and absolute accuracy

The digital samples leading to pixel values are acquired with a NI-DAQ card. The absolute accuracy is the ability of the device to precisely measure a voltage, and should not be confused with the resolution, which depends on the number of bytes used to quantize the voltage range [135].

This parameter depends on numerous factors such as the gain error, the offset precision, the system noise and the temperature drift [136]. However, in microscopy images, the absolute accuracy is not an

important parameter because what is interesting is only the *difference* of voltage between pixels. Thus the *relative* accuracy will rather determine the image quality.

A.6.2 Calculation for an ideal system

The acquisition card reads samples that are integers (coded on 12 or 16 bits). Several possibilities could be used to make the final image:
- the samples can be averaged, in the precision (12 or 16 bits).
- they can be averaged, but up-scaled to a higher precision (16 or 32 bits)
- they can be just summed up, then 32bits integer are used for the image array.
The last option keeps all the information contained in the detected samples, but the maximum value of the array depends on the pixel dwell time. The two first options give lighter images (on the disk), with an interesting averaging effect.

A.6.3 Accuracy calculation(s)

Let's measure the accuracy of the system, and see if it is limited by the quantization or not. The quantization (when converting an analog value to a digital number) is an important limitation of the system: for instance, measuring in the -10 to 10V range with 12 bits resolution leads to a relative accuracy of $20 * 1e3/2^{12} = 4.9$mV. Though, we must also take into account the other accuracy parameters.

As mentioned earlier, only the relative accuracy is consistent here : the noise of the system and the temperature drift are thus the only parameters to consider among those used for the absolute accuracy. We consider that the temperature does not vary much from pixel to pixel, and image to image, during an experiment (a calculation shows that this parameter is negligible compared to the other for variations of 1°C). The noise quantity can be calculated as [134] :

$$\text{NoiseUncertainty} = \frac{\text{RandomNoise} \times nb_\sigma}{\sqrt{N_{avg}}} \tag{A.11}$$

where nb_σ is the number of variance considered (usually 3), and N_{avg} is the number of points taken for to perform the average.
Table A.6 summarizes the NoiseUncertainty calculations for the two NI-DAQ cards, with 10 or the maximum average points i.e. $N_{avg,max} = \text{dwellTime} \times \text{samplingRate}_{\text{max}}$. It also gives the accuracy parameters and their equivalent in number of counts. Because the PMT returns a voltage in positive values (with a little negative offset of -0.13V), but the DAQ card always measure symmetrical voltage, only a little more than half of the count range (12bits or 16bits) is actually used. We see that for each card, the accuracy is NOT better than 1 count.

A.7 Spectra Physics laser control

A graphical user interface (GUI, Fig. A.20) was implemented in Python to control the Tsunami and Vanguard laser oscillators (see before), and the lok-to-clock synchronization module of the Tsunami. They are very practical for CARS microscopy, as the two lasers must be used, and the synchronization

Card	Resolution (mV)	RandomNoise (mV)	NoiseUncertainty (mV) if average = 10	NoiseUncertainty if max. average at max. rate and 20μs dwell time (mV)	total accuracy (mV)*	Corresponding counts*
6110 (12bits)	4.9	3.3	3.2	1.1	6	1.2
6259 (16bits)	0.3	0.28	0.27	0.19	0.49	1.6

Table A.6: Accuracy and other precision parameters of the two DAQ cards. * Taken at maximum averaging. For a -10/10V voltage range. Values are better for smaller ranges.

module can be changed in real-time with little efforts. The codes are available in the GitHub repository of ref. [155].

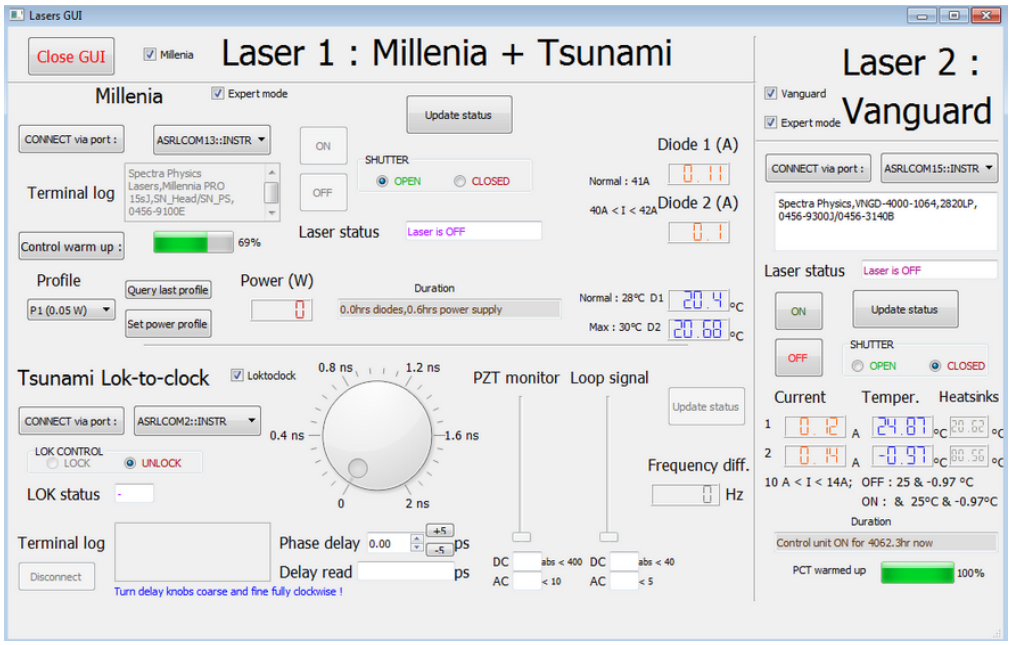

Figure A.20: GUI in Python for the control of the lasers, and their synchronization unit.

Appendix B

I-SHG: supplementary information

B.1 Beam diameter calculations in the interferometer

Here are calculated final (and intermediary) beam diameters for the I-SHG set-up, depending on the number of lenses used. For the different configurations, we refer to Fig. 3.12. Since only convex lenses are utilized, the notations are not algebraic, but the sign is used to differentiate the direction of light propagation, and its inverse.

B.1.1 Plane wave, paraxial

For the 3 lens configuration we have:

$$OA_{2,B} = (f'_{1,R} + f_{2,R}) - OA'_{1,B} \tag{B.1}$$

because the blue beam is not perfectly collimated, so the focus after L1 is located at a certain distance $OA'_{1,B}$ that will also serve as a point source for the lens L2.

$$OA'_{1,B} = \left(\frac{1}{f_{1,B}} - \frac{1}{OA_{1,B}}\right)^{-1} \text{ with } OA_{1,B} = d_{L0-L1} - OA'_{0,B} \tag{B.2}$$

Because the beam exiting L0 is almost collimated, the focus is at a large distance at:

$$OA'_{0,B} = \left(\frac{1}{f_{0,B}} - \frac{1}{f_{0,R}}\right)^{-1} \tag{B.3}$$

Then :

$$OA_{2,B} = \left(\left[-d_{L0-L1} + \left(\frac{1}{f_0^B} - \frac{1}{f_0^R}\right)^{-1}\right]^{-1} + \frac{1}{f_1^B}\right)^{-1} - \left(f_1^R + f_2^R\right) \tag{B.4}$$

It comes that:

$$d' = OA_{2,B} \tan\theta = \frac{OA_{2,B}}{OA'_{1,B}} \left(OA'_{0,B} - D_{L0-L1} \right) \frac{d}{OA'_{0,B}} \tag{B.5}$$

For the 2 lens configuration, the lens "0" (which is now noted "1") is displaced, such that the red beam is not collimated, but has its focus at a certain distance $OA'_{1,R}$. Then $OA_{2,B} = (OA'_{1,R} + f_{2,R}) - OA'_{1,B}$. The rest is the same and $OA_{1,B} = OA_{1,R} = \left(\frac{1}{f_{1,R}} - \frac{1}{OA'_{1,R}} \right)^{-1}$ because the SHG is supposed to be created exactly at the focus of the red beam. Then:

$$d' = OA_{2,B} \tan\theta = \frac{OA_{2,B}}{OA'_{1,B}} OA_{1,R} \frac{d}{f_1^R} \tag{B.6}$$

For both cases the final blue beam diameter is calculated just after the last lens. But what is important is its diameter just before the injection lens on the microscope, at a distance L from the L2 lens:

$$d'_f = d' \left(1 + \frac{L}{OA'_{2,B}} \right) \tag{B.7}$$

Because $OA'_{2,B} = \left(\frac{1}{f_{2,B}} - \frac{1}{OA_{2,B}} \right)^{-1}$, d'_f can be calculated although it depends on the used configuration (e.g. L = 1000 mm can be employed).
On table B.1 different calculated diameters for 2 or 3 lenses configuration are reported. Also, in the first case, the calculations are made with some non-perfect lenses such as the plano-convex ones that can be found e.g. at Thorlabs' (such as ref. LA1131-B), and the difference of diameter can be significant (up to x4). In the second case, the first 50mm lens that re-collimates the beam after the SHG creation is replaced by a perfect focusing system, such as an off-axis parabolic mirror: the diameter of the blue beam is then only x1.1-1.6 the red beam. When further optimizing, by replacing the last lens that recollimates with an achromatic doublet, this factor is only of 0.96-1.0.

B.1.2 Gaussian beam

The size of the waist w'_0 after a lens of focal f, placed at a distance s of the initial waist, and the distance to the new waist s' can be calculated by the Self's equations [192], [122]: $\frac{w'_0}{w_0} = \frac{1}{\sqrt{(1-s/f\ )^2 - (z_R/f\ )^2}}$ and $s' = \frac{f\left[s(s-f)+z_R^2\right]}{(s-f)^2+z_R^2}$.

After each lens, the first formula is used to calculate the size of the focal volume, considering the difference of focal length between the fundamental and SHG wavelength. It is then re-applied to determine the new beam size, if the beam gets re-collimated. The propagation of the beam is also taken into account with the formula: $w_z = w_0 \sqrt{1 + \frac{z}{z_R}^2}$ with $z_R = \frac{\pi {w_0}^2}{\lambda}$.

Hopefully, our conditions are paraxial at a good approximation, and the final diameter of the red beam is for instance approximately the same with a Gaussian beam or a plane wave (3.4mm vs 3.5 mm). Only when the most imperfect lenses are used (plano-convex), the ratio is different between the two methods (4.5 vs 0.46).

Furthermore, the Gaussian calculations can be useful for calculating what cannot be estimated with geometrical optics: the Rayleigh range. The beams being focused inside the calcites have a diameter of 7mm for the red one (excitation), and also for the blue (reference SHG) if a perfect lens is employed. For the 3 lens version, the Rayleigh range is just slightly higher, close to 8mm (see table B.1). This is a high value, useful since both beams need to be at their smallest diameter (∼focused) along the total thickness of calcites, which is up to 2*(15+5+30+5)=110mm.

	⌀ (mm)	Plano convex	1st lens = converging mirror	1st lens = converging mirror + achromatic for others
3 lenses	red ⌀	3.5 (3.6)	3.4 (3.5)	3.4 (3.5)
	Blue ⌀ after lens L2 at distance L	x4.5 (3.0)	x1.6 (0.6)	x0.96 (1.0)
2 lenses	red ⌀	4.1 (3.8)	4 (3.8)	4 (3.7)
	Blue ⌀ after lens L2 at distance L	x4.5 (0.46)	x1.1 (0.53)	x1.0 (1.0)

Table B.1: Beam diameter control in function of the configuration of lenses used in I-SHG. Initial beam diameter: 4mm. The beam is focused in calcite at 700mm distance, and a lens of 300mm is used to recollimate it. In parentheses is indicated the values calculated with a Gaussian beam.

B.2 Re-synchronization in 1S-ISHG

Figure 1 of the article in 9 explains how the voltage ramps and the pixel-by-pixel phase modulation works. In complementary, the (measured) different modes that the EOM can produce are shown in Fig. B.1: (a) 20μs, (b) 200μs and (c) 2000μs ramp times. The ramps must be re-synchronized ("re-sync") at each new line of the scan. For this, the trigger from the scanning motor is passed into a buffer cleaner that can detect the rising edges, and able to issue a pulse 0.4μs long. This pulse is TTL compatible (0-5V) and is sent to the EOM to re-synchronize the ramp train. At each pulse, the ramp is stopped at its position, and a new one starts.

B.3 Phase retrieval in I-SHG

B.3.1 Method of extraction

The intensity of a given pixel of an interferogram can be expressed as [79]:

$$I(x,y,\delta) = A_{ij} + B_{ij}\cos(\phi(x,y)+\delta) \Leftrightarrow I_{ij} = A_{ij} + B_{ij}\cos(\phi_i+\delta_j) \tag{B.8}$$

the right term being a translation of I in term of indices. When acquired, the signal is integrated over $\delta_i - \Delta/2$ and $\delta_i + \Delta/2$, where Δ is the phase-shift variation inside one interferogram:

$$I_i(x,y) = \frac{1}{\Delta}\int_{\delta_i-\Delta/2}^{\delta_i+\Delta/2} I(x,y,\delta)d\delta \tag{B.9}$$

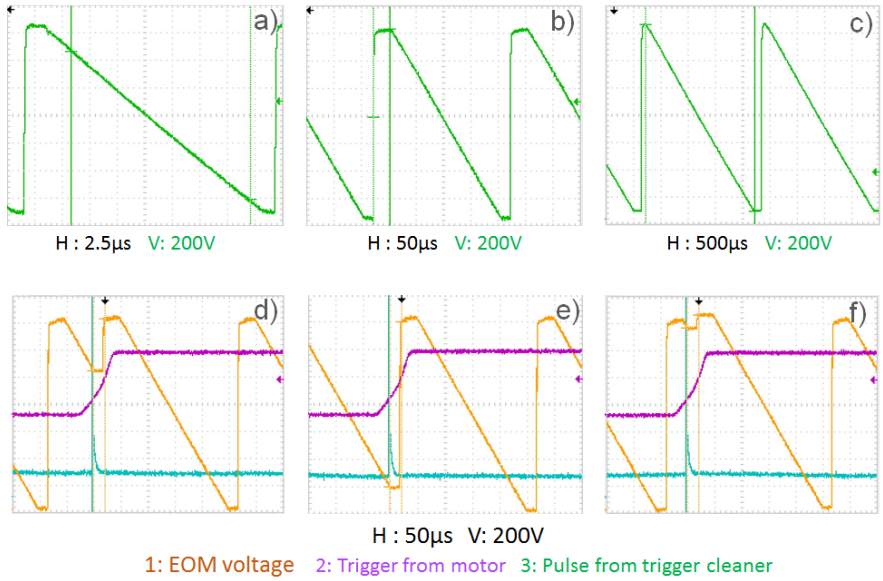

Figure B.1: Voltage ramps of the EOM for the different modes, and triggered synchronization. (Top) Different voltage ramps for the different modes: (a) 20μs, (b) 200μs and (c) 2000μs. (Bottom) When scanning with the motor, the ramps are re-synchronized at each lines: the motor's trigger is sent into a buffer cleaner, that issues a short pulse (0.4μs) at any rising edge (d,e,f). This pulse is used to trigger the "re-sync" of the ramps.

Under the *assumption* that $\Delta \approx 0$ (meaning that the interferogram is taken at a constant phase-shift):

$$I_{ij} = A_{ij} + B_{ij}\,\mathrm{sinc}(\Delta/2)\cos(\phi_i + \delta_j) = a_{ij} + b_{ij}\cos(\delta_i) + c_{ij}\sin(\delta_i) \tag{B.10}$$

where:

$$a_{ij} = A_{ij} \;\; ; \;\; b_{ij} = B_{ij}\,\mathrm{sinc}(\Delta/2)\cos(\phi_i) \;\text{ and }\; c_{ij} = -B_{ij}\,\mathrm{sinc}(\Delta/2)\sin(\phi_i) \tag{B.11}$$

Optionally, the constant term a_{ij} might be removed: $I_{ij}(0) - I_{ij}(\pi) \approx 2B_{ij}\,\mathrm{sinc}(\Delta/2)\cos(\phi_i + \delta_j)$, but a_{ij} is never rigorously equal to 0 as the interferograms show fluctuations, and the equation B.10 can be written the same in this case. Since δ_j is known, there are 3N unknown and M×N equations: it is directly clear that at least M = 3 different interferograms are needed. A least-square fitting can be used, which implies the following criteria:

$$\frac{\partial S_i}{\partial a_i} = \frac{\partial S_i}{\partial b_i} = \frac{\partial S_i}{\partial c_i} = 0 \;\text{ where }\; S_i = \sum_{j=1}^{M} \left({I_{ij}}^{theo} - I_{ij}\right)^2 = \sum_{j=1}^{M} \left(a_i + b_i\cos(\delta_j) + c_i\sin(\delta_j) - I_{ij}\right)^2 \tag{B.12}$$

X is defined as : $X_i = \begin{bmatrix} a_i \\ b_i \\ c_i \end{bmatrix}$ A system of equation can be solved :

$$A_i^{sys} \times X_i = I_i \;\text{ with }\; A_i^{sys} = \begin{bmatrix} 1 & A_{i1} + B_{i1}\cos(\delta_1) & A_{i1} + B_{i1}\sin(\delta_1) \\ . & . & . \\ . & . & . \\ . & . & . \\ 1 & A_{iN} + B_{iN}\cos(\delta_N) & A_{iN} + B_{iN}\sin(\delta_N) \end{bmatrix} \tag{B.13}$$

In Matlab, this just implies to use the function "\" : $X_i = A_i^{sys} \backslash I_i$. But a matrix inversion could also be employed : $X_i = A^{-1} B_i$, with:

$$A_i = \begin{bmatrix} N & \sum_{j=1}^{N} \cos(\delta_i) & \sum_{j=1}^{N} \sin(\delta_j) \\ \sum_{j=1}^{N} \cos(\delta_j) & \sum_{j=1}^{N} \cos^2(\delta_j) & \sum_{j=1}^{N} \cos(\delta_j)\sin(\delta_j) \\ \sum_{j=1}^{N} \sin(\delta_j) & \sum_{j=1}^{N} \cos(\delta_j)\sin(\delta_j) & \sum_{j=1}^{N} \sin^2(\delta_j) \end{bmatrix}$$
$$B_i(x,y) = \begin{bmatrix} \sum_{j=1}^{N} I_{ij}(x,y,\delta_j) \\ \sum_{j=1}^{N} I_{ij}(x,y,\delta_j)\cos(\delta_j) \\ \sum_{j=1}^{N} I_{ij}(x,y,\delta_j)\sin(\delta_j) \end{bmatrix} \tag{B.14}$$

where N is the number of interferogram (index j), i is the index of pixel.
The representation with the matrix inversion is more powerful than solving the system of equation, because A^{-1} needs to be calculated only once (and not at every pixel). Furthermore, a LU (Lower-Upper) decomposition of the matrix A_i can be used to get X_i and increase the speed even more, since the matrix inversion is exploited after in a matrix product. A matrix inversion is indeed often a highly time-consuming task in a program.

```
[L,U] = DecompositionLowerUpper(A);
Y = L \ B; % this is an easy, triangular solve
X = U \ Y; % this is another triangular solve
```

The phase φ_i and local interferometric contrast γ_i can be calculated as:

$$\varphi_i = \mathrm{atan2}(-c_i, b_i) \text{ and } \gamma_i = \frac{\sqrt{b_i^2 + c_i^2}}{a_i \,\mathrm{sinc}(\Delta/2)} \tag{B.15}$$

where atan2 is the four-quadrant arctan function, that can be used here because the numerator depends only on the sin and the denominator on the cos. As [79] points out, the phase can be calculated without any knowledge of the integration period Δ, provided it is the same for each interferogram. The influence of Δ is quite negligible: even for a quite large integration window of $\pi/2$, $\mathrm{sinc}(\Delta/2)$ =0.9, which is still close to 1.

B.3.2 Other methods of extraction

Synchronous detection

A special case of the least-square method is called synchronous detection [47, 24], when the matrix A is diagonal. In this case, the relative phase can be directly calculated for the whole image:

$$\varphi_{mat}(x,y) = \mathrm{Arctan}\left(\frac{\sum_{i=1}^{N} I_i(x,y)\sin(\delta_i)}{\sum_{i=1}^{N} I_i(x,y)\cos(\delta_i)} \right) \tag{B.16}$$

Some particular cases are expressed thereafter.

Methods 3, 4, 5 phases

We call I_1 (resp. I_2, I_3, I_4) the intensity of the interferogram at a given position (X, Y) where a phase-shift of $\alpha°$ (respectively $\alpha+90°$, $\alpha+180°$, $\alpha+270°$) has been applied. If the phase-shifts $-\alpha$, 0, α are chosen, the phase at a given position is then [47, 168]:

$$\varphi_{mat} = \text{Arctan}\left(\frac{1-\cos\alpha}{\sin\alpha}\frac{I_1 - I_3}{2I_2 - I_1 - I_3}\right) \tag{B.17}$$

An intelligent way of using 4 interferograms is also described in [47]:

$$\varphi_{mat} = \frac{1}{2}\left[\text{Arctan}\left(\frac{I_3 - I_2}{I_2 - I_1}\right) + \text{Arctan}\left(\frac{I_4 - I_3}{I_2 - I_3}\right)\right] = \text{Arctan}\left(\frac{I_4 - I_2}{I_3 - I_1}\right) \tag{B.18}$$

The left part is called the 3-and-3-averaged technique, and the right part the "4 buckets". The first one has the advantage of doing an average effect and thus reduces the error propagation through the phase-shifts [47].

Schwider and Hariharan then found a method to extend the number of phase-shifts from the basic equation by writing [47]:

$$\begin{cases} I_2 - I_4 = \tan\varphi_{\text{mat}}\,(I_1 - I_3) \\ I_2 - I_4 = \tan\varphi_{\text{mat}}\,(I_5 - I_3) \end{cases} \text{ so } \varphi_{mat} = \text{Arctan}\left(\frac{2\,(I_2 - I_4)}{2I_3 - I_5 - I_1}\right) \tag{B.19}$$

This provides a 5-buckets expression (the phase-shift between interferograms is 90°). This algorithm can be repeated N-times to find a 5+2N buckets expression. Similar derivations of the basic expressions can lead to various expressions: some are listed on Fig. B.2. All the phase-shifts are $\delta_i = (i-1)2\pi/N$ with i = 1 .. N.

The Carré method

We suppose that there are four phase-shifts with $\delta_i = -3\alpha/2\,; -\alpha/2\,; \alpha/2\,; 3\alpha/2$, then [168, 47]:

$$\varphi_{mat} = \text{Arctan}\left(\frac{\sqrt{(I_2 - I_3 + I_1 - I_4)\,(3\,(I_2 - I_3) - I_1 + I_4)}}{I_2 + I_3 - (I_1 + I_4)}\right) \tag{B.20}$$

The advantage here is that the value of α can be anything: there is no need to know it precisely, so no need for calibration. This algorithm is widely used in recent interferometric applications, and has even been generalized to more than 4 interferograms [106]. The real limitation of this method remains in the recasting of the phase from $[-\pi/2, \pi/2]$ (provided by the Arctan function) to the required $[-\pi, \pi]$ (thus removing the uncertainty). Unlike other techniques, this is not straightforward because the numerator (resp. denominator) of the argument of the Arctan does not directly rely to the cos (resp. sin) of the relative phase. Brutal recast like in [47] could work, but I have seen some recurrent problems on the boundaries.

$$\frac{-\sum_{i=1}^{N} I_i \sin\left(i\frac{2\pi}{N}\right)}{\sum_{i=1}^{N} I_i \cos\left(i\frac{2\pi}{N}\right)}$$ — N Bucket DFT

$$\frac{N}{D} = \frac{N_0 + N_{\pi/2}}{D_0 + D_{\pi/2}}$$ — Averaging $N+1$ technique

$$\frac{N}{D} = \frac{\sum_i N_i}{\sum_i D_i}$$ — Multiple averaging $N+m$ technique

$$\frac{\sum_{i=2}^{N} I_i \sin\left(i\frac{2\pi}{N}\right)}{\frac{I_1+I_{N+1}}{2} + \sum_{i=2}^{N} I_i \cos\left(i\frac{2\pi}{N}\right)}$$ — $N+1$ bucket type A

$$\frac{\frac{I_{N+1}-I_1}{2}\cot\left(\frac{2\pi}{N}\right) - \sum_{i=2}^{N} I_i \sin\left(i\frac{2\pi}{N}\right)}{\frac{I_1+I_{N+1}}{2} + \sum_{i=2}^{N} I_i \cos\left(i\frac{2\pi}{N}\right)}$$ — $N+1$ bucket type B

$$\frac{-\sum_{i=2}^{N}(i-1)(I_{i-1} - I_{2N-i+1})\sin\left(\frac{(i-1)2\pi}{N}\right)}{NI_N - \sum_{i=2}^{N}(i-1)(I_{i-1} - I_{2N-i+1})\sin\left(\frac{(i-1)2\pi}{N}\right)}$$ — WDFT

$$\frac{\frac{1}{4}(I_0 + I_1 - I_{N+2} - I_{N+3})\frac{\sin\left(\frac{3\pi}{N+2}\right)}{\sin^2\left(\frac{2\pi}{N+2}\right)} + \sum_{i=1}^{N+2} I_i \sin\left(\frac{2\pi}{N+2}\right)\left(i - \frac{N+5}{2}\right)}{\frac{1}{4}(I_0 - I_1 - I_{N+2} + I_{N+3})\frac{\cos\left(\frac{3\pi}{N+2}\right)}{\sin^2\left(\frac{2\pi}{N+2}\right)} + \sum_{i=1}^{N+2} I_i \cos\left(\frac{2\pi}{N+2}\right)\left(i - \frac{N+5}{2}\right)}$$ — $N+3$ bucket

Figure B.2: Expressions of $\tan\phi$ in different references, implying different number of phase-shifts (phase-shifts are spaced by $2\pi/N$). In order: [24], [130], [47], [116], [116], [209], [95]. Extracted and adapted from [130].

The best technique?

It should be noted that the reference [130] (around page 600) is a good basis for comparing phase extraction methods with a few or many frames. In particular, it emphasizes that the pixels-by-pixel least-square fitting using N frames is equivalent to the whole-frame methods with N frames. A high number of frames should then be chosen if the SNR is low, to act as an average effect. Otherwise, a number like 6 might be sufficient, regardless of the method employed. To deal with the precision problems and the uncertainty of the real phase-shifts, an advanced algorithm was created for the least square method (see section 3.2.4). The terms depending on the contrast γ and even on I_0 seem to cancel each other out. Same thing with other methods, like the "N phases" one. But we must keep in mind that a1 and a2 are calculated after the matrix inversion involving all the coefficients of the equation. If the contrast γ is weak and we have a signal in $I_0\gamma\cos(\phi) + b$, where b is the noise, b will have a greater impact than the case where γ is close to 1.

B.4 I-SHG treatment in MatLab - GUI

A routine to treat the raw images and plot the I-SHG results has been developed by Charles-André Couture, and later adapted by M. Rivard and can be found at [174],Annexe B.
In the wake of this work, I began to modify the function myself for some improvements. I soon realized that the data treatment - even if was simplified by the use of MatLab rather than a manual ImageJ routine - was sometimes very repetitive and lacked flexibility on the parameters adjustment. That is why a GUI seemed a good idea to increase the ergonomics. The main following features have also been

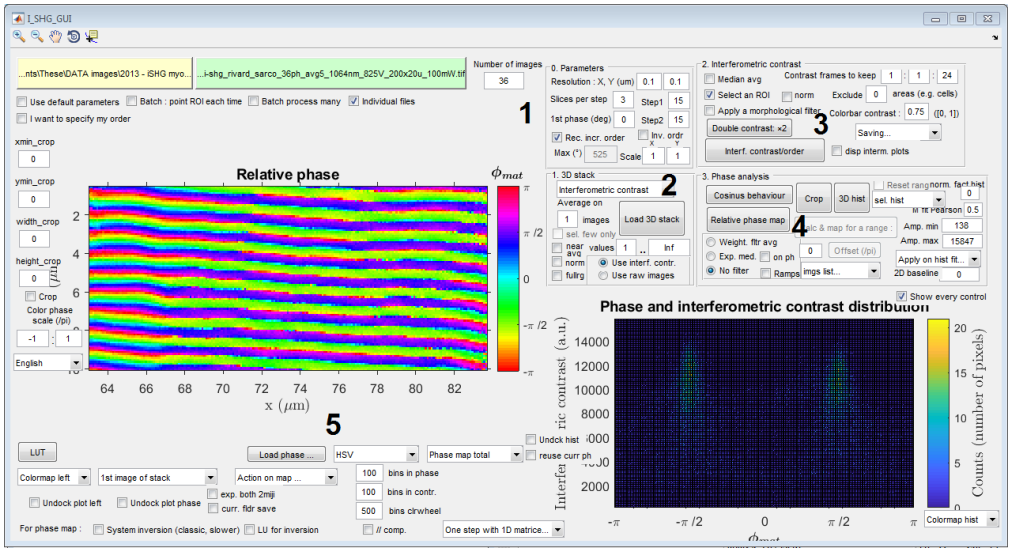

Figure B.3: The MatLab GUI for the data treatment of the iSHG images. (1) Setting of parameters. (2) Loading of images. (3) Interferometric contrast calculation. (4) Phase, amplitude calculations, histograms. (5) Display and advanced treatment and plotting.

implemented:
- the possibility to perform a mean or median averaging on the nearest neighbors on the raw SHG images, or on the contrast images
- this averaging (weighted or not) can be performed with a kernel of changeable size. It can also be done for the phase result, and be circular (modulo 2π), or not
- an optional normalization of the intensity level between interferograms
- an faster phase calculation using the lower-upper matrix decomposition
- the adaptation of the phase colormap with the curve fitting on the phase histogram: the colors reflect the widths of the peaks
- the possibility to fit the "bell curve" of the phase distribution with other functions than a Gaussian: a Lorentzian, a Voigt function, a von Mises, a product of a Gaussian and a Lorentzian, a sum of both, a Pearson VII with changeable parameter, and the possibility to use a manual window for the fit or not
- phase histograms plotted on a colorwheel, with changeable colormaps, and a display of the fit curve if applicable
- a direct plot of the result of the fit width on the theoretical abacus depending on the f ratio
- a direct plot of the correlation between SHG intensity and interferometric contrast
- a transfer into imageJ (via MIJI), conserving the colormap and scale
- a direct access to the correction of the phasemap by a reference, that can be a TIF image, a matrix or a surface

- the re-alignment of the calibration with the phase map (to compensate eventual shifts), mostly when using the I-SHG with a laser-scanning method
- some practical controls to modify the colormaps, scaling, display range, changing the LUT in real-time, etc.
- the possibility to exclude some frames in contrast, or for raw data before averaging (with an image quality control)
- the plotting of all the contrast frames in 3D
- an option to add or subtract a fixed offset to the phase map in order to be able to fit the distribution correctly or make a good comparison
- the plot of a line profile defined by user's choice
- the plot of the phase as a surface
- the 2D or 1D unwrapping of the phase map, or a wrapping if needed
- a correction of any tilt that the calculated image may have using a 2D surface that can be linear or parabolic, and options to derive this surface from images with two phase peaks
- a removal of specific lines/columns that the user specifies
- a correction of possible fluctuations on images by filtering their period
- an option to register the shift (i.e. correct it) between odd and even lines, for bidirectional stage-scanning
- an access to imaginary and real parts of the $\chi^{(2)}$ via the amplitude and phase
- the 3-steps algorithm to retrieve the exact phase-shifts, along with the phase, with vibrations-removal and tilt-correction as optional choices
- an option for batch treatment (large amount) of the images, with a customizable possibility to save some measurements.

Precision on the center of the histograms

It is common in statistics to consider that $x - \bar{x} = \frac{stddev}{\sqrt{N}}$ where stddev is the standard deviation, $x - \bar{x}$ is the error on the mean of a Gaussian distribution, and N is the size of the sample [100], [240]. When looking at cases where different noises are presents (background, shot-noise ...), Thompson [218] gives an expression for pixelated detectors. Before that, Bobroff [16] had studied the different cases of a Gaussian noise, Poison noise and background-limited detection: the SNR is an important parameter for the precision.

Appendix C

Polarization-resolved SHG and other multimodal techniques

C.1 Other existing techniques

To perform polarization SHG, other techniques can be used. A famous one is the Polarization-In-Polarization-Out (PIPO) that not only controls the polarization of the excitation light, but also analyzes the output SHG polarization [76]. This technique is less reliable than the P-SHG when working in strong focusing regime, or if the tissue is thick ([216],chap5), and on the whole more complicated to perform. Its advantage is the ability to directly calculate the chiral components and their out-of-plane polarity as in CD-SHG, in addition to the parameters calculated in P-SHG (orientation angle and anisotropy) [76].

Reference [55] goes even further by using unpolarized excitation light to ensure that the depolarization and birefringence effects in the biological sample will be limited. An analysis of the converted SHG is then used to measure the different parameters of orientation. A recent method should lastly be mentioned: a phasor approach to directly (without FFT) measure the fibrils orientation and anisotropy, and to order pixels by clusters of similar micro-structural features [166].

C.2 Comparison to other techniques of orientation mapper

3D Fourier transform SHG has emerged as a way to map the orientation directly from the intensity images, using the spatial patterns. It especially allows to classify isotropic and anisotropic regions inside a tissue [3]. We can argue that it is however highly dependent on the interferences from the SHG patterns, that sometimes hide the true structure of the material being imaged (see chap. 6). A MatLab software called CurveAlign [22] has been developed after FT SHG. It proves quite powerful when the filaments in SHG are very distinct, or when the interference patterns do not hide interesting features of the physical structure. There is also a general-purpose Fiji-ImageJ plugin called OrientationJ [183] [56] that could serve in the same circumstances. These libraries would however be of little use above a certain level of complexity, as e.g. in meniscus (chap. 4).

C.3 Polarization control

C.3.1 Generalities

The polarization may be shifted by the scanning system, as the incident angles on the mirror and following optics differ from 45°. The space between the scan lens and the tube lens is well-suited to insert some optical components, as the beam change will be made in the Fourier plane. There are three main ways to ensure a correct polarization at focus: In configuration (1) (see C.1), the polarization is

Key elements	Config. for linear polar.	Config. for circ. polar.	Power loss (linear polar.)	Purity of polar.
Polarizer (linear)	Sample rotation	$\lambda/4$ after polarizer	Few %*	10^5:1
Polarizer + $\lambda/4$	Rotatable polarizer	NO rotatable polarizer	67%	10^5:1
$\lambda/4 + \lambda/2$	rotate both	rotate both	Few %	100:1

Table C.1: Comparison of polarization schemes, and their performances. Note: all polarizers are linear. *: If the polarization can be rotated (rotated mount for the polarizer or an additional half-wave plate (HWP) before it)

filtered by a linear polarizer. A quarter-wave plate (QWP, $\lambda/4$) can be placed after to create a good circular polarization. It has to be on a rotation mount to be rotated 45° if a linear polarization is wanted (or removed). In that case, the effective linear polarization is changed by rotating the sample holder around its axis, which is rather difficult to perform in practice, and unsuitable for some samples.
In a 2nd configuration, a first polarizer and a QWP can create a perfect circular polarization. Then, another polarizer (on a rotating mount) can make the polarization linear, but at the cost of a 50% power loss. The switch between linear and circular polarization implies an insertion/removal of the polarizer.
In a 3rd configuration, a quarter wave-plate is used so that the input ellipticity is corrected [35]. The latter can be rotated to make the polarization circular, or linear. An HWP then allows to rotate the linear polarization, or to change between right-handed or left-handed circular polarization.

The circular polarization can be controlled with giant vesicles in membrane [35] to have a circularity close to 100%. This is also true for linear polarizations: the SHG anisotropy of tail tendon can be controlled within an optical clearing medium: the anisotropy is supposed to be close to unity [35].
Note that in cases where a dichroic (usually used to access to reflected light) has to be placed *after* the wave-plates, the polarization can still be corrected by creating a slightly elliptical polarization that will be transformed in a linear polarization by the coating of the dichroic mirror [40]. This correction must however be changed if the direction of the linear polarization is changed.

C.3.2 Outside a commercial microscope

The methods we have presented assumed that the same ellipticity is kept if the direction of polarization is rotated (a minimum ellipticity in the case of linear polarization). However, commercial microscopes - and in general every set-up that has different optical components - will affect the polarization in uncontrolled ways: polarization change by reflection on mirrors, and the well-known change due to dichroic mirrors. An option would be to put the retardation plates just before the objective [84], i.e. after all other optical components, however, it is usually impossible in commercial microscopes. It can also cause vibrations on the sample position, leading to artifacts [189]. Also, if the laser is scanned across the sample, the

beam might not pass through the waveplates with the same angle for every image's point. On the other hand, if the retardation plates are placed before the microscope, the polarization might be distorted by the scanning system (the reflections on the scanning mirrors are at different angles during the scan).

There is thus a real need for a relatively fast calibration of the polarization: a routine written in MatLab was proposed by [178]. I modified their version to suit our needs [157], in particular implementing other instruments to control the rotation of the waveplate and the power-meter (see Fig. C.1). Figure

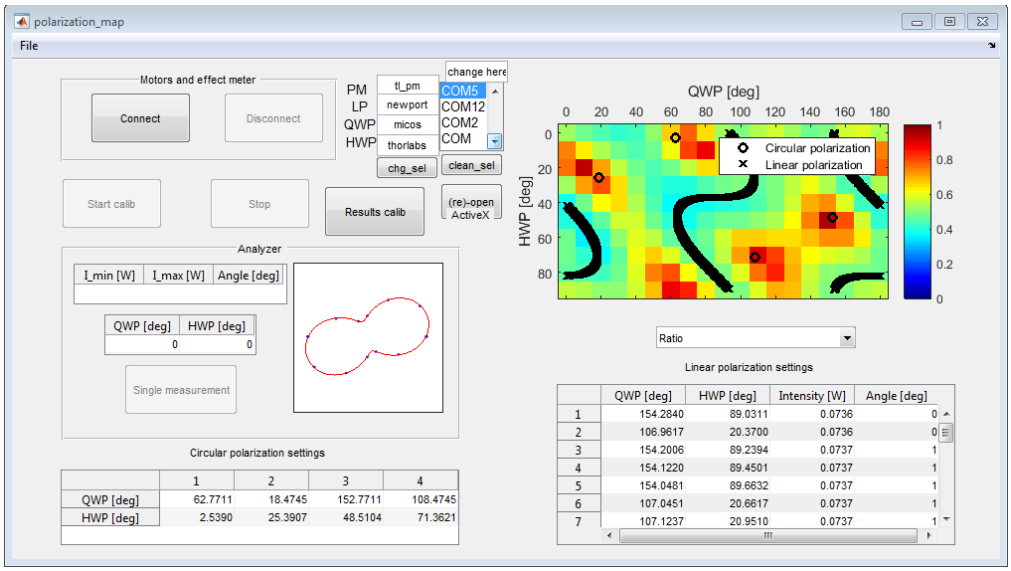

Figure C.1: The MatLab GUI for the calibration of the polarization.

C.2 shows the polarization pattern obtained by rotating the HWP in the range 0:10:90°at each position of the QWP in the range 0:10:180°, in the configuration of the digital galvos (no dichroic). Each pattern is obtained by rotating an analyzer before the power-meter in the range 0:30:180°. Finally, the ellipticity can be plotted (see Fig. C.3), and the linear polarization path can be represented to obtain maps that are similar to those found in the original publication [178]. On Fig. C.3, we can see that the linear polarizations (8-shape patterns) are not obtained at a constant angle of the QWP (which would be a vertical line), which means that just rotating the polarization direction is not sufficient: the ellipticity must be also tuned to obtain perfect linear polarization states. We can draw a path (in black on the figure) that follows these sets of angles where the polarization is linear, and use it for imaging in p-SHG. Of course, adding any other optical element will imply to do another calibration.

But to ensure the smallest ellipticity is not sufficient to have a linear polarization change from 0 to 180°. The path must also follow an increasing polarization direction angle (see Fig. C.4) left, A). Many paths on this map could provide the good polarization angles, but only one also matches the second map, to have the smallest ellipticity (B, right). Figure C.4,B also shows that measuring the polarizations profiles in a limited range for the QWP is sufficient to retrieve all the polarizations (linear and circular). Indeed, the result is the same as the full map presented on Fig. C.3 right.

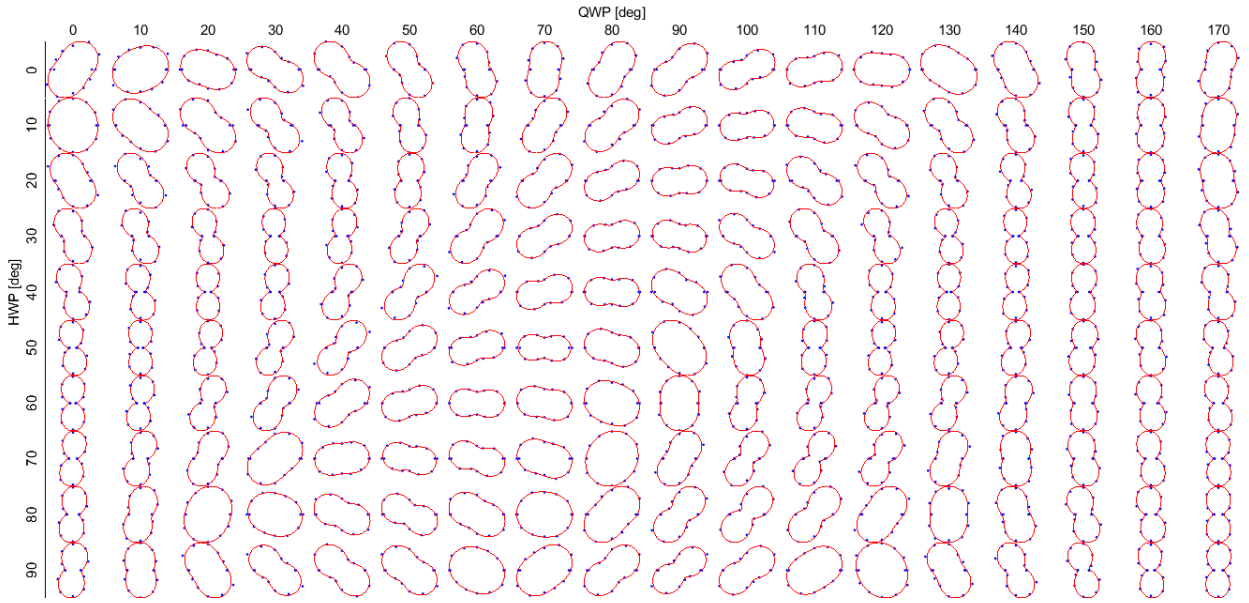

Figure C.2: Polarization characterization of our microscope with the digital galvos (no dichroic) configuration, in function of the angle of the half-wave plate (HWP) and the quarter-wave plate (QWP). Linear polarizations correspond to an 8-shape pattern, while circular polarizations are perfect circles (any shape in-between being elliptical polarizations).

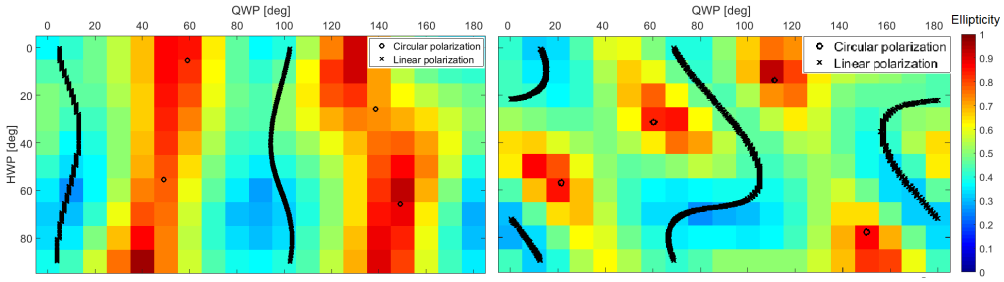

Figure C.3: Ellipticity map, as a function of both retardation plate angle (HWP and QWP). (Right) For the static path of the microscope (no scanning mirrors), with only one injection mirror. (Left) The same case, but with the dichroic splitter inserted after the injection. A clear difference of ellipticity can be seen if the dichroic mirror is used or not.

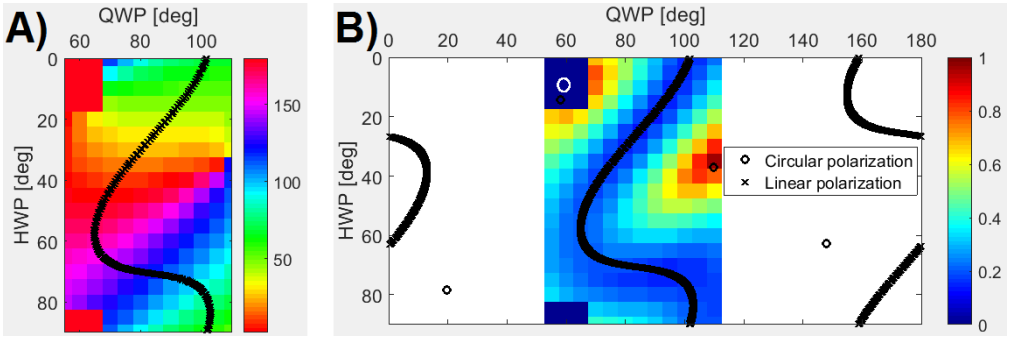

Figure C.4: A) Map of the polarization direction angles function of the QWP and HWP angles. B) Map of the ellipticity. Direct (stage) path with the dichroic filter.

C.4 CD-SHG

C.4.1 Circular difference

The circular difference exists in linear optics: it is the difference in optical signal between the illumination with a left-handed circular polarization (LHCP), and with a right-handed circular polarization (RHCP) [198]. This difference in SHG is even more enhanced by several orders of magnitude [198], and is hence a sensitive probe of chirality, as most of the material presenting an optical activity are chiral (see Fig. 2.1, right).

In SHG, the circular difference can be written as [153]:

$$\text{diff}_{SHG}^{CD} = 2\frac{I_{LHCP}^{2\omega} - I_{RHCP}^{2\omega}}{I_{LHCP}^{2\omega} + I_{RHCP}^{2\omega}} \tag{C.1}$$

This value is by definition in the interval [-2, 2].

C.4.2 CD in collagen

Collagen is a triple helix that will modify an input circular polarization if the helix is in the direction of the propagation of the light ([216], chap5). This molecule is indeed chiral, but more precisely homochiral, meaning only one handedness of the triple helix exists. The circular difference is therefore expected to change only with the position of the helix: it should be null if the helix is in the polarization plane, and have a positive (resp. negative) sign if the helix direction makes a positive (resp. negative) angle with the plane of polarization ([216], chap5). This is verified for the ideal case of the $LiIO_3$ crystal also having a C_∞ symmetry, but not for collagen fibrils due to the non-negligible contribution of magnetic dipoles to the optical activity! [190]. However, $|CD - SHG|$ values can still indicate if the fibrils are rather in-plane (small value) or out-of-plane (high value).

Non-linear tensor

For collagen, the non-linear tensor can be written as different terms:

$$\begin{aligned}
&\chi_{XXX}^{(2)} \\
&\chi_{XYY}^{(2)} = \chi_{XZZ}^{(2)} \\
&\chi_{YXY}^{(2)} = \chi_{ZXZ}^{(2)} = \chi_{YYX}^{(2)} = \chi_{ZZX}^{(2)} \\
&\chi_{YZX}^{(2)} = \chi_{YXZ}^{(2)} = -\chi_{ZYX}^{(2)} = -\chi_{ZXY}^{(2)}
\end{aligned} \tag{C.2}$$

The last ones in red are the chiral ones: an inversion of the indices X, Y or Z cannot give the same tensor element, contrary to the other terms. The SHG intensity writes - if all the tensor components are

in phase - as:

$$I_{2\omega} = \frac{(I_\omega)^2}{4}\cos^2\psi \left[\left|\left(\chi^{(2)}_{XXX} - \chi^{(2)}_{XYY}\right)\cos^2\psi + 2\chi^{(2)}_{YXY}\sin^2\psi\right|^2 + 4\left|\chi^{(2)}_{YXY}\right|^2 + 8\left|\chi^{(2)}_{YXZ}\right|^2\sin^2\psi\right] \tag{C.3}$$

This is valid for any circular polarization (RHCP or LHCP), see [216], chap5. We directly see that if the collagen helix is in the plane of polarization (i.e. $\psi = 0$), this expression simplifies, with the chiral terms being null. Yet there will be a CD contrast if the chiral components are not in phase with respect to the other (achiral) ones. This implies that their imaginary part is not null [75], which is linked to magnetic or quadrupole-dipole interactions.

The effect of the ellipticity

Figure C.5 shows the effect of an incorrect ellipticity of the circular polarization used to perform the CD measurement, on a horse meniscus. We see (a, left) that an ellipticity as good as 0.9 is not sufficient, as there are too many pixels with a + sign, whereas a correct ellipticity of 0.98 (b, right) reveals the correct map, with pixels more symmetrical *w.r.t.* 0. The bad calibration for the CD even hide some details of

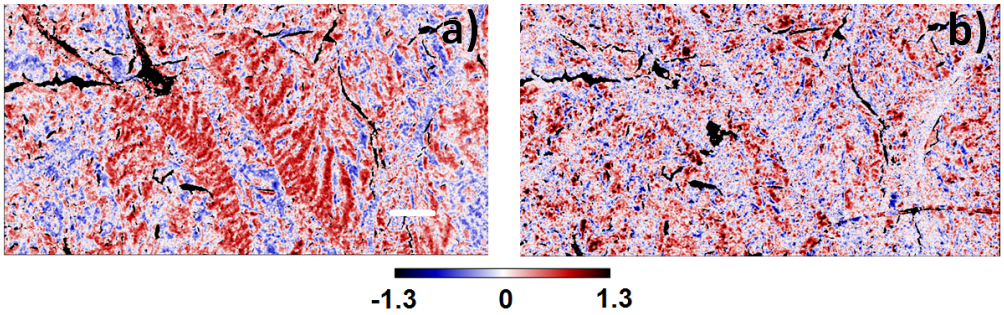

Figure C.5: Meniscus images in CD-SHG, central part (adult horse). a) With a circular polarization having a 0.9 ellipticity. b) With an ellipticity of 0.98. The image with a too low ellipticity shows too many red values (CD with + sign), while the one with a correct ellipticity shows the good map, more centered on the white color (values around 0). Scale-bar = 200μm.

the tissue like the white stripes corresponding to the tie fibers. In conclusion, an ellipticity close to 0.99 is required to do a proper CD-SHG measurement.

C.4.3 Other contributions to the circular difference

The chiral components in collagen is known to have little contribution to the signal if the structure is orthogonal to the propagation of the excitation beam [56]. Also, the circular difference can reveal a contribution due to the anisotropy of the sample [198, 199], which gives rise to a CD signal even if the sample is achiral (see [118] for an example in LiNbO3). The magnetic or quadrupolar contributions could also play a role in the CD signal [153, 128].

C.5 Mosaic end batch-treatment for p-SHG and CD-SHG

The GUI for mosaic reconstruction (used in galvos scanning of large areas), and P-SHG+CD-SHG batch treatment, is shown in Fig. C.6, of which we list here the main features. (1): normalization of the frame with a parabola fit (if needed) and calibration loading.
2: parameters of the mosaic (number of steps...).
3: Mode: p-SHG or forward and backward or both.
4: result (forward image), 5: backward image, hidden by the window for contrast adjustment.

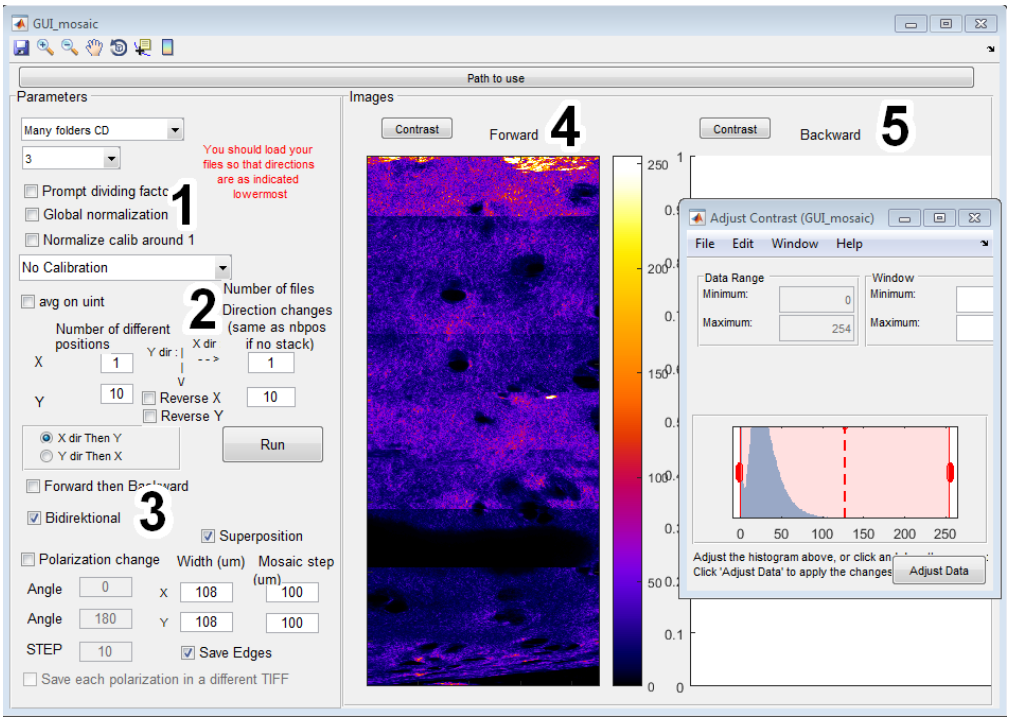

Figure C.6: GUI (MatLab) for mosaic reconstruction for mosaic and p-SHG+CD-SHG batch treatment.